Copyright
by
Daniel Adam Steck
2001

The Dissertation Committee of Daniel Adam Steck certifies that this
is the approved version of the following dissertation:

QUANTUM CHAOS, TRANSPORT, AND DECOHERENCE IN ATOM OPTICS

Committee:

Mark G. Raizen, Supervisor

Rafael de la Llave

Daniel J. Heinzen

Philip J. Morrison

Qian Niu

QUANTUM CHAOS, TRANSPORT, AND DECOHERENCE IN ATOM OPTICS

by

DANIEL ADAM STECK, B.S.

DISSERTATION

Presented to the Faculty of the Graduate School of
The University of Texas at Austin
in Partial Fulfillment
of the Requirements
for the Degree of

DOCTOR OF PHILOSOPHY

THE UNIVERSITY OF TEXAS AT AUSTIN
December 2001

Acknowledgements

Experimental research is often a collaborative endeavor, and the work presented in this dissertation is certainly no exception. During the past six years I have had the pleasure of working with a number of bright and enthusiastic people that I would like to mention here.

First of all, I would like to thank my advisor, Mark Raizen. Mark is always brimming with intriguing new ideas, and he has an exceptional sense for interesting physics problems. Mark has provided an exciting and supportive research environment for his students. I have truly enjoyed and greatly benefited from spending the past few years under his guidance.

I have collaborated with Windell Oskay on all of the research in this dissertation. I cannot imagine having done the experiments in this dissertation without Windell's remarkable productivity and superior technical prowess. This is especially true of the chaos-assisted tunneling experiments in Chapter 6, where the two of us managed an enormously complicated experiment and took enough data to literally choke our computer. Windell's rock-solid and extensive LabVIEW code (which featured its own web page so that we could check on the status of the experiment from anywhere in the world) enabled the 12 and 33 day (running 24/7) data marathons that produced all of the CAT results. It was also great to work with someone that shares my ardor for doing things the "right" way, and I have appreciated his attention to detail. I should also note that Windell is responsible for the cool 3D renderings in this dissertation, including the nice surface plots of the data in Chapter 6. It has been a pleasure knowing Windell both in and out of the lab, who has excellent taste in movies, art, italian cuisine, chocolate, and computers.

I worked with Bruce Klappauf from nearly the beginning of my graduate studies to build up the cesium experiment from scratch, and he worked on the early kicked-rotor experiments in Chapter 4. Bruce is not only laid back and very easy to work with, but also good at simply making things work. His insight, creativity, and curiosity made him a great asset to the lab as well as a great guy to hang out with.

Our postdoc Valery Milner also worked on the later kicked-rotor experiments on quantum–classical correspondence in Chapter 4. It seemed that every time he touched the Ti:sapphire laser, he would set a new record for its output power. His deftness in handling the laser was a crucial factor in enabling these experiments. Valery is also an imaginative and intelligent problem solver, and I have enjoyed many physics discussions with him.

I would also like to acknowledge the other students working on the cesium experiment. Alex Mück and Nicole Helbig, two Würzburg students, took on challenging projects to implement a new measurement technique and a high-intensity laser source, while at the same time providing colorful company. The cesium experiment will be in good hands with the next generation of students, Jay Hanssen, Todd Meyrath, and Chuanwei Zhang, whatever the experiment becomes in the future. Special thanks to Jay and Todd for helping to babysit the experiment during the final “datathon.”

I also enjoyed interacting with people over on the sodium side of the lab. Cyrus Bharucha has been a great friend and roommate in addition to being a talented physicist in the laboratory, continually posing interesting puzzles and questions, always with a cheerful demeanor. I have profited immensely from many memorable and long discussions with Kirk Madison, whose peculiar sense of humor and fervor for physics (and many other things) have made him a terrific colleague and friend. Martin Fischer is an exceptionally skilled experimentalist, with a broad knowledge of physics and a singular ability to explain things clearly. His advice, insight, and presence in the lab contributed much to my development as a scientist.

Thanks also go to Pat Morrow, who provided good advice and a lot of great experimental knowledge when I first arrived, as well as help in getting the Ti:sapphire laser to flash. Postdoc Steve Wilkinson brought a great deal of experience to the lab and was also a great source of knowledge when I was starting out. Many other members of the Raizen Lab made it a great place to be, even though I didn't get to work directly with them: John Robinson, Braulio Gutiérrez-Medina, Artëm Dudarev, Kevin Henderson (whose digital camera I used to take the photographs in this dissertation), Artur Widera, Patrick Bloom, Greg Henry, Arnaud Cursente, Wes Campbell, and Fred the mouse. Thanks also to Adrienne Lipoma and Julie Horn for keeping the lab running smoothly.

I have learned much during my graduate studies, due in no small part to the presence of many top-notch researchers at UT. In particular, I would like to mention Bala Sundaram, who is a truly brilliant guy and has been a great source of knowledge about classical and quantum chaos; Matt Choptuik, whose skill and willingness to help were invaluable in enabling my high-performance computing efforts; and Phil Morrison, from whom I learned a tremendous amount about classical Hamiltonian dynamics.

The Physics Department staff at UT was also of inestimable help. Les Deavers and later Allan Schroeder ran a group of top-notch machinists, whose services were indispensable during the construction phases of the experiment. I would also like to thank the administrative staff, especially Norma Kotz, Glenn Suchan, Dorothy Walker, and Olga Vorloou, for all their assistance.

Of course, I could not have come this far without a good start in physics, and the University of Dayton was an ideal place to be an undergraduate. I am grateful to have had such a great group of faculty and fellow students to nurture my yearning to study physics. Special thanks to Perry Yaney, who gave me my first taste of research, and who was a great mentor in so many ways. I would also like to thank Leno Pedrotti, from whom I garnered a love of things quantum; John Erdei, who piqued my interest in chaotic systems (and from whom I learned of the demonstration in Fig. 1.1); Bob Brecha, who alerted me to the fact that there were really great things going on in Mark's lab here at UT; and Mike O'Hare, for running a great department. The experience and knowledge gained in my undergraduate research under Brian Kennedy was also of much value in my later research. Thanks also to Alba Hurlbut, my high school physics teacher, for encouraging me to go into physics.

I would like to thank Windell Oskay, Patrick Bloom, Kirk Madison, Rafael de la Llave, Phil Morrison, Daniel Heinzen, Martin Fischer, Jay Hanssen, and Todd Meyrath for valuable comments and corrections. This dissertation has also benefited from discussions with Simon Gardiner, Salman Habib, Kurt Jacobs, Amaury Mouchet, and Vitali Averbukh.

I would also like to acknowledge financial support from a National Science Foundation Graduate Research Fellowship during the first three years and a Fannie and John Hertz Foundation Fellowship during the final three years of my graduate studies. The research effort as a whole was supported by the National Science Foundation, the Robert A. Welch Foundation, the Sid W. Richardson Foundation, and the U.S.–Israeli Binational Science Foundation. I performed some of the computations in this dissertation on supercomputers at the Texas Advanced Computing Center.

Finally, I would like to thank my parents, Raymond and Shitsuko Steck, for encouraging me to follow my interests and fostering in me a curiosity for how things work.

D. A. S.
Austin, Texas
October, 2001

QUANTUM CHAOS, TRANSPORT, AND DECOHERENCE IN ATOM OPTICS

Publication No. ____________________

Daniel Adam Steck, Ph.D.
The University of Texas at Austin, 2001

Supervisor: Mark G. Raizen

This dissertation details an experimental investigation of the center-of-mass motion of cesium atoms in a time-dependent lattice of light. The research described here proceeds along two general lines. The first group of experiments considers a realization of the quantum kicked rotor, where the optical lattice is applied in a series of short, periodic pulses. In the regime where the classical description of this system is strongly chaotic, the quantum and classical dynamics differ remarkably due to dynamical localization, which is a manifestation of the quantum suppression of classical chaos. Because this quantum localization is a coherent effect, it should be vulnerable to noise or coupling to the environment, providing a mechanism for restoring classical behavior at the macroscopic level. The experimental results confirm that dynamical localization can be destroyed by adding noise and dissipation in a controlled way, and furthermore they show that quantitative agreement between the experiment and a classical model can be reached with a sufficient level of applied noise.

The second line of research considers the weakly chaotic regime, where stable and chaotic regions coexist in phase space. The optical lattice is modulated sinusoidally in these experiments to realize the amplitude-modulated pendulum. Careful preparation of the initial atomic state, including stimulated Raman velocity selection, is necessary to resolve the phase-space features. Coherent tunneling oscillations are observed between two symmetry-related islands of stability in phase space. Because the classical transport between the islands is forbidden by the system dynamics, as opposed to a potential barrier, the tunneling in this experiment is an example of dynamical tunneling. Additionally, the experimental data indicate through multiple signatures that the tunneling is enhanced by the presence of the chaotic region in phase space, an effect known as chaos-assisted tunneling.

Table of Contents

Acknowledgements **iv**

Abstract **viii**

List of Tables **xv**

List of Figures **xvi**

Chapter 1. Introduction **1**

1.1 Classical Chaos 1
  1.1.1 Phase Space 6
  1.1.2 Integrability and Chaos 11
1.2 Quantum Chaos 14
  1.2.1 Quantum Chaology 16
  1.2.2 Chaos in Quantum Mechanics 18
  1.2.3 Experiments in Quantum Chaos 20
  1.2.4 On the "Usefulness" of Quantum Chaos 21
1.3 Decoherence 22
  1.3.1 Suppression of Quantum Superposition 24
  1.3.2 Classical Chaotic Evolution 28
  1.3.3 Experiments on Decoherence 32
1.4 Atom Optics 33
  1.4.1 The Dipole Force and Optical Lattices 34
  1.4.2 Atom Optics and Quantum Chaos 36

Chapter 2. Atomic Motion in an Optical Standing Wave **39**

2.1 Overview 39
2.2 Atom-Field Interaction 40
  2.2.1 Digression: Unitary Transformations and Field Operators 42

2.3 Schrödinger Equation 44
2.4 Adiabatic Approximation 46
  2.4.1 Master Equation Approach 47
2.5 Complications 50
  2.5.1 Spontaneous Emission 50
  2.5.2 Stochastic Dipole Force 51
  2.5.3 Nonlinearities of the Potential 51
  2.5.4 Velocity Dependence 53
  2.5.5 Multilevel Structure of Cesium 53
  2.5.6 Collisions 54
  2.5.7 Experimental Values 55
2.6 Generalization to Two Nonidentical Traveling Waves 56
2.7 Quantum Dynamics in a Stationary Standing Wave 58
  2.7.1 Bragg Scattering 59
  2.7.2 Band Structure 63
  2.7.3 Boundary Conditions 66

Chapter 3. Experimental Apparatus I **67**

3.1 Overview 67
3.2 DBR Laser 68
  3.2.1 Construction and Operation 68
  3.2.2 Saturated Absorption Spectroscopy 70
3.3 Grating-Stabilized Diode Laser 75
  3.3.1 Construction and Operation 75
  3.3.2 Frequency Control 79
3.4 Ti:sapphire Laser 81
  3.4.1 Laser Design and Construction 82
  3.4.2 Laser Operation and Control 83
  3.4.3 Intensity Calibration 88
3.5 Vacuum System 89
  3.5.1 Magnetic Field Control 92
3.6 Imaging System 94
3.7 Measurement Technique 95
3.8 Control Electronics 99

Chapter 4. Localization and Decoherence in the Kicked Rotor 101
4.1 Overview 101
4.2 Rescaling 102
4.3 Standard Map 103
4.4 Classical Transport 105
  4.4.1 Diffusion and Correlations 106
  4.4.2 Accelerator Modes 108
  4.4.3 External Noise 111
  4.4.4 Finite-Pulse Effects 114
4.5 Quantum Transport 117
  4.5.1 Quantum Mapping 117
  4.5.2 Dynamical Localization 119
  4.5.3 Quantum Resonances 122
  4.5.4 Delocalization 125
  4.5.5 Quantum Correlations 128
4.6 Quantitative Study of Delocalization 132
  4.6.1 Classical Model of the Experiment 133
  4.6.2 Data and Results 140
    4.6.2.1 Detailed Study: Destruction of Exponential Localization . . 143
    4.6.2.2 Detailed Study: Regime of Classical Anomalous Diffusion . . 147
4.7 Comparison with a Universal Theory of Quantum Transport 151
4.8 Calculation of the Correlations 156
  4.8.1 Classical Correlations 156
  4.8.2 Quantum Correlations 159

Chapter 5. Experimental Apparatus II 162
5.1 Overview 162
5.2 Cooling in a Three-Dimensional Optical Lattice 162
5.3 Stimulated Raman Velocity Selection 168
  5.3.1 Stimulated Raman Transitions: General Theory 168
  5.3.2 Pulse-Shape Considerations 174
  5.3.3 Implementation of Stimulated Raman Transitions 178

5.3.4 Optical Pushing and Hyperfine State Detection 183
5.3.5 Hyperfine Magnetic Sublevel Optical Pumping 185
5.3.6 Implementation of Stimulated Raman Velocity Selection 188
5.3.7 Raman Cooling 189
5.4 Interaction-Potential Phase Control 190
5.5 State-Preparation Sequence 193
5.6 Calibration of the Optical Potential 196
5.6.1 Anharmonicity 197
5.6.2 Quantum Effective Potentials 198
5.6.2.1 Wigner-Function Derivation 200
5.6.3 Calibration by Simulation 203

Chapter 6. Chaos-Assisted Tunneling 204
6.1 Overview 204
6.2 Barrier Tunneling 205
6.3 Dynamical Tunneling 208
6.3.1 Tunneling in Atom Optics 211
6.3.2 Broken Symmetry 216
6.3.3 Tunneling Dependence on Wave-Packet Location 221
6.4 Chaos-Assisted Tunneling 223
6.4.1 Singlet-Doublet Crossings 226
6.4.2 Comparison with Integrable Tunneling 228
6.4.3 Tunneling Dependence on Parameter Variations 233
6.4.4 Floquet Spectra 239
6.4.5 High Temporal Resolution Measurements 243
6.4.6 Transport in the Strongly Coupled Regime 248
6.5 Noise Effects on Tunneling 250
6.5.1 Chebyshev Filter Response 254

Appendices 257

Appendix A. Cesium D Line Data **258**
A.1 Overview 258
A.2 Cesium Physical and Optical Properties 258
A.3 Hyperfine Structure 260
  A.3.1 Energy Level Splittings 260
  A.3.2 Interaction with Static External Fields 262
    A.3.2.1 Magnetic Fields 262
    A.3.2.2 Electric Fields 265
  A.3.3 Reduction of the Dipole Operator 266
A.4 Resonance Fluorescence 267
  A.4.1 Symmetries of the Dipole Operator 267
  A.4.2 Resonance Fluorescence in a Two-Level Atom 269
  A.4.3 Optical Pumping 270
    A.4.3.1 Circularly ($\sigma^\pm$) Polarized Light 272
    A.4.3.2 Linearly (π) Polarized Light 273
    A.4.3.3 One-Dimensional $\sigma^+ - \sigma^-$ Optical Molasses 273
    A.4.3.4 Three-Dimensional Optical Molasses 274
A.5 Data Tables 276

Appendix B. Phase Space Gallery I: Standard Map **288**

Appendix C. Phase Space Gallery II: Amplitude-Modulated Pendulum **297**

Bibliography **310**

Vita **341**

List of Tables

2.1 Numerical estimates for deviations from an ideal optical lattice 55

A.1 Fundamental Physical Constants 276
A.2 Cesium Physical Properties 276
A.3 Cesium D_2 Transition Optical Properties 277
A.4 Cesium D_1 Transition Optical Properties 277
A.5 Cesium D Transition Hyperfine Structure Constants 277
A.6 Cesium D Transition Magnetic/Electric Field Interaction Parameters . . 278
A.7 Cesium Dipole Matrix Elements and Saturation Intensities 278
A.8 Cesium Relative Hyperfine Transition Strength Factors $S_{FF'}$ 278
A.9 Cesium D_2 Transition Dipole Matrix Elements 279
A.10 Cesium D_2 Transition Dipole Matrix Elements 279
A.11 Cesium D_2 Transition Dipole Matrix Elements 279
A.12 Cesium D_2 Transition Dipole Matrix Elements 280
A.13 Cesium D_2 Transition Dipole Matrix Elements 280
A.14 Cesium D_2 Transition Dipole Matrix Elements 280
A.15 Cesium D_1 Transition Dipole Matrix Elements 281
A.16 Cesium D_1 Transition Dipole Matrix Elements 281
A.17 Cesium D_1 Transition Dipole Matrix Elements 281
A.18 Cesium D_1 Transition Dipole Matrix Elements 282
A.19 Cesium D_1 Transition Dipole Matrix Elements 282
A.20 Cesium D_1 Transition Dipole Matrix Elements 282

List of Figures

1.1 Numerical instability in the standard map 5
1.2 Pendulum phase space 8
1.3 Weakly driven pendulum phase space 9
1.4 Strongly driven pendulum phase space 10
1.5 Numerical time-reversal of the classical and quantum kicked rotor 17

2.1 Level diagram for second-order Bragg scattering 60
2.2 Band structure of an optical standing wave potential 63
2.3 Dependence of allowed energies on the quasimomentum 64

3.1 DBR laser collimating lens mount assembly 71
3.2 Photograph of DBR laser system 72
3.3 Optical table layout 73
3.4 DBR laser saturated-absorption spectrum 74
3.5 Grating-stabilized laser diode assembly 77
3.6 Photograph of the grating-stabilized laser system 78
3.7 Repump laser saturated absorption spectrum (photodiode output) 80
3.8 Repump laser saturated absorption spectrum (lock-in output) 81
3.9 Ti:sapphire laser schematic layout 84
3.10 Ti:sapphire laser photograph (overall view) 85
3.11 Ti:sapphire laser photograph (cavity detail) 86
3.12 Vacuum chamber photograph (overall) 90
3.13 Vacuum chamber photograph (main section) 91
3.14 Schematic of experimental sequence 96
3.15 Measured momentum distribution of MOT atoms 98

4.1 Diffusion rate vs. K in the standard map 108
4.2 Standard-map trajectories with and without Lévy flights 110
4.3 Diffusion rate plot for various amplitude noise levels 114

4.4 Phase space comparison between δ-kicks and square pulses 115
4.5 Experimental momentum evolution with dynamical localization 121
4.6 Experimental measurement of dynamical localization (log plot) 122
4.7 Quantum resonances in experiment and simulation 124
4.8 Enhanced energy growth due to delocalization by optical molasses 126
4.9 Optical molasses effects on quantum kicked rotor evolution 127
4.10 Experimental verification of the Shepelyansky scaling for K_q 130
4.11 Influence of accelerator modes on momentum distributions 131
4.12 Systematic effects in the experiment on measured energies 134
4.13 Experimental laser pulse for kicked-rotor realization 135
4.14 Amplitude noise effects on energy vs. K curves 141
4.15 Experimental and classical ensemble energies with noise, $K = 11.2$ . . . 144
4.16 Experimental and classical ensemble energy evolution, $K = 11.2$ 145
4.17 Experimental and classical momentum distributions, $K = 11.2$ 146
4.18 Experimental and classical ensemble energies with noise, $K = 8.4$ 148
4.19 Experimental and classical ensemble energy evolution, $K = 8.4$ 149
4.20 Experimental and classical momentum distributions, $K = 8.4$ 150
4.21 Quantum diffusion theory fit to a localized case 152
4.22 Quantum diffusion theory fit to a noise-driven case 153
4.23 Quantum diffusion theory fit to an anomalous transport case 154

5.1 Diagram of three-dimensional lattice geometry 163
5.2 Stimulated Raman transition energy levels 169
5.3 Spectral excitation profile due to a square Raman pulse 176
5.4 Time evolution of Raman-excited population 177
5.5 Comparison of square and Blackman pulse excitation profiles 178
5.6 Stimulated Raman implementation optical layout 179
5.7 Energy-level scheme for reversible stimulated Raman tagging 180
5.8 Optical layout of pumping and pushing beams for Raman tagging 183
5.9 Experimental Raman Rabi oscillations in copropagating mode 185
5.10 Experimental Raman Rabi oscillations in counterpropagating mode . . . 186
5.11 Experimental Raman-transition profiles in copropagating mode 187

5.12 Photograph of optical lattice phase-control setup 192
5.13 Electro-optic modulator response to a sudden phase change 193
5.14 Schematic picture of state-preparation sequence 194
5.15 Comparison of classical and quantum pendulum motion 199
5.16 Experimentally measured pendulum oscillation periods 202

6.1 Tunneling doublet in the quartic double well potential 205
6.2 Two-level avoided crossing 207
6.3 Phase space for the quartic double-well potential 209
6.4 Experimental initial condition in phase space 214
6.5 Observation of coherent tunneling oscillations 215
6.6 Detail of momentum distributions showing tunneling oscillations 215
6.7 Influence of Raman-pulse duration on tunneling 217
6.8 Tunneling measurement without Raman velocity selection 218
6.9 Influence of Raman-pulse detuning on tunneling 219
6.10 Simulation of Raman tag width effects on tunneling 220
6.11 Influence of spatial displacement of the initial condition on tunneling . . 222
6.12 Displaced initial conditions for various time delays 223
6.13 Three-level avoided crossing 227
6.14 Corresponding pendulum phase space 229
6.15 Comparison of modulated-pendulum tunneling to Bragg scattering 230
6.16 Modulated-pendulum tunneling for $\bar{k} = 1.04$ 231
6.17 Tunneling variation vs. α, for $\bar{k} = 2.08$ 234
6.18 Tunneling rate vs. α, for $\bar{k} = 2.08$ 235
6.19 Tunneling for $\alpha = 8.0$, for $\bar{k} = 2.08$ 236
6.20 Tunneling for $\alpha = 9.7$, for $\bar{k} = 2.08$ 236
6.21 Tunneling variation vs. α, for $\bar{k} = 1.04$ 237
6.22 Tunneling rate vs. α, for $\bar{k} = 1.04$ 238
6.23 Calculated Floquet spectrum for $\bar{k} = 2.077$ 240
6.24 Calculated Floquet spectrum for $\bar{k} = 1.039$ 241
6.25 Fine time step evolution, $\bar{k} = 2.08$, $\alpha = 7.7$ 243
6.26 Fine time step evolution, $\bar{k} = 2.08$, $\alpha = 11.2$ 244

6.27 Fine time step evolution, $\bar{k} = 1.04$, $\alpha = 10.5$ 245
6.28 Evolution of classical phase space at different sampling phases 246
6.29 Strongly coupled transport, $\bar{k} = 2.08$, $\alpha = 17.0$ 249
6.30 Strongly coupled transport, $\bar{k} = 2.08$, $\alpha = 18.9$ 250
6.31 Illustration of amplitude noise applied to the optical lattice intensity . . 251
6.32 Effects of amplitude noise on tunneling, $\bar{k} = 2.08$ 252
6.33 Effects of amplitude noise on tunneling, $\bar{k} = 1.04$ 253
6.34 Chebyshev filter frequency response 254

A.1 Dependence of cesium vapor pressure on temperature 283
A.2 Cesium D_2 transition hyperfine structure 284
A.3 Cesium D_1 transition hyperfine structure 285
A.4 Cesium $6^2S_{1/2}$ level hyperfine structure in an external magnetic field . . 286
A.5 Cesium $6^2P_{1/2}$ level hyperfine structure in an external magnetic field . . 286
A.6 Cesium $6^2P_{3/2}$ level hyperfine structure in an external magnetic field . . 287
A.7 Cesium $6^2P_{3/2}$ level hyperfine structure in an external electric field . . . 287

Chapter 1

Introduction

1.1 Classical Chaos

The study of chaos in dynamical systems originated near the end of the 19th century [1–4]. At the time, Newtonian mechanics gave an impressively accurate description of the motion of the bodies in the solar system, even prompting (somewhat serendipitously) the discovery of Neptune, in order to explain a discrepancy between the predicted and observed trajectories of Uranus. Although the problem of the dynamics of three gravitationally interacting bodies was not (and still is not) analytically solvable in general, much headway was made in the prediction of planetary locations by first considering only the interaction of each planet with the sun, and then taking into account the perturbations due to the interactions of the planets with each other. The apparent clock-like regularity of the solar system and the accuracy with which the planetary motion could be computed prompted the question of the stability of the solar system: would the solar system continue in its usual fashion, with the planets maintaining their regular orbits, or could the motion of the planets change drastically in the future? Showing that the solar system is indeed stable, which amounts to showing that successive corrections (perturbations) to the planetary motion converge, was at the time considered quite important. In fact, it was posed by Weierstrass, after a comment by Dirichlet, as one of the prize questions in a contest, organized by Mittag-Leffler, in honor of King Oscar II of Sweden and Norway. Henri Poincaré submitted a complex and innovative entry that demonstrated the stability in the three-body problem and was named the winning entry. However, after its publication it was pointed out that Poincaré had made a significant error in his proof. Mittag-Leffler's rather drastic response was to recall and destroy every copy of the issue of *Acta Mathematica* in which Poincaré's proof appeared. Poincaré subsequently produced a revised work that instead appeared as the prize-winning entry; however, this revised work contained the opposite conclusion: the stability of the solar system could not be guaranteed. The ideas embodied in this work prompted Poincaré's later famous statement of how minute differences in the initial conditions of a system can lead to wildly different outcomes. This is the key notion of chaotic dynamical systems, which has the consequence that small but inevitable errors in our knowledge of the state of a system necessarily forbid accurate, long-term predictions of the system's evolution. Thus, despite the deterministic nature of chaotic systems, their dynamics are inherently unpredictable, and they appear to be random.

Despite Poincaré's remarkable achievement, the study of chaos did not really take off for several decades, although there were several important results during this period by George Birkhoff and Carl Ludwig Siegel, among others. In the 1950's and 60's the problem of stability in the three-body problem was revisited, and an important result was obtained in stages by Andrei N. Kolmogorov, Vladimir I. Arnol'd, and Jürgen Moser, in the celebrated KAM theorem [1, 2, 5]. This result restored the stability of the solar system in the sense that it showed that certain configurations are stable while others were unstable (at least in restricted versions of the solar system). Furthermore, if the aforementioned perturbations are small, then most of the possible configurations are stable. So, although the stability of the solar system seems to be assured, this whole series of events resulted in the important recognition of the possibility of chaos.

The study of chaotic systems began in earnest with the advent of computers, which facilitated the study of the inherent complexity of chaotic systems. This line of study began with the work of Edward Lorenz, who found this same sort of instability in numerical "experiments" studying a hydrodynamic system, which served as a very basic model for the atmosphere [6]. Since then, chaos has been found to be ubiquitous both in physics as well as in other disciplines, having found applications in such diverse phenomena as plasma confinement [7], laser dynamics [8], chemical reactions [9], cardiac rhythms [10], and disease epidemiology [11]. Chaos is also important in the study of dynamical systems, as chaos is the rule rather than the exception, despite the traditional textbook view of physics.

The term "chaos" was introduced [12] to refer to this "deterministic randomness" in dynamical systems. However, it is still difficult to provide a definition of chaos that is universally accepted. On the other hand, it is possible to point out some important characteristics of systems that we refer to as being chaotic:

1. As mentioned before, a *dynamical instability* leading to unpredictability is a central characteristic of chaos. Furthermore, this instability should be *exponential* rather than *linear* in time, since in the linear case predictability is possible even in the presence of a slight uncertainty if a sufficiently long history of the system is known. In the exponential (chaotic) case, however, no additional predictive power is gained by knowing the system history beyond the initial condition [13]. These properties can be more formally quantified using the *Lyapunov exponent* and the *Kolmogorov-Sinai entropy* [14, 15].

2. The instability is purely *deterministic* and intrinsic to the dynamics; the chaos is not explained by external noise [13].

3. The instability should be *global* in the sense that chaotic behavior occurs for a range of conditions and is not limited to a set of zero measure in phase space (defined below), as in the unstable configuration of a perfectly inverted pendulum. Also, the chaotic trajectories should be *ergodic*, so that they eventually wander throughout the possible range of chaotic trajectories (although it is possible to find disconnected regions of chaos in weakly perturbed Hamiltonian systems, as we briefly discuss below, and in dissipative systems, the trajectories are only ergodic over the "attracting set").

4. The system should be in some sense *bounded*, to avoid trivial exponential separation of trajectories, as in $x(t) = x_0 \exp(t)$ for different x_0. To keep the trajectories confined as they separate from each other, there must be some notion of "stretching and folding," as exemplified in the Smale horseshoe map [16]. Another related property is that each point on a chaotic trajectory should lie arbitrarily close to a periodic trajectory (i.e., a trajectory that repeats itself in finite time) [17].

5. The physical model of the system should be *simple*. It is surprising that simple systems such as the three-body problem can give rise to such complicated and unpredictable behavior, but complicated behavior is *not* surprising in a system with many degrees of freedom. So, for example, although Brownian motion is unpredictable, a deterministic physical model would include the collisional interactions of a macroscopic number of gas molecules; hence, we would not call this system chaotic. (Note that there are methods for analyzing data to distinguish low-dimensional chaos from such high-dimensional noise [18, 19].)

When we return to the concept of integrability below, we can be more precise about the meaning of chaos, at least in Hamiltonian systems.

As an example of the distinction between determinism and predictability in chaotic systems, consider the *standard map*, which models one of the two classically chaotic systems presented in this dissertation. The standard map is a set of two equations,

$$\begin{aligned} p_{n+1} &= p_n + K \sin x_n \\ x_{n+1} &= x_n + p_{n+1} \quad , \end{aligned} \tag{1.1}$$

where the sole parameter K controls the "degree of chaos" of the map. This mapping is iterated to determine a *trajectory* (x_0, p_0), (x_1, p_1), …, (x_n, p_n). These equations are, of course, deterministic, in that there is no random element involved. In fact, though this map looks quite simple, it gives rise to rich and complicated dynamics. The characteristic lack of predictability in this map is illustrated in Fig. 1.1, where the standard map is iterated with the same initial condition on four different computers. Even though

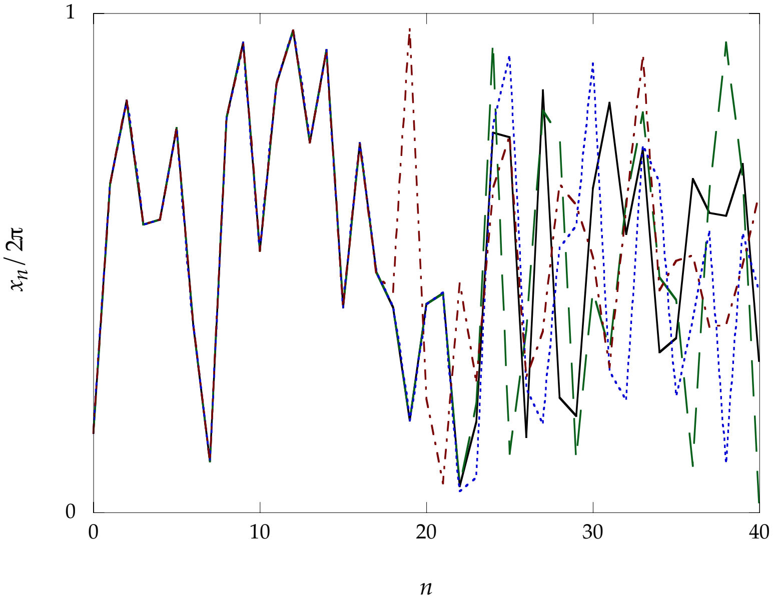

Figure 1.1: Numerical iteration of the standard map, illustrating the inherently unpredictable nature of chaotic systems. The same FORTRAN77 code was executed on four modern computers to iterate the standard map for $K = 10$ and the initial condition $(x_0, p_0) = (1, 1)$. The spatial coordinate x_n (taken modulo 2π) is plotted for the first 40 iterations of the standard map. Although nominally the same (64-bit, or around 15-digit) "double precision" numerical representation was used on the different computers, slight differences in the numerical rounding methods among the processors are rapidly amplified as the iterations progress. Hence, the trajectories are identical only for the first few iterations, and they become completely uncorrelated after about 25 iterations. The processors employed here were a Motorola PowerPC 750 (solid line), an Intel Pentium III (dashed line), a MIPS/SGI R10000 (dotted line), and a Cray SV1 processor (dash-dotted line).

the results should be identical among the four computers, they only agree for around 16 iterations. Beyond this point the trajectories diverge, and prediction clearly becomes meaningless. In principle, it is possible to make meaningful predictions over a larger number of iterations by using greater precision in the computations. However, a *linear* increase in prediction time requires an *exponential* increase in the numerical precision. More importantly, for modeling physical systems, the precision with which the initial state of the system is known nearly always limits the prediction time.

Despite this lack of predictability, chaotic systems can still be meaningfully studied. The unpredictability that we have indicated thus far is for a trajectory evolving from a particular initial state. The numerically generated trajectory, referred to as a *pseudotrajectory*, diverges away from the real trajectory with the same initial condition; however, it is often possible to find another real trajectory with a slightly different initial condition that *shadows* the pseudotrajectory in the sense that it remains close to the pseudotrajectory for long times. This shadowing occurs for arbitrarily long times in a restricted class of systems ("hyperbolic systems," which are comparatively rare), but shadowing occurs also for generic (nonhyperbolic) chaotic systems for long times between "glitches" [20–22]. An important consequence of this effect is that *global* or *statistical* predictions regarding ensembles of trajectories are still meaningful and can be accurately computed, implying a *robustness* or *structural stability* under sufficiently small perturbations [13]. So, the study of chaotic systems involves a shift to asking different kinds of questions, and in this way much progress has been made in uncovering universal structure and behavior in chaotic systems. This notion was recognized early on by Poincaré, who developed a geometric approach to studying dynamical systems that we introduce in the next section.

1.1.1 Phase Space

Now we explore the concept of *phase space*, whose graphical depiction, the *phase portrait*, is a powerful tool for visualizing the behavior of dynamical systems. The phase space of a dynamical system is the space of points that completely specify the state of the system. In a coordinate representation, a dynamical system can be expressed as a set of first-order differential equations:

$$\begin{aligned}\partial_t x_1 &= f_1(x_1, x_2, \ldots, x_n)\\ \partial_t x_2 &= f_2(x_1, x_2, \ldots, x_n)\\ &\vdots\\ \partial_t x_n &= f_n(x_1, x_2, \ldots, x_n)\end{aligned} \tag{1.2}$$

(where $\partial_t \equiv \partial/\partial t$). This dynamical system is *autonomous*, since the f_i do not explicitly depend on time, but an external periodic drive can be accounted for by introducing time as an auxiliary coordinate [14]. Then the phase space for this system is the set of all n-tuples $(x_1, x_2, \ldots, x_n)$. The location in phase space at a particular time together with the model functions f_i then completely specify the state of the system for all values of the time parameter t.

In this work we are interested in *Hamiltonian systems*. These systems are characterized by a Hamiltonian function $H(x_i, p_i, t)$, such that the dynamics in terms of the "canonical coordinates" x_i and p_i are given by Hamilton's equations:

$$\begin{aligned} \partial_t x_i &= \partial_{p_i} H \\ \partial_t p_i &= -\partial_{x_i} H \ . \end{aligned} \tag{1.3}$$

The phase space is then simply the space of the canonical positions x_i and momenta p_i. In the special case where the Hamiltonian is independent of time, the system is said to be *conservative* in that the energy (the particular value of H for a given phase-space point) is a conserved quantity, which follows directly from Eqs. (1.3). For time-dependent Hamiltonian systems, the energy is not conserved, but all Hamiltonian systems are characterized by the more general conservation property that volumes in phase space are preserved under time evolution as a consequence of Liouville's theorem (and as a special case of Poincaré's integral invariants) [5].

The simplest Hamiltonian systems that one can consider are of one dimension (or one *degree of freedom*) and time-independent, where the two-dimensional phase space is spanned by the pair of variables (x, p). The trajectories in this phase space are simply the surfaces of constant energy, because energy is a conserved quantity. We illustrate such a phase space by considering the pendulum, where the Hamiltonian is

$$H(x,p) = \frac{p^2}{2} - \cos x \ . \tag{1.4}$$

The phase portrait for the pendulum is shown in Fig. 1.2. There are several interesting features to note in the phase portrait. One type of motion, known as "libration" (or "oscillation"), appears as a set of elliptical contours, along which the trajectories flow in the clockwise direction. These trajectories correspond to the pendulum motion one observes in the operation of a grandfather clock, and they emanate from a stable *fixed point* at $(x, p) = (0, 0)$, which corresponds to the resting configuration of the pendulum. Another fixed point occurs at $(x, p) = (\pi, 0)$ (which is equivalent to the point $(-\pi, 0)$ because of the spatial periodicity of the Hamiltonian), and describes the stationary but unstable configuration of an inverted pendulum. Another distinct type of motion is "rotation," which appears as a set of curves that do not cross the $p = 0$ axis. For this motion the trajectories flow to the right in the upper half-plane and to the left in the lower half-plane. These trajectories correspond to more rapid motion of the pendulum such that the pendulum does not reverse direction as in the librational case, but rather continues

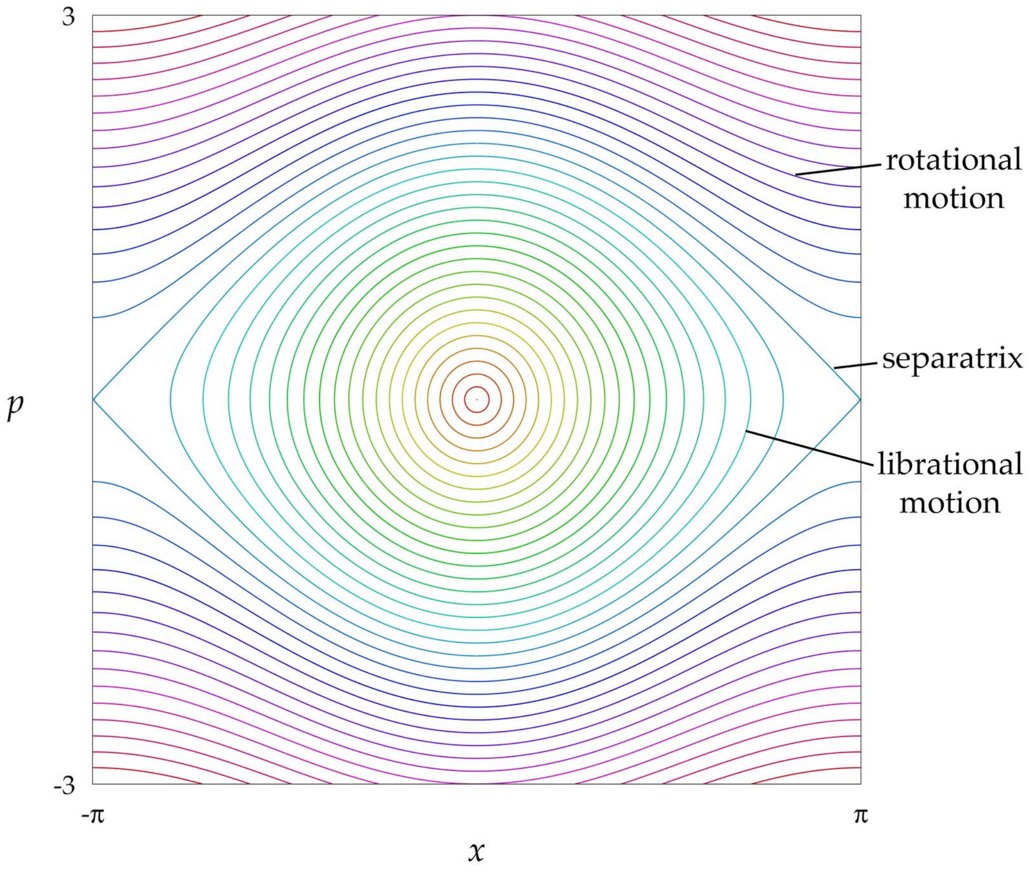

Figure 1.2: Plot of the phase space for the pendulum. The curves (trajectories) are the level sets of the pendulum Hamiltonian, Eq. (1.4). The different colors correspond to trajectories beginning from different initial conditions.

"over the top." The boundary between the two types of motion is the *separatrix*, which passes through the unstable fixed point. From this example, we can see that the phase portrait gives a concise, visual summary of the possible dynamics of a system (although the time-dependence of the trajectories must still be extracted from the equations of motion).

In the experiments described later on, we study time-periodic ("driven"), one-dimensional Hamiltonian systems. In this case, the phase space is of higher dimension

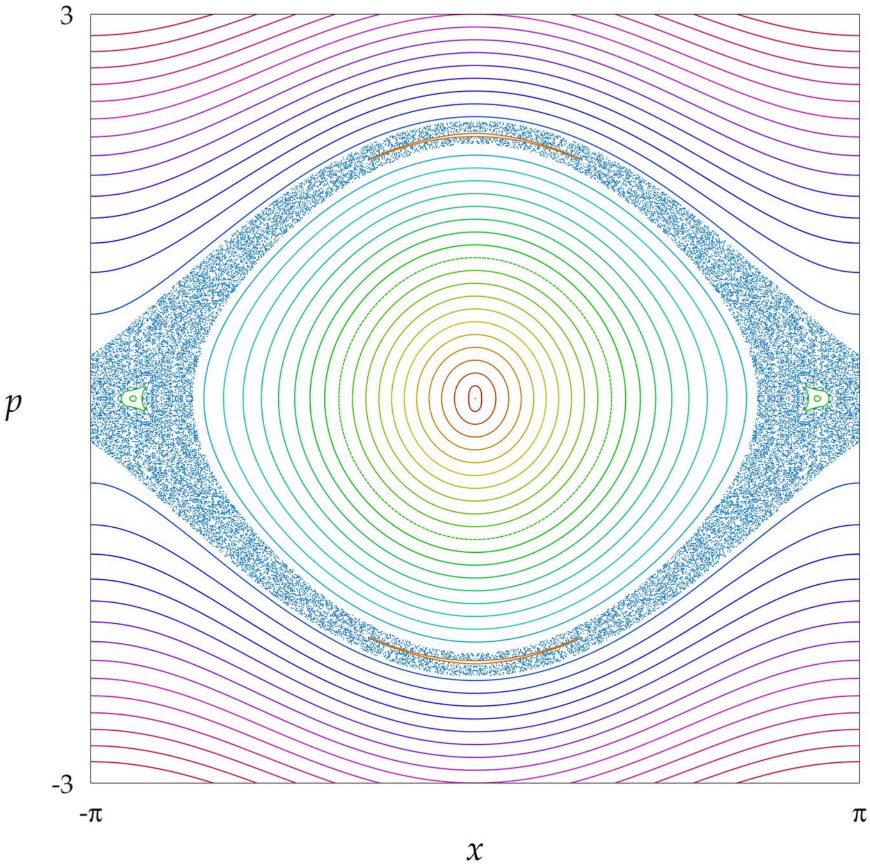

Figure 1.3: Phase space (Poincaré section) of a pendulum with a weak amplitude drive, with Hamiltonian $H = p^2/2 - (1 + 0.05\cos t)\cos x$. This "stroboscopic" plot is sampled at every $t = 2\pi n$ for integer n. As expected from KAM theory, most of the stable structure of the pendulum is left unchanged by the weak drive. However, the separatrix has broken down into a disordered region of chaos.

than in the time-independent case, since time acts as an effective extra dimension. In fact, it can be shown that these systems (referred to as $1\frac{1}{2}$-degree-of-freedom systems) are formally equivalent to two-degree-of-freedom systems [23]. So, the flow of these systems cannot be represented in a planar plot in the same way as one-dimensional systems. However, one can instead use a reduced phase plot, known as a *Poincaré surface of section*, which is a plane of constant t, modulo the period of the external drive. The plot constructed in this way consists of the intersections of the trajectories with the surface of section, which appear as dots in the plane, each corresponding to the coor-

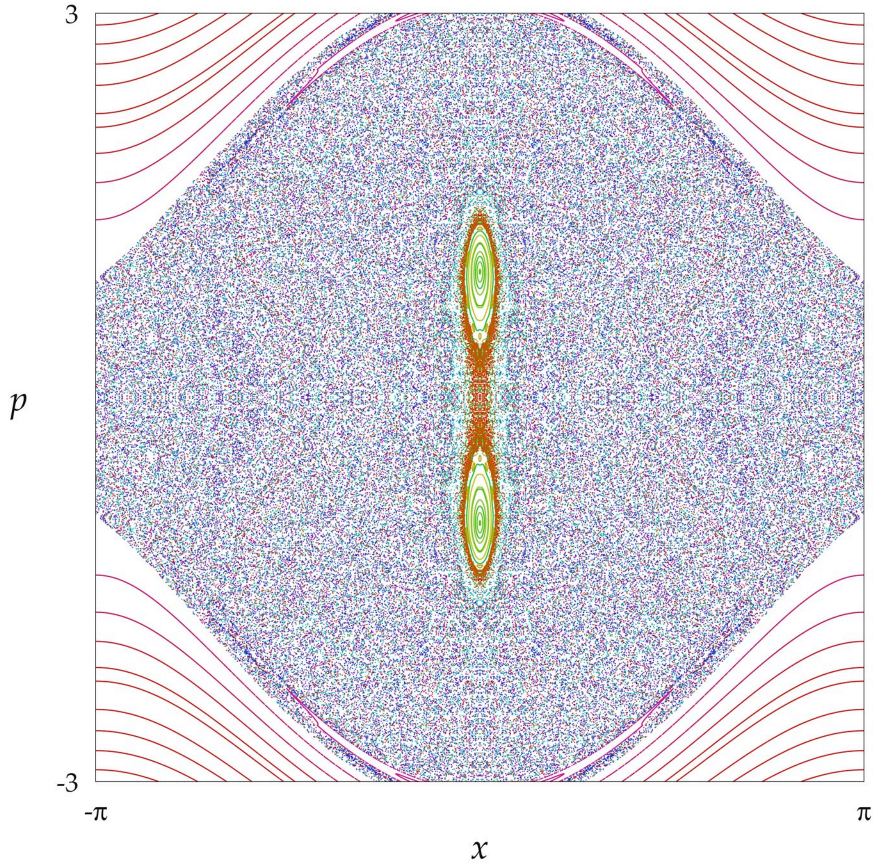

Figure 1.4: Phase space (Poincaré section) of a pendulum with a strong amplitude drive, with Hamiltonian $H = p^2/2-(1+\cos t)\cos x$. The stronger modulation here, compared to Fig. 1.3, breaks down most of the stable pendulum structure, resulting in widespread chaos.

dinates (x, p) plotted once per drive period. This phase portrait still captures the full dynamics, since each point in the phase plot uniquely determines all the successive points in the trajectory. Sample phase portraits of this type are shown in Fig. 1.3, for the pendulum with a weak, sinusoidal amplitude modulation, and in Fig. 1.4, for a strongly amplitude-modulated pendulum, corresponding to the system studied in much greater detail in Chapter 6. This surface-of-section technique also works for two-dimensional autonomous systems, which have four coordinates in the full phase space, since the conserved energy eliminates one of the coordinates, and the phase plane is taken to be at a constant value of another of the coordinates (where the intersections are also usually only plotted for one direction of passage through the surface). This technique can be used to study systems with more than two degrees of freedom, but then the location in the phase plane no longer uniquely determines the rest of the trajectory.

1.1.2 Integrability and Chaos

Now we will specialize our discussion of chaos to Hamiltonian systems, which will be our main interest in this work. Before doing so, however, we note that nonlinearity is an essential ingredient for producing chaotic behavior. Returning to the general dynamical system described by Eqs. (1.2), if this system is linear, then the equations can be expressed in terms of a matrix as

$$\partial_t x_i = \sum_j M_{ij}\, x_j \quad . \tag{1.5}$$

This linear system of equations then has the solution [24]

$$x_i(t) = \sum_j \exp(\mathbf{M}t)_{ij}\, x_j(0) \quad , \tag{1.6}$$

where $\exp(\mathbf{A})$ is the matrix exponential of the square matrix $\mathbf{A}$, which is defined in terms of the usual Taylor series expansion of the exponential function and exists for any matrix. Hence, linear systems are quasiperiodic (i.e., having a discrete frequency spectrum) in steady state and therefore predictable; by contrast, chaotic systems are characterized by continuous power spectra [13, 14].

Turning back now to Hamiltonian systems, we can see that no chaos occurs in one-dimensional autonomous Hamiltonian systems, because the existence of a conserved quantity, the energy $E(x,p)$, allows for the solution [23]

$$t = \int_{x(0)}^{x} dx' \, [\partial_p H(x',p)]^{-1} \ , \tag{1.7}$$

where p is regarded as a function of x and E. This solution must then be inverted to obtain $x(t)$ (and hence $p(t)$). So, the phase-space trajectories are regular for all one-dimensional autonomous Hamiltonians, as is the case for the pendulum example in Fig. 1.2 (indeed, any continuous dynamical system of the form of Eqs. (1.2) with $n = 2$ is free of chaotic behavior [14]). As a result, Hamiltonian systems of one degree of freedom are said to be *integrable*.

The important point of integrability in one dimension is the existence of a constant of the motion. In the case of N degrees of freedom, the system is integrable if there exist N independent constants of the motion I_k that are *in involution*, which means that their Poisson brackets (taken pairwise) vanish:

$$\{I_j, I_k\}_{\mathrm{P}} := \sum_{i=1}^{N} [(\partial_{x_i} I_j)(\partial_{p_i} I_k) - (\partial_{p_i} I_j)(\partial_{x_i} I_k)] = 0 \ \ (\forall \, j,k \in \{1,\ldots,N\}) \ . \tag{1.8}$$

These constants of the motion are related by Noether's theorem [3] to symmetries of the system (in the one-dimensional case, the constance of the energy is a consequence of the time-invariance of the Hamiltonian). The existence of these constants insures that the motion of trajectories in the $2N$-dimensional phase space is restricted to N-dimensional surfaces; under slightly more restrictive assumptions, these surfaces are N-tori, and there exists a canonical transformation to *action-angle* coordinates, in which the dynamics are similar to that of a free particle (and hence not chaotic) [25]. *Separable* systems, where the Hamiltonian has the form

$$H(x_1,\ldots,x_N,p_1,\ldots,p_N) = H_1(x_1,p_1) + \cdots + H_N(x_N,p_N) \ , \tag{1.9}$$

form a special class of higher-dimensional, integrable systems. These systems are clearly integrable, because they are composed of uncoupled one-dimensional systems.

Generic Hamiltonian systems do not possess the high degree of symmetry required for integrability. In the case of the $1\frac{1}{2}$-degree-of-freedom systems studied in this work, the external periodic drive breaks the time-invariance of the Hamiltonian and thus opens up the possibility for chaotic behavior. When discussing the formation of chaos in Hamiltonian systems, it is common to start with an integrable system (such as the pendulum in Fig. 1.2) and view the symmetry-breaking interaction as a perturbation. When a weak perturbation is added, as in Fig. 1.3, *nonlinear resonances* between the degrees of freedom can occur. By the Poincaré-Birkhoff fixed-point theorem [5], these resonances produce pendulum-like structures in the phase space (for weak perturbations). In Fig. 1.3, several nonlinear resonances are apparent, including the original structure of the unperturbed pendulum around the stable fixed point as well as two other pairs of resonances (although arbitrarily many more are present on smaller scales). Note that the corresponding structure in the unperturbed pendulum is not in itself a nonlinear resonance, though, because it is not the direct result of coupling between two degrees of freedom. Although a single (isolated) resonance does not result in chaotic behavior [26], the presence of multiple resonances causes their separatrices to broaden into chaotic regions [27] (or homoclinic "tangles" [5, 28]), as is shown by the diffuse area around the central resonance in Fig. 1.3. Picturesquely, these resonances are referred to as "islands of stability in a sea of chaos."

As expected from KAM theory, the weak perturbation in Fig. 1.3 leaves most of the stable structure intact. The invariant surfaces that survive the perturbation are thus referred to as "KAM surfaces." For the much stronger perturbation in Fig. 1.4, most of the stable structure has degenerated into chaos. The chaotic region in this system is bounded in momentum, though, because for sufficiently large momentum the kinetic energy dominates the perturbing interaction, restoring stability. The chaotic motion due to the interaction of the resonances can be thought of as competition between different stable motions, where the trajectory is not dominated by any one of the motions (as is the case for trajectories in an island of stability).

1.2 Quantum Chaos

The field of quantum chaos, which brings together the study of classical chaotic dynamics and quantum-mechanical systems, is a relatively new area of study, especially considering how long the fundamental ideas of its two parent fields have been around. Interestingly, the first notions of quantum chaos seem to have predated quantum mechanics itself: the problem of "Chladni figures," the patterns of dust formed on thin, rigid, vibrating plates, was understood in the 19th century for plates with simple shapes, but not for plates with irregular borders [29]. (Actually, this problem belongs to a more general class of "wave chaos" problems, but as in microwave cavities and surface waves in fluids, these systems are equivalent to quantum "billiard" systems in the sense of time-independent quantum mechanics [29].) Einstein [30] realized as early as 1917 that there could be problems quantizing classical systems in the "old" quantum theory, where the classical tori with actions given by a multiple of Planck's constant $\hbar$ were associated with quantum states (according to the Bohr-Sommerfeld and later the Einstein-Brillouin-Keller quantization rules) [5, 31, 32]. This quantization procedure, while emphasizing the connection with the underlying classical description, obviously fails for chaotic systems where action-angle variables do not exist. The advent of the "new" (Schrödinger/Heisenberg) quantum mechanics effectively sidestepped these problems by creating a very different formalism, and it was not until much later that these ideas were once again appreciated [5]. Indeed, most of the progress in the field of quantum chaos has been made only during the last quarter century.

As in classical Hamiltonian systems, there is a sense of integrability in quantum systems. Symmetries also lead to conserved quantities in quantum mechanics in the form of quantum numbers, which are the eigenvalues of operators that "generate" the transformation under which the system is invariant. For an N-dimensional quantum problem, if there are N operators $\hat{I}_k$ associated with conserved quantities that pairwise commute,

$$[\hat{I}_j, \hat{I}_k] := \hat{I}_j\hat{I}_k - \hat{I}_k\hat{I}_j = 0 \ \ (\forall\, j, k \in \{1, \ldots, N\}) \ \ , \tag{1.10}$$

the N ("simultaneous") operator eigenvalues completely specify the state of the system as well as its time evolution [3, 33]. This requirement on the quantum operators is formally analogous to the classical definition of integrability, since the existence of N constants in involution as in Eq. (1.8) implies the existence of N vector fields,

$$L_{I_k} = \sum_{i=1}^{N} (\partial_{p_i} H)\partial_{q_i} - (\partial_{q_i} H)\partial_{p_i} \tag{1.11}$$

(such that the flow of the trajectories along the L_{I_k} leaves I_k unchanged), that pairwise commute [23, 33]:

$$[L_{I_j}, L_{I_k}] = 0 \;\; (\forall j, k \in \{1, \ldots, N\}) \ . \tag{1.12}$$

Alternatively, the pairwise vanishing of the classical constants in the Poisson bracket carries over more directly to the quantum case in the form of the Moyal bracket [3, 33], defined in Section 1.3.2 below. In any case, quantum "nonintegrability" occurs when symmetries are broken, leading to the loss of "good" (conserved) quantum numbers.

Because classical nonintegrability leads to chaotic behavior, one might expect something similar to happen for quantum nonintegrable systems. Surprisingly, though, classical chaos is suppressed in quantum systems. This was discovered numerically in a seminal study by Casati, Chirikov, Izrailev, and Ford (CCIF) [34] of the quantum version of the standard map (1.1), obtained by quantizing the kicked-rotor Hamiltonian,

$$H = \frac{p^2}{2} + K \cos x \sum_n \delta(t - n) \ , \tag{1.13}$$

which generates the classical standard map. (We will treat this problem in detail in Chapter 4.) CCIF studied the kicked rotor in the regime where the phase space is characterized by widespread chaos. The classical signature of chaos here is diffusion of an ensemble of trajectories in momentum as they gain energy, on average, from the time-dependent potential. Quantum mechanically, though, CCIF found that the kicked rotor gains energy as in the classical case only for a short time, after which the diffusion is suppressed. This effect has come to be known as *dynamical localization*, and is a dramatic example of how quantum effects suppress classical chaos. Shepelyansky [35] has also provided a striking numerical demonstration of the suppression of chaos in the quantum kicked rotor, as we illustrate in Fig. 1.5. In this simulation, the classical and quantum systems evolve for some time from the same initial condition, and the suppression of energy growth by dynamical localization is evident in the quantum case. After evolving for some duration, a time-reversal is performed. In principle, both models should reverse their behavior and return to their initial conditions. The classical system only successfully contracts for a short time, though, and due to the buildup of numerical roundoff errors, the trajectories "forget" their history and the ensemble resumes diffusion, as expected for chaotic dynamics. The quantum system, on the other hand, makes a clean return to the initial state, indicating a robustness against perturbations and thus an absence of chaos. Note that such stability is expected in bounded quantum-mechanical systems, since they must have discrete spectra and thus exhibit almost-periodic dynamics [36].

1.2.1 Quantum Chaology

The apparent irony, then, of the field of quantum chaos is that it is the study of that which does not exist. Nonetheless, there are still some manifestations of the underlying classical disorder. One of the best-known examples is the disorder of the energy-levels in quantum nonintegrable systems, where the energy-level statistics are equivalent to those of random-matrix eigenvalues [3, 5, 37, 38]. Although the disorder in the spectra reflects the underlying (classical) dynamical disorder, this disorder is not unpredictable in the sense of dynamical chaos, because the spectral features can be computed with high accuracy [39]. The quantum-localization effect that we already discussed is another manifestation of the classical chaos. It has been shown [40, 41] that the kicked rotor can be mapped onto the Anderson localization problem [42], where a particle is spatially localized by the influence of a disordered potential. Thus in dynamical localization, the disorder that causes energy localization is not truly random (in the sense of an externally imposed randomness), but is generated dynamically by the underlying

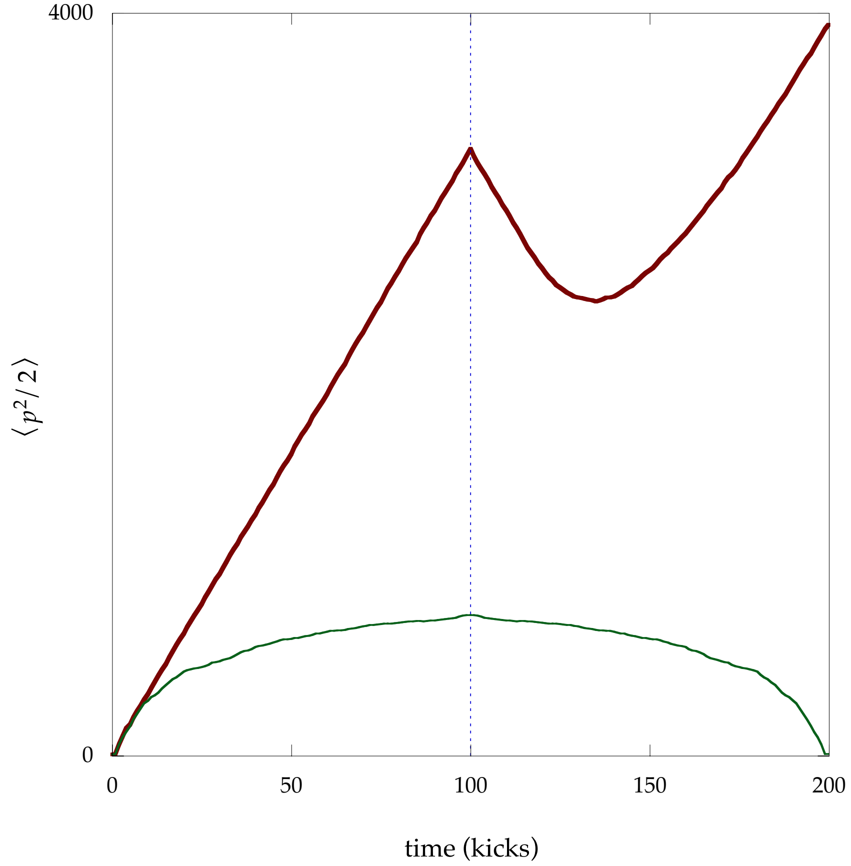

Figure 1.5: Comparison of classical (heavy solid line) and quantum (thin solid line) momentum transport in the kicked rotor for $K = 10$ and scaled Planck constant $\bar{k} = 1$ (simulation). The quantum initial condition is a Gaussian (minimum-uncertainty) wave packet with $\sigma_p = 2.5$, and the kinetic energy $\langle p^2/2 \rangle$ is plotted as a function of time; the classical evolution is the corresponding average for an ensemble of initial points picked according to the quantum distribution. The classical transport is diffusive, as characterized by the linear growth of energy. The quantum transport only shows diffusion for short times, and displays localization for longer times. At 100 kicks (marked by the dashed line), the direction of time is reversed. The classical ensemble resumes diffusive behavior after numerical errors build up in the simulation (thus converting the "special" trajectories that evolve back to the initial condition into generic, diffusing trajectories), which is typical for chaotic dynamics. The quantum system, on the other hand, retraces its steps back to its initial condition with high fidelity, indicating a lack of chaos. Note that in this quantum calculation, x is treated as an extended coordinate (as is the case in the experiment), necessitating a large (2×10^6 points) numerical grid to avoid aliasing effects.

classical chaos. The chaos-assisted tunneling effect that we discuss in Chapter 6 also reflects the disorder associated with the classical chaos. Since the tunneling rate is strongly influenced by the states inside the chaotic sea, and these states are very sensitive to changes in the system parameters, the tunneling rate shows strong fluctuations as a parameter varies. Similar fluctuations are also apparent, for example, in the conduction of mesoscopic semiconductor structures [29, 43], but it is worth reiterating that these symptoms of disorder are not chaotic in the classical sense.

In light of this suppression of chaos in quantum systems, Berry has introduced the term *quantum chaology* [44, 45] to refer to the study of the "fingerprints" or "signatures" of classical chaos in their quantized counterparts (of which the above phenomena are examples, as well as the "scarring" of eigenstates along unstable periodic orbits [46]). This is precisely the approach to quantum chaos adopted in this work, as we embark on a detailed investigation of localization, tunneling, and other quantum transport phenomena in classically chaotic systems.

1.2.2 Chaos in Quantum Mechanics

It is worth noting that one can also approach the problem of quantum chaos by asking what kinds of chaotic behaviors can be found in quantum systems. Part of the difficulty in carrying over classical chaos to quantum mechanics is that classical chaos is often defined in terms of the divergence of nearby trajectories, which do not have a straightforward quantum analog. If two nearly identical wave packets evolve, even in a nonintegrable system, the wave packets will remain close in the sense that their overlap integral is preserved under unitary time evolution; however, this is not a proper argument against chaos in quantum mechanics, as this argument applies also to the overlap integral of two classical phase space distributions evolving by the Liouville equation [16]. A variation on this idea is to look at sensitivity to parameter perturbations, rather than perturbations to the quantum state, to uncover some quantum sensitive dependence. Because of the sensitivity to parameter perturbations of quantum states associated with chaotic regions in phase space, the overlap of two initially identical wave packets evolving under slightly different Hamiltonians will drop exponentially under chaotic conditions, but will remain large in the stable case [47–50]. This idea has also been extended to studying the sensitivity of wave-packet evolution under randomly perturbed Hamiltonians, which shows a marked difference between stable and chaotic conditions [51, 52].

It is also possible to focus on the short-time quantum dynamics, where the behavior resembles that of classical chaos, as is apparent in the initial diffusive phase of the quantum kicked rotor [53] shown in Fig. 1.5. Furthermore, initially localized wave packets can also show exponential instability for short times [54–56], as expected for a similar classical distribution. Hence Chirikov [57] has advanced the notion of *finite-time* quantum chaos. There are also examples of genuine chaos where quantum mechanics is involved. Quantum systems can give rise to chaotic behavior when coupled to a classical system, as is the case for example with two-level atoms in a cavity coupled to a classical field [58–60] or in a quantum-mechanical oscillator coupled to a classical oscillator [61]. It has even been argued that chaos is possible in a purely quantum-mechanical system obtained by quantizing a classical chaotic system, although not by the usual quantization procedure, and this "configurational chaos" requires that the canonical momenta be unbounded [62–64]. (Another proposal for a purely quantum chaotic system [65] seems suspect in that the apparatus itself must become exponentially more complicated as the evolution continues, and additionally shows sensitivity to perturbations of the system parameters rather than to perturbations of the quantum state [66].)

Finally, we note that the concept of the trajectory is central to the de Broglie–Bohm formulation of quantum mechanics, so it is natural to look for chaotic behavior of these trajectories [67]. Interestingly, though, it has been found that the de Broglie–Bohm trajectories can be chaotic even for an integrable billiard [68], so in a sense there is "too much" chaos in the de Broglie–Bohm picture, in contrast to the "not enough" chaos in standard quantum mechanics. It is not clear, however, that these chaotic trajectories have any meaningful predictive power outside the statistical ensemble that reproduces the results of standard quantum mechanics.

1.2.3 Experiments in Quantum Chaos

By far the majority of progress in the field of quantum chaos has been theoretical, but now there has developed a large body of experiments to complement the theoretical advances. In this section we give a very brief and far from complete overview of experimental work in quantum chaos to illustrate the variety of systems in which the ideas of quantum chaos are important. An important first step towards experimental study in this area was taken with the work of Bayfield and Koch on the multiphoton ionization of hydrogen Rydberg atoms [69]. A discrepancy between the measured ionization thresholds and the predictions of classical models provided the first experimental evidence of dynamical localization [70–72]. Subsequently, Rydberg atom ionization experiments have given rise to a variety of interesting phenomena [73], including scarring effects [72, 74] and effects due to "metamorphoses" of classical resonances as the field strength is varied [75]. The spectroscopy of atoms in external fields also provides a frequency-domain arena for tests of quantum chaos, including level statistics [39, 76] and the influence of periodic orbits [77–79]. The statistics of resonances in atoms, molecules, and nuclei have also been shown to exhibit level-repulsion effects [33, 48].

As mentioned before, mesoscopic semiconductor structures provide an important arena for the study of quantum chaos [29]. Conductance measurements of semiconductor billiard structures show "universal conductance fluctuations" and weak localization effects with the application of strong magnetic fields [29, 43]. The tunneling current through quantum-well heterostructures ("resonant tunneling diodes") can also be understood in terms of unstable periodic orbits in a chaotic regime [80] and show effects due to scarring [81]. Semiconductor antidot lattices provide a different setting for studying conductance fluctuations with applied magnetic fields [82, 83], giving an experimental realization of the Lorentz gas [29]. Another related billiard-like system is the "quantum corral" [84], where a scanning tunneling microscope (STM) can be used to move individual atoms on a surface to build a confining structure for electrons.

A different class of experiments explores the area of "wave chaos," exploiting the formal equivalence of various other wave equations to the Schrödinger equation under certain circumstances. Perhaps the most notable among these are the microwave-cavity billiard experiments [29], in which such topics as level statistics [85], scarring [86], dynamical localization [87], chaos-assisted tunneling [88], and a trace formula [89] have been studied. This line of analysis has been extended to the study of deformed micro-disk cavity lasers, which act as open billiard systems in the optical domain [90]. A similar realization of wave chaos occurs with the mechanical vibrations of aluminum blocks [91, 92] or rigid plates [29, 93], and billiard-type experiments can be carried out using surface waves [94–96] or ultrasonic waves [97] in fluids. Many of these billiard-type experiments are reviewed in [29]. Finally, the equivalence of the electromagnetic equation in the paraxial approximation with the Schrödinger equation can be exploited to create an optical realization of the kicked rotor [98, 99].

Of course, the field of atom optics provides a clean and precise setting for experimental explorations of quantum chaos, including the dynamical localization effect that we have introduced, but we defer this discussion until Section 1.4.

1.2.4 On the "Usefulness" of Quantum Chaos

The field of quantum chaos is generally associated with fundamental interests in quantum mechanics, because of the initial motivation in this field to understand the interplay and correspondence of quantum and classical mechanics. However, it is worth pointing out that quantum chaos is also emerging as a field with important technological applications, and hence progress in this field is desirable also from an applied standpoint. One obvious area where these ideas will be important is in the semiconductor and microprocessor industries, where the nearly exponential increase in density of components will soon lead to sufficiently small devices that quantum effects will be significant. Present devices are strongly coupled to the environment at normal operating temperatures, so that the electron coherence length is very short and thus quantum effects are only important at very low temperatures, as in the conductance fluctuation experiments mentioned above. But when quantum effects take over, the semiconductor devices will obviously not have the high degree of symmetry necessary for integrability, so the charge transport in these devices will fall in the regime of quantum chaos. Along these same lines, the future development and demonstration of quantum computers [100] will require careful consideration of effects due to classical chaos to ensure proper operation [101].

As we have already discussed, quantum chaos has been important in the understanding of atomic spectra. Quantum chaos has also been shown to be of importance in the dynamical manipulation of atoms by light [102]. However, there are many more applications of quantum chaos outside of quantum mechanics in other wave systems. For example, quantum-chaos effects are important in the understanding of underwater acoustics [103]. We have also already mentioned the applicability of quantum chaos to the understanding of the mode structure of microwave cavity devices and mechanical vibrations. In a similar optical analogy, weakly deformed micro-disk semiconductor lasers show large improvements in directionality and intensity over normal whispering-gallery mode lasers, which is an application of wave chaos in an open system [90]. Finally, a fiber-optical switch for the communication industry has been proposed [104], based on the ideas of chaos-assisted tunneling, which we study in Chapter 6. In fact, a company (OpTun Ltd.) has been founded to develop these ideas.

1.3 Decoherence

The lack of long-time chaotic behavior in quantum mechanics seems to bring up difficulties in how the theories of quantum and classical physics are related. Specifically, since quantum mechanics is believed to be the more universal theory, it should in some sense "contain" classical mechanics as a limiting case. This idea, first advanced by Bohr, is known as the *Correspondence Principle*, and showing how classical-quantum correspondence arises remains even now a controversial and challenging problem. But because quantum mechanics does not support chaotic behavior in the sense of classical mechanics, it seems, oddly, that chaos cannot exist even in classical mechanics, if we are to believe in correspondence. In a simplistic view one might expect to recover classical mechanics by formally taking the limit $\hbar \rightarrow 0$ (of course, since Planck's constant $\hbar$ is indeed a constant, what we really mean is that we are taking the limit where the action of a system becomes arbitrarily large compared to $\hbar$). However, this limit is highly singular and not necessarily well-defined, as one can see from the form of the WKB wave function $\psi \sim \exp(iS(x)/\hbar)$ (where S is the action of the system) that applies in the "semiclassical" regime of small $\hbar$, which has an essential singularity at $\hbar = 0$.

One path to correspondence is suggested, for example, by the initially diffusive behavior in the kicked rotor that we noted above, which mimics the diffusion characteristic of classical chaos. It has been argued [39, 53, 105] that the "quantum break time" t_{B}, when the behavior crosses over from diffusive to localized, scales as $1/\hbar^2$, since in an energy-time uncertainty sense, this is the time required for the discrete spectrum to become "resolvable" by the system. Hence, it would seem that for macroscopic systems, the break time could become unobservably long because $\hbar$ would effectively be very small. However, there is a second time scale for quantum deviations from classical behavior, known as the "Ehrenfest time" t_{E}, which scales much more slowly, as $\log(1/\hbar)$. The existence of this time was pointed out originally by [106] for a specific model, and this time scale was discussed by [105, 107] in the context of the kicked rotor, by [108] for another driven, one-dimensional system, and by [109] for general chaotic systems. We will discuss the origin of this time scale in more detail below. The slow scaling of this time has dire consequences for correspondence, for although this time scale diverges as $\hbar \rightarrow 0$, in physical reality $\hbar$ is always some nonzero value, and thus spanning 30 orders of magnitude in $\hbar$ from a manifestly quantum regime to a manifestly classical regime yields a relatively minor change in t_{E}. By this argument, then, we would predict absurdly short times for which quantum effects should set in for classically chaotic systems

[110, 111]. Since this obviously violates common experience in the macroscopic world, there is clearly a need to resolve this discrepancy between the quantum and classical pictures.

One solution to this problem is embodied in the theory of *decoherence*. The key idea here is that macroscopic objects are in general not very well isolated from their "environment," which could, for example, include the internal (thermal) degrees of freedom or the ambient photons scattering off the object. Decoherence provides a mechanism by which the quantum coherence effects that suppress chaos can themselves be suppressed. Thus, even though it seems clear that classical behavior does not, in general, arise as a limit of the Schrödinger-equation description, it can arise as a limit of an "open" quantum description that takes into account the external influences on the system [112].

Broadly speaking, there are two "roles" of decoherence in explaining classical behavior as a consequence of quantum mechanics. The first is the suppression of quantum superposition states at the classical level, which addresses the famous Schrödinger cat paradox and is intimately related to the quantum-measurement problem [113, 114]. The second role of decoherence is in ensuring classical behavior in the dynamical evolution of a system. These two roles are, of course, closely related, but we will discuss them separately according to how they are applied in explaining classicality.

1.3.1 Suppression of Quantum Superposition

In Schrödinger dynamics, the state of the system is described by the wave function or state vector. For open systems, though, a more natural representation of the system is in terms of the *density operator*. For a state $|\psi\rangle$, the density operator is defined as

$$\hat{\rho} := |\psi\rangle\langle\psi| \ . \tag{1.14}$$

In this case the *density matrix* (the representation of the density operator in a particular basis) is highly redundant, because if the state vector has n components in some finite basis, the density matrix has n^2 components, but does not contain additional information. However, the density matrix has the advantage that it can be generalized to an ensemble in a straightforward way simply by averaging over the members $|\psi_j\rangle$ of the (usually large) ensemble,

$$\hat{\rho} := \frac{1}{N}\sum_j |\psi_j\rangle\langle\psi_j| \ . \tag{1.15}$$

A state corresponding to a wave vector as in (1.14) is referred to as a *pure state*, whereas an ensemble average as in (1.15) is a *mixed state*. The diagonal elements $\rho_{\alpha\alpha} = \langle\alpha|\hat{\rho}|\alpha\rangle$ of the density matrix are the *populations*, as they represent the probability of occupying the state $|\alpha\rangle$. The off-diagonal elements $\rho_{\alpha\beta} = \langle\alpha|\hat{\rho}|\beta\rangle$ ($\alpha \neq \beta$) contain the relative-phase information of the state, and are referred to as *coherences*. The important feature of the coherences to note here is that they have their maximum magnitude for a pure state. In a mixed state, if the phases of the various components are not aligned, the magnitudes of the coherences are reduced, falling to zero for a completely uncorrelated ensemble. Notice that because the coherences represent the potential for interference effects, they are in effect the "nonclassical" part of the density matrix. It is only the populations that have a sensible interpretation as classical probabilities.

The treatment of a system interacting with its environment begins typically by identifying the degrees of freedom associated with the "system" of interest and the "reservoir" which represents the environment. The combined system is then represented by the density operator $\hat{\rho}_{\mathrm{S+R}}$, and we assume that this combined system is now "closed" in the sense that there are no interactions with other systems that are not already described by this density operator. In a closed system, the density operator evolves according to the Schrödinger-von Neumann equation

$$\partial_t \hat{\rho} = -\frac{i}{\hbar}[H, \hat{\rho}] \ , \tag{1.16}$$

which gives the same evolution as the Schrödinger equation for the state vector. Hence a pure state, treated as a closed system, will evolve into a pure state as a consequence of the "unitarity" of the evolution equation. However, since we are generally interested in the system, which may have only a few degrees of freedom, we would like to ignore the information associated with the reservoir, which typically has many more degrees of freedom than we could possible monitor. One approach along these lines is suggested by the form for expectation values of operators in terms of the trace over the density matrix:

$$\langle \hat{A} \rangle = \mathrm{Tr}[\hat{A}\hat{\rho}] \ . \tag{1.17}$$

The average over the reservoir is then given by a partial trace taken over the reservoir degrees of freedom, resulting in a "reduced" density operator that describes only the state of the system:

$$\hat{\rho}_{\mathrm{S}} = \mathrm{Tr}_{\mathrm{R}}[\hat{\rho}_{\mathrm{S+R}}] \ . \tag{1.18}$$

In general, the evolution of $\hat{\rho}_{\mathrm{S}}$ depends on its history, but in the case where the reservoir is large, it should decorrelate rapidly, and so a Markovian approximation is justified. In this case it is possible to derive a *master equation* for the evolution of $\hat{\rho}_{\mathrm{S}}$ [115], which is similar to the unitary evolution equation (1.16) but with extra nonunitary terms describing the exchange of energy with the environment (dissipation or relaxation) and the redistribution of populations due to fluctuations in the environment (diffusion) [109, 116]. In terms of the density matrix, these new terms cause the evolution of a pure quantum state into a mixed quantum state, since the diffusion terms cause the coherences to be damped away [115, 116]. Although the interferences that were initially in the system still exist, they are moved out of the system and into the reservoir as the system and reservoir become entangled through their interaction [112].

The idea of decoherence, in its simplest form, is that the interaction with the environment can suppress the quantum coherences on a time scale that is many orders of magnitude shorter than the time scale associated with relaxation [116]. So, while the environment has a negligible impact on the "classical aspects" of the system, the coherences can be suppressed effectively instantaneously in a macroscopic system. The resulting diagonal density matrix can then be interpreted as a classical probability distribution.

The question that now arises is why the density operator should become diagonal in a particular basis and not some other. The answer depends, of course, on the nature of the environmental interaction. It has been argued [117–119] that the environment naturally selects a preferred ("pointer") basis, which consists of those states that are minimally affected by the environment (i.e., they become minimally entangled with the environment). These states are, in a sense, "robust" to the decoherence. This principle of "environment-induced superselection" [119] highlights the relation of decoherence to the measurement of a quantum system. Such a measurement necessarily entails an interaction with the environment, namely the measuring apparatus [120]. The nature of the interaction is tailored to the measurement of some observable, and the minimally coupled states are determined by a combination of the system Hamiltonian and the interaction Hamiltonian for the environmental coupling. A measurement may require a strong interaction that dominates the system Hamiltonian, so that the pointer states are the eigenvalues of the interaction Hamiltonian, leading naturally to the idea that measurement "collapses" the system into an eigenstate of the operator corresponding to the measured observable. The naturally selected states have also been demonstrated, for example, to be localized states in phase space in the case of an environmental coupling (of intermediate strength) to the position of a particle [119], coherent states for the weakly coupled harmonic oscillator [121], and energy eigenstates in the regime of weak coupling to the environment, where the system Hamiltonian is dominant [120]. Beyond the reduction to a classical mixture, decoherence addresses the issue of how a quantum system is forced into a definite state by the measurement interaction (notice that the only diagonal, pure-state density operators correspond to the basis states). The "measurement" is made by the environment, in that the entanglement with the environment transfers information to the environmental degrees of freedom. The statistical mixture that we are left with in the master-equation description is a reflection of our ignorance of the state of the environment, which in a macroscopic system is too complicated to keep track of even in principle. Since the outcome of the measurement is intimately tied to the immensely complicated environment, the measurement appears as a "random" collapse of the state vector. Thus, decoherence attempts to bring the measurement process back within the unitary evolution framework of quantum mechanics, without appealing to an extraneous notion of wave-function collapse, as in the orthodox interpretation of quantum mechanics [112, 116].

1.3.2 Classical Chaotic Evolution

So far, we have seen that the interaction with the environment can take a state with quantum features and convert it into a state that is sensible in a classical description. More important for the correspondence principle in dynamical systems, however, is to understand how decoherence can cause the *evolution* of a quantum system (which we have seen is particularly problematic in nonintegrable systems) to cross over to classical behavior.

One important tool for this discussion is the Wigner function (or distribution), which facilitates the description of quantum dynamics in phase space. The Wigner function is defined in terms of the density matrix as [122, 123]

$$W(x,p) := \frac{1}{\pi\hbar}\int_{-\infty}^{\infty} dx'\, e^{2ipx'/\hbar}\langle x - x'|\hat{\rho}|x + x'\rangle \ . \tag{1.19}$$

The Wigner function is not the only quantum phase-space distribution [124], but it has several features that make it preferable to other distributions. Each marginal distribution of the Wigner function, where one of the variables is integrated out, results in the probability distribution corresponding to the other variable. The Wigner function itself, however, is not a joint probability distribution, since it can take on negative values, which represent the interferences or coherences of the quantum state. The evolution of the Wigner function (for one degree of freedom) can be expressed in terms of the Moyal bracket of the Hamiltonian and the Wigner function [3, 125, 126],

$$\begin{aligned} \partial_t W(x,p) &= \{H, W\}_{\mathrm{M}} \\ &:= -\frac{2}{\hbar}H(x,p)\sin\left[\frac{\hbar}{2}\left(\overleftarrow{\partial_p}\,\overrightarrow{\partial_x} - \overleftarrow{\partial_x}\,\overrightarrow{\partial_p}\right)\right]W(x,p) \ , \end{aligned} \tag{1.20}$$

where the arrows on the derivative operators indicate the direction of operation. For a particle Hamiltonian in "standard form," $H = p^2/(2m) + V(x)$, the Moyal bracket can be written as the Poisson bracket plus quantum "correction" terms,

$$\partial_t W = \{H, W\}_{\mathrm{P}} + \sum_{n=1}^{\infty} \frac{(-1)^n \hbar^{2n}}{2^{2n}(2n+1)!} (\partial_x^{2n+1} V)(\partial_p^{2n+1} W) \ . \tag{1.21}$$

This equation is especially suitable for comparing the quantum evolution with the evolution of a classical ("Liouville") distribution ρ_{L},

$$\partial_t \rho_{\mathrm{L}}(x,p) = \{H, \rho_{\mathrm{L}}\}_{\mathrm{P}} \ , \tag{1.22}$$

which is described only by the Poisson bracket. Notice that formally setting $\hbar = 0$ in (1.21) recovers the Liouville evolution (1.22), so that correspondence seems easy in this formulation; however, it must be emphasized that taking the limit $\hbar \to 0$ for a quantum system is not trivial and may not be well defined without the assistance of external degrees of freedom.

It is immediately clear from the form of the Moyal bracket (1.21) that quantum-classical correspondence is particularly simple for "linear" systems, such as a free particle or a harmonic oscillator, because the quantum-correction terms vanish, yielding identical quantum and classical evolution equations. This point was recognized early on by Schrödinger, when he constructed the coherent states of the harmonic oscillator that mimic the classical oscillating trajectories [127]. Hence, all that is needed for correspondence in these systems is the action of decoherence for a mere instant (say, a single measurement), after which the quantum evolution preserves the classicality of the state. In the more general and challenging case, the nonlinearities of the system dynamically generate quantum interferences in the course of evolution [128]. The quantum terms cause the evolution to be unitary (notice that the classical evolution, even for a closed system, is manifestly nonunitary [129]), and thus it is these quantum terms that are responsible for the suppression of classical chaos. (Note that this is a much more meaningful way to treat the absence of chaos in quantum mechanics than simply appealing to the linearity of the Schrödinger equation.) The picture of quantum-classical divergence according to [109] is that because of the exponential stretching of a Liouville distribution under chaotic evolution, the distribution develops fine structure on a very short time scale. Since the quantum-correction terms involve derivatives of the Wigner function, they will be unimportant for an initially smooth distribution, but will quickly become important as fine structure develops due to the classical part of the evolution. From this argument, we expect the $\log(1/\hbar)$ breakdown time that we mentioned earlier as a consequence of exponential chaotic divergence. To achieve correspondence in the nonlinear regime, a single measurement at a single time during the evolution is insufficient to cause agreement between classical and quantum. For example, in the case of dynamical localization it is insufficient to decohere the system after the quantum break time, because although such an action would temporarily restore diffusive behavior, it would already be "too late," as the subsequent evolution could never catch up to the corresponding classical, continuously diffusing evolution. Rather, it is important to have continuous decoherence, which would effectively broaden the spectral components of the evolution and never allow the discreteness of the spectrum to become manifest. In the picture of [109], the interaction with the environment results in additional diffusive terms in the evolution equation (corresponding to the diffusion terms in the master equation for the density-matrix evolution) that tend to smooth the Wigner function. The resulting evolution is a balance between the usual evolution, which wants to generate fine structure, and the decoherence, which wants to destroy the same fine structure. For sufficiently strong noise, the fine structure can be tempered to the point where the quantum corrections remain unimportant, and the evolution is the same as that of the classical system subject to the same diffusive interaction. In the semiclassical limit, only a very small amount of noise is required to keep the quantum corrections under control (diffusion is only necessary on the scale of an $\hbar$ cell in phase space), so that the effect on the classical chaos is effectively negligible. This argument gives a nice picture of how decoherence can induce classical evolution, but we should note that there are some subtleties that may still need to be addressed for certain systems, including the kicked rotor [129].

In studying the decoherence due to environmental interaction, it is possible to use an approach based on the master equation [130–132] that models all of the effects due to the environment, or a simplified approach that employs an external noise source [107, 133, 134]. The latter approach is justified because the noise-induced diffusion (not dissipation) is mostly responsible for the decoherence [109, 135]. Furthermore, there are several levels at which correspondence has been examined in various theoretical studies. The most qualitative is the removal of nonclassical features by decoherence, including the destruction of scarred states [134] and the restoration of the irreversibility that is so conspicuously absent in unitary quantum evolution [126]. At the next level is the quantitative agreement of quantum and classical expectation values [131, 133, 136]. Although such quantitative agreement is important, the expectation values carry only a small amount of information about the system, which motivates the study of correspondence at the level of ensembles and distribution functions [110, 128]. Even here, though, it is possible to have agreement at the ensemble level even in a quantum regime [131], where it may still not be possible to associate classical trajectories with quantum evolution. Hence the strongest form of correspondence is obtained in a quantum trajectory approach, where a decoherence-influenced wave packet traces out a chaotic trajectory with the same properties as a corresponding classical trajectory (with noise added to the classical system to account for the "direct" contribution of the decoherence) [130, 132, 137, 138].

It has been argued that an appeal to the influence of the environment is not necessary for correspondence, but rather a coarse-graining, as for example manifested in the Husimi distribution [124], can serve to remove the nonclassical structure of the Wigner distribution [139]. However, as pointed out in [128], such an approach will not in general be successful because this coarse graining hides the nonclassical features in an essentially trivial way (because it can be reversed); it does not change the dynamical evolution of the quantum system, which as we have seen is certainly necessary for correspondence; and the coarse graining forbids correspondence at the trajectory level, which is in a sense the most impressive form of correspondence. The importance of environmental noise in explaining chaos is then somewhat ironic. Classical chaos is usually understood as arising solely from the system itself and not from an external noisy source, as we have pointed out in Section 1.1. At a deeper level, though, a certain amount of noise is necessary to obtain chaotic behavior from quantum mechanics. But because this noise level can be exceedingly small on macroscopic scales, the chaotic instability arises operationally from the "classical" dynamics rather than the perturbative noise.

1.3.3 Experiments on Decoherence

Despite the vast body of theoretical work on decoherence, there have been relatively few experiments dealing directly with the effects of decoherence on quantum systems. The situation is beginning to change now, though, due to the necessity of combating decoherence in systems where quantum coherence is very important, such as in quantum computers [100]. In linear systems, there have been several impressive and clean experiments. The most fundamental linear quantum problem, the two-slit experiment, has been realized as an atom interferometer, where light scattered by the atoms serves as a decohering measurement [140, 141]. Decoherence has also been studied in an entangled Rydberg atom/microwave cavity system [142], where the cavity acts as a measuring device for the internal atomic state. The decoherence of a superposition of motional states has also been studied in an ion trap [143, 144].

The first experimental studies in decoherence actually began with nonintegrable systems, where the effects of noise on the ionization of driven hydrogen [72, 145–147] and rubidium [148–151] Rydberg atoms were studied. Especially relevant to the work on correspondence that we discuss in Chapter 4 are Refs. [72, 145, 146], where noise added to the microwave driving of the Rydberg atoms led to improved agreement with classical predictions of ionization thresholds (which is an agreement at the expectation-value level, in contrast to the distribution correspondence that we present in Chapter 4). There has also been some work investigating the effects of temperature on conductance fluctuations in mesoscopic semiconductor quantum dots [152, 153]. Optical-analog experiments open up the possibility for decoherence experiments in wave-chaos systems, where perturbations to diffraction-grating positions in an optical kicked-rotor realization led to destruction of dynamical localization [98, 99]. Again, atom optics has contributed several experiments to this area, the discussion of which we defer until the next section.

1.4 Atom Optics

The field of *atom optics* is generally concerned with the manipulation of atoms using electromagnetic fields or material objects. In a sense, this field is the dual of traditional optics, where matter is used to manipulate electromagnetic (optical) fields. By far the majority of work in this field involves the optical manipulation of atoms, which is the case in this dissertation, although notable exceptions include the trapping of ions by electric fields [154], the trapping of neutral atoms in static magnetic traps [155], the reflection of atoms by the Casimir–van der Waals potential [156], and the diffraction of atoms by lithographically fabricated gratings [157]. The important concept in the optical manipulation of atoms is that light carries momentum. The momentum carried by photons is ordinarily very small, and macroscopic objects are generally immune to optical momentum effects. However, the momentum transferred to an atom when it scatters photons can have a very significant effect on its motion. Although the deflection of atoms by light ("radiation pressure") dates back to 1933 [158], it was not until the advent of lasers that much progress was made in this field. Subsequently the cooling of trapped ions using laser light was proposed [159, 160] and demonstrated soon thereafter [161, 162]. The development of trapping and cooling of neutral atoms introduced more difficulties, though, because the optical forces are so weak compared to the electric-field forces used in ion traps, and so thermal atoms from an atomic beam were very difficult to trap. But the slowing of a thermal beam of atoms [163] and the subsequent demonstration of laser cooling of neutral atoms in three dimensions (using "optical molasses," where laser light acts as an effective damping medium for the atoms) [164] led to magnetic [155] and optical [165] traps for atoms.

It was, however, the addition of a magnetic field to optical molasses that revolutionized atomic physics. This idea, due to Jean Dalibard [166], resulted in the efficient cooling and trapping of atoms from an atomic beam [167] in a device now known as the *magneto-optic trap* (MOT). The MOT uses optical molasses to cool atoms, while simultaneously taking advantage of the Zeeman shift of the atomic energy levels in a magnetic field to introduce a spatial dependence on the radiation pressure and hence confine the atoms to the center of the trap. The MOT was considerably simplified when it was demonstrated that atoms could also be trapped directly from an ambient atomic vapor [168], and it is now relatively simple to construct a very basic MOT [169]. The MOT is now a true workhorse in atomic physics, as it provides a convenient, cold, localized, and well-controlled sample of atoms that can be used as the starting point for a wide range of experiments [170], including Bose-Einstein condensation [171–173], atom interferometry [174], cold collisions and photoassociation spectroscopy [175], electric dipole moment searches [176], precision atomic clocks [177], and atom lithography [178, 179]. Indeed, all the experiments that we describe in this dissertation are performed with a cesium MOT loaded from atomic vapor, much like the setup in [168], as discussed further in Chapter 3. For some of the experiments that we will discuss, much more elaborate preparation of the atoms is necessary after the initial trapping and cooling of the atoms, as described in Chapter 5.

1.4.1 The Dipole Force and Optical Lattices

The forces used in a MOT are due to the absorption and spontaneous emission of light. Because the direction of a spontaneously emitted photon is random, this force is incoherent and results in the diffusion of momentum on the scale of the atomic recoil momentum due to a single photon scattering event (the “photon-recoil momentum”). Although this force is useful for the collection and preparation of atoms, the subsequent manipulation of atoms is greatly facilitated by the use of the *dipole force*, which does not involve dissipation or diffusion, and is thus a coherent interaction. The dipole force is a result of the interaction of an optical field and the atomic dipole moment induced by the field. The dipole interaction energy has the form $-\mathbf{d} \cdot \mathbf{E}$, where $\mathbf{d}$ is the atomic dipole moment and $\mathbf{E}$ is the electric field. Since the induced dipole moment is proportional to the applied field, the optical potential is proportional to the field intensity, and thus the dipole force is proportional to the gradient of the field intensity. In a photon picture, this force arises as a consequence of stimulated scattering of photons by the atom, where the redirection of a scattered photon results in a corresponding “recoil” by the atom. This effect is also known as the *ac Stark shift* or *light shift* of the atomic energy, and was first observed by Cohen-Tannoudji [180]. Thus, it is possible to create potentials to influence atomic motion by appropriately tailoring an optical-field profile. Also, if the optical field is tuned sufficiently far from the nearest atomic resonance, the interaction will be dominated by the dipole force, and spontaneous forces will be negligible.

One particular configuration in which the dipole force is important is the *optical lattice*, which is a periodic intensity pattern formed by the interference of multiple beams. Although there are many different possible configurations of optical lattices [181], the one that plays a central role in the experiments in this work is the simplest possible lattice, a standing wave of light, which is a one-dimensional, linearly polarized optical lattice. We discuss this configuration in detail in Chapter 2, but the basic result is that the atomic motion in such a standing wave is that of a quantum pendulum (without periodic boundary conditions). This system can then be viewed as an ideal one-dimensional crystal with long coherence times [182–184], leading to interesting and clean studies of effects in condensed-matter physics [185–189]. Viewed also as a one-dimensional dynamical system, this system gives rise to interesting tunneling effects [190–192], including non-exponential decay [193] and the quantum Zeno and anti-Zeno effects [194].

1.4.2 Atom Optics and Quantum Chaos

The fields of quantum chaos and atom optics became "entangled" with the proposal by Graham, Schlautmann, and Zoller [195] to observe dynamical localization in the deflection of an atomic beam crossing through a phase-modulated optical lattice. It was realized here in the group of Mark Raizen that the beam setup could be "collapsed" and performed with cold atoms prepared by a MOT and exposed to a modulated optical lattice in place. An apparatus using trapped sodium atoms was constructed [196, 197], and the manifestations of dynamical localization [198] and islands of stability (and other features in the transition from classical stability to chaos) in phase space [199] were studied in the phase-modulated lattice. (It was also in these experiments that the "ballistic-expansion imaging method" of measuring atomic momentum distributions was first employed. In this technique the atoms expand freely after the lattice interaction until they have expanded far beyond the initial MOT size, then they are frozen in place by optical molasses, and the distribution is photographed by a CCD camera.) In the phase-modulated system, the theoretical understanding of dynamical localization came about through an approximate mapping onto the kicked-rotor problem, and this system was soon also directly realized [200]. In these experiments, the dynamical evolution leading to localization was studied, along with the "quantum resonance" phenomenon, which is expected to give rise to ballistic transport but was manifested as a late-time Gaussian distribution. The atomic dynamics in an amplitude-modulated standing wave, which is the same system that we use in Chapter 6 to study chaos-assisted tunneling, were also studied using this apparatus to address the necessity of considering quantum chaos in analyzing a system as simple as atoms crossing transversely through an unmodulated optical lattice [102]. The work in this first-generation sodium apparatus is discussed in more detail in [201], as well as in two dissertations [196, 197].

The next natural direction of the quantum-chaos experiments was to examine the effects of decoherence, now that the quantum suppression of chaos had been observed. As these experiments involve transport to higher momenta than in the localized case, the sodium-based experiment was not suitable to carry out these studies [196]. To address these problems with the "momentum boundary" [202], we constructed a second-generation apparatus based on trapped cesium, which due to the longer wavelength of the atomic resonance and larger atomic mass effectively yields a better fidelity to the δ-kicked rotor over a wider momentum range (see Section 4.4.4 for details). The quantum-chaos experiments carried out on this new apparatus are reviewed in this dissertation as well as in Bruce Klappauf's dissertation [203], and meanwhile the sodium apparatus was put to good use in the tunneling and solid-state experimental efforts described in the previous section. The destruction of localization by amplitude noise in the kicks as well as dissipation due to the presence of a weak optical molasses were observed in this experiment [204], where it was found that late-time energy diffusion was increased, and the momentum distributions made a transition from the localized exponential profile to a classical-like Gaussian profile. Around the same time, the increased energy growth due to spontaneous emission induced by the optical lattice itself was observed by the group of Nelson Christensen [205], but it should be noted that there may be some difficulties in interpreting the results of this latter experiment due to the influences of the classical momentum boundary and the stochastic dipole force [206]. We subsequently extended this initial work on decoherence and showed that quantitative quantum-classical correspondence at the level of expectation values and momentum distributions could be achieved with a sufficient amount of amplitude noise, even in a manifestly quantum regime [207, 208]. This work on decoherence and correspondence in the kicked rotor is discussed in much more detail in Chapter 4.

There have also been several other interesting avenues of experiments on quantum chaos and quantum transport in atom optics. We revisited the quantum resonance phenomenon using the cesium apparatus, and due to much improved signal resolution and noise levels over the original study of [200], we were able to resolve the ballistic component of the motion [209]. There have also been related studies by the group of Keith Burnett [210, 211] on the kicked rotor near a quantum resonance but modified by a constant acceleration. Ballistic transport was likewise observed in these experiments, but the transport could be made directional (asymmetric) due to the influence of the acceleration. Continuing in the vein of global quantum nonintegrable transport, the suppression of diffusion by classical cantori was studied by the Christensen group [212], the effects of quasiperiodic kicking were studied by a group at the Université des Sciences et Technologies de Lille [213], and we provided experimental evidence for a universal theory of quantum diffusion by Jianxin Zhong, Qian Niu, Roberto Diener, and others [214]. More recently, work in this area has moved towards the study of mixed phase space using localized initial conditions. In this context we have observed chaos-assisted dynamical tunneling [215], and a collaboration of researchers at NIST-Gaithersburg under the direction of William Phillips and Steven Rolston and researchers at the University of Queensland under the direction of Gerard Milburn, Halina Rubinsztein-Dunlop, and Norman Heckenberg have also observed dynamical tunneling in a similar system (using a Bose-Einstein condensate) but in a more manifestly quantum and strongly coupled regime [216] (some earlier work of the Queensland group is discussed in [217]). Our work on chaos-assisted tunneling is described in detail in Chapter 6. Finally, we have performed experiments on a modified version of the kicked-rotor system that leads to spatial localization of the atoms, with applications to atom lithography. The results of this work will be presented in future publications [218, 219].

Chapter 2

Atomic Motion in an Optical Standing Wave

2.1 Overview

In this chapter we will motivate the experiments in this dissertation by considering the basic setup common to all of the experiments: the motion of an atom in a standing wave of far-detuned light. The basic conclusion of this chapter is that under the proper conditions, it is possible to ignore the internal electronic structure of the atom, and treat the atom as a point particle. Furthermore, the "reduced" atom moves under the influence of the effective center-of-mass Hamiltonian

$$H_{\text{eff}} = \frac{p^2}{2m} + V_0 \cos(2k_{\text{L}}x) \ , \tag{2.1}$$

where m is the atomic mass, k_{L} is the wave number of the laser light, and the potential amplitude V_0 is proportional to the laser intensity and inversely proportional to the detuning from the nearest atomic resonance (which in these experiments is one of the components of the cesium D_2 spectral line). This Hamiltonian is familiar, as it is formally equivalent to the plane-pendulum Hamiltonian. This motion is, of course, integrable, but this is nevertheless an important starting point for the realization of non-integrable systems, as both the amplitude and phase of the potential can be modulated to realize a variety of $1\frac{1}{2}$-degree-of-freedom systems.

We begin the analysis in Section 2.2, where we set up the problem of a two-level atom interacting with a laser field. We then examine the dynamical equations of motion for the atom and derive the atomic energy shift due to the field in Section 2.3. The adiabatic approximation, which is necessary to decouple the internal and external dynamics (and thus ignore the internal degrees of freedom), is reviewed in Section 2.4. In Section 2.5 we look at the deviations that can occur from the idealized picture represented by Eq. (2.1), such as several dissipative processes as well as the treatment of cesium (which has quite a complicated hyperfine level structure) as a two-level atom. We also estimate the magnitudes of these corrections for the experiments in this dissertation. Section 2.6 covers the more general case of when the two beams that form the optical lattice differ in amplitude and frequency. We will see that the former difference can be taken into account by using the geometric mean of the two intensities as a replacement for the intensity in the identical-beam case, and the frequency difference is equivalent to a nonzero velocity of the lattice. Finally, in Section 2.7, we examine some aspects of quantum motion in an optical lattice that will be important considerations for the experiments described in later chapters. Specifically, we will examine the how the momentum excitations due to the lattice are quantized in multiples of two photon recoil momenta ($2\hbar k_{\mathrm{L}}$) and how this quantization gives rise to Bragg scattering; we will also consider the band structure of the lattice, which is important in using a lattice for quantum-state preparation; and we examine the consequence of the lattice being an extended system, as opposed to a "true" pendulum that obeys periodic boundary conditions over one period of the potential.

2.2 Atom-Field Interaction

We begin our treatment with a general description of the atom-field interaction. We consider the one-dimensional problem of a two-level atom moving in a standing wave of light. The standing wave is described by the sum of two traveling waves,

$$\begin{aligned}\mathbf{E}(x,t) &= \hat{z}E_0[\cos(k_{\mathrm{L}}x-\omega_{\mathrm{L}}t)+\cos(k_{\mathrm{L}}x+\omega_{\mathrm{L}}t)]\\ &= \hat{z}E_0\cos(k_{\mathrm{L}}x)\left(e^{-i\omega_{\mathrm{L}}t}+e^{i\omega_{\mathrm{L}}t}\right)\\ &=: \mathbf{E}^{(+)}(x,t)+\mathbf{E}^{(-)}(x,t)\ \ ,\end{aligned}\tag{2.2}$$

where $\mathbf{E}^{(+)}$ and $\mathbf{E}^{(-)}$ are the positive- and negative-rotating components of the field, respectively (i.e., $\mathbf{E}^{(\pm)}\sim e^{-i(\pm\omega_{\mathrm{L}})t}$), E_0 is the amplitude of either one of the two constituent traveling waves, and $\omega_{\rm L}$ is the laser frequency.

The atomic free-evolution Hamiltonian is then given by

$$H_{\rm A} = \frac{p^2}{2m} + \hbar\omega_0 |{\rm e}\rangle\langle{\rm e}| \ , \tag{2.3}$$

where the excited and ground internal atomic states are $|{\rm e}\rangle$ and $|{\rm g}\rangle$, respectively, and ω_0 is the frequency of the atomic resonance. The atom-field interaction Hamiltonian is given (in the dipole approximation) by

$$H_{\rm AF} = -\mathbf{d}\cdot\mathbf{E} \ , \tag{2.4}$$

where $\mathbf{d}$ is the atomic dipole operator. Assuming that $|\omega_{\rm L} - \omega_0| \ll \omega_{\rm L} + \omega_0$, we can make the rotating-wave approximation (RWA), where terms rotating at twice the optical frequencies are replaced by their zero average value, with the result

$$\begin{aligned} H_{\rm AF} &= -\mathbf{d}^{(+)}\cdot\mathbf{E}^{(-)} - \mathbf{d}^{(-)}\cdot\mathbf{E}^{(+)} \\ &= -d_z^{(+)}E^{(-)} - d_z^{(-)}E^{(+)} \ , \end{aligned} \tag{2.5}$$

where we have decomposed the dipole operator into its positive- and negative-frequency parts,

$$\begin{aligned} \mathbf{d} &= \mathbf{d}^{(+)} + \mathbf{d}^{(-)} \\ &= (a + a^\dagger)\langle e|\mathbf{d}|g\rangle \ , \end{aligned} \tag{2.6}$$

$a := |{\rm g}\rangle\langle{\rm e}|$ is the atomic lowering operator, and we have taken the dipole matrix element $\langle e|\mathbf{d}|g\rangle$ to be real. We can also write the interaction Hamiltonian as

$$H_{\rm AF} = \frac{\hbar\Omega}{2}(a e^{i\omega_{\rm L}t} + a^\dagger e^{-i\omega_{\rm L}t})\cos k_{\rm L}x \ , \tag{2.7}$$

where we have defined

$$\Omega := -\frac{2\langle{\rm e}|d_z|{\rm g}\rangle E_0}{\hbar} \tag{2.8}$$

as the maximum Rabi frequency.

Before writing down the evolution equations, we make a transformation into the rotating frame of the laser field by defining the slowly varying excited state

$$|\tilde{\rm e}\rangle := e^{i\omega_{\rm L}t}|{\rm e}\rangle \tag{2.9}$$

and the stationary field amplitudes

$$\tilde{E}^{(\pm)} := e^{\pm i\omega_{\mathrm{L}}t}E^{(\pm)} \quad . \tag{2.10}$$

We can then rewrite the interaction Hamiltonian as

$$\begin{aligned}\tilde{H}_{\mathrm{AF}} &= -\tilde{\mathbf{d}}^{(+)} \cdot \tilde{\mathbf{E}}^{(-)} - \tilde{\mathbf{d}}^{(-)} \cdot \tilde{\mathbf{E}}^{(+)} \\ &= \frac{\hbar\Omega}{2}(\tilde{a} + \tilde{a}^\dagger)\cos k_{\mathrm{L}}x \quad ,\end{aligned} \tag{2.11}$$

where $\tilde{\mathbf{d}}^{(\pm)}$ and $\tilde{a}$ are defined as $\mathbf{d}^{(\pm)}$ and a were defined, but with $|\mathrm{e}\rangle$ replaced by $|\tilde{\mathrm{e}}\rangle$. In making the rotating-wave approximation, we have discarded the two terms that would have an explicit time dependence of $e^{\pm i2\omega_{\mathrm{L}}t}$ in Eq. (2.11), and in fact we have removed all of the explicit time dependence from this problem. Notice also that $|\tilde{\mathrm{e}}\rangle$ is additionally an eigenstate of the internal part of H_{A}, with eigenvalue $\hbar\omega_0 - \hbar\omega_{\mathrm{L}}$. Hence, in terms of the rotating frame excited state, the free atomic Hamiltonian becomes

$$\tilde{H}_{\mathrm{A}} = \frac{p^2}{2m} - \hbar\Delta_{\mathrm{L}}|\tilde{\mathrm{e}}\rangle\langle\tilde{\mathrm{e}}| \quad , \tag{2.12}$$

where $\Delta_{\mathrm{L}} := \omega_{\mathrm{L}} - \omega_0$ is the detuning of the laser from the atomic resonance. Again, this representation of the problem in the laser frame is interesting, because it shows that this *ac* interaction is equivalent to the problem of two states separated in energy by $\hbar\Delta_{\mathrm{L}}$ interacting with a *dc* electric field (after invoking the RWA).

2.2.1 Digression: Unitary Transformations and Field Operators

The result (2.12) also follows from formally applying the unitary transformation

$$U = \exp\left(i\omega_{\mathrm{L}}t|\mathrm{e}\rangle\langle\mathrm{e}|\right) \quad , \tag{2.13}$$

so that $|\tilde{\mathrm{e}}\rangle = U|\mathrm{e}\rangle$ (and $|\tilde{\mathrm{g}}\rangle = U|\mathrm{g}\rangle = |\mathrm{g}\rangle$), and then using the transformation law for a Hamiltonian under a time-dependent, unitary transformation [188]:

$$\tilde{H} = UHU^\dagger + i\hbar(\partial_t U)U^\dagger \quad . \tag{2.14}$$

However, this transformation does not correctly reproduce the rotating-frame interaction Hamiltonian (2.11). The problem lies in the fact that we have ignored the operator nature of the electric field. We can write the (single-mode) laser field as [220]

$$\mathbf{E}^{(+)}(x,t) = \hat{z}\mathcal{E}\, a_{\mathrm{F}} \cos(k_{\mathrm{L}}x)\, e^{-i\omega_{\mathrm{L}}t} \quad , \tag{2.15}$$

where a_{F} is the annihilation operator for the laser field,

$$a_{\mathrm{F}} = \sum_{n=1}^{\infty} |n-1\rangle\langle n|\sqrt{n} \quad , \tag{2.16}$$

and $\mathcal{E}$ is a constant that can be written in terms of the mode volume of the field and the photon energy [221]. In terms of the quantized field, the combined Hamiltonian corresponding to (2.3) and (2.4) becomes

$$\begin{aligned} H &= H_{\mathrm{A}} + H_{\mathrm{AF}} \\ &= \frac{p^2}{2m} + \hbar\omega_0|\mathrm{e}\rangle\langle\mathrm{e}| + \frac{\hbar g}{2}\left(a a_{\mathrm{F}}^\dagger e^{i\omega_{\mathrm{L}}t} + a^\dagger a_{\mathrm{F}} e^{-i\omega_{\mathrm{L}}t}\right)\cos k_{\mathrm{L}}x \quad , \end{aligned} \tag{2.17}$$

where $g := -2\langle\mathrm{e}|d_z|\mathrm{g}\rangle\mathcal{E}/\hbar$. This Hamiltonian is in the interaction picture with respect to the field evolution [222], because the field operators carry the explicit time dependence of the field (written out explicitly here). Thus, in addition to the transformation (2.13), we transform out of the interaction picture by applying the second transformation

$$U_{\mathrm{I}} = \exp\left(iH_{\mathrm{F}}t/\hbar\right) \quad , \tag{2.18}$$

where H_{F} is the field Hamiltonian, given by

$$H_{\mathrm{F}} = \hbar\omega_{\mathrm{L}}\left(a_{\mathrm{F}}^\dagger a_{\mathrm{F}} + \frac{1}{2}\right) \quad . \tag{2.19}$$

The resulting Hamiltonian is

$$\begin{aligned} \tilde{H} &= \frac{p^2}{2m} + \hbar\omega_0|\tilde{\mathrm{e}}\rangle\langle\tilde{\mathrm{e}}| + \frac{\hbar g}{2}\left(\tilde{a}\tilde{a}_{\mathrm{F}}^\dagger + \tilde{a}^\dagger\tilde{a}_{\mathrm{F}}\right)\cos k_{\mathrm{L}}x + \hbar\omega_{\mathrm{L}}\left(\tilde{a}_{\mathrm{F}}^\dagger\tilde{a}_{\mathrm{F}} + \frac{1}{2}\right) \\ &= \tilde{H}_{\mathrm{A}} + \tilde{H}_{\mathrm{AF}} + \tilde{H}_{\mathrm{F}} \quad , \end{aligned} \tag{2.20}$$

where the tildes indicate operators after transformation. This Hamiltonian is then in the Schrödinger picture with respect to the field, where the field time dependence is generated by the presence of $H_{\rm F}$. In the classical limit, the average photon number N of the laser field is very large, and in a coherent state the fractional uncertainty in N becomes vanishingly small. Hence, the field operators $a_{\rm F}$ can be replaced by $\sqrt{N}$, and the field Hamiltonian reduces to a constant energy offset (and thus can be neglected). Upon making the identification $\Omega = g\sqrt{N}$, we also recover the correct form for the rotating interaction Hamiltonian (2.11). Hence we have shown that the transformations (2.9) and (2.10) arise formally from different representations of the quantized field.

With the expression (2.15) for the field operator in hand, we make one final remark about the RWA. Since $\mathbf{E}^{(+)}$ annihilates a photon from the laser field, the terms left in Eq. (2.5) correspond to raising the atomic state while lowering the field state ($d_z^{(-)}E^{(+)}$) and lowering the atomic state while raising the field state ($d_z^{(+)}E^{(-)}$). Invoking the RWA, then, amounts to keeping only the energy-conserving (resonant) terms in the interaction Hamiltonian.

2.3 Schrödinger Equation

Since we assume that the detuning from resonance is large (i.e., $\Delta_{\rm L} \gg \Gamma$, where $1/\Gamma$ is the natural lifetime of $|{\rm e}\rangle$), we will neglect spontaneous emission and use the Schrödinger equation,

$$(\tilde{H}_{\rm A} + \tilde{H}_{\rm AF})|\psi\rangle = i\hbar\partial_t|\psi\rangle \ , \tag{2.21}$$

to describe the atomic evolution. It is convenient to decompose the state vector $|\psi\rangle$ into a product of internal and external states,

$$|\psi\rangle = |\psi_{\rm e}(t)\rangle\,|\tilde{\rm e}\rangle + |\psi_{\rm g}(t)\rangle\,|{\rm g}\rangle \tag{2.22}$$

where the $|\psi_i(t)\rangle$ are states in the center-of-mass space of the atom. In the following, we will associate all time dependence of the atomic state with the center-of-mass components of the state vector. Defining the coefficients $\psi_i(x,t) := \langle x|\psi_i(t)\rangle$, the equation of motion for the wave function $\langle x|\psi\rangle$ becomes

$$\begin{aligned} &i\hbar(\partial_t\psi_{\mathrm{e}}|\tilde{\mathrm{e}}\rangle + \partial_t\psi_{\mathrm{g}}|\mathrm{g}\rangle) = \\ &\qquad \frac{p^2}{2m}(\psi_{\mathrm{e}}|\tilde{\mathrm{e}}\rangle + \psi_{\mathrm{g}}|\mathrm{g}\rangle) - \hbar\Delta_{\mathrm{L}}\psi_{\mathrm{e}}|\tilde{\mathrm{e}}\rangle + \frac{\hbar\Omega}{2}(\psi_{\mathrm{e}}|\mathrm{g}\rangle + \psi_{\mathrm{g}}|\tilde{\mathrm{e}}\rangle)\cos k_{\mathrm{L}}x \ \ . \end{aligned} \tag{2.23}$$

Separating the coefficients of $|\tilde{\mathrm{e}}\rangle$ and $|\mathrm{g}\rangle$, we obtain the coupled pair of equations

$$\begin{aligned} i\hbar\partial_t\psi_{\mathrm{e}} &= \frac{p^2}{2m}\psi_{\mathrm{e}} + \left(\frac{\hbar\Omega}{2}\cos k_{\mathrm{L}}x\right)\psi_{\mathrm{g}} - \hbar\Delta_{\mathrm{L}}\psi_{\mathrm{e}} \\ i\hbar\partial_t\psi_{\mathrm{g}} &= \frac{p^2}{2m}\psi_{\mathrm{g}} + \left(\frac{\hbar\Omega}{2}\cos k_{\mathrm{L}}x\right)\psi_{\mathrm{e}} \ \ . \end{aligned} \tag{2.24}$$

for the wave functions $\psi_i(x,t)$.

At this point we mention that it is possible to find energy eigenstates of the coupled atom-field system. From (2.24), we can find the new (internal) eigenstates by diagonalizing the matrix

$$\begin{pmatrix} -\hbar\Delta_{\mathrm{L}} & \dfrac{\hbar\Omega}{2}\cos k_{\mathrm{L}}x \\ \dfrac{\hbar\Omega}{2}\cos k_{\mathrm{L}}x & 0 \end{pmatrix} \ \ , \tag{2.25}$$

where we have ignored the center-of-mass contributions to the Hamiltonian. The eigenvalues are given by

$$E_{1,2} = -\frac{\hbar\Delta_{\mathrm{L}}}{2} \pm \frac{\hbar}{2}\sqrt{\Delta_{\mathrm{L}}^2 + \Omega^2\cos^2 k_{\mathrm{L}}x} \ \ , \tag{2.26}$$

with corresponding eigenvectors [115, 223]

$$\begin{aligned} |1\rangle &= \sin\theta|\mathrm{g}\rangle + \cos\theta|\tilde{\mathrm{e}}\rangle \\ |2\rangle &= \cos\theta|\mathrm{g}\rangle - \sin\theta|\tilde{\mathrm{e}}\rangle \ \ . \end{aligned} \tag{2.27}$$

By convention the state $|1\rangle$ has the higher energy, and the angle θ is defined via

$$\tan 2\theta = -\frac{\Omega\cos k_{\mathrm{L}}x}{\Delta_{\mathrm{L}}} \quad \left(0 \le \theta < \frac{\pi}{2}\right) \ \ . \tag{2.28}$$

These states are known as the *dressed states* of the atom, and we see from Eq. (2.26) that the coupling to the field causes an avoided crossing in the energy level structure of the atom. For $\Delta_{\mathrm{L}} \gg \Omega$, we can expand the dressed-state energies (2.26), with the result

$$E_{1,2} = -\frac{\hbar\Delta_{\mathrm{L}}}{2} \pm \frac{\hbar\Delta_{\mathrm{L}}}{2} \pm \frac{\hbar\Omega^2}{4\Delta_{\mathrm{L}}} \cos^2 k_{\mathrm{L}}x + O\left(\frac{\Omega^4}{\Delta_{\mathrm{L}}^3}\right) \quad . \tag{2.29}$$

In this limit, the atom is essentially in only one of the dressed states, and so it is clear that the atom experiences an energy shift that depends sinusoidally on position. This shift in the energy levels is the *ac Stark shift*, and we will treat this phenomenon more precisely and directly in the next section, in the limit of large Δ_{L}.

2.4 Adiabatic Approximation

The equations of motion (2.24) can be greatly simplified by using the *adiabatic approximation*. We can motivate this approximation by examining the various time scales in the evolution of ψ_{e} and ψ_{g}. The kinetic-energy terms in Eqs. (2.24) induce variations on a time scale corresponding to several recoil frequencies $\omega_{\mathrm{r}} := \hbar k_{\mathrm{L}}^2/2m$, where $\omega_{\mathrm{r}} = 2\pi \cdot 2.07$ kHz for cesium. However, the pump-field terms induce motion on a time scale corresponding to the Rabi frequency (typically from zero to several hundred MHz), and the free evolution term induces motion of ψ_{e} on a time scale corresponding to Δ_{L} (typically several to many GHz); together, these terms induce internal atomic oscillations at the *generalized Rabi frequency* $\Omega_{\mathrm{gen}}(x) := \sqrt{\Omega^2 \cos^2 k_{\mathrm{L}}x + \Delta_{\mathrm{L}}^2} \simeq \Delta_{\mathrm{L}}$. Furthermore, in between these long and short time scales of external and internal atomic motion lies the damping time scale due to coupling with the vacuum, which corresponds to the natural decay rate Γ (for cesium, $\Gamma/2\pi = 5.2$ MHz). Because we are primarily interested in the slow center-of-mass atomic motion, and the internal atomic motion takes place for times much shorter than the damping time, it is a good approximation to assume that the internal motion is damped instantaneously to equilibrium (i.e., $\partial_t\psi_{\mathrm{e}} = 0$, because ψ_{e} is the variable that carries the natural internal free-evolution time dependence at frequency Δ_{L}, whereas ψ_{g} has no natural internal oscillation, because the state

$|\mathrm{g}\rangle$ is at zero energy). This approximation then gives a relation between ψ_e and ψ_g:

$$\left(\hbar\Delta_\mathrm{L} - \frac{p^2}{2m}\right)\psi_\mathrm{e} = \left(\frac{\hbar\Omega}{2}\cos k_\mathrm{L}x\right)\psi_\mathrm{g} \ . \tag{2.30}$$

We can then use this constraint to eliminate ψ_e in the second of Eqs. (2.24), with the result

$$i\hbar\partial_t\psi_\mathrm{g} = \left(\frac{p^2}{2m}\right)\psi_\mathrm{g} + \left(\frac{\hbar\Omega^2}{4\left(\Delta_\mathrm{L} - \dfrac{p^2}{2m\hbar}\right)}\cos^2 k_\mathrm{L}x\right)\psi_\mathrm{g} \ . \tag{2.31}$$

We have already assumed that $\hbar\Delta_\mathrm{L} \gg p^2/2m$, so we can ignore the momentum contribution to the cosine amplitude, and this equation becomes

$$i\hbar\partial_t\psi_\mathrm{g} = \left(\frac{p^2}{2m}\right)\psi_\mathrm{g} + V_0\cos(2k_\mathrm{L}x)\psi_\mathrm{g} \ , \tag{2.32}$$

where we have shifted the zero of the potential energy, and

$$\begin{aligned} V_0 &:= \frac{\hbar\Omega^2}{8\Delta_\mathrm{L}} \\ &= \frac{|\langle\mathrm{e}|d_z|\mathrm{g}\rangle|^2E_0^2}{2\hbar\Delta_\mathrm{L}} \ . \end{aligned} \tag{2.33}$$

Since the detuning is large, nearly all the population is contained in $|\mathrm{g}\rangle$, so the excited state completely drops out of the problem. Hence, the atom obeys the Schrödinger equation with the center-of-mass Hamiltonian

$$H = \frac{p^2}{2m} + V_0\cos(2k_\mathrm{L}x) \ , \tag{2.34}$$

and the atom behaves like a point particle in a sinusoidal potential, where the strength of the potential is given by (2.33). From Eq. (2.31), we see that the atomic momentum leads to a very small correction to the well depth V_0.

2.4.1 Master Equation Approach

It is also instructive to make the adiabatic approximation from the viewpoint of a master equation, where we can more explicitly see the effects of damping on the atomic motion. The master equation for the atomic evolution (i.e., the optical Bloch equations generalized to include center-of-mass motion) has the general form [224]

$$\partial_t\tilde{\rho}(t) = -\frac{i}{\hbar}[\tilde{H}_{\mathrm{A}} + \tilde{H}_{\mathrm{AF}}, \tilde{\rho}(t)] + V_{\mathrm{diss}}\tilde{\rho}(t) \tag{2.35}$$

in the rotating basis, where the density operator is given by $\tilde{\rho} := |\psi\rangle\langle\psi|$, with $|\psi\rangle$ as in (2.22). In this equation, the commutator describes the Hamiltonian evolution of the system, and the dissipation operator V_{diss} describes spontaneous emission. We can write out the effect of the dissipation operator more explicitly, with the result [225]

$$\begin{aligned}\partial_t\tilde{\rho}(t) = {} & -\frac{i}{\hbar}(\tilde{H}_{\mathrm{eff}}\tilde{\rho}(t) - \tilde{\rho}(t)\tilde{H}_{\mathrm{eff}}^{\dagger}) \\ & + \Gamma\int d\Omega f_{\mathrm{sc}}(\theta,\phi)e^{ik_{\mathrm{L}}x\sin\theta\cos\phi}a\rho a^{\dagger}e^{-ik_{\mathrm{L}}x\sin\theta\cos\phi} \quad ,\end{aligned} \tag{2.36}$$

where the effective, non-Hermitian Hamiltonian is given by

$$\tilde{H}_{\mathrm{eff}} = \tilde{H}_{\mathrm{A}} + \tilde{H}_{\mathrm{AF}} - i\frac{\hbar\Gamma}{2}|\tilde{\mathrm{e}}\rangle\langle\tilde{\mathrm{e}}| \quad , \tag{2.37}$$

$f_{\mathrm{sc}}(\theta,\phi)$ is the angular distribution of the scattered light, and $e^{ik_{\mathrm{L}}x\sin\theta\cos\phi}$ is the momentum-shift operator (projected along the x-axis) that describes the photon recoil of the atom as it returns to the ground state. Note that in writing down (2.37), we have assumed purely radiative damping. The non-Hermitian nature of this effective Hamiltonian accounts for the damping in the system, and causes the total population to decay; the ground-state creation term (the last term in (2.36)) returns the lost population to the ground state. We can then write out the equations for the density matrix elements $\tilde{\rho}_{ij}(x,x',t) := \langle x|\langle i|\tilde{\rho}|j\rangle|x'\rangle$ as

$$\begin{aligned}
\partial_t\tilde{\rho}_{\mathrm{gg}} &= -\frac{i}{\hbar}\left[\frac{p^2}{2m},\tilde{\rho}_{\mathrm{gg}}\right] - \frac{i\Omega}{2}\left(\cos k_{\mathrm{L}}x\tilde{\rho}_{\mathrm{eg}} - \tilde{\rho}_{\mathrm{ge}}\cos k_{\mathrm{L}}x\right) \\
&\qquad + \Gamma\int d\Omega f_{\mathrm{sc}}(\theta,\phi)e^{ik_{\mathrm{L}}x\sin\theta\cos\phi}\tilde{\rho}_{\mathrm{ee}}e^{-ik_{\mathrm{L}}x\sin\theta\cos\phi} \\
\partial_t\tilde{\rho}_{\mathrm{ee}} &= -\frac{i}{\hbar}\left[\frac{p^2}{2m},\tilde{\rho}_{\mathrm{ee}}\right] + \frac{i\Omega}{2}\left(\cos k_{\mathrm{L}}x\tilde{\rho}_{\mathrm{eg}} - \tilde{\rho}_{\mathrm{ge}}\cos k_{\mathrm{L}}x\right) - \Gamma\tilde{\rho}_{\mathrm{ee}} \\
\partial_t\tilde{\rho}_{\mathrm{ge}} &= -\frac{i}{\hbar}\left[\frac{p^2}{2m},\tilde{\rho}_{\mathrm{ge}}\right] - \left(\frac{\Gamma}{2} + i\Delta_{\mathrm{L}}\right)\tilde{\rho}_{\mathrm{ge}} - \frac{i\Omega}{2}\left(\cos k_{\mathrm{L}}x\tilde{\rho}_{\mathrm{ee}} - \tilde{\rho}_{\mathrm{gg}}\cos k_{\mathrm{L}}x\right) \\
\partial_t\tilde{\rho}_{\mathrm{eg}} &= -\frac{i}{\hbar}\left[\frac{p^2}{2m},\tilde{\rho}_{\mathrm{eg}}\right] - \left(\frac{\Gamma}{2} - i\Delta_{\mathrm{L}}\right)\tilde{\rho}_{\mathrm{eg}} - \frac{i\Omega}{2}\left(\cos k_{\mathrm{L}}x\tilde{\rho}_{\mathrm{gg}} - \tilde{\rho}_{\mathrm{ee}}\cos k_{\mathrm{L}}x\right) \quad .
\end{aligned} \tag{2.38}$$

We again assume that $\Delta_{\mathrm{L}} \gg \Gamma$ and note that the equations have fast internal driving terms (with frequencies comparable to or greater than Γ) and slow center-of-mass terms; this time, however, the equations of motion for the coherences (which are responsible for the population oscillations) have explicit damping terms. Since we are interested in the slow external motion, we can use the fact that the steady-state solution for $\tilde{\rho}_{\mathrm{ee}}$ is of order $(\Gamma/\Delta_{\mathrm{L}})^2$, whereas the steady state solutions for the coherences $\tilde{\rho}_{\mathrm{eg}}$ and $\tilde{\rho}_{\mathrm{ge}}$ are of order $\Gamma/\Delta_{\mathrm{L}}$ [222], so that we can neglect the $\tilde{\rho}_{\mathrm{ee}}$ terms on the right-hand sides of these equations. Now, we will assume that the quickly rotating coherences are damped to equilibrium on a time scale short compared to the external motion of interest, and hence set $\partial_t\tilde{\rho}_{\mathrm{ge}} = \partial_t\tilde{\rho}_{\mathrm{eg}} = 0$. Doing so leads to the adiabatic relations

$$\begin{aligned} \tilde{\rho}_{\mathrm{ge}} &= \frac{\Omega}{2\Delta_{\mathrm{L}}}\tilde{\rho}_{\mathrm{gg}} \cos k_{\mathrm{L}}x \\ \tilde{\rho}_{\mathrm{eg}} &= \frac{\Omega}{2\Delta_{\mathrm{L}}} \cos k_{\mathrm{L}}x \tilde{\rho}_{\mathrm{gg}} \ , \end{aligned} \tag{2.39}$$

where we have neglected the momentum and Γ terms in comparison to the Δ_{L} term. Substituting Eqs. (2.39) into the equation of motion for $\tilde{\rho}_{\mathrm{gg}}$ (and neglecting the $\tilde{\rho}_{\mathrm{ee}}$ term), we find

$$\partial_t\tilde{\rho}_{\mathrm{gg}} = -\frac{i}{\hbar}\left[\frac{p^2}{2m} + \frac{\hbar\Omega}{4\Delta_{\mathrm{L}}}\cos^2 k_{\mathrm{L}}x, \tilde{\rho}_{\mathrm{gg}}\right] \ . \tag{2.40}$$

This equation is simply the equation of motion for $\tilde{\rho}_{\mathrm{gg}}$ under the Hamiltonian

$$H_{\tilde{\rho}} = \frac{p^2}{2m} + \frac{\hbar\Omega^2}{4\Delta_{\mathrm{L}}}\cos^2 k_{\mathrm{L}}x \ , \tag{2.41}$$

which is equivalent to the Hamiltonian (2.34) when the zero-point of the potential is shifted. Notice that this adiabatic-elimination procedure is similar to the one commonly used to study laser cooling and trapping, where the excited state is eliminated, but spontaneous emission is not ignored; this procedure leads to a Fokker-Planck equation of motion for the atomic distribution [226].

From this approach, it is clear that the adiabatic approximation is good after a time on the order of $1/\Gamma$, when the coherences have damped away. After this initial transient, the adiabatic approximation remains good as long as any modulations of the standing wave take place over a time long compared to $1/\Omega_{\mathrm{gen}}$. This is clear from the dressed-state result (2.26), because such modulations will not excite transitions between the dressed states and thus cause the adiabatic approximation to break down. This argument thus sets limits on experiments where the lattice is pulsed, as in the atom-optical realization of the kicked rotor problem in Chapter 4.

2.5 Complications

Until this point we have argued that in the limit of large detuning Δ_{L} (compared to both the maximum Rabi frequency Ω and the atomic lifetime Γ), the motion of an atom in a standing wave of light is equivalent to a point particle moving conservatively in a sinusoidal potential. In this section we will discuss several ways in which the real atomic system differs from this idealized description.

2.5.1 Spontaneous Emission

In the parameter regime that we have discussed above, it is possible to use the results we have derived so far to estimate the rate of spontaneous emission due to the far-detuned light. From the form of the master equation (2.38), we see that the total rate of spontaneous emission is simply the product of the decay rate Γ and the excited-state population $\tilde{\rho}_{\mathrm{ee}} = |\psi_{\mathrm{e}}|^2$ (integrated over position). From Eq. (2.30), we have, after ignoring the momentum term,

$$|\psi_{\mathrm{e}}|^2 = \frac{\Omega^2}{4\Delta_{\mathrm{L}}^2} \cos^2 k_{\mathrm{L}} x |\psi_{\mathrm{g}}|^2 \ . \tag{2.42}$$

Performing a spatial average and using $|\psi_{\mathrm{g}}|^2 \simeq 1$, we find the scattering rate

$$R_{\mathrm{sc}} = \frac{\Gamma\Omega^2}{8\Delta_{\mathrm{L}}^2} \ . \tag{2.43}$$

A more careful treatment of the spontaneous emission rate yields (see Appendix A)

$$R_{\mathrm{sc}} = \frac{(\Gamma/2)\Omega^2 \cos^2 k_{\mathrm{L}} x}{2(\Delta_{\mathrm{L}}^2 + \Gamma^2/4) + \Omega^2 \cos^2 k_{\mathrm{L}} x} \ . \tag{2.44}$$

The momentum recoils from the emitted photons results in atomic momentum diffusion at the rate

$$D_{\mathrm{se}} = \frac{\hbar^2 k_{\mathrm{L}}^2 \Gamma \zeta^2}{4m} \frac{\Omega^2 \cos^2 k_{\mathrm{L}} x}{2(\Delta_{\mathrm{L}}^2 + \Gamma^2/4) + \Omega^2 \cos^2 k_{\mathrm{L}} x} \ , \tag{2.45}$$

where the kinetic energy diffusion coefficient D is defined such that $\langle p_x^2/(2m) \rangle$ grows asymptotically as Dt. Also, ζ^2 is the mean-square projection of the photon recoil along the direction of the standing wave (for radiation from a pure linearly oscillating dipole, $\zeta^2 = 2/5$; for light near the D_2 line of cesium, where the ground-state sublevels in either the $F_{\mathrm{g}} = 3$ or the $F_{\mathrm{g}} = 4$ manifold are uniformly populated, and the detuning Δ_{L} is large compared to the excited state hyperfine splittings, $\zeta^2 \approx 0.34$).

2.5.2 Stochastic Dipole Force

The dipole force on the atoms in the standing wave can also lead to momentum diffusion. The dipole moment of the atom fluctuates due to spontaneous emission, and this fluctuating dipole interacts with the field gradients in the standing wave to produce momentum diffusion at a rate [227, 228]

$$\begin{aligned} D_{\mathrm{sdf}} = {} & \frac{\hbar^2 k_{\mathrm{L}}^2 \Gamma}{2m} \frac{\Omega^2 \sin^2 k_{\mathrm{L}} x}{[2(\Delta_{\mathrm{L}}^2 + \Gamma^2/4) + \Omega^2 \cos^2 k_{\mathrm{L}} x]^3} \\ & \times \left[2\left(\Delta_{\mathrm{L}}^2 + \frac{\Gamma^2}{4}\right)^2 + \left(\frac{3}{4}\Gamma^2 - \Delta_{\mathrm{L}}^2\right) \Omega^2 \cos^2 k_{\mathrm{L}} x + \frac{3}{2} \Omega^4 \cos^4 k_{\mathrm{L}} x + \frac{\Omega^6}{\Gamma^2} \cos^6 k_{\mathrm{L}} x \right] \ . \end{aligned} \tag{2.46}$$

In writing down the diffusion rates (2.45) and (2.46), we have assumed nearly zero atomic velocity and ignored the velocity dependences of the diffusion rates [228].

2.5.3 Nonlinearities of the Potential

In Section 2.3, we saw how the center-of-mass potential

$$V(x) = \frac{\hbar \Omega^2}{8 \Delta_{\mathrm{L}}} \cos 2 k_{\mathrm{L}} x \tag{2.47}$$

arises from the energy shift of the dressed states (to lowest order in Ω^2) and the assumption that the atom is in only one dressed state. Here we describe the corrections to this potential due to the nonlinear dependence of the dressed-state energies on Ω^2 as well as the mixed steady-state populations of the dressed states. The potential obtained from the optical Bloch equations is [220, 227, 228]

$$V(x) = \frac{\hbar\Delta_{\mathrm{L}}}{2}\log\left(1 + \frac{\Omega^2}{2(\Delta_{\mathrm{L}}^2 + \Gamma^2/4)}\cos^2 k_{\mathrm{L}}x\right) \ . \tag{2.48}$$

Since we are primarily interested in the limit where Δ_{L} is large compared to both Γ and Ω, we can extract the first few Fourier components of (2.48),

$$V(x) = V_{02}\cos(2k_{\mathrm{L}}x) + V_{04}\cos(4k_{\mathrm{L}}x) + V_{06}\cos(6k_{\mathrm{L}}x) + \dots \ , \tag{2.49}$$

where, if we define the (maximum) saturation parameter s as

$$s := \frac{\Omega^2}{2(\Delta_{\mathrm{L}}^2 + \Gamma^2/4)} \ , \tag{2.50}$$

we find

$$\begin{aligned}
V_{02} &= (\hbar\Delta_{\mathrm{L}}/2)[2 + 4\left(1 - \sqrt{1+s}\right)/s] \\
V_{04} &= (\hbar\Delta_{\mathrm{L}}/2)[-(8 + 8s + s^2) + 4(2 + 3s + s^2)/\sqrt{1+s}]/s^2 \\
V_{06} &= (\hbar\Delta_{\mathrm{L}}/2)[2(32 + 48s + 18s^2 + s^3) \\
&\qquad\qquad - 4(16 + 32s + 19s^2 + 3s^3)/\sqrt{1+s}]/(3s^3) \ .
\end{aligned} \tag{2.51}$$

For small s, these become

$$\begin{aligned}
V_{02} &= \frac{\hbar\Delta_{\mathrm{L}}}{2}\left[\frac{1}{2}s - \frac{1}{4}s^2 + \frac{5}{32}s^3 - \frac{7}{64}s^4 + O(s^5)\right] \\
V_{04} &= \frac{\hbar\Delta_{\mathrm{L}}}{2}\left[-\frac{1}{16}s^2 + \frac{1}{16}s^3 - \frac{7}{128}s^4 + O(s^5)\right] \\
V_{06} &= \frac{\hbar\Delta_{\mathrm{L}}}{2}\left[\frac{1}{96}s^3 - \frac{1}{64}s^4 + O(s^5)\right] \ .
\end{aligned} \tag{2.52}$$

Hence, the corrected potential to order Ω^4 is

$$V(x) = \left(\frac{\hbar\Omega^2}{8\Delta_{\mathrm{L}}} - \frac{\hbar\Omega^4}{32\Delta_{\mathrm{L}}^3}\right)\cos 2k_{\mathrm{L}}x - \frac{\hbar\Omega^4}{128\Delta_{\mathrm{L}}^3}\cos 4k_{\mathrm{L}}x + O\left(\frac{\Omega^6}{\Delta^5}\right) \ , \tag{2.53}$$

where we have ignored the Γ dependence in s. The Stark shift is due to stimulated Raman and Rayleigh transitions among the motional states of the atom induced by the field; since these corrections are higher order in Ω^2, we can associate them with higher-order photon processes.

2.5.4 Velocity Dependence

In addition to diffusive effects and the saturation of the light-induced potential, there are velocity-dependent forces associated with motion in the standing wave. If we assume small velocities ($k_{\mathrm{L}} v \ll \Gamma$), then diabatic transitions between the dressed states are negligible, and the force to lowest order in v_x is [220, 227–229]

$$\mathbf{F_v} = v_x \hat{x} 2\hbar\Delta_{\mathrm{L}} k_{\mathrm{L}}^2 \sin^2 k_{\mathrm{L}}x \frac{\Gamma^2\Omega^2[2(\Delta_{\mathrm{L}}^2 + \Gamma/4) - \Omega^2\cos^2 k_{\mathrm{L}}x] - \Omega^6 \cos^4 k_{\mathrm{L}}x}{\Gamma[2(\Delta_{\mathrm{L}}^2 + \Gamma^2/4) + \Omega^2 \cos^2 k_{\mathrm{L}}x]^3} \quad . \quad (2.54)$$

For small Ω^2, this force can be understood in terms of optical molasses, where Doppler shifts cause an imbalance of spontaneous scattering between the two beams (leading to a cooling force for red detunings) [229]. For larger Ω^2, when the last term in (2.54) is dominant, this force can be understood in terms of the local steady-state dressed-level populations lagging behind the atomic position [220]; furthermore, in this regime, the sign of the force is opposite to the weak-field case, so that a red detuning actually leads to a heating force.

2.5.5 Multilevel Structure of Cesium

The results that we have derived in this chapter have assumed a two-level electronic structure of the atom. The cesium D_2 line, however, is far more complicated than a two-level atom as a result of hyperfine structure (Appendix A). The ground state is split into two hyperfine levels, $F = 3$ and $F = 4$ (where F is the hyperfine quantum number), which are separated by 9.2 GHz. Each of these levels additionally has $2F + 1$ magnetic sublevels (which are degenerate in the absence of fields), labeled by the quantum number m_F. The excited state is split into four sublevels, $F = 2$, 3, 4, and 5, with splittings between adjacent levels around 200 MHz, each with a corresponding set of magnetic sublevels.

From this proliferation of states it is not at all obvious that the two-level model is appropriate. The first important step in simplifying this structure is that the atoms should be initially optically pumped into one of the ground state levels (but not necessarily into only one magnetic sublevel). Then the atoms are only coupled to three of the excited states due to angular momentum conservation (i.e., $F' = 2$, 3, or 4 are excited for atoms pumped into the $F = 3$ ground state manifold, and $F = 4$ atoms can be excited to $F' = 3$, 4, or 5). In the limit where the detuning Δ_{L} is large compared to the excited-state hyperfine splittings, the excited states can be regarded as degenerate. In this limit, and for a linearly polarized standing wave, a symmetry then applies, which makes the dipole moment independent of m_F, and it has the value 2.2×10^{-29} C · m (see Appendix A for details).

The detuning is not arbitrarily large, however, with the consequence that the effective lattice potential depth V_0 depends slightly on m_F [230]. This effect can be accounted for by explicitly summing over the excited states to arrive at an effective dipole moment for each sublevel:

$$\frac{d_{\mathrm{eff}}^2(m_F)}{\Delta_{\mathrm{L}}} = \sum_{F'} \frac{|\langle F\ m_F|d_z|F'\ m_F\rangle|^2}{\Delta_{F'}} \quad . \tag{2.55}$$

Here, $\Delta_{F'}$ is the laser detuning from the $|F\ m_F\rangle \longrightarrow |F'\ m_F\rangle$ transition, and Δ_{L} is now the detuning with respect to an arbitrary reference point (since it drops out of the calculation of V_0). This dipole moment can then be used within the context of the two-level atom model.

2.5.6 Collisions

With experiments performed in a MOT, one obvious deviation from the single-atom picture is due to collisions between the atoms in the MOT cloud. We can give very rough estimates for the collision rate for the experimental conditions in a cesium MOT. The s-wave collision cross section for cesium atoms polarized in the $F = 4$, $m_F = 4$ state was measured to be 5×10^{-11} cm^2 at a temperature of 5 μK in [231]. Note that this cross section actually overestimates the situation in the unpolarized case. For the experiments in Chapter 4, the MOT density was 10^{11} cm^{-3}, and the mean velocity was around 3 cm/s for the initial condition. These values lead to an estimated collision probability of only 2%/ms. For the experiments in Chapter 6, the MOT density was much lower, around 10^8 cm^{-3}, as a result of velocity selection. After state preparation, the initial mean velocity was 0.8 cm/s, and thus the collision probability in this case was the much smaller 0.4%/s.

2.5.7 Experimental Values

To illustrate the magnitudes of the effects that we have discussed in this section, we calculate the values of these corrections (shown in Table 2.1) for several different sets

Table 2.1: Numerical values for the various effects described in Section 2.5. The three columns correspond to the three different experimental parameter regimes described in the text.

Parameter set	**Kicked Rotor**	**Tunneling**(1)	**Tunneling**(2)
R_{sc}(3)	$1.1\%/t_{\mathrm{p}}$(4)	$0.040\%/T$(5)	$0.010\%/\mu\mathrm{s}$
D_{sc}(6)	$0.0039\,\hbar\omega_{\mathrm{r}}/t_{\mathrm{p}}$	$1.3\times10^{-4}\,\hbar\omega_{\mathrm{r}}/T$	$3.5\times10^{-5}\,\hbar\omega_{\mathrm{r}}/\mu\mathrm{s}$
D_{sdf}(7)	$0.012\,\hbar\omega_{\mathrm{r}}/t_{\mathrm{p}}$	$4.0\times10^{-4}\,\hbar\omega_{\mathrm{r}}/T$	$1.0\times10^{-4}\,\hbar\omega_{\mathrm{r}}/\mu\mathrm{s}$
$\lvert(V_{02}-V_0)/V_0\rvert$(8)	0.23%	1.2×10^{-6}	6.3×10^{-6}
$\lvert V_{04}/V_0\rvert$(9)	0.058%	3.0×10^{-7}	1.6×10^{-6}
F_v(10)	$5.3\times10^{-8}\,\hbar k_{\mathrm{L}}/t_{\mathrm{p}}$	$-1.0\times10^{-11}\,\hbar k_{\mathrm{L}}/T$	$-2.7\times10^{-12}\,\hbar k_{\mathrm{L}}/\mu\mathrm{s}$
$\lvert\Delta V_0(m_F)/V_0(0)\rvert$(11)	1.6%	0.11%	0.11%
Collision rate	$\sim0.04\%/T$(12)	$\sim8\times10^{-8}/T$	$\sim4\times10^{-9}/\mu\mathrm{s}$

---

(1) Modulated standing wave interaction portion of the chaos-assisted tunneling experiment.
(2) State-preparation portion of the chaos-assisted tunneling experiment.
(3) Spontaneous emission rate, averaged over a lattice period.
(4) The pulse width $t_{\mathrm{p}} = 300$ ns is the relevant time scale for the kicked-rotor experiment.
(5) $T = 20\ \mu$s is a typical relevant time scale for the chaos-assisted tunneling experiment.
(6) Rate of diffusion due to spontaneous emission, averaged over a lattice period.
(7) Rate of diffusion due to stochastic dipole fluctuations, averaged over a lattice period.
(8) Correction to potential amplitude (relative to V_0).
(9) Amplitude of second harmonic potential component (relative to V_0).
(10) Velocity-dependent force, averaged over a lattice period for the recoil velocity ($v_{\mathrm{r}} = 3.5$ mm/s).
(11) Largest relative magnetic sublevel shift of V_0, normalized to the value for $m_F = 0$.
(12) The relevant time scale for this process is the $T = 20\ \mu$s period of the potential.

of experimental parameters. The first set of parameters corresponds to the experiments in Chapter 4, where the optical lattice was pulsed to realize the kicked rotor. In these experiments, the lattice was pulsed on for $t_{\mathrm{p}} = 300$ ns at a time; the maximum intensity used corresponds to a Rabi frequency of $\Omega/2\pi = 590$ MHz, and the lattice detuning was -6.1 GHz from the $F = 4 \longrightarrow F' = 5$ transition. The second set of parameters describes the chaos-assisted tunneling experiments of Chapter 6, where the lattice amplitude was modulated as a $\cos^2$ function in time. A typical modulation period T here was 20 μs, the detuning was $\Delta_{\mathrm{L}}/2\pi = -50$ GHz and a typical (time-averaged) Rabi frequency used was $\Omega/2\pi = 110$ MHz. The third set of parameters also applies to the chaos-assisted tunneling experiments, but to the state-preparation phase where the atoms evolved in a somewhat deeper lattice ($\Omega/2\pi = 250$ MHz), but shorter time scales apply, since the atoms evolved in the full lattice for 6 μs (and for an additional 300 μs as the lattice was gradually ramped up from zero intensity). The design of an experiment necessarily entails many compromises, but we were able to keep the effects discussed here to a very acceptable minimum.

2.6 Generalization to Two Nonidentical Traveling Waves

We now generalize the results derived so far to the case where the two traveling waves have different amplitudes and frequencies. In this case, the electric field is

$$\begin{aligned}
\mathbf{E}(x,t) &= \hat{z}[E_{01}\cos(k_{\mathrm{L1}}x - \omega_{\mathrm{L1}}t) + E_{02}\cos(k_{\mathrm{L2}}x + \omega_{\mathrm{L2}}t)] \\
&= \hat{z}\Big(E_{01}\, e^{i(k_{\mathrm{L1}}x - \delta_{\mathrm{L}}t/2)} + E_{02}\, e^{-i(k_{\mathrm{L2}}x - \delta_{\mathrm{L}}t/2)}\Big) e^{-i\omega_{\mathrm{L}}t} + \text{c.c.} \\
&=: \mathbf{E}^{(-)}(x,t) + \text{c.c.} \ ,
\end{aligned} \tag{2.56}$$

where $\omega_{\mathrm{L}} := (\omega_{\mathrm{L1}} + \omega_{\mathrm{L2}})/2$ is the mean laser frequency, $\delta_{\mathrm{L}} := \omega_{\mathrm{L1}} - \omega_{\mathrm{L2}}$ is the frequency splitting between the two traveling waves, and we assume that $|\delta_{\mathrm{L}}| \ll |\Delta_{\mathrm{L}}|$, with $\Delta_{\mathrm{L}} := \omega_{\mathrm{L}} - \omega_0$. Then, in the rotating-wave approximation, the interaction Hamiltonian becomes

$$\begin{aligned}
\tilde{H}_{\mathrm{AF}} &= -\tilde{\mathbf{d}}^{(+)} \cdot \tilde{\mathbf{E}}^{(+)} - \tilde{\mathbf{d}}^{(-)} \cdot \tilde{\mathbf{E}}^{(-)} \\
&= \frac{\hbar}{2}\Big(\Omega(x,t)a^{\dagger} + \Omega^{*}(x,t)a\Big) \ ,
\end{aligned} \tag{2.57}$$

where $\tilde{\mathbf{d}}$ and $\tilde{\mathbf{E}}$ are defined as before, and the time- and space-dependent Rabi frequency is defined by

$$\Omega(x,t) := -\frac{\langle \mathrm{e}|d_z|\mathrm{g}\rangle}{\hbar}\left(E_{01}e^{i(k_{\mathrm{L}1}x-\delta_{\mathrm{L}}t/2)} + E_{02}e^{-i(k_{\mathrm{L}2}x-\delta_{\mathrm{L}}t/2)}\right) \quad . \tag{2.58}$$

Writing out the Schrödinger equation yields the two coupled equations

$$\begin{aligned} i\hbar\partial_t\psi_{\mathrm{e}} &= \frac{p^2}{2m}\psi_{\mathrm{e}} + \frac{\hbar}{2}\Omega(x,t)\psi_{\mathrm{g}} - \hbar\Delta_{\mathrm{L}}\psi_{\mathrm{e}} \\ i\hbar\partial_t\psi_{\mathrm{g}} &= \frac{p^2}{2m}\psi_{\mathrm{g}} + \frac{\hbar}{2}\Omega^*(x,t)\psi_{\mathrm{e}} \quad . \end{aligned} \tag{2.59}$$

Making the adiabatic approximation gives the relation

$$\hbar\Delta_{\mathrm{L}}\psi_{\mathrm{e}} = \frac{\hbar}{2}\Omega(x,t)\psi_{\mathrm{g}} \quad , \tag{2.60}$$

and hence yields the equation of motion for the ground-state amplitude,

$$i\hbar\partial_t\psi_{\mathrm{g}} = \left(\frac{p^2}{2m}\right)\psi_{\mathrm{g}} + \frac{\hbar}{4\Delta_{\mathrm{L}}}|\Omega(x,t)|^2\psi_{\mathrm{g}} \quad . \tag{2.61}$$

From Eq. (2.58), we find that

$$\begin{aligned} |\Omega(x,t)|^2 &= \frac{|\langle \mathrm{e}|d_z|\mathrm{g}\rangle|^2}{\hbar^2}\left|E_{01}e^{i(k_{\mathrm{L}1}x-\delta_{\mathrm{L}}t/2)} + E_{02}e^{-i(k_{\mathrm{L}2}x-\delta_{\mathrm{L}}t/2)}\right|^2 \\ &= \frac{|\langle \mathrm{e}|d_z|\mathrm{g}\rangle|^2}{\hbar^2}\Big[|E_{01}|^2 + |E_{02}|^2 + 2E_{01}E_{02}\cos(2k_{\mathrm{L}}x - \delta_{\mathrm{L}}t)\Big] \quad , \end{aligned} \tag{2.62}$$

where $k_{\mathrm{L}} := (k_{\mathrm{L1}} + k_{\mathrm{L2}})/2$. Hence, we see that the atom obeys the center-of-mass Schrödinger equation ($i\hbar\partial_t\psi_{\mathrm{g}} = H\psi_{\mathrm{g}}$), where the Hamiltonian, after a potential offset has been subtracted, is given by

$$H = \frac{p^2}{2m} + V_0\cos(2k_{\mathrm{L}}x - \delta_{\mathrm{L}}t) \quad , \tag{2.63}$$

and

$$V_0 = \frac{|\langle \mathrm{e}|d_z|\mathrm{g}\rangle|^2 E_{01}E_{02}}{2\hbar\Delta_{\mathrm{L}}} \quad . \tag{2.64}$$

Thus, the motion is the same as before, except that the standing wave moves with velocity $\delta_{\mathrm{L}}/2k_{\mathrm{L}}$, and the potential depth is proportional to the geometric mean of the two traveling wave intensities. The velocity associated with the frequency difference is intuitive, as in a frame of reference moving with respect to an optical lattice, the two beams would be Doppler shifted in opposite senses, and would thus appear to have different frequencies.

2.7 Quantum Dynamics in a Stationary Standing Wave

Now that we have derived the equations of motion for an atom in an optical lattice, we will give an introduction to some aspects of the dynamics in the lattice that will be important in later chapters. Before continuing, though it is worth providing a set of scaled units in which to work. In order to simplify the Hamiltonian (2.34), we begin by noting that we have the freedom to independently rescale the coordinates to eliminate redundant parameters. There is a natural choice for the position scaling,

$$x' = 2k_{\mathrm{L}}x, \tag{2.65}$$

since the natural length scale is the $\lambda/2$ period of the standing-wave potential. In the pendulum, there is no explicit time scale that must be eliminated, so we are free to rescale such that Planck's constant is effectively unity. Thus, demanding that $[x', p'] = i$, we find that

$$p' = \frac{p}{2\hbar k_{\mathrm{L}}} \ . \tag{2.66}$$

Using these scalings in the unscaled Hamiltonian (2.34), we find

$$H' = \frac{p'^2}{2} + \alpha_{\mathrm{p}} \cos x' \tag{2.67}$$

upon identifying $8\hbar\omega_{\mathrm{r}}$ as the natural energy scale (recall that $\omega_{\mathrm{r}} = \hbar k_{\mathrm{L}}^2/2m$), so that $\alpha_{\mathrm{p}} = V_0/(8\hbar\omega_{\mathrm{r}})$ and $H' = H/(8\hbar\omega_{\mathrm{r}})$. Notice that this energy scaling implies a time scaling of $t' = 8\omega_{\mathrm{r}}t$, since we have already determined how action is scaled. In what follows we will drop the primes on the scaled units, and on occasion we will use unscaled units to emphasize particular points.

2.7.1 Bragg Scattering

The quantum-pendulum dynamics show a feature that is distinctly nonclassical: the momentum transferred from the potential to the atoms is quantized. To see this directly, we consider the Schrödinger equation in scaled units,

$$i\partial_t|\psi\rangle = \left(\frac{p^2}{2} + \alpha_{\mathrm{p}}\cos x\right)|\psi\rangle \ . \tag{2.68}$$

In the momentum representation, where $\psi(p) := \langle p|\psi\rangle$, the Schrödinger equation can be rewritten as

$$i\partial_t\psi(p) = \frac{p^2}{2}\psi(p) + \frac{\alpha_{\mathrm{p}}}{2}\left[\psi(p+1) + \psi(p-1)\right] \ . \tag{2.69}$$

This form follows from either recognizing $\exp(ikx)$ as a momentum-displacement operator, or by carrying out an explicit Fourier transform of the equation from the position to the momentum representation. So, the evolution in the standing wave imposes a "ladder" structure in momentum, such that an atom beginning in a plane-wave state $|p\rangle$ can only subsequently occupy the states $|p+n\rangle$ for integer n. In unscaled units, the quantization of the momentum is in multiples of $2\hbar k_{\mathrm{L}}$, which has a clear interpretation in terms of the stimulated scattering of lattice photons: if the atom absorbs a photon that was traveling in one direction and then re-emits it into the counterpropagating mode, the atom will recoil, changing its momentum by twice the photon momentum, or by $2\hbar k_{\mathrm{L}}$. Of course, the argument that we just considered was based on a classical treatment of the field, so it is the spatial periodicity of the potential that imposes the ladder structure in this model. However, as we will see in Chapter 5, the momentum transfer to the atoms can be viewed as a stimulated Raman transition between different motional states (say, $|p\rangle$ and $|p+1\rangle$). The coupling between these two levels is described by a Raman Rabi frequency (as in the two-level atom), given by

$$\Omega_{\mathrm{R}} = \frac{\Omega_1\Omega_2}{2\Delta_{\mathrm{L}}} \ , \tag{2.70}$$

where $\Omega_{1,2}$ are the Rabi frequencies associated separately with each traveling-wave component of the standing wave, and Δ_{L} is the mutual detuning to the atomic excited state (the relative frequency difference is constrained by energy conservation to be the splitting between the motional states). To connect with the notation that we have already used, $\Omega_1 = \Omega_2 = \Omega/2$ for the case of identical traveling waves, so that $\hbar\Omega_\mathrm{R} = V_0$, and thus V_0 also represents the strength of the Raman couplings.

The two-photon, stimulated Raman transition is an example of a *Bragg scattering* process [232–234]. In fact, it is the simplest ("first-order") form of Bragg scattering; in general, nth-order Bragg scattering is a $2n$-photon transition spanning an interval of $2n\hbar k_\mathrm{L}$ in momentum. The term "Bragg scattering" applies to the weakly coupled regime, where the intermediate states are not appreciably populated, and so the transition between the two distant momentum states can be treated as a two-level problem. In this regime, classical transport between these distinct momentum regions is forbidden, as the classical potential is not sufficiently strong to cause a correspondingly large change in the classical momentum. As such, Bragg scattering is an example of *dynamical tunneling*, which is quantum tunneling between regions in phase space between which classical transport is forbidden, but by the dynamics (here, the nature of asymptotically free-particle motion) rather than by a potential barrier.

Although the potential has a small amplitude, quantum coherence can build up

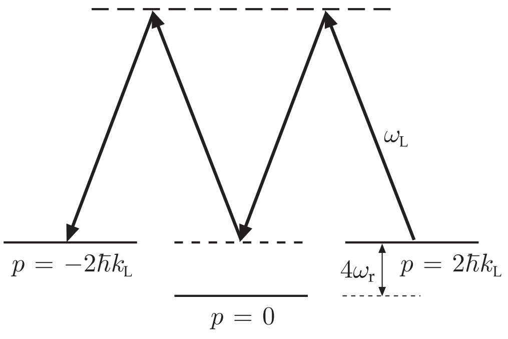

Figure 2.1: Level diagram for second-order Bragg scattering. This process occurs as a pair of two-photon Raman scattering processes, coupling the $2\hbar k_\mathrm{L}$ momentum level to the $-2\hbar k_\mathrm{L}$ level. The Bragg treatment is valid when the two-photon Rabi frequency Ω_R is small compared to the detuning $4\omega_\mathrm{r}$ from the intermediate state, which can then be adiabatically eliminated from the problem.

as the atoms sample the potential and cause the atoms to significantly change their motion. We will illustrate this process by considering the relatively simple case of second-order Bragg scattering, and then we will generalize our results to the nth-order case. We consider the case where the standing wave is stationary, so that only the states $|-2\hbar k_{\mathrm{L}}\rangle$ and $|2\hbar k_{\mathrm{L}}\rangle$ are resonantly coupled (we will stick to unscaled units for this derivation to emphasize the connection to the "quantum optics" view of the atomic motion) in the limit of small Ω_{R}. No other states will be substantially coupled by these fields, unless the Raman Rabi frequency is large enough to power-broaden the off-resonant transitions, which would not correspond to the Bragg regime. The relevant energy-level diagram is shown in Fig. 2.1, which shows that the detuning from the $|0\rangle$ motional state is simply the kinetic-energy shift. Neglecting couplings to other states (which are even further detuned than the $|0\rangle$ state), the Schrödinger equation for the three coupled momentum states then becomes

$$\begin{aligned} i\hbar\partial_t\psi(-2\hbar k_{\mathrm{L}},t) &= \frac{(2\hbar k_{\mathrm{L}})^2}{2m}\psi(-2\hbar k_{\mathrm{L}},t) + \frac{\hbar\Omega_{\mathrm{R}}}{2}\psi(0,t) \\ i\hbar\partial_t\psi(0,t) &= \frac{\hbar\Omega_{\mathrm{R}}}{2}[\psi(-2\hbar k_{\mathrm{L}},t)+\psi(2\hbar k_{\mathrm{L}},t)] \\ i\hbar\partial_t\psi(2\hbar k_{\mathrm{L}},t) &= \frac{(2\hbar k_{\mathrm{L}})^2}{2m}\psi(2\hbar k_{\mathrm{L}},t) + \frac{\hbar\Omega_{\mathrm{R}}}{2}\psi(0,t)\ . \end{aligned} \tag{2.71}$$

Adding an energy offset of $-4\hbar\omega_{\mathrm{r}}$, the equations become

$$\begin{aligned} i\hbar\partial_t\psi(\pm 2\hbar k_{\mathrm{L}},t) &= \frac{\hbar\Omega_{\mathrm{R}}}{2}\psi(0,t) \\ i\hbar\partial_t\psi(0,t) &= \frac{\hbar\Omega_{\mathrm{R}}}{2}[\psi(-2\hbar k_{\mathrm{L}},t)+\psi(2\hbar k_{\mathrm{L}},t)] - 4\hbar\omega_{\mathrm{r}}\psi(0,t)\ . \end{aligned} \tag{2.72}$$

Now we assume that $\Omega_{\mathrm{R}} \ll 4\omega_{\mathrm{r}}$, so that the population in the $|0\rangle$ state is $O(\Omega_{\mathrm{R}}^2/\omega_{\mathrm{r}}^2)$ and hence negligible. Additionally, we can make an adiabatic approximation for the evolution of the $|0\rangle$ state, by formally setting $\partial_t\psi(0,t)=0$, as we did in Section 2.4. Again, though, this is a shortcut for considering the density-matrix picture and replacing the rapidly-varying coherences with their locally average value (although this procedure is a result of coarse-graining here, rather than radiative damping as in the previous treatment). Doing so leads to the adiabatic relation

$$4\omega_{\mathrm{r}}\psi(0,t) = \frac{\Omega_{\mathrm{R}}}{2}[\psi(-2\hbar k_{\mathrm{L}},t) + \psi(2\hbar k_{\mathrm{L}},t)] \ , \tag{2.73}$$

which can be used to eliminate the intermediate state, resulting in a two-level evolution:

$$i\hbar\partial_t\psi(\pm 2\hbar k_{\mathrm{L}},t) = \frac{\hbar\Omega_{\mathrm{R}}^2}{16\omega_{\mathrm{r}}}[\psi(\pm 2\hbar k_{\mathrm{L}},t) + \psi(\mp 2\hbar k_{\mathrm{L}},t)] \ . \tag{2.74}$$

Hence the second-order Bragg Rabi frequency is $\Omega_{\mathrm{B},2} = \Omega_{\mathrm{R}}^2/8\omega_{\mathrm{r}}$. (The first term represents a Stark shift of $\Omega_{\mathrm{B},2}/2$, while the second term represents the Rabi-type coupling.) Comparing this expression to the form (2.70) for the two-photon Rabi frequency, we see that this second-order Bragg process can be viewed also as a Raman process of two Raman transitions, where the detuning to the intermediate state Δ_{L} is identified as $4\omega_{\mathrm{r}}$.

Continuing in this manner, the Bragg rate for nth-order scattering from $n\hbar k_{\mathrm{L}}$ to $-n\hbar k_{\mathrm{L}}$ is given by [233]

$$\Omega_{\mathrm{B},n} = \frac{\Omega_{\mathrm{R}}^n}{2^{n-1}\displaystyle\prod_{k=1}^{n-1}\delta_k} \ , \tag{2.75}$$

where δ_k is the detuning of the kth intermediate motional state. Notice that the intermediate detunings are given by $[n^2-(n-2)^2]\omega_{\mathrm{r}}$, $[n^2-(n-4)^2]\omega_{\mathrm{r}}$, …, $[n^2-(2-n)^2]\omega_{\mathrm{r}}$, so that this Bragg frequency can be written as

$$\Omega_{\mathrm{B},n} = \frac{\Omega_{\mathrm{R}}^n}{(8\omega_{\mathrm{r}})^{n-1}[(n-1)!]^2} \tag{2.76}$$

In scaled units, we can rewrite this frequency as

$$\Omega'_{\mathrm{B},n} = \frac{\alpha_{\mathrm{p}}^n}{[(n-1)!]^2} \ . \tag{2.77}$$

The transition frequency obviously becomes small for high-order Bragg processes, as the Rabi frequency decreases exponentially with the order. Nevertheless, Bragg oscillations of up to sixth [233] and eighth [235] order have been observed experimentally for an atomic beam crossing an optical standing wave.

2.7.2 Band Structure

As with any periodic potential, the eigenenergies for the atom in an optical lattice are grouped in bands, which are continuous intervals of allowed energies, separated by "band gaps" of forbidden energies. As this structure is relevant to some of the ex-

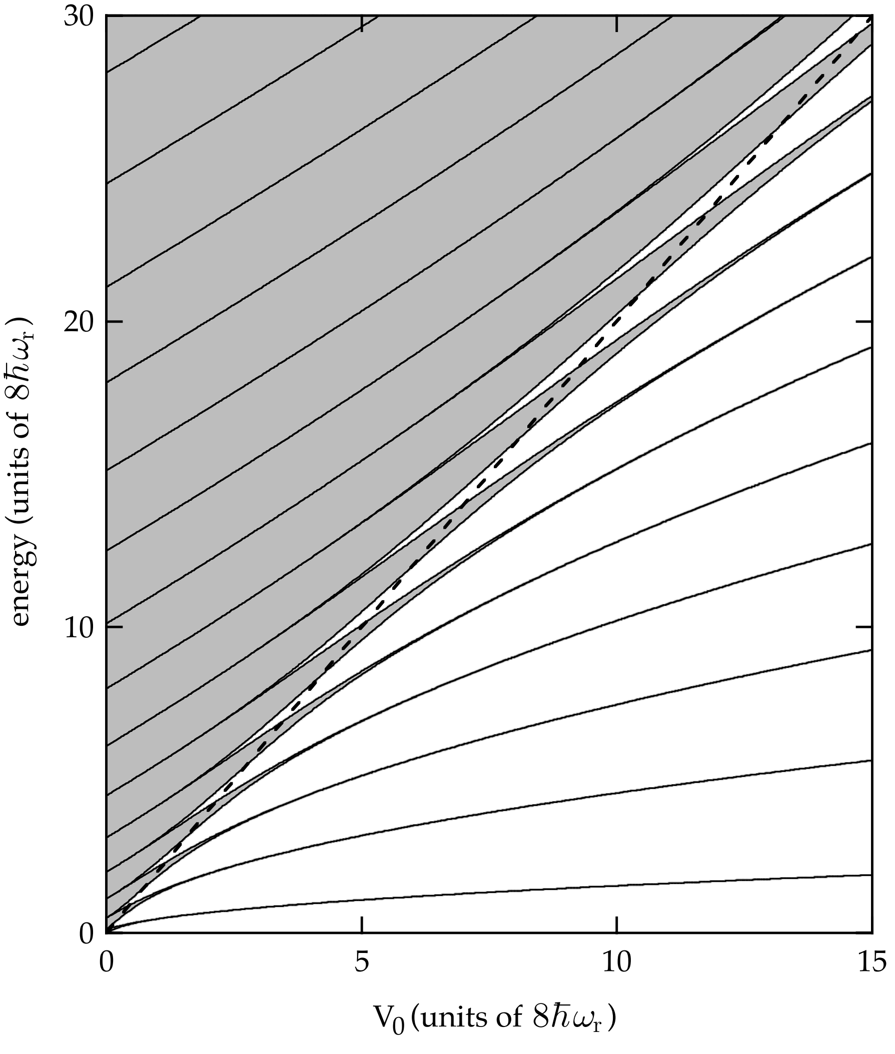

Figure 2.2: Plot of the allowed energy bands as a function of $V_0/8\hbar\omega_r$ (or equivalently α_p). The energies are also normalized to the natural unit scale $8\hbar\omega_r$, and are plotted relative to the potential minima. The shaded regions represent allowed energies, the solid lines represent the "edges" of the allowed bands, and the dashed line represents the energy of the peaks of the lattice.

periments performed in this dissertation, we will treat this subject briefly. From Floquet's theorem (or equivalently, Bloch's theorem), the spatial periodicity of the time-independent Schrödinger equation for an atom in an optical lattice,

$$\left(\frac{p^2}{2} + \alpha_{\rm p} \cos x\right) \psi = E\psi \ , \tag{2.78}$$

implies that the solutions will be plane waves modulated by a periodic function,

$$\psi_q = e^{iqx} u_q(x), \tag{2.79}$$

where $u_q(x + 2\pi) = u_q(x)$, and q is the "Floquet exponent" or "quasimomentum," which parameterizes the family of solutions. The eigenenergies and eigenfunctions can be computed using standard matrix-diagonalization methods to find solutions of the Mathieu equation [236–238]; the numerically calculated energy bands are plotted in Fig. 2.2 as a function of $\alpha_{\rm p}$. By convention, the quasimomentum is restricted to the

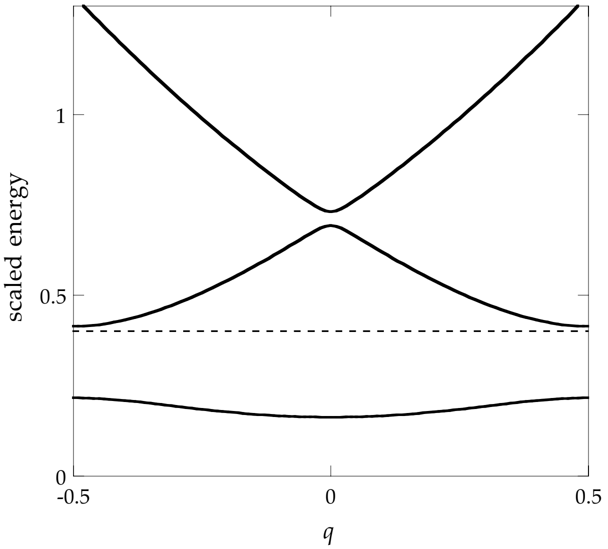

Figure 2.3: Plot of the lowest three energy bands for $\alpha_{\rm p} = V_0/8\hbar\omega_{\rm r} = 0.2$, where the band energy is plotted as a function of the quasimomentum q. This band structure is in the weakly coupled regime, where the lowest bands have significant curvature. The dashed line at the scaled energy of 0.4 marks the maximum potential energy of the lattice. The band gaps are a result of Bragg diffraction, which couples states with integer or half-integer quasimomentum and induces avoided crossings at these quasimomenta.

range $[-1/2, 1/2)$, and the integer part n of the full quasimomentum is called the "band index." Note that solutions with the same reduced quasimomentum q are similar in that they can be written in terms of plane-wave solutions with the same reduced quasimomentum:

$$\psi_{n,q} = \sum_{k=-\infty}^{\infty} c_{n,k} e^{i(k+q)x} \quad . \tag{2.80}$$

The energy bands are plotted as a function of the reduced quasimomentum for a small value of α_p in Fig. 2.3.

The band structure for small well depths can be understood in terms of Bragg scattering. In the free-particle case, the energy structure is that of a free particle, so that the energy is simply $q^2/2$, where we identify the quasimomentum with the real particle momentum. Bragg processes then couple certain degenerate pairs of the quasimomenta (the half-integer values), which are precisely the locations where the band gaps form. These band gaps can be viewed as avoided crossings of the energy as the quasimomentum varies. The avoided-crossing nature of the band gap is clear from the gaps plotted in Fig. 2.3, and the locations of the band gaps on the left edge of Fig. 2.2 are spaced according to n^2, as expected in the free-particle limit. As the bands make the transition to the deep-well limit (as in the right side of Fig. 2.2), they become narrow, as expected for trapped states. The band gaps becomes more uniform in size as well, as is expected for harmonic-oscillator states, which the lattice wave functions approach in the deep-well limit, when they only "see" the parabolic bottoms of the wells.

For our purposes there are two properties of the lattice wave functions that will be important. First, as long as the sinusoidal potential is the sole interaction potential for the atoms, the reduced quasimomentum is a constant of the motion, even if the lattice is temporally modulated. This property is simply a manifestation of the ladder structure that we already mentioned. The second property is that for slow changes of α_p, the band index is an adiabatic constant of the motion. This property is important in preparation of atomic states, because if the atoms can be cooled so that their momenta are within $(-\hbar k_\mathrm{L}, \hbar k_\mathrm{L})$ in free space, they will be loaded into the lowest energy band when the lattice is turned on adiabatically.

2.7.3 Boundary Conditions

Finally, we make a short comment on the nature of a “rotor” vs. a “particle,” and the relevance of these ideas to optical-lattice experiments. A pendulum in the usual sense has an angle as a coordinate, and the coordinate space is equivalent to a 1-torus. In an extended realization of the pendulum, as in the optical lattice, the coordinate space is extended and formally equivalent to a line. The identification of the two situations comes from the periodicity of the potential in the extended case. Classically, there is no problem making this identification, since one can always take the extended coordinate modulo the period of the potential. Quantum mechanically, however, the boundary conditions in the two cases can lead to drastically different energy-level structures. Specifically, the periodic boundary condition in the case of the rotor implies that the spectrum is discrete, because only the integer quasimomentum states exist. In other words, the periodic boundary conditions pick out an obviously special class of states (the $q = 0$ “symmetric ladder,” where each state is coupled to its degenerate partner via Bragg scattering) out of the possible continuum of ladders in the extended (particle) case. This difference has various consequences for atom-optics experiments, one of the most dramatic being that in Bragg scattering and chaos-assisted tunneling experiments, the transport only occurs for a relatively small set of states, which would naturally be selected in the case of a true rotor. In the case of dynamical localization as in Chapter 4, the localization still occurs in the particle case, although much of the theoretical analysis in the literature is for the rotor, which is obviously much simpler. Thus, despite this distinction, we will use the term “kicked rotor” to refer as well to the kicked particle.

Chapter 3

Experimental Apparatus I

3.1 Overview

Now we turn our attention to the experimental apparatus. In this chapter, we will confine our discussion to the basic parts of the apparatus that were necessary to carry out the experiments in Chapter 4. For the later experiments on chaos-assisted tunneling (Chapter 6), several major improvements were made to the apparatus, and these changes are discussed in Chapter 5.

The apparatus that we discuss here includes several parts. We begin by discussing the various laser systems involved in the experiment. Two diode lasers provided the light that trapped, cooled, and performed the measurements on the cesium atoms, and they are discussed separately in Sections 3.2 and 3.3. We will not discuss the general operation of a magneto-optic trap (MOT), as these traps have become quite commonplace (a nice discussion can be found in [169]); rather, we will give the specifics of our implementation and discuss how they impact the analysis of the experimental results. The optical lattice, which was the heart of the experiment, was provided by a home-built Ti:sapphire laser system, which is described in Section 3.4. For these experiments to work, the atoms had to be extremely well isolated from their surroundings, so they were trapped in an ultrahigh-vacuum system, detailed in 3.5. Finally, we discuss the experimental measurement procedure in Section 3.7 and the electronics needed to control the experiment in Section 3.8.

We will concentrate mostly on the salient features of the experiment, since much of the information in this chapter has already been covered in the dissertation of Bruce Klappauf [203].

3.2 DBR Laser

The basic operation of laser cooling in a MOT requires stabilized laser light tuned slightly to the red of an atomic transition. In the experiments here, we used the light from a distributed Bragg reflector (DBR) laser diode (model SDL-5712-H1, manufactured by SDL, Inc., which is no longer available as of the time of writing), which drove the $F = 4 \longrightarrow F' = 5$ hyperfine component of the cesium D_2 transition. The advantage of a DBR laser is that it incorporated a frequency-selective element that narrows its line width and causes it to lase near the desired wavelength (852 nm, in our case). The frequency of the laser is coarsely tuned by changing the diode temperature, and fine-tuning is achieved by adjusting the injection current. This particular laser nominally produced 100 mW of power with 180 mA of current, and incorporated a thermoelectric cooler and thermistor within the TO-3 package for convenient temperature stabilization.

3.2.1 Construction and Operation

The current and temperature controllers for the DBR laser were nuclear instrument module (NIM) style units that were designed and produced by Leo Hollberg's group at NIST-Boulder. These units worked extremely well, providing quiet current sources with reliable protection for the laser from electrical transients. The diode laser was also protected from electrical transients with several "protection diodes" in the cable connected to the laser diode, as suggested by [239]. The protection-diode circuit, placed only a few inches from the laser diode, comprised a fast 1N5711 diode connected across the laser diode, but in the opposite direction, to protect against reverse voltages; and four 1N914 diodes in series connected across and in the same direction as the laser diode, to protect against overvoltages. The DBR diode was mounted on a commercial, air-cooled heatsink mount (model SDL-800 heatsink, with a model SDL-800-H adaptor plate, both by SDL, Inc.). This mount was bolted to a stainless steel post, which was in turn clamped to the optical table. The laser light was collimated by an antireflection-coated lens, Rodenstock model 1403-.108-.020, which had a focal length of 5 mm and a numerical aperture of 0.5. The lens was originally mounted on a three-dimensional translation stage, for precise and flexible positioning. However, thermal creep in this setup necessitated a nearly daily adjustment of this lens to keep the beam line correctly aligned. To solve this problem, we implemented a method used in the ultracold atom group at the Laboratoire Kastler Brossel in Paris, illustrated in Fig. 3.1 (a photograph of the DBR laser assembly is also shown in Fig. 3.2). The lens, which came mounted in a cylindrical aluminum case, was bonded to the end of a rod using a small drop of five-minute epoxy. The rod was in turn attached to a rotation stage and then an x-y-z translation stage for precise positioning. The lens was then adjusted into the desired position over a V-grooved block that was attached directly to the laser diode heatsink mount. Two glass rods were then dropped gently onto the lens and V-groove, effectively filling in the space between them. This assembly was then bonded together by running beads of 24-hour epoxy using a syringe along the contact lines of the glass rods. After the epoxy was set, the bond for the positioning setup was broken. The setup (after the collimating lens) required minor adjustments for a few weeks as the bonds settled, but later the beam line became very stable, often remaining aligned for months without adjustment.

After collimation, the light was reshaped by an anamorphic prism pair (by Melles Griot) to be nearly circular, although the astigmatism of the beam required a cylindrical-lens telescope later in the beam line to maintain circularity. The beam then passed through two optical isolators (Conoptics, Inc. model 713), for 77 dB measured total isolation, because the DBR laser was especially sensitive to back reflections (compared to the grating-stabilized laser). This isolation came at a cost of 20% of the optical intensity. Another 10% of the light was split off for the saturated absorption setup used to frequency-lock the laser, as described below, leaving about 73 mW of power in the main beam. The beam was then double-passed through a tunable 60-100 MHz acousto-optic modulator (AOM), an IntraAction Corp. model ATD-801AL2. Since the laser was locked 195 MHz to the red of the $F = 4 \longrightarrow F' = 5$ "cycling" transition, the light after the double-pass setup could be tuned from -75 MHz to $+5$ MHz relative to the cycling transition. We used a detuning of -15 MHz for normal (loading) trap operation. This AOM also controlled the intensity of the trapping light. The beam was focused through a 25 μm pinhole to clean its spatial profile, leaving about 27 mW of power. The diverging beam after the pinhole was collimated, with a beam waist parameter $w_0 = 11$ mm, to ensure a uniform illumination of the atoms. This light was split with two 2" diameter beamsplitters (66% and 50%) into three beams of equal power. Each of these beams passed through a 1.5" diameter quarter-wave plate before entering the vacuum chamber that contained the MOT, to give the beams the appropriate circular polarization for proper MOT operation. The beams were retroreflected through another set of quarter-wave plates after they exited the chamber. This setup provided the usual six-beam $\sigma^+ - \sigma^-$ molasses configuration, and together with the anti-Helmholtz magnetic field coils (described below), provided the usual six-beam MOT configuration. A diagram of this beam line, along with the other two laser setups, is shown in Fig. 3.3.

3.2.2 Saturated Absorption Spectroscopy

The 10% of the beam that was picked off before the AOM was used to perform saturated absorption spectroscopy [239, 240] on the light for frequency stabilization. The thermal motions of cesium atoms in a vapor cell smear out the optical resonances, and the resulting Doppler line width [241] of cesium at room temperature is around 0.4 GHz. This width is much larger than the 5 MHz natural width of the cesium hyperfine resonances, and is even larger than the splittings between the excited hyperfine levels, so that these states cannot be resolved by simple absorption spectroscopy. The idea behind saturated absorption spectroscopy is that the atoms are illuminated by two counterpropagating beams of the same frequency (a "pump" and a "probe"), where the intensity of one of the beams (the probe) is monitored. The Doppler-broadened line will be apparent as usual, but at the resonance frequencies, the two beams will pick out the zero-velocity atoms, because only these atoms will be simultaneously pumped by both beams (for moving atoms, the two beams will be Doppler-shifted to two different frequencies). The spectral manifestation of this effect is that there are narrow "Lamb dips" in the Doppler-broadened background, because these atoms are more saturated at certain frequencies and thus are more transparent to the probe beam. The Lamb dips occur at the atomic hyperfine resonances and also at "crossover resonances," which occur halfway between pairs of hyperfine resonances (in these cases, the two beams pick out atoms moving such that the two Doppler-shifted beams excite two different hyperfine transitions, and thus still oversaturate the atoms). The widths of the Lamb dips are affected by many factors, including beam alignment, beam intensity, and cell pressure, but the width of the dips can be made comparable to the natural line width.

The saturated absorption spectrum thus provided high-resolution, frequency-

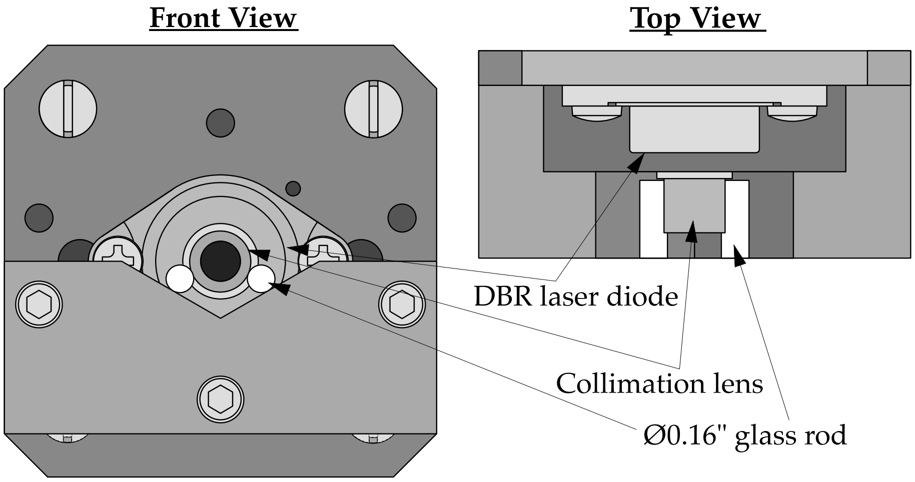

Figure 3.1: Diagram of DBR laser diode and collimation lens hardware. Only the front plate of the mounting heatsink is shown. A custom aluminum block with a V-groove was bolted to the front of the mounting plate. The collimation lens, which was mounted in a cylindrical aluminum housing, was held in place above the groove by two glass rods. The collimation lens, glass rods, and V-groove block were bonded together with 24-hour epoxy, resulting in a very stable configuration.

dependent spectral features by which the DBR laser frequency could be determined. In the sense of actively stabilizing the frequency of the laser, though, these dips are not so convenient, because it is necessary to lock to a sloping part of a spectral feature. It is possible to lock to the side of a Lamb dip, but then the laser frequency would be sensitive to the width of the dip, which could drift in time. A more convenient situation arises for a dispersive (as opposed to absorptive) line shape, where the maximum slope occurs at the center of the resonance. One way to obtain such a shape is through frequency-modulation (FM) spectroscopy [242]. In this technique the frequency of the laser light is modulated, and phase-sensitive detection produces the dispersive line shape. In our setup, the probe beam was modulated at 11 MHz using a Conoptics model 350-40 electro-optic phase modulator (EOM) before passing through a 75 mm long cesium vapor cell (made by Environmental Optical Sensors, Inc.), where it overlapped the

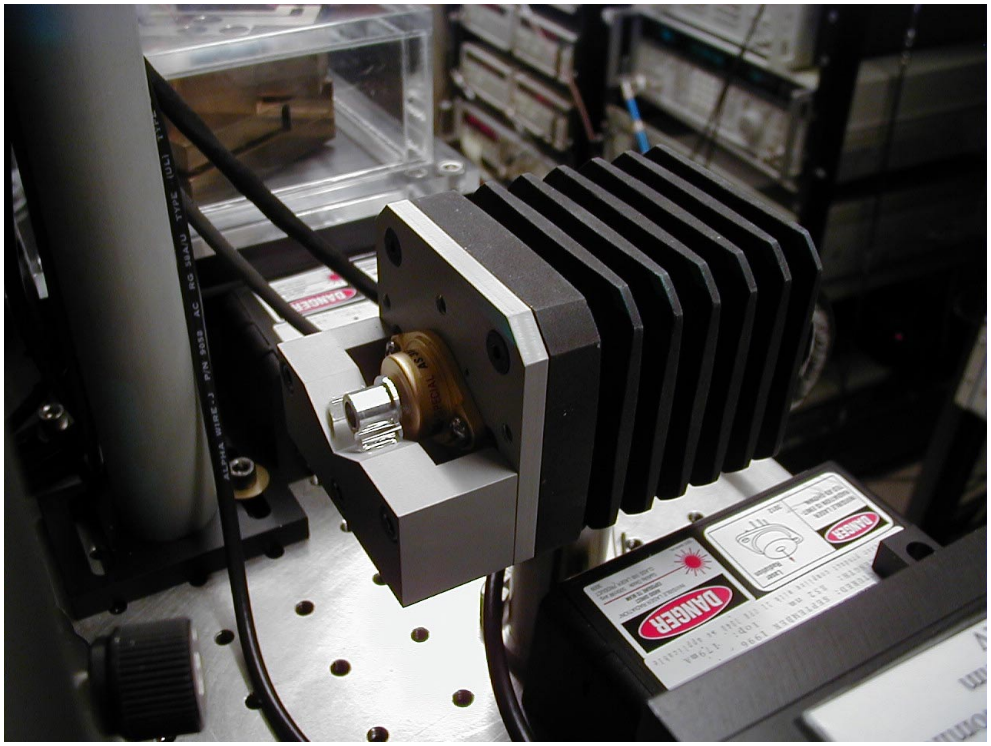

Figure 3.2: Photograph of the DBR laser, showing the laser itself inside the gold-toned TO-3 package, the mounting heatsink, and the collimation lens assembly.

counterpropagating pump beam. The probe was monitored with a New Focus model 1801 low-noise photodiode, and the photodiode signal was mixed with the phase-shifted signal that drove the EOM. Additionally, the pump beam was double-passed through a 70 MHz AOM, which was chopped on and off at 50 kHz. The mixed-down photodiode signal was then processed by a Stanford SR510 lock-in amplifier, with this chopping signal as the reference. The consequences (beyond the usual noise immunity of lock-in detection) of this pump-beam modulation were twofold: first, the spectrum was shifted to the red by 70 MHz, because the pump and probe beams were 140 MHz apart, and second, the Doppler contribution to the spectrum was suppressed, because only the Lamb dips (and not the Doppler-broadened absorption shape) were affected by the presence or absence of the pump beam. A spatial filter with a 75 μm pinhole placed in the input beam of this setup greatly enhanced the quality and reproducibility of the spectrum by

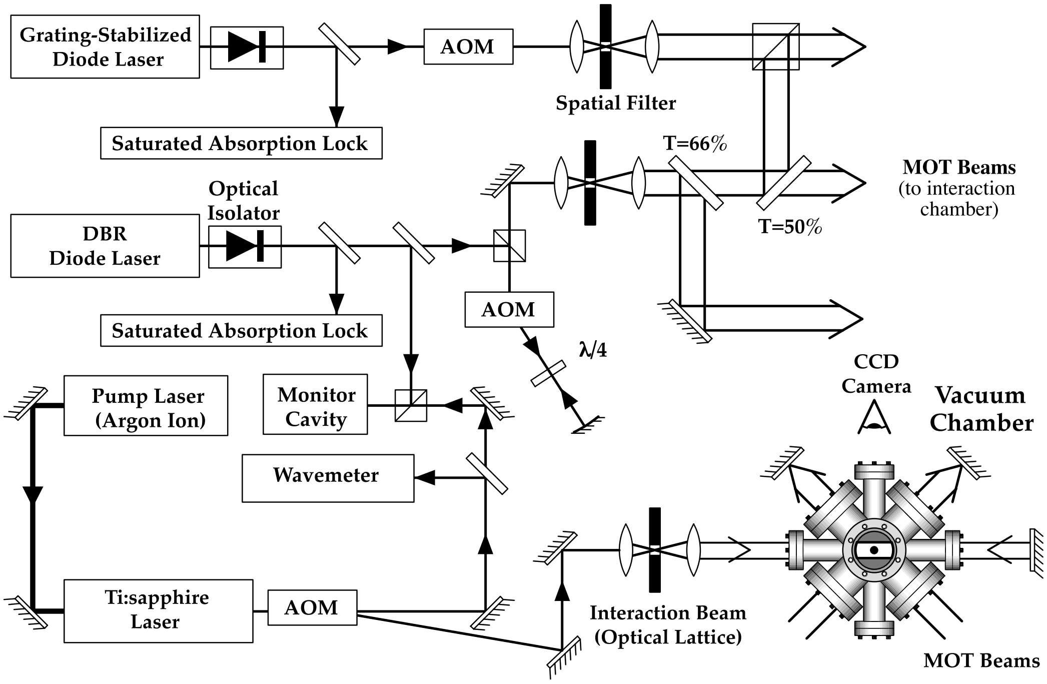
Grating-Stabilized Diode Laser
AOM
Spatial Filter
Saturated Absorption Lock
T=66%
MOT Beams
(to interaction chamber)
T=50%
Optical Isolator
DBR Diode Laser
AOM
Saturated Absorption Lock
λ/4
CCD Camera
Vacuum Chamber
Pump Laser (Argon Ion)
Monitor Cavity
Wavemeter
Ti:sapphire Laser
AOM
Interaction Beam (Optical Lattice)
MOT Beams

Figure 3.3: Layout of optical table, showing the schematic beam paths of the DBR diode laser (which provided the MOT trapping light), the external cavity diode laser (which provided the repumping light for the MOT), and the Ti:sapphire laser (which produced the optical lattice for the time-dependent interaction).

reducing fringes on the DBR laser beam, which had a relatively poor spatial mode quality. The measured spectrum for our setup is shown in Fig. 3.4. Because of the tunability requirements of the MOT trapping light, and the fact that the $F = 4 \longrightarrow F' = 4, 5$ crossover transition was the largest and cleanest feature in the spectrum, we locked the DBR laser to this crossover and shifted the laser frequency closer to the MOT cycling transition (before the beam entered the chamber) as described above. The laser was locked to the crossover resonance using a standard P-I feedback loop to the laser injection current. This detection and locking method was considerably more complex than the method implemented for the repumping laser diode, but the advantage of this setup was that the main beam that went to the chamber was not frequency-modulated. After active locking, the line width of the DBR laser was on the order of 1 MHz, which is not nearly as narrow as is possible with other (e.g., grating feedback) stabilization

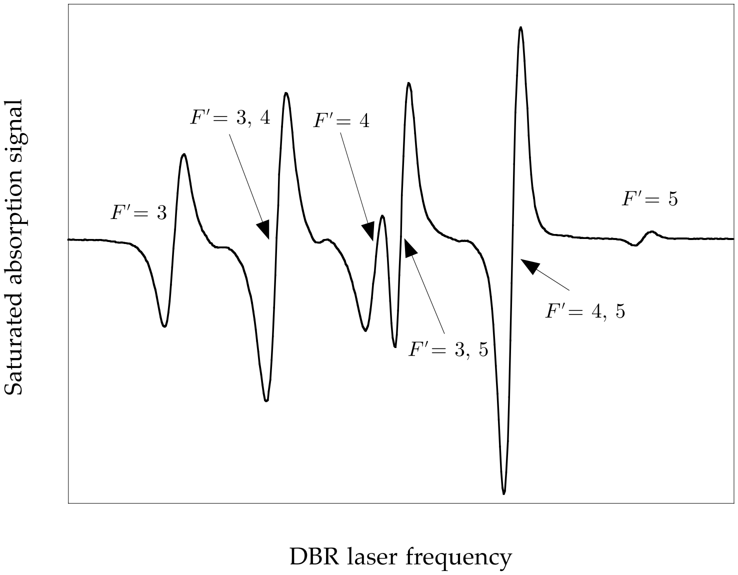

Figure 3.4: Saturated-absorption spectrum for the cesium D_2 line $F = 4 \longrightarrow F'$ hyperfine manifold, as measured by the DBR laser setup described in the text. The three excited-state hyperfine levels coupled to the $F = 4$ ground state are visible along with the three crossover transitions (labeled by pairs of quantum numbers) as dispersive resonances. The DBR laser was actively locked to the $F' = 4, 5$ crossover resonance during normal MOT operation.

techniques. It may have been possible to improve this line width electronically by using a much faster feedback loop, but this setup was certainly sufficient for the cooling and trapping of atoms. More details, as well as schematic diagrams, of this saturated absorption setup can be found in [203].

3.3 Grating-Stabilized Diode Laser

Although the $F = 4 \longrightarrow F' = 5$ trapping transition is in principle a closed cycling transition (because the $F' = 5$ state decays only to $F = 4$), the trapping light can off-resonantly excite one of the other excited hyperfine levels, which could then decay to the $F = 3$ "dark state," in which case the trapping laser would no longer cool the atom. The DBR laser alone was therefore insufficient on its own to trap cesium atoms. To address this problem, a "repumping" laser, tuned to the $F = 3 \longrightarrow F' = 4$ transition, was used to return atoms in the dark state to the cycling transition. For this repumping light, we employed a home-built, grating-stabilized (pseudo-external cavity) diode laser system [239, 243]. This laser system was constructed in the Littrow configuration, where a grating was placed in front of the laser such that the first-order diffracted beam was reflected back into the diode, while the zeroth-order light was taken as the laser output. The grating thus served as a wavelength-selective component, which narrowed and controlled the lasing frequency.

3.3.1 Construction and Operation

A diagram of the Littrow laser is shown in Fig. 3.5, and a photograph of the assembled laser is shown in Fig. 3.6. The diode laser was a model 5421-G1 laser by SDL, Inc., which is housed in a standard 9 mm package, and nominally produced 150 mW with 200 mA of injection current. The diode was mounted in a Thorlabs model LT230P-B collimation tube, which included a collimating lens with focal length 4.5 mm and numerical aperture 0.55. The collimation-tube assembly was mounted in a structure made of 954 aluminum bronze, which also supported the diffraction grating. This material had high strength and resistance to fatigue, which was important because the adjustability of the system relied on the flexing of thin sections of the structure, and the material also had reasonably good thermal conductivity, which facilitated temperature stabilization.

The diffraction grating was a 1/2”×1/2” section of an inexpensive Edmund Scientific E43,005 grating, which was 3/8” thick and blazed for 500 nm (17°). We had a 500 Å gold coating (over a 60 Å chromium coating to facilitate adhesion) evaporated onto the stock aluminum coating to improve the reflection efficiency. At the Littrow angle (31°), the coated grating diffracted 21% of the input power into the first (retroreflected) order and 67% into the zeroth-order beam. The grating angle was set by two New Focus 9300-series fine-adjustment screws, whose ball-ends contacted sapphire windows for precise and stable alignment. Additionally, the horizontal grating angle was controlled by a piezo stack, which provided electronic tuning capability. The piezo stack was assembled from three American Piezo Ceramics piezo discs, which were 8 mm in diameter and 2.54 mm thick. The stack had a maximum voltage of 1500 V, a capacitance of 39 pF, and a displacement of 1.35 μm at 1 kV (the laser tuning rate was 12 GHz/μm of displacement), and the stack was driven by a Trek model 601B-4 high-voltage (1 kV) amplifier, which had the upsetting habit of periodically self-destructing. Although we designed the pivot point of the horizontal adjustment to be near the optimal location [244], the laser could only be scanned for 1 GHz frequency intervals without mode hops. This restricted tunability was likely due to a competition between the pseudo-external cavity modes and the free-running laser diode modes. Some possible solutions would include using an antireflection-coated diode or scanning the injection current along with the grating angle to match the corresponding modes. However, this setup was certainly sufficient to scan continuously over the $F = 3 \longrightarrow F' = 4$ excited-state manifold, and has operated for years without mechanical intervention.

We used a second set of NIST current and temperature modules (as with the DBR laser) to control the laser, with the same protection diodes as in the DBR laser. The temperature of the aluminum bronze structure was monitored with a Fenwal Electronics

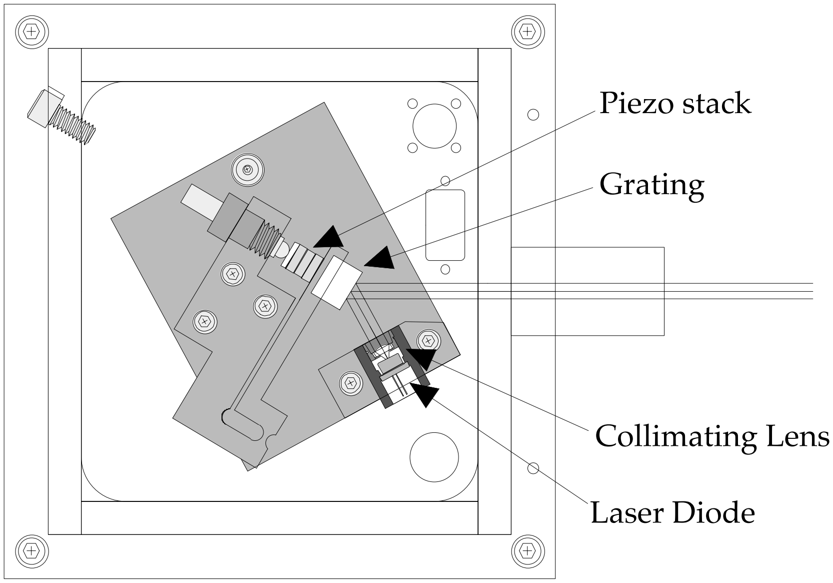

Top View

Piezo stack
Grating
Collimating Lens
Laser Diode

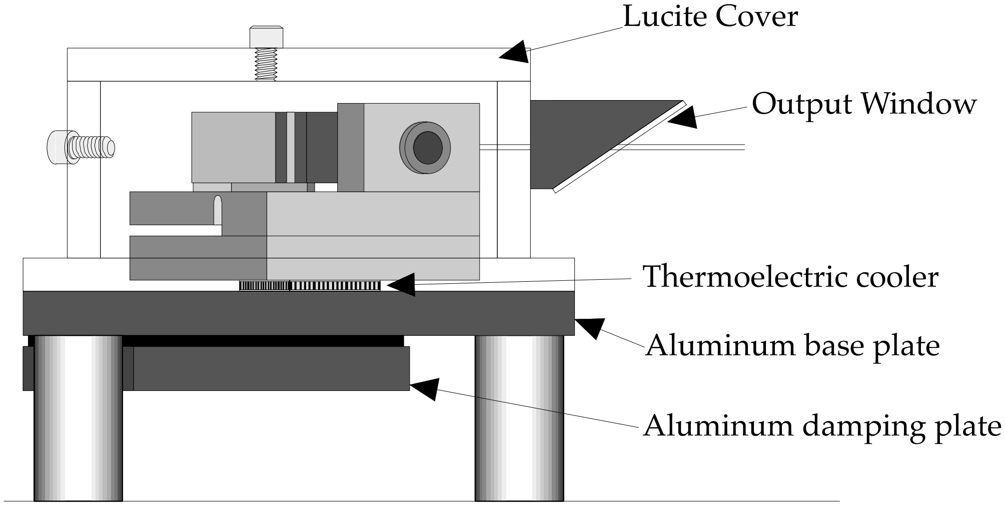

Side View

Lucite Cover
Output Window
Thermoelectric cooler
Aluminum base plate
Aluminum damping plate

Figure 3.5: Diagram of the grating-stabilized diode laser for driving the repumping transition for the MOT. The top view shows the main elements involved in the operation and tuning of the laser, while the bottom view shows how the laser assembly is mounted and thermally stabilized.

50 kΩ glass-bead thermistor, and a separate Analog Devices AD590 temperature sensor provided the panel reading on the NIST temperature controller. The bronze structure was attached to an aluminum base plate with nylon screws, and a Melcor CP1.0-127-05L thermoelectric cooler was sandwiched between them to provide active temperature control over the bronze structure. Because the diode laser was operated near room temperature, the aluminum plate was an adequate thermal reservoir. A Lucite cover provided thermal and also some acoustical isolation from the surroundings, and a microscope slide at Brewster's angle allowed the light to escape from the housing. The base plate was mounted rigidly to the optical table with four 1" diameter stainless steel posts, so that mechanical resonances would occur only at high frequencies. A second aluminum plate was bolted directly to the bottom of the base plate with a layer of 1/8" thick Sorbothane viscoelastic damping material between the two, in order to damp any vibrations of the

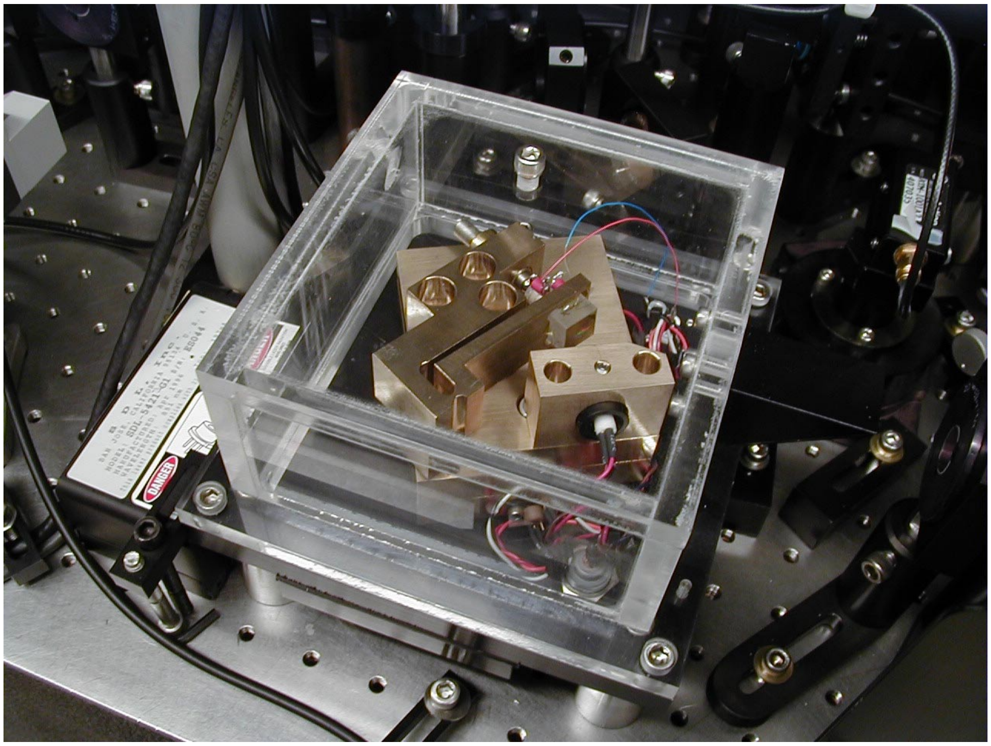

Figure 3.6: Photograph of the grating-stabilized laser assembly, used for the MOT repumping light.

base plate.

As in the case of the DBR laser, the Littrow laser output beam was passed through an anamorphic prism pair to make the beam circular before it passed through a single Conoptics isolator. The beam then made a single pass through a 100.5 MHz AOM, which shifted the frequency to the blue (because the laser was again locked to a crossover transition rather than the desired line itself) and provided intensity control for the repumping light. The beam was then spatially filtered and expanded to nearly the same size as the MOT beams, and was combined with only the vertical MOT beam (i.e., the beam along the symmetry axis of the anti-Helmholtz coils, described below) by a 1.5” polarizing cube beamsplitter before passing through the large quarter-wave plate mentioned above. With a typical operating current of 93 mA, this setup provided about 40 mW of power after the grating, and about 16 mW of repumping light after the spatial filter, which was far above the necessary intensity for proper MOT operation.

3.3.2 Frequency Control

The frequency of this laser was also locked via a saturated-absorption setup, which was considerably simplified compared to the setup for the DBR laser. The optical setup we used here is essentially the same as the one described in [239, 245]. About 10% of the repumping beam was split off of the main beam before the AOM, which then passed through a 3/8” thick uncoated window. The reflections from the window provided a pair of probe beams with about 1% of the main-beam intensity, and passed through a cesium vapor cell (identical to the vapor cell used in the DBR setup). The remainder of the picked-off beam formed the pump beam, overlapping one of the probe beams in the vapor cell in a counterpropagating fashion. The intensities of the probes were detected and subtracted by a differential photodetector. The Lamb dips only appeared on the probe beam that overlapped the pump beam, while the Doppler absorption profile appeared as a common mode signal on the two beams, and was thus removed by the subtraction. Again, from the standpoint of active frequency locking, it was convenient to have a dispersive signal. To achieve this, we dithered the laser frequency by applying a small 12 kHz signal to the piezo stack, and the subtracted photodiode signal was analyzed by an EG&G model 5204 lock-in amplifier. The dither had the disadvantage that the main repump beam was modulated, but the frequency excursion was not more than a few MHz, and the MOT operation was relatively insensitive to the repump characteristics, because the atoms spent a relatively small fraction of their time out of the cycling transition. The measured saturated-absorption spectrum for this setup is shown in Figs. 3.7 and 3.8 (see also [203] for other details of this setup, including a diagram of the optics and electronics). This signal was then fed back to the piezo control amplifier, using another P-I lock circuit based on the design in [245]. The laser was locked to the $F = 3 \longrightarrow F' = 3, 4$ crossover transition, which was the strongest feature in the spectrum, and the AOM shift of the main beam brought the repump light to the center of the $F = 3 \longrightarrow F' = 4$ repumping transition resonance. With this fairly simple setup,

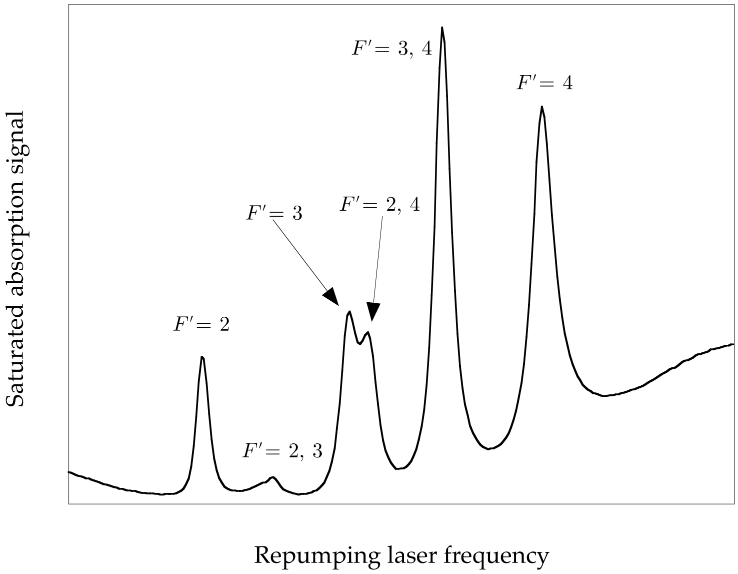

Figure 3.7: Saturated absorption spectrum for the cesium D_2 line $F = 3 \longrightarrow F'$ hyperfine manifold, as measured by the grating-stabilized (repumping) laser setup described in the text. The signal plotted here is the output of the differential photodiode, so the resonances appear as absorptive line shapes. The spectrum after additional processing by the lock-in amplifier to extract the dither information is shown in Fig. 3.8.

the diode laser remained locked to the proper frequency for hours, provided the optical table was not bumped too severely, and only required occasional adjustment of the injection current to move the laser mode-hop points away from the hyperfine resonances.

3.4 Ti:sapphire Laser

The two diode lasers worked quite well for cooling and trapping atoms, but to realize a clean optical lattice, we required a high-intensity, far-detuned source of light. These requirements were met by a home-built Ti:sapphire laser. This laser, when pumped by a Coherent Innova 90 argon-ion laser (producing about 8 W of power in multi-line mode) produced 0.5 W of single-mode light, tunable several nm around 852 nm. This laser (along with the associated control electronics) was originally a dye laser, built by Patrick Morrow, and was similar to a dye laser used in the sodium-based apparatus in

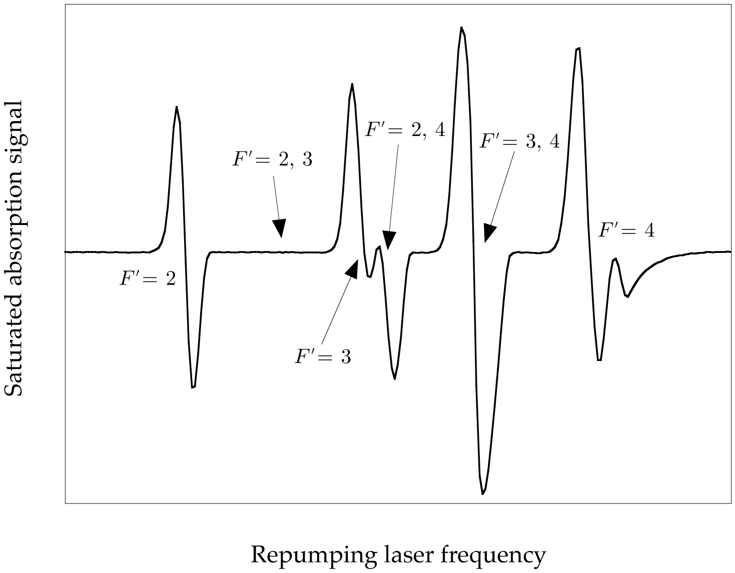

Figure 3.8: Saturated absorption spectrum for the cesium D_2 line $F = 3 \longrightarrow F'$ hyperfine manifold, as measured by the grating-stabilized (repumping) laser setup described in the text. The signal plotted here is the output of the lock-in amplifier, which extracts the frequency-dither information from the signal, so that the resonances are dispersive. This spectrum is otherwise the same as that shown in Fig. 3.7. During normal operation, the repump laser is actively locked to the $F = 3 \longrightarrow F' = 3, 4$ crossover resonance.

our laboratory [199, 246]. The dye laser and the subsequent conversion to a Ti:sapphire laser were based on designs by Jim Bergquist at NIST-Boulder.

3.4.1 Laser Design and Construction

The basic layout of the Ti:sapphire laser is shown in Fig. 3.9, and a photograph of the laser is shown in Fig. 3.10. The overall construction of the laser was a series of 1” thick aluminum plates mounted on four long 1” diameter Invar rods, providing a stable frame for mounting the laser components. The mirrors were mounted on plates that were in turn mounted on the main plates by extension springs and Bill Lees fine-adjustment screws.

The crystal itself was produced by Union Carbide. The crystal was doped with 0.05% titanium, with a guaranteed figure of merit $\geq$ 450, and was 6 mm in diameter and 20 mm long, with Brewster-cut ends. The crystal was mounted in a split copper disk, which was in turn water-cooled. We found that the water cooling was necessary for efficient laser operation.

The cavity was a four-mirror, folded-ring design. The two mirrors on either side of the crystal (in the beam path) were the “pump mirrors,” which allowed the argon-ion light in and out of the cavity. These mirrors were coated by VLOC (now a part of II-VI, Inc.), and were specified to transmit at least 90% at 488 and 514 nm, while maintaining at least 99.9% reflectivity at 852 nm. These two mirrors also had a 20 cm radius of curvature, while the other two mirrors were flat. The arrangement of the mirrors and crystal was such that the aberrations introduced by the Brewster surfaces and the off-axis curved mirrors cancelled [247], leading to clean Gaussian intensity profiles both inside the crystal and at the output coupler. The output coupler had a reflection coefficient of 97.3% (several other output couplers in the 90-95% range failed to give better output powers). The fourth mirror was small and mounted on a piezo stack to give rapid control over the cavity length. The cavity mode was focused to its tightest point inside the crystal (to a waist w_0 on the order of 40 μm), and the beam at the output coupler had a waist around 0.7 mm. The argon-ion beam was focused by a lens (175 mm focal length) to match the cavity mode inside the crystal, and the lens was tilted to compensate for the aberrations introduced by the Brewster-cut crystal end and the propagation through the slightly curved mirror (the axis of the tilt was perpendicular to the plane of the cavity mode).

The cavity also included several optical devices for stable, single-mode operation, some of which are visible in Fig. 3.11. An optical diode (optical rotator/Faraday rotator pair, manufactured by Coherent Laser Group for their model 899 Ti:sapphire laser) forced unidirectional lasing by rotating the polarization of light propagating in the wrong direction. A birefringent filter, also manufactured by Coherent, provided coarse frequency tuning, making use of the frequency-dependent polarization shift of three birefringent plates. Single-mode operation was enforced by a Coherent intracavity assembly (ICA), which housed two etalons, a thick etalon and a thin etalon. The thick etalon, which had a free spectral range (FSR) of 10 GHz, was dithered and actively locked to maximize the laser power. The thin etalon, with a 225 GHz FSR, was used to select the longitudinal cavity mode of operation, in roughly 10 GHz steps. The laser frequency could be tuned continuously by a pair of Brewster plates, mounted on galvanometer drives, to vary the cavity length; the two windows were arranged to cancel deflections caused by their synchronous rotation. The short-term line width of the laser was around 10 MHz, as measured by a Fabry-Perot cavity with a similar resolution, with fluctuations at the 100 MHz level during a data run.

3.4.2 Laser Operation and Control

The laser could be actively locked to arbitrary frequencies by using a polarization-based spectroscopic technique [248] to derive a dispersive lock signal from a 1.5 GHz FSR stable Invar Fabry-Perot cavity. The cavity resonance could be tuned continuously by adjusting the angle of a Brewster plate inside the cavity. In practice, though, the Ti:sapphire laser was stable enough that active frequency locking was unnecessary.

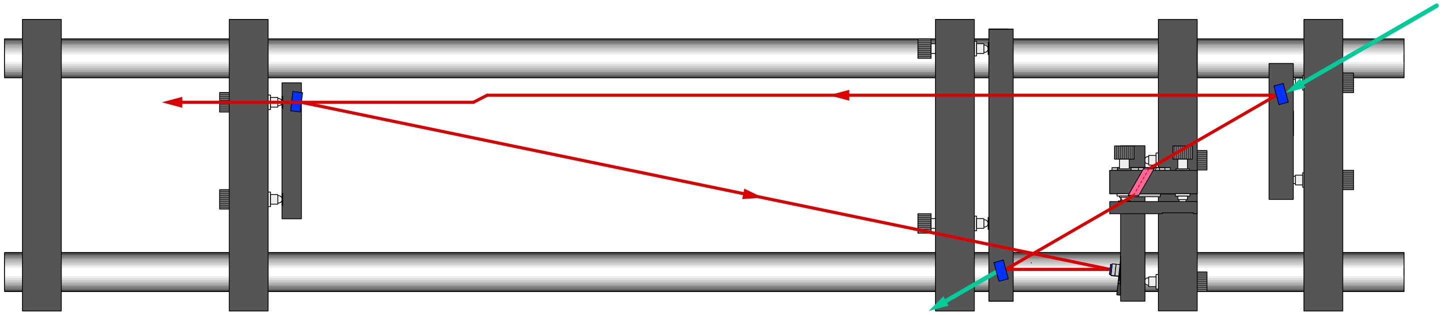

Figure 3.9: Diagram of the Ti:sapphire laser layout and beam paths. The structure of the laser consisted of thick aluminum plates mounted on four long Invar rods. Only the most basic optical elements are shown, including the four mirrors (shown in blue) and the Ti:sapphire crystal (shown in pink), where the beam path "jogs" in the right half of the diagram. The two mirrors adjacent to the crystal (in the sense of the beam path) transmitted the argon-ion laser pump light, which enters in the diagram from the upper right. The output coupler is the leftmost mirror. The jog in the uppermost leg of the beam path represents the location of the optical diode, which forced the lasing mode to oscillate in only one direction, indicated by the arrows. For a sense of scale, the uppermost leg of the beam path is about 64 cm long.

The frequency of the laser was monitored on a NIST LM-10 wavemeter (scanning Michelson interferometer), which measured the absolute laser wavelength by direct comparison to a known, stabilized HeNe reference laser. The resolution of the wavemeter was limited to about 500 MHz, so the Ti:sapphire beam was measured simultaneously with the DBR laser beam by a scanning "monitor" Fabry-Perot cavity with a 1.5 GHz FSR. The Ti:sapphire laser was tuned so that the resonances of the two lasers were aligned, and thus the frequency could be known to much better than 1.5 GHz. The Ti:sapphire beam intensity was controlled by an 80 MHz fast AOM (IntraAction model ATM-801A2-2), which shifted the frequency 80 MHz to the blue. Since the DBR laser beam (before the AOM) was 195 MHz to the red of the $F = 4 \longrightarrow F' = 5$ transition, and it was the zeroth-order beam of the Ti:sapphire AOM that was mea-

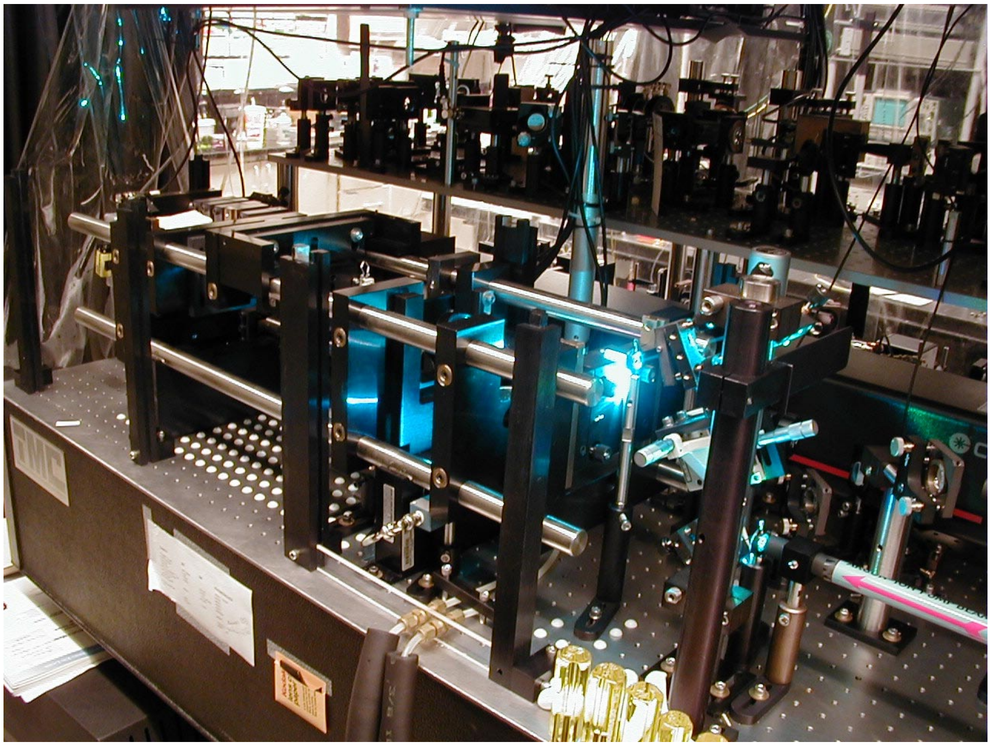

Figure 3.10: Overall photograph of the Ti:sapphire laser. The view is from the pump input end of the laser, and the pump light input periscope is visible here. The argon-ion laser is also visible behind and to the right of the Ti:sapphire laser.

sured by the cavity, the frequency of the optical lattice seen by the cesium atoms was $n \times 1.5$ GHz $-$ 115 MHz relative to the MOT cycling transition, when the two resonances were overlapped on the monitor cavity. For the experiments in Chapter 4, we used $n = -4$, for a detuning of -6.1 GHz.

The first-order AOM beam was spatially filtered by focusing through a 50 μm pinhole. The beam was then collimated with a waist parameter of 1.5 mm and sent to the vacuum chamber. This beam size was significantly larger than the size of the MOT atom cloud (which was Gaussian, with $\sigma_x = 0.15$ mm), to ensure uniform illumination of the atoms. The beam was retroreflected to form the optical lattice, using a mirror mounted directly to a vacuum-chamber window flange. This mounting method made the mirror position very rigid in the direction of the lattice, which was important be-

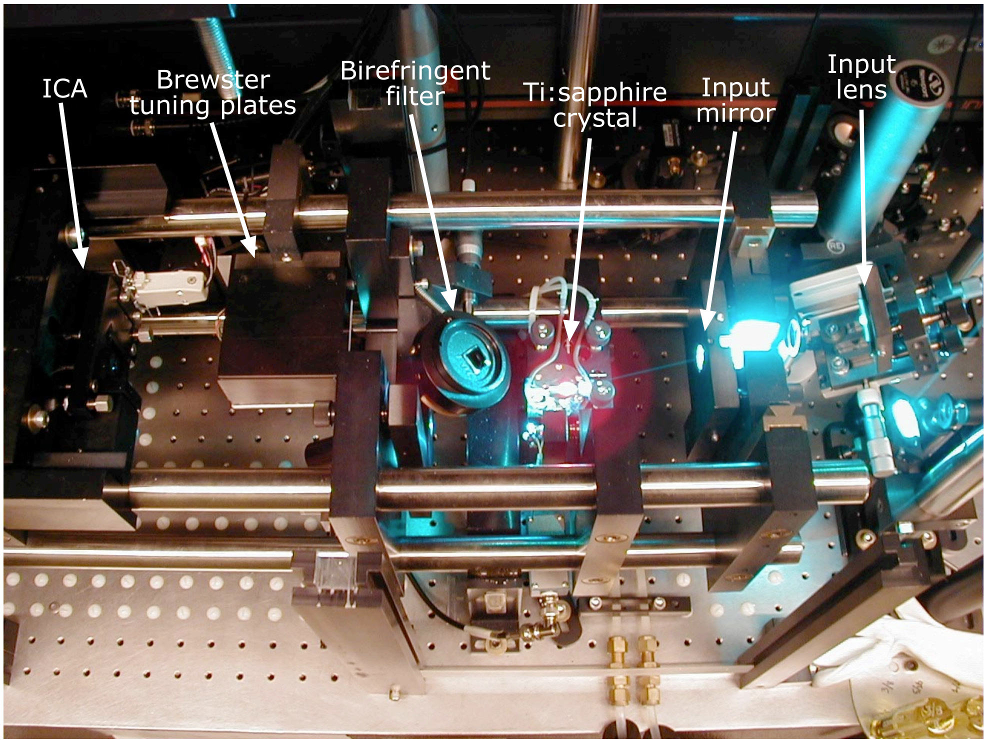

Figure 3.11: Overhead view of the interior of the Ti:sapphire laser, showing a clear view of the input light as it enters the crystal. Several of the frequency-stabilization components are also visible here.

cause the retroreflector position determined the spatial phase (and hence the positional stability) of the lattice. We measured the phase stability of the optical lattice with a Michelson interferometer setup, and found that the phase fluctuations over the time scales of the experiments (2 ms) were 8% of the lattice period, with typical ringing frequencies of around 600 Hz. This number is a generous upper bound, since the noise in the measurement was probably dominated by the motion of the beamsplitter and reference mirror. These optics were mounted on a Newport model 45 damped post and were hence not nearly as rigidly fixed in the direction of the standing wave. The dominant source of the phase instability was vibration from the cooling water flowing through the argon-ion laser, which was transmitted to the chamber and retroreflector through the optical table. The short-term (i.e., over a single 2 ms interaction with the atoms) noise on the intensity of the laser was measured to be 0.2% (rms) of the average intensity, with longer-term (i.e., on the order of seconds) fluctuations at the same level. (Note that the intrinsic noise of the New Focus model 1801 low-noise photodetector used for this measurement was of the same order as the laser intensity noise, and was thus subtracted to obtain the reported numbers.) The short-term fluctuations were dominated by an oscillation at 2.4 kHz, due to the dither of the thick etalon at the same frequency. The laser power also drifted by several to many percent over the course of hours as the room temperature drifted. For the experiments in Chapter 4, where the data were acquired over a few days, we manually kept the power at approximately the same level. For the experiments in Chapter 6, where the data were acquired in runs that took place continuously over more than a week at a time, a photodiode after the spatial filter monitored the laser intensity, and the computer scaled the control signals to compensate for laser drifts at the beginning of each run (i.e., about every 15-30 minutes). Also, if the power drifted by more than 1% from the initial power during a single data run, the entire run was discarded. This procedure was important, as the laser intensity was significantly different from the day to the night because of the difference in ambient temperature.

3.4.3 Intensity Calibration

As the local laser intensity and detuning determined the optical potential experienced by the atoms, it was important to have an accurate method for calibrating the laser intensity. Here we will discuss the calibration method used for the experments in Chapter 4. The beam power was measured using a Newport model 1825C power meter with a model 818-SL semiconductor detector (and a model 883-SL attenuator). The power meter had a NIST-traceable calibration, with a nominal absolute uncertainty of 2%. The intensity used for the well-depth calculation was reduced by 8% from this measured value to account for losses due to the vacuum chamber windows and other optics in the beam line after the point where the power was measured.

The beam diameter was measured using both a knife-edge method and an imaging method using a CCD camera. Both methods measured the beam profile approximately 2 m before the beam entered the chamber. The knife-edge method measured only the beam profile as the beam propagated to the chamber, while the CCD camera method measured the beam propagating both to and from the chamber by using beam splitters on kinematic mounts to pick off a sample of the beam for the camera. The knife-edge method involved scanning a knife edge across the beam using a micrometer-driven translation stage. The detector placed behind the knife edge thus measured the total intensity integrated over a half-plane. As the beam was quite Gaussian after the spatial filter, the detected signal could be well fit to an error-function model to yield the beam-waist parameter w_0 in the horizontal and vertical directions. In the CCD camera method, the picked-off beam passed through several attenuators and then into a Sony model XC-77 CCD video camera. The camera output was digitized using a ComputerEyes/RT SCSI frame grabber by Digital Vision, Inc., and the beam intensity profile was fit directly to a Gaussian model to obtain the beam-waist parameters. Some interference fringes due to reflections between the CCD surface and the protective window were visible on the beam, but did not significantly affect the measurement. The CCD images were valuable in ensuring that the beam spots were circular and nearly the same size before and after the chamber. Because the fitted spot sizes depended slightly on the beam intensity in the CCD method, this method was used only to obtain the relative spot sizes of the beam before and after the chamber, and the knife-edge measurement was used to set the absolute scale of the measurements. The local intensity used for well-depth calculations was also corrected for the specific widths of the MOT and laser beam size. The correction factor is

$$\eta_{\mathrm{MOT}} = \frac{w_0^2}{4\sigma_x^2 + w_0^2} \ , \tag{3.1}$$

where σ_x is the spatial standard deviation of the Gaussian MOT profile. This correction represents the average intensity experienced by the atoms relative to the intensity experienced by an atom at the center of the beam. For typical values of $\sigma_x = 0.15$ mm and $w_0 = 1.5$ mm, this correction factor is about 96%. Combining these measurements yielded an absolute potential amplitude that was correct to better than 10%. The oscillations in the diffusion rate $D(K)$ as a function of the laser intensity, as described in Chapter 4, provided an independent check of this calibration.

3.5 Vacuum System

The ultrahigh vacuum system, shown in Figs. 3.12 and 3.13, had as its main feature a large 10-way stainless steel cross, custom-fabricated by HPS (a division of MKS Instruments). The cross had six 4.25" ConFlat (CF) flanges, arranged along the three major axes to accept the large MOT trapping beams. Along the equatorial plane of the chamber, there were four 2.75" CF flanges between the four 4.25" flanges. Two of these smaller flanges provided access for the optical lattice, a third provided access for the main imaging system, and the fourth provided a path to the vacuum pump and cesium source. The flanges providing optical access were covered with zero-length (Kovar-sealed) glass viewports, which were antireflection (AR) coated by VLOC to have $\leq 0.25\%$ reflection per surface. The glass cells used in previous experiments [199] have the advantages of compact size and rapid magnetic field switching. The steel chamber used here, on the other hand, has the advantages of AR-coated windows, which largely suppress interference fringes on the beams, and optical access for large beams, like the MOT trapping and repumping beams. The chamber was mounted on a 5/8" thick aluminum plate (later changed to a G10 glass phenolic plate), which was in turn attached to the table via four 6" long stainless steel posts. All the viewport flanges had additional 1/4-20 tapped holes for mounting optics directly to the chamber.

A 20 l/s ion pump (Varian model 919-0236) maintained the vacuum in the chamber, and an HPS model 10000 5836 nude Bayard-Alpert ion gauge provided a means to monitor the chamber pressure (in addition to the ion pump current). From the ion-pump current, the vacuum pressure was around 8×10^{-8}, although it is likely that the actual pressure was substantially lower. With the proper magnetic bias field adjustment,

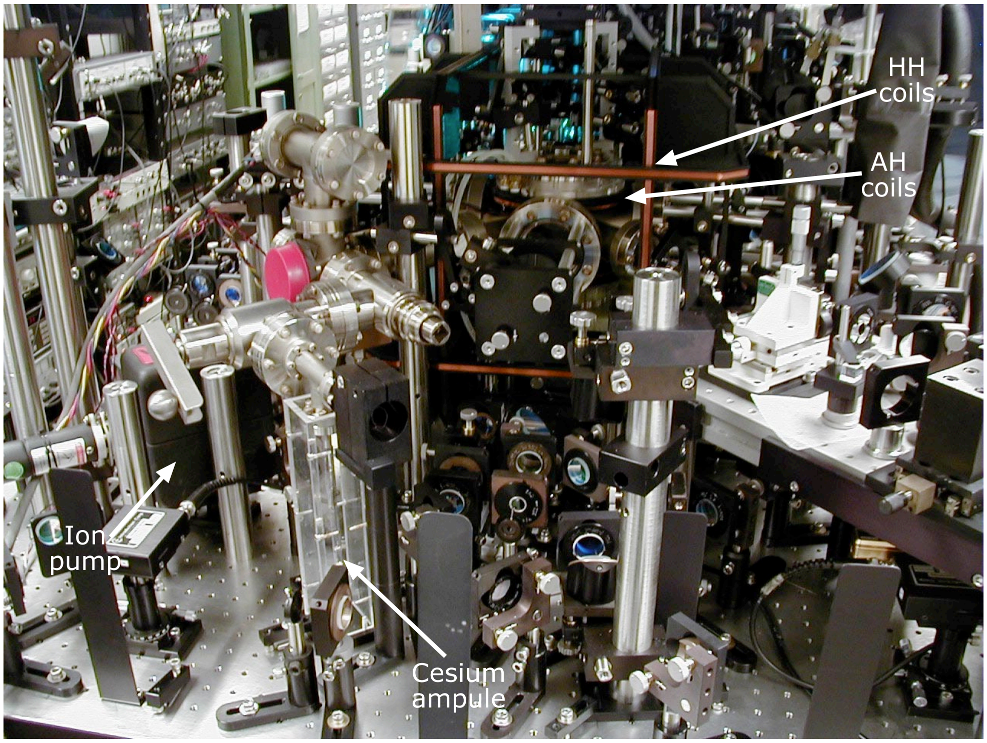

Figure 3.12: Photograph of the vacuum chamber. The rear section of the chamber is visible here, including the ion pump and cesium ampule. The main (trapping) chamber section is also visible, along with the anti-Helmholtz (AH) and Helmholtz (HH) coils.

the atoms could be released from the MOT by turning off the anti-Helmholtz coils (but not the optical molasses), and a substantial fraction could still be recaptured after 4 s by turning on the anti-Helmholtz fields again. With the measurements in [245], a lifetime of 4 s implies a pressure of 2×10^{-9} torr (assuming that cesium vapor dominated the background pressure). The readings from the ion gauge and ion pump were probably anomalously high due to cesium contamination.

We introduced cesium vapor into the chamber from a 1 g sample in a glass ampule, which was attached via a small CF flange (and a glass-metal seal) to a series pair of all-metal bakeable UHV 1.5" diameter vacuum valves (Varian model 951-5027). The inner valve was always fully open, and we installed it so that we could remove the cesium ampule without breaking vacuum in the main chamber by sealing both valves and break-

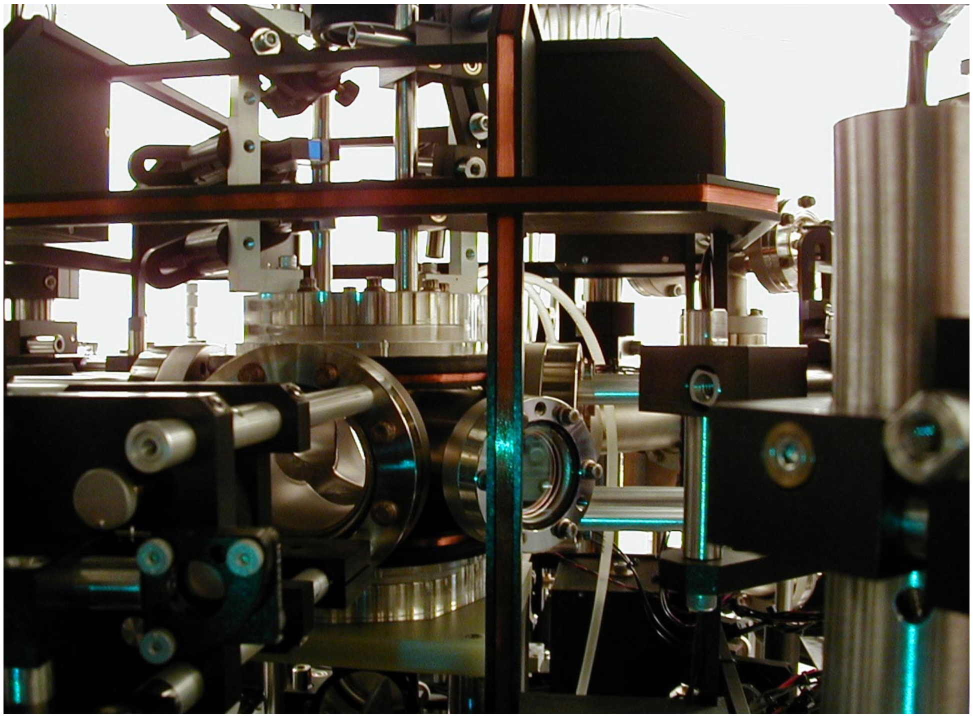

Figure 3.13: Photograph of the main (trapping) section of the vacuum chamber. This view looks into one of the large MOT trapping beam windows and the smaller optical lattice input window. The anti-Helmholtz and Helmholtz coils are more visible in this picture.

ing the CF seal between them. The second valve was usually closed hand-tight, and opened by a few turns to increase the cesium pressure in the main chamber whenever necessary (typically only once per week). At first, though, we heated the cesium ampule to 100°C for several days in order to build up enough vapor pressure to see trapped atoms in the MOT. This procedure coated the surfaces of the main chamber with cesium until it no longer acted as an effective pump for the cesium vapor. In an earlier attempt, we used a UHV variable leak valve (Varian model 951-5106) to introduce the cesium, but this valve did not have sufficient conductance to maintain a reasonable quantity of cesium in the chamber, even with substantial heating of the ampule. By contrast, the large-valve system required no temperature control of the cesium ampule.

To achieve good vacuum, we baked the chamber for three days at a maximum temperature of 220°C, with an additional day each for the gradual ramping up and down of the temperature. During the bake, the ion pump was off, but the chamber was pumped by a 70 l/s turbo pump through one of the all-metal bakeable valves. After this main bake, the second valve and cesium ampule were installed, and this subsection was separately baked for several days at a similar temperature while being pumped by the turbo pump through a pinch-off tube. After the second bake, we broke the ampule's inner glass seal using the included breaker and a strong magnet. Then the seal to the turbo pump was pinched off and we opened the valve to the main chamber.

3.5.1 Magnetic Field Control

The trapping action of a MOT relies on the presence of magnetic-field gradients in the trapping region. In our experiment these fields were generated by a pair of coils in the anti-Helmholtz configuration (where the coils form a mirror-image pair on either side of the atoms, but the currents in the two coils flow in opposite directions). The circular coils were 6.2" in diameter and each was wound from 202 turns of 24 gauge, Kapton-coated copper magnet wire onto a water-cooled aluminum form. The layers of the coil windings were fixed in place and further electrically insulated with clear fingernail polish. After winding, the coils measured 8.7 Ω and 2 mH each. The aluminum forms were attached to the chamber by Lucite clamps that gripped the two vertical flanges, such that the separation between the coils was about half their diameter. At a typical operating current of 3 A, the coils yielded a gradient of 11 G/cm along the symmetry axis of the coils (and thus half this value perpendicular to this axis, which follows from cylindrical symmetry and $\nabla \cdot \mathbf{B} = 0$). Although the coils generated 80 W of heat, they remained cold to the touch with 10°C water flowing through the forms at 10 gallons/hour.

The current through these coils was provided by two push-pull pairs of LM12 (National Semiconductor) high-current operational amplifiers, which were powered by a massive Sorenson DCR40-35A single-ended power supply. This circuit was capable of switching off the 3 A of current in the coils in 100 μs, but due to eddy currents in the chamber and the coil forms, the major part of the magnetic field damped away exponentially with a much longer time constant of 3 ms. The residual magnetic fields were not of substantial concern for the experiments in Chapter 4. However, the Raman velocity selection technique described in Chapter 5 is very sensitive to magnetic fields, and with this setup we could detect changing magnetic fields even 350 ms after the coil currents were extinguished. This time scale was much longer than expected for eddy currents in the chamber or coil forms, and even persisted when the aluminum chamber mounting plate was replaced with a phenolic plate. Thus, this long field decay was likely due to the presence of ferromagnetic Kovar in the chamber viewports.

The chamber was also enclosed within three pairs of Helmholtz coils, which allowed the magnetic field at the center of the chamber to be nulled out. Two of these coil pairs also provided the bias field for the optical pumping described in Chapter 5. These coils had a square profile, measured about 15" per side, and were separated by about 8" (with slight variations among the pairs so that they fit together properly and so that the coil spacings were 0.54 times the coil widths [249]). Each of these coils had 44 turns of the same wire used for the anti-Helmholtz coils, with about 6 Ω of resistance per coil. These coil pairs produced about 2 G/A of magnetic field along their respective axes. For typical operating conditions, where around 0.8 G was needed in the vertical direction to compensate for the magnetic field of the Earth, and a combined 1.5 G was pulsed on in the horizontal direction (using two coil pairs) for optical pumping, no special cooling was needed for these coils. These coils were driven by circuits that were similar to the anti-Helmholtz drivers, but were based on the Burr-Brown OPA2544T dual high-current op-amp, with the two sections operating in push-pull mode on a series pair of coils. The push-pull arrangement permitted bidirectional operation of all the coils, even though all the drivers (including the anti-Helmholtz drivers) were driven from a common single-ended power supply.

3.6 Imaging System

All measurements of the atoms in our experiments were performed by a CCD camera (Princeton Instruments TE/CCD-5122TK/1UV). The CCD chip was an array of 512 × 512 pixels, with each pixel approximately a 20 μm square. For low-noise operation, the CCD was chilled to around -30°C. The light was imaged by a Nikon 105 mm f/2.8 D macro lens, which reduced the image in the plane of the atoms by 1:1.8. The camera viewed the atoms through one of the smaller viewports in the chamber, such that the camera view was orthogonal to the optical lattice.

The action of the camera shutter was quite audible, and we designed the camera mount to minimize the transmission of vibration to the lasers and other components on the optical table. The camera was attached via a short post to an aluminum plate, which was sandwiched between two sheets of 1/8” thick Sorbothane rubber. This stack was clamped between an aluminum base plate and a third aluminum plate, so that the camera was vibrationally isolated from the base. The base plate was then mounted on a Newport model 45 vibration-damping post. The post was mounted on a large aluminum base plate that rested on the table through another intermediate layer of Sorbothane, and was clamped down with clamps padded with more rubber. With this setup, the shutter action vibrations were visible on the laser lock signals, but did not have a significant effect on the measurements.

The camera images were transferred to the Power Macintosh 7100 controlling computer via a Princeton ST-138 camera controller connected to a NuBus-style computer interface card. The data transfer took several seconds for large images, so for real-time alignment we used a separate and much less expensive Ikegami camera connected to a small CRT monitor. This camera viewed the MOT through the side edge of one of the MOT beam windows, so it also provided an independent view of the MOT.

3.7 Measurement Technique

With these experimental tools in hand, we can proceed with a discussion of the measurement methods for the data presented in the next chapter. The basic experimental sequence for these experiments is shown in Fig. 3.14. The sequence began by preparing a sample of cesium atoms by loading the MOT from ambient vapor. This trapping phase lasted for about 5 s. The atoms were cooled further by reducing the intensity of the trapping light to about 40% of its maximum value and increasing the detuning to 55 MHz (from the 15 MHz used during the initial trapping phase). This procedure resulted in an atomic sample that was approximately Gaussian in position and momentum, with typical sizes of $\sigma_x = 0.15$ mm and $\sigma_p/2\hbar k_{\mathrm{L}} = 4$ (corresponding to a one-dimensional temperature of 12 μK).

After this initial preparation, the trapping light and anti-Helmholtz fields were extinguished, and the atoms were exposed to the time-dependent optical lattice (in the form of a periodic pulse train, in Chapter 4). It was during this stage that the interactions of physical interest to us occured. Since we tracked the evolution of the atoms as they were exposed to the optical lattice, this stage lasted from zero to about 2 ms. This time was limited by both the capabilities of the control electronics as well as the requirement that the atoms not fall significantly compared to the 1.5 mm waist of the lattice during this time. During this interaction, the optical lattice modified the atomic momentum distribution, typically heating the center-of-mass motion of the

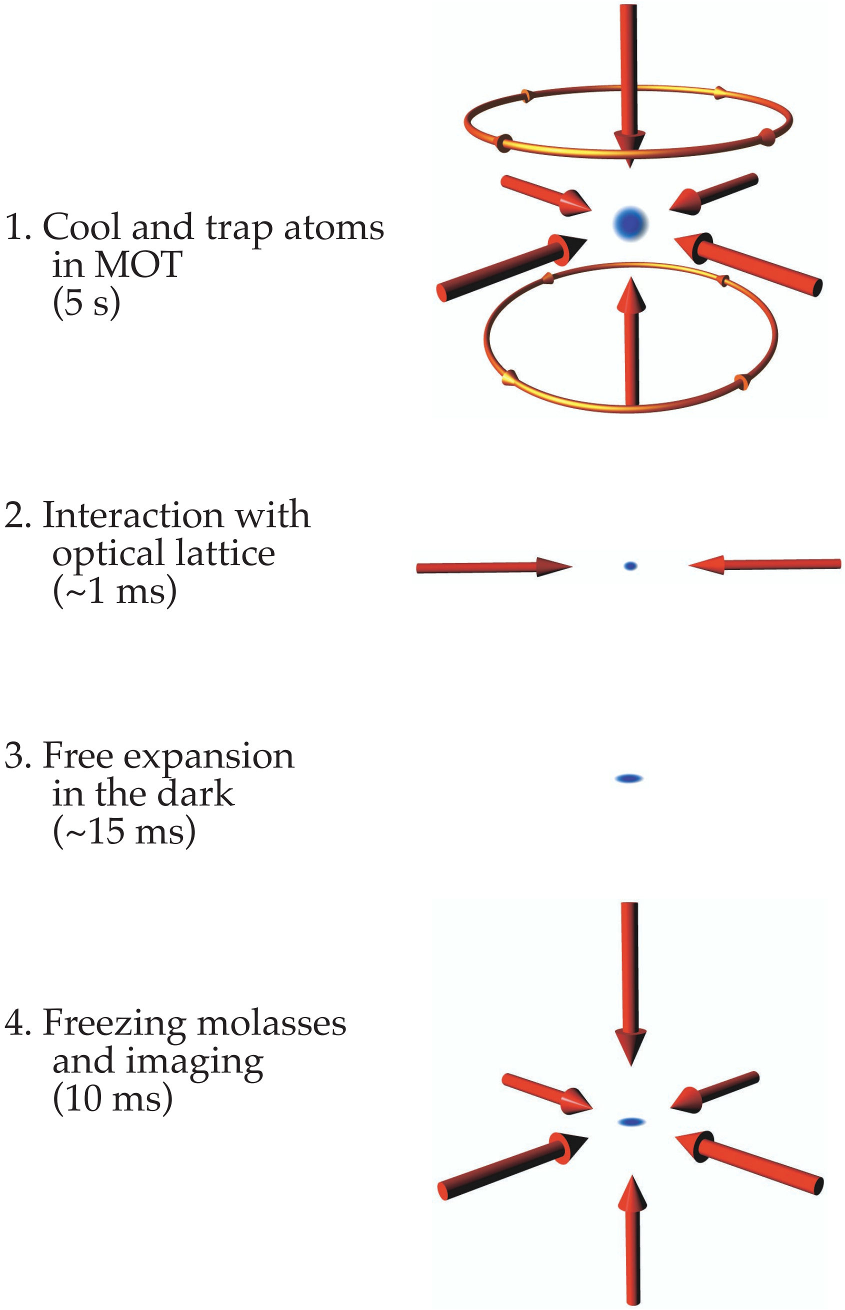
1. Cool and trap atoms
in MOT
(5 s)
2. Interaction with
optical lattice
(~1 ms)
3. Free expansion
in the dark
(~15 ms)
4. Freezing molasses
and imaging
(10 ms)

Figure 3.14: Schematic picture of the experimental sequence for the experiments in Chapter 4. (Graphics rendered by W. H. Oskay.)

atoms through the optical forces.

The next stage in the experimental sequence was the measurement of the atomic momenta. All laser light was extinguished, and the atoms were allowed to drift in the dark for 15 ms (or 20 ms for the experiments in Chapter 6; these quoted drift times include the variable lattice interaction times, so the time spent in the dark depended on the duration of the lattice interaction). During this time, the typical atom moved a distance that was large compared to the initial diameter of the cloud. Thus, assuming that the initial sample was a point source, the displacements of the atoms after the drift times was proportional to their corresponding momenta, and so the spatial distribution of the atoms had the same form as the momentum distribution. (More carefully, the final spatial distribution had the form of the momentum distribution convolved with the initial spatial distribution). To detect the momentum distribution, the atoms were illuminated by the MOT trapping light, but without the anti-Helmholtz magnetic fields. In this configuration, the cooling effect of these optical-molasses beams "froze" the atoms in place, and the atomic fluorescence was recorded on the CCD camera. The imaging time was kept relatively short (10 ms for the experiments of Chapter 4, 20 ms for Chapter 6) so that the atoms did not move significantly during the measurement. To avoid an effectively nonuniform exposure of the CCD as a result of the shutter opening (5 ms) and closing (12 ms) times, we pulsed the freezing molasses light on only when the shutter was fully open.

The two-dimensional intensity distributions from the camera were therefore a direct measurement of the two-dimensional momentum distributions of the atoms. Since we only care about the atomic momenta in the direction of the optical standing wave, we integrated over the transverse direction to obtain one-dimensional distributions. An example of such a distribution is shown in Fig. 3.15. This measurement is the simplest type of experiment, where no optical-lattice interaction is applied to the atoms, and hence constitutes a measurement of the momentum distribution of the MOT (which is the initial condition for the experiments in Chapter 4). The momentum distribution in the trap was mostly Gaussian, with broadened tails. Similar distributions have been observed by other groups, especially for strong magnetic-field gradients (e.g., [250, 251]). A good model for this momentum distribution is an incoherent sum of a Gaussian and an exponential distribution:

$$\frac{\eta_{\mathrm{g}}}{\sqrt{2\pi}\sigma_p}\exp\left(-\frac{p^2}{2\sigma_p^2}\right)+\frac{\eta_{\mathrm{e}}}{2\xi_p}\exp\left(-\frac{|p|}{\xi_p}\right) \quad . \tag{3.2}$$

The parameters for this model were determined from a best fit; the widths of the components are $\sigma_p/2\hbar k_{\mathrm{L}} = 3.9$ and $\xi_p/2\hbar k_{\mathrm{L}} = 13.0$, and the relative weights are $\eta_{\mathrm{g}} = 82\%$ and $\eta_{\mathrm{e}} = 18\%$. The measured distribution is plotted in Fig. 3.15 along with the best-fit function (3.2). To characterize the temperature of the atoms, we normally used a simple Gaussian model. When fitted to the same atomic distribution, this model accounts for 96% of the atomic population, with the remaining 4% augmenting the tails of the momentum profile. To minimize the convolution effects of the MOT cloud on the temperature measurements, we also measured the nearly Gaussian momentum distribution

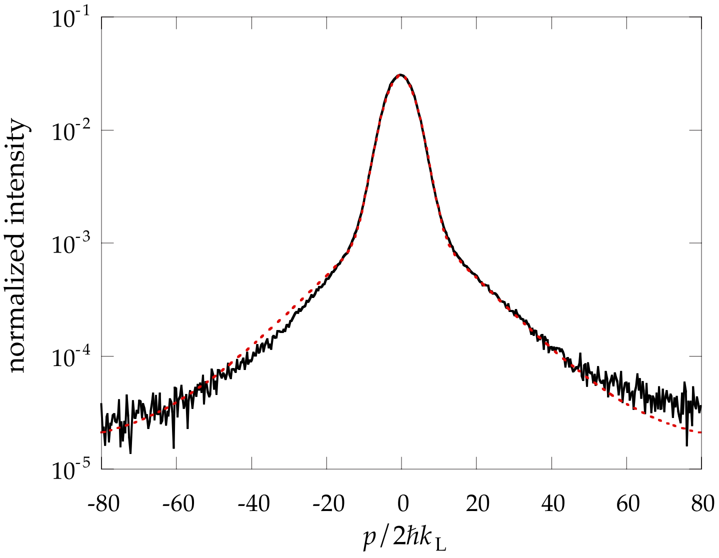

Figure 3.15: Plot of the momentum distribution in the MOT (solid line), with model distribution (3.2) (dotted line). Most of the atoms are in the main Gaussian component, while a smaller fraction is contained in the broad, non-Gaussian tails. This distribution corresponds to the initial conditions of our kicked-rotor experiments.

at several drift times. We could then extract the corresponding true σ_p by fitting Gaussian lineshapes to measurements at each drift time, and fitting these Gaussian widths to the model

$$\sigma_x(t_{\text{drift}}) = \sqrt{(\sigma_{x0})^2 + (\sigma_p t_{\text{drift}}/m)^2} \ , \tag{3.3}$$

where $\sigma_x(t_{\text{drift}})$ is the measured spatial width parameter of the expanded MOT, σ_{x0} is the spatial width parameter of the initial MOT, and t_{drift} is the drift time. This model is the exact convolution if the MOT spatial and momentum distributions are Gaussian.

3.8 Control Electronics

We give here a brief overview of the control electronics, and a more thorough discussion will be published separately [218]. For the experiments in Chapter 4, the entire experiment was controlled by a single Power Macintosh 7100/80 computer. All data acquisition and control software was programmed in LabVIEW. As mentioned above, the computer acquired the camera images via a NuBus interface card. The computer also used a National Instruments NB-MIO-16L-9 multipurpose I/O board. Although this board included many input and output functions, the functionality of this board was severely limited by the fact that its various sections could not be easily synchronized. This board was only used as a master trigger for the experiment and for control of the anti-Helmholtz fields, but precision timing was delegated to several external devices, including a Stanford Research Systems (SRS) DG535 timing/pulse generator and two SRS DS345 arbitrary waveform synthesizers. The computer programmed these timing devices through a National Instruments GPIB interface. The timing of various events was controlled with the DG535, while the optical lattice and MOT trapping beam intensities were controlled by the two DS345 synthesizers. To ensure precise timing, these three devices were slaved to a common frequency reference, and later all timing devices were slaved to a rubidium clock (LPRO model by EFRATOM) for extremely high absolute accuracy and stability.

For the more complex experiments in Chapter 6, the acquisition and control setup was upgraded considerably. Most of the control and data processing was handled by a fast Power Macintosh G4 (“Sawtooth”). However, because Princeton Instruments (now Roper Scientific) does not provide a PCI interface card for our camera controller, the old 7100 computer still acquired the camera images. The two LabVIEW processes on the two computers communicated via TCP. The more complex optical lattice intensity waveform was moved to an Agilent 33250A waveform synthesizer which has much better temporal resolution and waveform memory ($65,535$ samples with as fast as a 5 ns sampling rate, compared to the $16,299$ sample, 25 ns rate of the DS345). The new computer also handled many timing functions through a PCI-DIO-32HS digital interface by National Instruments, which outputs up to 32 channels of TTL data through 50 Ω drivers (at a clock rate of 1.25 MHz, in our setup). Other timing functions that required voltage levels other than TTL were handled by two DG535 units, and more complicated waveforms were generated by five DS345 synthesizers.

Chapter 4

Localization and Decoherence in the Kicked Rotor

4.1 Overview

Now we come to the first set of experiments discussed in this dissertation. In these studies, we focus on a realization of the kicked-rotor problem, formed by periodically pulsing on the optical standing wave. We will be concerned with the global (momentum) transport in the kicked rotor, since the classical and quantum transport are quite dramatically different due to dynamical localization. As we pointed out in Chapter 1, the difference between the quantum and classical behaviors is an apparent problem for correspondence. The goal of the research in this chapter is to directly address quantum–classical correspondence in the context of the kicked rotor. We will see that decoherence due to spontaneous emission or externally-imposed noise can destroy dynamical localization. Furthermore, we show that it is possible to obtain quantitative correspondence (at the global level of distributions and expectation values) in the presence of noise, even in a manifestly quantum regime.

The material presented in this chapter spans a number of previous publications from our group. The initial work on external noise and spontaneous emission effects was presented in [204]. The original confirmation of Shepelyansky's quantum scaling and the observation of a nonexponential late-time distribution were both presented in [252]. The effects of the finite pulses in the experiment were characterized in [202]. This earlier material is reviewed in [203], in more detail than we provide here. Later, we showed that we could observe ballistic transport at quantum resonance [209], even without subrecoil velocity selection. The quantitative studies of noise effects on quantum localization and the return to the classical limit were presented in [207, 208]. Finally, an experimental test of a universal quantum diffusion theory was presented in [214].

4.2 Rescaling

The atom-optics realization of the kicked rotor is described by the Hamiltonian

$$H(x,p,t) = \frac{p^2}{2m} + V_0 \cos(2k_{\mathrm{L}}x) \sum_n F(t-nT) \ . \tag{4.1}$$

Here, T is the kick period, and $F(t)$ is a pulse function of unit height and duration $t_{\mathrm{p}} \ll T$. Before proceeding, we will transform to scaled units to simplify our discussion, as we did for the pendulum in Chapter 1. As before, the spatial coordinate has a natural scaling,

$$x' := 2k_{\mathrm{L}}x \ . \tag{4.2}$$

This time, however, there is a natural time scale for the problem, which defines the scaling of the time coordinate,

$$t' := t/T \ . \tag{4.3}$$

The corresponding scaling of the pulse is given by

$$f(t') := F(t)/\eta \ , \tag{4.4}$$

where we have defined the pulse integral

$$\eta := T^{-1} \int_{-\infty}^{\infty} F(t)\, dt \propto t_{\mathrm{p}}, \tag{4.5}$$

so that the scaled pulse is normalized to unity (i.e., $\int_{-\infty}^{\infty} f(t)\, dt = 1$). If we define the constant

$$\bar{k} := 8\omega_{\mathrm{r}}T \ , \tag{4.6}$$

then the time scaling here is different from the pendulum time scaling by precisely this factor. This difference suggests that we should change the momentum scaling by the same factor,

$$p' := \frac{\bar{k}}{2\hbar k_{\mathrm{L}}} p \ . \tag{4.7}$$

Now the scaled coordinates obey the commutation relation,

$$[x', p'] = i\bar{k} \ , \tag{4.8}$$

and thus we can interpret $\bar{k}$ as a scaled Planck constant, which can be "tuned" by varying the period T. More concretely, this parameter measures the action scale of the system in physical units compared to $\hbar$. We can then use the energy transformation $H' := (\bar{k}/\hbar)TH$, and defining the stochasticity parameter as

$$K := \frac{\bar{k}T}{\hbar}\eta V_0 \ , \tag{4.9}$$

the Hamiltonian in scaled units takes the form

$$H(x, p, t) = \frac{p^2}{2} + K \cos x \sum_n f(t - n), \tag{4.10}$$

after dropping the primes. In this way we have reduced the classical system to a single parameter (K) and the quantum system to two parameters (K and $\bar{k}$). Note that in these units, the constant $\bar{k}$ also represents the quantization scale for momentum transfer, rather than unity as in the pendulum units or $2\hbar k_\mathrm{L}$ in unscaled units.

4.3 Standard Map

In the limit of arbitrarily short pulses, the pulse function $f(t)$ is replaced by the Dirac delta function $\delta(t)$,

$$H(x, p, t) = \frac{p^2}{2} + K \cos x \sum_n \delta(t - n) \ , \tag{4.11}$$

and this limit of the problem is commonly termed the "δ-kicked rotor." This limit is particularly convenient because the equations of motion can be reduced to a simple discrete map. From the form of the Hamiltonian (4.11), we note that during the kick, the potential term dominates the kinetic term. Between kicks, the potential term is zero, and the motion is that of a free rotor. Using these observations, we can integrate the equations of motion over one temporal period of the Hamiltonian.

Differentiating (4.11), Hamilton's equations of motion become

$$\begin{aligned} \partial_t p &= -\frac{\partial H}{\partial x} = K \sin x \sum_{n=-\infty}^{\infty} \delta(t - nT) \\ \partial_t x &= \frac{\partial H}{\partial p} = p \ . \end{aligned} \tag{4.12}$$

We will integrate Eqs. (4.12) to construct a map for x and p just *before* the nth kick. Letting ϵ be a small, positive number, we integrate the equation for p,

$$\int_{t_n-\epsilon}^{t_{n+1}-\epsilon} \partial_t p(t)\, dt = \int_{t_n-\epsilon}^{t_{n+1}-\epsilon} K \sin x \sum_n \delta(t-n)\, dt \ , \tag{4.13}$$

where $t_n = n$ is the time of the nth kick. This equation then becomes

$$p(t_{n+1} - \epsilon) - p(t_n - \epsilon) = K \sin x \ . \tag{4.14}$$

Similarly, we integrate the equation for x,

$$\int_{t_n-\epsilon}^{t_{n+1}-\epsilon} \partial_t x(t)\, dt = \int_{t_n-\epsilon}^{t_{n+1}-\epsilon} p\, dt \ , \tag{4.15}$$

which becomes

$$x(t_{n+1} - \epsilon) - x(t_n - \epsilon) = \epsilon\, p(t_n - \epsilon) + (1 - \epsilon)\, p(t_{n+1} - \epsilon) \ . \tag{4.16}$$

Then, letting $\epsilon \to 0$ and defining x_n and p_n to be the values of x and p just before the nth kick, we obtain the mapping

$$\begin{aligned} p_{n+1} &= p_n + K \sin x_n \\ x_{n+1} &= x_n + p_{n+1} \ . \end{aligned} \tag{4.17}$$

These equations, which constitute a one-parameter family of mappings parameterized by the *stochasticity parameter* K, are known as the *standard map* (or *Chirikov-Taylor map*), so named because of its broad importance in the study of Hamiltonian chaos. The significance of this widely studied map is due to both its simplicity, which makes it amenable to both analytical and numerical study, and the fact that many systems can be locally approximated by the standard map [27].

A number of standard-map phase plots are shown in Appendix B. The phase space for the standard map is clearly invariant under a 2π translation in x, because of the corresponding invariance of the mapping itself, and so x is usually taken to be within the interval $[0, 2\pi)$. What is perhaps less obvious is that the phase-space structure is also invariant under a 2π translation in p, as well. This point is more easily recognized from the Hamiltonian of the δ-kicked rotor (for which the standard-map phase space is a Poincaré section). Using a form of the Poisson sum rule,

$$\sum_{n=-\infty}^{\infty} \delta(t-n) = \sum_{n=-\infty}^{\infty} \cos(2\pi n t) \ , \tag{4.18}$$

we can rewrite the δ-kicked rotor Hamiltonian as

$$\begin{aligned} H(x,p,t) &= \frac{p^2}{2} + K\cos x \sum_{n=-\infty}^{\infty} \cos(2\pi n t) \\ &= \frac{p^2}{2} + \sum_{n=-\infty}^{\infty} K\cos(x - 2\pi n t) \ . \end{aligned} \tag{4.19}$$

From this form of the Hamiltonian, it is apparent that the δ-pulsed potential can be regarded as a superposition of an infinite number of unmodulated pendulum potentials moving with momentum $2\pi n$ for every integer n. The Hamiltonian is therefore invariant under boosts of $2\pi n$ in momentum, so the phase space is 2π-periodic in both x and p. Each of these pendulum terms is associated with a primary nonlinear resonance in the phase space, located at $(x,p) = (\pi, 2\pi n)$, and the interactions between these resonances result in chaos and rich structure in phase space.

4.4 Classical Transport

We will now consider the global behavior in the standard map. In particular, we will consider the transport in the limit of large K, where the phase space is predominantly chaotic (which operationally means $K \gtrsim 5$). Also in this limit, there are no Kolmogorov-Arnol'd-Moser (KAM) surfaces that span the phase space, dividing the phase space in the momentum direction and preventing chaotic transport to arbitrarily large momenta (this is true for any K above the Greene number, $K_{\mathrm{G}} \approx 0.971635$ [253]). Broadly speaking, invariant surfaces (KAM surfaces, which are traceable to invariant surfaces in the integrable limit, and islands of stability) confine trajectories, while chaotic trajectories are free to ergodically wander throughout the chaotic region. In the next section we will find that the chaotic motion can be thought of as being diffusive (like a random walk), although the presence of small but nevertheless important islands of stability complicate this diffusion picture.

4.4.1 Diffusion and Correlations

Focusing on the momentum transport in the standard map, we use the first equation in the standard map (4.17) to calculate the kinetic energy of a trajectory ensemble after n iterations:

$$\begin{aligned} E_n &:= \frac{\langle p_n^2 \rangle}{2} \\ &= \frac{1}{2} \sum_{m,m'=0}^{n-1} C_{m-m'} \quad . \end{aligned} \tag{4.20}$$

Here, the correlation functions C_m are defined as

$$C_{m-m'} := \langle K \sin x_m K \sin x_{m'} \rangle \quad . \tag{4.21}$$

(A similar discussion along these lines can be found in [105], but with a slightly different definition for the correlations.) The angle brackets here denote an average over the initial ensemble. For the purposes of the present analysis, we can take this average to be uniform over the unit cell in phase space, which is appropriate for the initial distribution of MOT atoms for the experimental parameters (for which the distribution is broad in both x and p compared to the unit cell size). The correlations also obviously depend only on the difference $m - m'$, as there is no explicit time dependence in the standard map.

The sum in Eq. (4.20) can be straightforwardly evaluated if one makes the approximation that the coordinate x_n is uniform and uncorrelated, as one might expect for very large K when the phase space is almost entirely chaotic. Doing so allows one to ignore the off-diagonal terms in the sum and gives the result

$$E_n = \frac{C_0}{2} n = \frac{K^2}{4} n \ . \tag{4.22}$$

The energy growth is hence diffusive (linear in time), with diffusion rate $D_{\mathrm{ql}}(K) = K^2/4$, which is known as the *quasilinear* diffusion rate. This quasilinear (random-phase) approximation is equivalent to assuming that the motion is a random walk in momentum, and thus the momentum distribution is asymptotically Gaussian with a width $\sim \sqrt{n}$.

The random-phase approximation is only valid in the limit of arbitrarily large K, however, and for finite K the higher-order correlations cannot always be neglected, even for trajectories within the chaotic region of phase space. Nonuniformities in the chaotic region, especially near the borders of stability islands, can lead to nonzero correlations, and thus to deviations of the diffusion rate from the quasilinear value. A more general expression for the (time-dependent) diffusion rate in terms of the higher-order correlations is

$$D_n := E_{n+1} - E_n = \frac{1}{2} \sum_{m=-n}^{n} C_m \ . \tag{4.23}$$

These corrections to the diffusion rate were treated analytically in [254, 255], where the series (4.23) was shown to be an asymptotic expansion in powers of Bessel functions of K. The result from [255] is

$$D(K) = \frac{K^2}{2} \left(\frac{1}{2} - J_2(K) - J_1^2(K) + J_2^2(K) + J_3^2(K) \right) \tag{4.24}$$

to second order in the Bessel functions (we defer the derivation of these results to Section 4.8). This expression represents the rate D_n of energy diffusion for long times n and large values of K; the higher-order terms in the expansion are assumed at this point to have only a small contribution, since they represent higher powers of $1/\sqrt{K}$. In this expression, it is often convenient to neglect $J_3^2(K) - J_1^2(K)$, which is $O(K^{-2})$, since for large K this difference is much smaller than $J_2^2(K)$, which is $O(K^{-1})$; however, these terms will be important when generalizing this result to account for amplitude noise below. This result shows that $D(K)$ oscillates about the quasilinear value, where the corrections become small compared to the quasilinear value as K becomes large.

4.4.2 Accelerator Modes

The diffusion rate expression in Eq. (4.24) is plotted in Fig. 4.1 along with the diffusion rate calculated in a simulation. The agreement is generally good, with the exception of the peaks in the diffusion curve, where the simulated diffusion rate greatly exceeds the analytical prediction. This discrepancy stems from the fact that we have so far assumed that the chaos causes the correlation series (4.23) to drop off rapidly (i.e., exponentially).

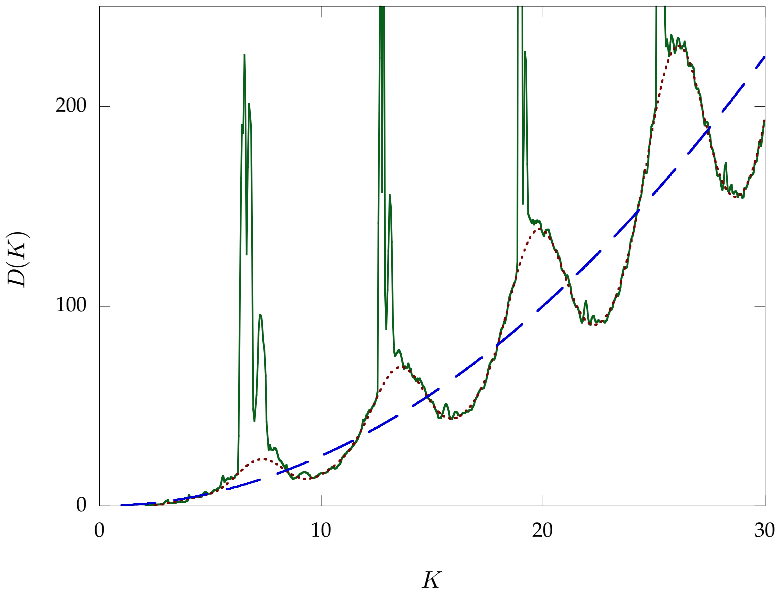

Figure 4.1: Dependence of the rate of energy diffusion D on the stochasticity parameter. The analytical diffusion expression [Eq. (4.24), dotted line] shows a significant oscillatory departure from the quasilinear prediction (dashed line). The simulated diffusion rate (solid line) is computed assuming an initial condition of 10^5 particles distributed uniformly over a unit cell in phase space, and is averaged over 1000 iterations of the standard map. The simulation agrees with Eq. (4.24) except at the peaks of the diffusion curve, where the diffusion is dramatically enhanced by the influence of accelerator modes.

However, the presence of small, stable islands (which are present for any value of K) can make the longer time correlations important, so that the correlation series decays slowly (i.e., like a power law [256, 257]), and as a result this series may not even rigorously converge.

The stable structures that cause the large deviations in Fig. 4.1 are the *accelerator modes* [27, 258, 259]. These structures are different from the usual stability islands in that they are boosted by a constant amount in momentum on each iteration. The main family of accelerator modes occur in the stability windows $(2\pi j) < K < \sqrt{(2\pi j)^2 + 16}$ (for integer j), where the corresponding accelerator mode hops monotonically by $2\pi j$ in momentum per iteration [27]. These intervals are precisely the locations of the strong deviations in Fig. 4.1; note that the $j = 0$ case simply corresponds to the primary resonances, as we discussed in the context of Eq. (4.19), whereas for $j > 0$ the accelerator modes are born by tangent bifurcations. From the inversion-symmetry properties of the standard map (i.e., invariance under the combined transformation $p \rightarrow -p$, $x \rightarrow -x$), we can see that the accelerator modes occur in pairs, which “stream” in opposite senses. The accelerator modes are obviously a peculiarity of the standard map, a result of the periodicity of the phase space in the momentum direction. Other systems, such as the experimental realization of the kicked rotor (which uses finite, not δ-function, kicks) can still exhibit *quasiaccelerator modes*, which behave like accelerator modes over a bounded region in phase space [15].

The behavior of the trajectories trapped within stable islands and accelerator modes is clearly different in nature from that of chaotic trajectories. However, these coherent phase-space structures can still have a strong influence over the behavior of chaotic trajectories. The boundaries of the islands, where the stable regions merge into the surrounding chaotic sea, are complicated and fractal in nature. This structure causes the island boundaries to be “sticky” in the sense that chaotic trajectories can become trapped for some finite time in the boundary layer. As the chaotic trajectories wander throughout the phase space, they will eventually wander close enough to any island

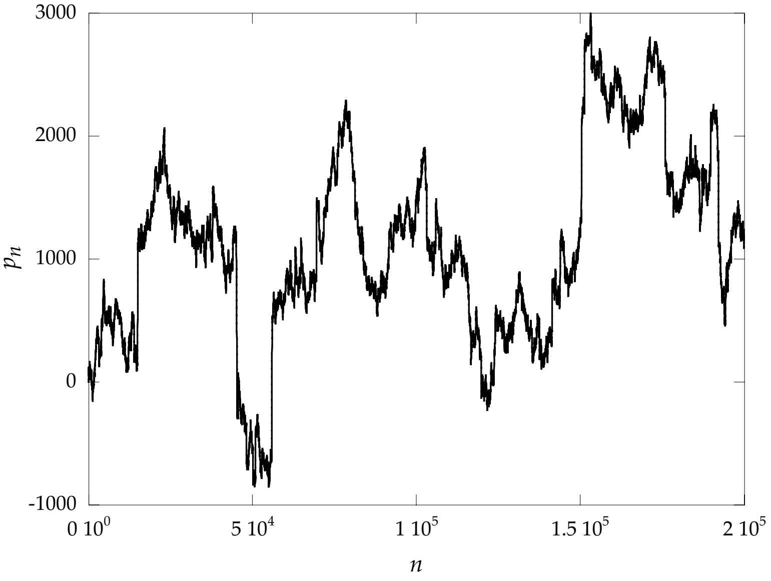

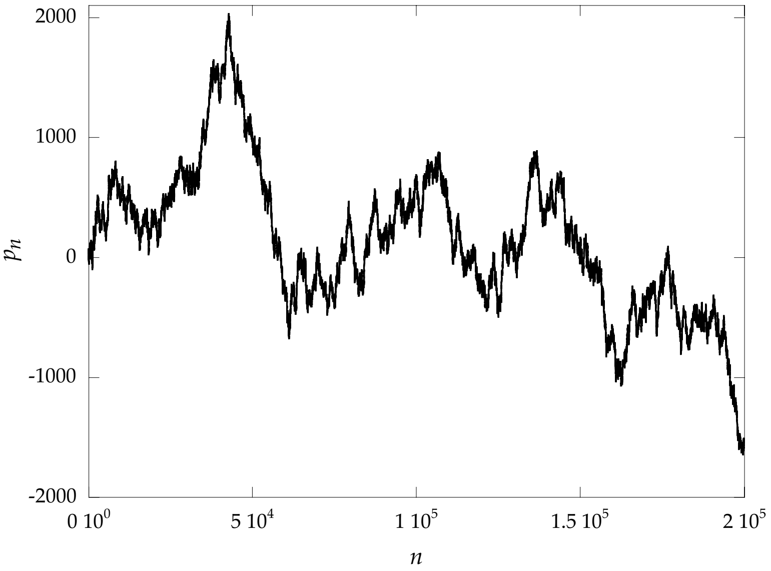

Figure 4.2: Upper graph: plot of the iterates p_n for a standard-map trajectory in the presence of accelerator modes, showing Lévy-flight behavior. The stochasticity parameter is $K = 6.52$, and the initial condition is $(x_0, p_0) = (3, 3.5)$. The Lévy flights are apparent as sudden jumps in momentum as a result of many successive steps in the same momentum direction. Lower graph: plot of the iterates p_n for a standard-map trajectory showing normal diffusive behavior. The stochasticity parameter is $K = 9.5$, and the initial condition is $(x_0, p_0) = (3, 3.5)$.

to become trapped. The self-similar structure of the boundary causes these trapping times to have a power-law distribution [256], and the resulting dynamics are characterized by Lévy-flight behavior, rather than simple diffusion [259]. The regular stability islands tend to trap trajectories at a fixed momentum, leading to reduced momentum transport, whereas the accelerator modes lead to streaming (with many correlated momentum steps), and therefore to enhanced momentum transport. This subdiffusive or superdiffusive behavior due to island structures is referred to as *anomalous diffusion* [257, 259–262]. The momentum distribution in this regime has asymptotically power-law tails, rather than Gaussian tails, and the kinetic energy scales as $E(t) \sim t^{\mu}$, where the transport exponent $\mu \neq 1$ for anomalous diffusion. The Lévy flights in a standard-map trajectory are apparent in Fig. 4.2, especially compared to a diffusive trajectory, shown also in this figure.

As the transport in the standard map is not strictly diffusive, the proper framework for the global dynamics is fractional kinetics [263–265]. However, since the stable islands in phase space are typically small for large K (the areas of the islands are asymptotically of the order K^{-2} [27]), it may take many kicks before the islands cause large deviations from diffusive behavior. Hence, for the time scales observed in our experiments (up to 80 kicks), it is appropriate to describe the classical dynamics as diffusive as long as large accelerator modes are not present. Operationally, Eq. (4.24) is an excellent approximation away from the main family of accelerator modes.

4.4.3 External Noise

The transport that we have studied is heavily influenced by correlations, and we might expect that noise will therefore also have substantial effects on the global dynamics. One type of decohering interaction that we will study more in Section 4.5.4 is spontaneous emission. To model the effects of spontaneous emission in the standard map, we could simply consider a fluctuating momentum perturbation that models the random momentum recoil of the atom in response to the photon scattering. We can compare this situation qualitatively to the results of Ref. [266] (see also [15]), which considers the generalized (noisy) mapping

$$\begin{aligned} p_{n+1} &= p_n + K \sin x_n + \delta p_n \\ q_{n+1} &= q_n + p_{n+1} + \delta x_n \ , \end{aligned} \tag{4.25}$$

where δp_n and δx_n are time-dependent random variables. In the case where δp_n and δx_n are chosen from a normal distribution, the diffusion rate from Eq. (4.24) becomes

$$\begin{aligned} D(K) = \frac{K^2 + 2\rho^2}{4} + \frac{K^2}{2}\bigg[&- J_2(K) e^{-(\sigma^2 + \rho^2/2)} \\ &- J_1^2(K) e^{-(\sigma^2+\rho^2)} + J_2^2(K) e^{-(2\sigma^2+\rho^2)} + J_3^2(K) e^{-(3\sigma^2+\rho^2)} \bigg], \end{aligned} \tag{4.26}$$

where ρ^2 is the variance of δp_n, and σ^2 is the variance of δx_n. The noise therefore affects the diffusion by exponentially damping the higher-order correlations, and the momentum perturbation also gives a direct contribution to the quasilinear term.

For the quantitative comparison of quantum and classical dynamics of the kicked rotor in Section 4.6, we used amplitude noise, where the value of K is randomly varied from kick to kick. This interaction has the advantage of being easy to apply and quantify compared to other decohering interactions such as spontaneous emission. We can also treat the effects of this noise on the classical correlations analytically, as we now discuss (again, some of the more gruesome details are left to Section 4.8). The standard map including amplitude noise is

$$\begin{aligned} p_{n+1} &= p_n + (K + \delta K_n) \sin x_n \\ q_{n+1} &= q_n + p_{n+1} \ , \end{aligned} \tag{4.27}$$

where δK_n is a random deviation for the nth kick, distributed according to $P(\delta K)$, with zero mean. The noise again modifies the correlations, and the generalization of (4.21) is

$$\begin{aligned} C_{m-m'} = \int & d(\delta K_m) \cdots d(\delta K_{m'}) P(\delta K_m) \cdots P(\delta K_{m'}) \\ & \times \langle (K + \delta K_m) \sin x_m (K + \delta K_{m'}) \sin x_{m'} \rangle, \end{aligned} \tag{4.28}$$

where there are $|m - m'| + 1$ integrals over the kick probability distribution, because the coordinate at the later time depends on all the kicks after the earlier time. As we can see from Section 4.8, each factor of K (the two factors of K and several factors of $J_n(K)$) in Eq. (4.24) enters as an independent random variable, so that the integration in (4.28) amounts to averaging over each factor independently. The resulting generalization of (4.24) is

$$D(K) = \frac{K^2 + \mathrm{Var}(\delta K)}{4} + \frac{K^2}{2}\left(-\mathcal{J}_2(K) - \mathcal{J}_1^{\,2}(K) + \mathcal{J}_2^{\,2}(K) + \mathcal{J}_3^{\,2}(K)\right). \tag{4.29}$$

In this equation, $\mathrm{Var}(\delta K)$ denotes the variance of $P(\delta K)$, and

$$\mathcal{J}_n(K) := \int_{-\infty}^{\infty} P(\delta K) J_n(K + \delta K)d(\delta K). \tag{4.30}$$

This expression makes it immediately clear how amplitude noise affects the diffusion rate: the integral in Eq. (4.30) is analogous to a convolution of the Bessel functions with the noise distribution. As the noise level is increased, the Bessel functions are smoothed out, and the correlations are effectively destroyed. This is especially true for long-term correlations, and indeed anomalous diffusion is suppressed in the presence of noise. At the same time, there is an increase in the quasilinear diffusion component, because the fluctuating kick strength leads to a fluctuating momentum perturbation, but this effect is generally small in comparison to the destruction of the correlations.

In the experiments, we considered exclusively the case of amplitude noise with a uniform probability distribution,

$$P(\delta K) = \begin{cases} 1/\delta K_{\mathrm{p-p}}, & \delta K \in (-\delta K_{\mathrm{p-p}}/2, \delta K_{\mathrm{p-p}}/2) \\ 0 & \text{elsewhere,} \end{cases} \tag{4.31}$$

where $\delta K_{\mathrm{p-p}}$ is the peak-to-peak deviation of the kick strength. When we quote the noise level used in our experiments, we are quoting the normalized peak-to-peak deviation $\delta K_{\mathrm{p-p}}/K$. For this noise, the variance, which characterized the contribution to the quasilinear diffusion, is $\mathrm{Var}(\delta K) = (\delta K_{\mathrm{p-p}})^2/12$, and from Eq. (4.30), the correlation contributions to the diffusion in (4.24) are simply convolved with a “box” window. For illustration, the function (4.29) is plotted for several different levels of amplitude noise in Fig. 4.3. Notice that for the 100% and 200% noise levels, the correlations are essentially destroyed, so that these noise levels cannot be considered perturbative; however, these noise levels are still small in the sense that their contribution to the quasilinear diffusion rate is significantly smaller than the zero-noise component.

4.4.4 Finite-Pulse Effects

In a real experiment, we obviously cannot realize exact δ-kicks, but we can use short laser pulses to work near this limit. The standard map is a valid model of the finite-pulse kicked rotor if the motion of the atom is negligible throughout the duration of the pulse, because this situation mimics the strobe-like nature of the δ-function pulses. This observation implies that the δ-kick approximation is valid within a bounded interval in momentum about $p = 0$. We can obtain a crude estimate for the momentum at which the δ-kick approximation breaks down by considering an atom moving with a velocity such that it travels over one period of the optical lattice over the duration t_p of the pulse. The momentum transferred to the atom is approximately zero, and thus the

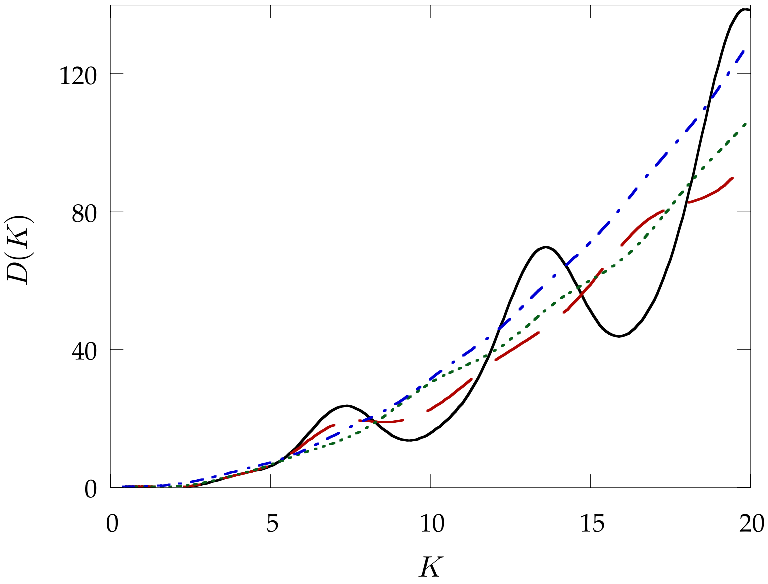

Figure 4.3: Plot of the diffusion expression (4.29) for several levels of amplitude noise (with uniformly-distributed statistics): no noise (solid line), 50% noise (dashed line), 100% noise (dotted line), and 200% noise (dot-dashed line). The oscillations, which represent short-term correlations, are smoothed out by the noise.

momentum p_b for this “boundary” is

$$\frac{p_\mathrm{b}}{2\hbar k_\mathrm{L}} = \frac{m\lambda^2}{8\pi\hbar t_\mathrm{p}}, \tag{4.32}$$

where all quantities are in physical units. The dependence of this boundary on the atomic mass m and the lattice wavelength λ motivated the use of a cesium-based apparatus for these experiments over the previous sodium-based apparatus, in order to realize an increase in $p_\mathrm{b}/2\hbar k_\mathrm{L}$ by a factor of 12 for fixed t_p.

We can make this momentum boundary effect due to finite pulses more precise by reconsidering the form (4.19) for the kicked-rotor Hamiltonian. We can write the

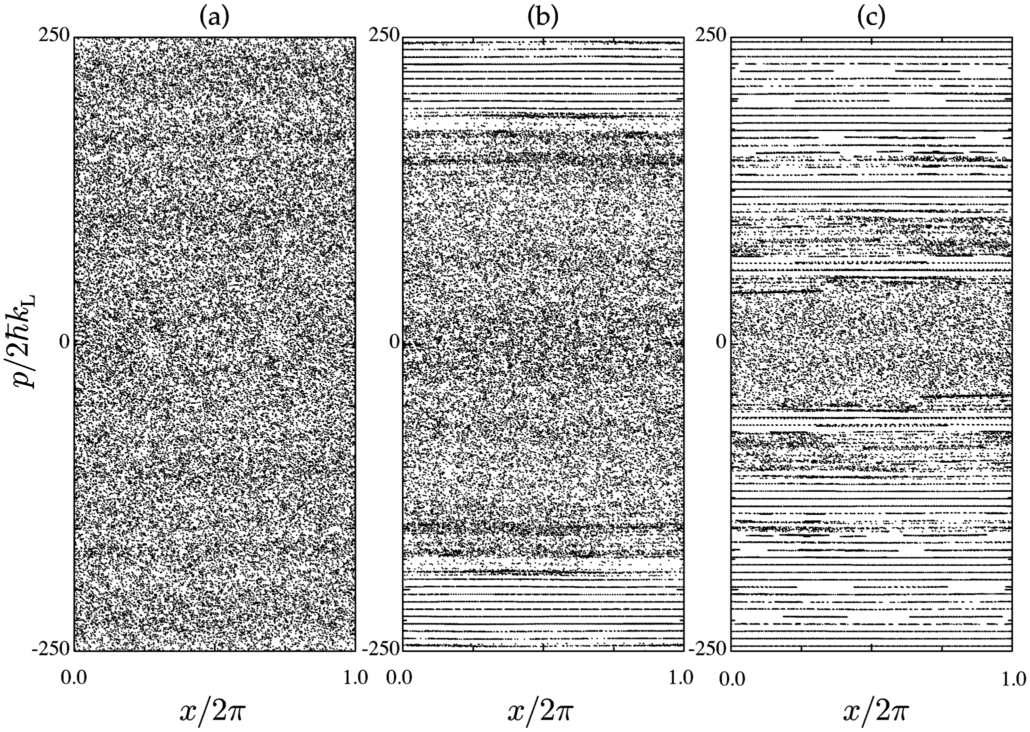

Figure 4.4: Phase-space plots for the kicked rotor with $K = 10.5$ in the cases of (a) δ-kicks, (b) square pulses with pulse width $t_\mathrm{p}/T = 0.014$, and (c) square pulses with $t_\mathrm{p}/T = 0.049$. Case (b) is similar to the pulses used in the experiments in this chapter. The effect of the finite pulses is to introduce KAM surfaces at large momenta in the otherwise chaotic phase space.

kicked-rotor Hamiltonian (4.10) for finite pulses as

$$H(x,p,t) = \frac{p^2}{2} + K\cos x \sum_{j=-\infty}^{\infty} c_j e^{-i2\pi jt} \ , \tag{4.33}$$

where the Fourier coefficient c_j is given by

$$c_j = \int_0^1 \sum_n f(t-n) e^{i2\pi jt}\, dt \ . \tag{4.34}$$

This Hamiltonian can in turn be rewritten as

$$H(x,p,t) = \frac{p^2}{2} + K \sum_{j=-\infty}^{\infty} |c_j| \cos(x - 2\pi jt + \phi_j) \ , \tag{4.35}$$

where we have defined the phases of the coefficients by $c_j = |c_j| \exp(i\phi_j)$, and we have used the fact that $c_j = c_{-j}^*$. Also, from the definition of $f(t)$, the coefficient c_0 of the stationary term is unity. In the case of δ-kicks, we saw that $c_j = 1$ holds true for all the coefficients. However, for finite pulses the Fourier weights drop off with increasing j, so that the primary resonances are attenuated at large momentum. Larger pulse widths imply a narrower spectrum, and hence a boundary at lower momentum, as we discovered using the simpler estimate above.

The effects of finite pulses are illustrated in Fig. 4.4, which shows the phase space for a δ-kicked rotor compared with two phase spaces corresponding to kicks with square pulse profiles. For the case of square pulses, we can define a momentum-dependent effective stochasticity parameter based on the Fourier transform argument as

$$K_{\text{eff}}(p) = K \text{sinc}\left(\frac{t_{\text{p}} p}{2}\right) \ , \tag{4.36}$$

where $\text{sinc}(x) = \sin(x)/x$, and p and t_{p} are scaled variables. This sinc profile is especially apparent in Fig. 4.4(c), where the phase space becomes stable as K_{eff} drops below ~ 1 (recall that the "stochasticity border" for the kicked rotor occurs near $K = 1$), becomes unstable again as it drops below ~ -1, and so on. The phase space in Fig. 4.4(b) corresponds closely to the situation in our experiments, and from this plot it is apparent that the momentum boundary occurs well outside the range of $|p/2\hbar k_{\text{L}}| < 80$ that we measure experimentally. More details about this momentum boundary and its effects on quantum transport can be found in [202, 204].

4.5 Quantum Transport

Now we turn to the subject of quantum transport in the kicked rotor. We introduced in Chapter 1 the dynamical localization phenomenon, where the quantum transport is in sharp contrast with the diffusive classical transport. The main symptom of dynamical localization is that momentum transport is frozen after the break time t_{B}. The underlying discrete-spectrum nature of the quantum dynamics also makes the quantum system numerically reversible, and hence manifestly nonchaotic, as we have also seen. In this section, we will examine several aspects of quantum transport in the kicked rotor, including some of the effects of noise on the quantum transport, and relate quantum and classical transport via their respective correlations.

4.5.1 Quantum Mapping

The equation of motion for the quantum δ-kicked rotor is just the Schrödinger equation,

$$i\bar{k}\partial_t|\psi\rangle = H|\psi\rangle \ , \tag{4.37}$$

where the Hamiltonian is given by Eq. (4.11). To derive a mapping for the quantum evolution, we start with the time-evolution operator $U(t,t_0)$ (so that $|\psi(t)\rangle = U(t,t_0)|\psi(t_0)\rangle$) for a system with a time-dependent Hamiltonian [267],

$$U(t,t_0) = \mathcal{T}\exp\left[-\frac{i}{\hbar}\int_{t_0}^{t} H(t')\,dt'\right] \ , \tag{4.38}$$

where $\mathcal{T}$ is the chronological (time-ordering) operator, which is necessary when $H(t)$ does not commute with itself at different times. Using a procedure similar to that used in the derivation of the classical standard map, we can write the kicked-rotor evolution operator as

$$U(n+1,n) = \exp\left(-\frac{ip^2}{2\bar{k}}\right)\exp\left(-\frac{iK\cos x}{\bar{k}}\right) \ , \tag{4.39}$$

where the "kick" operator acts on the state vector first, followed by the "drift" operator.

The quantum mapping in the form (4.39) is particularly suitable for calculations, because each component of the operator is diagonal in either the x or p representation, and thus is simple to apply to the wave function after appropriate Fourier transforms. Alternately, we can express the quantum mapping entirely in the momentum basis by using the generating function for the Bessel functions $J_n(x)$, with the result

$$\psi_{n+1}(p) = \exp\left(-\frac{ip^2}{2\bar{k}}\right) \sum_{l=-\infty}^{\infty} i^l J_l(K/\bar{k}) \psi_n(p - l\bar{k}) \ , \tag{4.40}$$

where $\psi_n(p)$ is the wave function in the momentum representation just before the nth kick. The ladder structure in momentum space is once again apparent in this form of the mapping. Also, since $J_n(x)$ drops off exponentially with n for $n > x$, each kick couples any given state to about $2K/\bar{k}$ other states.

Because the Hamiltonian for the kicked rotor is explicitly time-dependent, the energy is not a constant of the motion, and therefore there are no stationary states for the system. However, since the Hamiltonian is time periodic, we can define temporal *Floquet states* (or *quasienergy states*), in analogy with the spatial Floquet/Bloch solutions for the eigenstates of a periodic potential that we discussed in Chapter 2. We can write these states in an arbitrary representation as

$$\psi_\epsilon(t) = e^{-i\epsilon t/\bar{k}} u_\epsilon(t) \ , \tag{4.41}$$

where $u_\epsilon(t)$ is a periodic function of time (with the same unit period as the scaled Hamiltonian), and ϵ is the quasienergy of the state. These states are eigenstates of the one-period evolution operator,

$$U(n+1, n)\psi_\epsilon = e^{-i\epsilon/\bar{k}} \psi_\epsilon \ , \tag{4.42}$$

and thus are eigenstates in a stroboscopic sense, since their probability distribution is invariant under one period of time evolution.

Before continuing with the discussion of the quantum kicked rotor dynamics, it is useful to consider one more form for the quantum evolution equations. In the Heisenberg representation, we can integrate the Heisenberg equation of motion for the operators to obtain a map for the operators x_n and p_n just before the nth kick:

$$\begin{aligned} p_{n+1} &= p_n + K \sin x_n \\ x_{n+1} &= x_n + p_{n+1} \quad . \end{aligned} \tag{4.43}$$

This Heisenberg map has exactly the same form as the classical standard map (4.17), but with the classical variables replaced by quantum operators. What may seem surprising at first is that there is no mention of the quantum parameter $\bar{k}$. On iteration of the map, the sin function will operate on combinations of x and p, generating products of these operators at all orders, and thus Planck's constant enters via the commutation relation $[x, p] = i\bar{k}$. As we argued in Chapter 1, then, it is the nonlinearity that brings about quantum deviations from the classical behavior, and we also expect quantum effects to show up after repeated iterations of the map, rather than after a single time step.

4.5.2 Dynamical Localization

The work of Fishman, Grempel, and Prange (FGP) [40, 41, 268] marked an important milestone in the understanding of quantum localization. In this work, FGP showed that the quantum mapping for the kicked rotor could be written in a form that suggests a strong analogy with the problem of Anderson localization in one dimension [42, 268]. The Anderson problem considers the transport of an electron in a disordered potential, which consists of an array of barriers with flat regions between. The barriers are characterized by transmission and reflection probabilities, and classical particles that obey these particles would diffuse spatially throughout the potential. In the quantum case, if the barriers are arranged in a periodic fashion, there are certain particle energies that permit ballistic motion through the lattice (corresponding to the Bloch states of the system). This transport is analogous to the quantum resonance in the kicked rotor, to which we will return in Section 4.5.3. If the barriers are disordered, though, there is no resonance condition for long-range transport. In a path-summation picture [269], there are many paths by which an electron can travel to a distant site, but as a result of the disorder, the paths have random phases with respect to each other and thus tend to destructively interfere, effectively suppressing the quantum propagator for long-range transitions. The eigenfunctions in the Anderson problem are known to be exponentially localized, as opposed to the extended Bloch states. Additionally, FGP argued that although the kicked rotor has a dense point spectrum, the quasienergy spectrum is *locally* discrete in the sense that a localized excitation in momentum leads to a discrete spectrum, as states close together in quasienergy correspond to states that are widely separated in momentum [41].

In the Anderson-like form of the kicked rotor, the discrete "sites" are the plane-wave states in a momentum ladder, which are coupled by the kicks. The diagonal matrix elements that describe the lattice-site energies are pseudorandom [268] if $\bar{k}/2\pi$ is an irrational number (the rational case corresponds to the quantum-resonance phenomenon). In a more direct picture, the free phase evolution $\exp(-ip^2/2)$ between each kick causes the momentum-state phases to "twist," and the phases of widely separated momentum states become effectively randomized by this part of the evolution for generic values of $\bar{k}$. This pseudorandomness has essentially the same effect as the disorder in the Anderson problem, and thus the kicked-rotor Floquet states are likewise exponentially localized. This result provides a useful context for understanding dynamical localization, since the evolution to a localized state can be viewed as a dephasing of the quasienergy states. An initial momentum distribution that is narrow compared to a typical quasienergy state must be a coherent superposition of Floquet states. As time progresses, the precession of the phases of the basis states (each with different quasienergy) results in diffusive behavior for short times. At long times, when the basis states have completely dephased, the distribution relaxes to an incoherent sum of the exponentially localized basis states, resulting in an exponentially localized momentum distribution. For very long times, one also expects quantum recurrences as the basis states rephase [36], but these timescales are far beyond what we can observe experimentally.

An experimental measurement of dynamical localization is shown in Fig. 4.5.

This plot shows essentially the picture at which we just arrived: the initially narrow momentum distribution relaxes after a short time into a nearly stationary, exponential profile. The shapes of the distributions at various times are shown more clearly in Fig. 4.6. In this semilog plot, the exponential tails of the distribution at late times appear as straight lines. In viewing these measurements, it is important to realize that this localization is indeed dynamical localization and not the less interesting "adiabatic localization" [268], which is a result of the momentum boundary that we described above, and is a classical effect. The clean exponential tails that we observe make it clear that the dominant effect is dynamical localization, as adiabatic localization is characterized by more sharply truncated tails at the momentum boundaries [202, 203].

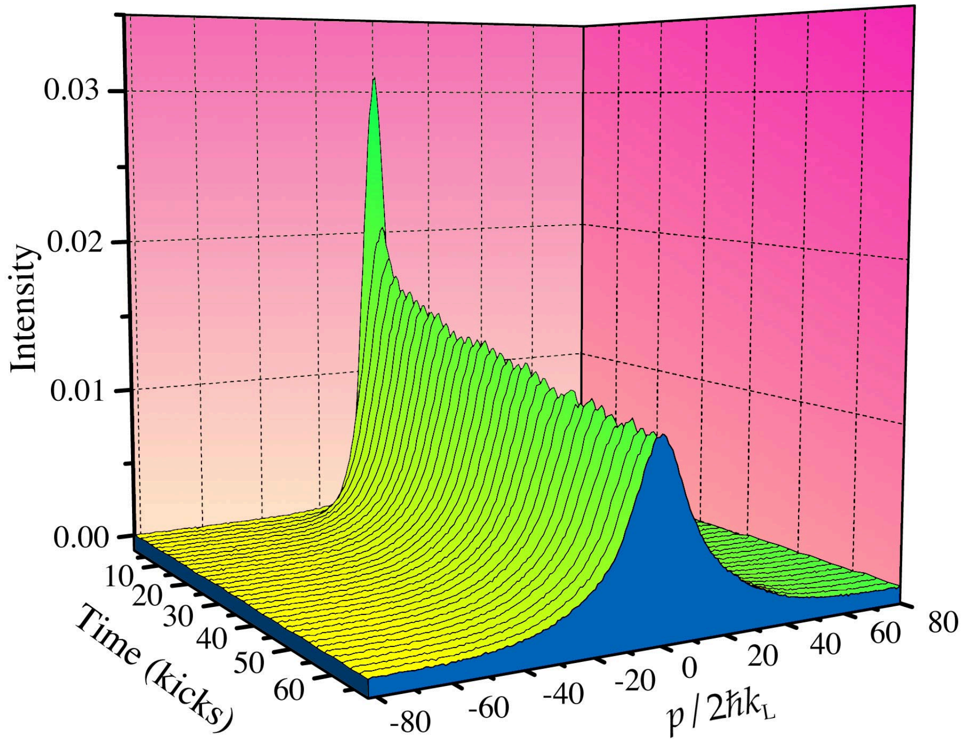

Figure 4.5: Experimental measurement of the momentum-distribution evolution in the kicked rotor, showing dynamical localization. Here $K = 11.5 \pm 10\%$, $T = 20$ μs ($\bar{k} = 2.077$), and $t_{\mathrm{p}} = 0.283$ μs. The nearly Gaussian initial distribution ($\sigma_p/2\hbar k_{\mathrm{L}} = 4.4$) relaxes rapidly to an exponential profile, which expands slowly.

The analysis that revealed the exponential nature of dynamical localization has implicitly assumed a kicked rotor, not a kicked particle. Since the continuous momentum space of the particle consists of many discrete, uncoupled, rotor-like momentum ladders, the same arguments apply to each ladder separately, and we expect localization to occur in a similar way in the experiment. In fact, if the momentum distribution is coarse-grained on the scale of $\bar{k}$, the particle momentum distribution evolves to a much smoother exponential profile than the rotor, due to averaging over the many ladders.

4.5.3 Quantum Resonances

In the cases where $\bar{k}/2\pi$ is a rational number, the motion is of quite a different (but still distinctly nonclassical) character. To illustrate the effect here, we consider the case of $\bar{k} = 4\pi$, and we restrict our attention to the "symmetric" momentum ladder, $p = s\bar{k}$ for integer s (i.e., we are assuming a kicked rotor, rather than a particle). The kinetic

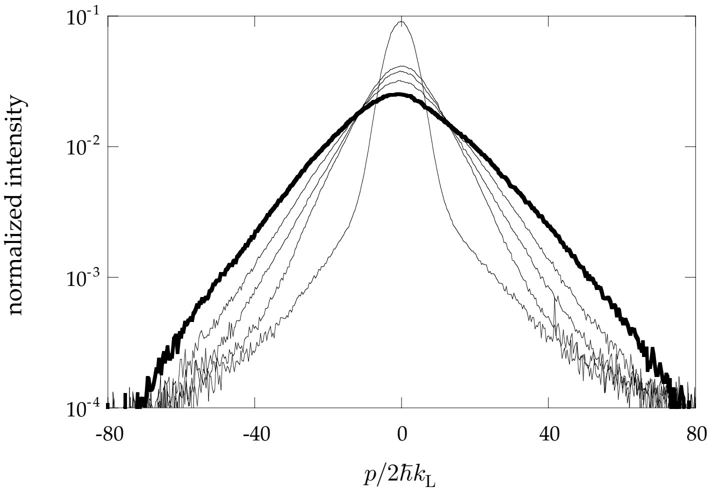

Figure 4.6: Experimentally measured momentum distribution evolution, shown for 0, 10, 20, 40, and 80 kicks ($K = 11.2 \pm 10\%, \bar{k} = 2.077$); the zero-kick case is the narrowest distribution, and the 80-kick distribution is highlighted in bold. Because the vertical axis in this plot is logarithmic, the tails of the localized (exponential) distribution appear as straight lines.

energy part of the evolution operator from (4.39),

$$\exp\left(-\frac{is^2\bar{k}}{2}\right) \quad , \tag{4.44}$$

collapses to unity, and the evolution operator for n kicks can be written as

$$\exp\left(-\frac{inK\cos x}{\bar{k}}\right) \quad . \tag{4.45}$$

This operator is equivalent to the operator for a single super-kick with stochasticity parameter nK. Recalling the analysis based on the expanded form (4.40) of the quantum standard map, the wave packet in this case will have propagating edges (asymptotically) at $p = \pm nK$. Correspondingly, the kinetic energy increases as t^2, which is characteristic of ballistic transport. This phenomenon is known as a quantum resonance [270, 271], and is related to the Talbot effect in wave optics [272].

The situation is obviously more complicated for the kicked-particle case, since the evolution operator does not trivially collapse for the other momentum ladders. The other states do not exhibit ballistic transport, but rather form a localized, Gaussian-like profile, which is narrower than the corresponding exponentially localized case [200]. An analytic treatment of the transport in this more general case can be found in [201]. The coexisting ballistic and localized behaviors at the $\bar{k} = 4\pi$ quantum resonance are visible in the measured and simulated evolutions in Fig. 4.7.

Experimentally, only the low-order quantum resonances (with $\bar{k}$ an integer or half-integer multiple of 2π) cause visible deviations from localization, as the higher-order resonances can take extremely long times to become manifest. The other low-order case that we have studied is the “antiresonance” at $\bar{k} = 2\pi$. For the symmetric momentum ladder, the kinetic-energy part of the evolution operator collapses to $(-1)^s$ for the state $p = s\bar{k}$, which effectively amounts to a time-reversal operator ($p \rightarrow -p$). In this case, an initial state on this ladder reconstructs itself every other kick. In the general particle case, the behavior is similar to that of the $\bar{k} = 4\pi$ resonance [209].

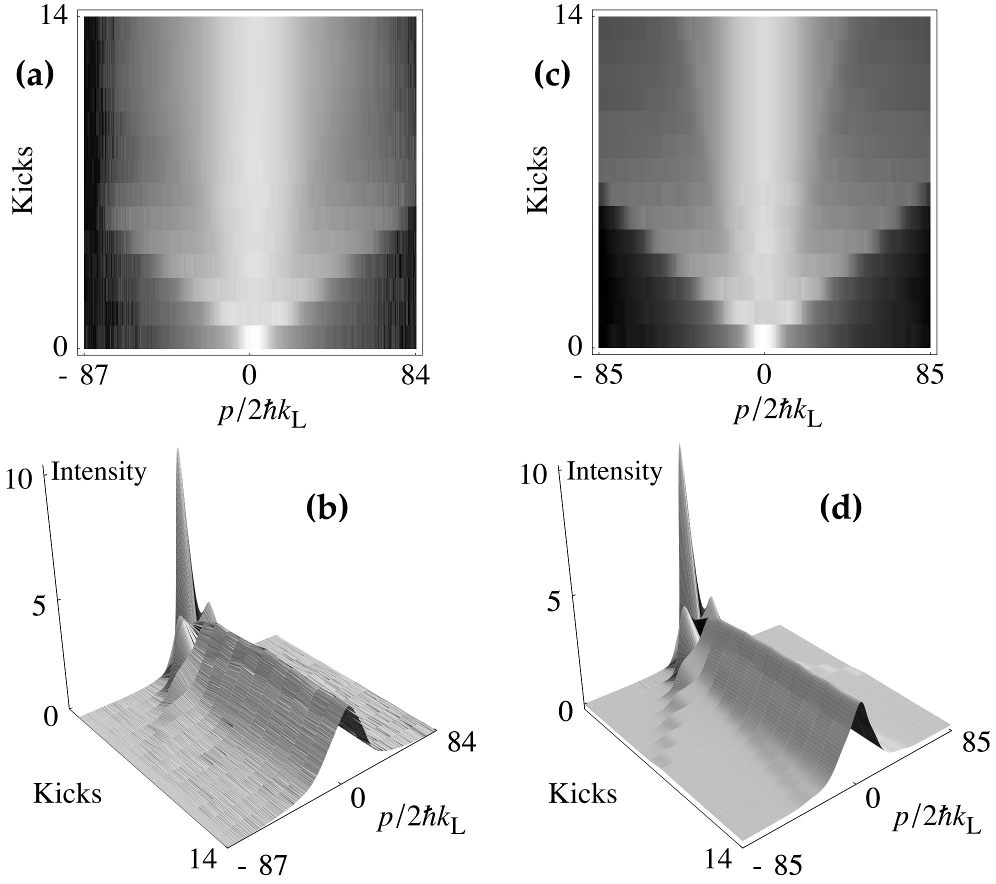

Figure 4.7: Experimental observation of ballistic transport at quantum resonance. The evolution of the atomic momentum distribution is plotted for the experimental measurement (a, b) and quantum simulation (c, d). The parameters are $\bar{k} = 4\pi$ ($T = 121$ μs) and $K = 184$. The simulation assumed square pulses with $t_\mathrm{p} = 0.295$ ns, and used an initial condition constructed directly from the experimentally measured initial distribution. In order to obtain good qualitative agreement and avoid numerical artifacts, a large simulation (that averaged over an ensemble of 50 wave packets, with centers distributed uniformly in position, and employed a grid spanning $p/2\hbar k_\mathrm{L} = \pm 256$ with a resolution of $\Delta p/2\hbar k_\mathrm{L} = 1/1024$, binned over $2\hbar k_\mathrm{L}$ for a smooth distribution) was necessary.

4.5.4 Delocalization

We now turn to the concept of the destruction of localization in the quantum kicked rotor. As the deviation from the classical dynamics is primarily a result of long-time quantum correlations, dynamical localization should be susceptible to external noise and environmental interaction, either of which would suppress these correlations. Note that noise and environmental interaction are fundamentally different in nature: noise is a unitary process, and is hence reversible in principle, whereas the latter case is an interaction with a very large (i.e., possessing many degrees of freedom) external system (reservoir), which is an inherently irreversible process. However, a noisy (stochastic) perturbation is the important effect of the environment, as we argued in Chapter 1, so that from an experimental point of view, these two situations are effectively equivalent. For the quantitative study of delocalization in Section 4.6, we chose to study noise effects because of the high degree of experimental control over the noise implementation. The first theoretical study of the influence of noise on the quantum kicked rotor appeared in [35], where it was found that a sufficiently strong random perturbation could restore diffusion at the classical rate. Soon thereafter, a more detailed theoretical treatment was presented by Ott, Antonsen, and Hanson [133], who showed that if the scaled Planck constant is sufficiently small, classical diffusion is restored, even for small amounts of added noise.

In the heuristic picture presented in [268], the noise can be characterized by a coherence time t_c, beyond which quantum coherence is destroyed. In the case of weak noise, where $t_\mathrm{c} \gg t_\mathrm{B}$, the noise restores diffusion after the break time at a rate proportional to $1/t_\mathrm{c}$, which is much slower than the initial classical-like diffusion phase. If, on the other hand, the coherence time is less than the break time, then we expect (for small $\hbar$) that localization is completely destroyed and classical behavior is restored.

We will now examine experimental evidence that localization can be destroyed by interaction with optical molasses. This situation is effectively an interaction with a dissipative environment, which causes momentum perturbations due to the photon absorption and emission and also dissipation of kinetic energy due to the cooling effect of the molasses. The effect on the kinetic energy evolution is plotted in Fig. 4.8 for several different values of the spontaneous scattering rate. Qualitatively, the energy diffusion increases with increasing scattering rate. This increased heating cannot be explained in terms of trivial photon-recoil heating because the molasses cools the distribution, and so the increased heating indicates the destruction of localization. The corresponding effect of the molasses light on the momentum distribution evolution is shown in Fig. 4.9. The exponential profile is again evident in the zero-noise case. As the spontaneous emission is applied, the late-time distribution becomes rounder, taking on a Gaussian profile in the cases of 5.3% and 13% scattering probability per kick (this seems to disagree with [273], where it is claimed that the distributions remain "essentially exponential" with scattering rates around 5%/kick).

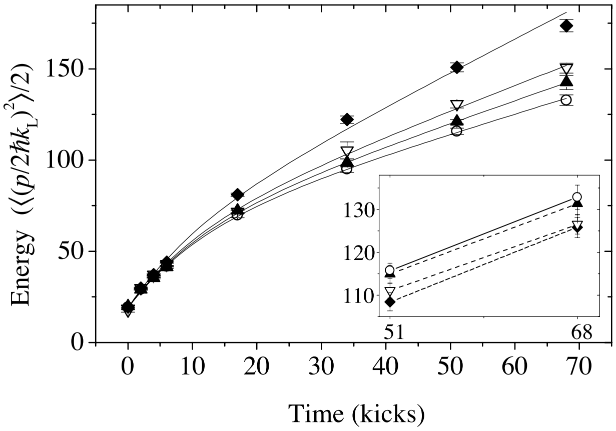

Figure 4.8: Experimental observation of decoherence due to spontaneous photon scattering in optical molasses. The scattering probabilities are 0% (circles), 1.2% (filled triangles), 5.0% (open triangles), and 13% (diamonds) per kick, and the kicked-rotor parameters are $K = 11.9 \pm 10\%$ and $\bar{k} = 2.077$. Although spontaneous emission generally causes momentum diffusion and therefore heating of the atomic sample, the optical molasses cools the atoms, as shown in the inset, where the molasses interaction was added *after* the lattice kicks. Thus, the enhanced diffusion in this dissipative case is due only to the destruction of localization.

The reader may notice in Fig. 4.8 that the late-time energy growth in the zero-noise case, while slower than the short-time growth, is still nonzero, as we might expect from a simple picture of localization. However, "perfect" localization is not necessarily expected over the time scales considered in the experiment, as we can see from the quantum simulation in Fig. 1.5. We have verified that this late-time growth is not due to the nonideal effects of the optical lattice discussed in Chapter 2 by varying the lattice detuning while keeping V_0 constant by compensating with a corresponding lattice intensity change. The other sources of noise are small, but it is difficult to rule out residual phase noise of the lattice (caused by mechanical vibrations of the retroreflecting mirror) as a contribution to late-time diffusion. (Recall that we have characterized the phase

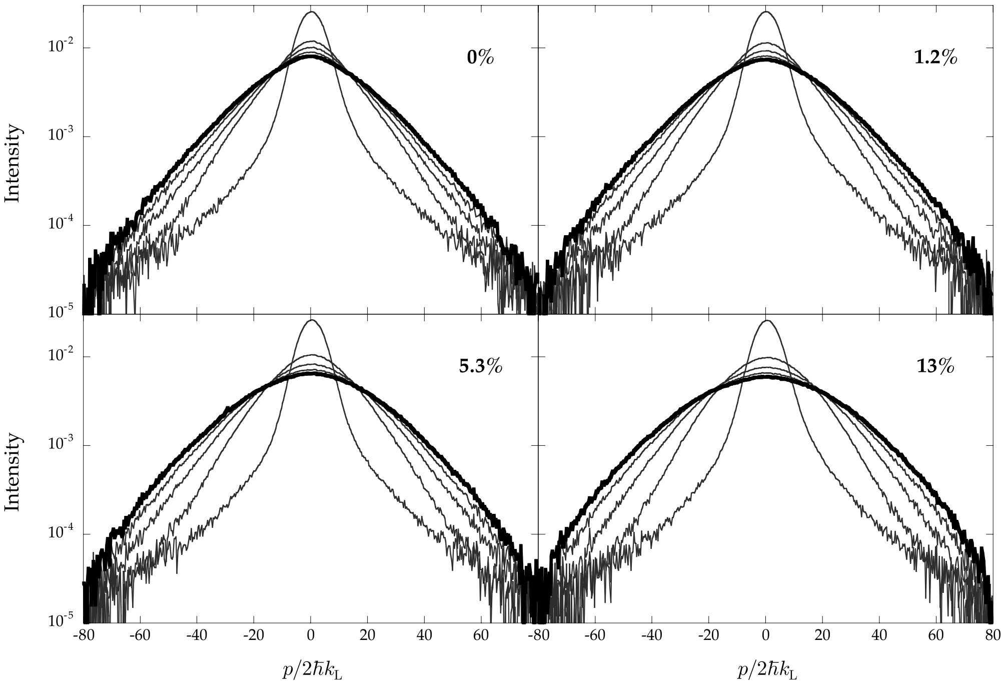

Figure 4.9: Experimental study of how the dissipative optical molasses interaction influences the momentum distributions in the quantum kicked rotor. The scattering rates here, 0%, 1.2%, 5.3%, and 13%, correspond closely to those displayed in Fig. 4.8. At the higher scattering rates, the late-time distribution makes a transition from the localized exponential profile to a classical-like Gaussian shape (which appears parabolic in these semilog plots).

noise in the optical lattice in Section 3.4.2).

We have also studied the effects of amplitude noise in the quantum kicked rotor (we examine these results in Section 4.6), as well as noise in the time between kicks and spontaneous emission from a far-detuned traveling wave applied between kicks. All of these noises cause a similar transition from localization to classical-like diffusion at late times. The different types of noise should in principle be different in nature. Amplitude noise is "ladder-preserving," which means that atoms can still only change momentum by $2\hbar k_{\mathrm{L}}$ at a time, even with this perturbation. Other types of noise, such as spontaneous emission, are "nonperturbative" in the sense that they can break this ladder symmetry. As a result of the interaction of the previously uncoupled ladders, this noise can lead to more effective destruction of localization [105, 268, 274]. A quantitative comparison between perturbative and nonperturbative noises is difficult, though, and we cannot distinguish any differences based on our current data. A clean quantitative study would probably best be accomplished with different types of noise than we have studied, which could be for example a perturbation by a second lattice with a different period [274] (realized by crossed but not counterpropagating laser beams).

4.5.5 Quantum Correlations

The above analysis leading to exponential quantum localization was based on dynamically generated disorder, and therefore we might expect that correlations also play an important role in the quantum dynamics. Shepelyansky showed numerically [35] and analytically [275] that whereas the classical correlations drop off quickly with time (when any residual stable structures are too small to affect the dynamics on a short time scale, i.e., away from the accelerator modes), the quantum correlations persisted for much longer times than the corresponding classical correlations. In contrast, for cases of smaller K (and hence more stability), the quantum and classical correlations were similar after the break time. This difference in the correlations is intuitively clear from Eq. (4.23). For localization, the long-time quantum correlations near the break time must be negative, bringing this sum to nearly zero, in order for the diffusion to freeze. For the quantum resonance case, the correlation series must have a long positive tail, such that the sum (4.23) diverges.

Shepelyansky also made another important observation regarding the quantum correlations, which will be important for the interpretation of the results presented here. In particular, he calculated the first few quantum correlations and found that they had approximately the same form as the corresponding classical correlations upon the substitution [105, 275, 276]

$$K \longrightarrow K_{\mathrm{q}} := \frac{\sin(\bar{k}/2)}{\bar{k}/2} K \ . \tag{4.46}$$

(Note, however, that the correlations used in [276] were defined without the factor of K^2 that appears in Eq. (4.21).) Hence, a good approximation for the initial quantum diffusion rate in the absence of noise is

$$D_{\mathrm{q}}(K, \bar{k}) = \frac{K^2}{2} \left(\frac{1}{2} - J_2(K_{\mathrm{q}}) - J_1^2(K_{\mathrm{q}}) + J_2^2(K_{\mathrm{q}}) + J_3^2(K_{\mathrm{q}}) \right) \ , \tag{4.47}$$

where, as in the classical calculation, it is assumed that the initial quantum distribution is uniform over the unit cell in the classical phase space. Consequently, there is an oscillatory dependence of the initial quantum diffusion rate on K_{q} that is closely related to the underlying classical dynamics. However, the oscillations are shifted due to the quantum scaling factor in (4.46). Since the width of the localized distribution (the *localization length*) is related to the initial diffusion rate by the heuristic/numerical result [268, 276],

$$t_{\mathrm{B}} \approx \xi = \frac{D_{\mathrm{q}}}{\bar{k}^2} \tag{4.48}$$

(where ξ is the localization length of the Floquet states, so that the momentum probability distributions have the form $\exp[-|p - p_0|/(\xi/2)]$), these oscillations are also apparent in the long-time quantum distributions.

This oscillatory structure and the confirmation of the quantum scaling is shown in Fig. 4.10, where the experimentally measured energy is plotted for a fixed interaction time as a function of K_q. The correct quantum scaling causes the oscillations in these curves to match for different $ƙ$. At the maxima of these curves, the late-time momentum distributions are not exponential, having more of a curved profile in the tails, as shown in Fig. 4.11. This effect is likely an influence of the accelerator modes and possibly other stable structures. Theoretical work has shown that classical anomalous transport enhances fluctuations in the Floquet-state localization lengths [277], and the deviations of the quasienergy states from a purely exponential shape may also be due to classical correlations [278]. We will also return to this issue of the late-time distribution shape in Section 4.7.

Notice that to reach the classical limit in our experiment, the short-term correlations must also be modified by the noise. This is especially true in view of the shift caused by the quantum scaling factor in (4.46), which shifts the diffusion oscillations by

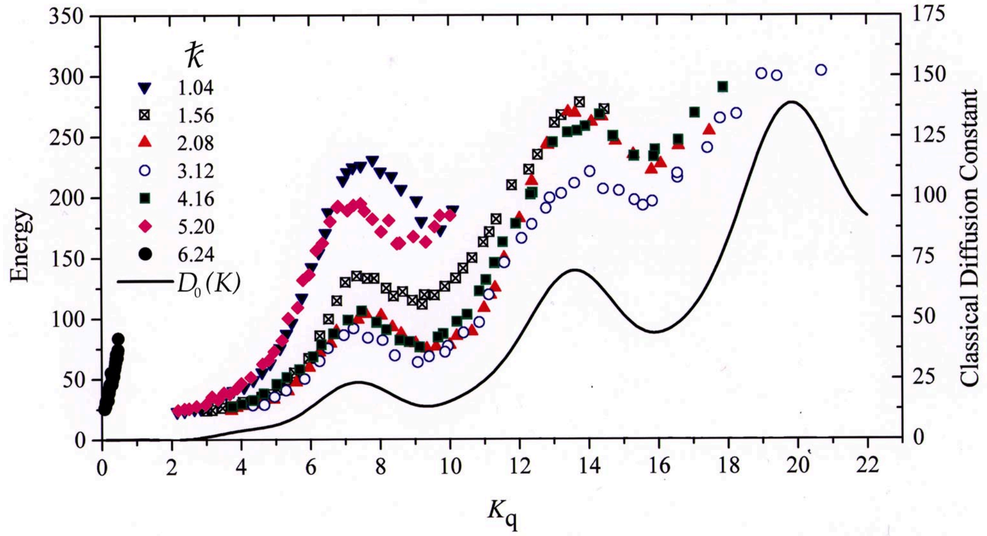

Figure 4.10: Experimental verification for the scaling of K_q. The measured ensemble kinetic energy is plotted for a fixed time as a function of the rescaled stochasticity parameter for several values of $ƙ$. The measurement times are 35 kicks ($ƙ = 1.04, 1.56, 2.08, 3.12, 4.16$), 28 kicks ($ƙ = 5.20$), and 24 kicks ($ƙ = 6.24$). The solid line is a plot of the classical (standard map) diffusion rate, Eq. (4.24). The locations of the oscillatory structures match well when plotted in terms of the rescaled K, supporting the validity of the K_q scaling.

about 20% in K for the typical experimental value $\bar{k} = 2.08$ in the experiments here. It is possible to generalize the work of Shepelyansky leading to Eq. (4.47) to include amplitude noise in essentially the same way as in the classical calculation, with the result (see Section 4.8 for details)

$$D_{\mathrm{q}}(K,\bar{k}) = \frac{K^2 + \mathrm{Var}(\delta K)}{4} + \frac{K^2}{2}\left(-\mathcal{Q}_2(K_{\mathrm{q}}) - \mathcal{Q}_1^2(K_{\mathrm{q}}) + \mathcal{Q}_2^2(K_{\mathrm{q}}) + \mathcal{Q}_3^2(K_{\mathrm{q}})\right), \tag{4.49}$$

where

$$\mathcal{Q}_n(K_{\mathrm{q}}) := \int_{-\infty}^{\infty} P(\delta K) J_n(K_{\mathrm{q}} + \delta K_{\mathrm{q}}) d(\delta K), \tag{4.50}$$

and $\delta K_{\mathrm{q}} = \delta K \sin(\bar{k}/2)/(\bar{k}/2)$. Thus, the short-time quantum correlations are washed out in much the same way as the classical correlations, as in Eq. (4.29). However, since the locations of the classical and quantum oscillations in $D(K)$ are different for our operating parameters, we can conclude that in order to observe good correspondence between quantum and classical evolution, the applied noise must be very strong (i.e.,

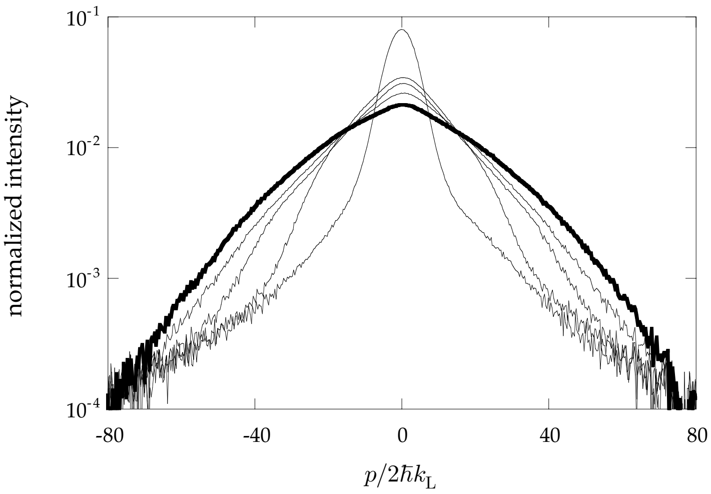

Figure 4.11: Experimentally measured momentum-distribution evolution, shown for 0, 10, 20, 40, and 80 kicks. In this plot, $K = 8.4 \pm 10\%$, $\bar{k} = 2.077$, corresponding to a peak in the quantum diffusion curve (as in Fig. 4.10). The zero-kick case is the narrowest distribution, and the 80-kick distribution is highlighted in bold. The late-time distribution is qualitatively different from the exponentially localized case in Fig. 4.6, which corresponds to a minimum in the quantum diffusion curve.

we must have t_{c} on the order of one kick, so that all the higher-order correlations are destroyed). In this case, both quantum and classical diffusion will proceed at the quasilinear rate, since the diffusion oscillations will be destroyed (as in Fig. 4.3), and the global behavior will be the same. For lower levels of noise, we might expect to recover diffusive behavior in the quantum system (if the long-time correlations responsible for localization are destroyed), but possibly at a rate that does not match the classical prediction. Heuristically, in the picture of [105, 133], the noise causes diffusion in momentum at a rate $2D$, and we can expect coherence to be broken when diffusion occurs on the scale $\bar{k}$ between neighboring momentum states, so that

$$t_{\mathrm{c}} = \frac{\bar{k}^2}{2D} \quad . \tag{4.51}$$

For the case of uniformly distributed amplitude noise, this estimate becomes

$$t_{\mathrm{c}} = \frac{24\bar{k}^2}{(\delta K_{\mathrm{p-p}})^2} \quad . \tag{4.52}$$

We can insert some values corresponding to the data to be analyzed in Section 4.6.2.1, where $K = 11.2$ and $\bar{k} = 2.08$. In order to break localization, we must have $t_{\mathrm{c}} \sim t_{\mathrm{B}}$, which is around 10 kicks in the experimental data, thus requiring about 30% amplitude noise. To obtain good correspondence, however, requires $t_{\mathrm{c}} \sim 1$ for quasilinear diffusion, and thus the higher noise value of around 90%. These simple estimates are in reasonable agreement with the experimental data.

4.6 Quantitative Study of Delocalization

Up to this point, we have shown that noise can lead to a loss of localization, with distributions that have a classical form. However, we have not yet addressed the more interesting question of whether the experimental data match the classical prediction in the presence of noise. Answering this question in a quantitative way requires a nontrivial amount of effort in carefully modeling the experiment in order to make an accurate classical prediction for comparison with the experimental data.

4.6.1 Classical Model of the Experiment

In order to facilitate an accurate comparison of the experimental data to the classical limit of the kicked rotor, we have performed classical Monte Carlo simulations of the experiment. In these simulations, a large number (2×10^5) of classical trajectories were computed, each with a distinct realization of amplitude noise; momentum distributions and ensemble energies were then extracted from this set of trajectories. Additionally, we accounted for several different systematic effects that were present in our experiment, in order to provide the best possible classical baseline for comparison with the experimental data. In the remainder of this section we describe in detail each of the systematic effects that we have accounted for and how we have included them in the comparison of the data to theory.

The effects that we will describe in this section are illustrated in Fig. 4.12. This plot compares the energy evolution for different cases where different corrections are accounted for. As each correction is (cumulatively) taken into account, the resulting energy curve is lower and less linear. Indeed, there is quite a large difference between the uncorrected, linear δ-kick curve that one might expect to observe and the fully corrected curve. The importance of this rather technical discussion of experimental details is clear: without carefully taking into account these systematic effects, one might mistakenly attribute curvature in the experimental energy data to residual quantum localization effects. It is also important to emphasize that these effects cause a reduction in the dynamic range of the experimental measurements, but they do not change the underlying physics in a fundamental way. Finally, we note that most of these systematic effects are such that it is either impractical or impossible to compensate for them with a simple correction to the experimental data. In this sense, the "energies" that we use in our comparisons are not true energies, but relatively complicated functions of the true energies and many other experimental parameters. It is therefore the ability to take these effects into account in the classical simulations that allows for a meaningful quantitative comparison between our experiment and classical theory.

The first, and perhaps most important, effect that we account for is the detailed pulse shape $f(t)$ of our kicks. The nonzero temporal width of the pulses leads to an effective reduction in the kick strength at higher momenta, as we discussed in Section 4.4.4, and so it is important to accurately model the experimental pulses in order to reproduce the correct tails in the momentum distributions. It turns out that our experimental pulses are well modeled by the function

$$f(t) = \frac{1}{2\eta_{\mathrm{erf}}}\left[\mathrm{erf}\left(\frac{(t-t_1)\sqrt{\pi}}{\delta t_1}\right) - \mathrm{erf}\left(\frac{(t-t_2)\sqrt{\pi}}{\delta t_2}\right)\right] \quad , \tag{4.53}$$

where $t_2 - t_1 = 295$ ns is the full width at half maximum (FWHM) of the pulse, $\delta t_1 = 67$ ns is the rise time of the pulse (defined such that a straight line going from 0 to 100% of the pulse height in time δt_1 matches the slope of the rising edge at the

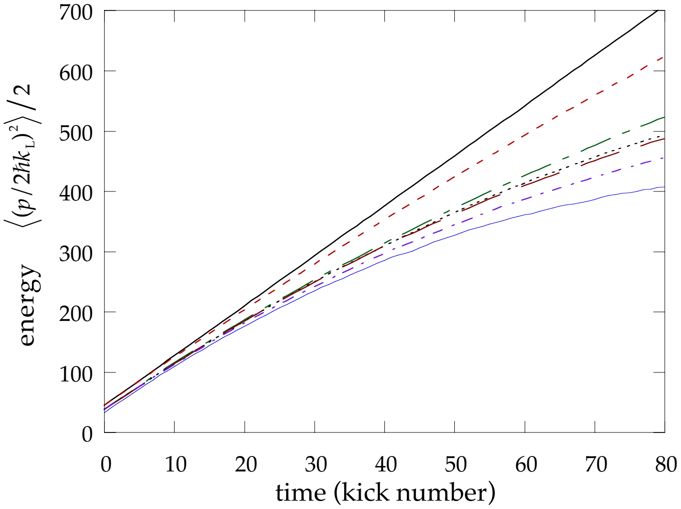

Figure 4.12: Example of how the systematic effects described in the text can affect the measured energies. Shown are the simulated average energy evolution for typical operating parameters ($K = 11.2$, 100% noise level) and typical parameters for the systematic corrections. The solid curve is the ideal case, corresponding to the δ-kicked rotor with no corrections; the successively lower curves represent the cumulative result as each effect is accounted for (in the order of presentation in the text): nonzero pulse duration (dashed), MOT (detection) beam profile (long dot-dash), clipping due to width of CCD chip (dotted), profile of interaction beam/transverse atomic motion (long dashes), correction for free-expansion measurement (dot-dash), and vertical-offset bias (thin solid).

half-maximum point), $\delta t_2 = 72$ ns,

$$\operatorname{erf}(x) := \frac{2}{\sqrt{\pi}} \int_0^x \exp(-t^2)\,dt \tag{4.54}$$

is the error function, and η_{erf} is a normalization factor, which takes the value $t_2 - t_1$ for small values of $\delta t_{1,2}/(t_2 - t_1)$. The function (4.53) is plotted along with a measured optical pulse in Fig. 4.13. The rise and fall times in the pulse were mainly due to the response time of the switching AOM for the Ti:sapphire laser beam and the rise time of the SRS DS345 arbitrary-waveform synthesizer that drives the AOM controller. It should be noted that although the agreement between the pulse model and the experimentally measured pulses is excellent, Eq. (4.53) is merely an empirical model of our observed pulse profiles. In the simulations, the classical equations of motion were directly integrated, using Eq. (4.53) for the kick profile.

The next effect that we consider is due to the Gaussian profile of the optical molasses laser beams. Recall that to measure momentum distributions, we imaged the light scattered by the atoms from the molasses beams after a free-expansion time. Since

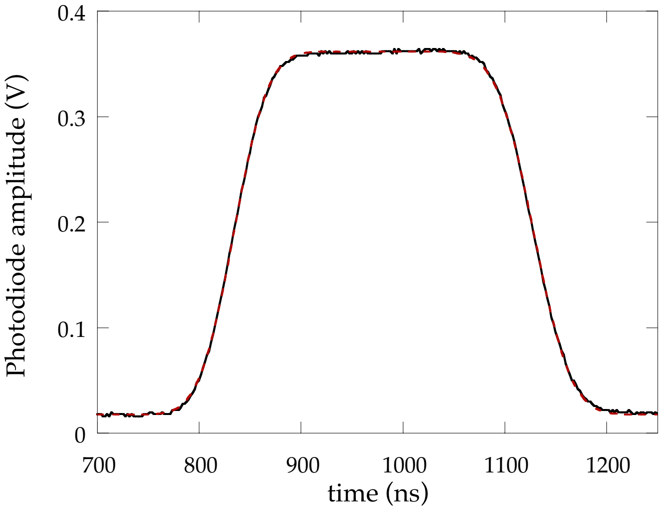

Figure 4.13: Model function (4.53) for the experimental pulses (dashed line) compared to an actual experimental pulse as measured on a fast photodiode (solid line). The two curves are nearly indistinguishable.

the light was not uniform over the atomic cloud, the scattering rate due to atoms with momentum p is given by

$$R_{\mathrm{sc}} = N(p)\left(\frac{\Gamma}{2}\right)\frac{(I(x)/I_{\mathrm{sat}})}{1+4\,(\Delta/\Gamma)^2+(I(x)/I_{\mathrm{sat}})} \quad , \tag{4.55}$$

where $N(p)$ is the number density of atoms with momentum p, $I(x)$ is the local intensity at spatial position x, Γ is the excited state decay rate, and I_{sat} is the saturation intensity ($=$ 2.70 mW/cm^2 for approximately isotropic pumping on the trapping transition). Also, in the free expansion measurement, the unscaled variables x and p are related by

$$x = v_{\mathrm{r}}(p/\hbar k_{\mathrm{L}})t_{\mathrm{drift}} \quad , \tag{4.56}$$

where $v_{\mathrm{r}} = 3.5$ mm/s is the velocity corresponding to a single photon recoil, and t_{drift} is the free drift time of the momentum measurement. The spatial intensity profile of the six beams is given by

$$I(x) = 2I_0\left[e^{-2x^2/w_0^2} + 2e^{-(x^2+2z^2)/w_0^2}\right] \quad , \tag{4.57}$$

where I_0 is the intensity at the center of one of the six beams, $w_0 = 11$ mm is the beam-radius parameter of the Gaussian beams, z is the vertical position of the atoms (transverse to the standing wave, in the direction of gravity), the first term represents the two vertical beams, and the last term represents the four horizontal beams, each at 45° to and in the horizontal plane with the standing wave. To account for this effect, we applied a correction to the classical simulation of the form

$$f_{\mathrm{mol}}(x) = \frac{f_{\mathrm{I}}(x)}{c_2 + f_{\mathrm{I}}(x)}, \tag{4.58}$$

where $f_{\mathrm{I}}(x) = I(x)/2I_0$ is a scaled intensity profile, and $c_2 = [1+4(\Delta/\Gamma)^2][I_{\mathrm{sat}}/(2I_0)]$. The value of c_2 was determined to be 5.94 by fitting the correction (4.58) to a known exponentially localized distribution for various drift times; this value is in reasonable agreement with the expected value of c_2 from the laser parameters.

The finite extent of our imaging CCD camera chip also had an impact on our measurements. We set up our imaging system such that a typical localized distribution was just contained within the imaged area after a 15 ms drift. For strongly noise-driven cases, though, the momentum distribution could extend significantly past the edges of the imaged area. This effect had little impact on the measured momentum distributions, since it only restricted the measurable range of momentum. However, the energies computed from this momentum distribution are sensitive to this truncation, even if the population in the truncated wings is small. The result is a systematic reduction in the measured energy. It was straightforward to model this effect in the simulations by rejecting trajectories that fall outside the experimental window.

Another effect that we accounted for is the transverse position of the atoms in the standing-wave beams. Although the spatial size of the beam (with $1/e^2$ radius $w_0 = 1.5\,\mathrm{mm}$) was large compared to the size of the initial MOT cloud ($\sigma_x = 0.15\,\mathrm{mm}$), the variation in kick strength over the atomic distribution must be accounted for, especially as the evolution progresses and the atoms move further out transversely. Hence each atom sees an effective kick strength of $K_{\mathrm{max}} \exp[2(y(t)^2 + z(t)^2)/w_0^2]$, where the transverse coordinates y and z are given in scaled units by

$$\begin{aligned} y(t) &= y_0 + p_{y0}t \\ z(t) &= z_0 + p_{z0}t - gt^2/2 \ . \end{aligned} \tag{4.59}$$

In these equations, we have used the scaled gravitational acceleration g, which is related to the acceleration in physical units by $g = 2k_{\mathrm{L}}T^2 g_{\mathrm{phys}}$. In the simulations, each particle was given initial transverse positions y_0 and z_0 according to a Gaussian distribution that matched the measured MOT size, and initial momenta p_{y0} and p_{z0} that matched the momentum distribution measured along the standing wave. It should be noted that this correction may actually increase or decrease the final energies compared to an uncorrected simulation using the mean value of K, even though the mean value of K effectively decreases with time. This is because a subset of the atoms may completely dominate the diffusion if they are located more closely to one of the maxima of $D(K)$. For the beam waist/MOT size ratio used here, there is a spread in K of around 5% in our initial distribution.

We additionally accounted for a systematic effect that occured in our free-expansion measurement technique. This technique relied on allowing the atomic cloud to expand freely for 15 ms after the interaction with the standing wave in order to convert the spatial distribution of the atoms into an effective momentum distribution. However, the interaction with the standing wave lasted as long as 1.6 ms for these experiments. Since we define the drift time as the time from the beginning of the standing-wave interaction to the beginning of the camera exposure, the drift time effectively becomes smaller as the number of kicks in the experiment increases. There is no simple way to directly correct for this effect, so we included this effect in our simulations by simulating the free-expansion process. The initial spatial distribution was chosen (in scaled units) to be uniform in the range $[-\pi, \pi)$, which is extremely small compared to the spatial distribution after the expansion. We did not choose the distribution from the MOT spatial distribution to account for convolution effects; these effects have been approximately accounted for already, since the initial momentum distribution used in the simulations is the measured momentum distribution, which was already convolved with the initial spatial distribution. Then the effective momentum of each particle measured by the free-expansion method is given by

$$p_{\text{eff}}(t) = x(t) + \left(\frac{t_{\text{drift}} - t}{t_{\text{drift}}}\right) p(t) \ , \tag{4.60}$$

where all quantities in this equation are scaled.

The final effect that we took into account was due to variations in the background levels measured by the data acquisition (Princeton Instruments) camera. Although we performed background subtraction, which greatly improved our signal-to-noise ratio, the offset levels after the subtraction were generally nonzero, due to fluctuations (from drifts in the camera electronics) and constant offsets (from physical effects in the imaging of the atomic cloud). To enhance the reproducibility of our data, we used the following procedure to fix the zero level of our measured distributions: the 40 lowest points (out of 510 total) in the distribution were averaged together and defined to be the zero level. The disadvantage of this technique is that it resulted in a slight negative bias in the offset level from the "true" distribution. For typical measurements of localized distributions, the bulk of the distribution was contained well within the imaged region. In these cases, the measured values near the edges of the imaged region were small compared to those in the center of the distribution, and the error in the offset was negligible. However, for strongly noise-driven cases, a significant fraction of the distribution could fall outside the imaged region, as noted above. In these cases, the lowest 40 values were then significantly different from the true zero level, and our procedure introduced a significant bias. It was straightforward to mimic this process in the simulations, but in some data sets it was possible to restore the correct offset level. For our typical studies of the transition from localized to delocalized behavior, the only cases that were significantly biased are the strongly noise-driven cases, which behaved essentially classically (as we will see later). Then one can assume that the biased cases can be modeled as Gaussian distributions, with the MOT beam profile correction applied to them, and obtain the correct offset by fitting the model function to the measured distribution. This *ansatz* was justified by the essentially perfect fit of the model function whenever its use was appropriate. Using this idea, we implemented an automatic procedure for restoring the correct offset in the data sets where the procedure was sensible (Figs. 4.15-4.20). In other data (Fig. 4.14), such as measurements of exponentially localized distributions with very long localization lengths, such a procedure was clearly inappropriate, and this effect was instead accounted for in the corresponding simulations.

There are a few other effects that we did not account for in the simulations, including spontaneous emission, the stochastic dipole force, collisions between atoms, and other sources of noise, most notably phase jitter in the standing wave (we have discussed all these effects in more detail in Chapter 2). These effects cause decoherence, but they were sufficiently weak that at low levels of applied amplitude noise, quantum effects were easily observed, and at high amplitude noise levels, the applied noise dominated any effects that these other processes might have had. Thus, these effects did not hinder our ability to study quantum-classical correspondence in our system.

We also note that the corrections we have mentioned lend themselves well to classical Monte Carlo simulations, whereas with other methods it would be quite cumbersome to take the many aspects of the experiment into account. A similar, quantum-mechanical analysis is much more difficult, however, as one would need to average over many wave packets in a Monte Carlo approach to obtain good convergence, and the evolution for a single quantum wave packet requires much more computation than for a single classical particle.

4.6.2 Data and Results

In this section we will explore a detailed experimental study of the quantum kicked rotor dynamics in the presence of amplitude noise, using the classical model for comparison. An overview of these results appears in Fig. 4.14, where the energies from the experiment and classical model are shown as a function of the kick strength K, for four different levels of amplitude noise. The energies are plotted at the fixed time of 35 kicks. In the case of no applied noise, one can clearly see the oscillations that correspond to Eqs. (4.24) and (4.47). Additionally, the shift in the locations of the experimental oscillations from their classical counterparts is evident; for the value of $\bar{k} = 2.08$ used in all the experiments shown here, the shift is 20% above the classical value. Although in some locations the quantum (experimentally observed) energies are larger than the classical (numerically calculated) energies due to the shift of the oscillations, the experimental energies are smaller on average than the classical energies because of quantum localization effects.

As the noise is added, the oscillations in the energy curves become washed out, as one expects from Eqs. (4.29) and (4.49). Additionally, the difference between the experimental and classical curves becomes less apparent, until the highest noise level (80%), where there is excellent agreement between the two curves. In accordance with our previous discussion, good correspondence only occurs when the noise level is

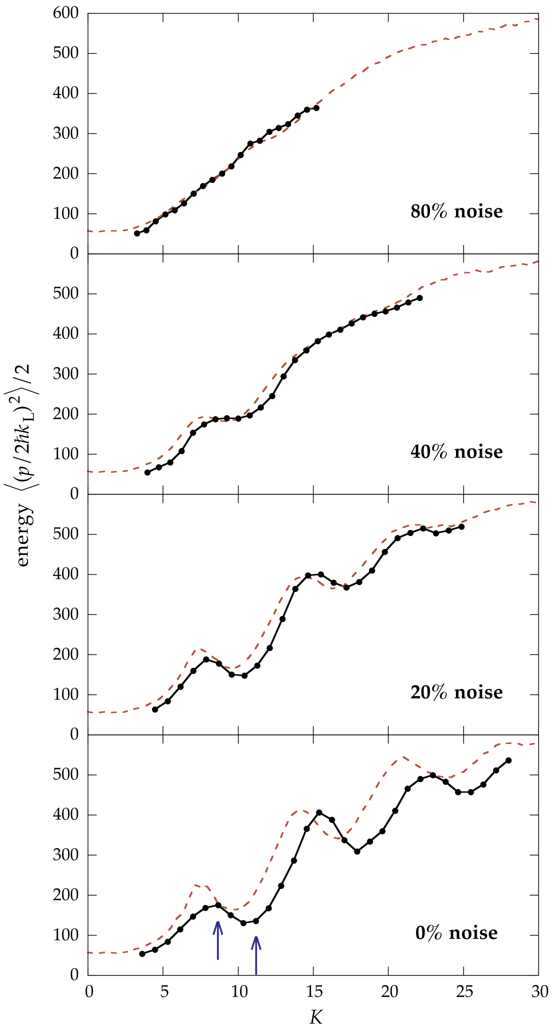

Figure 4.14: Plot of the experimentally measured energy (points connected by solid lines) and energy from the classical model (dashed line) as a function of the stochasticity parameter K, for several different levels of applied amplitude noise. All the plotted energies are measured at the fixed time of 35 kicks. The oscillations and the shift due to quantum effects, corresponding to Eqs. (4.24) and (4.47) with $\text{\it k}\!\!\!^{-} = 2.08$, are evident in the case with no applied noise. On average, the experimental energies at the lower noise levels are smaller than their classical counterparts due to localization effects. However, for the strongest noise level shown here (80%), there is good agreement between the two energy curves. For this figure, no adjustments have been made to the measured values of K, and the error bars for the energy values are suppressed, but are typically smaller than the corresponding dots. Each experimental point is an average over 10 realizations of amplitude noise. Two arrows in the zero-noise case mark the locations of detailed study that are described in the following two subsections.

sufficiently large to destroy the short-time quantum and classical correlations, and hence the oscillations in the diffusion curves.

To fill out this picture of the kicked-rotor behavior, detailed views of the experimental and classical dynamics at two values of K appear below. The two values of K in these detailed measurements correspond to a minimum and a maximum of the quantum energy curve in Fig. 4.14; these locations are indicated as arrows in the zero-noise plot in this figure. As we mentioned above, the dynamics are qualitatively different at these two locations. At the minima of the experimental diffusion curve, exponential localization occurs. However, at the maxima, the late-time distributions that we measured in our experiment are nonexponential; this behavior is a fingerprint of the underlying classical anomalous diffusion.

In Figs. 4.15-4.20, we contrast the behavior of the experimental and classical systems at these two values of K. The behaviors at small noise levels have several interesting differences, but as we have already seen, the behavior at high noise levels is similar in that there is good correspondence between the experiment and the classical simulations. In Figs. 4.15 and 4.18, we see the behaviors of the energies at the minimum and maximum of the experimental diffusion curve, respectively, at a fixed time (50 kicks) as the level of noise varies. The time evolutions of the energies are shown in Figs. 4.16 and 4.19 for the two values of K at various levels of noise. Finally, the corresponding evolutions of the momentum distributions themselves are shown in Figs. 4.17 and 4.20. We will discuss these results for the two values of K separately in the following presentation.

Before proceeding, though, a few remarks are in order about the comparisons between the experiment and the corresponding classical dynamics performed in this paper. The classical model contains many experimental parameters beyond the two that are really important for the quantum kicked rotor dynamics (K and $\bar{k}$). For the purposes of comparison, these extra parameters were not treated as fitting parameters; instead, they were all fixed to their experimentally measured values. However, the stochasticity parameter K, which is by far the largest source of uncertainty in the experiments, was sometimes adjusted by a few percent from its measured value (but well within the experimental uncertainty of $\pm 10\%$) in order to obtain better correspondence. To be precise about these adjustments, the measured values of K are quoted in each figure caption along with the value used in the classical simulations. Finally, as noted before, although statistical errors for our energy measurements are quoted in each figure, they are of limited utility in determining the quality of the correspondence between the experimental results and classical simulations. The main reason for this statement is the long-term optical alignment and laser drifts that result in long-term drifts in K, which can result in local systematic shifts in energies between different curves (or even points within a curve) in each figure. This effect is not properly accounted for by either the statistical error estimates or the simulations, which used a single value of K for an entire data set. For example, in Figs. 4.16 and 4.19, it is not possible to distinguish different levels of agreement between the data and simulations for the 60-200% noise levels, although some pairs of curves may appear to agree more closely than others. Indeed, it is important to realize that the momentum distributions are the most reliable tool for studying correspondence, since they contain much more information and tend to be less sensitive to the problems we have mentioned. The energies, on the other hand, are still valuable as a concise summary of the large amount of information presented here.

4.6.2.1 Detailed Study: Destruction of Exponential Localization

We now focus on the behavior at the minimum of the experimental diffusion curve, as indicated by the rightmost arrow in Fig. 4.14. In this regime, the atoms localize in an exponential distribution at late times. In Fig. 4.15, there is a large difference between the experimental and classical energies after 50 kicks when no noise is applied. This difference is due to both dynamical localization and the misalignment of the quantum and classical diffusion oscillations, which gives the classical system a larger initial diffusion rate. As noise is added, both the experimental data and the classical simulations exhibit increased diffusion, as the short-time correlations are washed out. The increase in the experimental diffusion is larger than the classical diffusion because quantum localization is destroyed. At high noise levels, the agreement between experiment and classical simulation is good. Additionally, both curves exhibit a characteristic dip in the energy around 150% noise levels. This somewhat surprising effect is a result of residual short-time correlations, which persist at noise levels as high as 100%, where they enhance diffusion slightly above the quasilinear value.

Similar behavior occurs in the time evolution of the energies shown in Fig. 4.16. When there is no applied noise, the experimental energy grows initially more slowly than the classical energy, and then saturates and diffuses slowly. As we noted before, this slow diffusion may be due to residual decohering effects in our experiment, such as

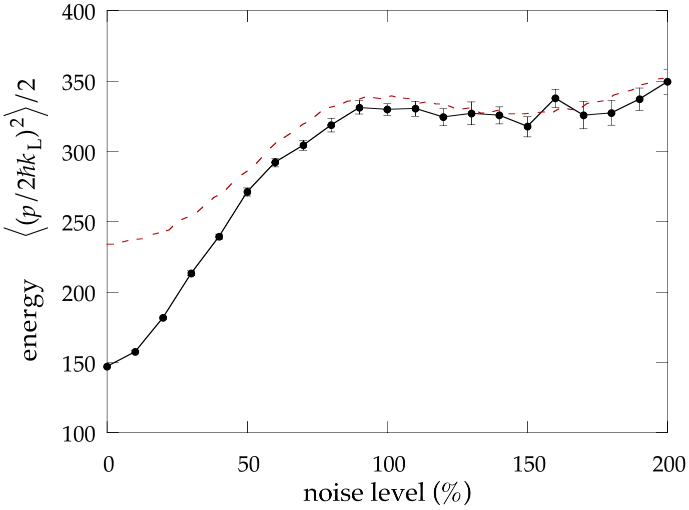

Figure 4.15: Experimentally measured energy (points and solid lines) and energy from the classical model (dashed line) as the noise level is changed, for a fixed time (50 kicks) and stochasticity parameter (the experimental value is $K = 11.2 \pm 10\%$, the classical simulation corresponds to $K = 10.9$). At the lowest noise levels, there is a significant difference between the experimental and classical energies, due to both localization and differences in short-term correlations, which disappears for high noise levels. The error bars represent statistical scatter among the 18 noise realizations comprised in each point, but do not account for long-term drifts or systematic uncertainties (see note in text). The value of K used here corresponds to the rightmost arrow in Fig. 4.14.

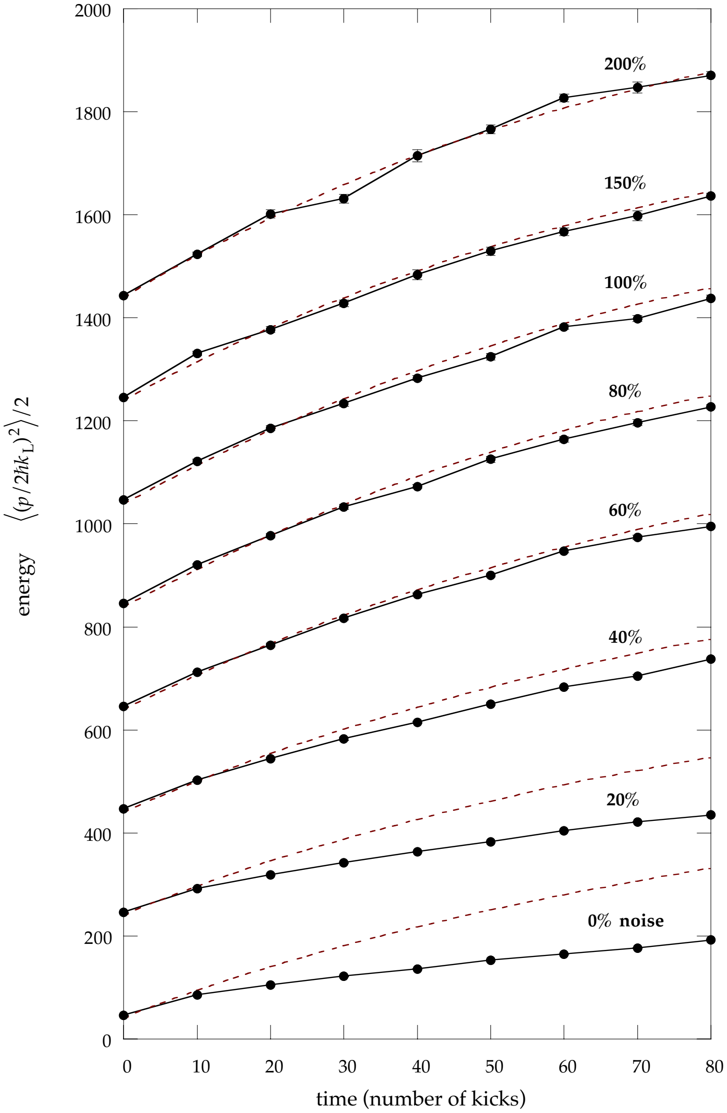

Figure 4.16: Experimentally measured energy (points and solid lines) and energy from the classical model (dashed line) as a function of time, for various levels of applied noise. The experimentally measured stochasticity parameter is $K = 11.2 \pm 10\%$, and the simulation corresponds to $K = 11.2$. The experimental data points are averages over 15 distinct realizations of amplitude noise, and data for successive noise levels are offset vertically by 200 for clarity. The agreement between the experimental data and the classical model is excellent for noise levels of 60% and above. The value of K used here corresponds to the rightmost arrow in Fig. 4.14.

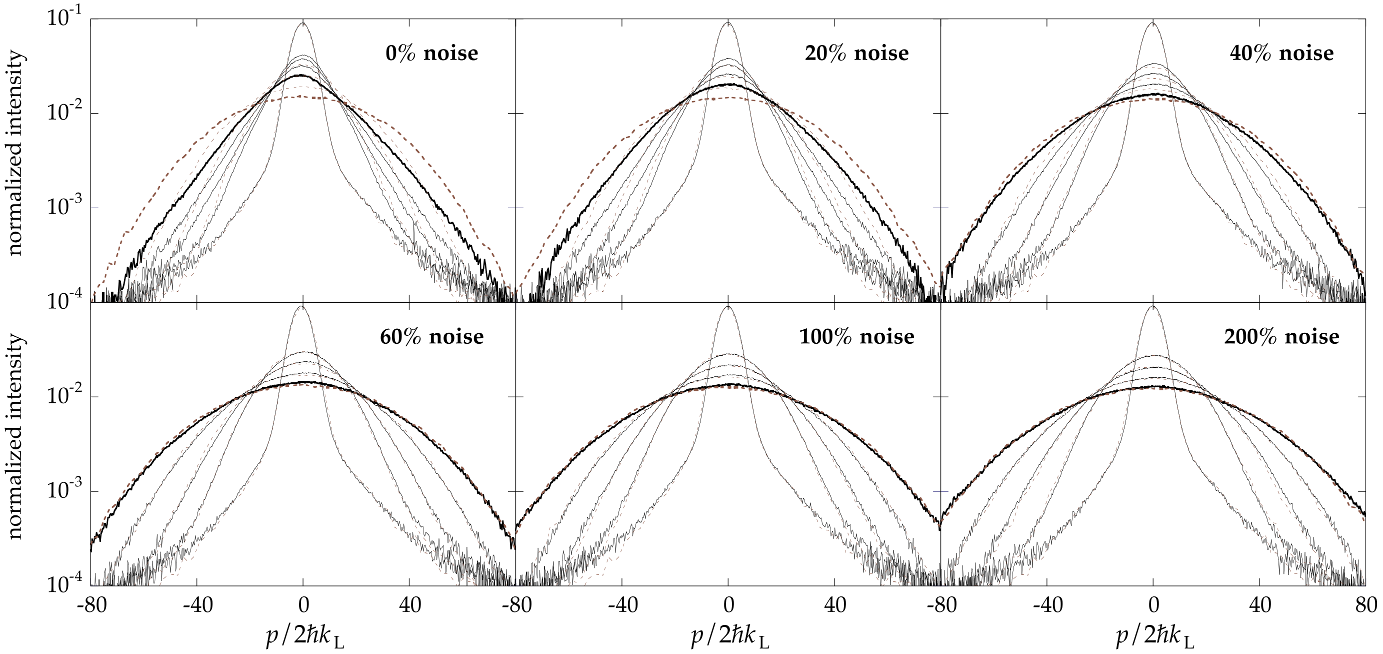

Figure 4.17: Evolution of the momentum distributions, for both the experiment (solid) and classical model (dashed), at various levels of applied noise. The experimentally measured stochasticity parameter is $K = 11.2 \pm 10\%$, and the simulation corresponds to $K = 11.2$. The times shown, in order of increasing width, are 0, 10, 20, 40, and 80 kicks, with the final distributions emphasized in bold. In the zero-noise case, the contrast between the exponentially localized experimental distribution and the classical Gaussian distribution is evident. For the largest three levels of noise shown, the experimental and classical distributions are nearly indistinguishable. The data and simulations presented in this figure are the same as those used to calculate the energies in Fig. 4.16, and the value of K used here corresponds to the rightmost arrow in Fig. 4.14 (the "valley" in the experimental curve).

phase noise in the standing wave. As noise is added, the diffusion is enhanced in both cases, and for high noise levels the energy growth in the experiment is quite similar to that observed in the simulations.

Finally, the transition to classical behavior in the experiment is most dramatically evident in the momentum distributions in Fig. 4.17. In the zero-noise case, the experimental distribution evolves from the initial, nearly Gaussian form to the exponentially localized distribution (shown in bold), which is characteristic of dynamical localization. The classical distribution, on the other hand, evolves to the broader, Gaussian distribution that one expects from classical physics. When a small amount of noise (20%) is applied, the final experimental distribution is broader and has a rounded appearance, but is still quite far away from the classical Gaussian distribution. With 40% noise, the final experimental distribution has made the transition to a Gaussian profile, but the evolution still does not quite match that of the classical evolution. For the highest levels of noise shown (60-200%), the evolutions of the experimental and classical distributions are nearly identical, providing strong evidence that the experiment is behaving classically.

4.6.2.2 Detailed Study: Regime of Classical Anomalous Diffusion

We now focus on a different regime than in the last section. Here we consider the behavior at a peak in the experimental diffusion curve, indicated by the leftmost arrow in Fig. 4.14. This location in the diffusion curve corresponds to a regime of classical anomalous diffusion. As in the previous case, there is a significant difference in the energy after 50 kicks in the absence of noise, as seen in Fig. 4.18. The difference in this figure is much larger than in Fig. 4.14 because of the much later time used in the plot (50 vs. 35 kicks). As noise is applied, the experimental energy increases. This behavior is consistent with the breaking of localization, although it is not completely clear that localization occurs in this regime, because of the nonexponential form of the long-time momentum distributions. By contrast, the classical energy is initially reduced by the applied noise, due to the destruction of the classical correlations. Again, for high noise levels the behavior in the experiment is well described by the classical model.

From the evolution of the energies in Fig. 4.19, we see that the differences between the behaviors of the atoms and the classical model are more subtle than in the case of the previous section. When there is no applied noise, the experimental data show a faster initial diffusion than one would expect classically; at later times, the diffusion seems to saturate, suggesting that localization effects are setting in, and the diffusion proceeds more slowly than in the classical model. The energy difference in this case is smaller than one might expect from Fig. 4.18, due to slight differences in the intensity and beam diameter of the kicking laser light between the two data runs (notice that

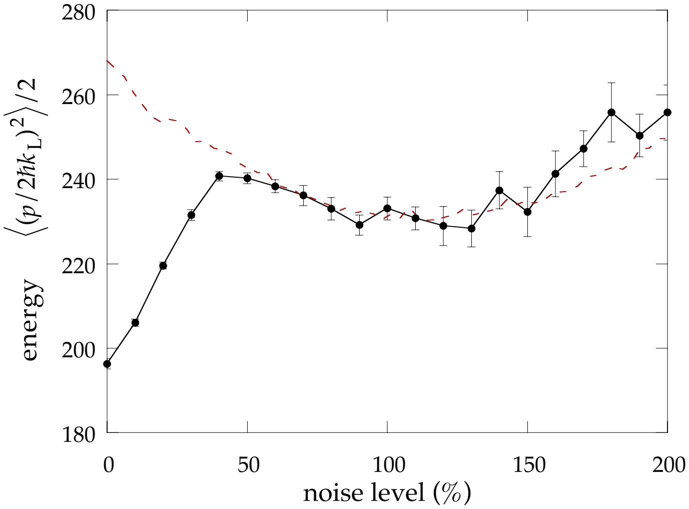

Figure 4.18: Experimentally measured energy (points and solid lines) and energy from the classical model (dashed line) as the noise level is changed, for a fixed time (50 kicks) and stochasticity parameter (the experimental value is $K = 8.4 \pm 10\%$, the classical simulation corresponds to $K = 8.4$). As in the case of Fig. 4.15, there is a large discrepancy between the experimental and classical energies at the lowest noise levels, which disappears for high noise levels. Experimental data are averaged over 18 realizations of noise. The value of K used here corresponds to the leftmost arrow in Fig. 4.14. Note the larger discrepancy for zero noise in this figure, since the time displayed here is later than that used in Fig. 4.14. Note also that the vertical scale used here is magnified compared to that of Fig. 4.15.

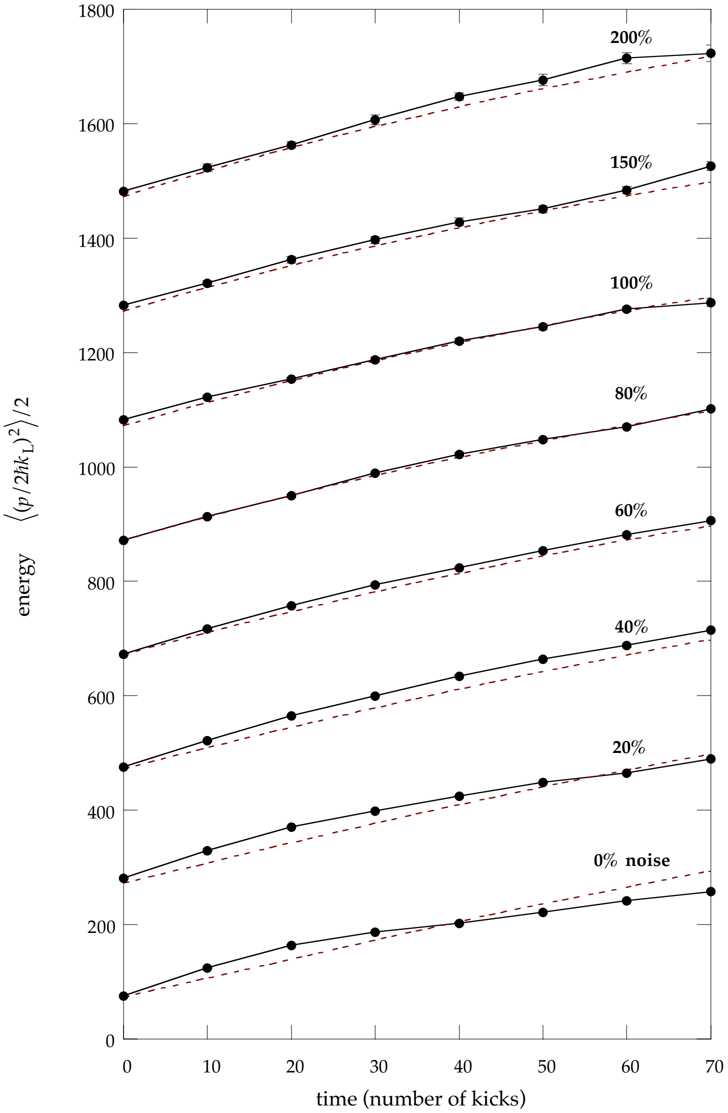

Figure 4.19: Experimentally measured energy (points and solid lines) and energy from the classical model (dashed line) as a function of time, for various levels of applied noise. The experimentally measured stochasticity parameter is $K = 8.4 \pm 10\%$, and the simulation corresponds to $K = 8.7$. The experimental data points are averages over 15 distinct realizations of amplitude noise, and data for successive noise levels are offset vertically by 200 for clarity. The agreement between the experimental data and the classical model is again excellent for noise levels of 60% and above. The value of K used here corresponds to the leftmost arrow in Fig. 4.14.

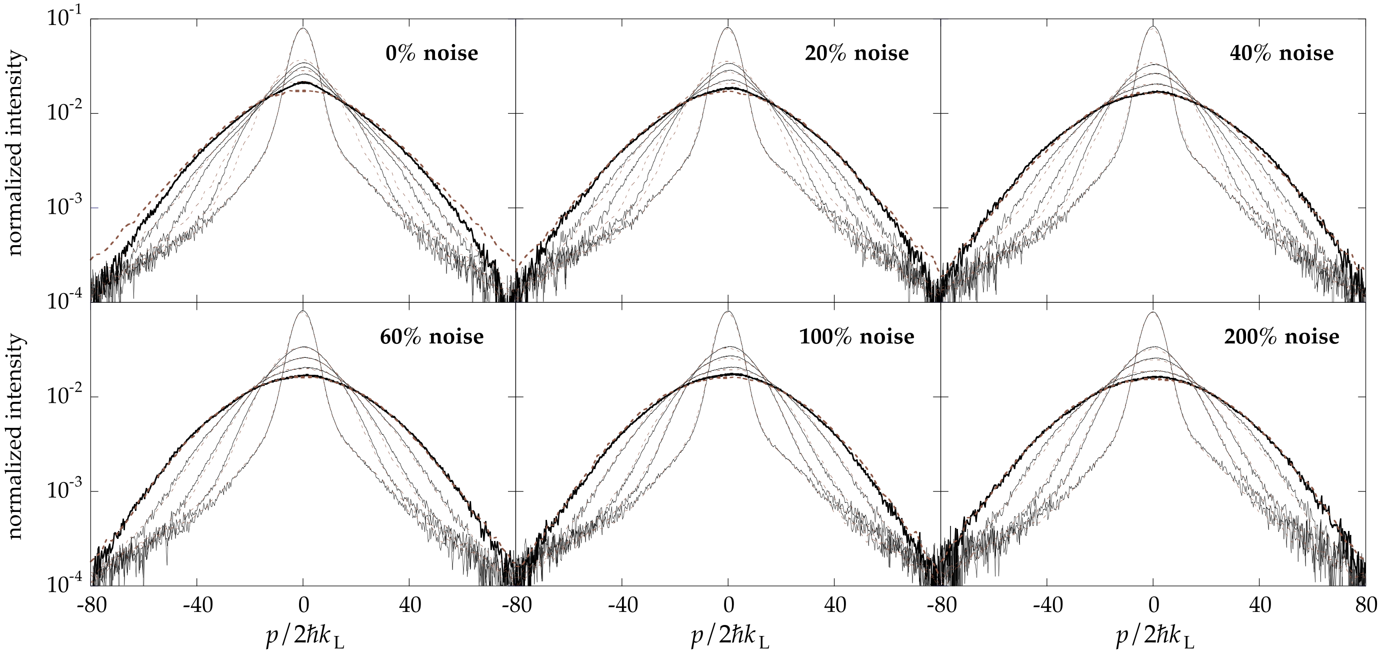

Figure 4.20: Evolution of the momentum distributions, for both the experiment (solid) and classical model (dashed), at various levels of applied noise. The experimentally measured stochasticity parameter is $K = 8.4 \pm 10\%$, and the simulation corresponds to $K = 8.7$. The times shown, in order of increasing width, are 0, 10, 20, 40, and 70 kicks, with the final distributions emphasized in bold. In the zero-noise case, the quantum distribution does not exhibit exponential localization, as observed in previous work, but the behavior is distinctly nonclassical. For the largest three levels of noise shown, the experimental and classical distributions are again nearly indistinguishable. The data and simulations presented in this figure are the same as those used to calculate the energies in Fig. 4.19, and the value of K used here corresponds to the leftmost arrow in Fig. 4.14 (the "peak" in the experimental curve).

this value of K corresponds to a steeply sloped region in the classical diffusion curve). As noise is added, the saturation is less pronounced, until the 40% noise level, where the diffusion occurs more quickly than in the classical model, with little indication of saturation. Above this level, the experiment agrees well with the classical model, and the short-time correlations are evidently small.

The momentum distributions for this case are shown in Fig. 4.20. In the zero-noise case, the experimental distribution after 70 kicks (highlighted in bold) has a characteristic profile, rounded and nonexponential in shape. One might be tempted to attribute this shape to the systematic effects that we have discussed, which affect the tails of an exponential distribution with a very long localization length. However, the region over which the distribution is rounded is well within the domain where the systematic effects are not significant. The final classical distribution also has tails that extend well beyond those of the experimental measurement. As noise is introduced, the experimental profile becomes more Gaussian, and the classical diffusion rate is reduced slightly. As in the previous section, the final experimental distribution for 40% noise is Gaussian, but the evolution does not quite proceed at the same rate (as one can most readily see from the distributions at intermediate times). The difference, though, is that the quantum diffusion occurs more quickly than the classical expectation, whereas in the previous section the diffusion occurred more slowly than in the classical model. Again, for the highest levels of noise shown (60-200%), the experimental evolutions are in excellent agreement with the classical model, and hence classical behavior is restored.

4.7 Comparison with a Universal Theory of Quantum Transport

Beyond examining the problem of quantum–classical correspondence, these experimental results are also useful for studying details of quantum transport. Specifically, we can compare these results with a recent quantum diffusion theory by Jianxin Zhong, Roberto Diener, Qian Niu, and others [214]. This theory concerns the shape of the tails of a spreading quantum wave packet, described by the stretched exponential function

$$P(x,t) \sim \exp(-|x/w|^\gamma) \ , \tag{4.61}$$

where $w(t)$ is the time-dependent width parameter. The exponent γ here is stationary, and is within the range $[1, \infty)$. This diffusion theory then relates this exponent to the scaling exponent for the width parameter,

$$w(t) \sim t^\beta \ , \tag{4.62}$$

via the universal relation

$$\gamma = 1/(1-\beta) \ . \tag{4.63}$$

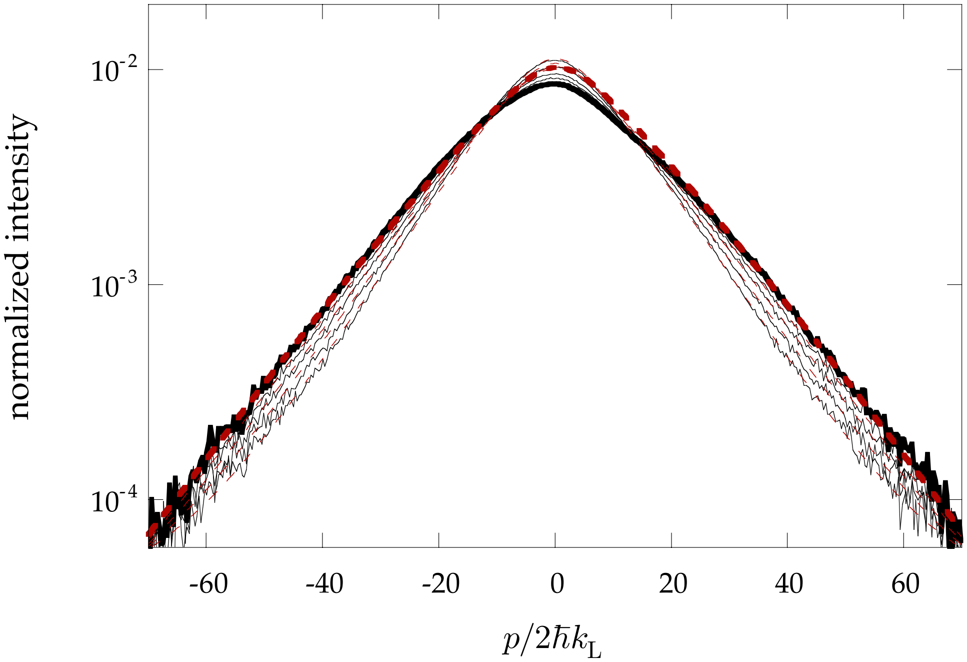

Figure 4.21: Comparison of the diffusion theory in Eqs. (4.61-4.63) to the experimental momentum distribution evolution, for the exponentially localized case. The experimental distributions for $K = 11.2$, $\bar{k} = 2.08$, and times of 30, 40, 50, 60, and 70 kicks are shown as solid lines, and the simultaneous best fit to the tails of all the distributions is shown as dashed lines. The 70 kick cases are highlighted in bold. The fitted exponents here are $\gamma = 1.06 \pm 0.19$ and $\beta = 0.06 \pm 0.17$, in good agreement with the expectations for dynamical localization.

This relation is expected to hold for lattice-type models with Schrödinger equations of the form

$$i\partial_t\psi(n,t) = V(n)\psi(n,t) + \sum_{n'} h(n,n')\psi(n',t) \ , \tag{4.64}$$

where $\psi(n,t)$ is the amplitude at the nth lattice site, $V(n)$ is the lattice-site potential energy, and $h(n,n')$ is the "hopping integral," which describes the couplings between the sites (for the common "tight-binding" models, only nearest-neighbor sites are directly coupled). As we mentioned above, the kicked rotor can be written in this form, where the lattice describes the ladder in momentum space, and so this spatial-diffusion picture describes the momentum transport in the kicked rotor. This theory has been jus-

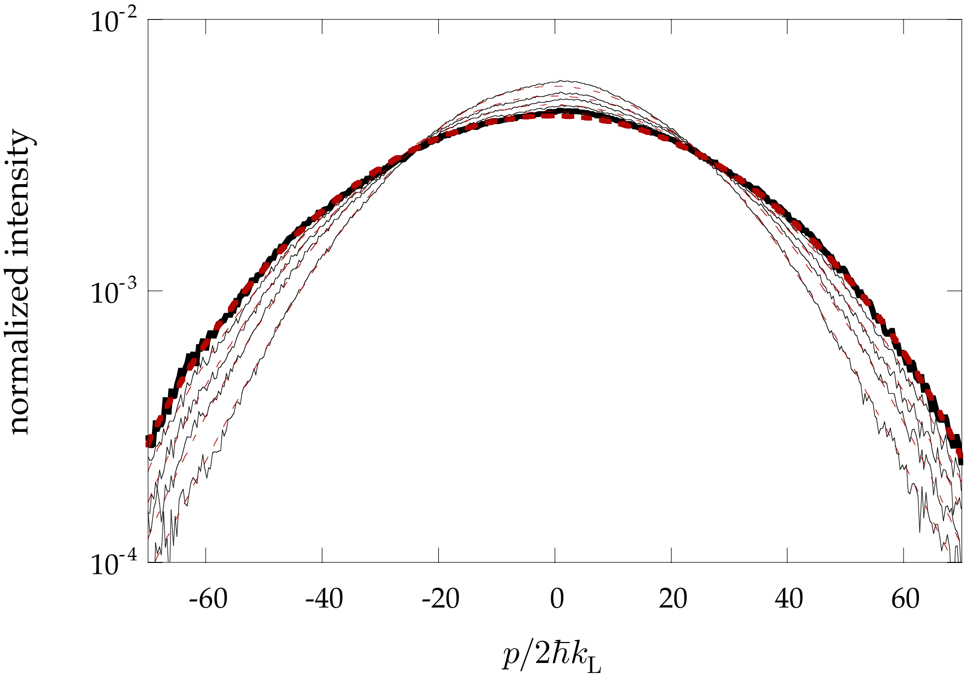

Figure 4.22: Comparison of the diffusion theory in Eqs. (4.61-4.63) to the experimental momentum distribution evolution, for a case driven by 200% amplitude noise. The experimental distributions for $K = 11.2$, $\bar{k} = 2.08$, and times of 30, 40, 50, 60, and 70 kicks are shown as solid lines, and the simultaneous best fit to the tails of all the distributions is shown as dashed lines. The 70 kick cases are highlighted in bold. The fitted exponents here are $\gamma = 2.03 \pm 0.14$ and $\beta = 0.51 \pm 0.03$, consistent with normal (classical) diffusion.

tified on the basis of numerical simulations in a variety of systems, as well as a general theoretical argument based on a stationary-phase approximation in the coarse-grained generalized master equation [214], and is valid asymptotically in the tails of the distributions at long times.

This theory makes sense in several situations that we have already discussed, such as exponential localization ($\gamma = 1$, $\beta = 0$), noise-induced (classical-like) diffusion ($\gamma = 2$, $\beta = 1/2$), and ballistic transport ($\gamma \to \infty$, $\beta \to 1$). What is more interesting, though, is that the universal relation should also hold in the intermediate cases of "quantum anomalous diffusion." Since we have observed a case of quantum transport (the behavior at the peaks of the diffusion curves, as in Fig. 4.11) that does not fall

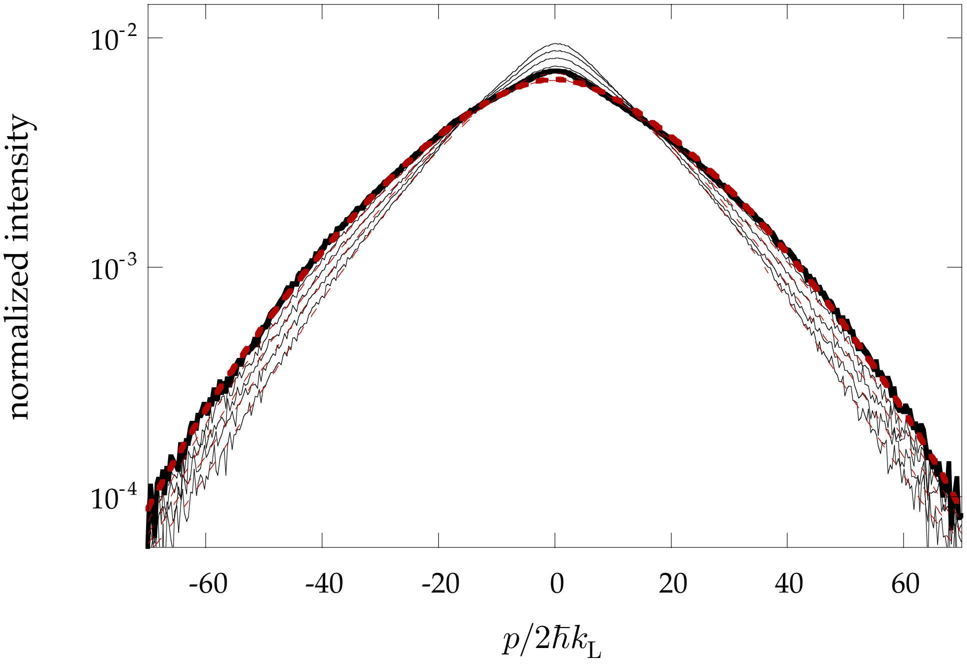

Figure 4.23: Comparison of the diffusion theory in Eqs. (4.61-4.63) to the experimental momentum distribution evolution, for the case influenced by classical anomalous transport. The experimental distributions for $K = 8.4$, $\bar{k} = 2.08$, and times of 30, 40, 50, 60, and 70 kicks are shown as solid lines, and the simultaneous best fit to the tails of all the distributions is shown as dashed lines. The 70 kick cases are highlighted in bold. The fitted exponents here are $\gamma = 1.48 \pm 0.16$ and $\beta = 0.32 \pm 0.07$, consistent with quantum anomalous diffusion.

cleanly in any of the extreme cases, it is interesting to use this theory to study this case.

To compare the theory with the experimental results, we have performed fits of the distributions (4.61) to experimental distributions at 30, 40, 50, 60, and 70 kicks. To focus on the asymptotic behavior, we excluded the data at the earlier times (0, 10, and 20 kicks), and the center portions of the data (bounded by $|p/2\hbar k_\mathrm{L}| \sim 15$) were also excluded. The distributions were likewise truncated outside $|p/2\hbar k_\mathrm{L}| \sim 70$ to exclude the regions of poor signal-to-noise ratio that might have skewed the fits. All the distributions for a given case were fit simultaneously, using a common fitting exponent γ. The scaling relation (4.62) was enforced by the constraint

$$w(t) = w_0 + \alpha t^\beta \quad , \tag{4.65}$$

where w_0 and α are fitting parameters, and β was constrained by the relation (4.63). In the fit, each distribution was convolved with the initial momentum distribution and then corrected for the known response of the detection system (i.e., the nonuniformity of the Gaussian imaging laser beams). To account for shot-to-shot variations in the backgrounds of the CCD camera photographs, it was necessary to include the vertical offsets and the amplitudes of the distributions as fitting parameters. The fits were stabilized by constraining vertical offsets to a two-parameter linear model and the amplitudes to a three-parameter quadratic model; these constraints were justified on physical grounds and on the basis of fits where these parameters were treated independently. The other effects discussed in Section 4.6.1 were not explicitly accounted for, and thus influenced the vales of the fitted parameters. In order to emphasize the tails of the distribution during the fit, the logarithms of the data were computed before being sent to the Marquardt-Levenberg fitting routine. The uncertainties quoted here primarily reflect the sensitivity of the fits to the choice of cutoff locations.

We have applied this fit to three sets of data. The first corresponds to exponential localization (Fig. 4.21), where the fitted exponents were $\gamma = 1.06 \pm 0.19$ and $\beta = 0.06 \pm 0.17$. These values are consistent with the expected values. The second case is the strongest case (200%) of amplitude noise that we considered above (Fig. 4.22), where the fitted values of $\gamma = 2.03 \pm 0.14$ and $\beta = 0.51 \pm 0.03$ are also consistent with the expected values for regular diffusion. Finally, in the regime of classical anomalous diffusion (Fig. 4.23), the fitted values were $\gamma = 1.48 \pm 0.16$ and $\beta = 0.32 \pm 0.07$, indicating intermediate behavior of quantum anomalous diffusion. In all three cases, the tails of the experimental distributions match very well with the fitted distributions.

4.8 Calculation of the Correlations

We will now run through the calculation of the correlations that we have used in this chapter. These correlations were calculated using probabilistic methods [254], including an elegant path-summation method [255], but here we will follow the direct approach used by Shepelyansky [275] for calculating the quantum correlations.

4.8.1 Classical Correlations

Beginning with the generalized standard map,

$$\begin{aligned} p_{n+1} &= p_n + K_n \sin x_n \\ q_{n+1} &= q_n + p_{n+1} \quad , \end{aligned} \tag{4.66}$$

which allows for different kick strengths on each iteration, we wish to calculate the correlation function

$$C_n := \langle K_0 \sin x_0 K_n \sin x_n \rangle, \tag{4.67}$$

where we will take the average over the initial distribution to be uniform over phase space. To evaluate this function, we need to calculate the exponentials e^{ix_m} of the iterated coordinates, in view of the form

$$C_n = K_0 K_n \left\langle e^{ix_0} e^{ix_n} - e^{ix_0} e^{-ix_n} \right\rangle + \text{c.c.} \tag{4.68}$$

of the correlation functions.

We will proceed by calculating the first few correlations before generalizing to the arbitrary case. If we use the generating function for the Bessel functions $J_n(x)$,

$$\exp\left[\left(t-\frac{1}{t}\right)\frac{z}{2}\right]=\sum_s J_s(z)t^n \quad , \tag{4.69}$$

we can let $t=\exp(ix)$ and $z=K$ to obtain

$$\exp(iK\sin x)=\sum_s J_s(K)e^{isx} \quad . \tag{4.70}$$

This relation allows the evaluation of the first iterated exponential,

$$\begin{aligned} e^{ix_1} &= \exp[i(x_0+p_0+K_0\sin x_0)] \\ &= \sum_{s_0} J_{s_0}(K_0)e^{i(s_0+1)x_0}e^{ip_0} \quad . \end{aligned} \tag{4.71}$$

We can iterate this procedure to obtain the next two exponentials. After reversing the order of the indices, we obtain

$$\begin{aligned} e^{ix_2} &= \sum_{s_0,s_1} J_{s_0}[K_1]J_{s_1}[K_0(s_0+2)]e^{i(s_1+s_0+1)x_0}e^{i(s_0+2)p_0} \\ e^{ix_3} &= \sum_{s_0,s_1,s_2} J_{s_0}[K_2]J_{s_1}[K_1(s_0+2)]J_{s_2}[K_0(2s_0+s_1+3)] \\ &\qquad\qquad \times e^{i(s_2+s_1+s_0+1)x_0}e^{i(2s_0+s_1+3)p_0} \end{aligned} \tag{4.72}$$

At this stage the pattern of the iteration is apparent. We can define the recurrence relations

$$\begin{aligned} \alpha_0 &= s_0+1 \\ \alpha_{n+1} &= \alpha_n+s_{n+1} \end{aligned} \tag{4.73}$$

and

$$\begin{aligned} \beta_0 &= 1+\alpha_0 \\ \beta_{n+1} &= \beta_n+\alpha_n \quad , \end{aligned} \tag{4.74}$$

and then write the nth iterated exponential as

$$e^{ix_n}=\sum_{s_0\cdots s_{n-1}} J_{s_0}(K_{n-1}\beta_0)J_{s_1}(K_{n-2}\beta_1)\cdots J_{s_{n-1}}(K_0\beta_{n-1})e^{i\alpha_{n-1}x_0}e^{i\beta_{n-1}p_0} \quad . \tag{4.75}$$

Now it is straightforward to evaluate the correlations (4.67), as the phase-space averages amount to projections into a Fourier basis, with the general result

$$\begin{aligned} C_n = \frac{K_0K_n}{2}\sum_{s_0\cdots s_{n-1}} & J_{s_0}(K_{n-1}\beta_0)J_{s_1}(K_{n-2}\beta_1)\cdots J_{s_{n-1}}(K_0\beta_{n-1}) \\ & \times (\delta_{\alpha_{n-1},1}-\delta_{\alpha_{n-1},-1})\delta_{\beta_{n-1},0} \quad , \end{aligned} \tag{4.76}$$

where $\delta_{n,n'}$ is the Kronecker symbol. Thus, the first few correlations evaluate to

$$\begin{aligned}
C_0 &= \frac{K_0^2}{2} \\
C_1 &= 0 \\
C_2 &= -\frac{K_0 K_2}{2} J_2(K_1) \\
C_3 &= \frac{K_0 K_3}{2} [J_3(K_1) J_3(K_2) - J_1(K_1) J_1(K_2)] \\
C_4 &= \frac{K_0 K_4}{2} [J_2(K_1) J_2(K_3) + O(K^{-3/2})] \ ,
\end{aligned} \tag{4.77}$$

where K is the statistical average of the K_n. For the normal standard map, $K_n = K$ for all n, and inserting these correlations into Eq. (4.20), we recover the diffusion rate (4.24). On the other hand, for amplitude noise, it is appropriate to average the K_n over their probability distributions, as in (4.28). Doing so, we recover the noise-modified diffusion result (4.29). Notice that for the case of uniformly distributed amplitude noise, Eq. (4.29) can be integrated analytically, with the somewhat unenlightening result,

$$\begin{aligned}
D(K, \delta K_{\mathrm{p-p}}) = \frac{K^2}{4} &+ \frac{\delta K_{\mathrm{p-p}}^2}{48} \\
&+ \frac{K^2}{2} \bigg\{ - \mathcal{J}_2(K, \delta K_{\mathrm{p-p}}) + \mathcal{J}_2^2(K, \delta K_{\mathrm{p-p}}) \\
&\qquad + \frac{4}{\delta K_{\mathrm{p-p}}} [J_2(K^+) - J_2(K^-)]^2 \\
&\qquad - \frac{4}{\delta K_{\mathrm{p-p}}} [J_0(K^+) - J_0(K^-)][J_2(K^+) - J_2(K^-)] \bigg\} \ ,
\end{aligned} \tag{4.78}$$

where $K^\pm := K \pm \delta K_{\mathrm{p-p}}/2$,

$$\begin{aligned}
\mathcal{J}_2(K, \delta K_{\mathrm{p-p}}) = \frac{1}{\delta K_{\mathrm{p-p}}} \bigg\{ & K^+ J_0(K^+) - K^- J_0(K^-) - 2[J_1(K^+) - J_1(K^-)] \\
& - \frac{\pi}{2} [J_0(K^+) \mathbf{H}_1(K^+) - J_1(K^+) \mathbf{H}_0(K^+)] \\
& + \frac{\pi}{2} [J_0(K^-) \mathbf{H}_1(K^-) - J_1(K^-) \mathbf{H}_0(K^-)] \bigg\} \ ,
\end{aligned} \tag{4.79}$$

and the $\mathbf{H}_n(x)$ are the Struve functions of order n.

4.8.2 Quantum Correlations

The calculation of the quantum correlations follows along similar lines to the classical calculation, but is somewhat more complex. The derivation here follows the work of Shepelyansky [275, 276]. The goal here is to calculate the (symmetrized) quantum correlation function

$$C_{\mathrm{q},n} = \frac{K_0 K_n}{2} \langle\psi_0|(\sin x_n \sin x_0 + \sin x_0 \sin x_n)|\psi_0\rangle \ , \tag{4.80}$$

which is averaged with respect to the initial state $|\psi_0\rangle$. The coordinates x_n and p_n here are Heisenberg-picture operators, which obey equations formally equivalent to the classical standard map, as we have indicated above. The initial state is again approximately uniform over phase space, so that

$$\langle\psi_0|e^{imx_0}e^{inp_0}|\psi_0\rangle = \delta_{m,0}\delta_{n,0} \ . \tag{4.81}$$

We begin as before, calculating the first iterated exponential

$$e^{ix_1} = e^{i(x_0+p_0+K_0\sin x_0)} = \exp\left[-p_0 + ix_0 + \frac{K_0}{2}e^{ix_0} - \frac{K_0}{2}e^{-ix_0}\right] \ . \tag{4.82}$$

To factor this exponential, we use two special cases of the Baker–Campbell–Hausdorff relation [279]. The first is

$$\exp(A+B) = \exp\left(B\frac{e^c-1}{c}\right)\exp(A) \tag{4.83}$$

for operators A and B such that $[A,B] = cB$. The second case is

$$\exp(A+B) = \exp(A)\exp(B)\exp\left(-\frac{1}{2}[A,B]\right) = \exp(B)\exp(A)\exp\left(\frac{1}{2}[A,B]\right) \ , \tag{4.84}$$

if $[A,[A,B]] = [B,[A,B]] = 0$. After factorization, the result is

$$e^{ix_1} = \exp\left(i\frac{2K_0}{\bar{k}}\sin(\bar{k}/2)\sin(x_0+\bar{k}/2)\right)e^{ix_0}e^{ip_0}e^{i\bar{k}/2} \ . \tag{4.85}$$

We can then apply the identity (4.70), with the result

$$e^{ix_1} = \sum_{s_0} J_{s_0}(K_{\mathrm{q},0})\exp\left[i\frac{\bar{k}}{2}(s_0+1)\right]e^{i(s_0+1)x_0}e^{ip_0} \ , \tag{4.86}$$

where $K_{\mathrm{q},0} := K_0 \sin(\bar{k}/2)/(\bar{k}/2)$. The general case is then obtained by iterating this relation and then normally ordering the operators (i.e., so that all the p_0 are on the right). Shepelyansky's result is

$$e^{ix_n} = \sum_{s_0 \cdots s_{n-1}} J_{s_0}(K_{\mathrm{q},n-1}\beta_0) J_{s_1}(K_{\mathrm{q},n-2}\beta_1) \cdots J_{s_{n-1}}(K_{\mathrm{q},0}\beta_{n-1}) e^{i\gamma_{n1}} e^{i\alpha_{n-1}x_0} e^{i\beta_{n-1}p_0} \ , \tag{4.87}$$

where the functions α_n and β_n are defined as before, and we have defined an additional function by the relations

$$\begin{aligned} \gamma_0 &= \frac{\bar{k}}{2}(s_0 + 1) \\ \gamma_{n+1} &= \gamma_n + \frac{\bar{k}}{2} s_n(\alpha_n + \beta_n) + \frac{\bar{k}}{2}\alpha_n^2 \ . \end{aligned} \tag{4.88}$$

We can then define the function

$$\begin{aligned} R(n,r) &:= \frac{1}{2}\langle\psi_0|[\exp(-irx_0)\exp(ix_n) + \exp(ix_n)\exp(-irx_0)]|\psi_0\rangle \\ &= \frac{1}{2}\sum_{s_0 \cdots s_{n-1}} J_{s_0}(K_{\mathrm{q},n-1}\beta_0) J_{s_1}(K_{\mathrm{q},n-2}\beta_1) \cdots J_{s_{n-1}}(K_{\mathrm{q},0}\beta_{n-1}) \\ &\qquad \times (1 + e^{-i\beta_{n-1}\bar{k}q}) e^{i\gamma_{n1}} \delta_{\alpha_{n-1},q}\, \delta_{\beta_{n-1},0} \ , \end{aligned} \tag{4.89}$$

in terms of which we can write the correlation function as

$$C_{\mathrm{q},n} = \frac{K_0 K_n}{4}[R(n,-1) - R(n,1)] + \mathrm{c.c.} \ . \tag{4.90}$$

The first few of these quantum correlations evaluate to

$$\begin{aligned} C_{\mathrm{q},0} &= \frac{K_0^2}{2} \\ C_{\mathrm{q},1} &= 0 \\ C_{\mathrm{q},2} &= -\frac{K_0 K_2}{2} J_2(K_{\mathrm{q},1}) \\ C_{\mathrm{q},3} &= \frac{K_0 K_3}{2}[J_3(K_{\mathrm{q},1})J_3(K_{\mathrm{q},2}) - J_1(K_{\mathrm{q},1})J_1(K_{\mathrm{q},2})] \\ C_{\mathrm{q},4} &= \frac{K_0 K_4}{2}[J_2(K_{\mathrm{q},1})J_2(K_{\mathrm{q},3}) + O(K_{\mathrm{q}}^{-3/2})] \ , \end{aligned} \tag{4.91}$$

Hence, we see that the first few quantum correlations have essentially the same form as the classical correlations in Eqs. (4.77), but with the quantum scaling factor applied to the arguments of the Bessel functions. The diffusion-rate results in the case of the normal quantum kicked rotor (4.47) and the amplitude-noise case (4.49) then proceed as in the classical case.

Chapter 5

Experimental Apparatus II

5.1 Overview

In this chapter we discuss several modifications to the experimental apparatus described in Chapter 3. These improvements were necessary to prepare localized atomic wave packets in phase space for the experiments in Chapter 6. The first step towards such localized initial states is further cooling of the atoms beyond what is possible in a typical MOT. We accomplished this additional cooling in a three-dimensional, far-detuned optical lattice, as we discuss in Section 5.2. Further velocity selection well below the recoil limit was accomplished using two-photon, stimulated Raman transitions. We will examine the theory of stimulated Raman transitions as well as their experimental implementation in Section 5.3. It was also necessary to have control over the spatial phase of the optical lattice, so that the wave packet could be shifted to various initial locations in phase space. This spatial control was accomplished through an electro-optic phase modulator placed before the standing-wave retroreflector, as described in Section 5.4. Finally, we trace through the entire state-preparation sequence, using all these atom-optics tools, in Section 5.5, and we discuss the calibration of the optical-lattice potential in the modified setup in Section 5.6.

5.2 Cooling in a Three-Dimensional Optical Lattice

Using the standard techniques of cooling and trapping in a MOT, as described in Chapter 3, we were limited to temperatures on the order of 10 μK for the initial conditions of the experiment. It is desirable, however, to have much lower temperatures for the initial conditions, especially looking towards experiments with minimum-uncertainty wave packets in phase space. Although it has been shown that temperatures below 3 μK can be achieved in cesium using a standard six-beam MOT [280], our MOT temperatures were substantially higher due to residual magnetic fields from eddy currents in the stainless steel vacuum chamber after the field coils were switched off. One successful approach to achieving additional cooling beyond that of a standard MOT is cooling in a three-dimensional optical lattice. Several methods for cooling in three-dimensional optical lattices have been demonstrated [281–284], but the method implemented here was based on the setup developed by the group of David Weiss [285–289].

The 3D optical lattice was formed by five beams, as illustrated in Fig. 5.1. Three of the beams were in the horizontal plane; two of these beams counterpropagate, and the third is perpendicular to the other two. These beams formed a two-dimensional interference pattern, consisting of a lattice of spots with maximum intensity. This pattern

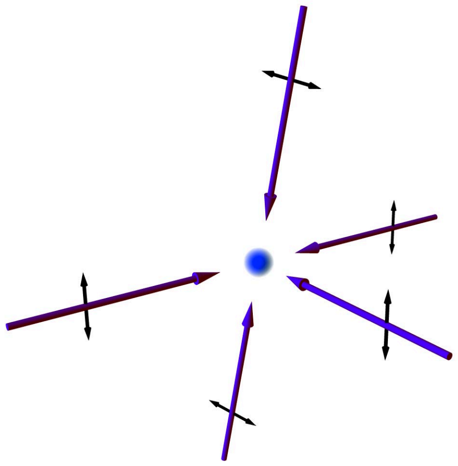

Figure 5.1: Configuration of the beams forming the three-dimensional lattice for additional cooling of the atoms. Five total beams form the lattice, and the directions of the linear polarizations of each beam are indicated. Each of the beams is orthogonal to or counterpropagating with respect to the other beams. The two vertical beams are decoupled from the three horizontal beams by an 80 MHz frequency shift. (Graphics rendered by W. H. Oskay.)

thus forms confining potential wells for red-detuned light, but not for blue-detuned light, where the intensity maxima form scattering barriers for the atoms, resembling the Lorentz gas. The use of three beams for this two-dimensional lattice is important, in that using the minimum number of beams to determine a lattice ensures that the structure of the interference pattern will be stable to phase perturbations [290]. In the original implementation of this lattice [286, 287], four beams (in two counterpropagating pairs) were used to form the horizontal part of the lattice. Because the interference pattern could change its periodicity by a factor of two as the phase of one of the beams varied, the authors in that experiment implemented interferometric stabilization of the beam phases [289]. In the realization here, we simply omitted one of the four beams to gain relatively easy stability at the expense of lattice intensity. The omission of one of the beams was important in allowing long-term storage of the atoms in the lattice, as we describe below, as well as repeatable atomic temperatures.

The other two beams in the 3D lattice counterpropagated in the vertical direction, and they were approximately perpendicular to the three horizontal beams. These beams were offset in frequency by 80 MHz with respect to the horizontal beams. In this arrangement, the interferences with the horizontal lattice oscillate on a time scale that is very fast compared to atomic motion time scales, and thus it is appropriate to regard the vertical beams as decoupled from the horizontal beams in terms of analyzing the interference pattern. Hence, the vertical beams produced a normal 1D standing-wave lattice, which confined the atoms vertically, and the three horizontal beams confined the atoms in the other two dimensions.

Cooling in 3D lattices proceeds by applying the usual MOT beams to the atoms in the lattice. There are several mechanisms by which lattice cooling achieves much lower temperatures than a standard MOT. The first mechanism is that of "adiabatic cooling" [181], where the application of the lattice acts as an effective refrigerator cycle for cooling the atoms. When the atoms are loaded into the lattice from the initial MOT, they are heated by the increasing potential in order to gain local confinement in the lattice wells. Laser cooling by the MOT beams proceeds as usual, cooling the atoms from the heated temperature back down to normal MOT temperatures. When the lattice is then adiabatically shut off (together with the MOT beams), the temperature is further lowered at the expense of local confinement, in which we are not necessarily interested. An important feature of the lattice configuration implemented here is that because all the light is linearly polarized and far-detuned, the magnetic (Zeeman) sublevels all experience the same energy shift due to the light, and sub-Doppler cooling mechanisms that rely on such degenerate level structure (polarization-gradient cooling [291]) proceed as in the free-MOT case. This mechanism was especially important for the setup here, as the atoms could be stored in the lattice until after the magnetic fields decayed, allowing for much better polarization-gradient cooling than we could achieve in the standard MOT. It was also important to extinguish the MOT beams adiabatically, as they likewise produced an optical lattice due to the six-beam interference. The second mechanism for better cooling in the lattice relates to suppression of the absorption of rescattered light in the MOT. The second-hand absorption of photons that have already been spontaneously scattered by MOT atoms, or "radiation trapping," leads to temperature and density limitations in free-space MOTs [292, 293]. These rescattering events are particularly problematic in that they may be much more likely to be absorbed than regular MOT photons, because their cross section for absorption is independent of detuning due to the possibility of taking part in a two-photon stimulated scattering event [288, 294]. In the *festina lente* regime [294], however, where the photon scattering rate (due to lattice photons, as we will mention below) is small compared to the trap oscillation frequency (and thus the vibrational-level splitting), the recoil heating due to these reabsorption events is suppressed [288, 294]. This is because most of the rescattered photons in this regime are scattered elastically in the tight-confinement (Lamb-Dicke) limit, and the probability of an atom changing its vibrational level by scattering such a rescattered photon is small. This suppression of rescatter heating is further enhanced by a third mechanism in lattice cooling, where the cooling proceeds in analogy to a dark

MOT [295]. This mechanism obtains because the normal repumping light used in the regular MOT is extinguished after the initial cooling phase in the lattice. Most of the atoms are thus in the dark ($F = 3$) hyperfine level, and so the cooling light only affects a small fraction of the atoms at a given time. The far-detuned lattice light provides slow repumping to the trapping transition. Thus, the lifetime for a given vibrational level is set by the scattering rate of optical-lattice light, and not the near-resonant MOT light. Finally, cooling in the lattice has the additional benefit that atoms are separated in individual lattice sites, and thus light-assisted collision losses and other collisional effects are suppressed, resulting in a nearly density-independent cooling rate [285].

For the realization here, the light was produced by the same Ti:sapphire laser that provided the 1D time-dependent interaction lattice. An 80 MHz AOM picked off light for the 3D lattice just before the similar pickoff AOM for the 1D lattice light. Another 80 MHz AOM split this beam into two parts, the first order (+80 MHz) having about 1/3 of the light, with the remainder in the unshifted zeroth order. These two beams were spatially filtered by focusing through 50 μm diameter pinholes. The upshifted light formed the vertical lattice beams, while the unshifted portion was further split in two with a half-wave plate and a polarizing beam-splitter cube to form the horizontal beams. These three beams were all focused onto retroreflecting mirrors on the opposite sides of the chamber so that the beam waist w_0 was 500 μm at their intersection; one of the horizontal, retroreflected beams was blocked to form the five-beam geometry described above. Each of the beams had approximately 90 mW of power. The lattice had a typical detuning of 50 GHz to the red of the $F = 3 \longrightarrow F'$ transition multiplet (or 40 GHz to the red of $F = 4 \longrightarrow F'$), leading to an oscillation frequency in the vertical direction of around 170 kHz (in the harmonic-oscillator approximation) and a scattering rate of around 1 kHz at beam center.

The procedure for lattice cooling began with about 5 s of loading the regular MOT from the background vapor. The optical molasses light intensity was then lowered to 60% of the loading value, and the detuning was increased to 37 MHz (from the

13 MHz used during the loading phase). At the same time, the 3D lattice was turned on adiabatically to minimize the heating of the atoms. The intensity followed the temporal profile $I(t) = I_{\max}(1 - t/\tau)^{-2}$ (for $-800\ \mu\mathrm{s} < t < 0$) [281, 287], where the time constant τ was 30 μs. During this lattice-loading phase, the anti-Helmholtz fields and repump light were both left on to encourage rapid binding of the atoms to the 3D lattice. After a total of 22 ms in this loading phase, the magnetic fields and repump light were extinguished, and the molasses light was raised back up to 100% intensity. The 3D lattice was maintained at full intensity during the subsequent 298 ms storage time, but the molasses light was ramped linearly down to 77% intensity by the end of this period. This long storage time was sufficient to allow the magnetic fields to decay mostly away (to 70 mG or better, when compensated properly by the Helmholtz coils), although a slowly varying magnetic field was still detectable using the stimulated Raman spectroscopy described below. Then the MOT and 3D lattice beams were ramped down adiabatically according to a similar profile, $I(t) = I_0(1 + t/\tau)^{-2}$ (with the same time constant), over 800 μs. The molasses light began its ramping down about 20 μs before the 3D lattice beams, giving the optimum final temperature.

This lattice-cooling procedure led to an atomic population in the $F = 3$ level with a 1D temperature (in the horizontal direction) of 400 nK, or $\sigma_p/2\hbar k_{\mathrm{L}} = 0.7$. Between 50% and 90% of the atoms remained trapped in the lattice during the cooling cycle, depending sensitively on how well the lattice was aligned. The vertical temperature of 500 nK ($\sigma_p/2\hbar k_{\mathrm{L}} = 0.8$) was somewhat higher; the temperature could be made more isotropic by changing the relative beam powers, but at the expense of the horizontal temperature, which was the only important temperature for the experiments here. The lattice worked well over detunings of 25-70 GHz (from $F = 3 \longrightarrow F'$); for closer detunings the final temperature began to rise, and at larger detunings, the fraction retained in the lattice dropped off.

For some experiments, it was necessary to prepare the atoms in the $F = 4$ hyperfine level. This could be conveniently achieved by pulsing on the repumping light for 100 μs after the lattice and molasses fields were extinguished, at the expense of temperature (the final temperature was typically 700 nK after repumping). To implement stimulated Raman velocity selection, as we discuss in the next section, further optical pumping to the $F = 4, m_F = 0$ Zeeman sublevel was necessary, as we discuss in Section 5.3.5.

5.3 Stimulated Raman Velocity Selection

Now we consider the implementation of two-photon, stimulated Raman transitions in cesium for subrecoil (i.e., smaller than the single-photon momentum) velocity selection. After giving a general overview of the theory behind stimulated Raman transitions and velocity selection, we will give the details of our implementation as well as a discussion of optical pumping and internal state selection necessary for a clean velocity-selection method.

5.3.1 Stimulated Raman Transitions: General Theory

We consider the atomic energy level structure shown in Fig. 5.2, where two ground states $|\mathrm{g}_{1,2}\rangle$ are coupled to a manifold of excited states $|\mathrm{e}_n\rangle$ by two optical fields. Our goal is to show that under suitable conditions, the atomic population can be driven between the ground states as in a two-level system. We restrict our attention to the case where the fields propagate along a common axis. In the counterpropagating case, the combined optical field has the form

$$\begin{aligned}\mathbf{E}(x,t) &= \hat{\epsilon}_1 E_{01}\cos(k_1 x - \omega_{\mathrm{L}1} t) + \hat{\epsilon}_2 E_{02}\cos(k_2 x + \omega_{\mathrm{L}2} t)\\ &= \mathbf{E}^{(+)}(x,t) + \mathbf{E}^{(-)}(x,t)\ \ ,\end{aligned} \tag{5.1}$$

where $\mathbf{E}^{(\pm)}(x,t)$ are the positive and negative rotating components of the field, given by

$$\mathbf{E}_1^{(\pm)}(x,t) = \frac{1}{2}\left(\hat{\epsilon}_1 E_{01} e^{\pm ik_1 x} e^{\mp i\omega_{\mathrm{L}1} t} + \hat{\epsilon}_2 E_{02} e^{\mp ik_2 x} e^{\mp i\omega_{\mathrm{L}2} t}\right)\ \ , \tag{5.2}$$

and $\hat{\epsilon}_{1,2}$ are the unit polarization vectors of the two fields. The results that we will derive also apply to the copropagating case as well upon the substitution $k_2 \to -k_2$.

The free atomic Hamiltonian can then be written

$$H_\mathrm{A} = \frac{p^2}{2m} + \hbar\omega_{\mathrm{g}_1}|\mathrm{g}_1\rangle\langle\mathrm{g}_1| + \hbar\omega_{\mathrm{g}_2}|\mathrm{g}_2\rangle\langle\mathrm{g}_2| + \sum_n \hbar\omega_{\mathrm{e}_n}|\mathrm{e}_n\rangle\langle\mathrm{e}_n| \ , \tag{5.3}$$

and the atom-field interaction Hamiltonian is

$$H_\mathrm{AF} = -\mathbf{d}^{(+)}\cdot\mathbf{E}^{(-)} - \mathbf{d}^{(-)}\cdot\mathbf{E}^{(+)} \ , \tag{5.4}$$

where we have made the rotating-wave approximation, we have assumed that $\omega_{21} := \omega_{\mathrm{g}_2} - \omega_{\mathrm{g}_1} \ll \omega_{\mathrm{eg}_j} := \max\{\omega_{\mathrm{e}_n}\} - \omega_{\mathrm{g}_j}$, and we have in mind that the $|\mathrm{e}_n\rangle$ are nearly degenerate. Additionally, we have decomposed the dipole operator $\mathbf{d}$ into its positive- and negative-rotating components,

$$\begin{aligned}\mathbf{d} &= \mathbf{d}^{(+)} + \mathbf{d}^{(-)}\\ &= \sum_n \left(a_{1n}\langle\mathrm{e}_n|\mathbf{d}|\mathrm{g}_1\rangle + a_{2n}\langle\mathrm{e}_n|\mathbf{d}|\mathrm{g}_2\rangle\right) + \sum_n \left(a_{1n}^\dagger\langle\mathrm{e}_n|\mathbf{d}|\mathrm{g}_1\rangle + a_{2n}^\dagger\langle\mathrm{e}_n|\mathbf{d}|\mathrm{g}_2\rangle\right) \ ,\end{aligned} \tag{5.5}$$

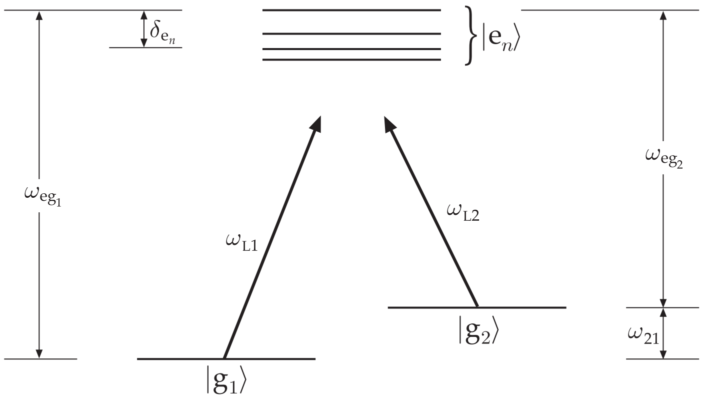

Figure 5.2: Energy level diagram for stimulated Raman transitions. Each ground level $|\mathrm{g}_j\rangle$ is coupled to the excited-state manifold $|\mathrm{e}_n\rangle$ via two laser fields, which are tuned so that their detunings from the excited-state manifold are nearly the same.

where $a_{jn} := |\mathrm{g}_j\rangle\langle\mathrm{e}_n|$ is an annihilation operator. Substituting (5.5) into (5.4), we find

$$\begin{aligned} H_{\mathrm{AF}} = &-\sum_n \frac{1}{2}\langle\mathrm{e}_n|\hat{\epsilon}_1\cdot\mathbf{d}|\mathrm{g}_1\rangle E_{01}(a_{1n}e^{ik_1x}e^{-i\omega_{\mathrm{L}1}t} + a_{1n}^\dagger e^{-ik_1x}e^{i\omega_{\mathrm{L}1}t}) \\ &-\sum_n \frac{1}{2}\langle\mathrm{e}_n|\hat{\epsilon}_2\cdot\mathbf{d}|\mathrm{g}_2\rangle E_{02}(a_{1n}e^{-ik_2x}e^{-i\omega_{\mathrm{L}2}t} + a_{2n}^\dagger e^{ik_2x}e^{i\omega_{\mathrm{L}2}t}) \ . \end{aligned} \tag{5.6}$$

In writing this expression, we have assumed the detunings $\Delta_{\mathrm{L}j} := \omega_{\mathrm{L}j} - \omega_{\mathrm{eg}_j}$ are nearly equal; hence, to make this problem more tractable, we assume that the field $\mathbf{E}_j$ couples only $|\mathrm{g}_j\rangle$ to the $|\mathrm{e}_n\rangle$. After solving this problem we will treat the cross-couplings as a perturbation to our solutions. If we define the Rabi frequency

$$\Omega_{jkn} := \frac{-\langle\mathrm{e}_n|\hat{\epsilon}_k\cdot\mathbf{d}|\mathrm{g}_j\rangle E_{0k}}{\hbar} \ , \tag{5.7}$$

which describes strength of the coupling from level $|\mathrm{g}_j\rangle$ through field $\mathbf{E}_k$ to level $|\mathrm{e}_n\rangle$, we arrive at

$$\begin{aligned} H_{\mathrm{AF}} = &\sum_n \frac{\hbar\Omega_{11n}}{2}(a_{1n}e^{ik_1x}e^{-i\omega_{\mathrm{L}1}t} + a_{1n}^\dagger e^{-ik_1x}e^{i\omega_{\mathrm{L}1}t}) \\ &+\sum_n \frac{\hbar\Omega_{22n}}{2}(a_{1n}e^{-ik_2x}e^{-i\omega_{\mathrm{L}2}t} + a_{2n}^\dagger e^{ik_2x}e^{i\omega_{\mathrm{L}2}t}) \end{aligned} \tag{5.8}$$

as a slightly more compact form for the interaction Hamiltonian.

Now, before examining the equations of motion, we transform the ground states into the rotating frame of the laser field, as in Chapter 2:

$$\begin{aligned} |\tilde{\mathrm{g}}_j\rangle &:= e^{-i\omega_{\mathrm{L}j}t}|\mathrm{g}_j\rangle \\ \tilde{E}_k^{(\pm)} &:= e^{\pm i\omega_{\mathrm{L}k}t}E_k^{(\pm)} \ . \end{aligned} \tag{5.9}$$

Also, for concreteness, we will take $\max\{\omega_{\mathrm{e}_n}\} = 0$. Then the rotating-frame, free-atom Hamiltonian is

$$\tilde{H}_{\mathrm{A}} = \frac{p^2}{2m} + \hbar\Delta_{\mathrm{L}1}|\tilde{\mathrm{g}}_1\rangle\langle\tilde{\mathrm{g}}_1| + \hbar\Delta_{\mathrm{L}2}|\tilde{\mathrm{g}}_2\rangle\langle\tilde{\mathrm{g}}_2| + \sum_n \hbar\delta_{\mathrm{e}_n}|\mathrm{e}_n\rangle\langle\mathrm{e}_n| \ , \tag{5.10}$$

where $\delta_{\mathrm{e}_n} := \omega_{\mathrm{e}_n} - \max\{\omega_{\mathrm{e}_n}\}$ (i.e., $\delta_{\mathrm{e}_n} \leq 0$). The interaction Hamiltonian in the rotating frame is

$$\begin{aligned}\tilde{H}_{\mathrm{AF}} &= -\tilde{\mathbf{d}}^{(+)}\cdot\tilde{\mathbf{E}}^{(-)} - \tilde{\mathbf{d}}^{(-)}\cdot\tilde{\mathbf{E}}^{(+)} \\ &= \sum_n \frac{\hbar\Omega_{11n}}{2}(\tilde{a}_{1n}e^{ik_1x} + \tilde{a}_{1n}^\dagger e^{-ik_1x}) + \sum_n \frac{\hbar\Omega_{22n}}{2}(\tilde{a}_{1n}e^{-ik_2x} + \tilde{a}_{2n}^\dagger e^{ik_2x}) \ ,\end{aligned} \tag{5.11}$$

where the annihilation operator $\tilde{a}_{jn}$ is defined in the same way as a_{jn}, but with $|\mathrm{g}_j\rangle$ replaced by $|\tilde{\mathrm{g}}_j\rangle$.

Turning to the equations of motion, we will manifestly neglect spontaneous emission, since $\Delta_{\mathrm{L}j} \gg \Gamma$, where Γ is the decay rate of $|\mathrm{e}_n\rangle$, by using a Schrödinger-equation description of the atomic evolution. Then we have

$$i\hbar\partial_t|\psi\rangle = (\tilde{H}_{\mathrm{A}} + \tilde{H}_{\mathrm{AF}})|\psi\rangle \ , \tag{5.12}$$

where the state vector can be factored into external and internal components as

$$|\psi\rangle = |\psi_{\mathrm{g}_1}\rangle|\tilde{\mathrm{g}}_1\rangle + |\psi_{\mathrm{g}_2}\rangle|\tilde{\mathrm{g}}_2\rangle + \sum_n |\psi_{\mathrm{e}_n}\rangle|\mathrm{e}_n\rangle \ . \tag{5.13}$$

Then if $\psi_\alpha(x,t) := \langle x|\psi_\alpha\rangle$, we obtain the equations of motion

$$\begin{aligned} i\hbar\partial_t\psi_{\mathrm{e}_n} &= \frac{p^2}{2m}\psi_{\mathrm{e}_n} + \frac{\hbar\Omega_{11n}}{2}e^{-ik_1x}\psi_{\mathrm{g}_1} + \frac{\hbar\Omega_{22n}}{2}e^{ik_2x}\psi_{\mathrm{g}_2} + \hbar(\delta_{\mathrm{e}_n} - \Delta_{\mathrm{L}})\psi_{\mathrm{e}_n} \\ i\hbar\partial_t\psi_{\mathrm{g}_1} &= \frac{p^2}{2m}\psi_{\mathrm{g}_1} + \sum_n \frac{\hbar\Omega_{11n}}{2}e^{ik_1x}\psi_{\mathrm{e}_n} + \hbar(\Delta_{\mathrm{L}1} - \Delta_{\mathrm{L}})\psi_{\mathrm{g}_1} \\ i\hbar\partial_t\psi_{\mathrm{g}_2} &= \frac{p^2}{2m}\psi_{\mathrm{g}_2} + \sum_n \frac{\hbar\Omega_{22n}}{2}e^{-ik_2x}\psi_{\mathrm{e}_n} + \hbar(\Delta_{\mathrm{L}2} - \Delta_{\mathrm{L}})\psi_{\mathrm{g}_2} \ , \end{aligned} \tag{5.14}$$

where we have boosted all energies by $-\hbar\Delta_{\mathrm{L}}$, with $\Delta_{\mathrm{L}} := (\Delta_{\mathrm{L}1} + \Delta_{\mathrm{L}2})/2$ (i.e., we applied an overall phase of $e^{i\Delta_{\mathrm{L}}t}$ to the state vector). Since we assume that $|\delta_{\mathrm{e}_n}| \ll |\Delta_{\mathrm{L}}|$ and $|\Delta_{\mathrm{L}2} - \Delta_{\mathrm{L}1}| \ll |\Delta_{\mathrm{L}}|$, it is clear that the ψ_{e_n} carry the fast time dependence at frequencies of order $|\Delta_{\mathrm{L}}| \gg \Gamma$. We are interested in motion on timescales slow compared to $1/\Gamma$, and the fast oscillations are damped by coupling to the vacuum on timescales of $1/\Gamma$, so we can adiabatically eliminate the ψ_{e_n} by making the approximation that they damp to equilibrium instantaneously ($\partial_t \psi_{\mathrm{e}_n} = 0$). Also, we use $p^2/2m \ll \hbar|\Delta_{\mathrm{L}}|$, with the result,

$$\psi_{\mathrm{e}_n} = \frac{\Omega_{11n}}{2(\Delta_{\mathrm{L}} - \delta_{\mathrm{e}_n})} e^{-ik_1x} \psi_{\mathrm{g}_1} + \frac{\Omega_{22n}}{2(\Delta_{\mathrm{L}} - \delta_{\mathrm{e}_n})} e^{ik_2x} \psi_{\mathrm{g}_2} \ . \tag{5.15}$$

Notice that in deriving this relation, it was important to choose the proper energy shift $-\hbar\Delta_{\mathrm{L}}$ to minimize the natural rotation of the states that remain after the adiabatic elimination; indeed, if the resonance condition that we will derive is satisfied, the two ground states have no natural oscillatory time dependence. This procedure would be much more clear in a density-matrix treatment (as in Section 2.4.1), where the oscillating coherences would be eliminated, but this description is cumbersome due to the number of energy levels in the problem. Using this relation in the remaining equations of motion, we obtain two coupled equations of motion for the ground states,

$$\begin{aligned} i\hbar\partial_t \psi_{\mathrm{g}_1} &= \frac{p^2}{2m}\psi_{\mathrm{g}_1} + [\hbar\Delta_{\mathrm{L}1} + \hbar\omega_{\mathrm{AC}1}]\psi_{\mathrm{g}_1} + \frac{\hbar\Omega_{\mathrm{R}}}{2} e^{i(k_1+k_2)x}\psi_{\mathrm{g}_2} \\ i\hbar\partial_t \psi_{\mathrm{g}_2} &= \frac{p^2}{2m}\psi_{\mathrm{g}_2} + [\hbar\Delta_{\mathrm{L}2} + \hbar\omega_{\mathrm{AC}2}]\psi_{\mathrm{g}_2} + \frac{\hbar\Omega_{\mathrm{R}}}{2} e^{-i(k_1+k_2)x}\psi_{\mathrm{g}_1} \ , \end{aligned} \tag{5.16}$$

where we have removed the energy shift of $-\hbar\Delta_{\mathrm{L}}$. These equations are formally equivalent to the equations of motion for a two level atom, with Rabi frequency

$$\Omega_{\mathrm{R}} := \sum_n \frac{\Omega_{11n}\Omega_{22n}}{2(\Delta_{\mathrm{L}} - \delta_{\mathrm{e}_n})} \tag{5.17}$$

and Stark shifts

$$\omega_{\mathrm{AC}j} := \sum_n \frac{\Omega_{jjn}^2}{4(\Delta_{\mathrm{L}} - \delta_{\mathrm{e}_n})} \ . \tag{5.18}$$

These equations of motion are just the equations generated by the effective Raman Hamiltonian

$$\begin{aligned} H_{\mathrm{R}} = \frac{p^2}{2m} &+ \hbar(\Delta_{\mathrm{L}1} + \omega_{\mathrm{AC}1})|\tilde{\mathrm{g}}_1\rangle\langle\tilde{\mathrm{g}}_1| + \hbar(\Delta_{\mathrm{L}2} + \omega_{\mathrm{AC}2})|\tilde{\mathrm{g}}_2\rangle\langle\tilde{\mathrm{g}}_2| \\ &+ \hbar\Omega_{\mathrm{R}}\left(a_{\mathrm{R}} e^{i(k_1+k_2)x} + a_{\mathrm{R}}^\dagger e^{-i(k_1+k_2)x}\right) \ , \end{aligned} \tag{5.19}$$

where the Raman annihilation operator is defined as $a_{\mathrm{R}} := |\mathrm{g}_1\rangle\langle\mathrm{g}_2|$. Noting that the operator $\exp(-ikx)$ is a momentum-shift operator, so that $\exp(-ikx)|p\rangle = |p - \hbar k\rangle$ (and thus $\exp(-ikx)\psi(p) = \psi(p+\hbar k)$, where $\psi(p) := \langle p|\psi\rangle)$, it is clear from the form of the effective Raman Hamiltonian that a transition from $|\mathrm{g}_2\rangle$ to $|\mathrm{g}_1\rangle$ is accompanied by a kick to the left of two photon-recoil momenta, and the reverse transition is accompanied by a kick to the right of two photon recoils. We can write out the coupled equations of motion due to the Hamiltonian (5.19) more explicitly as

$$\begin{aligned} i\hbar\partial_t\psi_{\mathrm{g}_1}(p) &= \left[\frac{p^2}{2m} + \hbar\Delta_{\mathrm{L1}} + \hbar\omega_{\mathrm{AC1}}\right]\psi_{\mathrm{g}_1}(p) + \frac{\hbar\Omega_{\mathrm{R}}}{2}\psi_{\mathrm{g}_2}(p+2\hbar k_{\mathrm{L}}) \\ i\hbar\partial_t\psi_{\mathrm{g}_2}(p+2\hbar k_{\mathrm{L}}) &= \left[\frac{(p+2\hbar k_{\mathrm{L}})^2}{2m} + \hbar\Delta_{\mathrm{L2}} + \hbar\omega_{\mathrm{AC2}}\right]\psi_{\mathrm{g}_2}(p+2\hbar k_{\mathrm{L}}) + \frac{\hbar\Omega_{\mathrm{R}}}{2}\psi_{\mathrm{g}_1}(p) \ , \end{aligned} \tag{5.20}$$

where $2k_{\mathrm{L}} := k_1 + k_2$. The resonance condition for this transition $|p\rangle|\mathrm{g}_1\rangle \longrightarrow |p + 2\hbar k_{\mathrm{L}}\rangle|\mathrm{g}_2\rangle$ is

$$\left[\frac{(p+\hbar k_{\mathrm{L}})^2}{2m\hbar} + \Delta_{\mathrm{L2}} + \omega_{\mathrm{AC2}}\right] - \left[\frac{p^2}{2m\hbar} + \Delta_{\mathrm{L1}} + \omega_{\mathrm{AC1}}\right] = 0 \ , \tag{5.21}$$

which can be rewritten as

$$4\omega_{\mathrm{r}}\left(\frac{p+\hbar k_{\mathrm{L}}}{\hbar k_{\mathrm{L}}}\right) + (\Delta_{\mathrm{L2}} - \Delta_{\mathrm{L1}}) + (\omega_{\mathrm{AC2}} - \omega_{\mathrm{AC1}}) = 0 \ . \tag{5.22}$$

Here, we have defined the recoil frequency as before by $\omega_{\mathrm{r}} := \hbar k_{\mathrm{L}}^2/2m = 2\pi \cdot 2.0663$ kHz for the cesium D_2 transition. The first term is just the Doppler shift of the two optical fields due to motion at the average of the upper and lower state momenta. In the copropagating case, this term is typically negligible.

Finally, we account for the effects of the cross-couplings that we previously ignored. The lifetimes of the two ground states are in practice extremely long, so that the line width of the Raman transition is quite narrow, being limited only by the finite interaction time. Since it is assumed that the Raman resonance condition (5.21) is approximately true, the Raman cross-coupling is much further away from resonance than the intended coupling (typically several orders of magnitude in cesium), so this extra Raman coupling can be neglected in a secondary rotating-wave approximation. However, the cross-couplings can induce additional ac Stark shifts of the ground levels. So, we simply modify (5.18) to include these extra shifts:

$$\begin{aligned} \omega_{\mathrm{AC1}} &:= \sum_n \frac{\Omega_{11n}^2}{4(\Delta_{\mathrm{L}} - \delta_{\mathrm{e}_n})} + \sum_n \frac{\Omega_{12n}^2}{4(\Delta_{\mathrm{L}} - \delta_{\mathrm{e}_n} - \omega_{21})} \\ \omega_{\mathrm{AC2}} &:= \sum_n \frac{\Omega_{22n}^2}{4(\Delta_{\mathrm{L}} - \delta_{\mathrm{e}_n})} + \sum_n \frac{\Omega_{21n}^2}{4(\Delta_{\mathrm{L}} - \delta_{\mathrm{e}_n} + \omega_{21})} \quad . \end{aligned} \tag{5.23}$$

These additional Stark shifts may not in general be negligible compared to the original Stark shifts.

We can also obtain an estimate of the spontaneous emission rate by using (5.15) to write the total excited state population in terms of the density matrix elements:

$$\begin{aligned} R_{\mathrm{sc}} &= \Gamma \sum_n \rho_{\mathrm{e}_n\mathrm{e}_n} \\ &= \sum_n \frac{\Gamma\Omega_{11n}^2}{4(\Delta_{\mathrm{L}} - \delta_{\mathrm{e}_n})^2}\rho_{\mathrm{g}_1\mathrm{g}_1} + \sum_n \frac{\Gamma\Omega_{22n}^2}{4(\Delta_{\mathrm{L}} - \delta_{\mathrm{e}_n})^2}\rho_{\mathrm{g}_2\mathrm{g}_2} \\ &\quad + \sum_n \frac{\Gamma\Omega_{11n}\Omega_{22n}}{4(\Delta_{\mathrm{L}} - \delta_{\mathrm{e}_n})^2} e^{-i2k_{\mathrm{L}}x}\rho_{\mathrm{g}_1\mathrm{g}_2} + \sum_n \frac{\Gamma\Omega_{11n}\Omega_{22n}}{4(\Delta_{\mathrm{L}} - \delta_{\mathrm{e}_n})^2} e^{i2k_{\mathrm{L}}x}\rho_{\mathrm{g}_2\mathrm{g}_1} \quad . \end{aligned} \tag{5.24}$$

Here, $\rho_{\alpha\alpha}$ is the population in state $|\alpha\rangle$, with $\rho_{\mathrm{g}_1\mathrm{g}_1} + \rho_{\mathrm{g}_2\mathrm{g}_2} \simeq 1$, and this result assumes implicitly that $\Delta_{\mathrm{L1}} \approx \Delta_{\mathrm{L2}}$. The second two terms represent an enhancement or suppression of spontaneous scattering due to atomic coherences; for example, the state

$$|\psi\rangle = \eta(\Omega_{22n} e^{ik_{\mathrm{L}}x} |\psi_{\mathrm{g}_1}\rangle - \Omega_{11n} e^{-ik_{\mathrm{L}}x} |\psi_{\mathrm{g}_2}\rangle) \tag{5.25}$$

(where η is the appropriate normalization factor) is dark, since R_{sc} vanishes for this state. However, this state is only dark if the cross-couplings can be ignored. More realistically, the scattering rate can be modeled as an incoherent sum over all the couplings of the form $(\Gamma\Omega^2/4\Delta^2)\rho_{\mathrm{g}_j\mathrm{g}_j}$, including other fields that are not directly involved in the Raman transition (such as the EOM carrier field, discussed in Section 5.3.3).

5.3.2 Pulse-Shape Considerations

Since the velocity-selective Raman pulses are generally used to “tag” a subset of an atomic distribution according to their momentum, it is important to consider the impact of the temporal pulse profile on the tagged distribution. The simplest pulse profile is the square profile, where the light is turned on at a constant intensity for some duration. Assuming that the atoms are all initially in the same internal atomic state, the tagging process is described by the solution of the optical Bloch equations for the excited state population of a two-level atom with Rabi frequency Ω_R, Raman detuning Δ_R (given by the left-hand side of Eq. (5.22)), and with all initial population in the ground Raman state:

$$\rho_\mathrm{ee}(t) = \frac{\Omega_\mathrm{R}^2}{\Omega_\mathrm{R}^2 + \Delta_\mathrm{R}^2} \sin^2\left(\frac{1}{2}\sqrt{(\Omega_\mathrm{R}^2 + \Delta_\mathrm{R}^2)}\, t\right) \quad . \tag{5.26}$$

From Eq. (5.22), we see that a detuning of $\Delta_\mathrm{R} = 4\omega_\mathrm{r}$ corresponds to a momentum shift of $\hbar k_\mathrm{L}$. This lineshape has wings that decay relatively slowly, with a series of locations where the lineshape goes to zero. The locations of the zeros for an interaction time of δt is given by

$$\Delta_\mathrm{R} = \sqrt{\frac{4n^2\pi^2}{(\delta t)^2} - \Omega_\mathrm{R}^2} \tag{5.27}$$

for positive integer n. This relation simplifies for specific interaction times; for example, for a "π-pulse" of duration $\delta t = \pi/\Omega_\mathrm{R}$, the locations are at $\Delta_\mathrm{R} = \Omega_\mathrm{R}\sqrt{4n^2-1}$, and for a $\pi/2$-pulse of duration $\delta t = \pi/(2\Omega_\mathrm{R})$, the locations are $\Delta_\mathrm{R} = \Omega_\mathrm{R}\sqrt{16n^2-1}$. These zeros were important in a previous implementation of Raman cooling [296, 297], where the first zero of the profile (5.26) was placed at zero momentum to form a dark interval where atoms would accumulate. The square-pulse excitation lineshape is plotted in Fig. 5.3 for a $\pi/2$-pulse, a π-pulse, and a 2π-pulse. Note that for the important case of the π-pulse, the central population lobe is characterized by a half width at half maximum of $0.799 \cdot \Omega$.

It is also important to note that because one typically excites a range of detunings with a velocity-selective Raman pulse, the transferred population does not undergo simple sinusoidal Rabi oscillations. For a square pulse, the excitation profile (5.26) must be averaged over the atomic velocity distribution. In the limit of a broad velocity distribution, the excited population is proportional to

$$\begin{aligned}\int_{-\infty}^{\infty} \rho_{\mathrm{ee}}(t)\,d\Delta_{\mathrm{R}} &= \frac{\pi\Omega_{\mathrm{R}}}{2}\mathit{Ji}_0(\Omega_{\mathrm{R}}t)\\ &= \frac{\pi\Omega_{\mathrm{R}}^2 t}{2}\left\{J_0(\Omega_{\mathrm{R}}t) + \frac{\pi}{2}[J_1(\Omega_{\mathrm{R}}t)\mathbf{H}_0(\Omega_{\mathrm{R}}t) - J_0(\Omega_{\mathrm{R}}t)\mathbf{H}_1(\Omega_{\mathrm{R}}t)]\right\}\ , \end{aligned} \tag{5.28}$$

where the $J_n(x)$ are ordinary Bessel functions, the $\mathbf{H}_n(x)$ are Struve functions, and $\mathit{Ji}_n(x) := \int_0^x J_n(x')dx'$. The population in this case still oscillates as a function of time, but with some damping. This function is plotted in Fig. 5.4. Notice that for short times, the function (5.28) reduces to $(\pi/2)\Omega_{\mathrm{R}}^2 t + O(t^2)$, so that one can associate a nonzero transition rate, proportional to Ω_{R}^2 (which is in turn proportional to the product of the laser intensities), as long as $\Omega_{\mathrm{R}}t \ll 1$.

An alternative approach, based on the Blackman pulse profile, was used by the Chu group for Raman cooling [298, 299]. This profile, when normalized to have unit

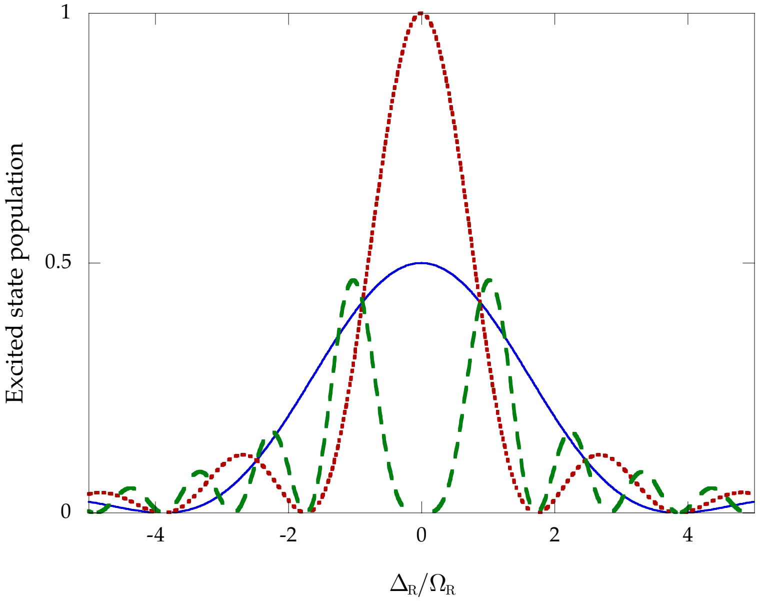

Figure 5.3: Plot of Eq. (5.26), showing excited state population as a function of the detuning from resonance, for three pulse durations: $\pi/2$-pulse, corresponding to an interaction time of $\delta t = \pi/(2\Omega_{\mathrm{R}})$, (solid line); a π-pulse, corresponding to $\delta t = \pi/\Omega_{\mathrm{R}}$ (dotted line); and a 2π-pulse, for $\delta t = 2\pi/\Omega_{\mathrm{R}}$ (dashed line).

area, can be written as

$$f_{\mathrm{B}}(t) = \frac{1}{0.42\tau}[-0.5\cos(2\pi t/\tau) + 0.08\cos(4\pi t/\tau) + 0.42] \ , \tag{5.29}$$

where τ is the duration (support) of the pulse. The Blackman profile has the property that the tails in the Fourier spectrum are suppressed relative to the square pulse. Hence, the Raman excitation spectrum of the Blackman pulse falls off much more sharply than the corresponding square-pulse spectrum, as shown in Fig. 5.5. However, the implementation of Blackman pulses in a setup where the Raman beams induce an ac Stark shift of the transition is more complicated, since the Raman frequency must be chirped to match the Stark shift in order to get good frequency resolution. (For an 800 μs, square π-pulse, the Raman transition was Stark shifted by around -2 kHz in this setup, which is larger than the 500 Hz effective half-width of the selected momentum group.) Due to the frequency stability issues of the RF electronics discussed below, the experiments in this dissertation used only square Raman pulses.

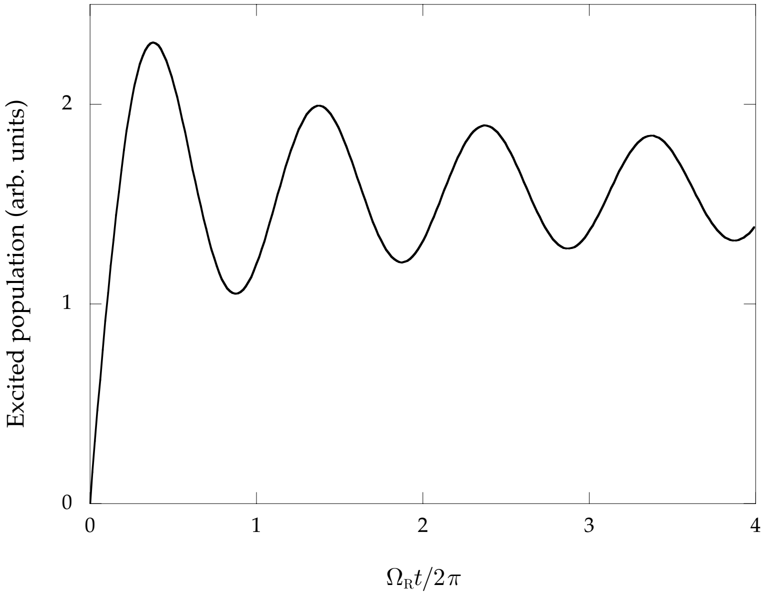

Figure 5.4: Plot of Eq. (5.28), showing excited state population evolution resulting from a square, velocity-selective Raman pulse in a broad atomic velocity distribution. The location of the first minimum is determined by the second zero of $J_0(x)$, which is at $\Omega_{\mathrm{R}}t \approx 0.879 \cdot 2\pi$.

5.3.3 Implementation of Stimulated Raman Transitions

The basic hardware setup for implementing stimulated Raman transitions is shown in Fig. 5.6. The Ti:sapphire laser that provided the light for the 1D and 3D optical lattices also provided the light to drive the Raman transitions. A 40 MHz AOM, placed after the two AOMs for the optical lattices and before the wave meter and Fabry-Perot cavity, was used to to pick off the Raman light from the main Ti:sapphire beam line.

The method used to generate the two laser frequencies to drive cesium Raman transitions is similar to the implementation in [300]. The first-order beam from the Raman AOM was split into two components by a 50% beam splitter (or more precisely, a half-wave plate with a polarizing beam-splitter cube). One of the split beams was sent through a New Focus model 4851, 9.28 GHz electro-optic phase modulator (EOM), which put sidebands at ±9.28 GHz on the beam. The driving signal was derived from the 10 MHz output of a highly stable and accurate EFRATOM LPRO rubidium oscil-

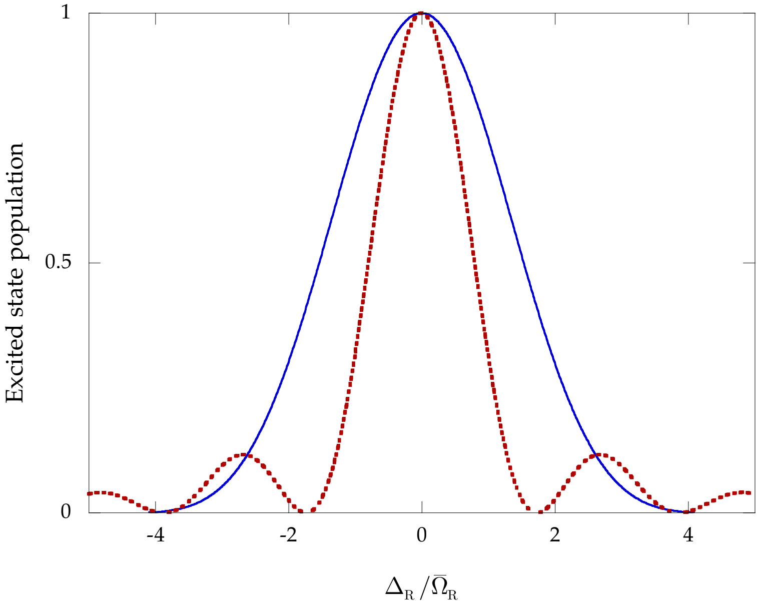

Figure 5.5: Plot of the excitation profile for a Blackman pulse (solid line) and for a square pulse (dotted line). Both pulses are π-pulses and have the same total temporal duration (and hence the same average Rabi frequency $\bar{\Omega}_R$).

lator, which was quadrupled in frequency and then converted to 9.28 GHz by a Delphi Components, Inc. dielectric resonant oscillator (DRO). The DRO output was amplified by a QuinStar Technology, Inc. model CPA09092535-1 solid state amplifier, which was specified to have 25 dB of gain (with 35 dBm maximum output power) at 9.28 GHz. The amplifier output was protected by a Sierra Microwave Technology model SMC-8010 microwave circulator, so that any back-reflections would be terminated into a 50 Ω resistive load rather than the amplifier output port. The signal was transferred to the phase modulator through a 1 m long, Times Microwave Systems LMR-400 cable, which has low loss at 9.28 GHz compared to standard semirigid (RG-402) coaxial wire. The EOM converted about 7% of the carrier into each of the sidebands. The beam was then spatially filtered by focusing through a 40 μm pinhole, converted to circular polarization

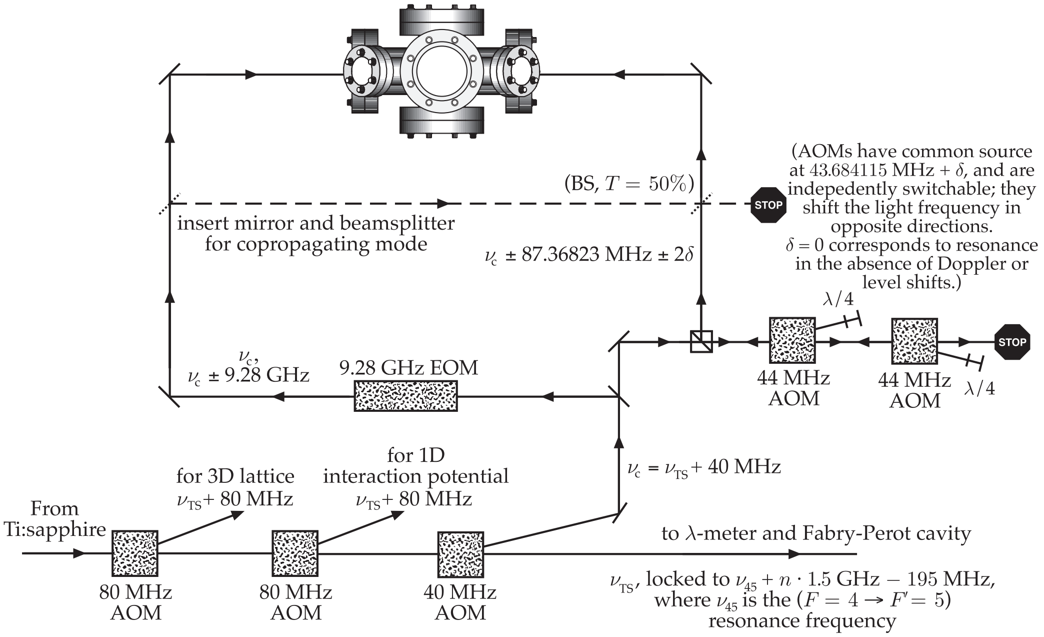
(BS, $T = 50\%$)
STOP
insert mirror and beamsplitter for copropagating mode
ν_c ± 87.36823 MHz ± 2δ
(AOMs have common source at 43.684115 MHz + δ, and are indepedently switchable; they shift the light frequency in opposite directions. $\delta = 0$ corresponds to resonance in the absence of Doppler or level shifts.)
$\lambda/4$
STOP
44 MHz AOM
44 MHz AOM
$\lambda/4$
ν_c, ν_c ± 9.28 GHz
9.28 GHz EOM
$\nu_c = \nu_{TS} + 40$ MHz
for 3D lattice ν_{TS}+ 80 MHz
for 1D interaction potential ν_{TS}+ 80 MHz
From Ti:sapphire
to λ-meter and Fabry-Perot cavity
80 MHz AOM
80 MHz AOM
40 MHz AOM
ν_{TS}, locked to $\nu_{45} + n \cdot 1.5$ GHz $-$ 195 MHz, where ν_{45} is the ($F = 4 \rightarrow F' = 5$) resonance frequency

Figure 5.6: Optical layout for implementing stimulated Raman transitions with a high-frequency electro-optic modulator (EOM). The EOM put 9.28 GHz sidebands on the carrier frequency ν_c, and the counterpropagating beam was shifted up or down in frequency by one of two acousto-optic modulators (AOMs), depending on the desired direction of the photon momentum transfer. An extra mirror and beam splitter could be inserted on kinematic mounts to convert the system to copropagating mode.

by a zero-order half-wave plate, and sent into the chamber. This (collimated) beam had a waist parameter w_0 of around 2 mm as it entered the chamber.

The other beam propagated through two 44 MHz tunable AOMs. These AOMs were arranged in a double-pass configuration, with one double-passing the $+1$ order and the other using the -1 order. With this arrangement the output beam could be shifted by ± 88 MHz depending on which AOM was switched on, with some tunability. The output of the double-pass configuration was also sent into the vacuum chamber after spatial filtering through a 35 μm pinhole. This beam also had a waist parameter w_0 of around 2 mm in the chamber, and was likewise circularly polarized after passing through a zero-order half-wave plate. The two beams propagated along nearly the same axis as the 1D lattice (with about 1° of horizontal angular separation), to give velocity selectivity in the dimension of interest. The idea behind this arrangement is that the AOM-shifted light and one of the sidebands on the other beam provide the two frequencies to drive the Raman transition. The AOM frequency shift was important to decouple all other pairs of light, so that the other EOM sideband and the EOM carrier had no influence on the atoms besides a Stark shift and some additional spontaneous scattering. The shift was

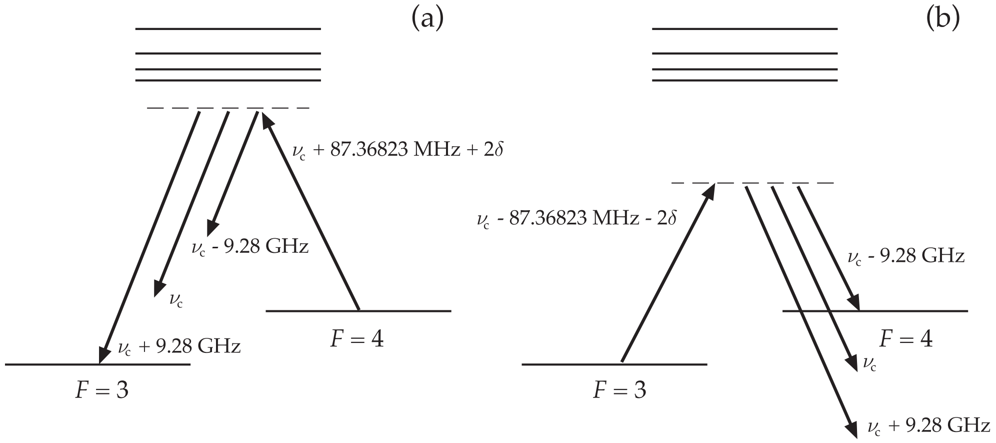

Figure 5.7: Energy-level scheme in cesium for the optical setup in Fig. 5.6. The configuration shown in (a) is for the case when one of the double-passed AOMs shifted the light up by 87 MHz, while case (b) is for the case where the light was shifted down by 87 MHz.

particularly important in decoupling the carrier, which in velocity-selective mode would form a standing wave with the counterpropagating beam. With the frequency shift, this standing wave moved far too quickly ($\sim 10^4$ photon recoils) to have any effect on the atomic motion. Since the ground-state splitting ω_{21} is exactly $2\pi \cdot 9.192\ 631\ 770$ GHz, driving the AOMs at 43.684 115 MHz (which induces a shift of ± 87.368 230 MHz) put the Raman transition directly on resonance in the absence of Stark, magnetic, or Doppler shifts.

The tunable RF signal that drove the AOMs needed to be extremely stable, and thus was derived from synthesized signal generators. In the original setup, the signal from a Fluke 6080A/AN synthesizer, operating at 150 MHz, was doubled in frequency by a Mini-Circuits FK-5 doubler. Since the synthesizer had an analog frequency-modulation (FM) input which could change the frequency by up to ±1 MHz, the doubler effectively increased the "throw" of the synthesizer to ±2 MHz. The analog FM input was controlled by a Stanford Research Systems DS345 arbitrary waveform synthesizer, connected by a double-shielded coaxial cable to reduce noise contamination on the FM signal. The doubled signal was mixed by a Mini-Circuits ZP-3LH mixer with the output of a WaveTek model 2047 synthesizer, which operated at about 343.7 MHz, to obtain the difference frequency at 43.7 MHz. The mixer output was then amplified by an IntraAction model PA-4 power amplifier and then fed into the appropriate AOM. The synthesizers were both slaved to the Rb oscillator mentioned above for extremely good accuracy and stability, but the analog input of the Fluke unit caused the output frequency to have long-term drifts (over the course of a day) at the kHz level, which is at the same level as the Fourier width of the Raman selection pulse. Hence, this setup was not suitable for a reliable Raman velocity selection solution, and so the Fluke unit was replaced by a Hewlett-Packard model 8662A synthesizer. The HP unit was much more stable, having drifts at the 100 Hz level over the course of a day, but also had a much smaller FM range of ±25 kHz. So, the HP unit was more useful for Raman velocity selection, while the Fluke unit was more useful for wide-range sweeps (e.g., while looking for Raman signals initially or beginning to null out magnetic fields). It was also useful to have rapid control of the Raman detuning to chirp the detuning during a pulse, which improved the quality of the spectra in coarse spectral sweeps. For the Raman velocity selection in the state-preparation sequence described below, the FM input on the HP unit was disabled, and the Raman detuning was set by programming the HP unit via the GPIB interface. In this mode, where the FM input was deselected, the RF system had extremely good frequency stability, with a drift at the level of 1 Hz/day.

This configuration allows for two distinct possibilities for driving Raman transitions. When the two beams are counterpropagating, the Raman transitions are velocity-selective, as we argued in the previous section. By choosing which way the double-passed beams are shifted, one also chooses the direction of momentum that the beams impart to the atoms. This idea is illustrated in Fig. 5.7, which shows the optical frequencies in the context of the energy levels of cesium. When the double-passed beam is shifted up in frequency, it drives the $F = 4 \longrightarrow F'$ part of the transition, while the upper sideband on the EOM beam drives the $F = 3 \longrightarrow F'$ part. The lower sideband and the carrier are too far away from resonance to have a significant effect. When the double-passed beam is shifted to the red, however, as in Fig. 5.7(b), the double-passed beam drives the $F = 3 \longrightarrow F'$ part of the Raman transition, while the lower sideband of the EOM beam drives the $F = 4 \longrightarrow F'$ part. The mutual detuning of the Raman beams from resonance is now effectively 9 GHz larger, but the imparted momentum for a given Raman transition is in the opposite direction. For the $F = 3 \longrightarrow F = 4$ Raman transition, the case of Fig. 5.7(a) corresponds to a leftward kick in Fig. 5.6, while the case of Fig. 5.7(b) corresponds to a rightward kick. This dual-AOM arrangement is useful for an implementation of stimulated Raman cooling, as we discuss briefly below, although for the experiments in this dissertation, we only used one of the AOMs (inducing a positive frequency shift) to drive velocity-selective transitions.

This setup could also be operated in copropagating mode by inserting a mirror to deflect the phase-modulated beam after the spatial filter and inserting a 50%

non-polarizing cube beam splitter to combine the two beams with the same polarization. This configuration was useful for nulling the background magnetic fields, as these Raman transitions are much more efficient than in the counterpropagating case (since atoms moving at all velocities can still undergo transitions), and the only energy shifts are Stark and Zeeman shifts. By minimizing the splittings between the resonances due to these copropagating-mode transitions, we could null the background fields to about 10 mG, although we tolerated background fields at the 70 mG level because of long-term drifts in the field-control electronics.

5.3.4 Optical Pushing and Hyperfine State Detection

With this setup, it is possible to drive Raman transitions in cesium, but it is still necessary to have a measurement scheme to detect the internal state populations. Beginning with cooling in the 3D optical lattice, the atoms were cooled in the $F = 3$ ground hyperfine level. As discussed above, a brief repumping pulse transferred the atoms to the $F = 4$ level. At this point we could drive Raman transitions back to the $F = 3$ level. To detect the population transferred by the Raman process, we turned on a beam resonant with the $F = 4 \longrightarrow F' = 5$ cycling transition to accelerate the $F = 4$ atoms to high velocity, leaving only the $F = 3$ atoms in the interaction region; these atoms could then be detected by the usual freezing molasses method or used as a starting point for further

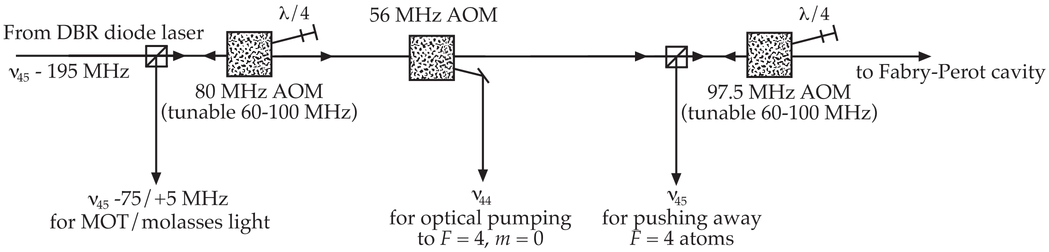
From DBR diode laser
ν_{45} - 195 MHz
$\lambda/4$
80 MHz AOM
(tunable 60-100 MHz)
56 MHz AOM
$\lambda/4$
to Fabry-Perot cavity
97.5 MHz AOM
(tunable 60-100 MHz)
ν_{45} -75/+5 MHz
for MOT/molasses light
ν_{44}
for optical pumping
to $F = 4$, $m = 0$
ν_{45}
for pushing away
$F = 4$ atoms

Figure 5.8: Optical layout for other beams needed for Raman tagging. The same laser is used to generate light for the MOT/molasses, the optical pumping into $F = 4, m_F = 0$, and for pushing $F = 4$ atoms out of the interaction region after the tagging.

atomic manipulation and experimentation. This pushing beam was combined with the phase-modulated Raman beam by a cube beam splitter before the half-wave plate, and thus was circularly polarized as it propagated along the Raman-beam axis. The beam also diverged rapidly (it passed through a 25.4 mm focal length lens about 0.5 m away from the atoms), so that it was large and uniform at the atomic cloud. This light was derived from the DBR laser beam line by a double-passed, 97.5 MHz fixed-frequency AOM, as shown in Fig. 5.8. The light was turned on at low level for 800 μs, accelerating the atoms to over $100 \cdot 2\hbar k_{\mathrm{L}}$. The circular polarization of this beam had the advantage that atoms were optically pumped into the $F = 4, m_F = 4 \longrightarrow F' = 5, m_F = 5$ cycling transition; atoms in this excited state do not decay (by dipole transitions) to the $F = 3$ ground level, and atoms in $F = 4, m_F = 4$ cannot be pumped off-resonantly to the $F' = 4$ excited level (by a dipole transition), so this transition is tightly closed. However, it was still important to use a sufficiently low light level during the first part of the pushing to avoid off-resonant excitation before the atoms were fully optically pumped. This procedure removed the $F = 4$ atoms from the detection region after the drift time with about 99.9% efficiency, with the remaining atoms forming a broad background in the momentum distribution measurements.

To detect the number of atoms transferred by the Raman interaction, we used the usual ballistic-expansion measurement. We ignored the spatial dependence of the CCD image and simply counted the total fluorescence, which after a background subtraction is proportional to the number of atoms in the $F = 3$ level. A sample measurement of Raman Rabi oscillations on resonance (for one of the Zeeman transitions) is shown in Fig. 5.9, which exhibits clean oscillations with a certain amount of damping. For comparison, the Raman Rabi oscillations in the counterpropagating arrangement are shown in Fig. 5.10. The oscillations in this configuration have lower contrast, as we expect from the previous theoretical discussion, and show much lower overall population transfer due to the velocity selectivity. Some detuning-dependent Raman selection profiles for the copropagating mode are shown in Fig. 5.11 for several interaction times.

5.3.5 Hyperfine Magnetic Sublevel Optical Pumping

One difficulty in implementing velocity selection via stimulated Raman transitions in cesium is due to the highly degenerate level structure. For a generic polarization state of the Raman fields, there are 15 possible transitions, each with possibly different Zeeman and Stark shifts, as well as different Rabi frequencies. To make this situation much cleaner, we implemented optical pumping of the atoms into the $F = 4, m_F = 0$ sublevel before driving the Raman transition. We effected this optical pumping using another beam derived from the DBR laser, this time with a 56 MHz AOM (as shown in Fig. 5.10) to shift the beam down in frequency to be on resonance with the $F = 4 \longrightarrow F' = 4$ transition. The beam was spatially filtered and introduced via the MOT beam window on the top of the chamber, so that its linear polarization direction was along the Raman-beam propagation axis. This light was pulsed on for 50 μs, beginning 66 μs before the end of the of the ramp-down time of the 3D optical lattice. Because the $F = 4, m_F = 0 \longrightarrow F' = 4, m_F' = 0$ transition is forbidden in the dipole approxima-

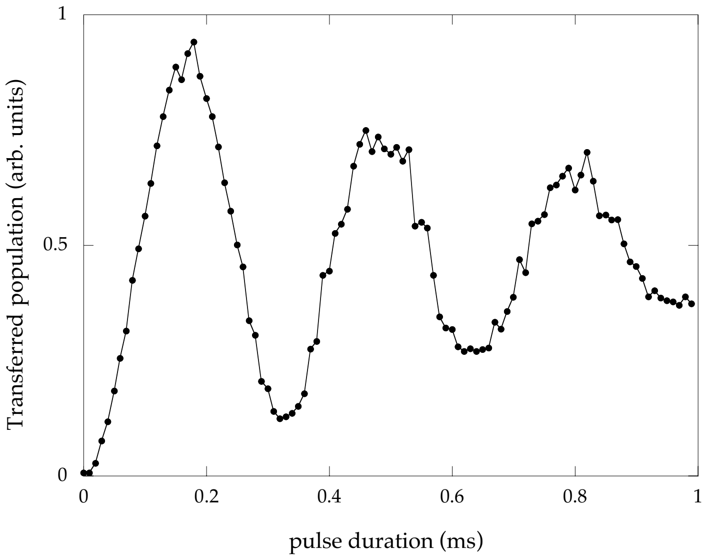

Figure 5.9: Example of an experimental measurement of excited population oscillations for a resonant, stimulated Raman transition in copropagating mode. The damping here is due mostly to spontaneous scattering of the Raman light. The data points here were not averaged over multiple measurements.

tion, the atoms accumulated in the $F = 4, m_F = 0$ sublevel after several fluorescence cycles. Atoms that decayed to the $F = 3$ ground level were returned to $F = 4$ by the usual repumping light, which was turned on at the same time as the optical-pumping light. The repumping light was left on until the end of the 3D lattice ramp-down time to ensure that all atoms were in the $F = 4$ ground level. Two of the Helmholtz coils were also pulsed on to provide a 1.5 G bias field along the polarization direction of the pumping light, which swamped other residual magnetic fields and thus prevented remixing of the magnetic sublevels. The coils were turned on 200 μs before the pumping light to allow transients to decay away. This procedure pumped most ($>95\%$) of the atoms into the proper magnetic sublevel. Because the Raman beams were circularly polarized, they drove the atoms from the $F = 4, m_F = 0$ level to the $F = 3, m_F = 0$ level via the $F' = 3, m_F = 1$ and $F' = 4, m_F = 1$ excited states. The atoms thus all experienced the same Raman Rabi frequency, and the Raman transition frequency was

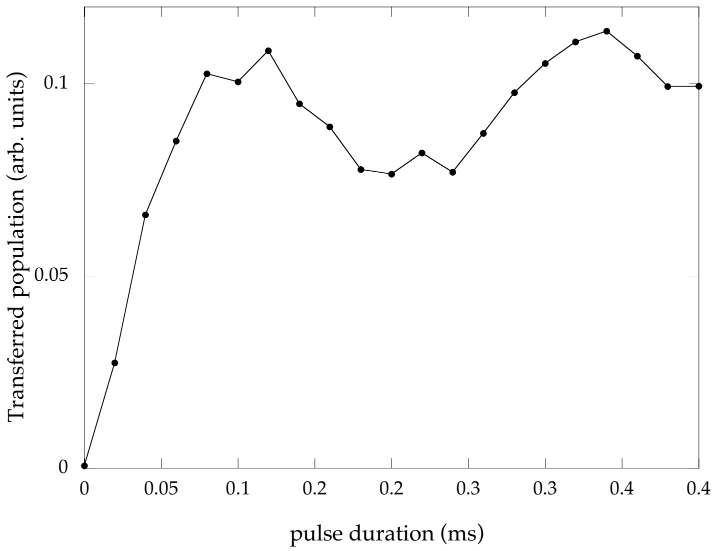

Figure 5.10: Example of an experimental measurement of excited population oscillations for a resonant, stimulated Raman transition in counterpropagating mode. The scale of the vertical axis is the same as in Fig. 5.9. The population transfer is much less efficient due to the velocity selectivity of the counterpropagating configuration. The oscillations also show an upwards trend due to relaxation of nonresonantly coupled atoms. The data points here were not averaged over multiple measurements.

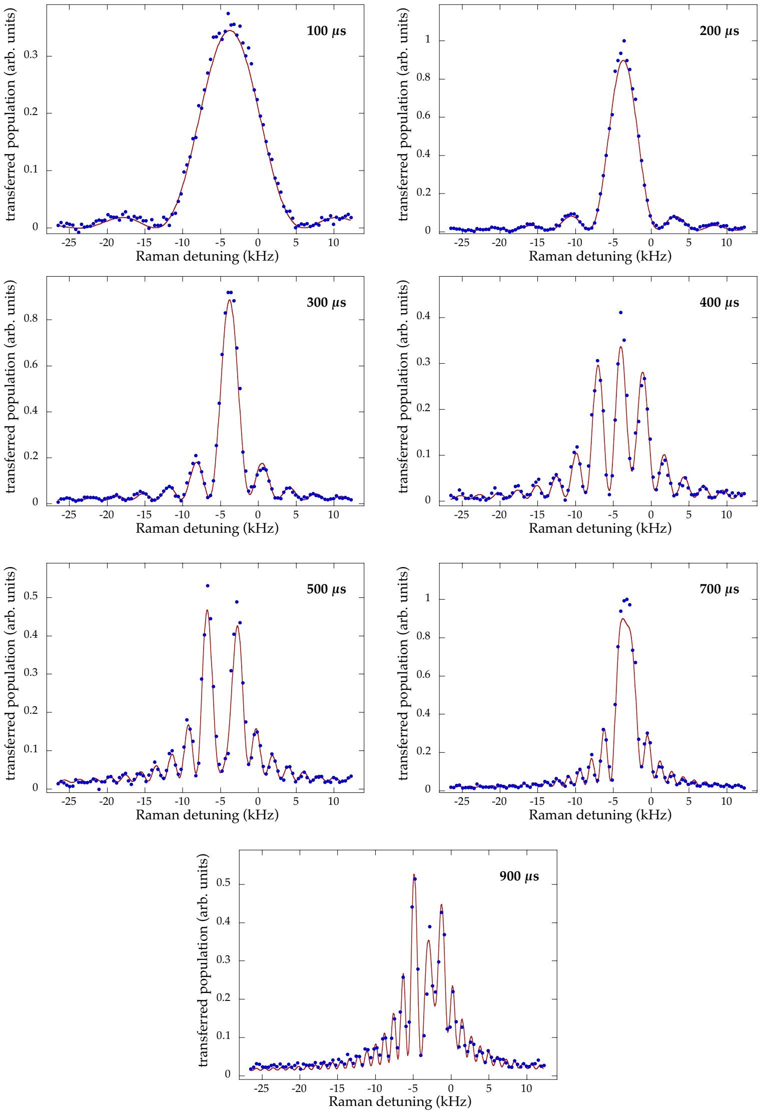

Figure 5.11: Experimental measurement of excited population vs. Raman detuning Δ_{R} for different interaction (square) pulse lengths. The data are shown as points, and the solid lines represent the best fit of a model based on direct integration of the Schrödinger equation for the two-level atom. The asymmetries of the profiles, which is not predicted by Eq. (5.26), can largely be explained by broadening due to the intensity variation of the Gaussian profile of the Raman beams over the atomic sample, which is included in the model. The model was fit simultaneously to all the distributions, and the fitted parameter values are: $\Omega_{\mathrm{R}} = 2\pi \cdot 2.1$ kHz, a coherence damping rate of 21 Hz, and a Raman beam waist $w_0 = 2$ mm (assuming a Gaussian MOT spatial profile with width parameter $\sigma_x = 0.15$ mm). The data points here were not averaged over multiple measurements.

insensitive to magnetic fields to first order (this transition is the cesium clock transition that currently defines the measurement of time). Because of the Zeeman shift due to the large bias field, any atoms left in other magnetic sublevels did not participate in the Raman transition. Unfortunately, these benefits came at the expense of temperature, which increased to 3 μK (or $\sigma_p/2\hbar k_{\text{L}} = 1.9$) after the optical pumping (beginning with atoms cooled in the 3D optical lattice). One possible improvement would be to implement sideband cooling into the $m_F = 0$ sublevel [301], but such a scheme requires a considerable increase in the complexity of the experiment.

5.3.6 Implementation of Stimulated Raman Velocity Selection

The 3D lattice cooling, Raman-field setup, pushing-beam setup, and optical-pumping procedure were all important for implementing velocity selection by stimulated Raman transitions. Typically, we selected atoms to be near $p = 0$ as a starting point for further quantum state preparation techniques. The procedure for Raman velocity selection (or “Raman tagging”) atoms near $p = 0$ was as follows:

1. Trap and cool atoms in the MOT, and then further cool the atoms in the 3D lattice.
2. Turn on the magnetic bias field along the direction of the Raman beams to define the quantization axis.
3. Use the optical pumping light (during the ramping down of the 3D lattice) to prepare atoms in $F = 4, m_F = 0$ sublevel.
4. Use the Raman beams (both with σ^+ polarization) in counterpropagating mode to tag atoms with $p = 2\hbar k_{\text{L}}$ in the $F = 4, m_F = 0$ state to the $F = 3, m_F = 0$ state with $p = 0$. The Raman pulse has appropriate intensity and duration to drive a π-pulse with the desired momentum width.
5. Use the resonant pushing light to remove atoms in $F = 4$.

The atoms were then further manipulated as desired, as described below, and then subjected to the 1D, time-dependent standing-wave interaction as described in the following chapter. In the typical experiment in Chapter 6, the Raman beams drove an 800 μs, square π-pulse. This pulse should result in a selected profile as in Eq. (5.26), with a half width at half maximum (HWHM) of $0.03 \cdot 2\hbar k_{\mathrm{L}}$. Because of the resolution limit set by the initial size of the MOT cloud, we could not directly verify this profile with our ballistic-expansion measurement, but the expansion rates and the scaling of the fluorescence of the selected atoms with the pulse duration were consistent with the theoretical expectation. This extreme velocity selection was crucial to the success of the experiments in Chapter 6, but had the unfortunate side effect that about 99.5% of the atoms (after 3D lattice cooling) were discarded, causing relatively weak signals in the measurements.

5.3.7 Raman Cooling

With the setup described above, it should in principle be possible to implement Raman cooling, where a large fraction of the atoms could be cooled into a narrow velocity slice as narrow as (or perhaps narrower than) the Raman-tagged slice. Raman cooling works in a repetitive cycle, where atoms at all velocities, except for those in a "target" region near zero momentum, are transferred from the $F = 4$ level to the $F = 3$ level by velocity-selective, stimulated Raman transitions. Then the repumping light is pulsed on to return the atoms to $F = 4$, but with slightly different momentum due to the fluorescence cycle. We implemented the dual-AOM scheme described above so that the direction of the momentum transfer due to the Raman transition could be reversed, and thus during the Raman tagging cycle the atoms on either side of the target region could be moved towards it. However, there are several technical challenges involved in implementing Raman cooling, the most severe of which is the presence of residual magnetic fields. For efficient cooling, the fields must be nulled to 1 mG or better [302], necessitating the use of a glass chamber (with no ferromagnetic materials) and μ-metal shielding, because the atoms are distributed among the magnetic sublevels. Furthermore, Raman cooling leaves a broad background in the momentum distribution [296, 302], which must be removed by a final tagging sequence as described above; however, we have noted that transitions associated with different sublevels proceed at different rates, making a clean π-pulse difficult. An optical pumping cycle after cooling would ruin the very cold temperatures, but selecting only atoms in a given sublevel would result in another large hit in atom number.

To circumvent these technical problems, we attempted a modified Raman-cooling procedure, which was performed in the presence of a bias field as above. In addition to the repumping, we also applied the optical pumping light during the recycling stage of each iteration. The target state in this case is the $F = 4, m_F = 0$ state simultaneously with $p = 0$, which is a much more stringent requirement. After a brief attempt, we were not able to cool using this technique, and we instead elected to use averaging as a more straightforward way to address the difficulty of small signals.

5.4 Interaction-Potential Phase Control

An important part of the state-preparation procedure for the experiments in Chapter 6 was the ability to change the phase of the one-dimensional optical lattice. One method for changing the phase is suggested by the analysis in Section 2.6, where we concluded that a frequency difference between the two traveling-wave components results in a moving standing wave. A phase shift can thus be obtained by introducing a pulsed frequency difference. From an experimental point of view, this method is not optimal because it requires splitting the beam, reducing the available intensity (relative to a retroreflecting setup), and it requires careful mode matching of the two traveling waves.

Because the optical lattice was formed by retroreflecting a laser beam in the setup here, the phase of the standing wave was set by the position of the retroreflector. Thus we could move the standing wave simply by moving the retroreflector. We could effectively move the retroreflector by inserting an electro-optic phase modulator

(EOM) in the beam path just before the retroreflector. Doing so gave direct electronic control of the optical path length between the atoms and the retroreflector. We used a Conoptics, Inc. model 360-40 EOM, which used a 40 mm long lithium tantalate (LTA) crystal, with a model 302 driver. The EOM had a 2.7 mm clear aperture, and we focused the optical lattice beam onto the retroreflector using a 300 mm focal length lens to ensure that the EOM did not clip the beam. The EOM was also aligned so that the beam propagated slightly off the EOM axis to avoid interference fringes (the reflections of the EOM were also minimized by antireflection coatings on the windows and index-matching fluid inside the housing). To avoid polarization-modulation effects, it was important to carefully set the EOM angle relative to the lattice-beam polarization. The lattice-beam polarization was set to be horizontal by a cube polarizer mounted just before the entry of the lattice into the chamber. On the other (retroreflecting) side of the chamber, we inserted another cube polarizer before the EOM and adjusted the EOM angle to minimize the signal rejected from the polarizer as the EOM phase was scanned.

In the previous setup of Chapter 3, the stability of the retroreflector was ensured by rigidly mounting it to the vacuum chamber. This new setup was too large to be mounted directly on the chamber, so we constructed a platform to mount the optics, as shown in Fig. 5.12. This platform consisted of a 1/2" thick aluminum plate (jig plate), which rested on a similar piece of 1/2" thick aluminum. A layer of 1/2" thick Sorbothane damping rubber was sandwiched between the two aluminum plates. The lower plate was mounted rigidly to the table by six stainless steel posts (1.25" diameter) in an irregular pattern. The optical-lattice beam propagated only 2" above the platform surface to minimize vibrations of the optical mounts. An interferometer constructed on the platform itself measured negligible vibrations, but was incapable of detecting center-of-mass vibrations of the platform, which also contributed to phase jitter of the optical lattice.

This setup provided good phase control over a large range in phase (the EOM controller had an 800 V range, where 250 V corresponds to a 2π phase shift of the lattice phase) on a fast ($\sim 1\ \mu$s) time scale. One caveat, however, is that fast changes in the phase could excite piezoelectric resonances of the EOM, where the crystal itself begins mechanically ringing as a result of the sudden excitation. This effect is illustrated in Fig. 5.13, where the EOM phase, as measured by a Michelson interferometer, shows ringing in response to a sudden step in the control voltage. The resonance occurred at 150 kHz, with a quality factor Q of about 12. Of the available options from Conoptics, this LTA modulator was the most suitable; the KD*P modulators have a smaller available phase range while exhibiting substantially worse ringing than the LTA modulator, even when the crystal is mechanically clamped, and the ADP modulators, which have no piezoelectric resonances, have poor transmission at 852 nm.

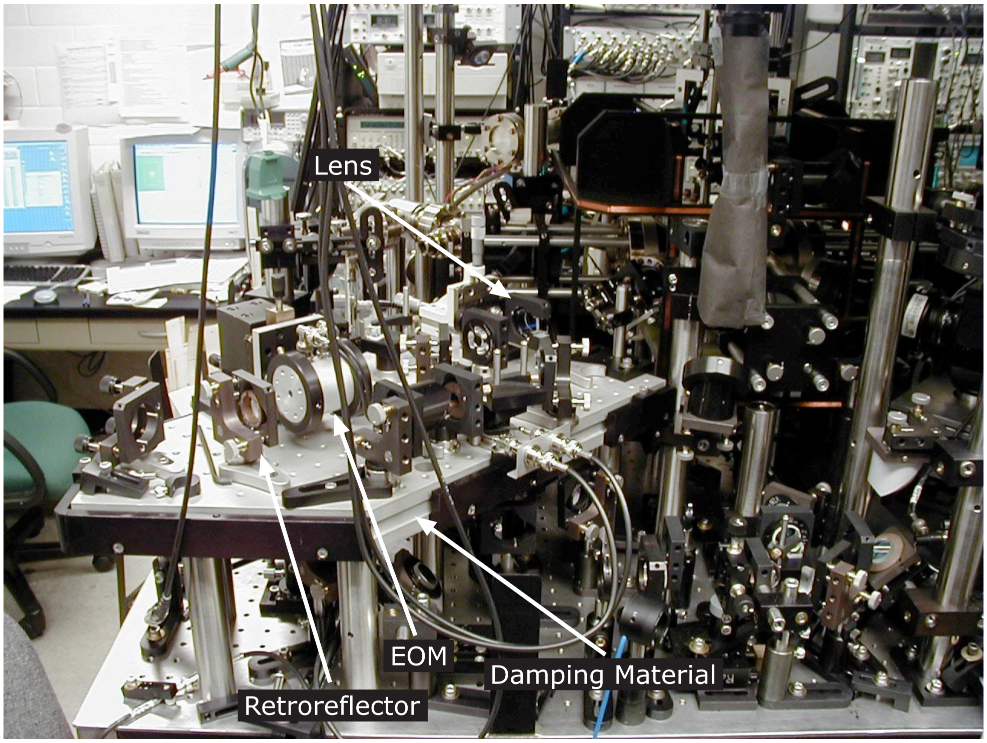

Figure 5.12: Photograph of the phase-control setup for the one-dimensional optical lattice. The components in this setup are shown mounted on the damped, raised, mounting table, and several components for the stimulated Raman optical setup are also visible both on the main and raised tables.

5.5 State-Preparation Sequence

Now we will discuss how the various tools presented in this chapter were used to prepare localized initial states in phase space. An overall schematic view of the procedure is illustrated in Fig. 5.14, which shows the condition of the state in phase space at various points in the process. This state-preparation procedure began with the Raman velocity selection process as in Section 5.3.6, which prepared a quantum state that was subrecoil in momentum but delocalized in space. The 1D optical lattice was then turned on adiabatically, with the same temporal profile and time constant (30 μs) as the 3D lattice, although here the leading edge of the profile was clipped 300 μs before the maximum intensity was reached. The lattice caused the atoms to become localized at the potential minima, at the expense of some heating in momentum. Because the initial momentum distribution was narrow compared to the photon recoil momentum $\hbar k_{\mathrm{L}}$, the resulting phase-space distribution had the discrete structure shown in Fig. 5.14. This

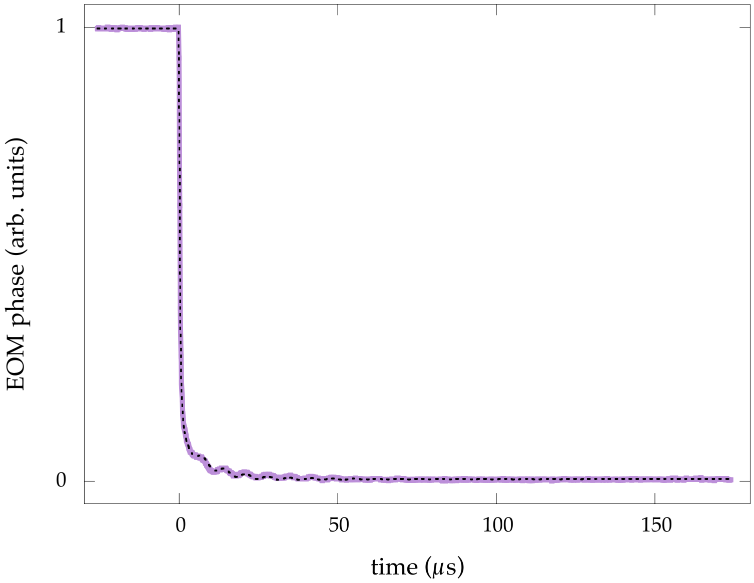

Figure 5.13: Response of the electro-optic modulator to a sudden phase step, as measured interferometrically. The fitted model (dashed line) is a sum of two pure exponentials of different time constants and a damped cosine: $f(t) = 0.87 \cdot \exp(-t/0.37\ \mu\mathrm{s}) + 0.11 \cdot \exp(-t/7.5\ \mu\mathrm{s}) + 0.011 \cdot \cos(2\pi t/6.8\ \mu\mathrm{s} - 0.79)\exp(-t/25\ \mu\mathrm{s}) + 0.004$ (for $t > 0$).

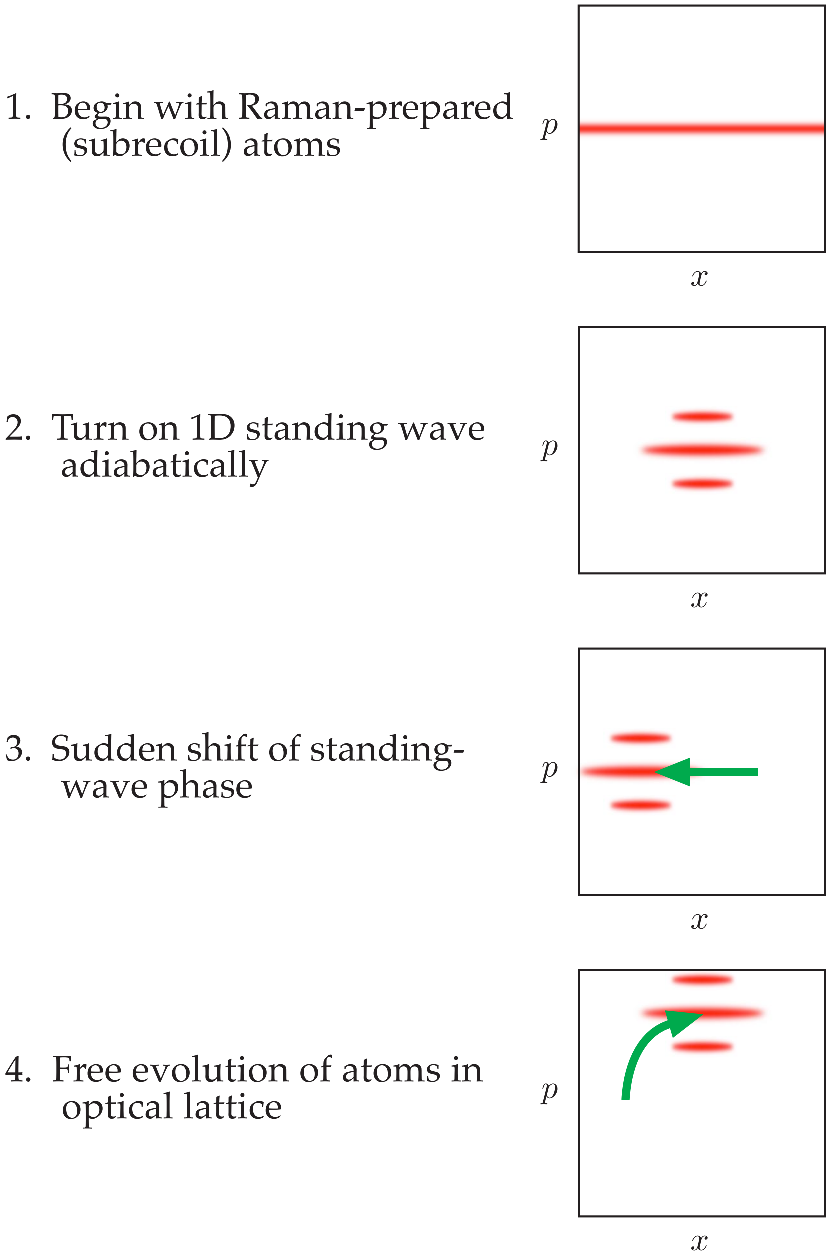
1. Begin with Raman-prepared (subrecoil) atoms
p
x
2. Turn on 1D standing wave adiabatically
p
x
3. Sudden shift of standing-wave phase
p
x
4. Free evolution of atoms in optical lattice
p
x

Figure 5.14: Schematic picture of the state-preparation sequence, beginning with the atoms prepared by subrecoil Raman velocity selection. The influence on the atoms in phase space is illustrated. The “striped” character of the distributions is a result of the discrete nature of the momentum transfer to the atoms.

structure can be understood intuitively in the discrete momentum transfer (in steps of $2\hbar k_{\mathrm{L}}$) from the lattice as it is turned on, and also indicates coherence of the wave packet over multiple potential wells. Recalling from Chapter 2 that for adiabatic processes the band index and quasimomentum are preserved, the atoms were loaded completely into the lowest energy band of the optical lattice. For deep wells (as used in the experiment), the lowest band is approximately the harmonic oscillator ground state (repeated in each well), and thus the overall distribution envelope was approximately a minimum-uncertainty Gaussian wave packet, modulo the standing-wave period. The structure of subrecoil "slices" in the distribution out of an overall Gaussian profile was important in the experiments in Chapter 6, and we will return to this issue in the discussion there.

After the atoms became localized in the lattice potential wells, the phase of the standing wave was shifted by around $1/4$ of the lattice period, which had the effect of displacing the atoms onto the gradients of the potential. They were then allowed to evolve in the stationary optical lattice, where they returned to the potential minima, acquiring momentum in the meantime. In a harmonic potential, this procedure amounts to a boost of the wave packet in momentum, where the distance in momentum is set by the amount of displacement. The anharmonicities in the optical lattice led to a slight distortion of the wave packet, although it was still mostly Gaussian. More importantly, the subrecoil structure of the wave packet was preserved because all of this motional control was induced by the lattice. We refer to this state preparation procedure by the acronym "SPASM," for "State Preparation through Atomic Sliding Motion."

To make this procedure more concrete, the experimental parameters for the first group of data in Chapter 6 (i.e., for $\alpha = 10.5$, $\bar{k} = 2.08$) were as follows: the Raman π-pulse selection time was 800 μs, giving a velocity slice with a HWHM of $0.03 \cdot 2\hbar k_{\mathrm{L}}$; the lattice was turned on to a depth of $\alpha_{\mathrm{p}} = 11.8$ (in the units of Section 2.7); the lattice phase was shifted by 0.25 of the lattice period, and the atoms evolved in the lattice for 6 μs, which was the time after which the atomic momentum was maximized; and the resulting distribution (in momentum) was peaked at $4.1 \cdot 2\hbar k_{\mathrm{L}}$, with a width

$\sigma_p = 1.1 \cdot 2\hbar k_\mathrm{L}$. For the second group of data ($\bar{k} = 2.08$, for various other values of α), the same Raman velocity selection parameters were used; the optical lattice was turned on to a maximum depth of $\alpha_\mathrm{p} = 16.4$; the lattice phase was shifted by 0.21 of the lattice period, and the atoms evolved for 4.5 μs in the lattice; and the prepared distribution was peaked at $4.2 \cdot 2\hbar k_\mathrm{L}$, with a width $\sigma_p = 1.7 \cdot 2\hbar k_\mathrm{L}$. For the third data group ($\bar{k} = 1.04$), the same Raman velocity selection was again used; the optical lattice was turned on to a maximum depth of $\alpha_\mathrm{p} = 30.9$; the lattice phase shift was 0.30 of the standing-wave period, after which the atoms evolved for 3.5 μs; and the momentum distribution was peaked at $8.2 \cdot 2\hbar k_\mathrm{L}$, with a width $\sigma_p = 2.1 \cdot 2\hbar k_\mathrm{L}$.

The procedure for carrying out the experiments in the following chapter is then very similar to the procedure in Chapter 3, albeit with a much more complicated state-preparation sequence inserted after the initial cooling and trapping of the cesium atoms. After the state-preparation sequence, the atoms were exposed to the temporally modulated optical lattice, where the dynamics of interest occurred. The atoms were then allowed to drift freely in the dark for 20 ms, and the freezing molasses and CCD camera enabled a measurement of the atomic momentum distribution by imaging the atomic fluorescence for 20 ms.

5.6 Calibration of the Optical Potential

After the introduction of a lens and EOM in the beam path of the 1D optical lattice, we found that the calibration method of Section 3.4.3 no longer produced reliable values for the optical potential depth. This was most likely due to the breakdown of the assumption that the beam waists measured at the knife edge and CCD camera were the same as the waist at the MOT. Thus, the CCD camera was only used to collimate the beam as much as possible: first, the beam was retroreflected with a temporary mirror before the (EOM) lens, and the beam was adjusted so that two beam spots on the CCD (going to and from the vacuum chamber) were approximately the same; then, the temporary mirror was removed, and the longitudinal position of the lens was adjusted to make the spots again equal, thus ensuring that the lens focused the beam onto the retroreflecting mirror.

The state-preparation method outlined above suggests another, *in situ* method to calibrate the potential amplitude. If the Raman velocity selection procedure is used to select a subrecoil momentum sample of the atoms, and the 1D lattice is adiabatically turned on to a large potential depth, an approximately minimum-uncertainty wave packet (modulo the period of the lattice) results, as mentioned above. If the EOM then provides a sudden but small phase shift, the atoms begin to oscillate in the lattice. The oscillation frequency serves as a direct measurement of the potential depth. In the simplest approximation, valid for large potential depths, the oscillations can be regarded as harmonic oscillations near the parabolic potential minima. Recalling from Chapter 2 that the unscaled Hamiltonian for atomic motion in the optical lattice has the form

$$H = \frac{p^2}{2m} - V_0 \cos(2k_{\mathrm{L}}x) \ , \tag{5.30}$$

we can expand the potential to $O(x^2)$ about $x = 0$ to obtain the equivalent harmonic oscillator, which has a period

$$T_{\mathrm{HO}} = \frac{\pi}{k_{\mathrm{L}}}\sqrt{\frac{m}{V_0}} \ . \tag{5.31}$$

However, for a given potential depth V_0, we would actually underestimate the true oscillation period as a result of two effects, anharmonic frequency shifts and quantum effective potential frequency shifts, which we now discuss.

5.6.1 Anharmonicity

Using the same unit scaling as in Chapter 2 (i.e., units where $\hbar = 1$), the pendulum Hamiltonian is

$$H = \frac{p^2}{2} - \alpha_{\mathrm{p}} \cos x \ . \tag{5.32}$$

For a particular value E of the Hamiltonian, we can write the pendulum period as [5]

$$T(k) = \frac{4}{\sqrt{\alpha_{\mathrm{p}}}} F\left(\frac{\pi}{2}, k\right) \ , \tag{5.33}$$

where $F(\theta, k)$ is the elliptic integral of the first kind, and

$$k = \sqrt{\frac{1}{2}(1 + E/\alpha_{\mathrm{p}})} \ . \tag{5.34}$$

Since $F(\pi/2, 0) = \pi/2$, the small-displacement (harmonic) frequency for this equation is

$$T_{\mathrm{HO}} = T(0) = \frac{2\pi}{\sqrt{\alpha_{\mathrm{p}}}} \ , \tag{5.35}$$

so that the fractional period shift due to the lattice anharmonicity is

$$\begin{aligned} \frac{T(k)}{T_{\mathrm{HO}}} &= \frac{2}{\pi} F\left(\frac{\pi}{2}, k\right) \\ &= 1 + \frac{k^2}{4} + O(k^4) \ . \end{aligned} \tag{5.36}$$

Thus, larger amplitudes of oscillation result in longer oscillation periods, which we expect from the fact that the lattice potential drops below the parabolic approximation away from the potential minima.

5.6.2 Quantum Effective Potentials

In addition to the classical anharmonic effects, the oscillation period in the lattice is also increased by the fact that we are considering a quantum wave packet. This effect is illustrated by the numerical simulations in Fig. 5.15. Because of the adiabatic loading of the atoms into the ground state of the lattice, we can invoke the harmonic approximation to argue that the state within a single well is approximately minimum-uncertainty Gaussian with momentum uncertainty $\sigma_p = (\alpha_{\mathrm{p}}/4)^{1/4}$ and spatial uncertainty $\sigma_x = (4\alpha_{\mathrm{p}})^{-1/4}$. From the Ehrenfest equations of motion for the mean values of x and p [303],

$$\begin{aligned} \partial_t \langle x \rangle &= \frac{\langle p \rangle}{m} \\ \partial_t \langle p \rangle &= -\langle \partial_x V(x) \rangle \ , \end{aligned} \tag{5.37}$$

we might expect that the quantum mean values oscillate as in the classical case, but where the potential is "smeared" out by the spatial extent of the wave packet. Performing a convolution of the pendulum potential with the spatial distribution of the Gaussian wave packet, we find that this *effective potential* is still sinusoidal, but with a reduced amplitude:

$$\alpha_{\text{eff}} = \alpha_{\text{p}} \exp\left(-\frac{1}{4\sqrt{\alpha_{\text{p}}}}\right) \ . \tag{5.38}$$

Because we have scaled the units so that $\hbar = 1$, the scaled well depth α_{p} represents the "degree of quantumness" of the pendulum, with larger values representing more classical behavior (and thus a smaller wave-packet area in phase space), as reflected in this quantum scaling factor. Hence, we should expect that the quantum wave packet moves with a longer period due to the reduced effective potential amplitude, and also that the wave packet motion will be further retarded by "classical" anharmonic effects in the effective potential.

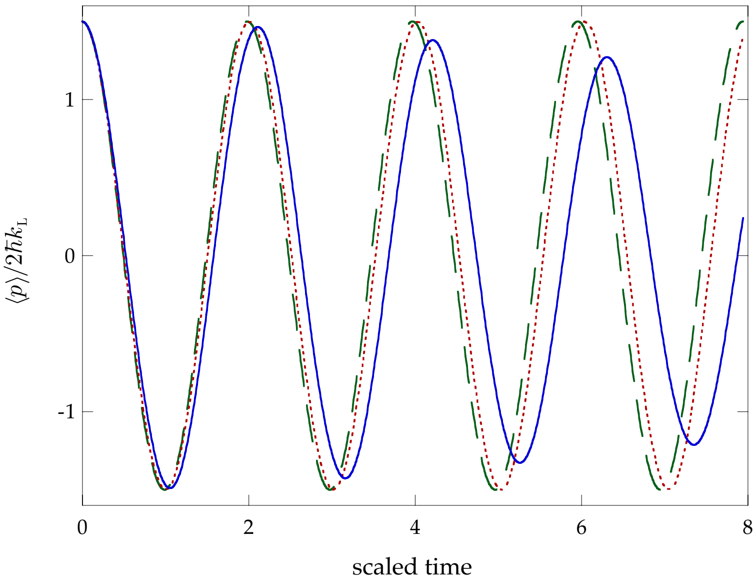

Figure 5.15: Comparison of simulated pendulum oscillations of the classical case in the harmonic approximation (dashed line) to the anharmonic classical pendulum oscillations (dotted line) and the oscillations of an initially minimum-uncertainty quantum wave packet (solid line). The slowing effects of the anharmonicity and quantum wave packet extent are evident here. The system parameters are $\alpha_{\text{p}} = 10$ (and $\hbar = 1$), with the wave packet and trajectories initially centered at $(x, p) = (0, 1.5)$.

5.6.2.1 Wigner-Function Derivation

Hug and Milburn [304] have recently produced a more formal derivation of a quantum scaling factor based on the Wigner-function dynamics, in the context of the amplitude-modulated pendulum. Here we adapt this calculation to the ordinary pendulum, since the derivation does not depend on the temporal modulation of the potential.

We begin with the general equation of motion for the Wigner function (which we introduced in Chapter 1 as the Moyal bracket),

$$\begin{aligned}\partial_t W(x,p) = -p\partial_x W(x,p) + \frac{i}{\bar{k}}\Bigg[&\sum_{s=0}^{\infty}\frac{1}{s!}\left(\frac{\bar{k}}{2i}\right)^s \partial_x^s V(x,t)\partial_p^s W(x,p)\\ &-\sum_{s=0}^{\infty}\frac{1}{s!}\left(-\frac{\bar{k}}{2i}\right)^s \partial_x^s V(x,t)\partial_p^s W(x,p)\Bigg]\ ,\end{aligned}\tag{5.39}$$

where we will keep the scaled Planck constant $\bar{k}$ explicit for the time being. We can then insert the pendulum potential,

$$V(x) = -\alpha_{\mathrm{p}}\cos(x)\ ,\tag{5.40}$$

with the result

$$\partial_t W = -p\partial_x W + \frac{\alpha_{\mathrm{p}}}{\bar{k}}\sin(x)\sum_{s=0}^{\infty}\frac{1}{s!}\left(\frac{\bar{k}}{2}\right)^s[1-(-1)^s]\partial_p^s W\ .\tag{5.41}$$

If make use of the Taylor expansion

$$W(x, p+\bar{k}/2) = \sum_{s=0}^{\infty}\frac{1}{s!}[\partial_p^s W(x,p)]\left(\frac{\bar{k}}{2}\right)^s\ ,\tag{5.42}$$

then Eq. (5.41) becomes

$$\partial_t W(x,p) = -p\partial_x W(x,p) + \frac{\alpha_{\mathrm{p}}}{\bar{k}}\sin(x)\left[W(x,p+\bar{k}/2) - W(x,p-\bar{k}/2)\right]\ .\tag{5.43}$$

The goal here to put this equation of motion into "classical form" (of a Liouville equation for a classical phase-space distribution) with an effective potential V_{eff}:

$$\partial_t W = -p\partial_x W + \partial_x V_{\mathrm{eff}}\partial_p W\ .\tag{5.44}$$

Hence, we can make the identification

$$\partial_x V_{\text{eff}} = \frac{\alpha_{\text{p}}}{\bar{k}} \sin(x) \frac{W\left(x, p+\bar{k}/2\right) - W\left(x, p-\bar{k}/2\right)}{\partial_p W(q,p)} \quad . \tag{5.45}$$

We now take the Wigner function to be Gaussian,

$$W(x,p,t) = \frac{1}{\pi \bar{k}} \exp\left[-\frac{\xi}{\bar{k}}(x - \langle x \rangle)^2 - \frac{1}{\bar{k}\xi}(p - \langle p \rangle)^2 \right] \quad , \tag{5.46}$$

where $\xi(t)$ is a time-dependent squeezing parameter. So, we can evaluate the terms in the effective potential,

$$\partial_p W(x,p) = -\frac{2(p - \langle p \rangle)}{\bar{k}\xi} W(x,p) \quad , \tag{5.47}$$

and

$$W(x, p \pm \bar{k}/2) = \exp\left(-\frac{\bar{k}}{4\xi} \right) \exp\left[\mp \frac{1}{\xi}(p - \langle p \rangle) \right] W(x,p) \quad , \tag{5.48}$$

and thus the effective potential becomes

$$V_{\text{eff}} = -\alpha_{\text{p}} \cos(x) \exp\left(-\frac{\bar{k}}{4\xi} \right) \frac{\sinh\left[\dfrac{1}{\xi}(p - \langle p \rangle) \right]}{\dfrac{1}{\xi}(p - \langle p \rangle)} \quad . \tag{5.49}$$

If we assume that the wave packet remains localized (which is implicit in assuming the Gaussian form), then the sinh ratio is approximately unity. Thus, the effective potential is the original potential compressed by a factor of $\exp[-\bar{k}/(4\xi)]$.

Turning to the quantum pendulum, we can select a preferred value of ξ based on the adiabatic loading into the lattice. Rewriting the Wigner function in terms of σ_x and σ_p and using $\sigma_x \sigma_p = \bar{k}/2$,

$$\begin{aligned} W(x,p) &= \frac{1}{\sqrt{2\pi\sigma_x}} \exp\left[-\frac{(x - \langle x \rangle)^2}{2\sigma_x^2} \right] \frac{1}{\sqrt{2\pi\sigma_p}} \exp\left[-\frac{(p - \langle p \rangle)^2}{2\sigma_p^2} \right] \\ &= \frac{1}{\pi \bar{k}} \exp\left[-\frac{-2\sigma_p^2}{\bar{k}^2}(x - \langle x \rangle)^2 - \frac{1}{2\sigma_p^2}(p - \langle p \rangle)^2 \right] \quad , \end{aligned} \tag{5.50}$$

we find that $\xi = 2\sigma_p^2/\bar{k} = \bar{k}/(2\sigma_x^2)$. Then, for the quantum pendulum in the harmonic oscillator approximation, we have $\bar{k} = 1$ and $\sigma_p^2 = \sqrt{\alpha_\mathrm{p}}/2$, so $\xi = \sqrt{\alpha_\mathrm{p}}$. Thus, the effective potential in this case is given by

$$V_\mathrm{eff}(x) = -\alpha_\mathrm{p}\cos(x)\exp\left(-\frac{1}{4\sqrt{\alpha_\mathrm{p}}}\right) \,, \tag{5.51}$$

which is the same result that we found in the simple Ehrenfest (Gaussian convolution) model.

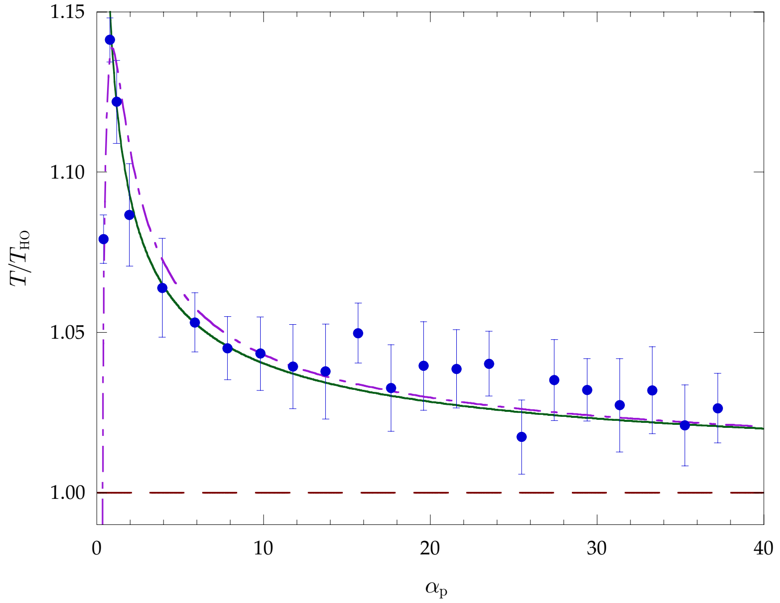

Figure 5.16: Experimentally measured oscillation periods in the optical lattice, normalized to the classical period in the harmonic-oscillator approximation, shown as a dashed line. For comparison the harmonic period in the quantum effective potential is also shown (solid), which agrees reasonably well with the data. Also shown is the splitting of the two lowest eigenstates (with zero quasimomentum) calculated for the sinusoidal potential (dot-dashed line). These latter two curves diverge for small α_p, where the Gaussian approximation for the ground state of the lattice breaks down. The experimental data points are averages over three measurements, and the error bars represent statistical variations among the repeated measurements. The α_p scale was calibrated by comparing the periods in the right half of the plot directly to quantum simulations, as described in the text.

5.6.3 Calibration by Simulation

From the above analysis, we can see that the situation is not entirely simple when deciding what oscillation frequency to expect, given a particular potential depth. To directly account for these effects, we compared the measured wave-packet oscillations to quantum-pendulum simulations. We first extracted the oscillation period of the experimental data, along with the maximum average momentum achieved by the atomic distribution, by fitting an exponentially damped cosine function to the measured $\langle p \rangle$ evolution data. Then a quantum simulation was set up for a minimum-uncertainty wave packet with the same maximum average momentum, and the α_{p} parameter in the simulation was adjusted until the simulated period matched the experimental period. The simulation was facilitated by the fact that the experiment used narrow Raman velocity selection, so that it was a good approximation to use only the discrete plane-wave basis $p = n2\hbar k_{\mathrm{L}}$ (for integer n). Although anharmonic effects were taken into account by using the same maximum momentum in the simulations, these calibrations were typically done with small EOM phase displacements (about 0.05 of the lattice period) to minimize these effects and maintain the Gaussian character of the wave packet as long as possible. When performed with several different lattice intensities, the resulting calibrated values of α_{p} typically agreed at the 3% level or better, although we quote a 5% uncertainty for all the well-depth values in Chapter 6 to account for other systematic effects (such as piezoelectric ringing of the EOM) in the calibration procedure. Fig. 5.16 shows a series of experimentally measured oscillation periods as a function of α_{p}, calibrated as described here.

Chapter 6

Chaos-Assisted Tunneling

6.1 Overview

We will now discuss experimental results on quantum dynamics in the case where the corresponding classical description is characterized by a mixed phase space, in which chaotic and stable regions coexist. This regime is distinctly different from the strongly chaotic regime of Chapter 4, and the study of this new regime is enabled by the state-preparation methods outlined in the previous chapter. The experiments study the atomic motion in a standing wave of light that is modulated sinusoidally in time. In particular, we will focus on tunneling between two islands of stability in the classical phase space of this system. Because the classical transport between the islands is forbidden by the system dynamics and not by a potential barrier, this tunneling is known as *dynamical tunneling*. We will investigate the salient details of the tunneling, including how the tunneling depends on the phase-space location of the initial condition and the role of symmetry in supporting the tunneling. More significantly, though, we will discuss how the presence of chaos in phase space can enhance the tunneling rate, and we will examine evidence for such *chaos-assisted tunneling* in the experimental results. This evidence includes a comparison to a dynamical tunneling process (Bragg scattering) that occurs in the integrable counterpart to the modulated system; a fast, secondary oscillation in the tunneling dynamics; and the dependence of the tunneling rate on the lattice intensity. Finally, we will see how noise destroys the quantum tunneling effect and restores classical-like behavior, and how the system is more sensitive to noise as the parameters move the dynamics closer to the classical limit.

A subset of the data presented here, including the observation of tunneling oscillations, the effects of location in phase-space and broken symmetry, a comparison to Bragg scattering, and the influence of a third (chaotic) state has been previously published in [215].

6.2 Barrier Tunneling

Before tackling the issue of tunneling in phase space, we will begin with the familiar problem of tunneling in a symmetric double-well potential, of which one example is shown in Fig. 6.1. In the limit where the barrier separating the wells is arbitrarily high, the system can be regarded as two isolated, identical potential wells, and thus the level structure of the combined system is a set of degenerate doublets. For a potential barrier of finite height, the doublet states are coupled because a state localized in one well "leaks" through the barrier and into the other well. In the weak-coupling regime, we can

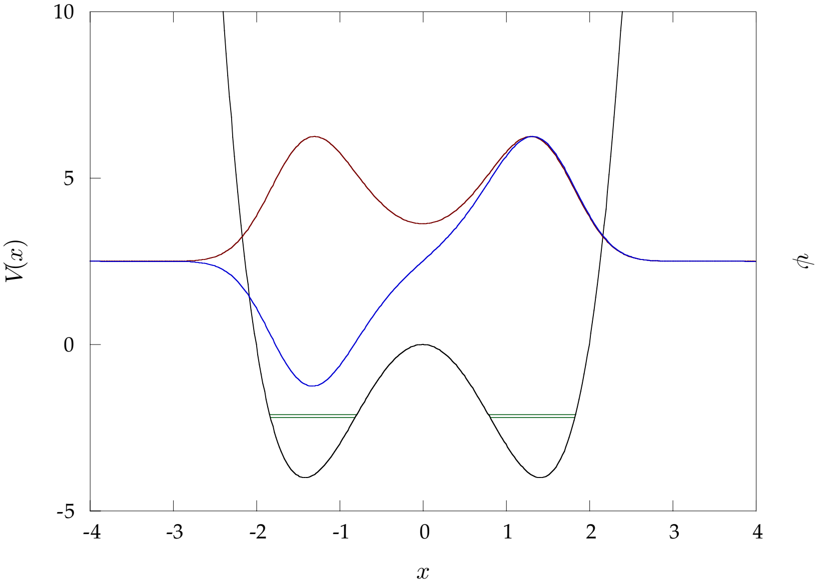

Figure 6.1: The ground-state tunneling doublet of the quartic double well potential, $H = p^2/2 + x^4 - 4x^2$ (with $\hbar = 1$). The symmetric-state energy is -2.20, and the antisymmetric-state energy is -2.10.

neglect the coupling of a particular doublet to other doublets, and thus the Hamiltonian for a doublet can be written as

$$H = \begin{pmatrix} E_0 & -\wp/2 \\ -\wp/2 & E_0 \end{pmatrix} \tag{6.1}$$

in the uncoupled basis $\{|\mathrm{L}\rangle, |\mathrm{R}\rangle\}$ (localized in the left and right well, respectively), where $\wp/2$ represents the coupling energy between the two states. The coupling matrix elements in this case are negative because the perturbation is a reduction of the potential from an arbitrarily large height. The eigenvalues of this Hamiltonian are $E_0 \pm \wp/2$, and the eigenvectors are the symmetric and antisymmetric combinations $(|\mathrm{L}\rangle \pm |\mathrm{R}\rangle)/\sqrt{2}$ of the uncoupled states. The antisymmetric state has the larger energy for positive $\wp$, which is consistent with the small-barrier limit of a single well. The lowest energy doublet for the quartic double well is shown in Fig. 6.1.

The doublet of a symmetric and an antisymmetric state can then fully describe the tunneling behavior. If we begin the evolution with a state localized in the left-hand well, it can be written approximately as the superposition $(|+\rangle + |-\rangle)/\sqrt{2}$, where $|+\rangle$ and $|-\rangle$ are the symmetric and antisymmetric doublet states, respectively. The time-dependent solution is

$$\begin{aligned} |\psi(t)\rangle &= \frac{1}{\sqrt{2}}\left(|+\rangle e^{i\wp t/2\hbar} + |-\rangle e^{-i\wp t/2\hbar}\right) \\ &= \cos\left(\frac{\wp t}{2\hbar}\right)|\mathrm{L}\rangle + i\sin\left(\frac{\wp t}{2\hbar}\right)|\mathrm{R}\rangle \ , \end{aligned} \tag{6.2}$$

up to an overall phase. Thus, as the two states dephase, the wave packet oscillates between the two wells with an angular frequency of $\wp/\hbar$. In the WKB (semiclassical) approximation, the tunnel splitting $\wp$ can be written [31, 305, 306]

$$\wp = \frac{\hbar\omega_0}{\pi}\exp\left(-\frac{1}{\hbar}\int_{x_1}^{x_2}\sqrt{2m(V(x)-E_0)}\,dx\right) \ , \tag{6.3}$$

where x_1 and x_2 are the two inner classical turning points at energy E_0, and ω_0 is the classical angular oscillation frequency in one of the uncoupled wells. This $A\exp(-S/\hbar)$

scaling of the tunneling rate with $\hbar$, where A is a smooth function of $\hbar$ and S is the imaginary part of the classical action along a (complex) path connecting the two tunneling regions, is characteristic of tunneling where only two states are involved [306, 307].

It is important to note that the tunneling here is facilitated by the reflection symmetry of the system. In a double well with small asymmetry (i.e., the energy difference between the wells is small compared to the uncoupled energy splittings), we can simply change the model Hamiltonian (6.1) to reflect an energy displacement of one well:

$$H = \begin{pmatrix} E_0 + \Delta & -\wp/2 \\ -\wp/2 & E_0 \end{pmatrix} . \tag{6.4}$$

In this model, Δ controls the asymmetry of the system. Comparing this Hamiltonian to the Hamiltonian (2.25) for a driven two-level atom in the rotating-wave approximation, we see that these two systems are formally equivalent. Thus the eigenvalues are

$$E_\pm = E_0 + \frac{1}{2}\left(\Delta \mp \sqrt{\Delta^2 + \wp^2}\right) , \tag{6.5}$$

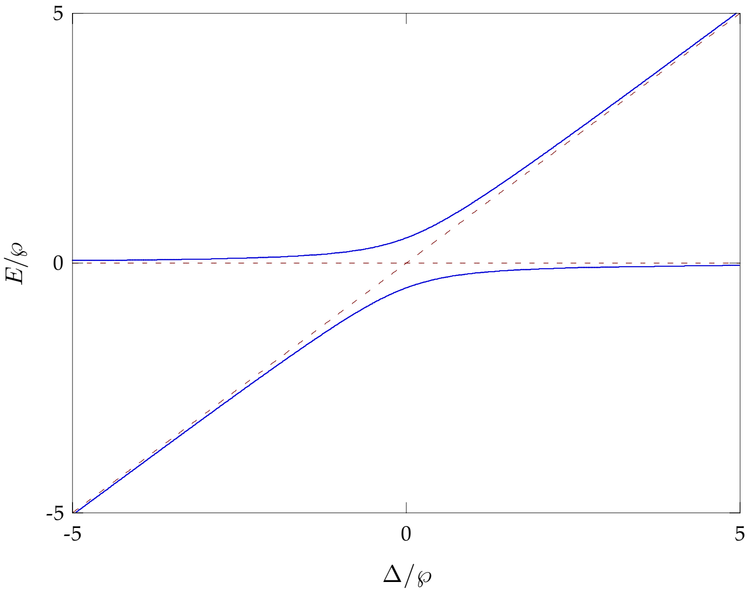

Figure 6.2: Illustration of an avoided crossing of a tunneling doublet as a function of the asymmetry parameter Δ, as described by Eq. 6.5. The dashed lines show the energies in the absence of any coupling.

and the corresponding eigenvectors are

$$\begin{aligned} |+\rangle &= \sin\theta|\mathrm{L}\rangle + \cos\theta|\mathrm{R}\rangle \\ |-\rangle &= \cos\theta|\mathrm{L}\rangle - \sin\theta|\mathrm{R}\rangle \ , \end{aligned} \tag{6.6}$$

where

$$\begin{aligned} \sin\theta &= \sqrt{\frac{1}{2}\left(1-\frac{\Delta}{\sqrt{\Delta^2+\wp^2}}\right)} \\ \cos\theta &= \sqrt{\frac{1}{2}\left(1+\frac{\Delta}{\sqrt{\Delta^2+\wp^2}}\right)} \ , \end{aligned} \tag{6.7}$$

or more compactly,

$$\tan(2\theta) = -\frac{\wp}{\Delta} \qquad \left(0 \le \theta < \frac{\pi}{2}\right) \ . \tag{6.8}$$

As in the two-level atom, the $|+\rangle$ and $|-\rangle$ states are the “dressed” states of the system, and the tunneling oscillations can be regarded as Rabi oscillations between the two wells. The asymmetry in the double well then corresponds to driving a two-level atom off resonance, and the coupling induces an avoided crossing of the two levels as a function of Δ, as illustrated in Fig. 6.2. In the asymmetric case, the eigenstates lose their symmetric and antisymmetric characters, reducing to the uncoupled states in the limit of large Δ. The tunneling proceeds at the generalized Rabi frequency $\sqrt{\wp^2+\Delta^2}$, which is faster than in the symmetric case, but the tunneling is suppressed in the sense that only a fraction $\wp^2/(\wp^2+\Delta^2)$ of the population in the initial well participates in the coherent tunneling oscillation. Hence, the symmetry is an important ingredient for producing the tunneling. For larger asymmetries, a state in one well may couple to a different state in the other well, causing this picture to break down; such “accidental” degeneracies can also lead to tunneling, even in the absence of symmetry.

6.3 Dynamical Tunneling

In the case of the double-well potential, the potential barrier is an obvious impediment to the classical transport between the two wells. However, it is useful to regard the classical transport more abstractly, from the point of view of the phase space of the double well, as shown in Fig. 6.3. Here the two wells are represented by regions surrounding stable (elliptic) fixed points. Classical trajectories within a single well are confined to nearly elliptical trajectories surrounding only one of the fixed points, while trajectories with enough energy to cross the potential barrier are represented by larger contours that surround both of the elliptic points. We can thus view these invariant surfaces along which the trajectories lie (which correspond to KAM surfaces in near-integrable systems) as barriers for the classical transport, because classical trajectories cannot cross these surfaces. This is true in a trivial sense for the double well, because all trajectories are confined to their corresponding surfaces. However, these invariant surfaces retain their role as barriers for classical transport in all systems with two degrees of freedom (or, equivalently, periodically driven systems with one degree of freedom), even when the system is not integrable. Trajectories can wander freely throughout chaotic regions, but invariant surfaces (including KAM surfaces, which survive in the presence of weak, nonintegrable perturbations) divide the phase space and cannot be crossed by any trajectory, as a consequence of the continuity and the deterministic character of the equations

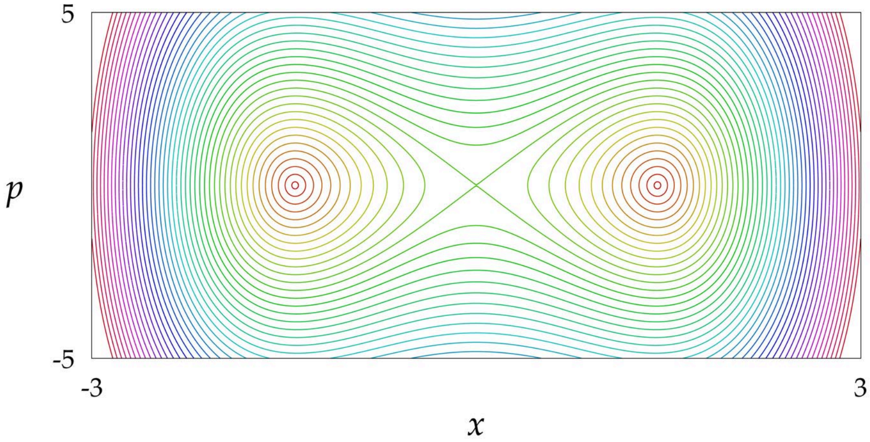

Figure 6.3: Phase space for the quartic double-well potential in Fig. 6.1. The barrier tunneling can be regarded as tunneling between classical invariant tori associated with the two wells. Classical transport between the wells is forbidden because the classical trajectories are confined along these invariant surfaces.

of motion. This is not true in systems with $N > 2$ degrees of freedom, because the N-dimensional invariant surfaces no longer partition the $(2N-1)$-dimensional surfaces of constant energy (thus allowing for Arnol'd diffusion [3]). For the systems that we will consider here, though, we can regard these invariant surfaces as being the fundamental barriers in phase space to classical transport.

Invariant surfaces are common in nearly integrable systems, and a potential barrier is not necessary for their existence. Davis and Heller first pointed out that *dynamical tunneling* could occur between two separated, symmetry-related stable regions in phase space, where the classical transport is forbidden by the dynamics and not by a potential barrier [308]. They considered tunneling between two types of oscillatory motion, which corresponds to tunneling between two islands of stability in phase space, in a two-dimensional, nonlinear potential with a reflection symmetry. Tunneling can also occur between other types of stable regions in phase space, such as bands of KAM surfaces in the phase space of the annular billiard [309].

In fact, the two essential ingredients for tunneling are the existence of a discrete symmetry and the separation of the (quasi)energy eigenstates in phase space [310]. The second ingredient is obviously fulfilled in the barrier-tunneling problem, because the low-energy states in the two wells are localized in their respective wells. In dynamical tunneling between two islands of stability, states are also localized in the islands, which support states similar to harmonic-oscillator states [311] (as one might expect from EBK quantization). As we have seen before, though, localization is natural in quantum nonlinear systems even with widespread chaos. Thus, there is also the possibility of "retunneling" [312] between quantum localized states in the Sinai billiard. Here, the transport is forbidden by quantum localization (but not classically), but oscillatory transport occurs anyway across this quantum "barrier." A similar tunneling effect can occur between symmetry-related, exponentially localized states in the kicked rotor [313].

Previous work in the area of dynamical tunneling has been restricted to spectroscopic observation of tunneling doublets. It has been pointed out [314, 315] that the experimental fluorescence-excitation spectrum of the benzophenone molecule in [316] shows doublet features that correspond to dynamical tunneling. In this molecule, there are two symmetry-related benzene rings, each of which can undergo twisting motions. The tunneling is between the two "local modes," where one ring twists while the other is at rest; the spectral doublets then correspond to the symmetric and antisymmetric combinations of the local modes. There is also experimental evidence for dynamical tunneling in wave analogies to quantum mechanics. The tunneling doublets have also been directly observed in the resonance spectroscopy of a microwave-cavity realization of the annular billiard [88]. Furthermore, the Shnirelman peak [310] in the level spacing distribution is a similar signature of dynamical tunneling, and has recently been observed in an acoustical resonator [93] and a microwave-cavity experiment [317]. Finally, there is an experimental effort, complementary to the one described here, to study dynamical tunneling of a Bose-Einstein condensate in an amplitude-modulated standing wave of light [216]. This experiment, while being similar in some respects to the experiments described below, considers tunneling between a different pair of resonances (second-order resonances [318]) than we consider later in this chapter.

6.3.1 Tunneling in Atom Optics

The basic experimental system that we used to study tunneling is very similar to that used in the kicked-rotor experiments in Chapter 4 (save for the substantially more complicated quantum-state preparation), the primary difference being the temporal dependence of the potential. To produce a more manageable, mixed classical phase space, the amplitude modulation of the potential was relatively smooth:

$$H = \frac{p^2}{2m} - 2V_0 \cos^2\left(\frac{\pi t}{T}\right) \cos(2k_{\mathrm{L}}x) \ . \tag{6.9}$$

The quantities here are as they were defined in Chapter 4. This Hamiltonian is again that of the pendulum, but with a sinusoidal variation of the potential amplitude in time from zero to $2V_0$ with period T. We can make a transformation into scaled units that is similar to the transformation used for the kicked rotor, since this system is effectively a kicked rotor with long, sinusoidal pulses:

$$\begin{aligned} x' &= 2k_{\mathrm{L}}x \\ p'/\bar{k} &= p/2\hbar k_{\mathrm{L}} \\ t' &= t/T \\ H' &= (\bar{k}T/\hbar)H \\ \alpha &:= (\bar{k}T/\hbar)V_0 \\ \bar{k} &:= 8\omega_{\mathrm{r}}T \quad . \end{aligned} \tag{6.10}$$

Here, we have chosen the time scaling so that the scaled period of the modulation is unity, α is the scaled amplitude of the potential (related to the amplitude in pendulum units by $\alpha = \bar{k}^2\alpha_{\mathrm{p}}$), and $\bar{k}$ is again the effective Planck constant in the scaled units. The Hamiltonian in scaled units, after dropping the primes, is

$$H = \frac{p^2}{2} - 2\alpha\cos^2(\pi t)\cos(x) \quad , \tag{6.11}$$

with the Schrödinger equation given by $H\psi = i\bar{k}\partial_t\psi$.

In the spirit of the analysis of Section 4.4.4, we can rewrite the potential as

$$V(x,t) = -\alpha\cos(x) - \frac{\alpha}{2}\cos(x+2\pi t) - \frac{\alpha}{2}\cos(x-2\pi t) \quad . \tag{6.12}$$

In this form, the potential appears as the sum of three pendulum-like terms with time-independent amplitude. Thus the modulated potential can be regarded as a combination of three pendulum potentials; two of these potentials are moving with momentum $\pm 2\pi$, and the third is stationary. When this system is sampled at integer times, these three terms produce primary resonances in phase space centered at $(x,p) = (0,\pm 2\pi)$ and $(0,0)$. This structure is evident in the phase spaces in Appendix C, especially for small α. For larger α, the resonances interact, producing a phase-space structure of bands of chaos surrounding the three main islands of stability. The tunneling that we consider here is between the two outer islands of stability, which are related to each other by reflection symmetry through the origin $(x,p) = (0,0)$. In configuration space, the tunneling occurs between a state of coherent motion in only one direction to a state of the oppositely directed motion. These two states each correspond to being tightly bound to one of the two moving components of the lattice. The center island does not directly participate in the tunneling.

To observe tunneling in the experiment, we used the state-preparation procedure described in Chapter 5. This procedure produced an initial state centered on one of the outer resonances with narrow slices taken out of the overall Gaussian profile (because of the narrow Raman velocity selection). A schematic representation of the initial condition for $\bar{k} = 2.08$ (corresponding to a 20 μs modulation period) and an 800 μs Raman-pulse duration is shown in Fig. 6.4 with the classical phase space for the experimental value of $\alpha = 10.5$. In this strongly driven regime, the center island has mostly dissolved into the chaotic sea, making this a clean regime for studying tunneling between the remaining two islands. The two islands are located $8 \cdot 2\hbar k_{\mathrm{L}}$ apart in momentum. The measured evolution of the momentum distribution in this case is plotted in Fig. 6.5, where the distribution was sampled every 2 modulation periods out to 80 periods. Four of these distributions are also shown in more detail in Fig. 6.6. Four coherent oscillations of the atoms between the islands are apparent before the transport is damped out. During the first oscillation, nearly half of the atoms appear in the secondary (tunneled) peak.

At this point, a few words are in order concerning the initial condition plotted in Fig. 6.4. The ellipses shown are the 50% contours of the atomic distribution in phase space. This depiction represents a classical distribution with the same x and p marginal distributions as the Wigner function for the initial state, but is not itself the correct Wigner function. The proper Wigner function for this state is more complicated, and can be constructed from the plotted distribution as follows. Whereas the distribution shown has momentum slices spaced by $\bar{k}$, the Wigner function has additional (positive) slices within the Gaussian profile between these slices, so that the spacing is $\bar{k}/2$. This combined structure is then repeated a distance π away in position, except that the slices added to the original three have negative amplitude in this new group. The population $\bar{k}/2$ away from the center of the wave packet integrates to zero when computing the

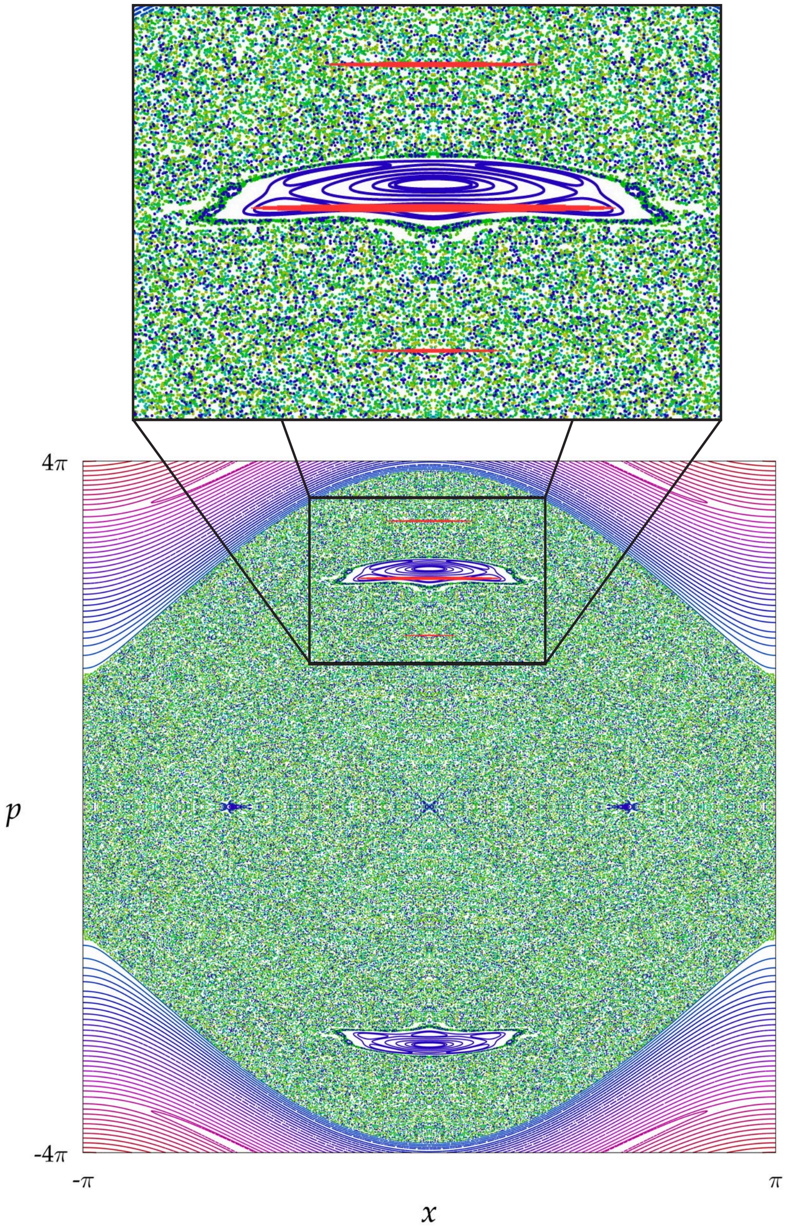

Figure 6.4: Phase space corresponding to the experimental conditions for the data in Fig. 6.5 ($\alpha = 10.5$). A schematic representation of the atomic initial state is superimposed in red on the upper island ($\bar{k} = 2.08$), showing the subrecoil structure that we expect from the state-preparation procedure. A magnified view of the upper island and initial quantum state is also shown.

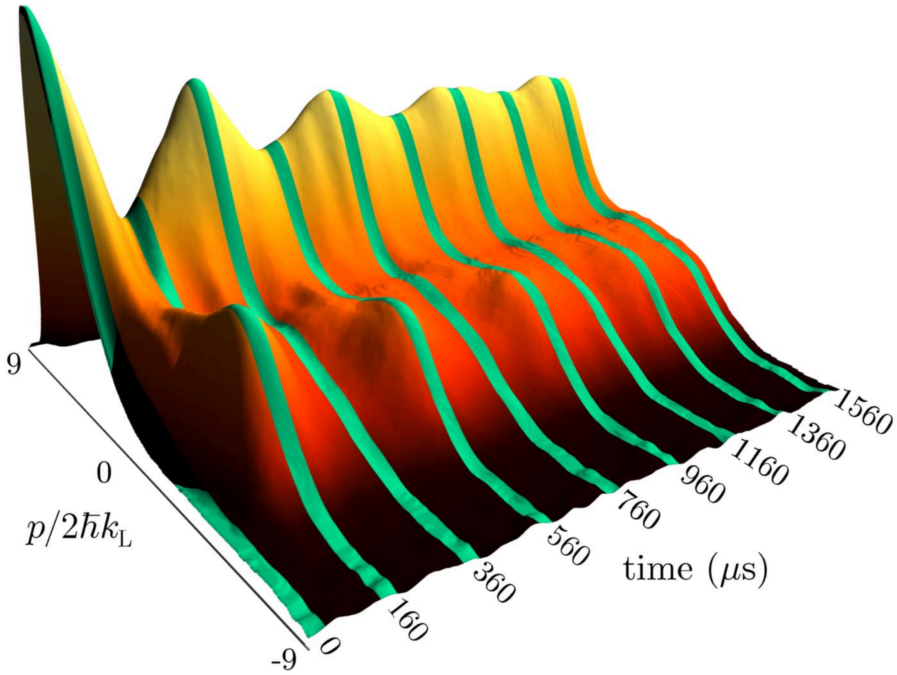

Figure 6.5: Observation of coherent tunneling oscillations in the momentum-distribution evolution between the two symmetry-related islands of stability, as shown in Fig. 6.4. The two island centers are separated in momentum by $8 \cdot 2\hbar k_{\mathrm{L}}$. In this plot, the distribution was sampled every 40 μs (every 2 modulation periods). Each of the distributions represent averages over 20 iterations of the experiment.

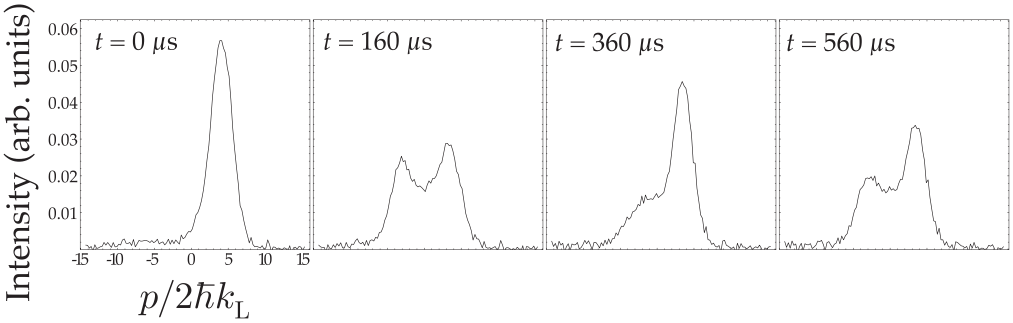

Figure 6.6: Detailed view of the first four highlighted distributions in Fig. 6.5, where it is clear that a significant fraction of the atoms tunnel to the other island. The distributions here were averaged over 100 iterations of the experiment.

p marginal distribution, and the population is only in the vicinity of the island when computing the x marginal distribution. These extra structures represent coherence of the wave packet over multiple wells of the potential, where the coherence length scales as the inverse of the width of the narrow slices. Finally, we note that the initial condition plotted here assumes a minimum-uncertainty Gaussian, but in the experiment the wave packet was distorted slightly by anharmonic evolution in the lattice during the state preparation.

6.3.2 Broken Symmetry

The subrecoil Raman velocity selection is important not only to produce a nearly uncertainty-limited wave packet, but also in order to satisfy a quantum symmetry required to observe tunneling. This symmetry stems from the discrete translational symmetry of the potential, as discussed in Chapter 2, which causes momentum transitions to occur in discrete steps of $\bar{k}$ (or $2\hbar k_{\mathrm{L}}$ in unscaled units). Thus the momentum state $|n\bar{k} + \delta\rangle$ (where n is an integer) is coupled to the $|-n\bar{k} + \delta\rangle$ state via 2-photon transitions. For $0 < |\delta| < \bar{k}/2$, these states are therefore not coupled to their symmetric reflections about $p = 0$. In the language of the double-well potential above, this situation is equivalent to an asymmetric double well, because the potential couples two states with a difference of $2n\bar{k}\delta$ in energy. Thus, complete tunneling only fully occurs for the $|n\bar{k}\rangle$ momentum states and is suppressed for states off this integer ladder. A deviation in momentum from this symmetric ladder is equivalent to a broken time-reversal symmetry [313], and the symmetric/antisymmetric doublet character can be sensitive to this broken symmetry [310]. This symmetry condition is automatically fulfilled for a rotor, because the periodic boundary conditions select the tunneling states, but in the case of a particle in an extended potential, as in the present experiment, careful state preparation is required to populate only the proper states. Thus the subrecoil velocity selection, coupled with the rest of the state-preparation sequence, fulfills the simultaneous goals of producing a wave packet localized on an island of stability and populating only states with momentum nearly an integer multiple of $\bar{k}$.

The importance of the subrecoil momentum selection is demonstrated in Fig. 6.7, where the evolution of $\langle p \rangle$ corresponding to the data in Fig. 6.5 (with an 800 μs Raman selection pulse) is shown, along with data for 400 and 200 μs Raman pulses. Shorter Raman pulses result in wider velocity slices, so that fewer of the atoms fulfill the symmetry condition, and thus the tunneling oscillations are suppressed as the Raman pulse duration decreases. Also shown is the case where the experiment was performed without

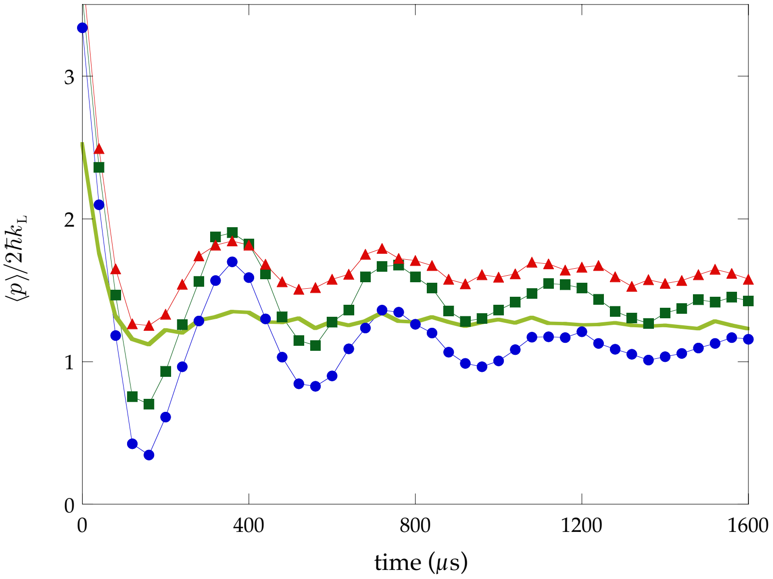

Figure 6.7: Comparison of tunneling oscillations for different Raman π-pulse durations, and thus selected velocity widths ($\alpha = 10.5$, $\bar{k} = 2.08$). The strongest oscillations shown here (circles) correspond to the longest (800 μs) Raman velocity selection pulse used, which implies a momentum slice with a HWHM of $0.03 \cdot 2\hbar k_L$. The data here are derived from the momentum distributions in Fig. 6.5. Also shown are data for a 400 μs selection pulse (corresponding to a HWHM of $0.06 \cdot 2\hbar k_L$) and a 200 μs selection pulse (corresponding to a HWHM of $0.12 \cdot 2\hbar k_L$), illustrating the reduced contrast in the tunneling oscillations as the pulse duration is decreased. The heavy solid line corresponds to a measurement where no Raman velocity selection was performed, but the atoms were subjected to the state-preparation sequence after cooling in the 3D lattice (where they have a HWHM in momentum of $0.8 \cdot 2\hbar k_L$). The tunneling oscillations are completely suppressed in this last case. The data were averaged over 20 (800 μs tag), 10 (400 μs tag), 5 (200 μs tag), and 1 (no Raman tag) iterations of the experiment.

any Raman velocity selection, and the state-preparation sequence in the 1D lattice was performed immediately after cooling in the 3D lattice. The momentum distribution after the atoms were released from the 3D lattice was not subrecoil, so the prepared wave packet was no longer minimum uncertainty (the wave-packet area in phase space was about three times the size of a minimum-uncertainty state). More importantly, though, there was no subrecoil structure in this last case, so that the tunneling oscillations are completely absent in the figure. The evolution of the momentum distribution in this case is shown in Fig. 6.8. There is perhaps a half of a tunneling oscillation at the beginning of the evolution, but the oscillations are again clearly suppressed. Most of the atoms have suppressed tunneling amplitudes, because they are too far away from the proper tunneling momenta. Also, because there is a continuum of states populated near the symmetric ladder, the different momentum classes tunnel at slightly different rates.

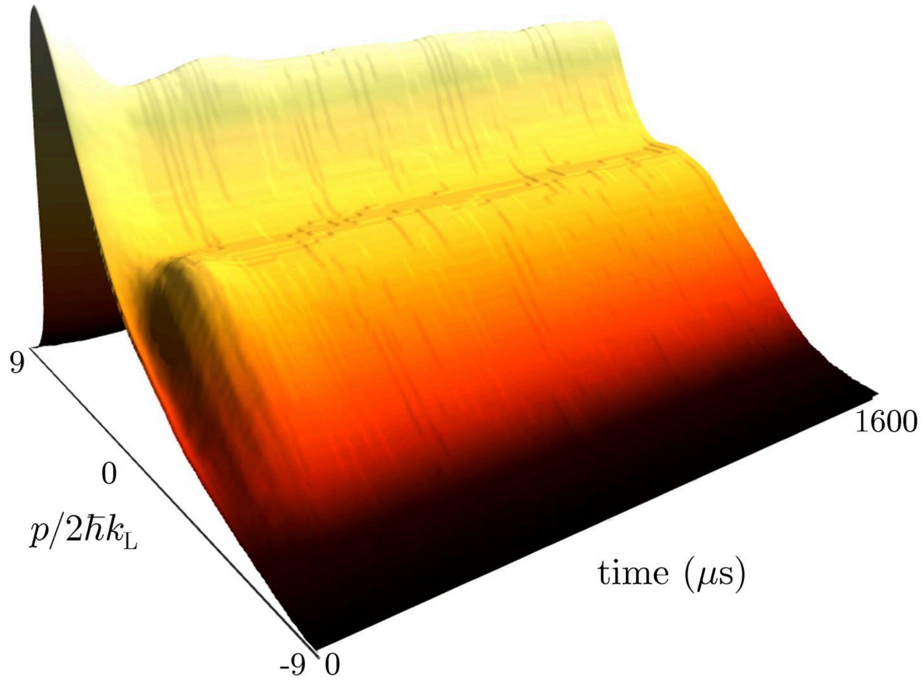

Figure 6.8: Evolution of the momentum distribution as in Fig. 6.5, but without Raman velocity selection. The tunneling oscillations are clearly suppressed here.

This situation provides another mechanism for damping of the coherent oscillations, similar to broadened excitation of a two-level atom.

We also studied this broken symmetry more directly by fixing the velocity-selection width at the minimum value and varying the locations of the velocity slices within the Gaussian profile. This was accomplished easily by slightly varying the detuning of the Raman pulse before loading the atoms into the standing wave. The experimental results are shown in Fig. 6.9, where the data with the optimum Raman detuning are compared to data with two other Raman detunings. As the detuning increases, the tunneling oscillations are again suppressed, being almost fully destroyed for an offset corresponding to $0.12 \cdot 2\hbar k_{\mathrm{L}}$ in momentum. The tunneling is thus quite sensitive to this broken symmetry.

Fig. 6.10 shows simulations of the tunneling oscillations that model the Raman

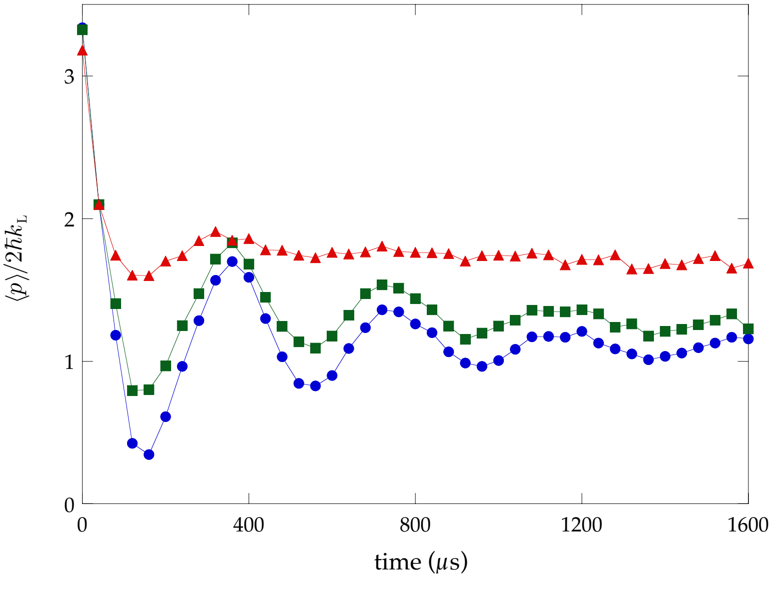

Figure 6.9: Comparison of tunneling oscillations for different Raman detunings ($\alpha = 10.5$, $k\!\!\!^{-} = 2.08$). The strongest oscillations observed (circles) correspond to Raman velocity selection at $p = 0$. The other two cases are for velocity selection at $p = 0.05 \cdot 2\hbar k_{\mathrm{L}}$ (squares), where the oscillations are partially suppressed, and $p = 0.12 \cdot 2\hbar k_{\mathrm{L}}$ (triangles), where the oscillations are almost completely suppressed.

tag widths in Fig. 6.7 as well as oscillations in the limit of arbitrarily narrow velocity selection (i.e., the rotor case). The simulation assumes an overall profile of a minimum-uncertainty wave packet with the same center and momentum width as in the experiment, along with ideal Raman π-pulse momentum-selection profiles. With no width, there are no signs of damping, and the tunneling is nearly complete. With wider momentum slices, a smaller fraction of the atoms successfully tunnels, and the tunneling oscillations become increasingly damped. The Raman tagging thus explains a substantial part of the incomplete tunneling and damping in the experiment. In principle, then, a Raman tagging pulse even longer than 800 μs could have provided more complete tunneling, although such a pulse was impractical, as the atoms would have fallen too far with respect to the beams over the course of the experimental sequence.

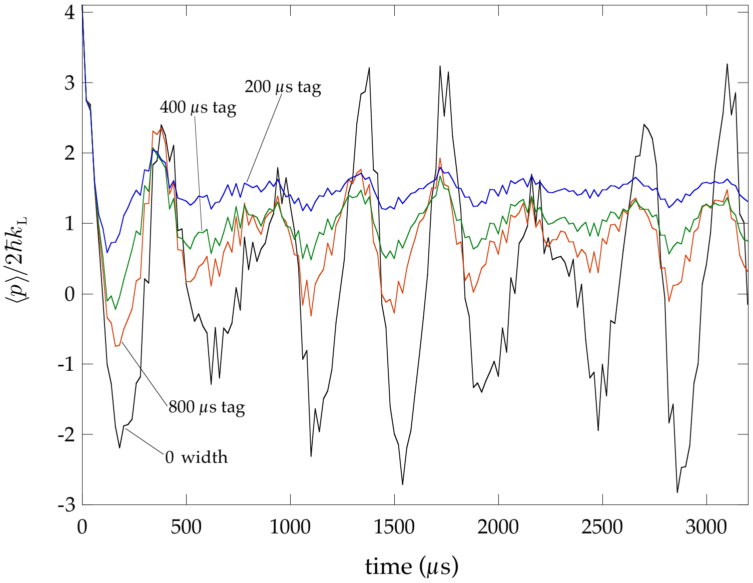

Figure 6.10: Simulation of the effects of the Raman tag width on the tunneling signal ($\alpha = 10.5$, $k\!\!\!{}^{-} = 2.077$). The average momentum $\langle p \rangle$ is plotted every 20 μs modulation period for a single, minimum-uncertainty wave packet with an overall Gaussian envelope (out of which the Raman-selected slices are taken) centered at $(x_0, p_0) = (0, 4.1 \cdot 2\hbar k_\mathrm{L})$, with $\sigma_p = 1.1 \cdot 2\hbar k_\mathrm{L}$, to model the experimental conditions in Fig. 6.7. This calculation assumes idealized (square) π-pulse lineshapes, as in Eq. (5.26), for the Raman pulse durations used in the experiment. The case of an arbitrarily narrow velocity selection is also shown, which maximizes the tunneling-oscillation amplitude.

Finally, the reader may have noticed that the average momenta $\langle p \rangle$ in the experimental plots are reduced in magnitude compared to what one might expect. This is especially evident at the beginning of the evolution, where the average momentum appears to be around $3.3 \cdot 2\hbar k_\mathrm{L}$, even though the distribution is peaked at $4.1 \cdot 2\hbar k_\mathrm{L}$. This effect is an artifact of the reduction of the distributions to average values, where the broad backgrounds of the distributions and the truncation at large momenta (the $\bar{k} = 2.08$ data are truncated beyond $\pm 9 \cdot 2\hbar k_\mathrm{L}$ and the $\bar{k} = 1.04$ data are truncated beyond $\pm 14.1 \cdot 2\hbar k_\mathrm{L}$) skew the computed means to have magnitudes that are smaller than their actual values.

6.3.3 Tunneling Dependence on Wave-Packet Location

To argue that the observed tunneling was indeed between islands of stability, it was important to demonstrate that the tunneling is sensitive to the location of the wave packet in phase space. Just after the state preparation sequence for the above experiments, the wave packet was moving. Thus, it was possible to displace the initial wave packet in the x-direction in phase space simply by inserting a time delay between the usual state-preparation procedure and the amplitude-modulated lattice phase of the experiment. Doing so produced a shift of the wave-packet center, where the distance was proportional to the time delay, along with a shear of the profile of the wave packet due to dispersion effects. Fig. 6.11 shows the usual zero-delay case compared to data with three different time delays, corresponding to displacements of 1/4, 1/2, and 1 full period of the lattice potential. Schematic plots of the initial conditions in the classical phase space are shown in Fig. 6.12 for these four cases. The tunneling oscillations are strongest for zero time delay, when the wave packet was centered on the island. For the 1/4-period displacement, the wave packet was centered in the chaotic region next to the island, and the tunneling oscillations are significantly suppressed. For the 1/2-period displacement, the wave packet was centered in the outer stability region, and the tunneling oscillations are almost completely suppressed. For the longest time delay, the wave packet was displaced by a full period of the potential and thus is again centered on the island. The tunneling oscillations return in this case, but with smaller amplitude due to the stretched character of the wave packet after the dispersive free evolution. Hence, it is clear that the islands of stability were important in supporting the tunneling in this experiment.

We have also displaced the center of the wave packet in the p-direction in phase space by changing the amplitude of the lattice phase shift during the state preparation (and adjusting the subsequent evolution period in the lattice accordingly). For the experimental parameters here, we varied the wave packet center in steps of $0.5 \cdot 2\hbar k_{\mathrm{L}}$, and

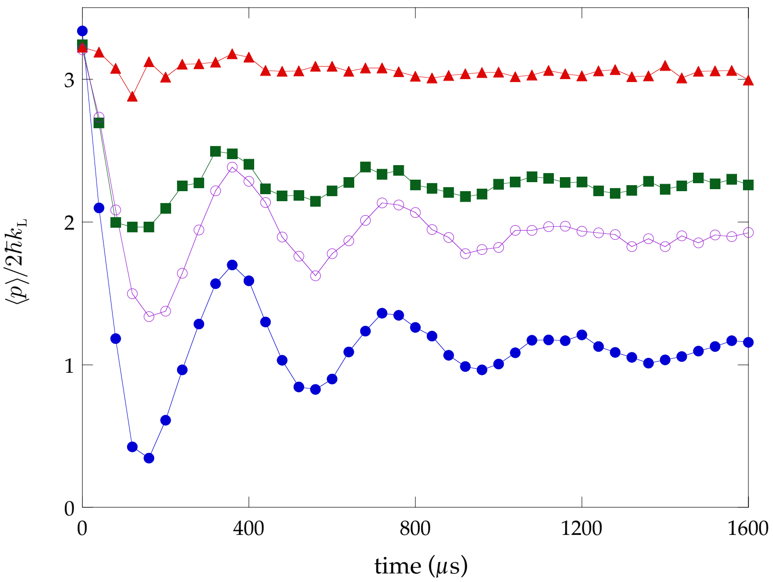

Figure 6.11: Comparison of chaos-assisted tunneling ($\alpha = 10.5$, $k\!\!\!^- = 2.08$) for different free-drift times before the standing-wave interaction, which amount to different displacements of the initial condition in the x-direction in phase space, as illustrated in Fig. 6.12. The strongest oscillations occur for zero drift time (filled circles), where the initial wave packet is centered on the island of stability as in Fig. 6.4. The oscillations are significantly suppressed for a 3.8 μs drift time (squares), which displaces the initial wave packet center by 1/4 of a period of the standing wave. Tunneling oscillations are completely suppressed for a 7.6 μs drift time (triangles), corresponding to a 1/2-period offset of the initial wave packet. For a 15.1 μs drift time (open circles), the wave packet is again centered on the island, and coherent oscillations are restored. The data here were averaged over 20 iterations of the experiment.

we observed strong tunneling when the wave packet was centered at $p/2\hbar k_{\mathrm{L}} = 3$, 3.5, and 4, while tunneling was suppressed at the other values outside this range.

6.4 Chaos-Assisted Tunneling

In considering the tunneling phenomenon in the experiment, we have thus far focused only on the role of the islands of stability in the tunneling. However, as we will now discuss, the chaotic region surrounding the islands is important in enhancing the tunneling

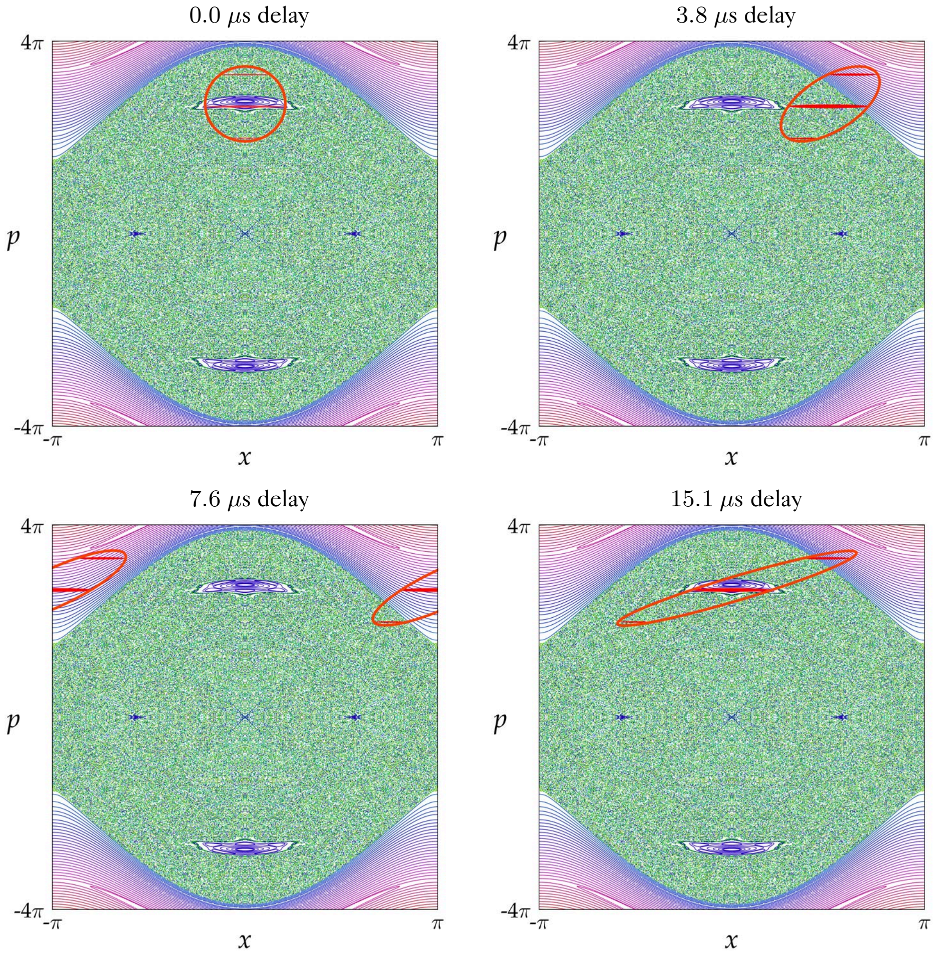

Figure 6.12: Initial conditions in phase space for the four time delays used in obtaining the data of Fig. 6.11. The large ellipse around the three narrow population slices in each case marks the overall profile of the wave packet to guide the eye.

process, and we will argue that the tunneling in the experiment is due to *chaos-assisted tunneling*.

The possibility of tunneling enhancement by classical chaos was first introduced in a numerical study by Lin and Ballentine [319], where it was found that the tunneling rate between islands of stability in the periodically driven, double-well potential could be orders of magnitude larger than the tunneling rate in the undriven (integrable) double well. While the presence of two islands related by a discrete symmetry is important in supporting the tunneling in this system [320], the authors attributed the increased tunneling rate to the presence of the chaotic region in the classical phase space. It was subsequently shown that the tunneling rate is correlated with the degree of overlap of the tunneling states with the chaotic region [321], which also points to the role of the chaotic sea as a catalyst for the tunneling. This enhancement of the tunneling was understood in [306, 322] (where the term "chaos-assisted tunneling" was introduced) in terms of an avoided crossing of the tunneling doublet with a third level associated with the chaotic region, which can greatly increase the tunnel splitting. Because the (quasi)energies of the chaotic states exhibit strong and irregular dependence of the system parameters, the tunneling rate also exhibits irregular fluctuations over orders of magnitude [323–325], sometimes reaching zero for exact crossings of the tunneling doublet (the "coherent destruction of tunneling" [326]). The smooth, universal dependence of the tunneling rate on $\hbar$, as mentioned above for the double-well tunneling, is therefore lost for chaos-assisted tunneling. In addition to this three-state picture, chaos-assisted tunneling has also been understood in terms of the dominance of indirect paths, which are multi-step paths that traverse the chaotic region, over direct paths, which tunnel in a single step and are responsible for regular (two-state) tunneling [327]. Thus, chaos-assisted tunneling occurs as small portions of the population from the initial wave packet break off, transport through the chaotic region, and then accumulate in the symmetric region, without a large population building up in the chaotic region [306, 328]. By contrast, direct tunneling occurs with an always negligible population in the intermediate region.

The sense in which we mean “chaos-assisted tunneling” here is the influence of the chaotic region on tunneling transport between symmetry-related regions in phase space, but this term has also been applied in the sense of open systems, where the tunneling implies an escape from a bound state. In this vein, chaos-assisted tunneling has been invoked to explain fluctuations in the energy and rate of ionization of Rydberg atoms in microwave fields [329], and also to explain mode lifetimes in weakly deformed optical micro-resonators [330].

Previous experimental work in chaos-assisted tunneling has been performed in the spectroscopy of a microwave resonator in the shape of an annular billiard [88]. The authors measured the dependence of the quasidoublet splittings on the locations of the states in phase space and on the eccentricity of the cavity, demonstrating an enhancement in the splitting for states near the border between the stable and chaotic regions. Chaos-assisted tunneling has also been invoked to explain features in the decay of superdeformed nuclear states to normal-deformed states [331], although the interpretation here is not entirely straightforward [328]. It is also worth noting that another atom-optics experiment studies tunneling of atoms in an optical lattice of double wells [332], where the classical description is chaotic as a result of the coupling of the center-of-mass motion to the spin state of the atom [333]. So far, though, the symptoms of chaos-assisted tunneling that we describe below have not been observed in this system. Other experiments [80, 81] consider the transport in the resonant tunneling diode, where a strong magnetic field induces chaos in the classical limit. However, the tunneling here is enhanced by energy resonances of states on either side of a barrier (corresponding to periodic orbits in the chaotic quantum-well region), and thus the tunneling is not enhanced by the chaos in the sense of this chapter.

6.4.1 Singlet-Doublet Crossings

We will now review the simplified three-state model introduced in [306, 322] because of its importance in understanding chaos-assisted tunneling and its utility in interpreting the experimental data. Because we are considering a periodically driven system, though, we will consider a Floquet-Hamiltonian model as in [334], rather than the original Hamiltonian model. We recall from Section 4.5.1 that the Floquet states are eigenstates of the unitary evolution operator $U(t+1,t)$ over one period of the modulation, with eigenvalue $\exp(-i\epsilon_n/\bar{k})$, where ϵ_n is the quasienergy. The eigenstates can also be written as

$$|\psi_n(t)\rangle = e^{-i\epsilon_n t/\bar{k}}|\chi_n(t)\rangle \ \ , \tag{6.13}$$

where the state $|\chi_n(t)\rangle$ is periodic in time with the same period as the modulation. Thus, the quasienergies represent the phase evolution of the Floquet states (in a stroboscopic sense), just as the energies govern the phase evolution of the energy eigenstates for autonomous systems. The periodic states $|\chi_n(t)\rangle$ are also eigenstates of the Floquet Hamiltonian [325],

$$\mathcal{H} := H - i\hbar\partial_t, \tag{6.14}$$

with eigenvalue ϵ_n. We will therefore construct a model Floquet Hamiltonian that captures the essence of chaos-assisted tunneling.

We consider a doublet of tunneling states, localized on the two islands of stability (regular regions), with quasienergies ϵ_r and $\epsilon_\mathrm{r} + \delta_\mathrm{r}$, so that δ_r parameterizes the tunneling rate in the absence of interaction with other levels. These states have opposite parity, and for the sake of concreteness, we can take the state with quasienergy ϵ_r to be of even parity. We also consider a third state in the chaotic region (although we note that three-level crossings can also be induced by states in other stable regions [327, 335, 336]), with quasienergy $\epsilon_\mathrm{r} + \Delta_\mathrm{c}$. Without loss of generality we may assume that this state has even parity; notice that the states in the chaotic region do not generally occur in narrowly spaced doublets, so that we can ignore the effect of the corresponding state of odd parity. The chaotic state does not interact with the odd member of the tunneling doublet, but we assume that there is some nonzero interaction between the two even states. We may then write the model Floquet Hamiltonian as [306, 322, 334]

$$\mathcal{H} = \left(\begin{array}{ccc} \epsilon_{\mathrm{r}} + \delta_{\mathrm{r}} & 0 & 0 \\ 0 & \epsilon_{\mathrm{r}} & \beta/2 \\ 0 & \beta/2 & \epsilon_{\mathrm{r}} + \Delta_{\mathrm{c}} \end{array} \right) , \tag{6.15}$$

where β represents the coupling between the chaotic state and the even regular state. Thus, the two coupled states undergo an avoided crossing, with quasienergy solutions of the same form as in the two-level case in Eqs. (6.5)-(6.8), while the odd regular state remains unchanged. This behavior is illustrated in Fig. 6.13. In the case where the coupling energy $\beta/2$ is large compared to the two-level splitting δ_{r} (which is the case

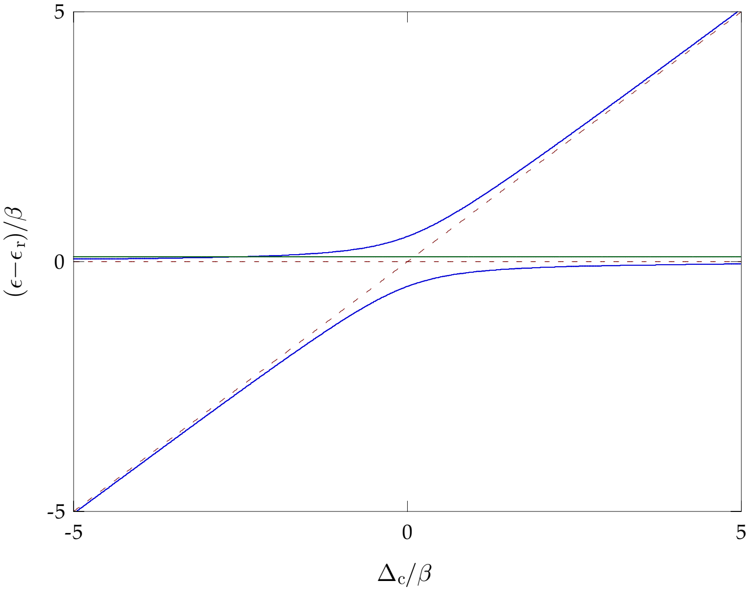

Figure 6.13: Illustration of a three-level avoided crossing of a tunneling doublet with a third (chaotic) state, as described by the model (6.15). The behavior of the three quasienergies is shown as a function of the detuning Δ_{c} of the chaotic state, for an unperturbed doublet splitting $\delta_{\mathrm{r}}/\beta = 0.1$. The chaotic state interacts with the regular state of the same parity (both shown as blue lines), and the other tunneling state (the green line) is unaffected by the crossing in this simple model. The dashed lines show the two repelling states in the absence of any coupling.

when the regular states have substantial overlap with the surrounding chaotic region), the tunnel splitting can be greatly enhanced, becoming of the order of $\beta/2$ between the odd state and either of the even states near the center of the crossing. As one might expect in an avoided crossing, the even regular state and the chaotic state exchange their character as Δ_c is swept through zero, as verified numerically in [337]. Thus, near the center of the crossing, the two even states each have population both in the islands and in the chaotic region, whereas away from the crossing it is possible to clearly distinguish a predominantly regular and predominantly chaotic even state. In a singet-doublet crossing, one expects a complicated time dependence, compared to the sinusoidal two-state tunneling, because three states will be excited by a wave packet localized on a single island. In general, the three splittings will all be different, leading to complicated beating in the time domain [334].

6.4.2 Comparison with Integrable Tunneling

The tunneling that we have studied is between two oppositely directed modes of motion. In unmodulated optical lattices, however, Bragg scattering is a well-known dynamical-tunneling mechanism, as we discussed in Section 2.7.1. Bragg scattering produces similar results to the tunneling that we have described, including sensitivity to the same broken symmetry that we discussed above, even though there is no classical chaos without a modulation of the lattice. It was therefore important to demonstrate that the tunneling here is not simply Bragg scattering, but that the amplitude modulation has a substantial effect on the tunneling dynamics. We have done this already to a certain extent by demonstrating that the initial state must be centered on the island of stability for tunneling to occur (Bragg scattering occurs between plane-wave states, which are delocalized in position, and thus should not be sensitive to spatial displacements of the initial condition). However, a direct comparison between tunneling in chaotic and integrable systems is also illuminating.

A sensible integrable counterpart of the modulated system arises by using the optical lattice with constant amplitude, where the potential depth is taken to be V_0. Doing so produces a pendulum, such that the lattice intensity is the same, on average, as in the amplitude-modulated system. The phase space for the pendulum corresponding to the experimental conditions in Fig. 6.4 is shown in Fig. 6.14, along with the same initial condition as before. The wave packet is centered outside the separatrix, so that classical transport to the opposite momentum region is also forbidden here. However,

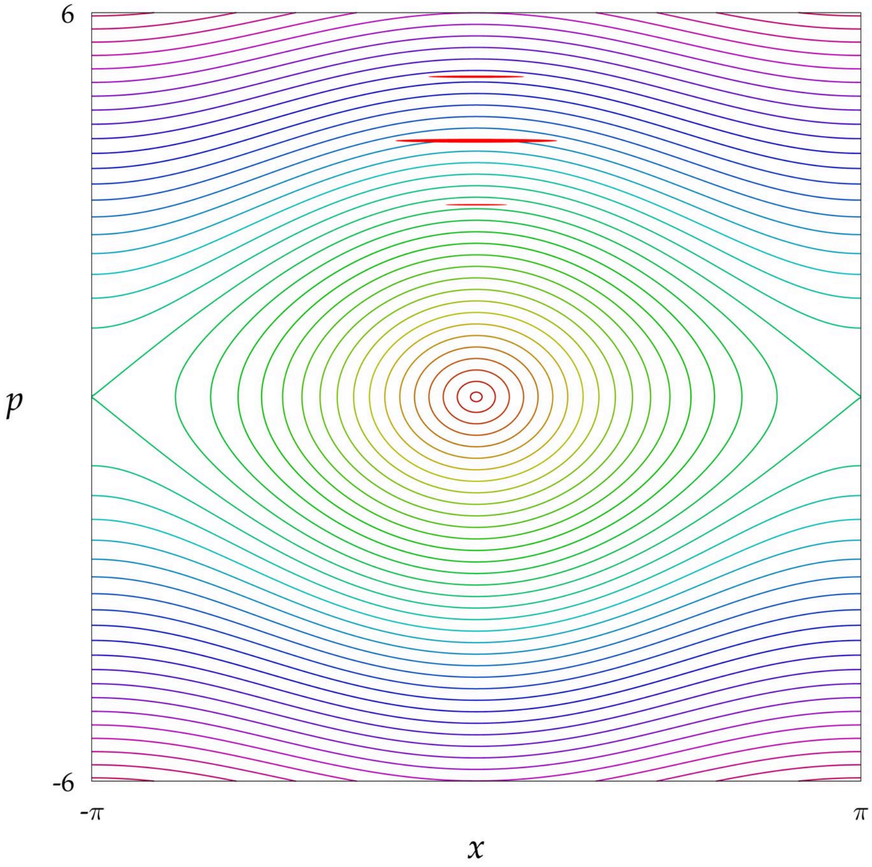

Figure 6.14: Phase space of the pendulum, with the same average potential amplitude as the modulated-pendulum case in Fig. 6.4. The same initial condition is also shown here. The initial state is centered outside the separatrix, so that classical transport to the opposite (symmetric) momentum region is also forbidden here. Notice that the momentum axis is in pendulum scaled units (i.e., multiples of $2\hbar k_{\mathrm{L}}$), rather than the scaled units for the modulated pendulum.

high-order Bragg scattering, which is a manifestation of quantum above-barrier reflection [338], allows quantum oscillatory transport between these momentum regions.

We recall from Section 2.7.1 that the Bragg oscillation frequency is

$$\Omega'_{\mathrm{B},n} = \frac{\alpha^n}{\bar{k}^{2n-1}[(n-1)!]^2} \ , \tag{6.16}$$

when adapted to the scaled units of the amplitude-modulated pendulum. In this form, it is not obvious that Bragg scattering has the expected universal dependence $\exp(-S/\bar{k})$ for two-state tunneling that we mentioned above. Since tunneling occurs from some initial momentum $(n/2)\bar{k}$ to $-(n/2)\bar{k}$ (for integer n) as an nth-order scattering process, the order n is effectively a function of $\bar{k}$. Then, in the semiclassical limit of large n, we

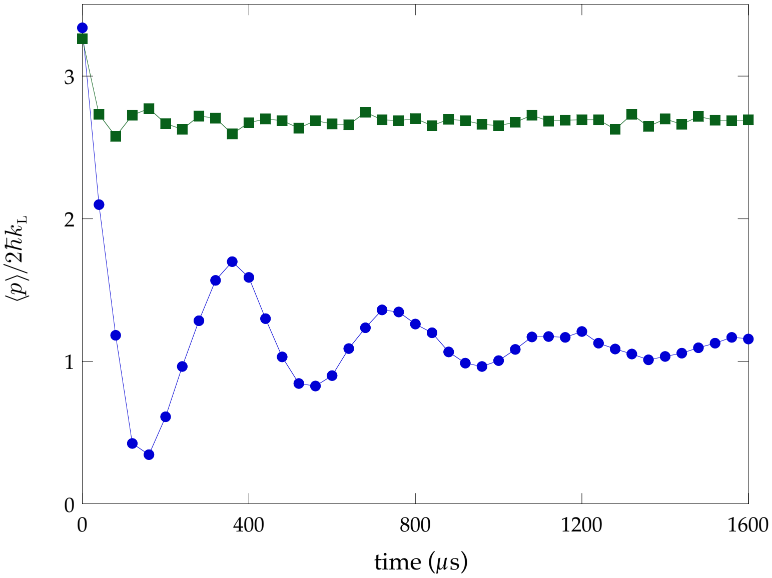

Figure 6.15: Comparison of chaos-assisted tunneling oscillations (circles) to transport in the corresponding quantum pendulum (squares). The experimental conditions are $\alpha = 10.5$ and $\bar{k} = 2.08$ in the modulated case, with the same average intensity used in the pendulum case. No tunneling oscillations are observed in the pendulum case over the interaction times studied in the experiment. The expected period for 8th-order Bragg scattering is 1 s, which is much longer than the 400 μs period of the tunneling between islands of stability. The data here were averaged over 20 iterations of the experiment.

can invoke Stirling's approximation, and the Bragg rate becomes

$$\Omega'_{\mathrm{B},n} \simeq \frac{1}{2\pi}\left[\frac{(2p)^2}{\alpha e^2}\right]^{-p/\bar{k}}, \tag{6.17}$$

which is consistent with the expected scaling with $\bar{k}$. Notice that the factor in the square braces is greater than unity, since to be in the Bragg regime (where population in the intermediate states can be adiabatically eliminated) the wave packet must be outside the classical pendulum separatrix, which implies that $|p| > 2\sqrt{\alpha}$.

The tunneling oscillations of Fig. 6.5 are compared with the behavior of the corresponding pendulum in Fig. 6.15. No tunneling oscillations are visible in the integrable case over the time scale studied in the experiment. Since the initial distribution is peaked near $4 \cdot 2\hbar k_{\mathrm{L}}$, the dominant transport process in the pendulum is 8th-order Bragg scattering. For $n = 8$, $\alpha = 10.5$, and $\bar{k} = 2.08$, the Bragg period is about 1 s, which

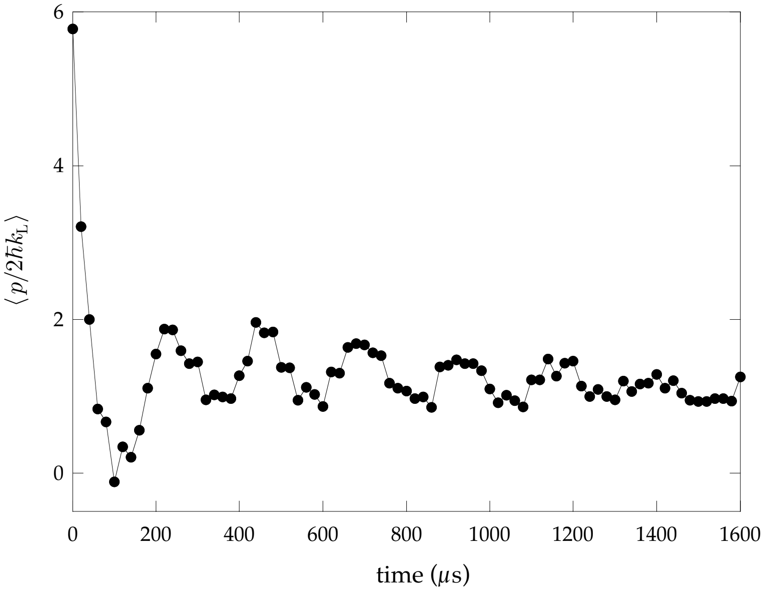

Figure 6.16: Tunneling oscillations for $\alpha = 11.2$, $\bar{k} = 1.04$ (10 μs modulation period). The corresponding two-state (integrable) tunneling mechanism is 16th-order Bragg scattering, which has an expected period of 20 years. The observed tunneling rate is clearly much smaller than the expected Bragg period. The data here were averaged over 10 iterations of the experiment.

is much longer than the 400 μs period of the tunneling oscillations in the chaotic case (and thus the experimental Bragg measurement is in accord with our expectations).

We have also demonstrated tunneling in a parameter regime that is closer to the classical limit ($\bar{k} = 1.04$), as shown in Fig. 6.16. The initial distribution here is peaked around $8 \cdot 2\hbar k_{\mathrm{L}}$, and so this coherent, 32-photon process is similar to 16th-order Bragg scattering. The expected Bragg period here is 20 years, which is long compared to the 250 μs period of the tunneling in the chaotic case, and is even long compared to the coherence time of a graduate student. Thus, it is clear that in some sense the chaos enhances the transport, in that the tunnel splittings are much larger in the chaotic case than in the corresponding integrable case.

Of course, it could be the case that the amplitude modulation enhances the two-level tunneling rate without the influence of a third, chaotic state, especially in view of the rapid dependence of the Bragg splitting on the lattice intensity. Although we provide additional experimental evidence for chaos-assisted tunneling below, we will now derive a simple estimate for the direct tunneling rate with the modulation. Since Bragg scattering represents the two-level transport mechanism in this system, and corresponds to a resonantly coupled two-level system if the proper momentum symmetry condition is satisfied, we can use the well-established solution to the two-level atom (without damping) exposed to a resonant driving field with time-dependent intensity [339]. In this case we define the pulse integral,

$$\phi = \int_0^t \Omega_{\mathrm{B},n}(t')\, dt' \quad , \tag{6.18}$$

in terms of which the tunneled population can be written as $\sin^2(\phi/2)$ (note that $\phi = \Omega_{\mathrm{B},n} t$ for constant drive, as in normal Bragg scattering). Since the tunneling period is substantially longer than the modulation period, we can simply average the Bragg rate over a modulation period, and thus the modulation enhances the two-level tunneling rate by a factor

$$\int_0^1 [2\cos^2(\pi t)]^n\, dt \tag{6.19}$$

for nth-order transport. This factor is about 50 for the $\bar{k} = 2.08$ case and about 9000 for the $\bar{k} = 1.04$ case. Neither of these numerical values is sufficiently large to explain the enormous differences in the tunneling rates in the integrable and chaotic cases.

6.4.3 Tunneling Dependence on Parameter Variations

To establish that the tunneling in the modulated lattice is chaos-assisted tunneling, it is also important to examine the dependence of the tunneling as the two experimental parameters (α and $\bar{k}$) are varied. As we noted above, the dependence of the tunneling rate should be very different for direct and chaos-assisted tunneling. In this section, we examine the variation of the tunneling as a function of α for two different values of $\bar{k}$. Operationally, α is a much more convenient parameter to vary, because it only requires a change in laser intensity, whereas $\bar{k}$ is more difficult because it requires changing both the laser intensity and the modulation period (to keep α fixed) as well as a new set of parameters for the SPASM state preparation (to maintain the initial condition at the same phase-space location). While we do not necessarily expect to see rapid variations in the tunneling rate as we vary α, due to inhomogeneous broadening (different atoms see different optical intensities, depending on their transverse location in the optical lattice, leading to about a 5% spread in α over the atomic sample), there are nevertheless signatures of three-state tunneling in the data.

The dependence of the tunneling oscillations in the measured evolution of $\langle p(t) \rangle$ is shown in Fig. 6.17 for $\bar{k} = 2.08$. Tunneling is visible in the range of α from about 7 to 14, but is suppressed outside this range. Below this range the tunneling is presumably too slow to be observed (see the Floquet-spectrum analysis in the next section), and above this range the outer islands have completely dissolved into the chaotic sea, so that we no longer expect clean tunneling to occur. The tunneling rates for this data are plotted in Fig. 6.18. The tunneling rate does not fluctuate strongly as α changes, but there are two interesting features to notice. The first is that the tunneling rate *decreases* as a function of α. This dependence is the opposite of our expectation of direct tunneling, where as we have seen above the tunneling rate should increase with α, following a power-law dependence. This behavior is thus strong evidence that the tunneling is chaos-assisted, where one or more chaotic levels has a definite influence on the doublet

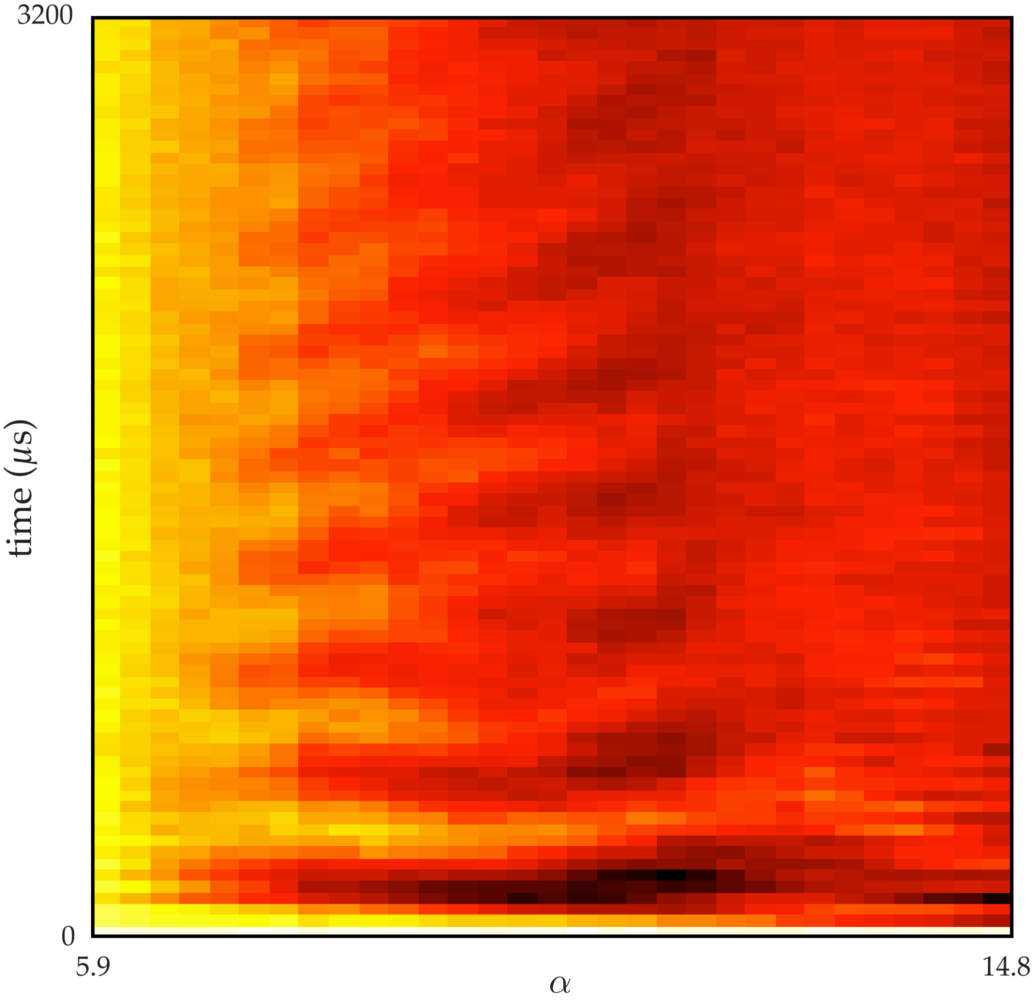

Figure 6.17: Dependence of the tunneling as the optical-lattice intensity α is varied for $\bar{k} = 2.08$ (20 μs modulation period). The color indicates the value of $\langle p \rangle$, with black representing the most negative values and white the most positive. The tunneling is absent at the extreme values of α shown here, but tunneling oscillations appear in the center of the α range. This behavior is consistent with the avoided-crossing mechanism for chaos-assisted tunneling. The data here were averaged over 10 iterations of the experiment.

splitting. The second feature to notice is that two frequencies are clearly resolvable in the tunneling in a comparatively narrow window in α (from about 8.5 to 10.5). The one- and two-frequency behaviors of the tunneling are illustrated in Fig. 6.19, where one tunneling frequency is evident (for $\alpha = 8.0$), and in Fig. 6.20, where the beating of two frequencies is clearly apparent (for $\alpha = 9.7$). Thus, there is some sensitivity of the tunneling to variations in α in this regime. This behavior is also consistent with the three-state model near the center of a singlet-doublet crossing. In this model, the initial wave packet populates a regular state (localized on the islands) and two hybrid states, which have population in both the islands and in the chaotic sea. There should thus be two frequencies associated with the tunneling, corresponding to the two splittings between the regular state and the two hybrid states. In general, these two splittings will not be equal, but should be similar near the center of the avoided crossing, leading to

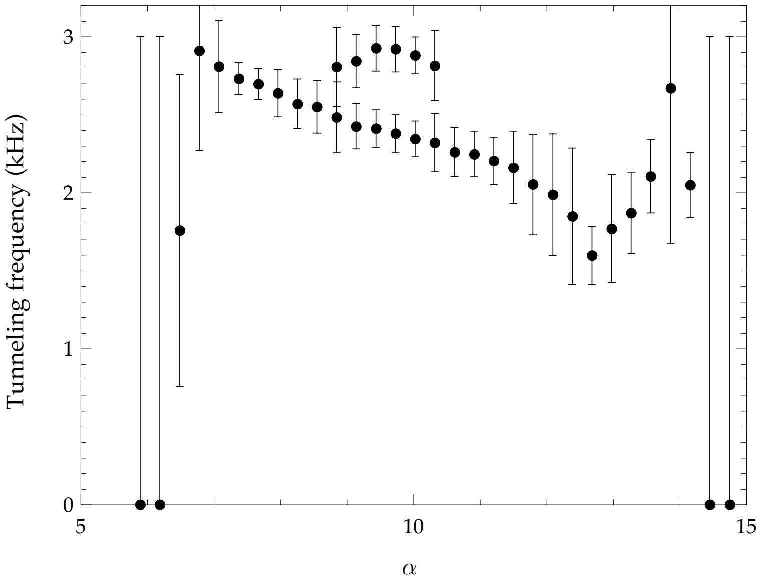

Figure 6.18: Dependence of the tunneling rate on the well depth α, for $\bar{k} = 2.08$ (20 μs modulation period). The periods were extracted from the data in Fig. 6.17 using both numerical Fourier transform and nonlinear fitting techniques. The error bars account for both fitting uncertainty and the width of the spectral peaks. In the range of α from 8.9 to 10.3, two distinct frequencies can be resolved in the tunneling data. The zero-frequency data points at the edges of the plot indicate that no tunneling frequency could be extracted from the data at these locations.

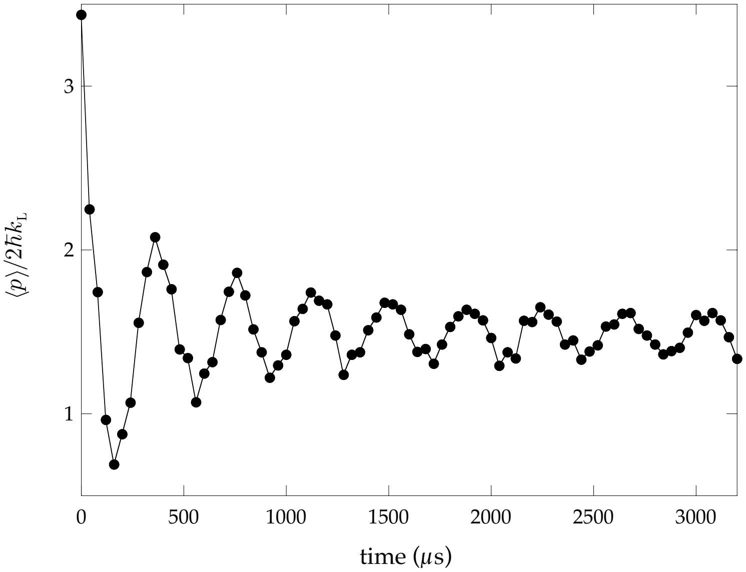

Figure 6.19: Example of tunneling oscillations from Fig. 6.17, where a single tunneling frequency persists for the maximum duration of the optical-lattice interaction. The parameters are $\alpha = 8.0$, $\bar{k} = 2.08$. The data points are connected by lines for clarity.

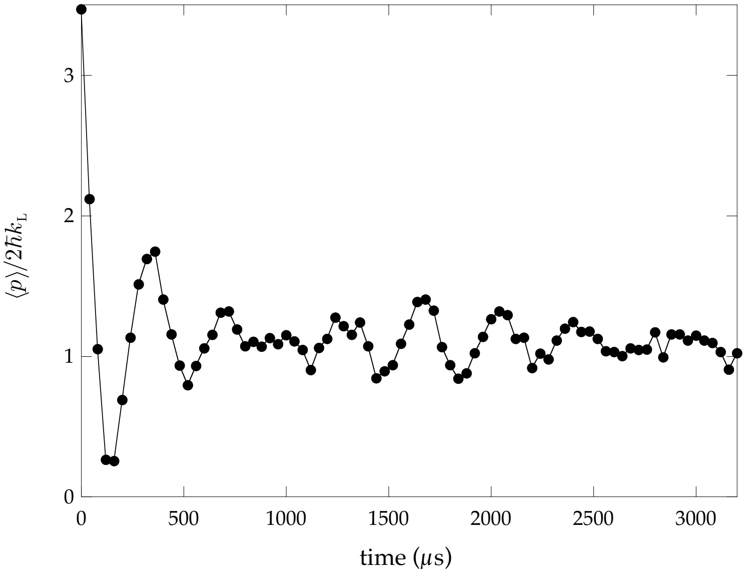

Figure 6.20: Example of tunneling oscillations from Fig. 6.17, where two tunneling frequencies are clearly present. The parameters are $\alpha = 9.7$, $\bar{k} = 2.08$. The data points are connected by lines for clarity.

two-frequency beating in the tunneling dynamics.

The variation of the tunneling behavior in the $\bar{k} = 1.04$ case is plotted in Fig. 6.21, with the extracted tunneling rates plotted in Fig. 6.22. The observed tunneling rates appear to have weaker dependence on α than in the $\bar{k} = 2.08$ case. However, the tunneling is only visible in a much narrower interval in α, from about 9.5 to

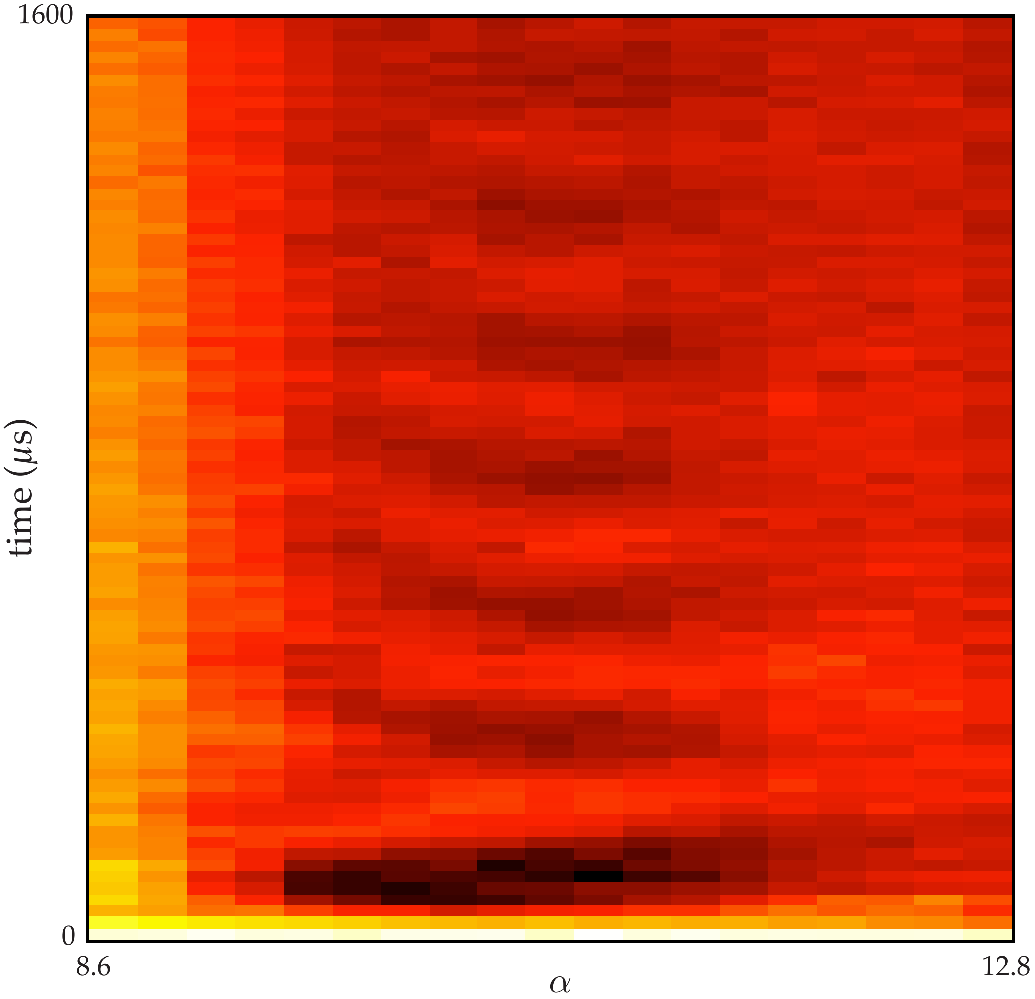

Figure 6.21: Dependence of the tunneling as the optical-lattice intensity α is varied for $\bar{k} = 1.04$ (10 μs modulation period). The color indicates the value of $\langle p \rangle$. The behavior here is qualitatively similar to the behavior in Fig. 6.17, but the tunneling occurs in a substantially narrower interval in α. The data were averaged over 10 iterations of the experiment.

12.5. Thus, in a sense, the tunneling here is more sensitive to variation in α than in the $\hbar\!\!\!k = 2.08$ case.

One question that remains is why the tunneling rate does not go smoothly to zero at the edges of the α intervals where tunneling is observed, especially at the lower end of the interval where the tunnel splitting is expected to become very small. In the experiment, the disappearance of the tunneling as α is swept comes about as the oscillations decrease in amplitude and become damped more quickly, until the oscillations are no longer discernible. One possible explanation is the change in the location of the two islands, which move to larger momentum as α increases (see the next section for an empirical expression for the island locations). In the experiment, the initial condition was held fixed as α is swept, so that there may have been less overlap with the tunneling Floquet states if the islands moved too far. However, over the intervals where

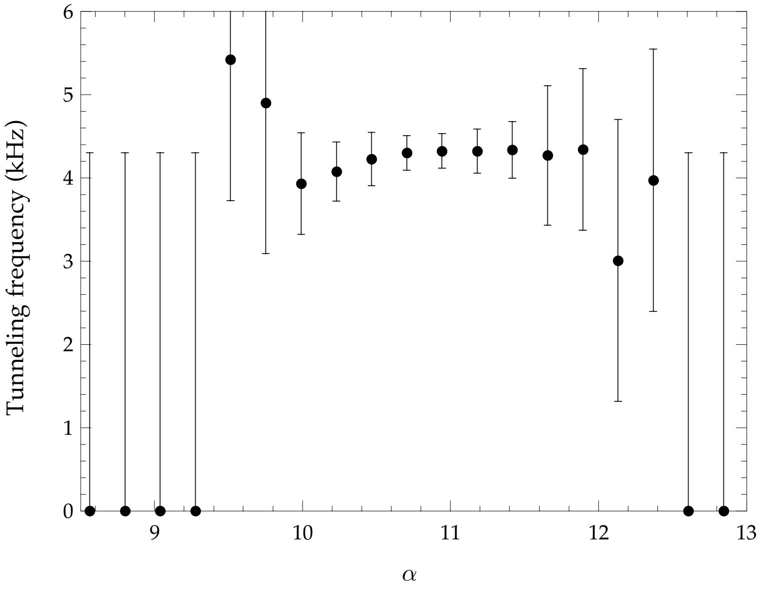

Figure 6.22: Dependence of the tunneling rate on the well depth α, for $\hbar\!\!\!k = 1.04$ (10 μs modulation period). The periods were extracted from the data in Fig. 6.21 using both numerical Fourier transform and nonlinear fitting techniques. The error bars account for both fitting uncertainty and the width of the spectral peaks. The zero-frequency data points at the edges of the plot indicate that no tunneling frequency could be extracted from the data at these locations.

tunneling was observed, the islands moved only by $\pm 0.3 \cdot 2\hbar k_{\mathrm{L}}$ for both the $\bar{k} = 2.08$ and the $\bar{k} = 1.04$ data sets, which is a substantially smaller amount than the respective $\sigma_p = 1.7 \cdot 2\hbar k_{\mathrm{L}}$ and $\sigma_p = 2.1 \cdot 2\hbar k_{\mathrm{L}}$ momentum uncertainties of the initial conditions in the two cases. Thus, misalignment of the initial conditions does not account for the disappearance of the tunneling at the extreme α values here. Another possible explanation lies in a suggestion by [340] that three-level tunneling is more robust to a symmetry-breaking interaction than two-level tunneling. Since the range of populated quasimomenta (and thus the degree of broken symmetry) is fixed by the Raman velocity selection, the tunneling away from the avoided crossings may simply disappear, as opposed to being manifested as a slow tunneling oscillation.

6.4.4 Floquet Spectra

In the context of understanding the observed tunneling dependence on α, it is useful to consider the quasienergy spectrum for this system. Computed spectra for the $\bar{k} = 2.077$ and $\bar{k} = 1.039$ cases are plotted in Figs. 6.23 and 6.24, respectively. These spectra only show the states with definite parity, falling on the symmetric ladder of momentum states $p = n\bar{k}$ (for integer n), corresponding to zero quasimomentum. The quasienergies were calculated by numerically constructing the unitary evolution operator for one period of the modulation and then diagonalizing the resulting operator. The even and odd tunneling states are also highlighted in these spectra. These states were identified by finding the states with maximum overlap with a minimum-uncertainty Gaussian wave packet that was centered on the fixed point of the island and had the same aspect ratio as the elliptical trajectories near the fixed point (i.e., where the linearized equations of motion are valid). The centers of the outer islands are given approximately by the empirical model

$$p_0 = \pm(2\pi + 0.1988 \cdot \alpha + 0.002953 \cdot \alpha^2 - 0.0000327 \cdot \alpha^3) \tag{6.20}$$

(with $x = 0$), which is accurate at about the 0.02% level from $\alpha = 0$ to the critical value $\alpha_{\mathrm{c}} \approx 11.54$ where these islands become unstable and bifurcate into pairs of islands. The aspect ratio of the elliptic invariant surfaces near the island centers is given approximately by the empirical model

$$\frac{\Delta p}{\Delta x} = \sqrt{\alpha(\alpha - \alpha_{\mathrm{c}})(-0.0439 + 0.00151 \cdot \alpha + 0.0000170 \cdot \alpha^2)} \ , \tag{6.21}$$

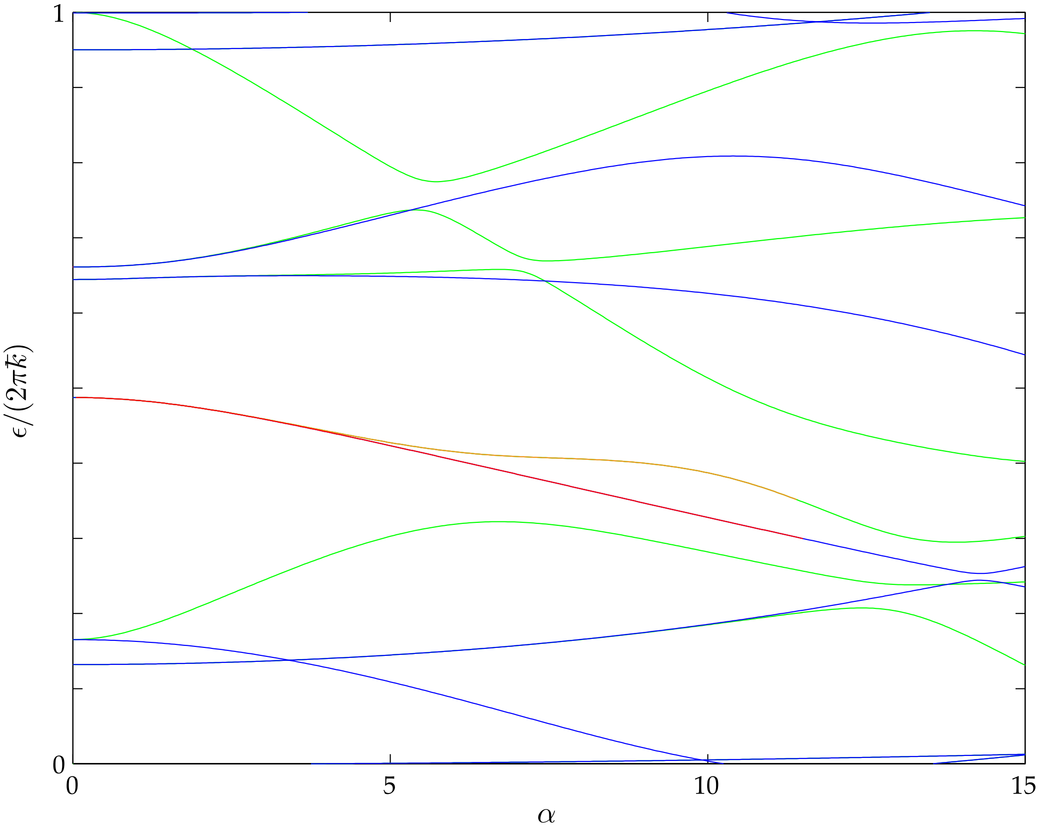

Figure 6.23: Calculated quasienergy spectrum for $\bar{k} = 2.077$, corresponding to a 20 μs modulation period. Quasienergies that correspond to states with large momentum (that do not interact with the states shown in this range of α) are suppressed, and the quasienergies shown are for the symmetric momentum ladder (zero quasimomentum). The quasienergies for even-parity Floquet states are shown in green, while the odd-parity states are shown in blue. The even (orange) and odd (red) states with maximal overlap with the outer stable islands are shown, up to the point where the islands bifurcate, as described in the text. The avoided-crossing behavior of the tunneling states is apparent over a broad range of α, where two chaotic states have a clear influence on the tunneling-doublet splitting.

which is accurate to the 1% level or better in the same range. The tunneling states are not identified for $\alpha > \alpha_c$, where it is difficult to assign states to the island remnants.

In the spectrum for $\bar{k} = 2.077$, the first avoided crossing (with an even-parity state of smaller quasienergy) does not occur until about $\alpha = 7$, where the splitting

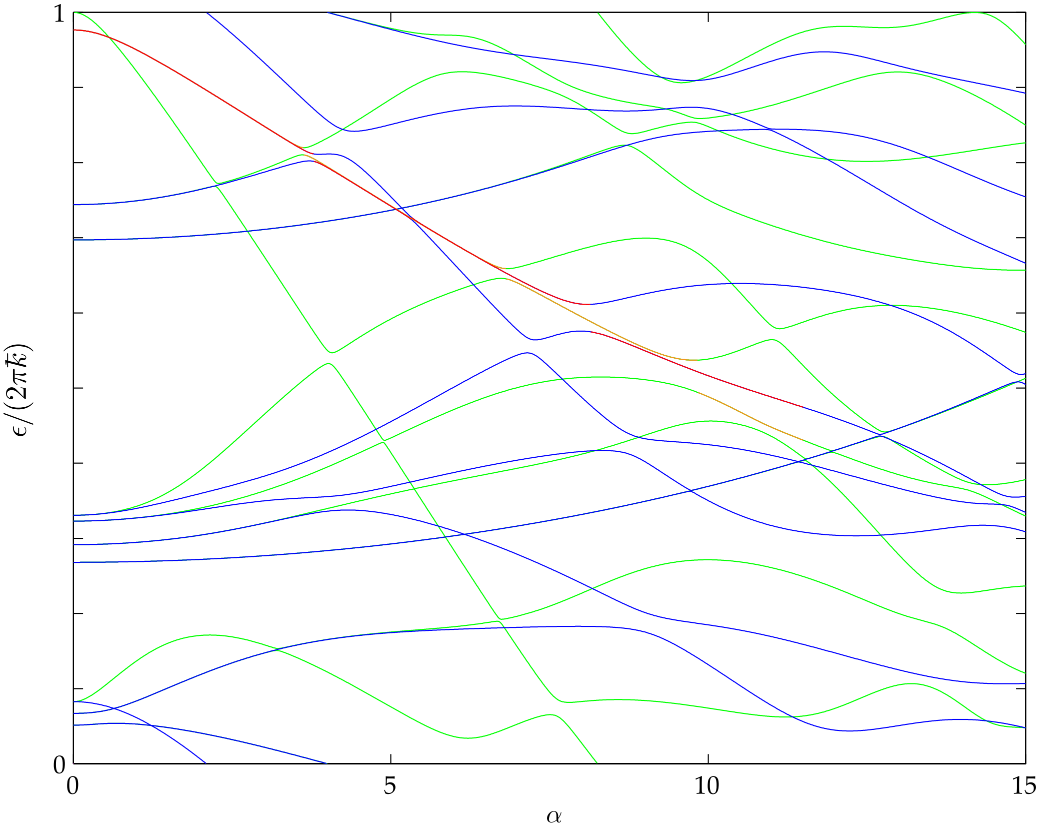

Figure 6.24: Calculated quasienergy spectrum for $\bar{k} = 1.039$, corresponding to a 10 μs modulation period. Quasienergies that correspond to states with large momentum (that do not interact with the states shown in this range of α) are suppressed, and the quasienergies shown are for the symmetric momentum ladder (zero quasimomentum). The quasienergies for even-parity Floquet states are shown in green, while the odd-parity states are shown in blue. The even (orange) and odd (red) states with maximal overlap with the outer stable islands are shown, up to the point where the islands bifurcate, as described in the text. Several avoided crossings of the tunneling doublet with chaotic states are apparent, although the splitting only becomes very large around $\alpha = 10$.

also first becomes significant. This behavior is consistent with the experimental data in Fig. 6.17, where tunneling oscillations are also first observed around $\alpha = 7$. Beyond this point, the two even-parity states maintain a similar distance from the odd tunneling state, and this holds true in the regime where two tunneling frequencies are visible in the data. These two even states then move back towards each other (and the odd tunneling state) as they interact with two other even states, and this behavior may explain the decreasing tunneling rate as a function of α, although it is again difficult to pinpoint the tunneling states in this regime of large α.

In the $\bar{k} = 1.039$ spectrum, the singlet-doublet crossings are much more apparent. There are several clear avoided crossings involving the tunneling doublet in the range shown, but it is not until the final avoided crossing before the islands become unstable that the splitting becomes large enough to observe experimentally. The experimental observation of tunneling beginning with $\alpha = 9.5$ is thus consistent with the spectrum, although another significant avoided crossing in the spectrum suggests that tunneling might also be visible in a very narrow region around $\alpha = 8$. The experimental tunneling stops around $\alpha = 12.5$, where the spectrum has become quite complicated and the tunneling doublet can no longer be identified.

The tunneling rates from the calculated spectra here are in good agreement with the observed rates in Figs. 6.18 and 6.22. For example, the two calculated tunneling rates for $\alpha = 10$ and $\bar{k} = 2.08$ are 3.0 kHz and 2.3 kHz, and the calculated tunneling rate for $\alpha = 11$ and $\bar{k} = 1.04$ is 4.0 kHz, all of which match the observed tunneling rates reasonably well. However, it should be noted that while these spectra provide a useful basis for understanding the data, an interpretation based solely on these spectra would most likely be too simplistic to be very useful. An accurate model would at minimum need to take into account the excitation of multiple Floquet states by the initial condition, the range of quasimomenta populated after the Raman velocity selection (as we have done in Fig. 6.10), and the averaging over a range of α due to the transverse profile of the optical-lattice beam.

6.4.5 High Temporal Resolution Measurements

All of the data so far in this chapter have been sampled only at a particular phase of the periodic driving, corresponding to integer times in the Hamiltonian (6.11). We will now study the dynamics on a much finer time scale, which will reveal additional interesting aspects of the tunneling dynamics. Figs. 6.25 and 6.26 show the tunneling dynamics for $k\!\!\!^{-} = 2.08$ (for two different values of α), and Fig. 6.27 shows the tunneling dynamics for $k\!\!\!^{-} = 1.04$; in all three figures, the momentum distribution was sampled 10 times per modulation period, and the duration of the measurement covers approximately one full period of the amplitude modulation. Besides the island-tunneling process, which is vis-

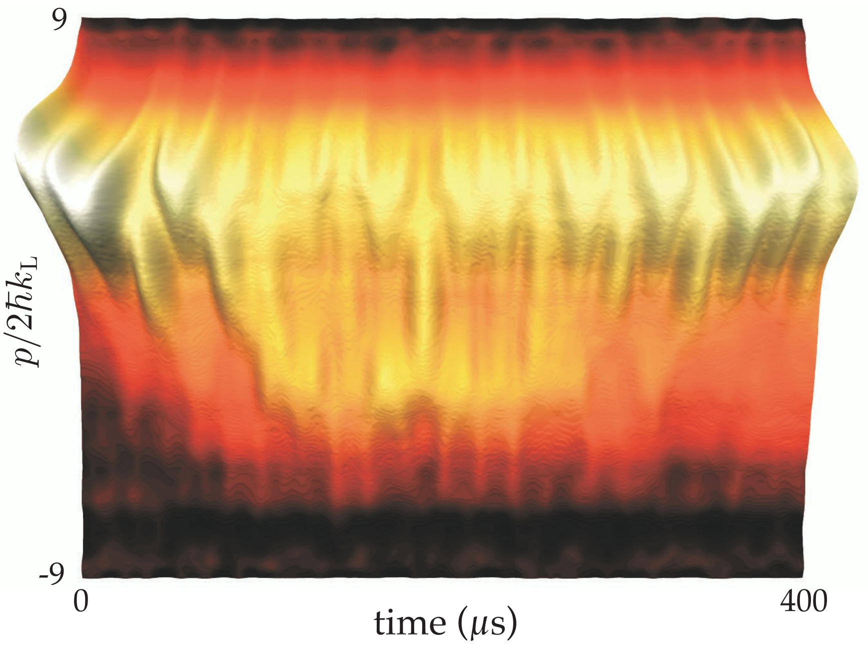

Figure 6.25: Experimental momentum-distribution evolution of chaos-assisted tunneling for $k\!\!\!^{-} = 2.08$ ($T = 20\ \mu$s) and $\alpha = 7.7$. The distribution was sampled every 2 μs out to 400 μs, covering the first full tunneling oscillation. The classical oscillations (with the same period as the modulation period) are evident, as well as more complicated oscillations into the intermediate chaotic/stable region near $p = 0$. The phase space (see Appendix C) is characterized by the two (symmetry-related) tunneling islands as well as a doublet of stable islands near $p = 0$. These distributions were averaged over 10 iterations of the experiment.

ible as the slowest oscillation, there are two other oscillatory motions that are common to the three plots. The more obvious of these features appears as a fast oscillation of the initial peak, with the same period as the modulation of the potential. As the atoms tunnel to the other island, the tunneled peak oscillates in a complementary fashion. This motion can be understood in terms of the classical phase-space dynamics. A particular phase space for this system assumes a particular sampling phase for the dynamics; for the phase spaces in Appendix C, the sampling phase is the same as that used for the previous data in this chapter. To understand the present phenomenon, though, it is necessary to examine the phase space as the sampling phase varies, as illustrated in Fig. 6.28. Because of the periodic time dependence of the potential, the time parameter acts as a

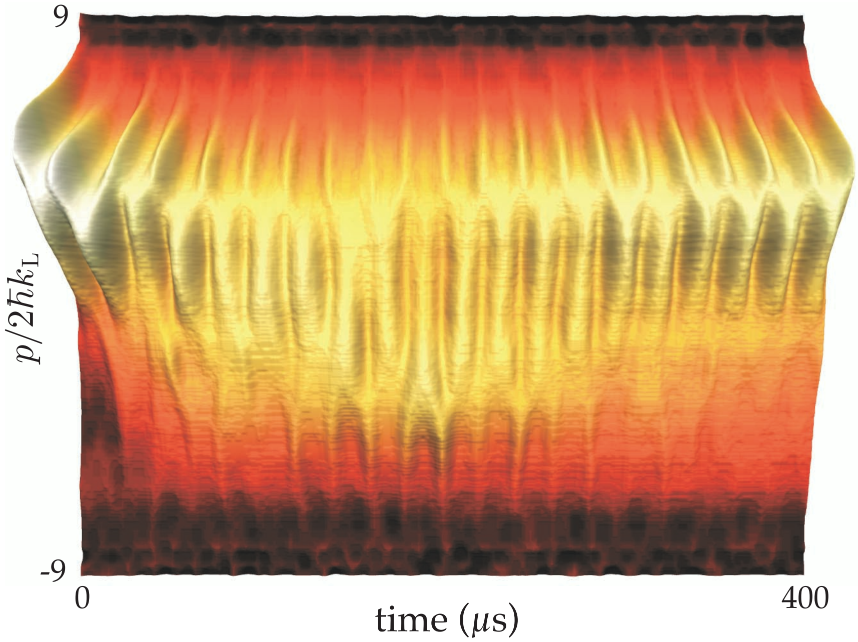

Figure 6.26: Experimental momentum-distribution evolution of chaos-assisted tunneling for $\bar{k} = 2.08$ ($T = 20\ \mu$s) and $\alpha = 11.2$. The distribution was sampled every 2 μs out to 400 μs, covering the first full tunneling oscillation. The conditions are otherwise similar to those in Fig. 6.25; the oscillations in the chaotic region occur in different locations, compared to the previous case. The phase space (see Appendix C) is characterized by the two (symmetry-related) tunneling islands with only small remnants of the island near $p = 0$. These distributions were averaged over 10 iterations of the experiment.

third dimension in phase space. Thus the islands of stability are “flux tubes” that confine classical trajectories in the higher-dimensional phase space [341], and the islands that appear in the phase plots (Poincaré sections) are cross sections of the flux tubes. As time varies continuously, then, the islands move in opposite directions in phase space according to their mean momenta. Additionally, the islands move in the momentum direction, becoming furthest apart in momentum for integer sampling times and closest together for half-integer times. This oscillation is only significant for relatively large values of α (away from the near-integrable regime), because of the mutual repulsion of the three primary resonances in phase space. Thus, the fast oscillations of the experimental

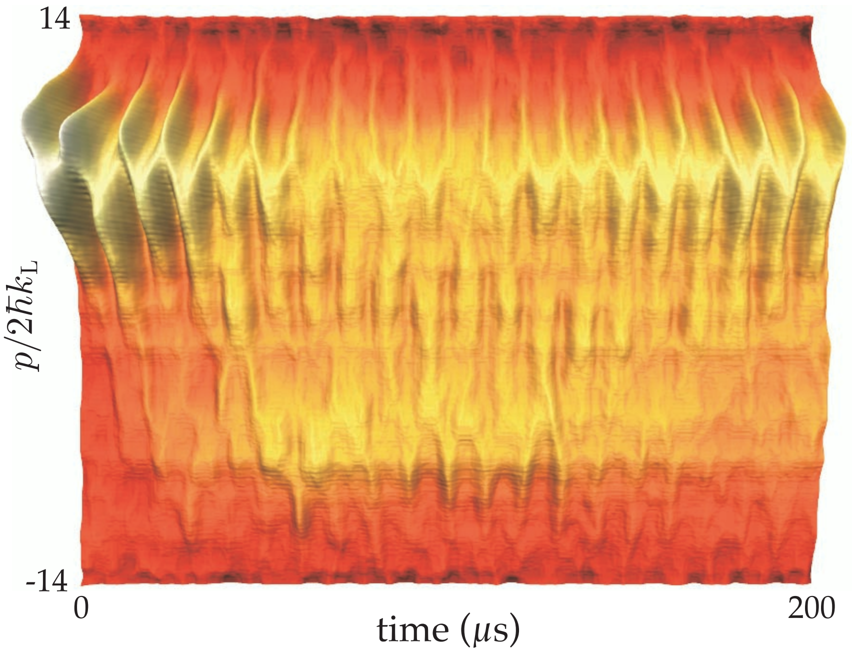

Figure 6.27: Experimental momentum-distribution evolution of chaos-assisted tunneling for $\bar{k} = 1.04$ ($T = 10$ μs) and $\alpha = 10.5$. The distribution was sampled every 1 μs out to 200 μs, covering the first full tunneling oscillation. The oscillations in the chaotic region here are more difficult to see than in Figs. 6.25 and 6.26, because of the smaller signal-to-noise ratio for these experimental conditions (the horizontal stripes are artifacts of the CCD camera). The phase space (see Appendix C) is characterized by the two (symmetry-related) tunneling islands with only small remnants of the island near $p = 0$. These distributions were averaged over 10 iterations of the experiment.

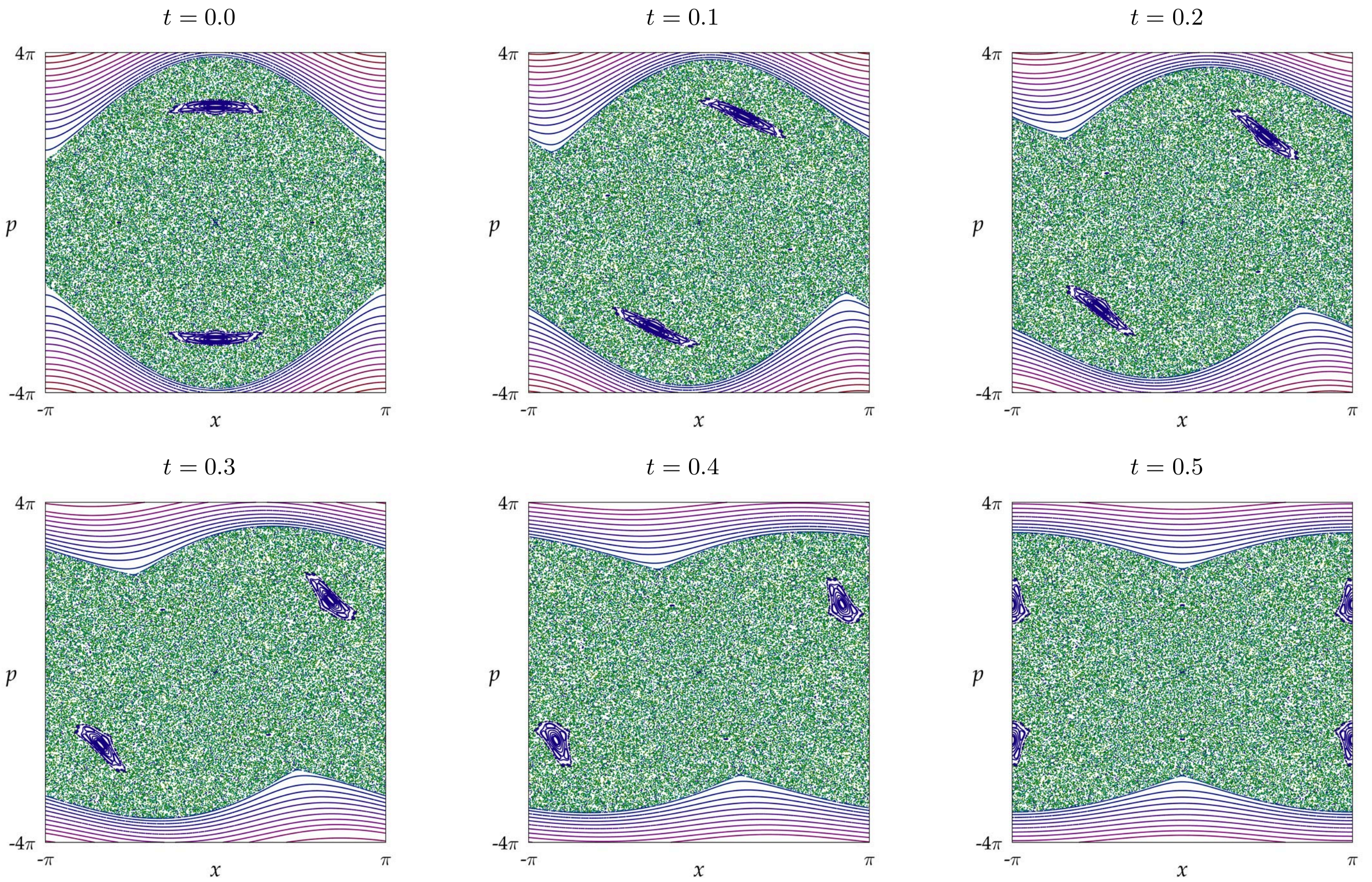

Figure 6.28: Classical phase space (for $\alpha = 10.5$), shown with different sampling phases in the first half of a modulation period. At the start of the modulation period, the islands of stability are separated maximally in momentum, but move inward as they drift away from $x = 0$, and return to their initial momenta by the end of the modulation period. The two islands always remain separated in momentum, and do not cross the $p = 0$ axis. The complementary motions of the two islands produce the fast oscillatory motions in Figs. 6.25-6.27.

momentum distributions can be attributed to the motion of the classical phase-space islands.

The second oscillatory feature is the more relevant effect for demonstrating chaos-assisted tunneling. This oscillation is slower than the classical oscillation but also is substantially faster than the tunneling oscillation. It appears as an occasional enhancement of probability in the (predominantly) chaotic region between the two islands. This effect is particularly dramatic in the case of $\alpha = 7.7$ and $\bar{k} = 2.08$ (Fig. 6.25). Here, the first part of the tunneling transport takes place in (at least) two steps through the chaotic sea, with the first chunk of probability crossing during the third period of the potential and the second crossing during the fifth and sixth periods of the potential. The population in the chaotic region is also enhanced at the time of maximum tunneling, where the population in the islands appears to jump in the center region for a short time (during the tenth modulation period). Similar behavior is evident for $\alpha = 11.2$ and $\bar{k} = 2.08$ (Fig. 6.26); in this case, this third oscillation is not as pronounced, but is still present. The details of this oscillation in the chaotic region are also slightly different than in the previous case. This is especially true at the moment of maximum tunneling, where the atoms are mostly in the two islands (unlike the case before, where the atoms were mostly in the chaotic region), but the chaotic region is populated during the modulation periods just before and after this time. In the case of $\alpha = 10.5$ and $\bar{k} = 1.04$ (Fig. 6.27), this oscillation is less visible because of the poorer signal/noise ratio (notice that the atoms are spread over a much larger region in momentum for this value of $\bar{k}$, resulting in an effectively smaller signal). Nonetheless, the tunneling again proceeds in chunks, with the transport visible as faint ridges crossing the chaotic region, especially near the ends of the first, second, fourth, and fifth modulation periods. The tunneling here in some sense resembles a Landau-Zener crossing [342], because the population crosses between the islands at the times of closest approach.

This appearance of probability in the chaotic region during the tunneling is precisely the behavior expected from the picture of chaos-assisted tunneling of [306, 328] that we mentioned above, where tunneling occurs as parts of the wave packet break away from the initially populated island, transport through the chaotic sea, and then reassemble in the symmetric destination island. We also recall from the analysis of the three-level model (6.15) of chaos-assisted tunneling that near the center of the avoided crossing, the tunneling rate is given by the splitting(s) between the odd-parity regular state taken pairwise with each of the two even-parity (regular/chaotic hybrid) states, which is of the order $\beta/2$. On the other hand, it is the beating between the two hybrid states that determines the appearance of population in the chaotic region, and this beating occurs at a rate of order β. Thus, we expect the oscillation of population to be substantially faster than the tunneling oscillation. The oscillations observed in the experiment do not appear to occur with a single frequency, so it may be necessary to include couplings to other chaotic states in order to account more accurately for this phenomenon.

6.4.6 Transport in the Strongly Coupled Regime

For even larger α than we have considered so far, the two symmetry-related islands of stability disappear, and the quantum transport undergoes a transition to qualitatively different behavior than the above tunneling. This strongly coupled behavior is illustrated in Figs. 6.29 and 6.30, where the momentum-distribution evolution is shown (sampled on a fine time scale) for two large values of α. For $\alpha = 17.0$ (Fig. 6.29), the three primary resonances have disappeared, leaving a chaotic region with only very small stable structures, while for $\alpha = 18.9$ (Fig. 6.30), there is a small island at the center of the phase space (see Appendix C). The experimental measurement shows erratic oscillations of the momentum distributions on a faster time scale than the tunneling observed above.

We can also understand this behavior qualitatively in terms of the Floquet states of the system. For very small α, the Floquet spectrum consists of nearly degenerate doublets associated with KAM tori, and as α increases the doublets break apart as their associated invariant structures become unstable [321, 334]. In the regime that we consider here, where the stable structures have disappeared, the splittings are on the order of the mean level spacing [334] due to level repulsion of the states in the chaotic region [48]. This behavior of the splittings is apparent in the spectra in Figs. 6.23 and 6.24. The Floquet states are no longer well localized in this regime, and thus the initial condition excites several states. The observed behavior is the result of complicated beating between the various populated states, and we expect a time dependence that is faster than the tunneling due to the relatively large splittings involved.

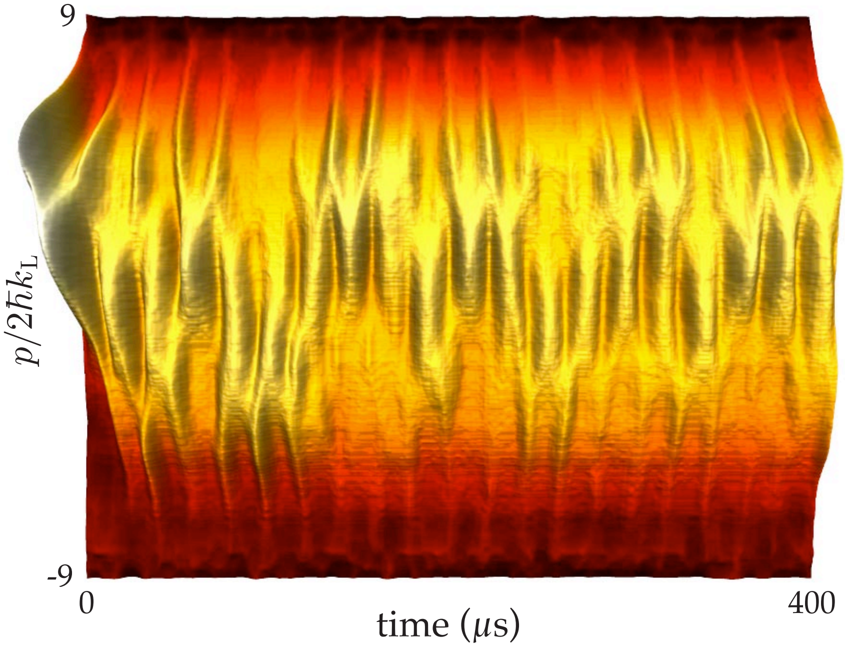

Figure 6.29: Experimental momentum-distribution evolution of chaos-assisted tunneling for $\bar{k} = 2.08$ ($T = 20$ μs) and $\alpha = 17.0$. The distribution was sampled every 2 μs out to 400 μs. The three primary islands of stability have dissolved into the chaotic region in the classical phase space for this value of α (see Appendix C). The experimental momentum distributions show erratic oscillations in time. These distributions were averaged over 10 iterations of the experiment.

6.5 Noise Effects on Tunneling

The tunneling that we have described here is obviously an effect of quantum coherence, and tunneling in classically chaotic systems is expected to be suppressed by dissipation [334, 343], measurement [344], and noise [345]. Here we consider the effects of a noisy perturbation of the optical-lattice intensity, so that the atomic center-of-mass Hamiltonian becomes

$$H = \frac{p^2}{2} - 2\alpha[1 + \varsigma(t)] \cos^2(\pi t) \cos(x) \ , \tag{6.22}$$

where $\varsigma(t)$ is a randomly fluctuating quantity with a probability distribution peaked at and symmetric about zero. This noise signal was generated digitally by picking normally distributed random deviates with a 10 MHz sampling rate. The noise was then

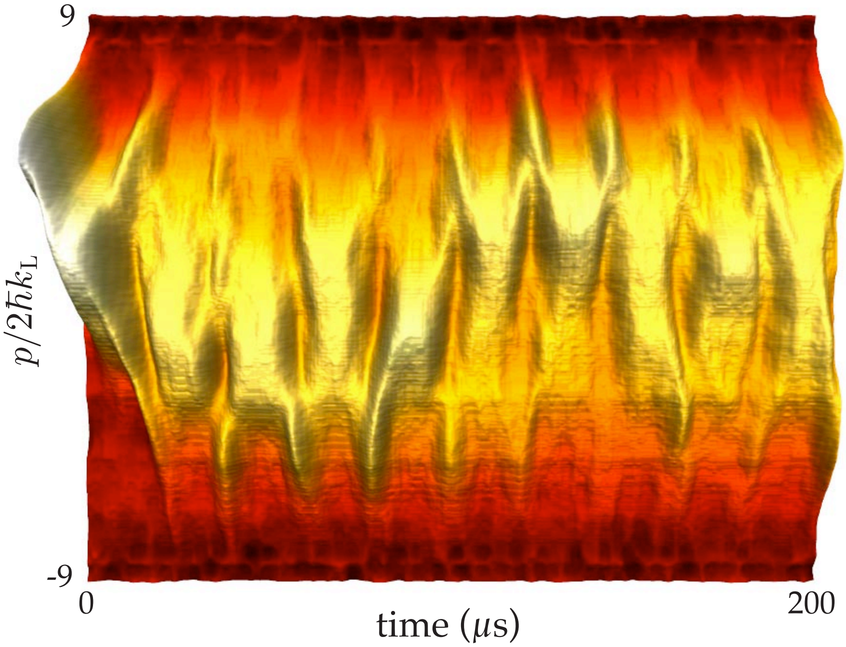

Figure 6.30: Experimental momentum-distribution evolution of chaos-assisted tunneling for $\bar{k} = 2.08$ ($T = 20\ \mu$s) and $\alpha = 18.9$. The distribution was sampled every 1 μs out to 200 μs. The two outer islands of stability are not present in the chaotic region in the classical phase space for this value of α (see Appendix C). The experimental momentum distributions show erratic oscillations in time. These distributions were averaged over 5 iterations of the experiment.

bandwidth-limited by a digital Chebyshev low-pass filter (see Section 6.5.1) before being applied to the AOM control signal. The cutoff frequency (0.5 MHz for the $\bar{k} = 2.08$, 20 μs modulation period data, and 1 MHz for the $\bar{k} = 1.04$, 10 μs modulation period data) was selected to be well within the 10 MHz modulation response of the AOM driver and to make the noise spectrum the same in scaled units for different modulation periods. The rms noise levels $\langle \varsigma^2(t) \rangle^{1/2}$ that we quote correspond to the noise levels after the low-pass filter. Because the instantaneous noise level is proportional to the mean intensity, truncation effects due to noise deviations falling outside the dynamic range of the laser were rare except in the largest noise case that we consider here (62% rms).

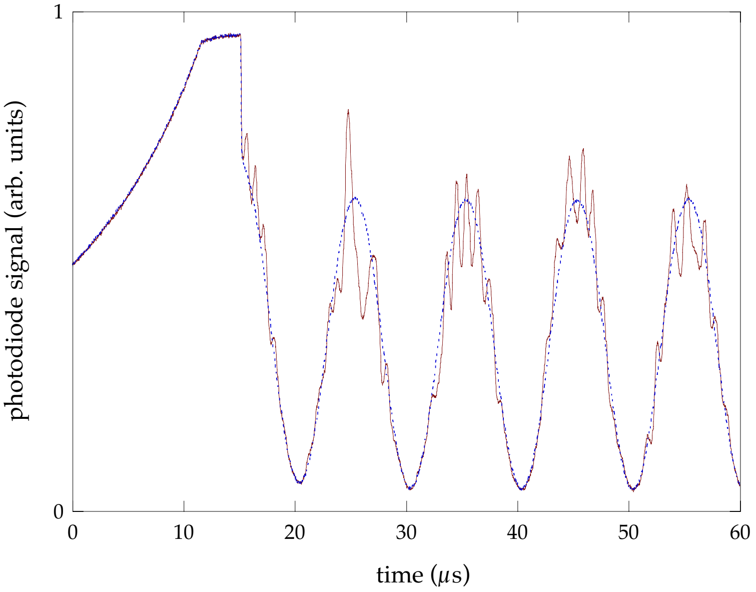

Figure 6.31: Illustration of amplitude noise applied to the optical lattice intensity, as measured by a fast photodiode. The end of the SPASM state-preparation sequence is visible at the beginning of the traces, where the lattice is ramped up and then remains at a high level for several μs after the lattice phase is shifted. The sinusoidal modulations begin immediately after the state preparation, and both the zero (dashed line) and 15.7% (solid line) rms deviation cases are shown here. The noise effects are most pronounced when the lattice is at the highest average intensity because the noise deviation is always proportional to the local average intensity. These traces correspond to the experimental settings for $\bar{k} = 1.04$, where the modulation period is 10 μs, and the noise is filtered with a 1 MHz cutoff frequency.

An example of the optical lattice intensity for one particular realization of the noise is illustrated in Fig. 6.31.

The response of the tunneling oscillations to the noise is illustrated in Fig. 6.32 for $\bar{k} = 2.08$ and 6.33 for $\bar{k} = 1.04$ ($\alpha = 11.2$ in both cases). As one might expect, the oscillations are destroyed as the noise level increases, causing damping of the oscillations on progressively shorter time scales. At the largest levels of noise, classical-like behavior (with noise) is recovered, in that the tunneling oscillations are suppressed. The noise also has the "direct" effect of causing relaxation to $p = 0$, because the noise permits transitions, both quantum and classical, out of the initial island of stability and into the chaotic sea. The more interesting feature of this data, though, is that because the value of α is fixed between the two measurements and the tunneling periods are approximately the same (in scaled units), we can compare the sensitivity of the system

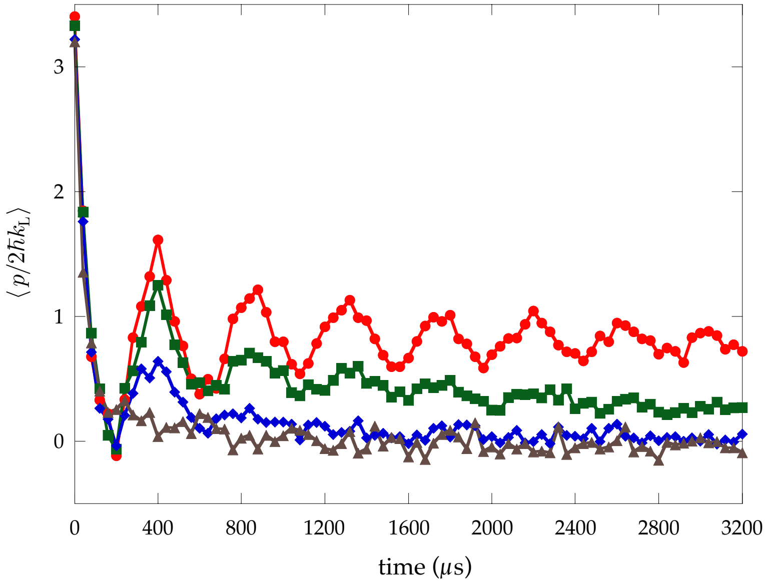

Figure 6.32: Effects of applied amplitude noise on the tunneling oscillations for $\alpha = 11.2$ and $\bar{k} = 2.08$. The rms noise levels are 0% (circles), 15.7% (squares), 31% (diamonds), and 62% (triangles). The tunneling is only completely suppressed at the 62% level, and thus is substantially less sensitive than in the $\bar{k} = 1.04$ case in Fig. 6.33. The data were averaged over 10 realizations of noise, and were sampled every 2 modulation periods.

to the noise for two different values of $\bar{k}$. From the data we see that the tunneling oscillations are suppressed at a much lower level of noise for the $\bar{k} = 1.04$ case than in the $\bar{k} = 2.08$ case (31% vs. 62% rms). Recalling that $\bar{k}$ is the dimensionless Planck constant in scaled units, this comparison indicates that the tunneling in this system is more sensitive to decoherence as the system moves towards the classical limit (i.e., to a larger action scale compared to $\hbar$). This behavior is consistent with theoretical expectations, because for smaller $\bar{k}$, the phase-space structure in chaotic systems saturates on a smaller scale [346], thus being more easily influenced by decoherence (which causes diffusion in phase space). Related experimental results have demonstrated that Schrödinger-cat superposition states in the phase of a cavity field [142], in an atom interferometer [140, 141], and in an ion trap [143, 144] are more sensitive to decoherence when the separation of the components of the state increases (i.e., as the spacing of the interference fringes decreases). The present experimental results are of a fundamen-

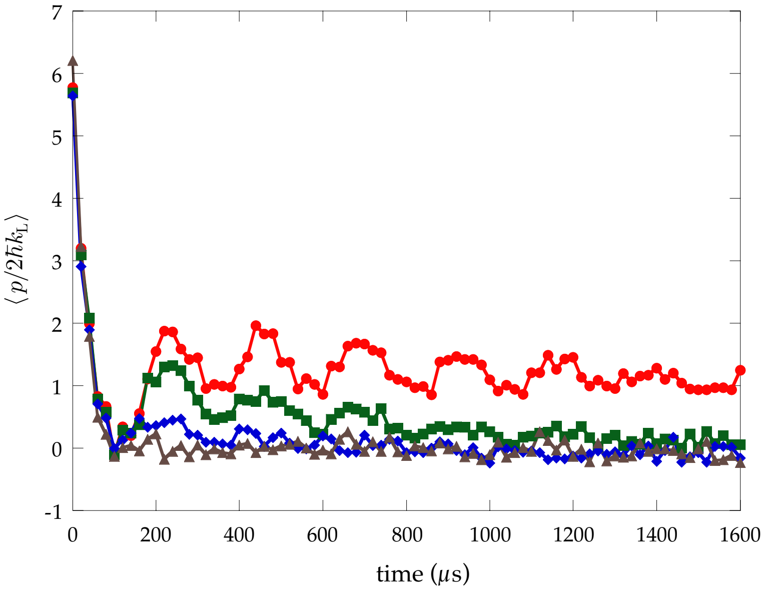

Figure 6.33: Effects of applied amplitude noise on the tunneling oscillations for $\alpha = 11.2$ and $\bar{k} = 1.04$. The rms noise levels are 0% (circles), 7.9% (squares), 15.7% (diamonds), and 31% (triangles). The tunneling is completely suppressed at the 31% level, and thus is more sensitive than in the $\bar{k} = 2.08$ case in Fig. 6.32. The data were averaged over 10 realizations of noise, and were sampled every 2 modulation periods.

tally different nature, though: while these other experiments study the decoherence of a superposition state produced by some state-preparation method, the interferences in the tunneling here are generated dynamically in this nonlinear system. It is also interesting to notice that since the applied noise here leads to a fluctuating force and thus to diffusion of the atomic momenta, this form of noise mimics a continuous measurement of the atomic positions [136, 347]. Thus, we might expect that the system may be more sensitive to noise that mimics a measurement of the atomic momentum, which would cause diffusion of the atomic position, rather than the momentum.

6.5.1 Chebyshev Filter Response

To more completely characterize the noise used in the experiment, we give a description of the filter applied to the noise before it was used to control the optical-lattice intensity. The low-pass Chebyshev filter is specified in terms of three parameters: the cutoff frequency ω_c, the order N, and the passband ripple parameter ε. The frequency

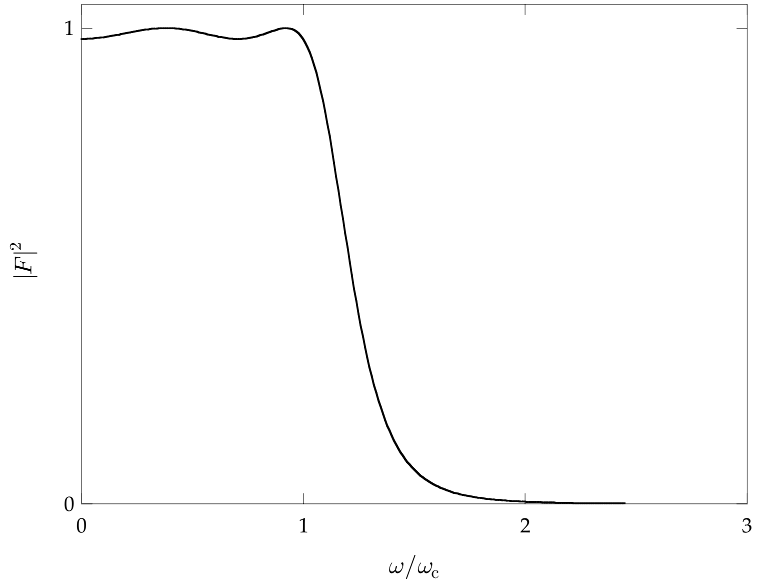

Figure 6.34: Plot of the frequency (power) response function $|F|^2$ of the digital Chebyshev filter used in the experiment, with order $N = 4$ and 0.1 dB passband ripple.

response of this filter is specified by the locations of the N poles in the complex s-plane,

$$s_k = -\sinh(v_0)\cos\left(\frac{k\pi}{2N}\right) - i\cosh(v_0)\sin\left(\frac{k\pi}{2N}\right) \quad , \tag{6.23}$$

where

$$v_0 = \frac{\sinh^{-1}(1/\varepsilon)}{N} \quad , \tag{6.24}$$

for $k = (1-N), (3-N), \ldots, (N+1)$ [348]. Thus the complex frequency-transfer function can be written as

$$F(s) = \eta \prod_k \frac{1}{s - s_k} \quad , \tag{6.25}$$

where $s = -i\omega/\omega_\mathrm{c}$, and η is a normalization factor. The (normalized) squared modulus of the frequency-response function is then [348]

$$|F(s)|^2 = \frac{1}{1 + \varepsilon^2 C_N^2(\omega/\omega_\mathrm{c})} \quad , \tag{6.26}$$

where

$$C_N(\omega) = \cos(N\cos^{-1}(\omega)) \tag{6.27}$$

is the Nth-order Chebyshev polynomial. Thus, the normalization factor can be written as $\eta = (\prod_k s_k)/\sqrt{1 + \varepsilon^2 \cos^2(N\pi/2)}$. The passband ripple is also commonly specified in terms of another parameter a, which is expressed in terms of ε as

$$a = 10\log(1 + \varepsilon^2) \quad , \tag{6.28}$$

if a is quoted in (positive) dB.

In the experiment, a white noise series (i.e., a series of independent, normally distributed, random deviates) was generated at the 10 MHz sampling rate of the Agilent 33250A waveform synthesizer that controlled the 1D optical lattice intensity. To avoid unattainably large deviations, the Gaussian distribution of these deviates was truncated beyond three standard deviations. The waveform was then filtered using the built-in function in LabView. For the $k\!\!\!^{-} = 1$ (10 μs modulation period) case, the 1 MHz cutoff frequency resulted in an effective reduction of the rms deviation of the waveform by a factor of about 0.4965. To produce equivalent noise levels in the $\bar{k} = 2$ ($20\ \mu$s modulation period) case, where the cutoff frequency was 500 kHz, the noise level was first multiplied by $\sqrt{2}$, thus compensating for the different ratio of the sampling frequency to the cutoff frequency.

Appendices

Appendix A

Cesium D Line Data

A.1 Overview

In this appendix we review many of the physical and optical properties of cesium that are relevant to the experiments in this dissertation. In particular, we give parameters that are useful in treating the mechanical effects of light on cesium atoms. The atomic parameters for the D_1 and D_2 optical transitions are given, although only the D_2 transition values are relevant to the work in this dissertation. The measured numbers are given with their original references, and the calculated numbers are presented with an overview of their origin along with references to more comprehensive discussions of their underlying theory.

A.2 Cesium Physical and Optical Properties

Some useful fundamental physical constants are given in Table A.1. The values given are the 1998 CODATA recommended values, as listed in [349]. Some of the overall physical properties of cesium are given in Table A.2. Cesium has 55 electrons, only one of which is in the outermost shell. ^{133}Cs is the only stable isotope of cesium, and is the only isotope we consider in this reference. The mass is taken from the high-precision measurement of [350], and the density, melting point, boiling point, and heat capacities are taken from [351]. The vapor pressure at 25°C and the vapor pressure curve in Fig. A.1 are taken from the vapor pressure model given by [352], which is

$$\begin{aligned}\log_{10} P_{\mathrm{v}} &= -219.482\,00 + \frac{1088.676}{T} \\ &\qquad - 0.083\,361\,85\,T + 94.887\,52 \log_{10} T \qquad \text{(solid phase)} \\ \log_{10} P_{\mathrm{v}} &= 8.221\,27 - \frac{4006.048}{T} \\ &\qquad - 0.000\,601\,94\,T - 0.196\,23 \log_{10} T \qquad \text{(liquid phase)},\end{aligned} \tag{A.1}$$

where P_v is the vapor pressure in torr, and T is the temperature in K. The ionization limit is the minimum energy required to ionize a cesium atom; this value is taken from Ref. [353].

The optical properties of the cesium D line are given in Tables A.3 and A.4. The properties are given separately for each of the two D-line components; the D_2 line (the $6^2\mathrm{S}_{1/2} \longrightarrow 6^2\mathrm{P}_{3/2}$ transition) properties are given in Table A.3, and the optical properties of the D_1 line (the $6^2\mathrm{S}_{1/2} \longrightarrow 6^2\mathrm{P}_{1/2}$ transition) are given in Table A.4. Of these two components, the D_2 transition is of much more relevance to current quantum and atom optics experiments, because it has a cycling transition that is used for cooling and trapping cesium. The frequencies ω_0 of the transitions were measured using an optical frequency comb [354, 355]; the vacuum wavelengths λ and the wave numbers k_L are then determined via the following relations:

$$\lambda = \frac{2\pi c}{\omega_0} \qquad k_\mathrm{L} = \frac{2\pi}{\lambda}\ . \tag{A.2}$$

The air wavelength $\lambda_\mathrm{air} = \lambda/n$ assumes index of refraction of $n = 1.000\,268\,21$, corresponding to dry air at a pressure of 760 torr and a temperature of 22°C. The index of refraction is calculated from the Edlén formula [356]:

$$\begin{aligned} n_\mathrm{air} = 1 + \Bigg[&\left(8342.13 + \frac{2\,406\,030}{130 - \kappa^2} + \frac{15\,997}{38.9 - \kappa^2}\right) \\ &\times \left(\frac{0.001\,388\,23\,P}{1 + 0.003\,671\,T}\right) - f\left(5.722 - 0.0457\kappa^2\right)\Bigg] \times 10^{-8}\ . \end{aligned} \tag{A.3}$$

Here, P is the air pressure in torr, T is the temperature in °C, κ is the vacuum wave number $k_\mathrm{L}/2\pi$ in $\mu\mathrm{m}^{-1}$, and f is the partial pressure of water vapor in the air, in torr. This formula is appropriate for laboratory conditions and has an estimated uncertainty of $\leq 10^{-8}$. The lifetime is an average of two recent measurements; the first [357] used a fast beam laser technique, yielding lifetimes of $35.07(10)$ ns for the $6^2\mathrm{P}_{1/2}$ state and $30.57(7)$ ns for the $6^2\mathrm{P}_{3/2}$ state, while the second [358] used a photon-counting method, giving lifetimes of $34.75(7)$ ns ($6^2\mathrm{P}_{1/2}$) and $30.41(10)$ ns ($6^2\mathrm{P}_{3/2}$) state. The former measurement is taken to supersede several measurements by some of the same experimenters using the same technique [359, 360], and another measurement of comparable quoted uncertainty ($29.9(2)$ ns for the $6^2\mathrm{P}_{3/2}$ state) [361] is excluded because of a substantial disagreement with all recent precision measurements [357]. Another precise measurement of the ratios of the D_1 and D_2 transition strengths [362] was not accounted for in the values quoted here. A general discussion of precision lifetime measurement methods can be found in [363]. Inverting the lifetime gives the decay rate, which is also the natural (homogenous) line width of the emitted radiation.

The recoil velocity v_r is the change in the cesium atomic velocity when absorbing or emitting a resonant photon, and is given by

$$v_\mathrm{r} = \frac{\hbar k}{m} \ . \tag{A.4}$$

The recoil energy $\hbar\omega_\mathrm{r}$ is defined as the kinetic energy of an atom moving with velocity $v = v_\mathrm{r}$, which is

$$\hbar\omega_\mathrm{r} = \frac{\hbar^2 k^2}{2m} \ . \tag{A.5}$$

The Doppler shift of an incident light field of frequency ω_L due to motion of the atom is

$$\Delta\omega_\mathrm{d} = \frac{v_\mathrm{atom}}{c}\omega_\mathrm{L} \tag{A.6}$$

for small atomic velocities relative to c. For an atomic velocity $v_\mathrm{atom} = v_\mathrm{r}$, the Doppler shift is simply $2\omega_\mathrm{r}$. Finally, if one wishes to create a standing wave that is moving with respect to the lab frame, the two traveling-wave components must have a frequency difference determined by the relation

$$v_\mathrm{sw} = \frac{\Delta\omega_\mathrm{sw}}{2\pi}\frac{\lambda}{2} \ , \tag{A.7}$$

because $\Delta\omega_\mathrm{sw}/2\pi$ is the beat frequency of the two waves, and $\lambda/2$ is the spatial periodicity of the standing wave. For a standing wave velocity of v_r, Eq. (A.7) gives $\Delta\omega_\mathrm{sw} = 4\omega_\mathrm{r}$.

A.3 Hyperfine Structure

A.3.1 Energy Level Splittings

The $6^2\mathrm{S}_{1/2} \longrightarrow 6^2\mathrm{P}_{3/2}$ and $6^2\mathrm{S}_{1/2} \longrightarrow 6^2\mathrm{P}_{1/2}$ transitions are the components of a fine-structure doublet, and each of these transitions additionally have hyperfine structure. The fine structure is a result of the coupling between the orbital angular momentum $\mathbf{L}$ of the outer electron and its spin angular momentum $\mathbf{S}$. The total electron angular momentum is then given by

$$\mathbf{J} = \mathbf{L} + \mathbf{S} \ , \tag{A.8}$$

and the corresponding quantum number $\mathbf{J}$ must lie in the range

$$|L - S| \leq J \leq L + S \ . \tag{A.9}$$

(Here we use the convention that the magnitude of $\mathbf{J}$ is $\sqrt{J(J+1)}\hbar$, and the eigenvalue of J_z is $m_J\hbar$.) For the ground state in cesium, $L = 0$ and $S = 1/2$, so $J = 1/2$; for the first excited state, $L = 1$, so $J = 1/2$ or $J = 3/2$. The energy of any particular level is shifted according to the value of J, so the $L = 0 \longrightarrow L = 1$ (D line) transition is split into two components, the D_1 line ($6^2\mathrm{S}_{1/2} \longrightarrow 6^2\mathrm{P}_{1/2}$) and the D_2 line ($6^2\mathrm{S}_{1/2} \longrightarrow 6^2\mathrm{P}_{3/2}$). The meaning of the energy level labels is as follows: the first number is the principal quantum number of the outer electron, the superscript is $2S + 1$, the letter refers to L (i.e. $\mathrm{S} \leftrightarrow L = 0$, $\mathrm{P} \leftrightarrow L = 1$, etc.), and the subscript gives the value of J.

The hyperfine structure is a result of the coupling of $\mathbf{J}$ with the total nuclear angular momentum $\mathbf{I}$. The total atomic angular momentum $\mathbf{F}$ is then given by

$$\mathbf{F} = \mathbf{J} + \mathbf{I} \ . \tag{A.10}$$

As before, the magnitude of $\mathbf{F}$ can take the values

$$|J - I| \leq F \leq J + I \ . \tag{A.11}$$

For the cesium ground state, $J = 1/2$ and $I = 7/2$, so $F = 3$ or $F = 4$. For the excited state of the D_2 line ($6^2\mathrm{P}_{3/2}$), F can take any of the values 2, 3, 4, or 5, and for the D_1 excited state ($6^2\mathrm{P}_{1/2}$), F is either 3 or 4. Again, the atomic energy levels are shifted according to the value of F.

Because the fine structure splitting in cesium is large enough to be resolved by many lasers (~ 42 nm), the two D-line components are generally treated separately. The hyperfine splittings, however, are much smaller, and it is useful to have some formalism to describe the energy shifts. The Hamiltonian that describes the hyperfine structure for each of the D-line components is [364, 365]

$$H_{\mathrm{hfs}} = A_{\mathrm{hfs}} \mathbf{I} \cdot \mathbf{J} + B_{\mathrm{hfs}} \frac{3(\mathbf{I} \cdot \mathbf{J})^2 + \frac{3}{2} \mathbf{I} \cdot \mathbf{J} - I(I+1)J(J+1)}{2I(2I-1)J(2J-1)} \ , \tag{A.12}$$

which leads to a hyperfine energy shift of

$$\Delta E_{\mathrm{hfs}} = \frac{1}{2} A_{\mathrm{hfs}} K + B_{\mathrm{hfs}} \frac{\frac{3}{2} K(K+1) - 2I(I+1)J(J+1)}{2I(2I-1)2J(2J-1)} \ , \tag{A.13}$$

where

$$K = F(F+1) - I(I+1) - J(J+1) \ , \tag{A.14}$$

A_{hfs} is the magnetic dipole constant, and B_{hfs} is the electric quadrupole constant (although the term with B_{hfs} applies only to the excited manifold of the D_2 transition and not to the levels with $J = 1/2$). These constants for the cesium D line are listed in Table A.5. The value for the ground state A_{hfs} constant is the recommended value from Ref. [365]. The constants listed for the $6^2\mathrm{P}_{3/2}$ manifold were taken from a more recent and precise measurement by Tanner and Wieman [366]. The $A_{\rm hfs}$ constant for the $6^2\rm P_{1/2}$ manifold is a weighted average of a frequency-comb measurement ($A_{\rm hfs} = 291.922(20)$ MHz) [355] and a crossed-beam laser spectroscopy measurement ($A_{\rm hfs} = 291.89(8)$ MHz) [367]. The energy shift given by (A.13) is relative to the unshifted value (the "center of gravity") listed in Table A.3. The hyperfine structure of the $\rm D_2$ line, along with the energy splitting values, is diagrammed in Fig. A.2.

A.3.2 Interaction with Static External Fields

A.3.2.1 Magnetic Fields

Each of the hyperfine (F) energy levels contains $2F + 1$ magnetic sublevels that determine the angular distribution of the electron wave function. In the absence of external magnetic fields, these sublevels are degenerate. However, when an external magnetic field is applied, their degeneracy is broken. The Hamiltonian describing the atomic interaction with the magnetic field is

$$\begin{aligned} H_B &= \frac{\mu_{\rm B}}{\hbar}(g_S\mathbf{S} + g_L\mathbf{L} + g_I\mathbf{I})\cdot\mathbf{B} \\ &= \frac{\mu_{\rm B}}{\hbar}(g_S S_z + g_L L_z + g_I I_z)B_z \ , \end{aligned} \qquad (\text{A.15})$$

if we take the magnetic field to be along the z-direction (i.e., along the atomic quantization axis). In this Hamiltonian, the quantities g_S, g_L, and g_I are respectively the electron spin, electron orbital, and nuclear "g-factors" that account for various modifications to the corresponding magnetic dipole moments. The values for these factors are listed in Table A.6, with the sign convention of [365]. The value for g_S has been measured very precisely, and the value given is the CODATA recommended value. The value for g_L is approximately 1, but to account for the finite nuclear mass, the quoted value is given by

$$g_L = 1 - \frac{m_{\rm e}}{m_{\rm nuc}} \ , \qquad (\text{A.16})$$

which is correct to lowest order in $m_{\rm e}/m_{\rm nuc}$, where $m_{\rm e}$ is the electron mass and $m_{\rm nuc}$ is the nuclear mass [368]. The nuclear factor $g_I$accounts for the entire complex structure of the nucleus, and so the quoted value is an experimental measurement [365].

If the energy shift due to the magnetic field is small compared to the fine-structure splitting, then J is a good quantum number and the interaction Hamiltonian can be written as

$$H_B = \frac{\mu_{\rm B}}{\hbar}(g_J J_z + g_I I_z)B_z \ . \qquad (\text{A.17})$$

Here, the *Landé factor* g_J is given by [368]

$$\begin{aligned} g_J &= g_L \frac{J(J+1) - S(S+1) + L(L+1)}{2J(J+1)} + g_S \frac{J(J+1) + S(S+1) - L(L+1)}{2J(J+1)} \\ &\simeq 1 + \frac{J(J+1) + S(S+1) - L(L+1)}{2J(J+1)} \quad , \end{aligned} \tag{A.18}$$

where the second, approximate expression comes from taking the approximate values $g_S \simeq 2$ and $g_L \simeq 1$. The expression here does not include corrections due to the complicated multielectron structure of cesium [368] and QED effects [369], so the values of g_J given in Table A.6 are experimental measurements [365].

If the energy shift due to the magnetic field is small compared to the hyperfine splittings, then similarly F is a good quantum number, so the interaction Hamiltonian becomes [370]

$$H_B = \mu_{\mathrm{B}}\, g_F\, F_z\, B_z \quad , \tag{A.19}$$

where the hyperfine Landé g-factor is given by

$$\begin{aligned} g_F &= g_J \frac{F(F+1) - I(I+1) + J(J+1)}{2F(F+1)} + g_I \frac{F(F+1) + I(I+1) - J(J+1)}{2F(F+1)} \\ &\simeq g_J \frac{F(F+1) - I(I+1) + J(J+1)}{2F(F+1)} \quad . \end{aligned} \tag{A.20}$$

The second, approximate expression here neglects the nuclear term, which is a correction at the level of 0.1%, since g_I is much smaller than g_J.

For weak magnetic fields, the interaction Hamiltonian H_B perturbs the zero-field eigenstates of H_{hfs}. To lowest order, the levels split linearly according to [364]

$$\Delta E_{|F\, m_F\rangle} = \mu_{\mathrm{B}}\, g_F\, m_F\, B_z \quad . \tag{A.21}$$

The approximate g_F factors computed from Eq. (A.20) and the corresponding splittings between adjacent magnetic sublevels are given in Fig. A.2. The splitting in this regime is called the *anomalous Zeeman effect*.

For strong fields where the appropriate interaction is described by Eq. (A.17), the interaction term dominates the hyperfine energies, so that the hyperfine Hamiltonian perturbs the strong-field eigenstates $|J\, m_J\, I\, m_I\rangle$. The energies are then given to lowest order by [371]

$$\begin{aligned} E_{|J\,m_J\,I\,m_I\rangle} = A_{\text{hfs}} m_J m_I & \\ & + B_{\text{hfs}} \frac{3(m_J m_I)^2 + \frac{3}{2} m_J m_I - I(I+1)J(J+1)}{2J(2J-1)I(2I-1)} \\ & + \mu_{\text{B}}(g_J\,m_J + g_I\,m_I)B_z \ . \end{aligned} \tag{A.22}$$

The energy shift in this regime is called the *Paschen-Back effect*.

For intermediate fields, the energy shift is more difficult to calculate, and in general one must numerically diagonalize $H_{\text{hfs}} + H_B$. A notable exception is the *Breit-Rabi formula* [364, 370, 372], which applies to the ground-state manifold of the D transition:

$$E_{|J=1/2\,m_J\,I\,m_I\rangle} = -\frac{\Delta E_{\text{hfs}}}{2(2I+1)} + g_I\,\mu_{\text{B}}\,m\,B \pm \frac{\Delta E_{\text{hfs}}}{2}\left(1 + \frac{4mx}{2I+1} + x^2\right)^{1/2} \ . \tag{A.23}$$

In this formula, $\Delta E_{\text{hfs}} = A_{\text{hfs}}(I + 1/2)$ is the hyperfine splitting, $m = m_I \pm m_J = m_I \pm 1/2$ (where the ± sign is taken to be the same as in (A.23)), and

$$x = \frac{(g_J - g_I)\mu_{\text{B}}\,B}{\Delta E_{\text{hfs}}} \ . \tag{A.24}$$

In order to avoid a sign ambiguity in evaluating (A.23), the more direct formula

$$E_{|J=1/2\,m_J\,I\,m_I\rangle} = \Delta E_{\text{hfs}} \frac{I}{2I+1} \pm \frac{1}{2}(g_J + 2I g_I)\mu_{\text{B}}\,B \tag{A.25}$$

can be used for the two states $m = \pm(I + 1/2)$. The Breit-Rabi formula is useful in finding the small-field shift of the "clock transition" between the $m_F = 0$ sublevels of the two hyperfine ground states, which has no first-order Zeeman shift. Using $m = m_F$ for small magnetic fields, we obtain

$$\Delta\omega_{\text{clock}} = \frac{(g_J - g_I)^2 \mu_{\text{B}}^2}{2\hbar\Delta E_{\text{hfs}}} B^2 \tag{A.26}$$

to second order in the field strength.

If the magnetic field is sufficiently strong that the hyperfine Hamiltonian is negligible compared to the interaction Hamiltonian, then the effect is termed the *normal Zeeman effect* for hyperfine structure. For even stronger fields, there are Paschen-Back and normal Zeeman regimes for the fine structure, where states with different J can mix, and the appropriate form of the interaction energy is Eq. (A.15). Yet stronger fields induce other behaviors, such as the quadratic Zeeman effect [370], which are beyond the scope of the present discussion.

The level structure of cesium in the presence of a magnetic field is shown in Figs. A.4-A.6 in the weak-field (anomalous Zeeman) regime through the hyperfine Paschen-Back regime.

A.3.2.2 Electric Fields

An analogous effect, the *dc Stark effect*, occurs in the presence of a static external electric field. The interaction Hamiltonian in this case is [373–375]

$$H_E = -\frac{1}{2}\alpha_0 E_z^2 - \frac{1}{2}\alpha_2 E_z^2 \frac{3J_z^2 - J(J+1)}{J(2J-1)} \ , \tag{A.27}$$

where we have taken the electric field to be along the z-direction, α_0 and α_2 are respectively termed the *scalar* and *tensor polarizabilities*, and the second (α_2) term is nonvanishing only for the $J = 3/2$ level. The first term shifts all the sublevels with a given J together, so that the Stark shift for the $J = 1/2$ states is trivial. The only mechanism for breaking the degeneracy of the hyperfine sublevels in (A.27) is the J_z contribution in the tensor term. This interaction splits the sublevels such that sublevels with the same value of $|m_F|$ remain degenerate. An expression for the hyperfine Stark shift, assuming a weak enough field that the shift is small compared to the hyperfine splittings, is [373]

$$\begin{aligned} \Delta E_{|J\,I\,F\,m_F\rangle} = &-\frac{1}{2}\alpha_0 E_z^2 \\ &- \frac{1}{2}\alpha_2 E_z^2 \frac{[3m_F^2 - F(F+1)][3X(X-1) - 4F(F+1)J(J+1)]}{(2F+3)(2F+2)F(2F-1)J(2J-1)} \ , \end{aligned} \tag{A.28}$$

where

$$X = F(F+1) + J(J+1) - I(I+1) \ . \tag{A.29}$$

For stronger fields, when the Stark interaction Hamiltonian dominates the hyperfine splittings, the levels split according to the value of $|m_J|$, leading to an electric-field analog to the Paschen-Back effect for magnetic fields.

The static polarizability is also useful in the context of optical traps that are very far off resonance (i.e., several to many nm away from resonance, where the rotating-wave approximation is invalid), since the optical potential is given in terms of the ground-state polarizability as $V = -1/2\alpha_0 E^2$, where E is the amplitude of the optical field. A more accurate expression for the far-off resonant potential arises by replacing the static polarizability with the frequency-dependent polarizability [376]

$$\alpha_0(\omega) = \frac{(\hbar\omega_0)^2 \alpha_0}{(\hbar\omega_0)^2 - (\hbar\omega)^2} \ , \tag{A.30}$$

where ω_0 is the resonant frequency of the lowest-energy transition (i.e., the D_1 resonance); this approximate expression is valid for light tuned to the red of the D_1 line.

The cesium polarizabilities are tabulated in Table A.6. Notice that the *differences* in the excited state and ground state scalar polarizabilities are given, rather than the excited state polarizabilities, since these are the quantities that were actually measured experimentally. The polarizabilities given here are in SI units, although they are often given in cgs units (units of cm^3) or atomic units (units of a_0^3, where the Bohr radius a_0 is given in Table A.1). The SI values can be converted to cgs units via $\alpha[\text{cm}^3] = 5.95531 \times 10^{-22}\,\alpha[\text{Hz/(V/cm)}^2]$ [376], and subsequently the conversion to atomic units is straightforward.

The level structure of cesium in the presence of an external dc electric field is shown in Fig. A.7 in the weak-field regime through the electric hyperfine Paschen-Back regime.

A.3.3 Reduction of the Dipole Operator

The strength of the interaction between cesium and nearly-resonant optical radiation is characterized by the dipole matrix elements. Specifically, $\langle F\ m_F|e\mathbf{r}|F'\ m_F'\rangle$ denotes the matrix element that couples the two hyperfine sublevels $|F\ m_F\rangle$ and $|F'\ m_F'\rangle$ (where the primed variables refer to the excited states and the unprimed variables refer to the ground states). To calculate these matrix elements, it is useful to factor out the angular dependence and write the matrix element as a product of a Clebsch-Gordan coefficient and a reduced matrix element, using the Wigner-Eckart theorem [377]:

$$\langle F\ m_F|er_q|F'\ m_F'\rangle = \langle F\|er\|F'\rangle\langle F\ m_F|F'\ 1\ m_F'\ q\rangle\ . \tag{A.31}$$

Here, q is an index labeling the component of $\mathbf{r}$ in the spherical basis, and the doubled bars indicate that the matrix element is reduced. We can also write (A.31) in terms of a Wigner 3-j symbol as

$$\langle F\ m_F|er_q|F'\ m_F'\rangle = \langle F\|er\|F'\rangle(-1)^{F'-1+m_F}\sqrt{2F+1}\begin{pmatrix} F' & 1 & F \\ m_F' & q & -m_F \end{pmatrix}\ . \tag{A.32}$$

Notice that the 3-j symbol (or, equivalently, the Clebsch-Gordan coefficient) vanishes unless the sublevels satisfy $m_F = m_F' + q$. This reduced matrix element can be further simplified by factoring out the F and F' dependence into a Wigner 6-j symbol, leaving a further reduced matrix element that depends only on the L, S, and J quantum numbers

[377]:

$$\begin{aligned}\langle F\|er\|F'\rangle &\equiv \langle J\ I\ F\|er\|J'\ I'\ F'\rangle \\ &= \langle J\|er\|J'\rangle(-1)^{F'+J+1+I}\sqrt{(2F'+1)(2J+1)}\left\{\begin{matrix} J & J' & 1 \\ F' & F & I\end{matrix}\right\} \ .\end{aligned} \tag{A.33}$$

Again, this new matrix element can be further factored into another 6-j symbol and a reduced matrix element involving only the L quantum number:

$$\begin{aligned}\langle J\|er\|J'\rangle &\equiv \langle L\ S\ J\|er\|L'\ S'\ J'\rangle \\ &= \langle L\|er\|L'\rangle(-1)^{J'+L+1+S}\sqrt{(2J'+1)(2L+1)}\left\{\begin{matrix} L & L' & 1 \\ J' & J & S\end{matrix}\right\} \ .\end{aligned} \tag{A.34}$$

The numerical value of the $\langle J = 1/2\|er\|J' = 3/2\rangle$ (D_2) and the $\langle J = 1/2\|er\|J' = 1/2\rangle$ (D_1) matrix elements are given in Table A.7. These values were calculated from the expression [222]

$$\frac{1}{\tau} = \frac{\omega^3}{3\pi\epsilon_0\hbar c^3}\frac{2J+1}{2J'+1}|\langle J\|e\mathbf{r}\|J'\rangle|^2 \ . \tag{A.35}$$

Note that all the equations we have presented here assume the normalization convention

$$\sum_{M'}\left|\langle J\ M|er|J'\ M'\rangle\right|^2 = \sum_{M'q}\left|\langle J\ M|er_q|J'\ M'\rangle\right|^2 = \left|\langle J\|er\|J'\rangle\right|^2 \ . \tag{A.36}$$

There is, however, another common convention (used in Ref. [363]) that is related to the convention used here by $(J\|er\|J') = \sqrt{2J+1}\,\langle J\|er\|J'\rangle$.

The dipole matrix elements for specific $|F\ m_F\rangle \longrightarrow |F'\ m_F'\rangle$ transitions are listed in Tables A.9-A.20 as multiples of $\langle J\|er\|J'\rangle$. The tables are separated by the ground-state F number (3 or 4) and the polarization of the transition (where σ^+-polarized light couples $m_F \longrightarrow m_F' = m_F + 1$, π-polarized light couples $m_F \longrightarrow m_F' = m_F$, and σ^--polarized light couples $m_F \longrightarrow m_F' = m_F - 1$).

A.4 Resonance Fluorescence

A.4.1 Symmetries of the Dipole Operator

Although the hyperfine structure of cesium is quite complicated, it is possible to take advantage of some symmetries of the dipole operator in order to obtain relatively simple expressions for the photon scattering rates due to resonance fluorescence. In the spirit of treating the D_1 and D_2 lines separately, we will discuss the symmetries in this section implicitly assuming that the light is interacting with only one of the fine-structure components at a time. First, notice that the matrix elements that couple to any single excited state sublevel $|F'\ m'_F\rangle$ add up to a factor that is independent of the particular sublevel chosen,

$$\sum_{q\,F} |\langle F\ (m'_F + q)|er_q|F'\ m'_F\rangle|^2 = \frac{2J+1}{2J'+1}|\langle J\|er\|J'\rangle|^2\ , \tag{A.37}$$

as can be verified from the dipole matrix element tables. This factor of $(2J{+}1)/(2J'{+}1)$ (which is 1 for the D_1 line or $1/2$ for the D_2 line) is the same factor that appears in Eq. (A.35), and is a consequence of the normalization convention (A.36). The interpretation of this symmetry is simply that all the excited state sublevels decay at the same rate Γ, and the decaying population "branches" into various ground state sublevels.

An additional symmetry arises from summing the matrix elements from a single ground-state sublevel to the levels in a particular F' energy level:

$$\begin{aligned} S_{FF'} &:= \sum_q (2F'+1)(2J+1)\begin{Bmatrix} J & J' & 1 \\ F' & F & I \end{Bmatrix}^2 |\langle F\ m_F|F'\ 1\ (m_F - q)\ q\rangle|^2 \\ &= (2F'+1)(2J+1)\begin{Bmatrix} J & J' & 1 \\ F' & F & I \end{Bmatrix}^2\ . \end{aligned} \tag{A.38}$$

This sum $S_{FF'}$ is independent of the particular ground state sublevel chosen, and also obeys the sum rule

$$\sum_{F'} S_{FF'} = 1. \tag{A.39}$$

The interpretation of this symmetry is that for an *isotropic* pump field (i.e. a pumping field with equal components in all *three* possible polarizations), the coupling to the atom is independent of how the population is distributed among the sublevels. These factors $S_{FF'}$ (which are listed in Table A.8) provide a measure of the relative strength of each of the $F \longrightarrow F'$ transitions. In the case where the incident light is isotropic and couples two of the F levels, the atom can be treated as a two-level atom, with an effective dipole moment given by

$$|d_{\text{iso,eff}}(F \longrightarrow F')|^2 = \frac{1}{3}S_{FF'}|\langle J||e\mathbf{r}||J'\rangle|^2\ . \tag{A.40}$$

The factor of $1/3$ in this expression comes from the fact that any given polarization of the field only interacts with one (of three) components of the dipole moment, so that it is appropriate to average over the couplings rather than sum over the couplings as in (A.38).

When the light is detuned far from the atomic resonance ($\Delta \gg \Gamma$), the light interacts with several hyperfine levels. If the detuning is large compared to the excited-state frequency splittings, then the appropriate dipole strength comes from choosing any ground state sublevel $|F\ m_F\rangle$ and summing over its couplings to the excited states. In the case of π-polarized light, the sum is independent of the particular sublevel chosen:

$$\sum_{F'}(2F'+1)(2J+1)\left\{\begin{array}{ccc} J & J' & 1 \\ F' & F & I \end{array}\right\}^2 |\langle F\ m_F|F'\ 1\ m_F\ 0\rangle|^2 = \frac{1}{3}\ . \tag{A.41}$$

This sum leads to an effective dipole moment for far detuned radiation given by

$$|d_{\text{det,eff}}|^2 = \frac{1}{3}|\langle J||e\mathbf{r}||J'\rangle|^2\ . \tag{A.42}$$

The interpretation of this factor is also straightforward. Because the radiation is far detuned, it interacts with the full $J \longrightarrow J'$ transition; however, because the light is linearly polarized, it interacts with only one component of the dipole operator. Then, because of spherical symmetry, $|\hat{d}|^2 \equiv |e\hat{r}|^2 = e^2(|\hat{x}|^2 + |\hat{y}|^2 + |\hat{z}|^2) = 3e^2|\hat{z}|^2$. Note that this factor of 1/3 also appears for $\sigma^{\pm}$ light, but only when the sublevels are uniformly populated (which, of course, is not the equilibrium configuration for these polarizations). The effective dipole moments for this case and the case of isotropic pumping are given in Table A.7.

A.4.2 Resonance Fluorescence in a Two-Level Atom

In these two cases, where we have an effective dipole moment, the atoms behave like simple two-level atoms. A two-level atom interacting with a monochromatic field is described by the *optical Bloch equations* [222],

$$\begin{aligned}
\dot{\rho}_{\text{gg}} &= \frac{i\Omega}{2}(\tilde{\rho}_{\text{ge}} - \tilde{\rho}_{\text{eg}}) + \Gamma\rho_{\text{ee}} \\
\dot{\rho}_{\text{ee}} &= -\frac{i\Omega}{2}(\tilde{\rho}_{\text{ge}} - \tilde{\rho}_{\text{eg}}) - \Gamma\rho_{\text{ee}} \\
\dot{\tilde{\rho}}_{\text{ge}} &= -(\gamma + i\Delta)\tilde{\rho}_{ge} - \frac{i\Omega}{2}(\rho_{\text{ee}} - \rho_{\text{gg}})\ ,
\end{aligned} \tag{A.43}$$

where the ρ_{ij} are the matrix elements of the density operator $\rho := |\psi\rangle\langle\psi|$, $\Omega := -\mathbf{d}\cdot\mathbf{E_0}/\hbar$ is the resonant Rabi frequency, $\mathbf{d}$ is the dipole operator, $\mathbf{E_0}$ is the electric field amplitude ($\mathbf{E} = \mathbf{E_0}\cos\omega_{\text{L}}t$), $\Delta := \omega_{\text{L}} - \omega_0$ is the detuning of the laser field from the atomic resonance, $\Gamma = 1/\tau$ is the natural decay rate of the excited state, $\gamma := \Gamma/2 + \gamma_{\text{c}}$ is the "transverse" decay rate (where γ_{c} is a phenomenological decay rate that models collisions), $\tilde{\rho}_{\text{ge}} := \rho_{\text{ge}}\exp(-i\Delta t)$ is a "slowly varying coherence," and $\tilde{\rho}_{\text{ge}} = \tilde{\rho}^*_{\text{eg}}$. In writing down these equations, we have made the rotating-wave approximation and used a master-equation approach to model spontaneous emission. Additionally, we have ignored any effects due to the motion of the atom and decays or couplings to other auxiliary states. In the case of purely radiative damping ($\gamma = \Gamma/2$), the excited state population settles to the steady state solution

$$\rho_{ee}(t \to \infty) = \frac{(\Omega/\Gamma)^2}{1 + 4\,(\Delta/\Gamma)^2 + 2\,(\Omega/\Gamma)^2} \quad . \tag{A.44}$$

The (steady state) total photon scattering rate (integrated over all directions and frequencies) is then given by $\Gamma\rho_{ee}(t \to \infty)$:

$$R_{\mathrm{sc}} = \left(\frac{\Gamma}{2}\right) \frac{(I/I_{\mathrm{sat}})}{1 + 4\,(\Delta/\Gamma)^2 + (I/I_{\mathrm{sat}})} \quad . \tag{A.45}$$

In writing down this expression, we have defined the *saturation intensity* I_{sat} such that

$$\frac{I}{I_{\mathrm{sat}}} = 2\left(\frac{\Omega}{\Gamma}\right)^2 \quad , \tag{A.46}$$

which gives (with $I = (1/2)c\epsilon_0 E_0^2$)

$$I_{\mathrm{sat}} = \frac{c\epsilon_0\Gamma^2\hbar^2}{4|\hat{\epsilon}\cdot\mathbf{d}|^2} \quad , \tag{A.47}$$

where $\hat{\epsilon}$ is the unit polarization vector of the light field, and $\mathbf{d}$ is the atomic dipole moment. With I_{sat} defined in this way, the on-resonance scattering cross section σ, which is proportional to $R_{\mathrm{sc}}(\Delta = 0)/I$, drops to $1/2$ of its weakly pumped value σ_0 when $I = I_{\mathrm{sat}}$. Additionally, the saturation intensity depends on the polarization of the pumping light as well as the atomic alignment, although the smallest saturation intensity ($I_{\mathrm{sat}(m_F=\pm 4 \to m_F'=\pm 5)}$, discussed below) is often quoted as a representative value. Some saturation intensities corresponding to the discussions in Section A.4.1 are given in Table A.7. A more detailed discussion of the resonance fluorescence from a two-level atom, including the spectral distribution of the emitted radiation, can be found in Ref. [222].

A.4.3 Optical Pumping

If none of the special situations in Section A.4.1 applies to the fluorescence problem of interest, then the effects of optical pumping must be accounted for. A discussion of the effects of optical pumping in an atomic vapor on the saturation intensity using a rate-equation approach can be found in Ref. [378]. Here, however, we will carry out an analysis based on the generalization of the optical Bloch equations (A.43) to the degenerate level structure of cesium. The appropriate master equation for the density matrix of a $F_\mathrm{g} \to F_\mathrm{e}$ hyperfine transition is [224, 379–381]

$$
\begin{aligned}
\frac{\partial}{\partial t}\tilde{\rho}_{\alpha\, m_\alpha,\, \beta\, m_\beta} = {} & \left.\begin{aligned} -\frac{i}{2}\Bigg[& \delta_{\alpha\mathrm{e}}\sum_{m_\mathrm{g}} \Omega(m_\alpha, m_\mathrm{g})\,\tilde{\rho}_{\mathrm{g}\, m_\mathrm{g},\,\beta\, m_\beta} - \\
& \delta_{\mathrm{g}\beta}\sum_{m_\mathrm{e}} \Omega(m_\mathrm{e}, m_\beta)\,\tilde{\rho}_{\alpha\, m_\alpha,\,\mathrm{e}\, m_\mathrm{e}} \\
& + \delta_{\alpha\mathrm{g}}\sum_{m_\mathrm{e}}\Omega^*(m_\mathrm{e}, m_\alpha)\,\tilde{\rho}_{\mathrm{e}\,m_\mathrm{e},\,\beta\,m_\beta} - \\
& \delta_{\mathrm{e}\beta}\sum_{m_\mathrm{g}}\Omega^*(m_\beta, m_\mathrm{g})\,\tilde{\rho}_{\alpha\,m_\alpha,\,\mathrm{g}\,m_\mathrm{g}}\Bigg]
\end{aligned}\right\}\text{(pump field)} \\
& \left.\begin{aligned}
- \quad & \delta_{\alpha\mathrm{e}}\delta_{\mathrm{e}\beta}\,\Gamma\,\tilde{\rho}_{\alpha\,m_\alpha,\,\beta\,m_\beta} \\
- \quad & \delta_{\alpha\mathrm{e}}\delta_{\mathrm{g}\beta}\,\frac{\Gamma}{2}\,\tilde{\rho}_{\alpha\,m_\alpha,\,\beta\,m_\beta} \\
- \quad & \delta_{\alpha\mathrm{g}}\delta_{\mathrm{e}\beta}\,\frac{\Gamma}{2}\,\tilde{\rho}_{\alpha\,m_\alpha,\,\beta\,m_\beta} \\
+ \quad & \delta_{\alpha\mathrm{g}}\delta_{\mathrm{g}\beta}\,\Gamma\sum_{q=-1}^{1}\Big[\tilde{\rho}_{\mathrm{e}\,(m_\alpha+q),\,\mathrm{e}\,(m_\beta+q)} \\
& \qquad \times\langle F_\mathrm{e}\;(m_\alpha+q)|F_\mathrm{g}\;1\;m_\alpha\;q\rangle \\
& \qquad \times\langle F_\mathrm{e}\;(m_\beta+q)|F_\mathrm{g}\;1\;m_\beta\;q\rangle\Big]
\end{aligned}\right\}\text{(dissipation)} \\
& \left.\begin{aligned}
+ \quad & i(\delta_{\alpha\mathrm{e}}\delta_{\mathrm{g}\beta} - \delta_{\alpha\mathrm{g}}\delta_{\mathrm{e}\beta})\;\Delta\;\tilde{\rho}_{\alpha\,m_\alpha,\,\beta\,m_\beta}
\end{aligned}\right\}\text{(free evolution)}
\end{aligned}
\tag{A.48}
$$

where

$$\Omega(m_\mathrm{e}, m_\mathrm{g}) = (-1)^{m_\mathrm{e}-m_\mathrm{g}}\langle F_\mathrm{e}\;m_\mathrm{e}|F_\mathrm{g}\;1\;m_\mathrm{g}\;(m_\mathrm{e}-m_\mathrm{g})\rangle\;\Omega_{-(m_\mathrm{e}-m_\mathrm{g})} \tag{A.49}$$

is the Rabi frequency between two magnetic sublevels,

$$\Omega_{-q} = -\frac{2\langle F_\mathrm{e}||er||F_\mathrm{g}\rangle E^{(+)}_{-q}}{\hbar} \tag{A.50}$$

is the overall Rabi frequency with polarization $(-q)$ ($E^{(+)}_{-q}$ is the field amplitude associated with the positive-rotating component, with polarization $(-q)$ in the spherical basis), and δ is the Kronecker delta symbol. This master equation ignores coupling to F levels other than the ground (g) and excited (e) levels; hence, this equation is appropriate for a cycling transition such as $F = 4 \longrightarrow F' = 5$. Additionally, this master equation assumes purely radiative damping and, as before, does not describe the motion of the atom.

To calculate the scattering rate from a Zeeman-degenerate atom, it is necessary to solve the master equation for the steady-state populations. Then, the total scattering rate is given by

$$R_{\mathrm{sc}} = \Gamma P_{\mathrm{e}} = \Gamma \sum_{m_{\mathrm{e}}} \rho_{\mathrm{e}\,m_{\mathrm{e}},\,\mathrm{e}\,m_{\mathrm{e}}} \quad , \tag{A.51}$$

where P_e is the total population in the excited state. In addition, by including the branching ratios of the spontaneous decay, it is possible to account for the polarization of the emitted radiation. Defining the scattering rate $R_{\mathrm{sc},\,-q}$ for the polarization $(-q)$, we have

$$R_{\mathrm{sc},\,-q} = \sum_{m_{\mathrm{e}}\, m_{\mathrm{g}}} |\langle F_{\mathrm{e}}\; m_{\mathrm{e}} | F_{\mathrm{g}}\; 1\; m_{\mathrm{g}}\; q\rangle|^2 \rho_{\mathrm{e}\,m_{\mathrm{e}},\,\mathrm{e}\,m_{\mathrm{e}}} \quad , \tag{A.52}$$

where, as before, the only nonzero Clebsch-Gordan coefficients occur for $m_{\mathrm{e}} = m_{\mathrm{g}} + q$. As we have defined it here, $q = \pm 1$ corresponds to $\sigma^{\pm}$-polarized radiation, and $q = 0$ corresponds to π-polarized radiation. The angular distribution for the $\sigma^{\pm}$ scattered light is simply the classical radiation pattern for a rotating dipole,

$$f_{\mathrm{sc}}^{\pm}(\theta, \phi) = \frac{3}{16\pi}(1 + \cos^2\theta) \quad , \tag{A.53}$$

and the angular distribution for the π-scattered light is the classical radiation pattern for an oscillating dipole,

$$f_{\mathrm{sc}}^{0}(\theta, \phi) = \frac{3}{8\pi}\sin^2\theta \quad . \tag{A.54}$$

The net angular pattern will result from the interference of these three distributions.

In general, this master equation is difficult to treat analytically, and even a numerical solution of the time-dependent equations can be time-consuming if a large number of degenerate states are involved. In the following discussions, we will only consider some simple light configurations interacting with the $F = 4 \longrightarrow F' = 5$ cycling transition that can be treated analytically. Discussions of Zeeman-degenerate atoms and their spectra can be found in Refs. [381–385].

A.4.3.1 Circularly ($\sigma^{\pm}$) Polarized Light

The cases where the atom is driven by either σ^+ or σ^- light (i.e. circularly polarized light with the atomic quantization axis aligned with the light propagation direction) are straightforward to analyze. In these cases, the light transfers its angular momentum to the atom, and thus the atomic population is transferred to the state with the largest corresponding angular momentum. In the case of the $F = 4 \longrightarrow F' = 5$ cycling transition, a σ^+ driving field will transfer all the atomic population into the $|F = 4, m_F = 4\rangle \longrightarrow |F' = 5, m'_F = 5\rangle$ cycling transition, and a σ^- driving field will transfer all the population into the $|F = 4, m_F = -4\rangle \longrightarrow |F' = 5, m'_F = -5\rangle$ cycling transition. In both cases, the dipole moment $d_{(m_F=\pm4 \rightarrow m_F=\pm5)}$ is given in Table A.7. Note that these dipole moments are only valid in steady state. If the pumping field is weak, the "settling time" of the atom to its steady state can be long, resulting in a time-dependent effective dipole moment (and saturation intensity). For example, beginning with a uniform sublevel population in the $F = 4$ ground level, the saturation intensity will begin at 2.70 mW/cm^2 and equilibrate at 1.10 mW/cm^2 for a circularly polarized pump. Also, if there are any "remixing" effects such as collisions or magnetic fields not aligned with the axis of quantization, the system may equilibrate to some other configuration.

A.4.3.2 Linearly (π) Polarized Light

If the light is π-polarized (linearly polarized along the quantization axis), the equilibrium population distribution is more complicated. In this case, the atoms tend to accumulate in the sublevels near $m = 0$. Gao [381] has derived analytic expressions for the equilibrium populations of each sublevel and showed that the equilibrium excited-state population is given by Eq. (A.44) if Ω^2 is replaced by

$$g_S(2F_\mathrm{e} + 1)|\Omega_0|^2 \ , \tag{A.55}$$

where Ω_0 is the only nonzero component of the Rabi-frequency vector and g_S is a (constant) geometric factor that accounts for the optical pumping. For the cesium $F = 4 \longrightarrow F' = 5$ cycling transition, this factor has the value $g_S = 4420/92377 \approx 0.04785$, leading to a steady-state saturation intensity of $I_\mathrm{sat} = 2.09$ mW/cm^2.

A.4.3.3 One-Dimensional $\sigma^+ - \sigma^-$ Optical Molasses

We now consider the important case of an optical molasses in one dimension formed by one σ^+ and one σ^- field (e.g., by two right-circularly polarized, counterpropagating laser fields). These fields interfere to form a field that is linearly polarized, where the polarization vector traces out a helix in space. Because the light is linearly polarized everywhere, and the steady-state populations are independent of the polarization direction (in the plane orthogonal to the axis of quantization), the analysis of the previous section applies. When we apply the formula (A.45) to calculate the scattering rate, then, we simply use the saturation intensity calculated in the previous section, and use the total intensity (twice the single-beam intensity) for I in the formula.

A.4.3.4 Three-Dimensional Optical Molasses

Finally, we consider an optical molasses in three dimensions, composed of six circularly polarized beams. This optical configuration is found in the commonly used six-beam magneto-optic trap (MOT). However, as we shall see, this optical configuration is quite complicated, and we will only be able to estimate the total rate of fluorescence.

First, we will derive an expression for the electric field and intensity of the light. A typical MOT is formed with two counterpropagating, right-circularly polarized beams along the z-axis and two pairs of counterpropagating, left-circularly polarized beams along the x- and y-axes. Thus, the net electric field is given by

$$\begin{aligned}\mathbf{E}(\mathbf{r},t) = \frac{E_0}{2}e^{-i\omega t}\Bigg[&e^{ikz}\left(\frac{\hat{x}-i\hat{y}}{\sqrt{2}}\right) + e^{-ikz}\left(\frac{\hat{x}+i\hat{y}}{\sqrt{2}}\right)\\ &+ e^{ikx}\left(\frac{\hat{y}+i\hat{z}}{\sqrt{2}}\right) + e^{-ikx}\left(\frac{\hat{y}-i\hat{z}}{\sqrt{2}}\right)\\ &+ e^{iky}\left(\frac{\hat{z}+i\hat{x}}{\sqrt{2}}\right) + e^{-iky}\left(\frac{\hat{z}-i\hat{x}}{\sqrt{2}}\right)\Bigg] + \text{c.c.}\\ = \sqrt{2}E_0 e^{-i\omega t}\Big[&(\cos kz - \sin ky)\hat{x} + (\sin kz + \cos kx)\hat{y} + (\cos ky - \sin kx)\hat{z}\Big] .\end{aligned} \tag{A.56}$$

Hence, the polarization is linear everywhere, but the orientation of the polarization vector is strongly position-dependent. The corresponding intensity is given by

$$I(\mathbf{r}) = I_0\Big[6 - 4(\cos kz \sin ky + \cos ky \sin kx - \sin kz \cos kx)\Big] , \tag{A.57}$$

where $I_0 := (1/2)c\epsilon_0 E_0^2$ is the intensity of a single beam. The six beams form an intensity lattice in space, with an average intensity of $6I_0$ and a discrete set of points with zero intensity. Note, however, that the form of this interference pattern is specific to the set of phases chosen here, since there are more than the minimal number of beams needed to determine the lattice pattern.

It is clear that this situation is quite complicated, because an atom moving in this molasses will experience both a changing intensity and polarization direction. The situation becomes even more complicated when the magnetic field gradient from the MOT is taken into account. However, we can estimate the scattering rate if we ignore the magnetic field and assume that the atoms do not remain localized in the lattice, so that they are, on the average, illuminated by all polarizations with intensity $6I_0$. In this case, the scattering rate is given by the two-level atom expression (A.45), with the saturation intensity corresponding to an isotropic pump field ($I_{\text{sat}} = 2.70\ \text{mW/cm}^2$ for the $F = 4 \longrightarrow F' = 5$ cycling transition, ignoring the scattering from any light tuned to the $F = 3 \longrightarrow F' = 4$ repump transition). Of course, this is almost certainly an overestimate of the effective saturation intensity, since sub-Doppler cooling mechanisms will lead to optical pumping and localization in the light maxima [251]. These effects can be minimized, for example, by using a very large intensity to operate in the saturated limit, where the scattering rate approaches $\Gamma/2$.

This estimate of the scattering rate is quite useful since it can be used to calculate the number of atoms in an optical molasses from a measurement of the optical scattering rate. For example, if the atoms are imaged by a CCD camera, then the number of atoms N_{atoms} is given by

$$N_{\text{atoms}} = \frac{8\pi\Big[1 + 4(\Delta/\Gamma)^2 + (6I_0/I_{\text{sat}})\Big]}{\Gamma(6I_0/I_{\text{sat}})t_{\text{exp}}\eta_{\text{count}}d\Omega} N_{\text{counts}} \ , \tag{A.58}$$

where I_0 is the intensity of one of the six beams, N_{counts} is the integrated number of counts recorded on the CCD chip, t_{exp} is the CCD exposure time, η_{count} is the CCD camera efficiency (in counts/photon), and $d\Omega$ is the solid angle of the light collected by the camera. An expression for the solid angle is

$$d\Omega = \frac{\pi}{4}\left(\frac{f}{(f/\#)d_0}\right)^2 \ , \tag{A.59}$$

where f is the focal length of the imaging lens, d_0 is the object distance (from the MOT to the lens aperture), and $f/\#$ is the f-number of the imaging system.

A.5 Data Tables

Table A.1: Fundamental Physical Constants (1998 CODATA recommended values [349])

Speed of Light	c	$2.997\,924\,58 \times 10^{8}$ m/s (exact)
Permeability of Vacuum	μ_0	$4\pi \times 10^{-7}\mathrm{N/A}^2$ (exact)
Permittivity of Vacuum	ϵ_0	$(\mu_0 c^2)^{-1}$ (exact) $= 8.854\,187\,817\ldots \times 10^{-12}$ F/m
Planck's Constant	h	$6.626\,068\,76(52) \times 10^{-34}$ J·s $4.135\,667\,27(16) \times 10^{-15}$ eV·s
	$\hbar$	$1.054\,571\,596(82) \times 10^{-34}$ J·s $6.582\,118\,89(26) \times 10^{-16}$ eV·s
Elementary Charge	e	$1.602\,176\,462(63) \times 10^{-19}$ C
Bohr Magneton	μ_B	$9.274\,008\,99(37) \times 10^{-24}$ J/T $h \cdot 1.399\,624\,624(56)$ MHz/G
Atomic Mass Unit	u	$1.660\,538\,73(13) \times 10^{-27}$ kg
Electron Mass	m_e	$5.485\,799\,110(12) \times 10^{-4}$ u $9.109\,381\,88(72) \times 10^{-31}$ kg
Bohr Radius	a_0	$0.529\,177\,208\,3(19) \times 10^{-10}$ m
Boltzmann's Constant	k_B	$1.380\,650\,3(24) \times 10^{-23}$ J/K

Table A.2: Cesium Physical Properties.

Atomic Number	Z	55	
Total Nucleons	$Z+N$	133	
Atomic Mass	m	132.905 451 931(27) u $2.206\,946\,50(17) \times 10^{-25}$ kg	[350]
Density at 25°C	ρ_m	1.93 g/cm^3	[351]
Melting Point	T_M	28.44 °C	[351]
Boiling Point	T_B	671 °C	[351]
Specific Heat Capacity	c_p	0.242 J/g·K	[351]
Molar Heat Capacity	C_p	32.210 J/mol·K	[351]
Vapor Pressure at 25°C	P_v	1.3×10^{-6} torr	[352]
Nuclear Spin	I	7/2	
Ionization Limit	E_I	31 406.467 66(15) cm^{-1} 3.893 905(15) eV	[353]

Table A.3: Cesium D_2 ($6^2\mathrm{S}_{1/2} \longrightarrow 6^2\mathrm{P}_{3/2}$) Transition Optical Properties.

Frequency	ω_0	$2\pi \cdot 351.725\ 718\ 50(11)$ THz	[354]
Wavelength (Vacuum)	λ	852.347 275 82(27) nm	
Wavelength (Air)	λ_{air}	852.118 73 nm	
Wave Number (Vacuum)	$k_{\mathrm{L}}/2\pi$	11 732.307 104 9(37) cm^{-1}	
Lifetime	τ	30.517(57) ns	[357, 358]
Decay Rate/ Natural Line Width (FWHM)	Γ	$32.768(62) \times 10^6\ \mathrm{s}^{-1}$ $2\pi \cdot 5.2152(98)$ MHz	
Recoil Velocity	v_{r}	3.5225 mm/s	
Recoil Energy	ω_{r}	$2\pi \cdot 2.0663$ kHz	
Doppler shift ($v_{\mathrm{atom}} = v_{\mathrm{r}}$)	$\Delta\omega_{\mathrm{d}}(v_{\mathrm{atom}} = v_{\mathrm{r}})$	$2\pi \cdot 4.1327$ kHz	
Frequency shift for standing wave moving with $v_{\mathrm{sw}} = v_{\mathrm{r}}$	$\Delta\omega_{\mathrm{sw}}(v_{\mathrm{sw}} = v_{\mathrm{r}})$	$2\pi \cdot 8.2653$ kHz	

Table A.4: Cesium D_1 ($6^2\mathrm{S}_{1/2} \longrightarrow 6^2\mathrm{P}_{1/2}$) Transition Optical Properties.

Frequency	ω_0	$2\pi \cdot 335.116\ 048\ 807(41)$ THz	[355]
Wavelength (Vacuum)	λ	894.592 959 86(11) nm	
Wavelength (Air)	λ_{air}	894.353 09 nm	
Wave Number (Vacuum)	$k_{\mathrm{L}}/2\pi$	11 178.268 160 7(14) cm^{-1}	
Lifetime	τ	34.855(57) ns	[357, 358]
Decay Rate/ Natural Line Width (FWHM)	Γ	$28.690(47) \times 10^6\ \mathrm{s}^{-1}$ $2\pi \cdot 4.5662(75)$ MHz	
Recoil Velocity	v_{r}	3.3561 mm/s	
Recoil Energy	ω_{r}	$2\pi \cdot 1.8758$ kHz	
Doppler shift ($v_{\mathrm{atom}} = v_{\mathrm{r}}$)	$\Delta\omega_{\mathrm{d}}(v_{\mathrm{atom}} = v_{\mathrm{r}})$	$2\pi \cdot 3.7516$ kHz	
Frequency shift for standing wave moving with $v_{\mathrm{sw}} = v_{\mathrm{r}}$	$\Delta\omega_{\mathrm{sw}}(v_{\mathrm{sw}} = v_{\mathrm{r}})$	$2\pi \cdot 7.5031$ kHz	

Table A.5: Cesium D Transition Hyperfine Structure Constants.

Magnetic Dipole Constant, $6^2\mathrm{S}_{1/2}$	$A_{6^2\mathrm{S}_{1/2}}$	$h \cdot 2.298\ 157\ 942\ 5$ GHz (exact)	[365]
Magnetic Dipole Constant, $6^2\mathrm{P}_{1/2}$	$A_{6^2\mathrm{P}_{1/2}}$	$h \cdot 291.920(19)$ MHz	[355, 367]
Magnetic Dipole Constant, $6^2\mathrm{P}_{3/2}$	$A_{6^2\mathrm{P}_{3/2}}$	$h \cdot 50.275(3)$ MHz	[366]
Electric Quadrupole Constant, $6^2\mathrm{P}_{3/2}$	$B_{6^2\mathrm{P}_{3/2}}$	$h \cdot -0.53(2)$ MHz	[366]

Table A.6: Cesium D Transition Magnetic and Electric Field Interaction Parameters.

Electron spin g-factor	g_S	2.002 319 304 373 7(80)	[349]
Electron orbital g-factor	g_L	0.999 995 87	
Fine structure Landé g-factor	g_J ($6^2\mathrm{S}_{1/2}$)	2.002 540 32(20)	[365]
	g_J ($6^2\mathrm{P}_{1/2}$)	0.665 90(9)	[365]
	g_J ($6^2\mathrm{P}_{3/2}$)	1.3340(3)	[365]
Nuclear g-factor	g_I	$-0.000\ 398\ 853\ 95(52)$	[365]
Clock transition Zeeman shift	$\Delta\omega_{\mathrm{clock}}/\mathrm{B}^2$	$2\pi \cdot 427.45$ Hz/G^2	
Ground-state polarizability	$\alpha_0(6^2\mathrm{S}_{1/2})$	$h \cdot 0.1001(20)$ Hz/(V/cm)^2	[376]
D$_1$ scalar polarizability	$\alpha_0(6^2\mathrm{P}_{1/2}) - \alpha_0(6^2\mathrm{S}_{1/2})$	$h \cdot 0.2415(24)$ Hz/(V/cm)^2	[386]
D$_2$ scalar polarizability	$\alpha_0(6^2\mathrm{P}_{3/2}) - \alpha_0(6^2\mathrm{S}_{1/2})$	$h \cdot 0.308\ 60(60)$ Hz/(V/cm)^2	[387]
D$_2$ tensor polarizability	$\alpha_2(6^2\mathrm{P}_{3/2})$	$h \cdot -0.065\ 29(37)$ Hz/(V/cm)^2	[387]

Table A.7: Cesium Dipole Matrix Elements and Saturation Intensities.

D$_2$($6^2\mathrm{S}_{1/2} \longrightarrow 6^2\mathrm{P}_{3/2}$) Transition Dipole Matrix Element	$\langle J = 1/2 \Vert er \Vert J' = 3/2 \rangle$	4.4754(59) ea_0 $3.7944(50) \times 10^{-29}$ C·m
Effective Dipole Moment and Saturation Intensity ($F = 4 \rightarrow F' = 5$) (isotropic light polarization)	$d_{\mathrm{iso,eff}}(F = 4 \rightarrow F' = 5)$	2.0199(27) ea_0 $1.7126(23) \times 10^{-29}$ C·m
	$I_{\mathrm{sat(iso,eff)}}(F = 4 \rightarrow F' = 5)$	2.7020(36) mW/cm^2
Effective Far-Detuned Dipole Moment and Saturation Intensity (D$_2$ line, π-polarized light)	$d_{\mathrm{det,eff,D_2}}$	2.5839(34) ea_0 $2.1907(29) \times 10^{-29}$ C·m
	$I_{\mathrm{sat(det,eff,D_2)}}$	1.6512(22) mW/cm^2
Dipole Moment and Saturation Intensity, $\lvert F = 4, m_F = \pm 4\rangle \rightarrow \lvert F' = 5, m_F' = \pm 5\rangle$ cycling transition ($\sigma^{\pm}$-polarized light)	$d_{(m_F = \pm 4 \rightarrow m_F' = \pm 5)}$	3.1646(42) ea_0 $2.6831(36) \times 10^{-29}$ C·m
	$I_{\mathrm{sat}(m_F = \pm 4 \rightarrow m_F' = \pm 5)}$	1.1008(15) mW/cm^2
D$_1$($6^2\mathrm{S}_{1/2} \longrightarrow 6^2\mathrm{P}_{1/2}$) Transition Dipole Matrix Element	$\langle J = 1/2 \Vert er \Vert J' = 1/2 \rangle$	3.1840(37) ea_0 $2.6995(31) \times 10^{-29}$ C·m
Effective Far-Detuned Dipole Moment and Saturation Intensity (D$_1$ line, π-polarized light)	$d_{\mathrm{det,eff,D_1}}$	1.8383(21) ea_0 $1.5586(18) \times 10^{-29}$ C·m
	$I_{\mathrm{sat(det,eff,D_1)}}$	2.5008(29) mW/cm^2

Table A.8: Cesium Relative Hyperfine Transition Strength Factors $S_{FF'}$.

D$_2$ ($6^2\mathrm{S}_{1/2} \longrightarrow 6^2\mathrm{P}_{3/2}$) transition	S_{45}	11/18	S_{34}	15/56
	S_{44}	7/24	S_{33}	3/8
	S_{43}	7/72	S_{32}	5/14
D$_1$ ($6^2\mathrm{S}_{1/2} \longrightarrow 6^2\mathrm{P}_{1/2}$) transition	S_{44}	5/12	S_{34}	3/4
	S_{43}	7/12	S_{33}	1/4

Table A.9: Cesium D_2 ($6^2S_{1/2} \longrightarrow 6^2P_{3/2}$) Dipole Matrix Elements for σ^+ transitions ($F = 4, m_F \longrightarrow F', m_F' = m_F + 1$), expressed as multiples of $\langle J = 1/2||er||J' = 3/2\rangle$.

$m_F =$	-4	-3	-2	-1	0	1	2	3	4
$F' = 5$	$\sqrt{\frac{1}{90}}$	$\sqrt{\frac{1}{30}}$	$\sqrt{\frac{1}{15}}$	$\sqrt{\frac{1}{9}}$	$\sqrt{\frac{1}{6}}$	$\sqrt{\frac{7}{30}}$	$\sqrt{\frac{14}{45}}$	$\sqrt{\frac{2}{5}}$	$\sqrt{\frac{1}{2}}$
$F' = 4$	$\sqrt{\frac{7}{120}}$	$\sqrt{\frac{49}{480}}$	$\sqrt{\frac{21}{160}}$	$\sqrt{\frac{7}{48}}$	$\sqrt{\frac{7}{48}}$	$\sqrt{\frac{21}{160}}$	$\sqrt{\frac{49}{480}}$	$\sqrt{\frac{7}{120}}$	
$F' = 3$	$\sqrt{\frac{7}{72}}$	$\sqrt{\frac{7}{96}}$	$\sqrt{\frac{5}{96}}$	$\sqrt{\frac{5}{144}}$	$\sqrt{\frac{1}{48}}$	$\sqrt{\frac{1}{96}}$	$\sqrt{\frac{1}{288}}$		

Table A.10: Cesium D_2 ($6^2S_{1/2} \longrightarrow 6^2P_{3/2}$) Dipole Matrix Elements for π transitions ($F = 4, m_F \longrightarrow F', m_F' = m_F$), expressed as multiples of $\langle J = 1/2||er||J' = 3/2\rangle$.

$m_F =$	-4	-3	-2	-1	0	1	2	3	4
$F' = 5$	$-\sqrt{\frac{1}{10}}$	$-\sqrt{\frac{8}{45}}$	$-\sqrt{\frac{7}{30}}$	$-\sqrt{\frac{4}{15}}$	$-\sqrt{\frac{5}{18}}$	$-\sqrt{\frac{4}{15}}$	$-\sqrt{\frac{7}{30}}$	$-\sqrt{\frac{8}{45}}$	$-\sqrt{\frac{1}{10}}$
$F' = 4$	$-\sqrt{\frac{7}{30}}$	$-\sqrt{\frac{21}{160}}$	$-\sqrt{\frac{7}{120}}$	$-\sqrt{\frac{7}{480}}$	0	$\sqrt{\frac{7}{480}}$	$\sqrt{\frac{7}{120}}$	$\sqrt{\frac{21}{160}}$	$\sqrt{\frac{7}{30}}$
$F' = 3$		$\sqrt{\frac{7}{288}}$	$\sqrt{\frac{1}{24}}$	$\sqrt{\frac{5}{96}}$	$\sqrt{\frac{1}{18}}$	$\sqrt{\frac{5}{96}}$	$\sqrt{\frac{1}{24}}$	$\sqrt{\frac{7}{288}}$	

Table A.11: Cesium D_2 ($6^2S_{1/2} \longrightarrow 6^2P_{3/2}$) Dipole Matrix Elements for σ^- transitions ($F = 4, m_F \longrightarrow F', m_F' = m_F - 1$), expressed as multiples of $\langle J = 1/2||er||J' = 3/2\rangle$.

$m_F =$	-4	-3	-2	-1	0	1	2	3	4
$F' = 5$	$\sqrt{\frac{1}{2}}$	$\sqrt{\frac{2}{5}}$	$\sqrt{\frac{14}{45}}$	$\sqrt{\frac{7}{30}}$	$\sqrt{\frac{1}{6}}$	$\sqrt{\frac{1}{9}}$	$\sqrt{\frac{1}{15}}$	$\sqrt{\frac{1}{30}}$	$\sqrt{\frac{1}{90}}$
$F' = 4$		$-\sqrt{\frac{7}{120}}$	$-\sqrt{\frac{49}{480}}$	$-\sqrt{\frac{21}{160}}$	$-\sqrt{\frac{7}{48}}$	$-\sqrt{\frac{7}{48}}$	$-\sqrt{\frac{21}{160}}$	$-\sqrt{\frac{49}{480}}$	$-\sqrt{\frac{7}{120}}$
$F' = 3$			$\sqrt{\frac{1}{288}}$	$\sqrt{\frac{1}{96}}$	$\sqrt{\frac{1}{48}}$	$\sqrt{\frac{5}{144}}$	$\sqrt{\frac{5}{96}}$	$\sqrt{\frac{7}{96}}$	$\sqrt{\frac{7}{72}}$

Table A.12: Cesium D_2 ($6^2S_{1/2} \longrightarrow 6^2P_{3/2}$) Dipole Matrix Elements for σ^+ transitions ($F = 3, m_F \longrightarrow F', m'_F = m_F + 1$), expressed as multiples of $\langle J = 1/2||er||J' = 3/2\rangle$.

$m_F =$	-3	-2	-1	0	1	2	3
$F' = 4$	$\sqrt{\frac{5}{672}}$	$\sqrt{\frac{5}{224}}$	$\sqrt{\frac{5}{112}}$	$\sqrt{\frac{25}{336}}$	$\sqrt{\frac{25}{224}}$	$\sqrt{\frac{5}{32}}$	$\sqrt{\frac{5}{24}}$
$F' = 3$	$\sqrt{\frac{3}{32}}$	$\sqrt{\frac{5}{32}}$	$\sqrt{\frac{3}{16}}$	$\sqrt{\frac{3}{16}}$	$\sqrt{\frac{5}{32}}$	$\sqrt{\frac{3}{32}}$	
$F' = 2$	$\sqrt{\frac{5}{14}}$	$\sqrt{\frac{5}{21}}$	$\sqrt{\frac{1}{7}}$	$\sqrt{\frac{1}{14}}$	$\sqrt{\frac{1}{42}}$		

Table A.13: Cesium D_2 ($6^2S_{1/2} \longrightarrow 6^2P_{3/2}$) Dipole Matrix Elements for π transitions ($F = 3, m_F \longrightarrow F', m'_F = m_F$), expressed as multiples of $\langle J = 1/2||er||J' = 3/2\rangle$.

$m_F =$	-3	-2	-1	0	1	2	3
$F' = 4$	$-\sqrt{\frac{5}{96}}$	$-\sqrt{\frac{5}{56}}$	$-\sqrt{\frac{25}{224}}$	$-\sqrt{\frac{5}{42}}$	$-\sqrt{\frac{25}{224}}$	$-\sqrt{\frac{5}{56}}$	$-\sqrt{\frac{5}{96}}$
$F' = 3$	$-\sqrt{\frac{9}{32}}$	$-\sqrt{\frac{1}{8}}$	$-\sqrt{\frac{1}{32}}$	0	$\sqrt{\frac{1}{32}}$	$\sqrt{\frac{1}{8}}$	$\sqrt{\frac{9}{32}}$
$F' = 2$		$\sqrt{\frac{5}{42}}$	$\sqrt{\frac{4}{21}}$	$\sqrt{\frac{3}{14}}$	$\sqrt{\frac{4}{21}}$	$\sqrt{\frac{5}{42}}$	

Table A.14: Cesium D_2 ($6^2S_{1/2} \longrightarrow 6^2P_{3/2}$) Dipole Matrix Elements for σ^- transitions ($F = 3, m_F \longrightarrow F', m'_F = m_F - 1$), expressed as multiples of $\langle J = 1/2||er||J' = 3/2\rangle$.

$m_F =$	-3	-2	-1	0	1	2	3
$F' = 4$	$\sqrt{\frac{5}{24}}$	$\sqrt{\frac{5}{32}}$	$\sqrt{\frac{25}{224}}$	$\sqrt{\frac{25}{336}}$	$\sqrt{\frac{5}{112}}$	$\sqrt{\frac{5}{224}}$	$\sqrt{\frac{5}{672}}$
$F' = 3$		$-\sqrt{\frac{3}{32}}$	$-\sqrt{\frac{5}{32}}$	$-\sqrt{\frac{3}{16}}$	$-\sqrt{\frac{3}{16}}$	$-\sqrt{\frac{5}{32}}$	$-\sqrt{\frac{3}{32}}$
$F' = 2$			$\sqrt{\frac{1}{42}}$	$\sqrt{\frac{1}{14}}$	$\sqrt{\frac{1}{7}}$	$\sqrt{\frac{5}{21}}$	$\sqrt{\frac{5}{14}}$

Table A.15: Cesium D$_1$ ($6^2\mathrm{S}_{1/2} \longrightarrow 6^2\mathrm{P}_{1/2}$) Dipole Matrix Elements for σ^+ transitions ($F = 4, m_F \longrightarrow F', m'_F = m_F + 1$), expressed as multiples of $\langle J = 1/2||er||J' = 1/2\rangle$.

$m_F =$	-4	-3	-2	-1	0	1	2	3	4
$F' = 4$	$\sqrt{\frac{1}{12}}$	$\sqrt{\frac{7}{48}}$	$\sqrt{\frac{3}{16}}$	$\sqrt{\frac{5}{24}}$	$\sqrt{\frac{5}{24}}$	$\sqrt{\frac{3}{16}}$	$\sqrt{\frac{7}{48}}$	$\sqrt{\frac{1}{12}}$	
$F' = 3$	$\sqrt{\frac{7}{12}}$	$\sqrt{\frac{7}{16}}$	$\sqrt{\frac{5}{16}}$	$\sqrt{\frac{5}{24}}$	$\sqrt{\frac{1}{8}}$	$\sqrt{\frac{1}{16}}$	$\sqrt{\frac{1}{48}}$		

Table A.16: Cesium D$_1$ ($6^2\mathrm{S}_{1/2} \longrightarrow 6^2\mathrm{P}_{1/2}$) Dipole Matrix Elements for π transitions ($F = 4, m_F \longrightarrow F', m'_F = m_F$), expressed as multiples of $\langle J = 1/2||er||J' = 1/2\rangle$.

$m_F =$	-4	-3	-2	-1	0	1	2	3	4
$F' = 4$	$-\sqrt{\frac{1}{3}}$	$-\sqrt{\frac{3}{16}}$	$-\sqrt{\frac{1}{12}}$	$-\sqrt{\frac{1}{48}}$	0	$\sqrt{\frac{1}{48}}$	$\sqrt{\frac{1}{12}}$	$\sqrt{\frac{3}{16}}$	$\sqrt{\frac{1}{3}}$
$F' = 3$		$\sqrt{\frac{7}{48}}$	$\sqrt{\frac{1}{4}}$	$\sqrt{\frac{5}{16}}$	$\sqrt{\frac{1}{3}}$	$\sqrt{\frac{5}{16}}$	$\sqrt{\frac{1}{4}}$	$\sqrt{\frac{7}{48}}$	

Table A.17: Cesium D$_1$ ($6^2\mathrm{S}_{1/2} \longrightarrow 6^2\mathrm{P}_{1/2}$) Dipole Matrix Elements for σ^- transitions ($F = 4, m_F \longrightarrow F', m'_F = m_F - 1$), expressed as multiples of $\langle J = 1/2||er||J' = 1/2\rangle$.

$m_F =$	-4	-3	-2	-1	0	1	2	3	4
$F' = 4$		$-\sqrt{\frac{1}{12}}$	$-\sqrt{\frac{7}{48}}$	$-\sqrt{\frac{3}{16}}$	$-\sqrt{\frac{5}{24}}$	$-\sqrt{\frac{5}{24}}$	$-\sqrt{\frac{3}{16}}$	$-\sqrt{\frac{7}{48}}$	$-\sqrt{\frac{1}{12}}$
$F' = 3$			$\sqrt{\frac{1}{48}}$	$\sqrt{\frac{1}{16}}$	$\sqrt{\frac{1}{8}}$	$\sqrt{\frac{5}{24}}$	$\sqrt{\frac{5}{16}}$	$\sqrt{\frac{7}{16}}$	$\sqrt{\frac{7}{12}}$

Table A.18: Cesium D_1 ($6^2S_{1/2} \longrightarrow 6^2P_{1/2}$) Dipole Matrix Elements for σ^+ transitions ($F = 3, m_F \longrightarrow F', m'_F = m_F + 1$), expressed as multiples of $\langle J = 1/2||er||J' = 1/2\rangle$.

$m_F =$	-3	-2	-1	0	1	2	3
$F' = 4$	$-\sqrt{\frac{1}{48}}$	$-\sqrt{\frac{1}{16}}$	$-\sqrt{\frac{1}{8}}$	$-\sqrt{\frac{5}{24}}$	$-\sqrt{\frac{5}{16}}$	$-\sqrt{\frac{7}{16}}$	$-\sqrt{\frac{7}{12}}$
$F' = 3$	$-\sqrt{\frac{1}{16}}$	$-\sqrt{\frac{5}{48}}$	$-\sqrt{\frac{1}{8}}$	$-\sqrt{\frac{1}{8}}$	$-\sqrt{\frac{5}{48}}$	$-\sqrt{\frac{1}{16}}$	

Table A.19: Cesium D_1 ($6^2S_{1/2} \longrightarrow 6^2P_{1/2}$) Dipole Matrix Elements for π transitions ($F = 3, m_F \longrightarrow F', m'_F = m_F$), expressed as multiples of $\langle J = 1/2||er||J' = 1/2\rangle$.

$m_F =$	-3	-2	-1	0	1	2	3
$F' = 4$	$\sqrt{\frac{7}{48}}$	$\sqrt{\frac{1}{4}}$	$\sqrt{\frac{5}{16}}$	$\sqrt{\frac{1}{3}}$	$\sqrt{\frac{5}{16}}$	$\sqrt{\frac{1}{4}}$	$\sqrt{\frac{7}{48}}$
$F' = 3$	$\sqrt{\frac{3}{16}}$	$\sqrt{\frac{1}{12}}$	$\sqrt{\frac{1}{48}}$	0	$-\sqrt{\frac{1}{48}}$	$-\sqrt{\frac{1}{12}}$	$-\sqrt{\frac{3}{16}}$

Table A.20: Cesium D_1 ($6^2S_{1/2} \longrightarrow 6^2P_{1/2}$) Dipole Matrix Elements for σ^- transitions ($F = 3, m_F \longrightarrow F', m'_F = m_F - 1$), expressed as multiples of $\langle J = 1/2||er||J' = 1/2\rangle$.

$m_F =$	-3	-2	-1	0	1	2	3
$F' = 4$	$-\sqrt{\frac{7}{12}}$	$-\sqrt{\frac{7}{16}}$	$-\sqrt{\frac{5}{16}}$	$-\sqrt{\frac{5}{24}}$	$-\sqrt{\frac{1}{8}}$	$-\sqrt{\frac{1}{16}}$	$-\sqrt{\frac{1}{48}}$
$F' = 3$		$\sqrt{\frac{1}{16}}$	$\sqrt{\frac{5}{48}}$	$\sqrt{\frac{1}{8}}$	$\sqrt{\frac{1}{8}}$	$\sqrt{\frac{5}{48}}$	$\sqrt{\frac{1}{16}}$

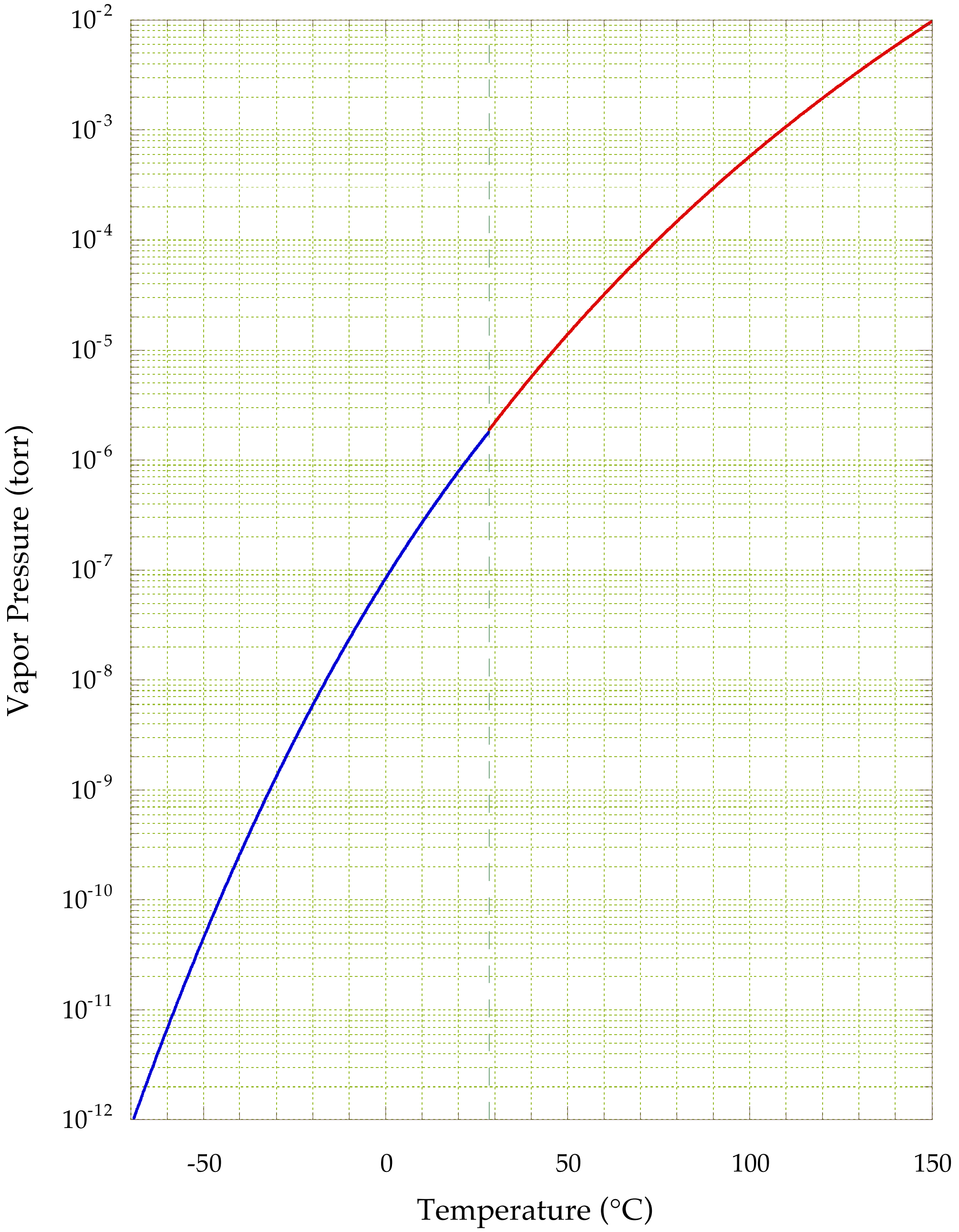

Figure A.1: Vapor pressure of cesium from the model of Eqs. (A.1). The vertical line indicates the melting point.

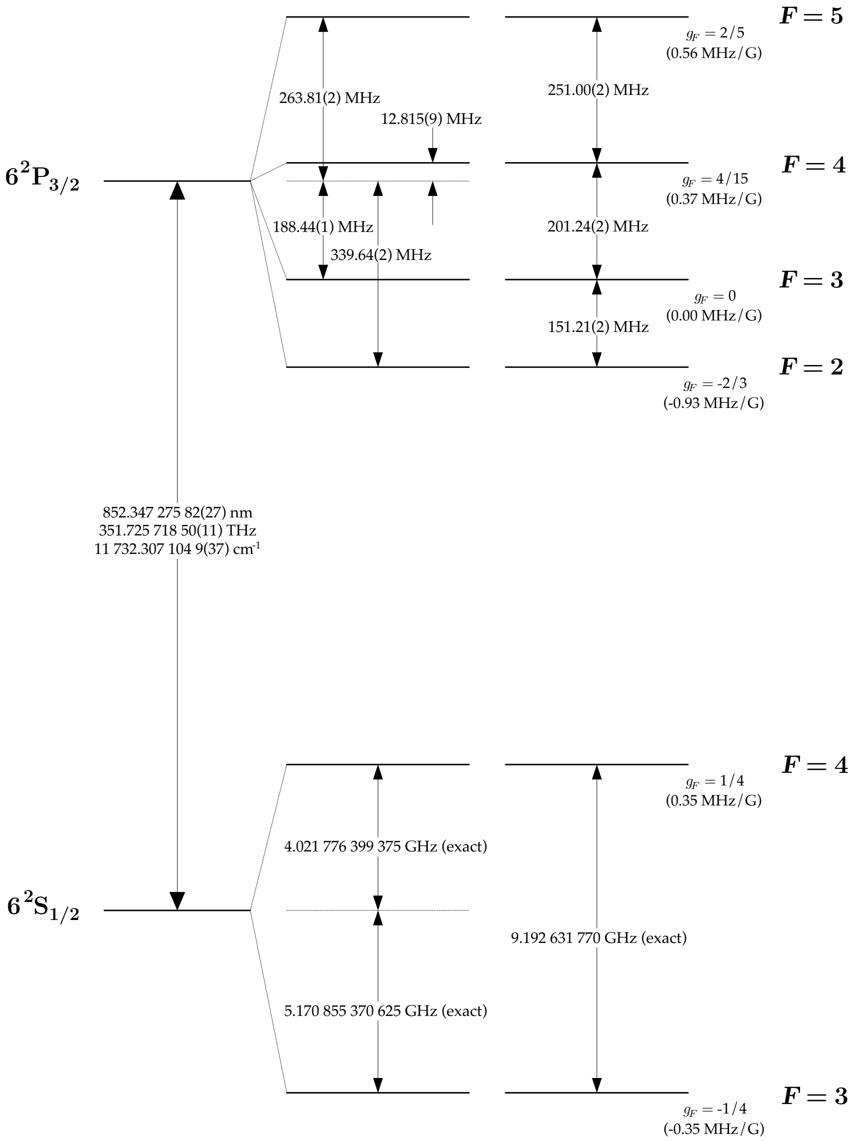
$6^2P_{3/2}$
$6^2S_{1/2}$
F = 5
F = 4
F = 3
F = 2
F = 4
F = 3
263.81(2) MHz
12.815(9) MHz
188.44(1) MHz
339.64(2) MHz
251.00(2) MHz
201.24(2) MHz
151.21(2) MHz
$g_F = 2/5$
(0.56 MHz/G)
$g_F = 4/15$
(0.37 MHz/G)
$g_F = 0$
(0.00 MHz/G)
$g_F = -2/3$
(-0.93 MHz/G)
852.347 275 82(27) nm
351.725 718 50(11) THz
11 732.307 104 9(37) cm^{-1}
4.021 776 399 375 GHz (exact)
5.170 855 370 625 GHz (exact)
9.192 631 770 GHz (exact)
$g_F = 1/4$
(0.35 MHz/G)
$g_F = -1/4$
(-0.35 MHz/G)

Figure A.2: Cesium D_2 transition hyperfine structure, with frequency splittings between the hyperfine energy levels. The excited-state values are taken from [366], and the ground-state values are exact, as a result of the current definition of the second. The approximate Landé g_F-factors for each level are also given, with the corresponding Zeeman splittings between adjacent magnetic sublevels.

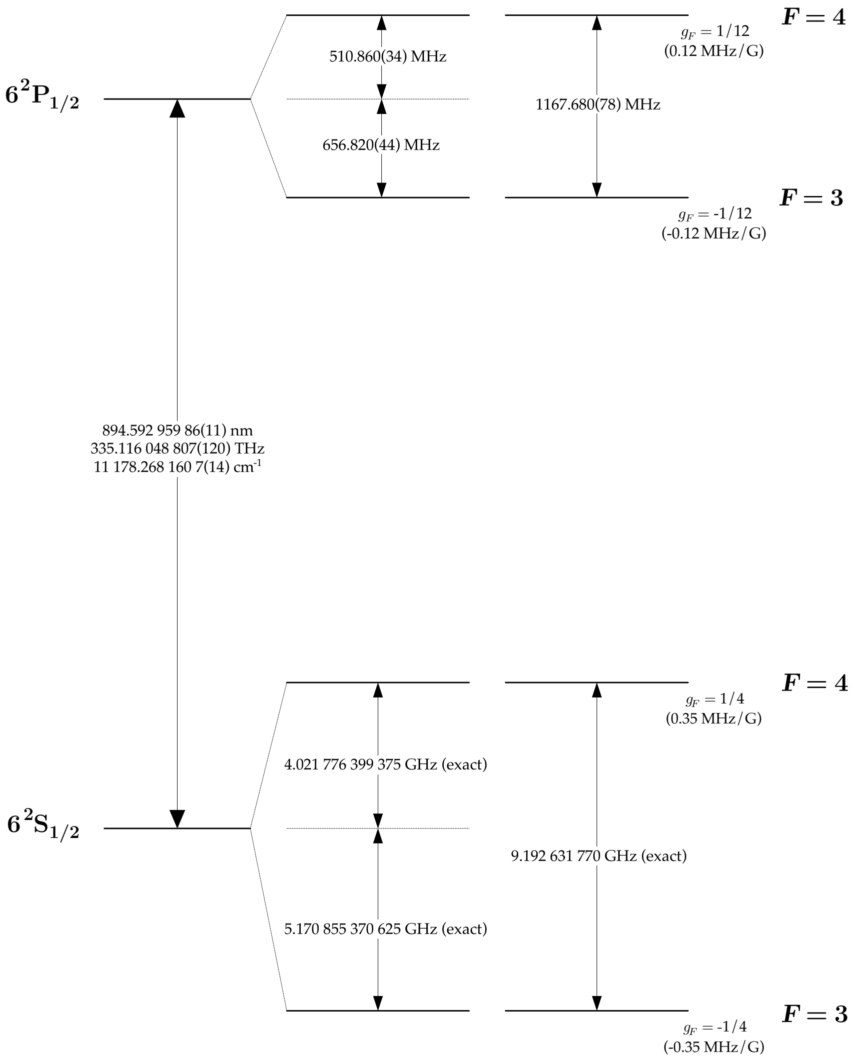
$6^2P_{1/2}$
510.860(34) MHz
656.820(44) MHz
1167.680(78) MHz
$g_F = 1/12$
(0.12 MHz/G)
$F = 4$
$g_F = -1/12$
(-0.12 MHz/G)
$F = 3$
894.592 959 86(11) nm
335.116 048 807(120) THz
11 178.268 160 7(14) cm^{-1}
$6^2S_{1/2}$
4.021 776 399 375 GHz (exact)
5.170 855 370 625 GHz (exact)
9.192 631 770 GHz (exact)
$g_F = 1/4$
(0.35 MHz/G)
$F = 4$
$g_F = -1/4$
(-0.35 MHz/G)
$F = 3$

Figure A.3: Cesium D_1 transition hyperfine structure, with frequency splittings between the hyperfine energy levels. The excited-state values are taken from [355, 367], and the ground-state values are exact, as a result of the current definition of the second. The approximate Landé g_F-factors for each level are also given, with the corresponding Zeeman splittings between adjacent magnetic sublevels.

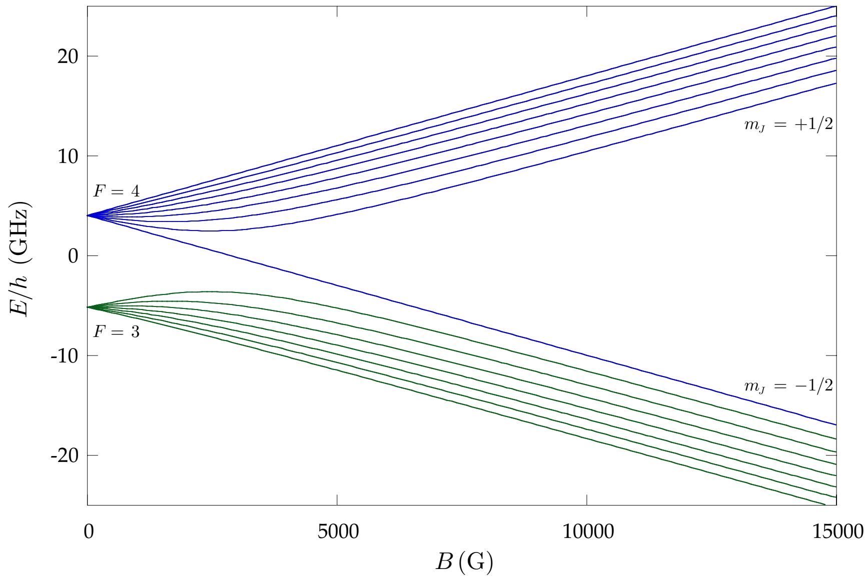

Figure A.4: Cesium $6^2\mathrm{S}_{1/2}$ (ground) level hyperfine structure in an external magnetic field. The levels are grouped according to the value of F in the low-field (anomalous Zeeman) regime and m_J in the strong-field (hyperfine Paschen-Back) regime.

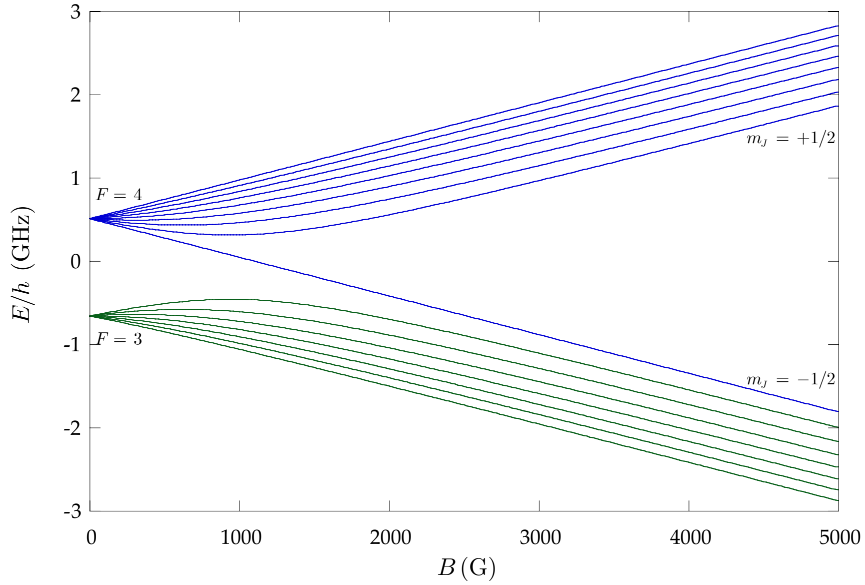

Figure A.5: Cesium $6^2\mathrm{P}_{1/2}$ (D_1 excited) level hyperfine structure in an external magnetic field. The levels are grouped according to the value of F in the low-field (anomalous Zeeman) regime and m_J in the strong-field (hyperfine Paschen-Back) regime.

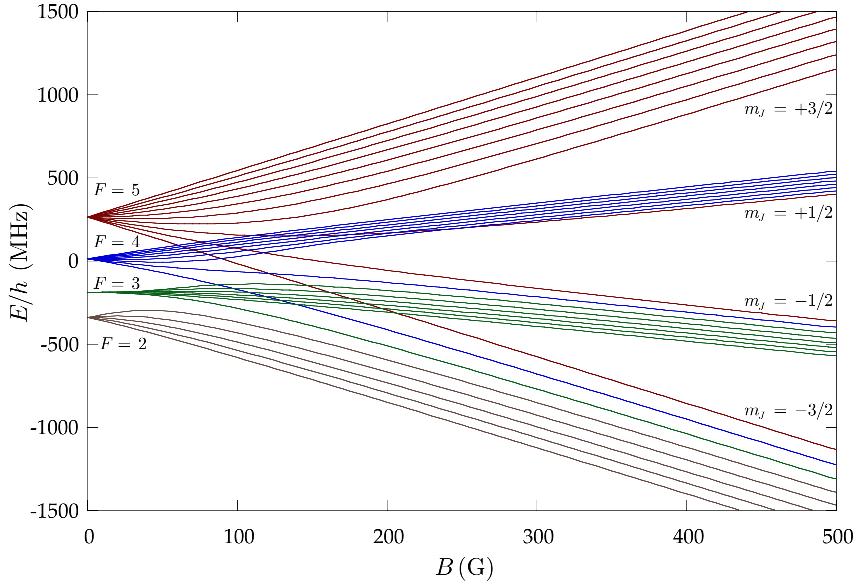

Figure A.6: Cesium $6^2P_{3/2}$ (D_2 excited) level hyperfine structure in an external magnetic field. The levels are grouped according to the value of F in the low-field (anomalous Zeeman) regime and m_J in the strong-field (hyperfine Paschen-Back) regime.

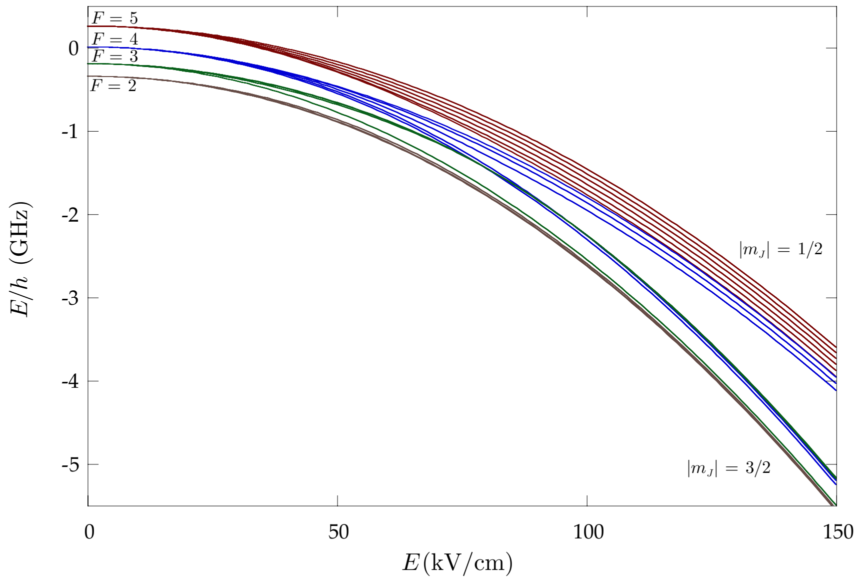

Figure A.7: Cesium $6^2P_{3/2}$ (D_2 excited) level hyperfine structure in a constant, external electric field. The levels are grouped according to the value of F in the low-field (anomalous Zeeman) regime and $|m_J|$ in the strong-field ("electric" hyperfine Paschen-Back) regime. Levels with the same values of F and $|m_F|$ (for a weak field) are degenerate.

Appendix B

Phase Space Gallery I: Standard Map

In this appendix we take a stroll through the phase space of the standard map as it becomes increasingly chaotic. As we have seen in Chapter 4, the standard map is actually a one-parameter family of maps, given by

$$\begin{aligned} p_{n+1} &= p_n + K \sin x_n \\ x_{n+1} &= x_n + p_{n+1} \quad . \end{aligned} \tag{B.1}$$

The stochasticity parameter K controls the "degree of chaos" of the dynamics.

For $K = 0$, the momentum is a constant of the motion, so the phase space is simply the set of contours of constant p. For small K, the map is weakly perturbed. Most of the tori are distorted but still present, with only very small chaotic regions (as expected from the KAM theorem), and several resonances become visible (as expected from the Poincaré–Birkhoff theorem). The phase space structure becomes especially rich when K is near Greene's number (≈ 0.971635) [253], which is the critical value at which the last KAM surface (i.e., invariant torus that spans the phase space, partitioning the chaotic regions into disconnected cells) is destroyed, and the chaotic transport makes a phase transition from local to global diffusion. Beyond this value, much of the stable structure breaks down, leaving mostly the primary resonances, until they become unstable at $K = 4$. The phase space then becomes mostly chaotic, with some islands popping back up now and then (such as the accelerator modes near $K = 2\pi$ and 4π).

In the graphics that follow, the iterates of the standard map are plotted for various stochasticity parameters. The phase plots here show about 40 different trajectories, with around 8000 iterations per trajectory. To retain the symmetry of the phase space, the symmetric image $(2\pi - x, 2\pi - p)$ of each (x, p) point is also plotted. The colors in the diagrams mark different trajectories, serving the dual purposes of heightening the contrast between phase-space structures and making it clear when mixing behavior is present. Because of the 2π-periodicity of the phase space in both x and p, only one unit cell of the phase space is shown.

The phase-space plots in this and the next gallery were hand-coded directly in the POSTSCRIPT graphics language, which is a powerful and efficient tool for producing complex graphics. These rather small graphics files can then be printed on standard laser printers, and the printer's processor performs the iteration mapping or numerical integration to determine the locations of the points. To save space in the PDF-formatted version of this document (and for more consistent color and intensity), these phase spaces were rasterized prior to inclusion in this LaTeX document. An earlier example of using POSTSCRIPT for plotting the phase space of an iterated map can be found in [388].

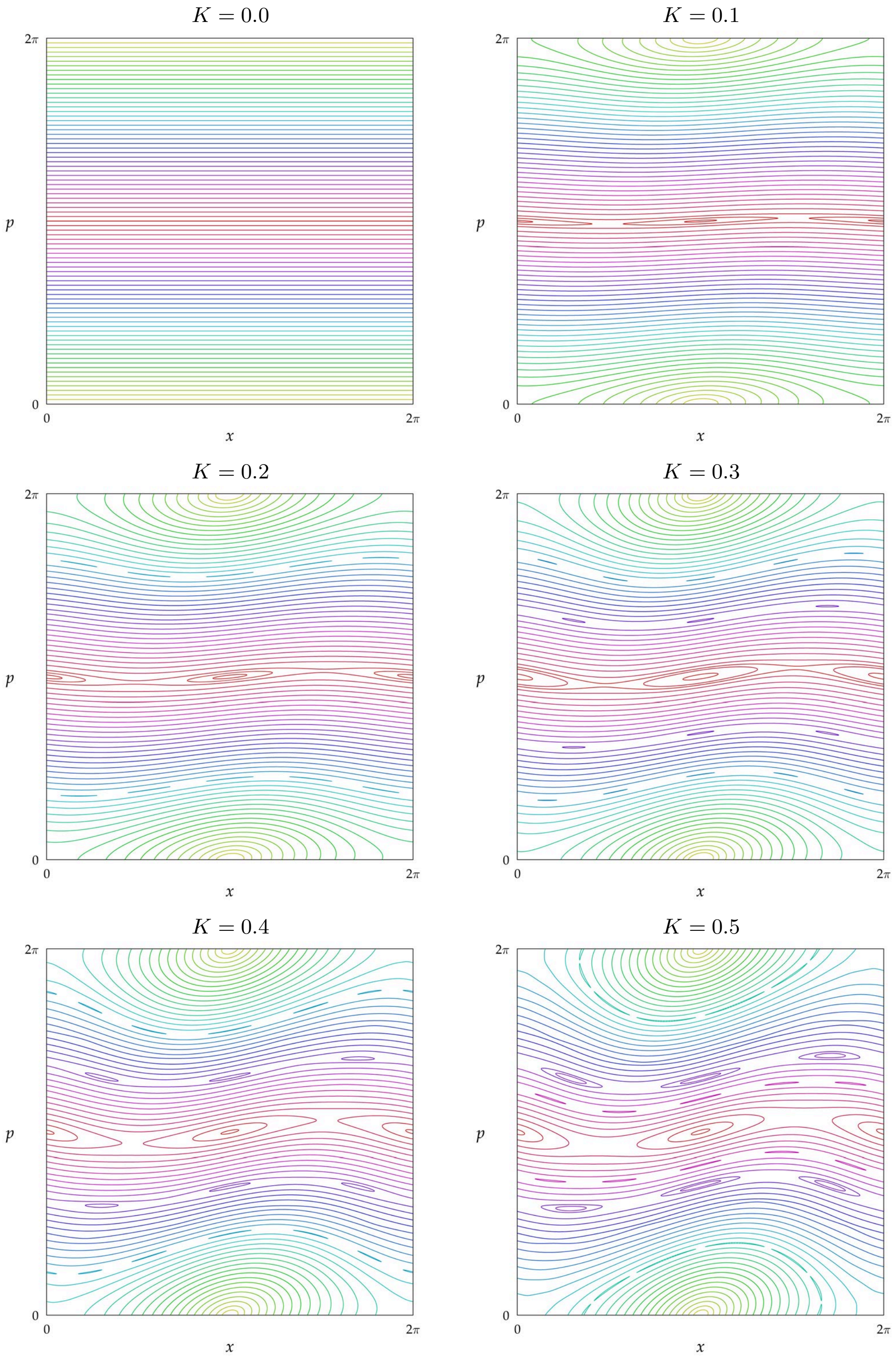
$K = 0.0$
$K = 0.1$
$K = 0.2$
$K = 0.3$
$K = 0.4$
$K = 0.5$
p
x
0
2π

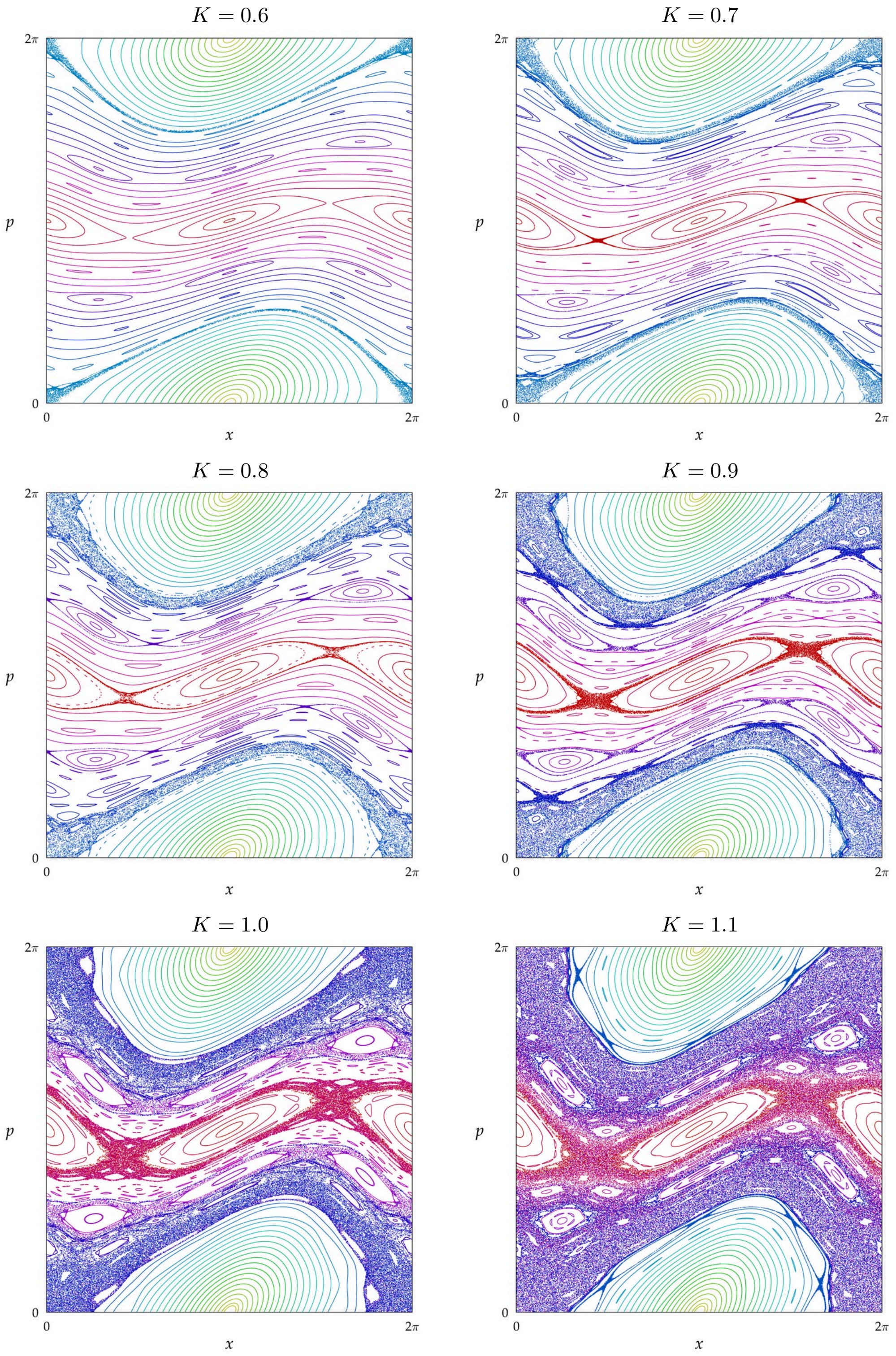
$K = 0.6$
$K = 0.7$
$K = 0.8$
$K = 0.9$
$K = 1.0$
$K = 1.1$
2π
p
0
0
2π
x

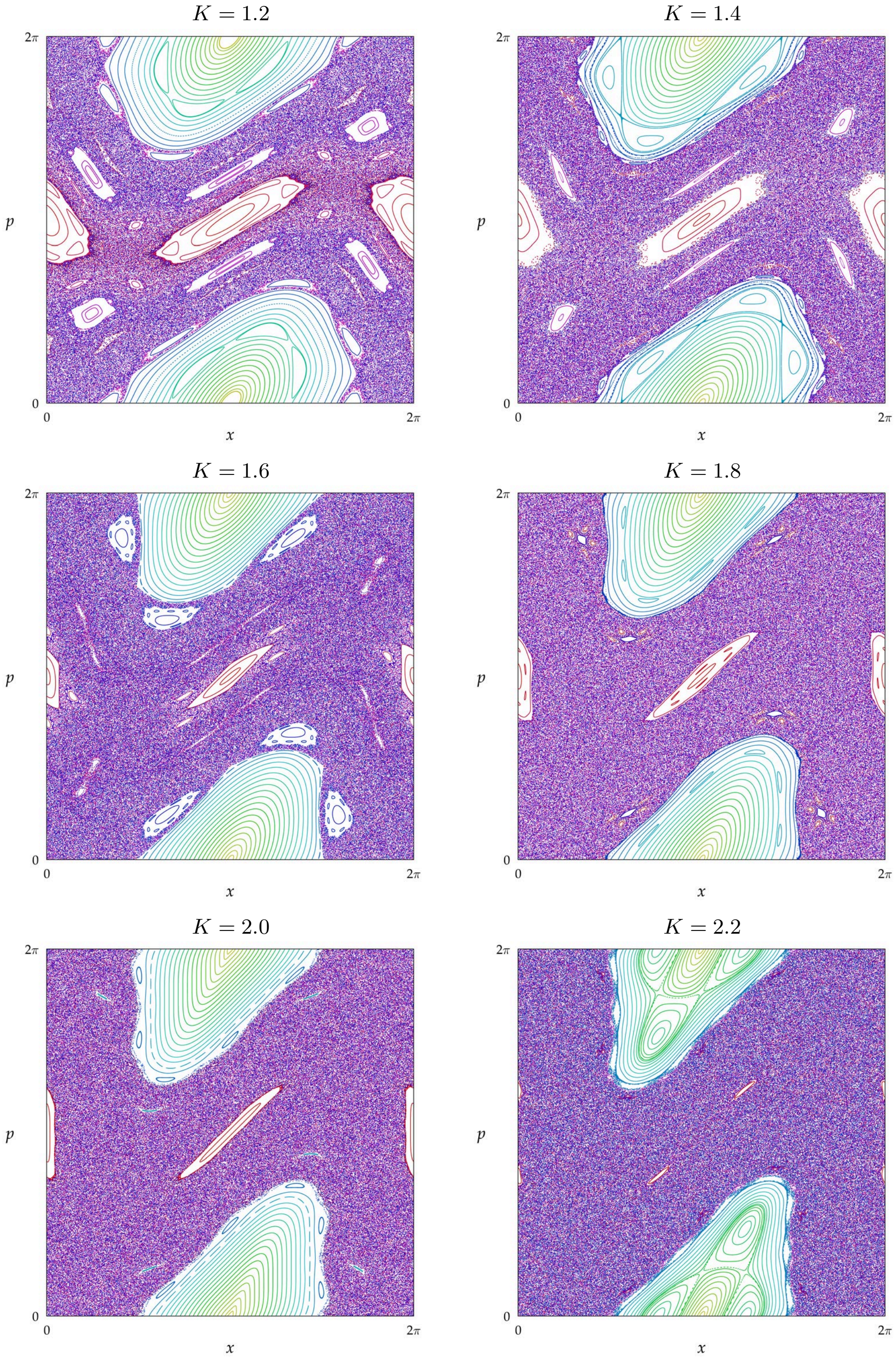
$K = 1.2$
$K = 1.4$
$K = 1.6$
$K = 1.8$
$K = 2.0$
$K = 2.2$
p
x
0
2π

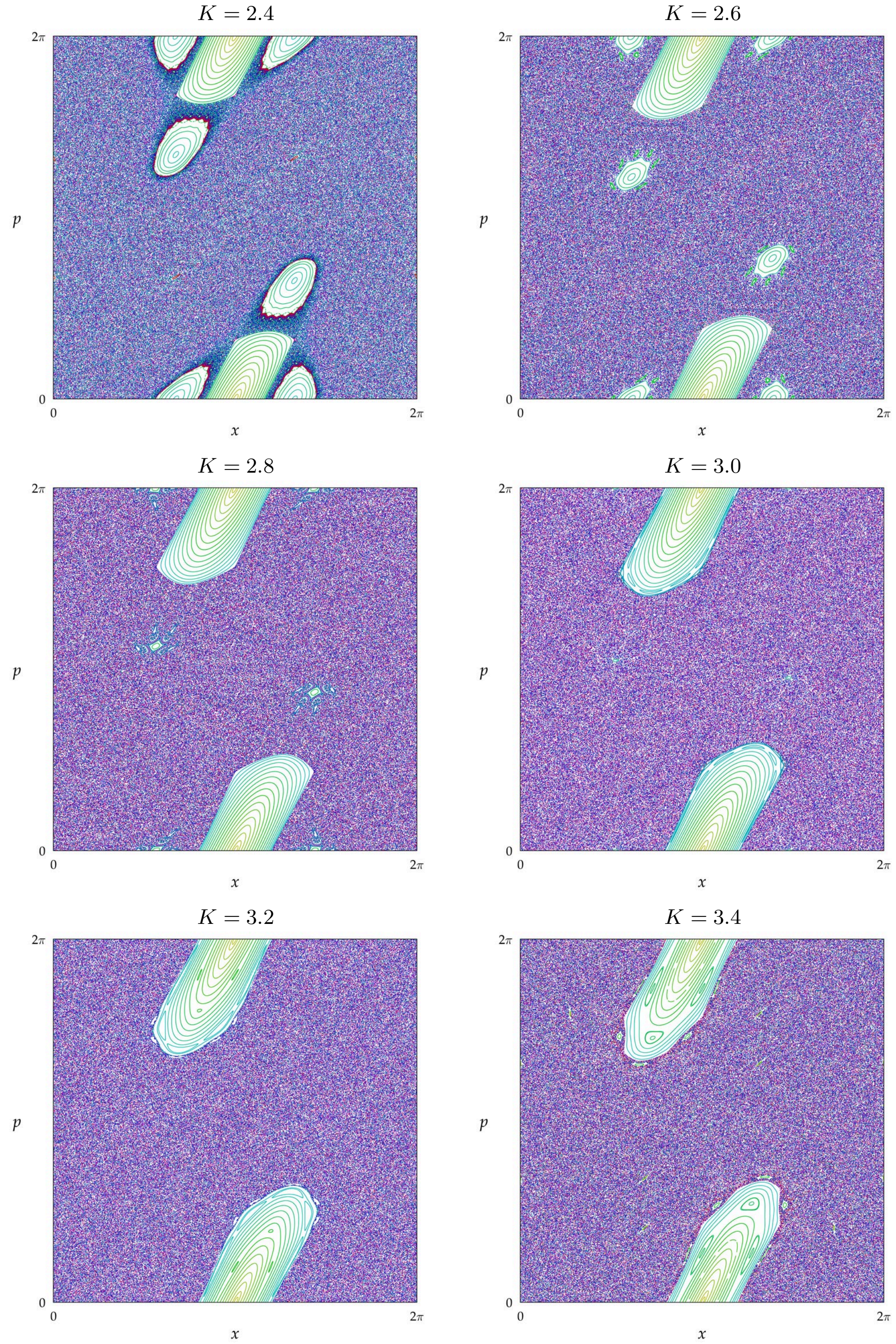
$K = 2.4$
$K = 2.6$
$K = 2.8$
$K = 3.0$
$K = 3.2$
$K = 3.4$
2π
p
0
x

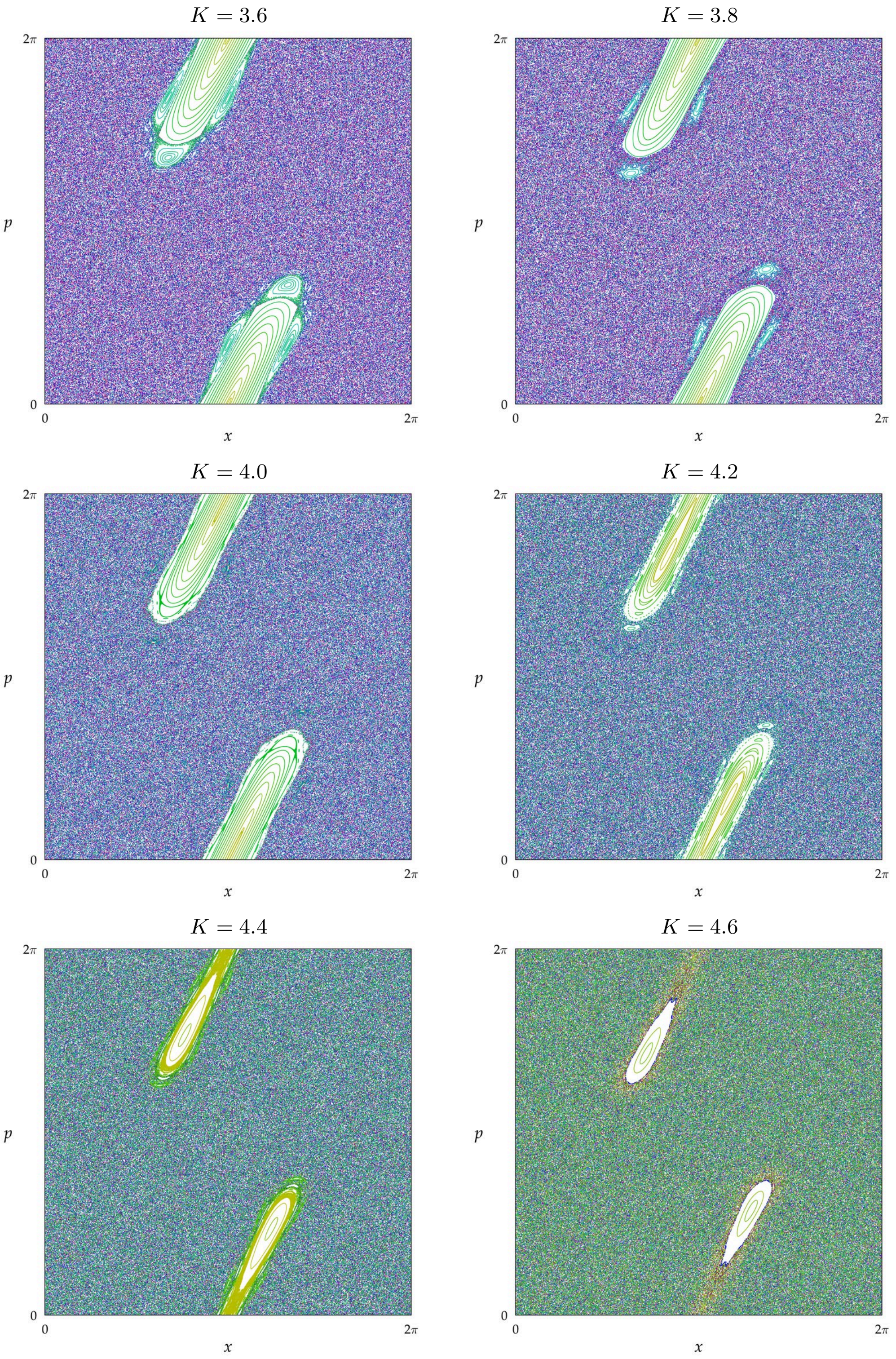
$K = 3.6$
$K = 3.8$
$K = 4.0$
$K = 4.2$
$K = 4.4$
$K = 4.6$
2π
p
0
x

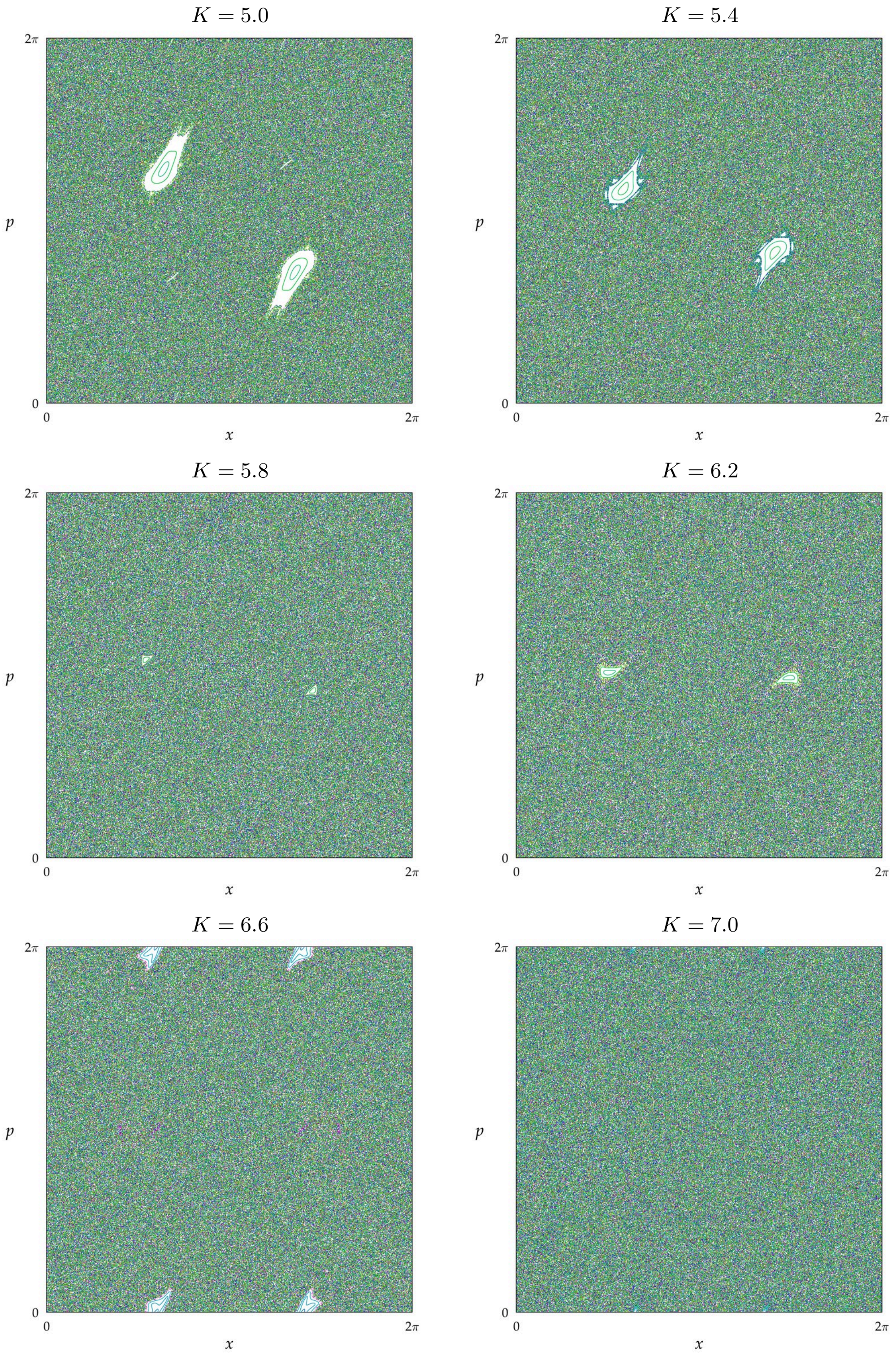
$K = 5.0$
$K = 5.4$
$K = 5.8$
$K = 6.2$
$K = 6.6$
$K = 7.0$
2π
p
0
0
2π
x

$K = 8.0$

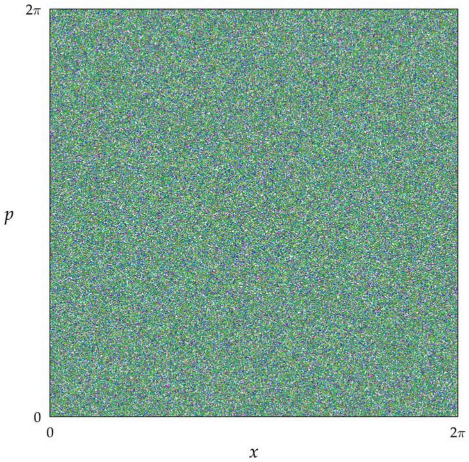

$K = 9.0$

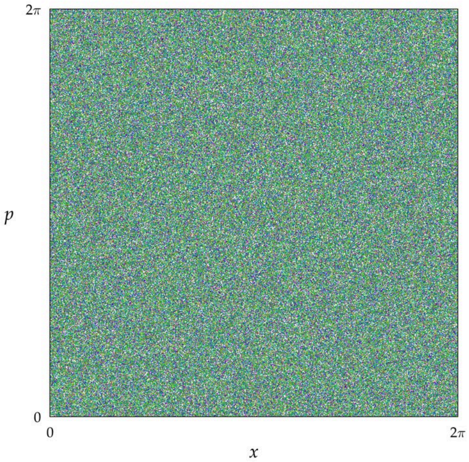

$K = 10.0$

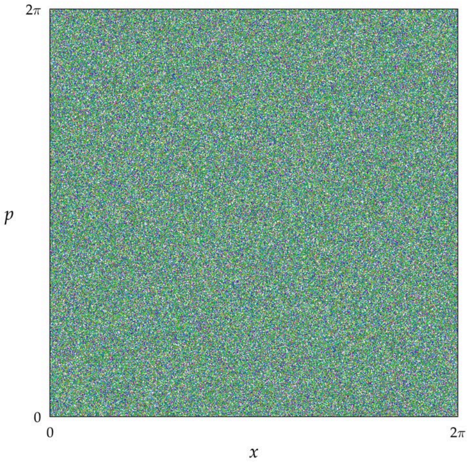

$K = 11.0$

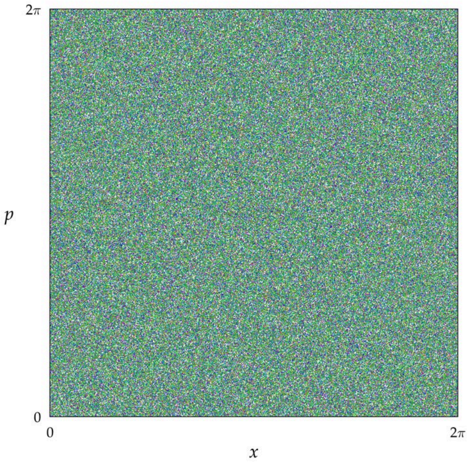

$K = 12.5$

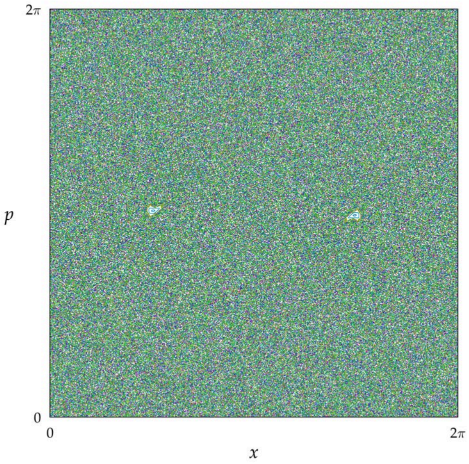

$K = 12.8$

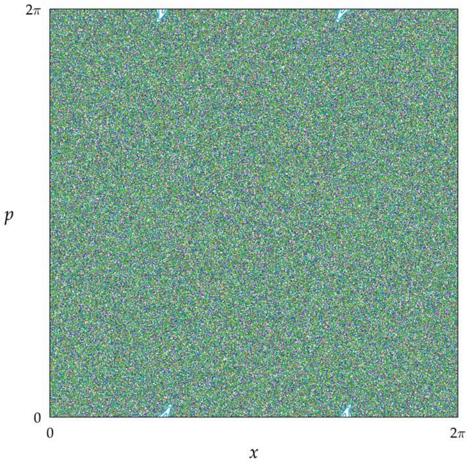

Appendix C

Phase Space Gallery II: Amplitude-Modulated Pendulum

Now we examine the phase space for the other system that we study in this dissertation, the amplitude-modulated pendulum. This system is described by the Hamiltonian

$$H(x, p, t) = \frac{p^2}{2} - 2\alpha \cos^2(\pi t) \cos(x) \ , \tag{C.1}$$

which is just the pendulum Hamiltonian with a single-frequency modulation of the well depth. As the time dependence here can be decomposed into three frequencies, the phase-space is dominated by the three corresponding primary resonances, located at $p = 0$ and $p = \pm 2\pi$. These three resonances form as α increases from zero, and they dissolve into the surrounding chaotic sea as α continues to grow. Especially dramatic is the "molting" behavior of the islands, where they grow an island chain and then shed it into the chaotic sea; this can be seen, for example, for a period-4 chain in the center island around $\alpha = 3.2$, and a period-4 island chain in the outer islands around $\alpha = 5.2$. Also interesting is that the remnants of the center island disappear around $\alpha = 11$, but the island makes a strong reappearance around $\alpha = 18$.

In the following graphics, the trajectory coordinates are plotted, sampled at unit times $t = n$ (for integer n). The phase plots here show about 60 different trajectories, with around 4000 iterations per trajectory. To retain the symmetry of the phase space, the three symmetric images $(x, -p)$, $(-x, p)$, and $(-x, -p)$ of each (x, p) point is also plotted.

The phase-space plots in this gallery were again hand-coded directly in POSTSCRIPT, where the code contained two embedded integrators, a fixed-step, second-order Stoermer routine and a fourth-order Runge-Kutta routine. Despite the lower order of the Stoermer method, it was much more accurate for the same step size than the Runge-Kutta integrator. These graphics files were again rasterized before inclusion in the PDF-formatted version of this document, as they require extensive processing time compared to the standard-map phase plots.

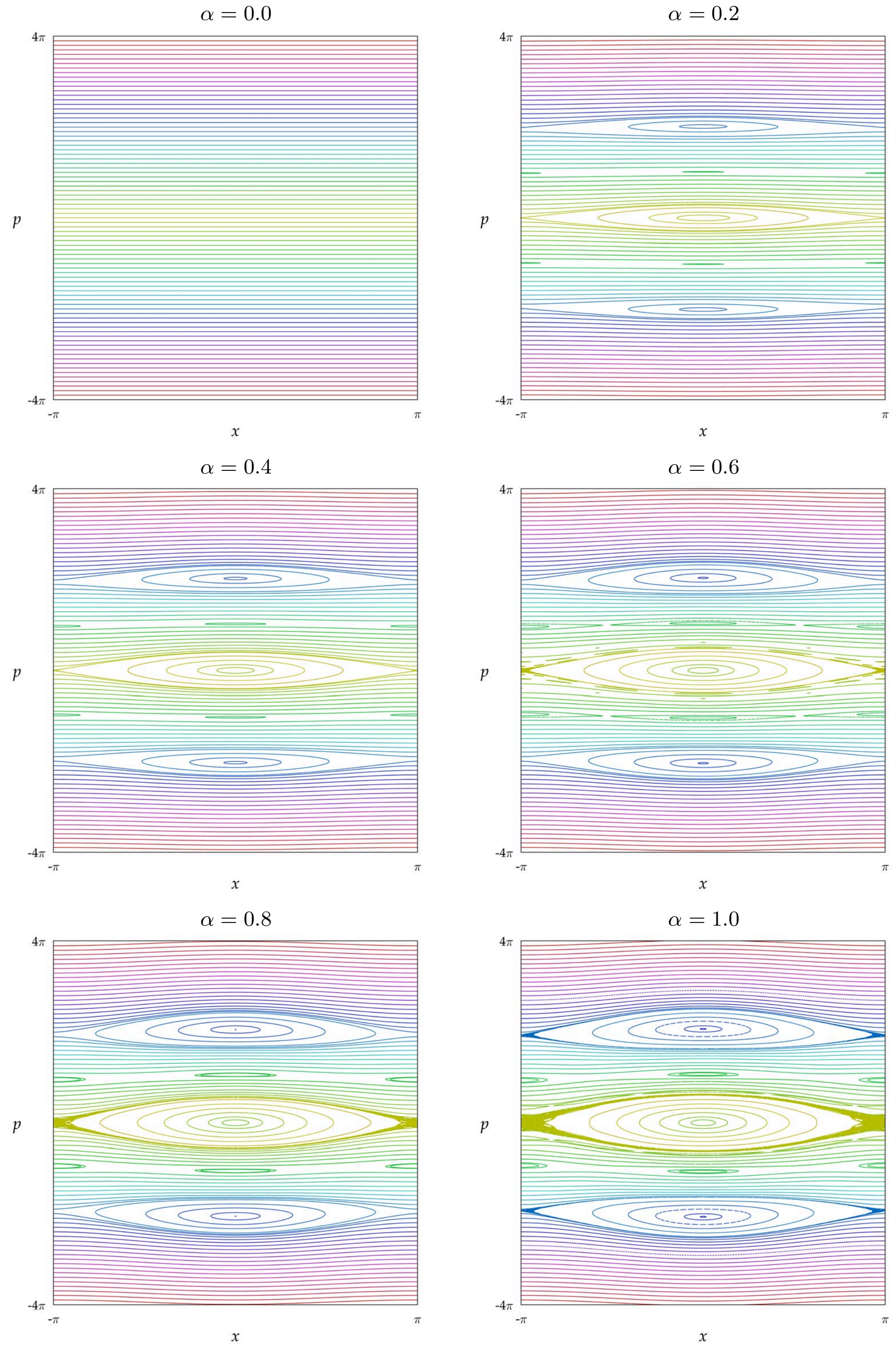
$\alpha = 0.0$
$\alpha = 0.2$
$\alpha = 0.4$
$\alpha = 0.6$
$\alpha = 0.8$
$\alpha = 1.0$
4π
-4π
p
$-\pi$
π
x

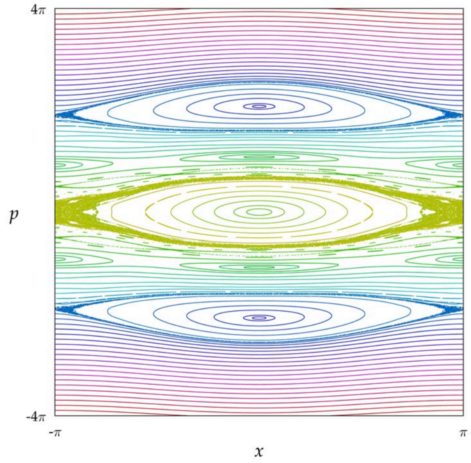
$\alpha = 1.2$

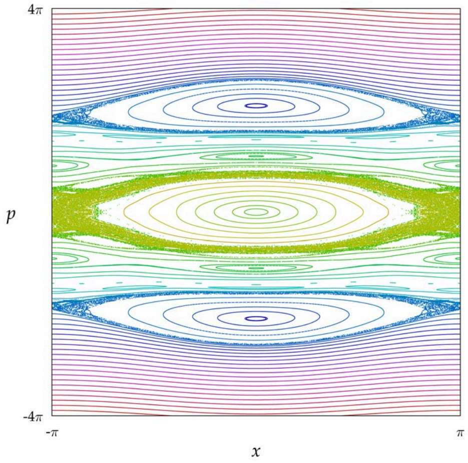
$\alpha = 1.4$

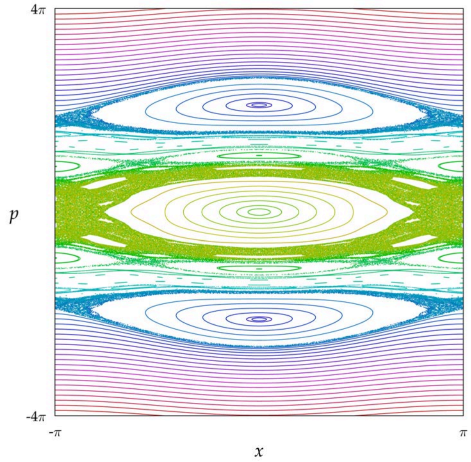
$\alpha = 1.6$

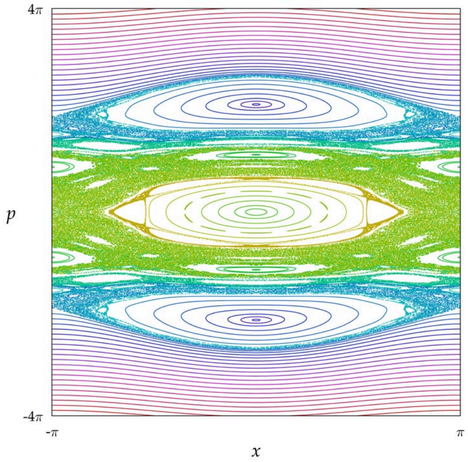
$\alpha = 1.8$

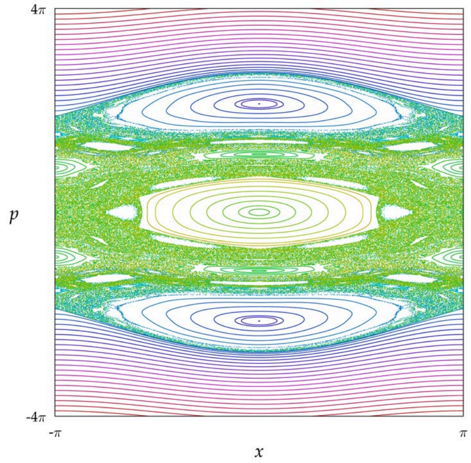
$\alpha = 2.0$

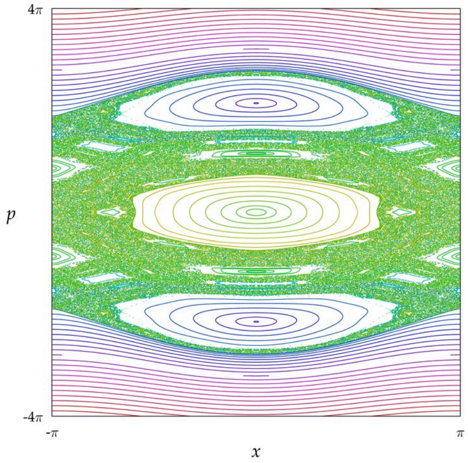
$\alpha = 2.2$

$\alpha = 2.4$

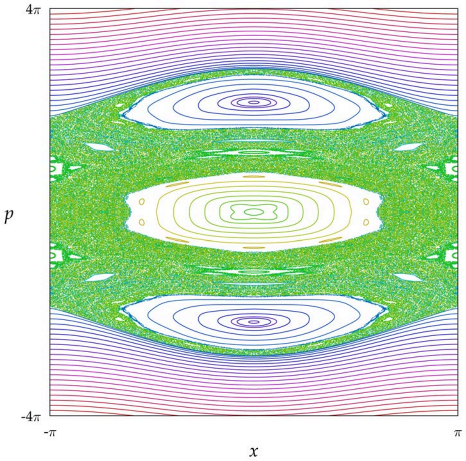

$\alpha = 2.6$

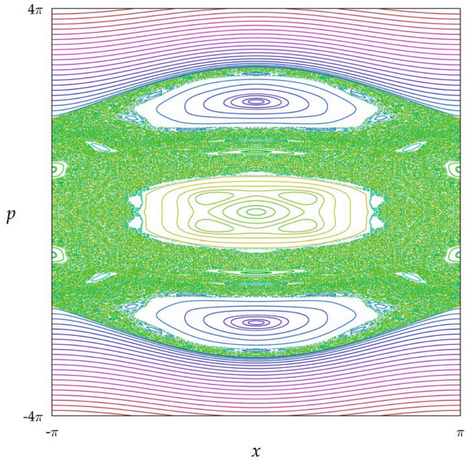

$\alpha = 2.8$

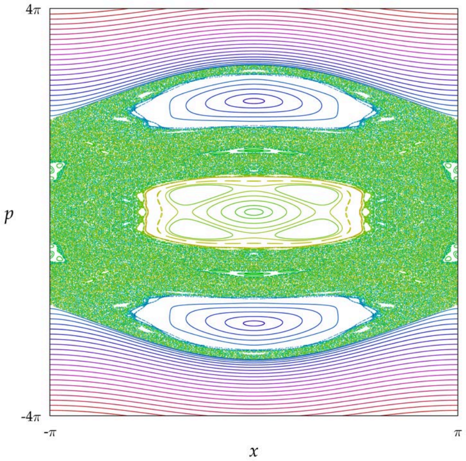

$\alpha = 3.0$

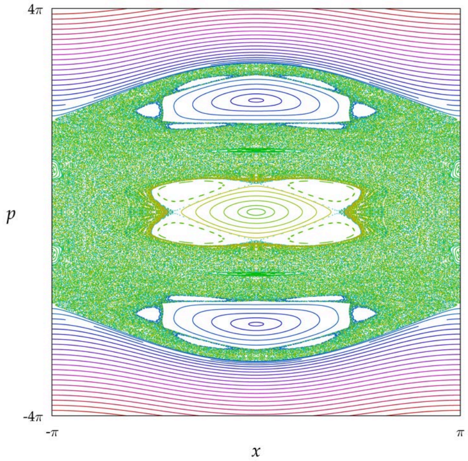

$\alpha = 3.2$

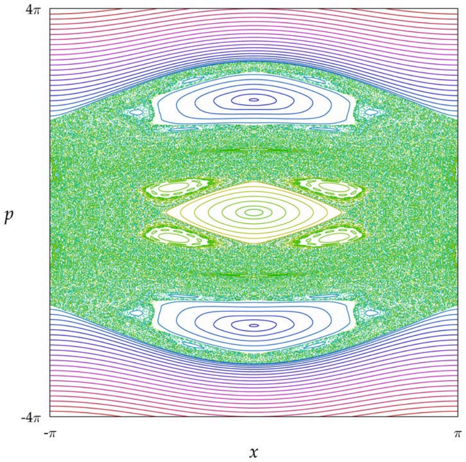

$\alpha = 3.4$

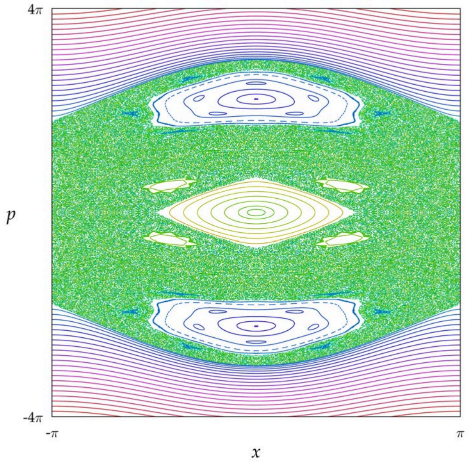

$\alpha = 3.6$

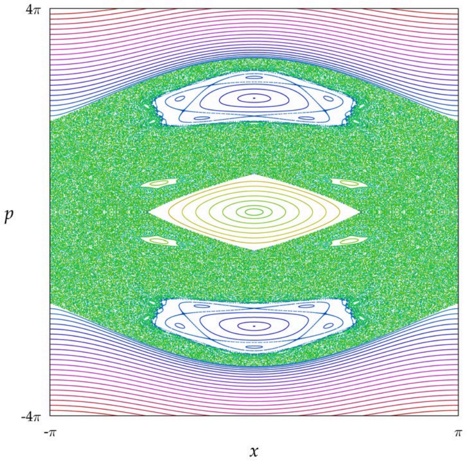

$\alpha = 3.8$

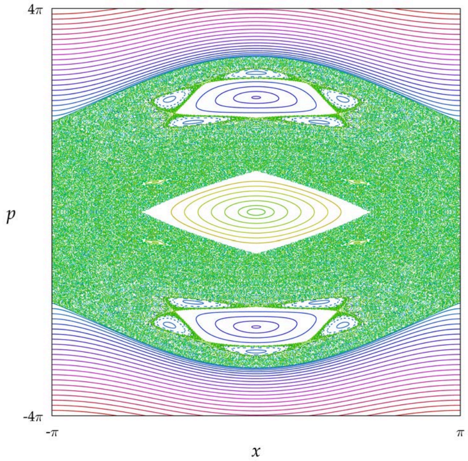

$\alpha = 4.0$

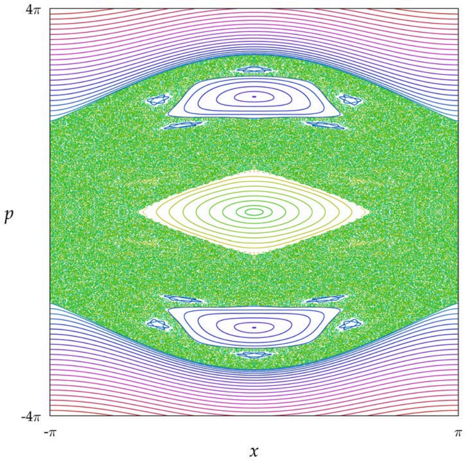

$\alpha = 4.2$

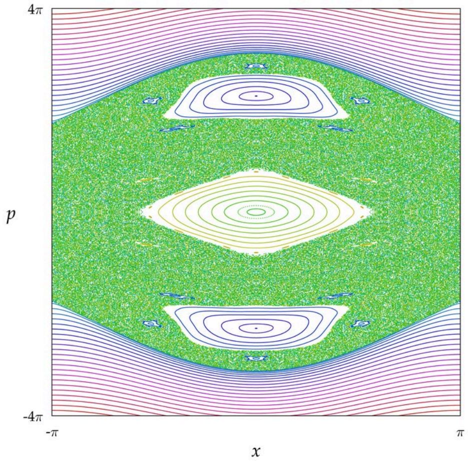

$\alpha = 4.4$

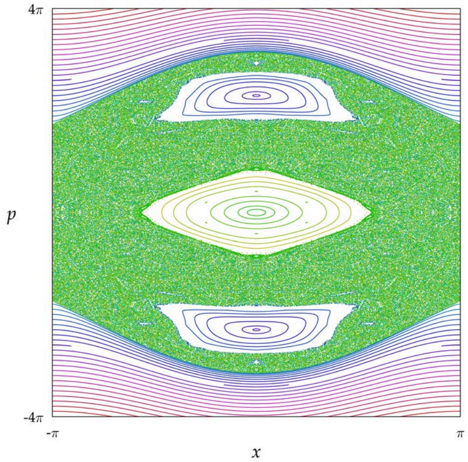

$\alpha = 4.6$

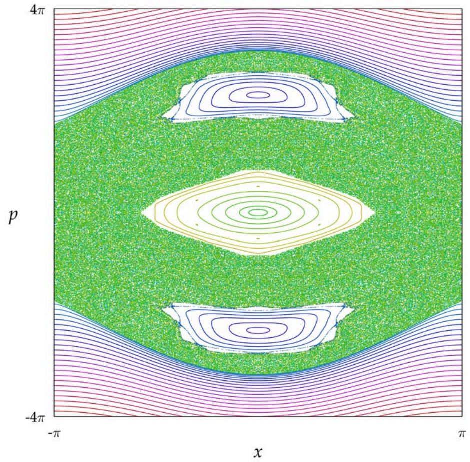

$\alpha = 4.8$

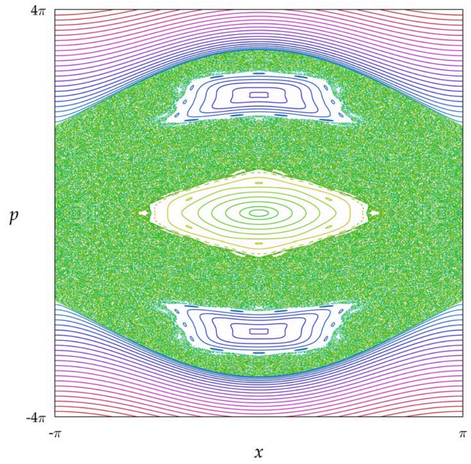

$\alpha = 5.0$

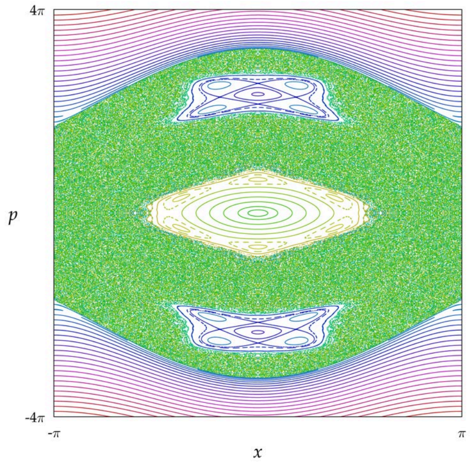

$\alpha = 5.2$

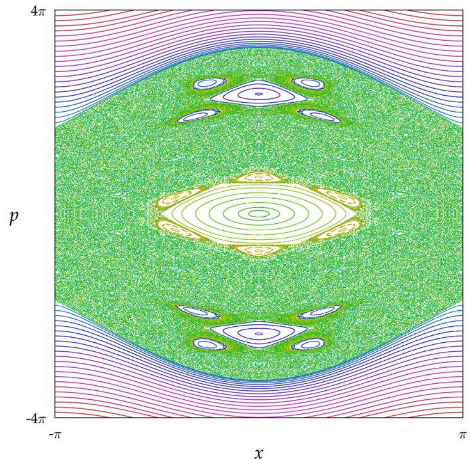

$\alpha = 5.4$

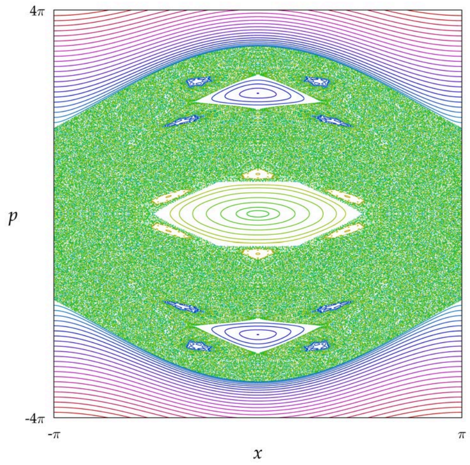

$\alpha = 5.6$

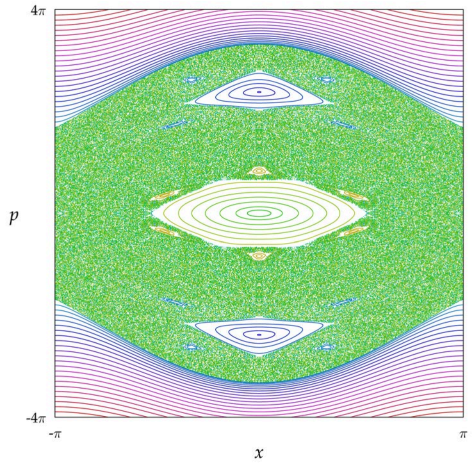

$\alpha = 5.8$

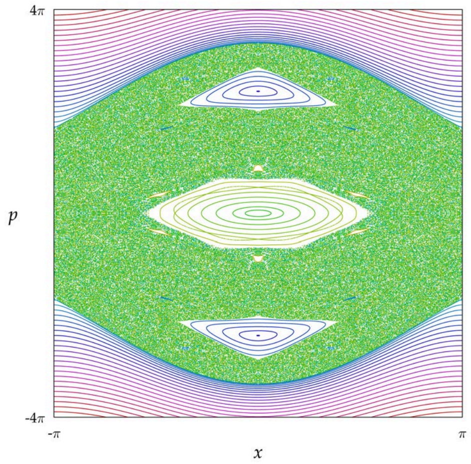

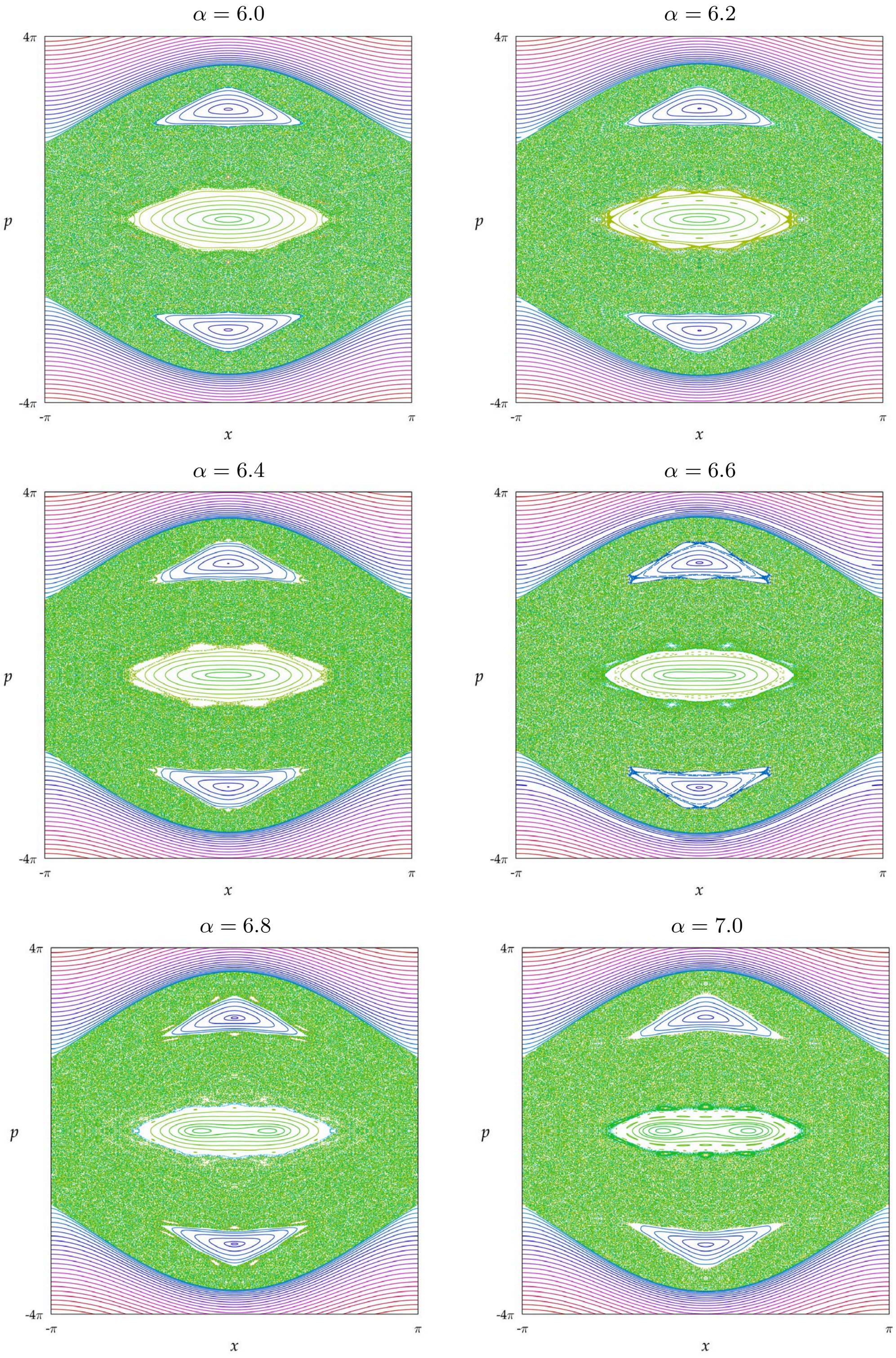
$\alpha = 6.0$
$\alpha = 6.2$
$\alpha = 6.4$
$\alpha = 6.6$
$\alpha = 6.8$
$\alpha = 7.0$
4π
-4π
$-\pi$
π
p
x

$\alpha = 7.2$

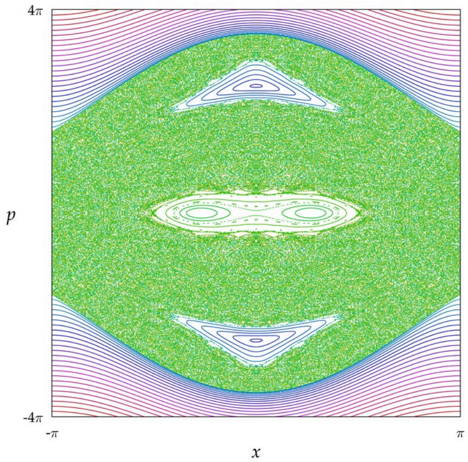

$\alpha = 7.4$

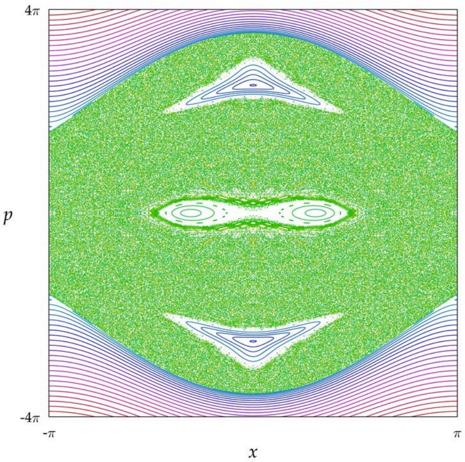

$\alpha = 7.6$

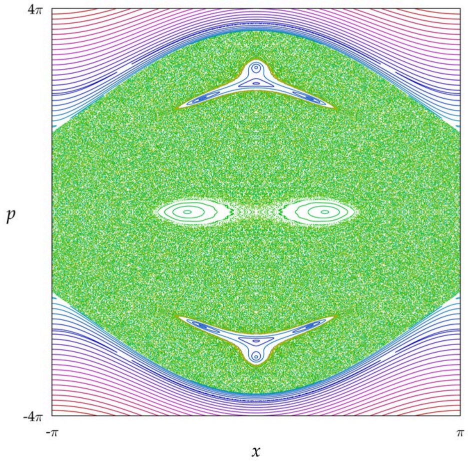

$\alpha = 7.8$

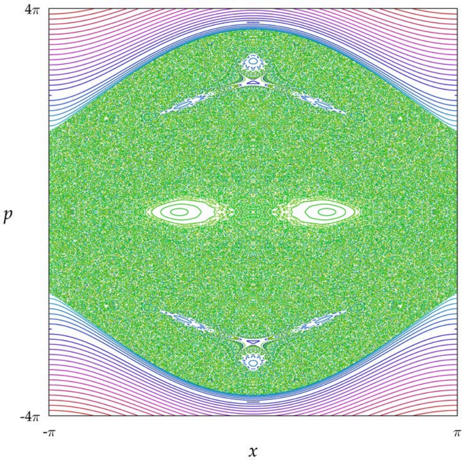

$\alpha = 8.0$

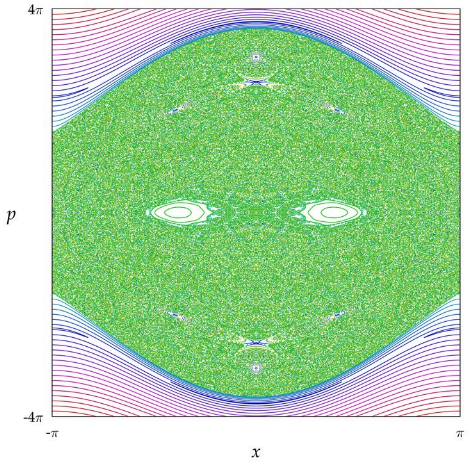

$\alpha = 8.2$

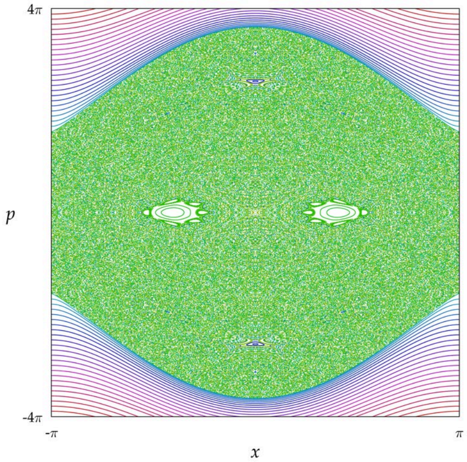

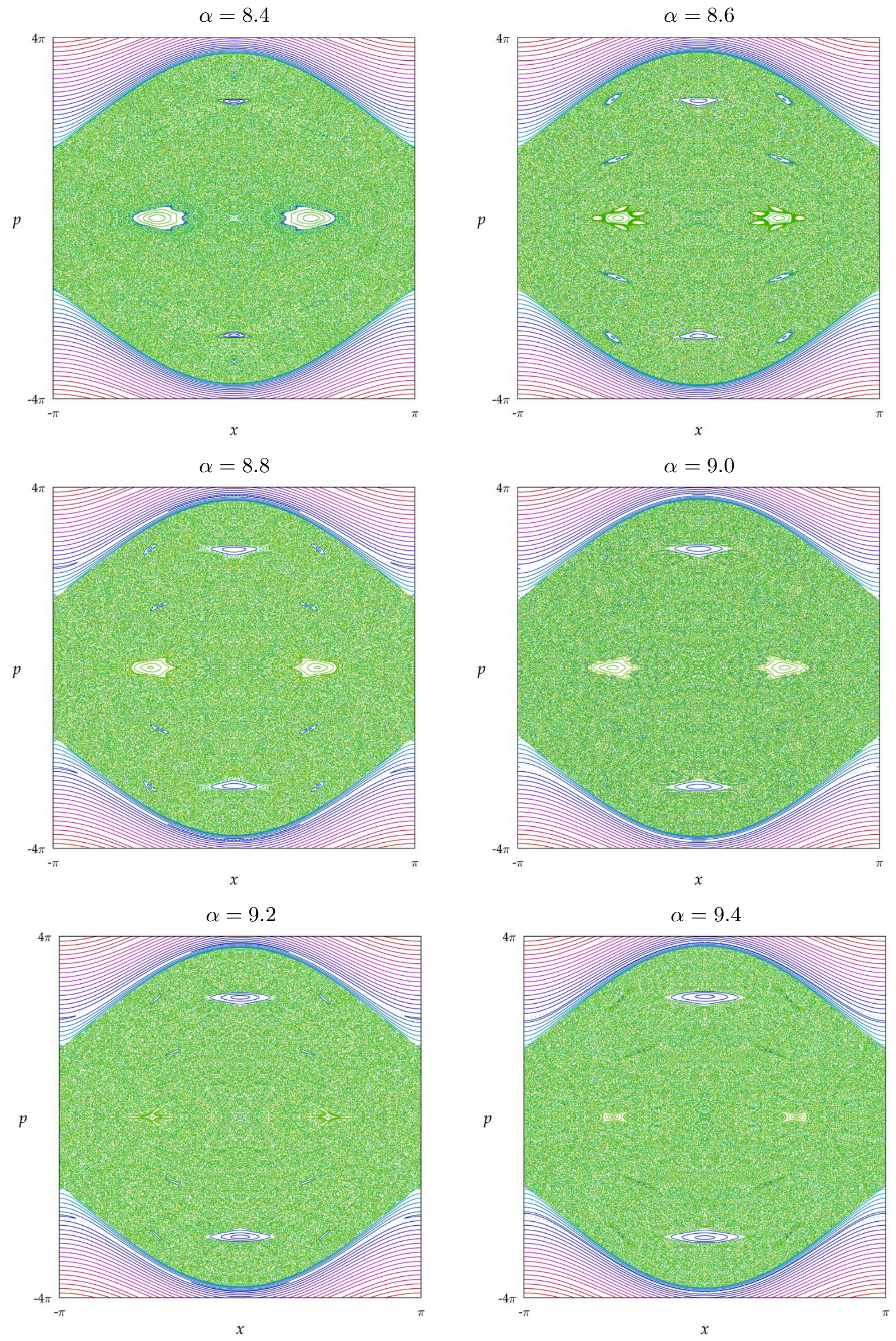
$\alpha = 8.4$
$\alpha = 8.6$
$\alpha = 8.8$
$\alpha = 9.0$
$\alpha = 9.2$
$\alpha = 9.4$
4π
-4π
$-\pi$
π
p
x

$\alpha = 9.6$

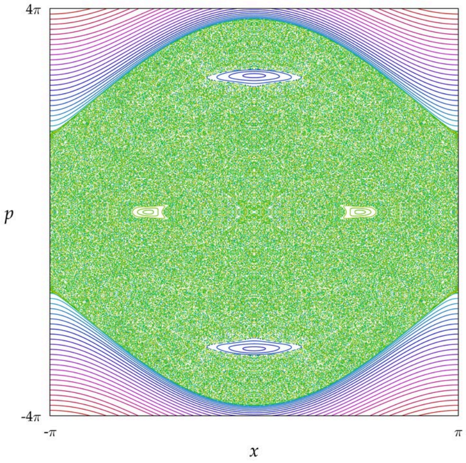

$\alpha = 9.8$

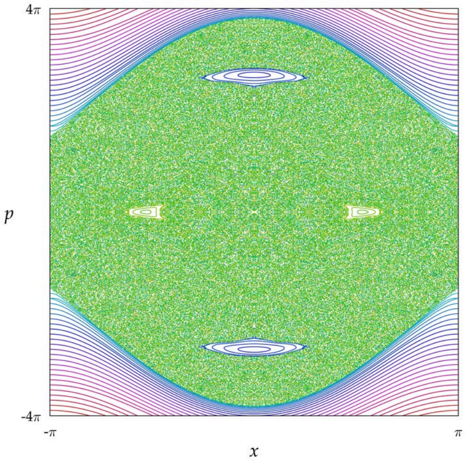

$\alpha = 10.0$

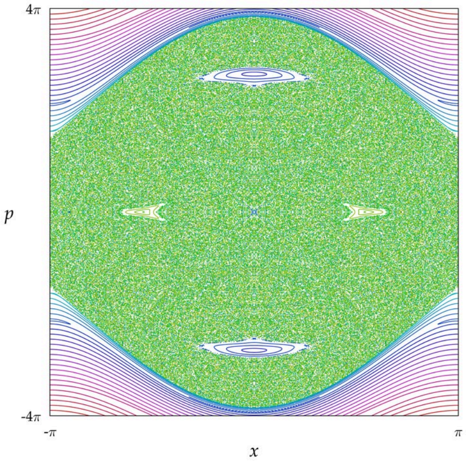

$\alpha = 10.4$

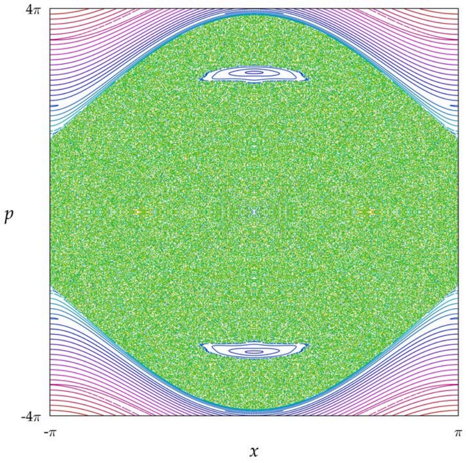

$\alpha = 10.8$

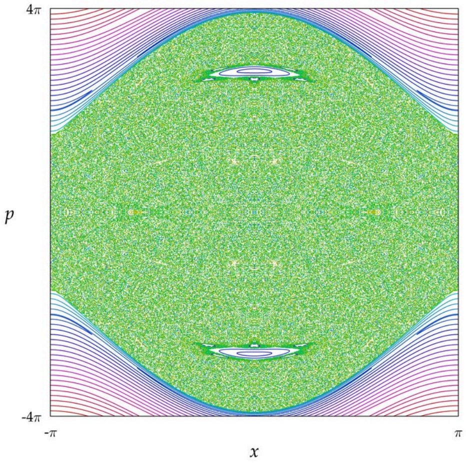

$\alpha = 11.2$

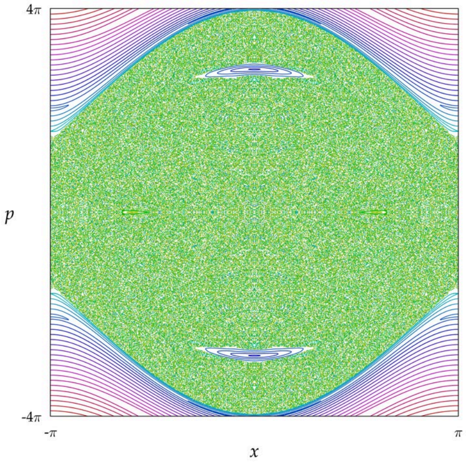

$\alpha = 11.6$

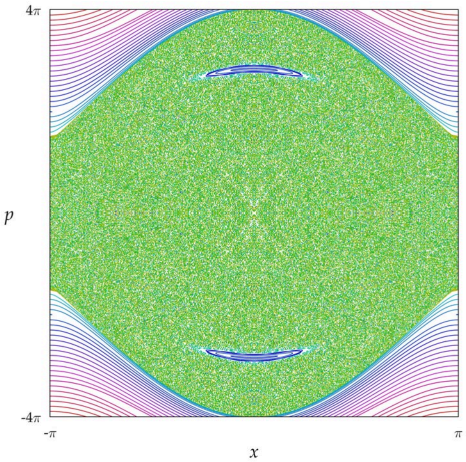

$\alpha = 12.0$

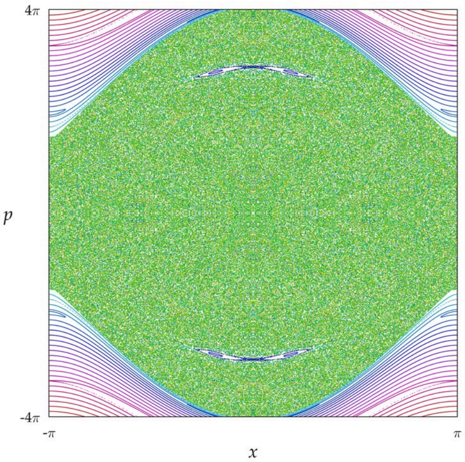

$\alpha = 12.4$

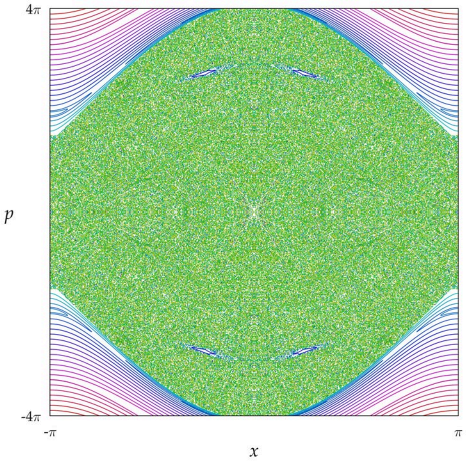

$\alpha = 12.8$

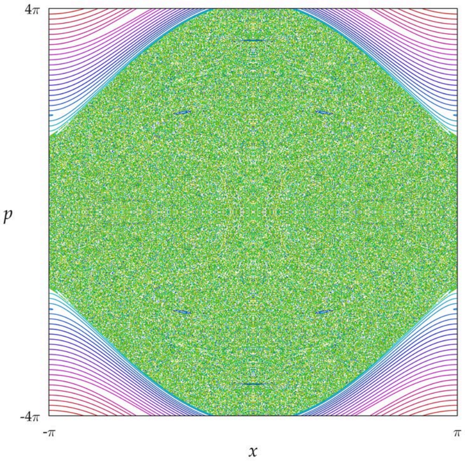

$\alpha = 13.2$

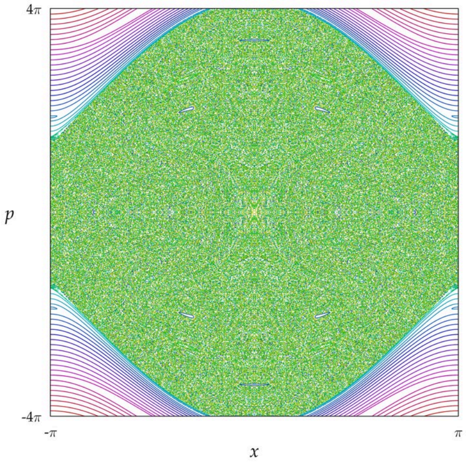

$\alpha = 13.6$

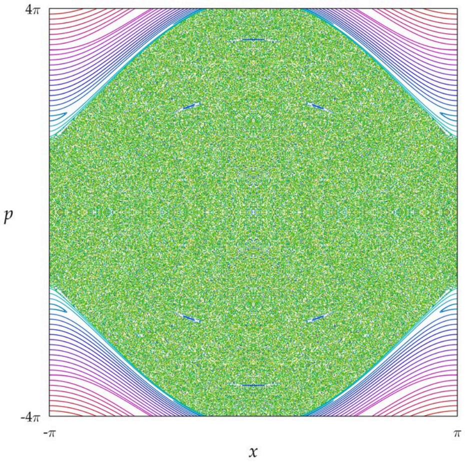

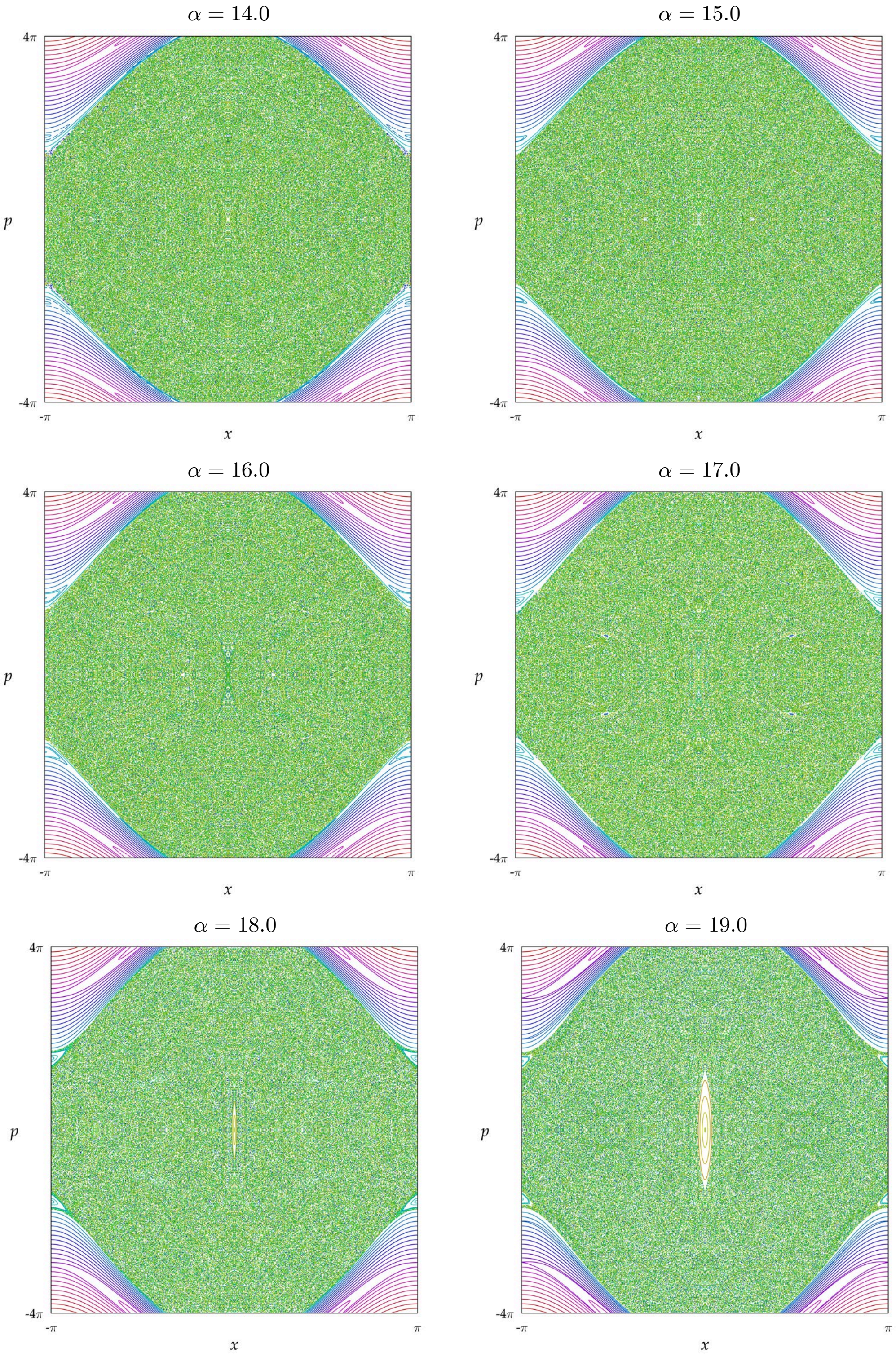
α = 14.0
α = 15.0
α = 16.0
α = 17.0
α = 18.0
α = 19.0
4π
-4π
-π
π
p
x

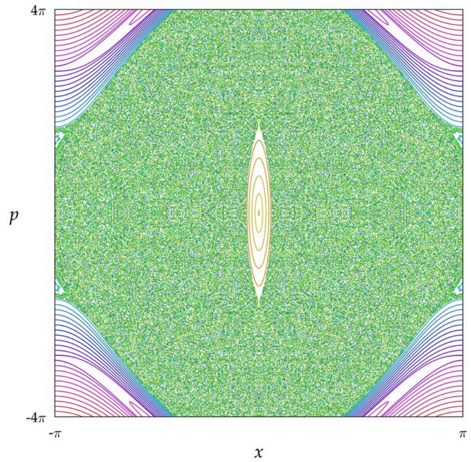
$\alpha = 20.0$

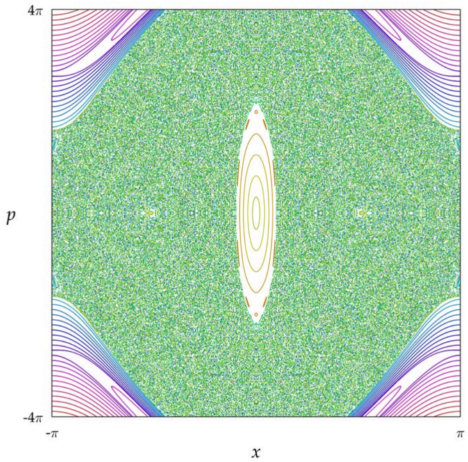
$\alpha = 22.0$

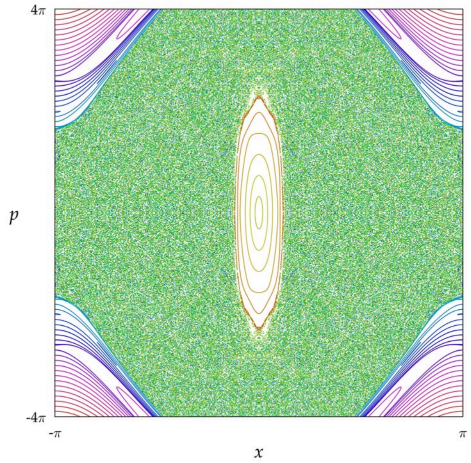
$\alpha = 24.0$

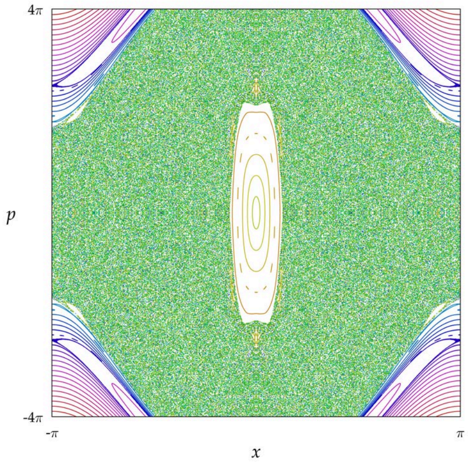
$\alpha = 26.0$

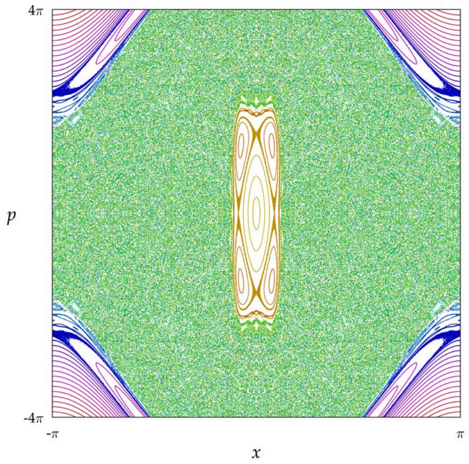
$\alpha = 28.0$

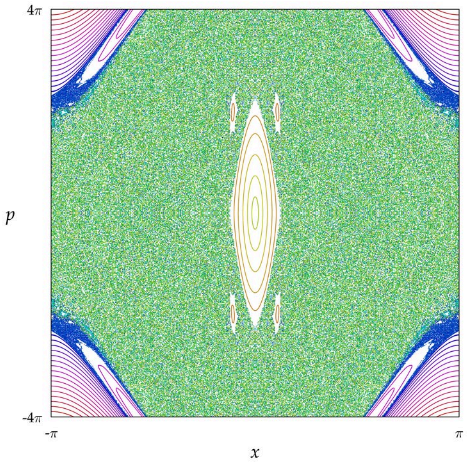
$\alpha = 30.0$

Bibliography

[1] Jürgen Moser, *Stable and Random Motions in Dynamical Systems* (Princeton University Press, Princeton, 1973).

[2] Jürgen Moser, "Is the Solar System Stable?" *Math. Intell.* **1**, 65 (1978).

[3] L. E. Reichl, *The Transition to Chaos in Conservative Classical Systems: Quantum Manifestations* (Springer-Verlag, New York, 1992).

[4] Ivars Peterson, *Newton's Clock: Chaos in the Solar System* (W. H. Freeman, New York, 1993).

[5] Michael Tabor, *Chaos and Integrability in Nonlinear Dynamics: An Introduction* (Wiley, New York, 1989).

[6] Edward N. Lorenz, "Deterministic Nonperiodic Flow," *J. Atmos. Sci.* **20**, 130 (1963).

[7] R. D. Hazeltine and J. D. Meiss, *Plasma confinement* (Addison-Wesley, Redwood City, 1992).

[8] Rajarshi Roy, T. W. Murphy, Jr., T. D. Maier, Z. Gills, and E. R. Hunt, "Dynamical Control of a Chaotic Laser: Experimental Stabilization of a Globally Coupled System," *Phys. Rev. Lett.* **68**, 1259 (1992).

[9] Reuben H. Simoyi, Alan Wolf, and Harry L. Swinney, "One-Dimensional Dynamics in a Multicomponent Chemical Reaction," *Phys. Rev. Lett.* **49**, 245 (1982).

[10] Leon Glass, Alvin Shrier, and Jacques Bélair, "Chaotic cardiac rhythms," in *Chaos*, Arun V. Holden, Ed. (Princeton University Press, Princeton, 1986).

[11] W. M. Schaffer and M. Kot, "Differential systems in ecology and epidemiology," in *Chaos*, Arun V. Holden, Ed. (Princeton University Press, Princeton, 1986).

[12] Tien-Yien Li and James A. Yorke, "Period Three Implies Chaos," *Am. Math. Monthly* **82**, 985 (1975).

[13] Boris V. Chirikov, "Time-Dependent Quantum Systems," in *Chaos and Quantum Physics: Proceedings of the Les Houches Summer School, Session LII, 1–31 August 1989*, M.-J. Giannoni, A. Voros, and J. Zinn-Justin, Eds. (North-Holland, Amsterdam, 1991).

[14] Edward Ott, *Chaos in Dynamical Systems* (Cambridge University Press, Cambridge, 1993).

[15] A. J. Lichtenberg and M. A. Lieberman, *Regular and Chaotic Dynamics*, second ed. (Springer-Verlag, New York, 1992).

[16] Robert C. Hilborn, *Chaos and Nonlinear Dynamics: An Introduction for Scientists and Engineers* (Oxford University Press, Oxford, 1994).

[17] Robert L. Devaney, *An Introduction to Chaotic Dynamical Systems*, second ed. (Addison-Wesley, Reading, 1989).

[18] George Sugihara and Robert M. May, "Nonlinear forecasting as a way of distinguishing chaos from measurement error in time series," *Nature* **344**, 734 (1990).

[19] A. A. Tsonis and J. B. Elsner, "Nonlinear prediction as a way of distinguishing chaos from random fractal sequences," *Nature* **358**, 217 (1992).

[20] Celso Grebogi, Stephen M. Hammel, James A. Yorke, and Tim Sauer, "Shadowing of Physical Trajectories in Chaotic Dynamics: Containment and Refinement," *Phys. Rev. Lett.* **65**, 1527 (1990).

[21] Tim Sauer and James A. Yorke, "Rigorous verification of trajectories for the computer simulation of dynamical systems," *Nonlinearity* **4**, 961 (1991).

[22] Tim Sauer, Celso Grebogi, and James A. Yorke, "How Long Do Numerical Chaotic Solutions Remain Valid?" *Phys. Rev. Lett.* **79**, 59 (1997).

[23] Philip J. Morrison, class notes for PHY 385K: Classical Mechanics, The University of Texas at Austin (Spring, 1996).

[24] L. Mirsky, *An Introduction to Linear Algebra* (Dover, Mineola, 1990).

[25] P. J. Morrison, "Hamiltonian description of the ideal fluid," *Rev. Mod. Phys.* **70**, 467 (1998).

[26] Grayson H. Walker and Joseph Ford, "Amplitude Instability and Ergodic Behavior for Conservative Nonlinear Oscillator Systems," *Phys. Rev.* **188**, 416 (1969).

[27] Boris V. Chirikov, "A Universal Instability of Many-Dimensional Oscillator Systems," *Phys. Rep.* **52**, 263 (1979).

[28] Alfredo M. Ozorio de Almeida, *Hamiltonian Systems: Chaos and Quantization* (Cambridge University Press, Cambridge, 1988).

[29] H.-J. Stöckmann, *Quantum Chaos: An Introduction* (Cambridge University Press, Cambridge, 1999).

[30] A. Einstein, "Zum Quantensatz von Sommerfeld und Epstein," *Verh. Deutsch. Phys. Ges.* **19**, 82 (1917).

[31] Matthias Brack and Rajat K. Bhaduri, *Semiclassical Physics* (Addison-Wesley, Reading, 1997).

[32] George M. Zaslavsky, "Stochasticity in Quantum Systems," *Phys. Rep.* **80**, 157 (1981).

[33] Bruno Eckhardt, "Quantum Mechanics of Classically Non-Integrable Systems," *Phys. Rep.* **163**, 205 (1988).

[34] G. Casati, B. V. Chirikov, F. M. Izraelev, and Joseph Ford, "Stochastic Behavior of a Quantum Pendulum under a Periodic Perturbation," in *Stochastic Behavior in Classical and Quantum Hamiltonian Systems: Proceedings of the Volta Memorial Conference, Como, 1977 (Lecture Notes in Physics Vol. 93)*, G. Casati and J. Ford, Eds. (Springer-Verlag, Berlin, 1979).

[35] D. L. Shepelyansky, "Some Statistical Properties of Simple Classically Stochastic Quantum Systems," *Physica D* **8**, 208 (1983).

[36] T. Hogg and B. A. Huberman, "Recurrence Phenomena in Quantum Dynamics," *Phys. Rev. Lett.* **48**, 711 (1982).

[37] Steven W. McDonald and Allan N. Kaufman, "Spectrum and Eigenfunctions for a Hamiltonian with Stochastic Trajectories," *Phys. Rev. Lett.* **42**, 1189 (1979).

[38] O. Bohigas, M. J. Giannoni, and C. Schmit, "Characterization of Chaotic Quantum Spectra and Universality of Level Fluctuation Laws," *Phys. Rev. Lett.* **52**, 1 (1984).

[39] D. Delande, "Quantum Chaos in Atomic Physics," in *Coherent Atomic Matter Waves: Proceedings of the Les Houches Summer School, Session LXXII, 27 July – 27 August 1999*, R. Kaiser, C. Westbrook, and F. David, Eds. (Springer-Verlag, Berlin, 2001).

[40] Shmuel Fishman, D. R. Grempel, and R. E. Prange, "Chaos, Quantum Recurrences, and Anderson Localization," *Phys. Rev. Lett.* **49**, 509 (1982).

[41] D. R. Grempel, R. E. Prange, and Shmuel Fishman, "Quantum dynamics of a nonintegrable system," *Phys. Rev. A* **29**, 1639 (1984).

[42] P. W. Anderson, "Absence of Diffusion in Certain Random Lattices," *Phys. Rev.* **109**, 1492 (1958).

[43] C. M. Marcus, A. J. Rimberg, R. M. Westervelt, P. F. Hopkins, and A. C. Gossard, "Conductance Fluctuations and Chaotic Scattering in Ballistic Microstructures," *Phys. Rev. Lett.* **69**, 506 (1992).

[44] M. V. Berry, "Quantum chaology," *Proc. R. Soc. Lond. A* **413**, 183 (1987).

[45] Michael Berry, "Some Quantum-to-Classical Asymptotics," in *Chaos and Quantum Physics: Proceedings of the Les Houches Summer School, Session LII, 1–31 August 1989*, M.-J. Giannoni, A. Voros, and J. Zinn-Justin, Eds. (North-Holland, Amsterdam, 1991).

[46] Eric J. Heller, "Bound-State Eigenfunctions of Classically Chaotic Hamiltonian Systems: Scars of Periodic Orbits," *Phys. Rev. Lett.* **53**, 1515 (1984).

[47] Asher Peres, "Instability of Quantum Motion of a Chaotic System," in *Chaos and Quantum Chaos: Proceedings of the Adriatico Research Conference on Quantum Chaos*, H. A. Cerdeira, R. Ramaswamy, M. C. Gutzwiller, and G. Casati, Eds. (World Scientific, Singapore, 1991).

[48] Fritz Haake, *Quantum Signatures of Chaos*, second ed. (Springer-Verlag, Berlin, 2001).

[49] S. A. Gardiner, J. I. Cirac, and P. Zoller, "Quantum Chaos in an Ion Trap: The Delta-Kicked Harmonic Oscillator," *Phys. Rev. Lett.* **79**, 4790 (1997).

[50] Simon Alexander Gardiner, *Quantum Measurement, Quantum Chaos, and Bose–Einstein Condensates*, Doctoral dissertation, Leopold–Franzens–Universität Innsbruck (2000).

[51] Rüdiger Schack and Carlton M. Caves, "Hypersensitivity to Perturbations in the Quantum Baker's Map," *Phys. Rev. Lett.* **71**, 525 (1993).

[52] Rüdiger Schack, Giacomo M. D'Ariano, and Carlton M. Caves, "Hypersensitivity to Perturbations in the quantum kicked top," *Phys. Rev. E* **50**, 972 (1994).

[53] B. V. Chirikov, F. M. Izrailev, and D. L. Shepelyansky, “Dynamical Stochasticity in Classical and Quantum Mechanics,” *Sov. Sci. Rev. C* **2**, 209 (1987).

[54] M. Toda and K. Ikeda, “Quantal Lyapunov Exponent,” *Phys. Lett. A* **124**, 165 (1987).

[55] Ronald F. Fox and T. C. Elston, “Chaos and the quantum-classical correspondence in the kicked pendulum,” *Phys. Rev. E* **49**, 3683 (1994).

[56] Boon Leong Lan, “Wave-packet initial motion, spreading, and energy in the periodically kicked pendulum,” *Phys. Rev. E* **50**, 764 (1994).

[57] Boris V. Chirikov, “The Problem of Quantum Chaos,” in *Quantum Chaos: Proceedings of the Eighth Chris Engelbrecht Summer School on Theoretical Physics, Blydepoort, Eastern Transvaal, South Africa, 13–24 January 1992*, W. Dieter Heiss, Ed. (Springer-Verlag, Berlin, 1992).

[58] P. I. Belobrov, G. M. Zaslavskiĭ, and G. Kh. Tartakovskiĭ, “Stochastic breaking of bound states is a system of atoms interacting with a radiation field,” *Sov. Phys. JETP* **44**, 945 (1977). Translation of *Zh. Eksp. Teor. Fiz.* **71**, 1799 (1976).

[59] P. W. Milonni, J. R. Ackerhalt, and H. W. Galbraith, “Chaos in the Semiclassical N-Atom Jaynes-Cummings Model: Failure of the Rotating-Wave Approximation,” *Phys. Rev. Lett.* **50**, 966 (1983). Also **51**, 1108(E) (1983).

[60] Ronald F. Fox, “Quantum Chaos in Two-Level Quantum Systems,” in *The Ubiquity of Chaos*, Saul Krasner, Ed. (Am. Assoc. Adv. Sci., Washington, D.C., 1990).

[61] Fred Cooper, John F. Dawson, Dawn Meredith, and Harvey Shepard, “Semiquantum Chaos,” *Phys. Rev. Lett.* **72**, 1337 (1994).

[62] B. V. Chirikov, F. M. Izrailev, and D. L. Shepelyansky, “Quantum Chaos: Localization vs. Ergodicity,” *Physica D* **33**, 77 (1988).

[63] Stefan Weigert, “Quantum chaos in the configurational quantum cat map,” *Phys. Rev. A* **48**, 1780 (1993).

[64] Asher Peres, “Chaotic evolution in quantum mechanics,” *Phys. Rev. E* **53**, 4524 (1996).

[65] R. Blümel, “Exponential Sensitivity and Chaos in Quantum Systems,” *Phys. Rev. Lett.* **73**, 428 (1994).

[66] Rüdiger Schack, "Comment on 'Exponential Sensitivity and Chaos in Quantum Systems,'" *Phys. Rev. Lett.* **75**, 581 (1995). A comment on [65].

[67] D. Bohm and B. J. Hiley, *The Undivided Universe* (Routledge, London, 1993).

[68] O. F. de Alcantara Bonfim, J. Florencio, and F. C. Sá Barreto, "Chaotic dynamics in billiards using Bohm's quantum mechanics," *Phys. Rev. E* **58**, R2693 (1998).

[69] J. E. Bayfield and P. M. Koch, "Multiphoton Ionization of Highly Excited Hydrogen Atoms," *Phys. Rev. Lett.* **33**, 258 (1974).

[70] E. J. Galvez, B. E. Sauer, L. Moorman, P. M. Koch, and D. Richards, "Microwave Ionization of H Atoms: Breakdown of Classical Dynamics for High Frequencies," *Phys. Rev. Lett.* **61**, 2011 (1988).

[71] J. E. Bayfield, G. Casati, I. Guarneri, and D. W. Sokol, "Localization of Classically Chaotic Diffusion for Hydrogen Atoms in Microwave Fields," *Phys. Rev. Lett.* **63**, 364 (1989).

[72] Peter M. Koch, "Microwave 'ionization' of excited hydrogen atoms: How non-classical local stability brought about by scarred separatrix states is affected by broadband noise and by varying the pulse envelope," *Physica D* **83**, 178 (1995).

[73] R. Blümel and W. P. Reinhardt, *Chaos in Atomic Physics* (Cambridge University Press, Cambridge, 1997).

[74] Peter M. Koch, "Experimental evidence for the influence of 'scars' in hydrogen atoms driven by strong magnetic fields," *Chaos* **2**, 131 (1992).

[75] J. E. Bayfield, S. Y. Luie, L. C. Perotti, and M. P. Skrzypkowski, "Ionization steps and phase-space metamorphoses in the pulsed microwave ionization of highly excited hydrogen atoms," *Phys. Rev. A* **53**, R12 (1996).

[76] Dominique Delande, "Chaos in Atomic and Molecular Physics," in *Chaos and Quantum Physics: Proceedings of the Les Houches Summer School, Session LII, 1–31 August 1989*, M.-J. Giannoni, A. Voros, and J. Zinn-Justin, Eds. (North-Holland, Amsterdam, 1991).

[77] U. Eichmann, K. Richter, D. Wintgen, and W. Sandner, "Scaled-Energy Spectroscopy and Its Relation with Periodic Orbits," *Phys. Rev. Lett.* **61**, 2438 (1988).

[78] J. Main, G. Wiebusch, and K. H. Welge, "Spectroscopy of the classically chaotic hydrogen atom in magnetic fields," *Comm. At. Mol. Phys.* **25**, 233 (1991).

[79] Martin C. Gutzwiller, *Chaos in Classical and Quantum Mechanics* (Springer-Verlag, New York, 1990).

[80] T. M. Fromhold, L. Eaves, F. W. Sheard, M. L. Leadbeater, T. J. Foster, and P. C. Main, "Magnetotunneling Spectroscopy of a Quantum Well in the Regime of Classical Chaos," *Phys. Rev. Lett.* **72**, 2608 (1994).

[81] P. B. Wilkinson, T. M. Fromhold, L. Eaves, F. W. Sheard, N. Miura, and T. Takamasu, "Observation of 'scarred' wavefunctions in a quantum well with chaotic electrons dynamics," *Nature* **380**, 608 (1996).

[82] D. Weiss, M. L. Roukes, A. Menschig, P. Grambow, K. von Klitzing, and G. Weimann, "Electron Pinball and Commensurate Orbits in a Periodic Array of Scatterers," *Phys. Rev. Lett.* **66**, 2790 (1991).

[83] D. Weiss, K. Richter, A. Menschig, R. Bergmann, H. Schweizer, K. von Klitzing, and G. Weimann, "Quantized Periodic Orbits in Large Antidot Arrays," *Phys. Rev. Lett.* **70**, 4118 (1993).

[84] M. F. Crommie, C. P. Lutz, D. M. Eigler, and E. J. Heller, "Quantum Corrals," *Physica D* **83**, 98 (1995).

[85] H.-J. Stöckmann and J. Stein, "'Quantum' Chaos in Billiards Studied by Microwave Absorption," *Phys. Rev. Lett.* **64**, 2215 (1990).

[86] S. Sridhar, "Experimental observation of scarred eigenfunctions of chaotic microwave cavities," *Phys. Rev. Lett.* **67**, 785 (1991).

[87] L. Sirko, Sz. Bauch, Y. Hlushchuk, P. M. Koch, R. Blümel, M. Barth, U. Kuhl, and H.-J. Stöckmann, "Observation of dynamical localization in a rough microwave cavity," *Phys. Lett. A* **266**, 331 (2000).

[88] C. Dembowski, H.-D. Gräf, A. Heine, R. Hofferbert, H. Rehfeld, and A. Richter, "First Experimental Evidence for Chaos-Assisted Tunneling in a Microwave Annular Billiard," *Phys. Rev. Lett.* **84**, 867 (2000).

[89] C. Dembowski, H.-D. Gräf, A. Heine, T. Hesse, H. Rehfeld, and A. Richter, "First Experimental Evidence of a Trace Formula for Billiard Systems Showing Mixed Dynamics," *Phys. Rev. Lett.* **86**, 3284 (2001).

[90] Claire Gmachl, Federico Capasso, E. E. Narimanov, Jens U. Nöckel, A. Douglas Stone, Jérôme Faist, Deborah L. Sivco, and Alfred Y. Cho, "High-Power Directional Emission from Microlasers with Chaotic Resonators," *Science* **280**, 1556 (1998).

[91] R. L. Weaver, "Spectral statistics in elastodynamics," *J. Acoust. Soc. Am.* **85**, 1005 (1989).

[92] C. Ellegaard, T. Guhr, K. Lindemann, H. Q. Lorensen, J. Nygård, and M. Oxborrow, "Spectral Statistics of Acoustic Resonances in Aluminum Blocks," *Phys. Rev. Lett.* **75**, 1546 (1995).

[93] T. Neicu, K. Schaadt, and A. Kudrolli, "Spectral properties of a mixed system using an acoustical resonator," *Phys. Rev. E* **63**, 026206 (2001).

[94] P. E. Lindelof, J. Nørregaard, and J. Hanberg, "New Light on the scattering mechanisms in Si inversion layers by weak localization experiments," *Phys. Scr.* **T14**, 17 (1986).

[95] R. Blümel, I. H. Davidson, W. P. Reinhardt, H. Lin, and M. Sharnoff, "Quasilinear ridge structures in water surface waves," *Phys. Rev. A* **45**, 2641 (1992).

[96] A. Kudrolli, Mathew C. Abraham, and J. P. Gollub, "Scarred patterns in surface waves," *Phys. Rev. E* **63**, 026208 (2001).

[97] P. A. Chinnery and V. F. Humphrey, "Experimental visualization of acoustic resonances within a stadium-shaped cavity," *Phys. Rev. E* **53**, 272 (1996).

[98] Baruch Fischer, Amir Rosen, Alexander Bekker, and Shmuel Fishman, "Experimental observation of localization in the spatial frequency domain of a kicked optical system," *Phys. Rev. E* **61**, R4694 (2000).

[99] Amir Rosen, Baruch Fischer, Alexander Bekker, and Shmuel Fishman, "Optical kicked system exhibiting localization in the spatial frequency domain," *J. Opt. Soc. Am. B* **17**, 1579 (2000).

[100] Andrew Steane, "Quantum computing," arXiv.org preprint quant-ph/9708022 (1997).

[101] B. Georgeot and D. L. Shepelyansky, "Emergence of Quantum Chaos in Quantum Computer Core and How to Manage It," arXiv.org preprint quant-ph/0005015 (2000).

[102] J. C. Robinson, C. F. Bharucha, K. W. Madison, F. L. Moore, Bala Sundaram, S. R. Wilkinson, and M. G. Raizen, "Can a Single-Pulse Standing Wave Induce Chaos in Atomic Motion?" *Phys. Rev. Lett.* **76**, 3304 (1996).

[103] Bala Sundaram and G. M. Zaslavsky, "Wave analysis of ray chaos in underwater acoustics," *Chaos* **9**, 483 (1999).

[104] Ilya Vorobeichik, Meir Orenstein, and Nimrod Moiseyev, "Quantum accelerator modes: A tool for atom optics," *IEEE J. Quant. Electron.* **34**, 1772 (1998).

[105] Doron Cohen, "Quantum chaos, dynamical correlations, and the effect of noise on localization," *Phys. Rev. A* **44**, 2292 (1991).

[106] G. P. Berman and G. M. Zaslavsky, "Condition of Stochasticity in Quantum Nonlinear Systems," *Physica A* **91**, 450 (1978).

[107] S. Adachi, M. Toda, and K. Ikeda, "Potential for Mixing in Quantum Chaos," *Phys. Rev. Lett.* **61**, 655 (1988).

[108] Zbyszek P. Karkuszewski, Jakub Zakrzewski, and Wojciech H. Zurek, "Breakdown of correspondence in chaotic systems: Ehrenfest versus localization times," nlin.CD/0012048 v3 (2001).

[109] Wojciech Hubert Zurek and Juan Pablo Paz, "Decoherence, Chaos, and the Second Law," *Phys. Rev. Lett.* **72**, 2508 (1994).

[110] S. Adachi, M. Toda, and K. Ikeda, "Recovery of Liouville dynamics in quantum mechanically suppressed chaotic behavior," *J. Phys. A* **22**, 3291 (1989).

[111] Wojciech Hubert Zurek and Juan Pablo Paz, "Zurek and Paz Reply," *Phys. Rev. Lett.* **75**, 351 (1995). A reply to the comment on [109] by [139].

[112] E. Joos and H. D. Zeh, "The Emergence of Classical Properties Through Interaction with the Environment," *Z. Phys. B* **59**, 223 (1985).

[113] John Archibald Wheeler and Wojciech Hubert Zurek (Eds.), *Quantum Theory and Measurement* (Princeton University Press, Princeton, 1993).

[114] D. Giulini, E. Joos, C. Kiefer, J. Kupsch, I.-O. Stamatescu, and H. D. Zeh, *Decoherence and the Appearance of a Classical World in Quantum Theory* (Wiley, New York, 1992).

[115] Claude Cohen-Tannoudji, Jacques Dupont-Roc, and Gilbert Grynberg, *Atom–Photon Interactions* (Wiley, New York, 1992).

[116] Wojciech H. Zurek, "Decoherence and the Transition from Quantum to Classical," *Physics Today* p. 36 (October 1991). See also the follow-up discussion in *Physics Today* (April 1993).

[117] W. H. Zurek, "Pointer basis of quantum apparatus: Into what mixture does the wave packet collapse?" *Phys. Rev. D* **24**, 1516 (1981).

[118] W. H. Zurek, "Environment-induced superselection rules," *Phys. Rev. D* **26**, 1862 (1982).

[119] Juan Pablo Paz, Salman Habib, and Wojciech H. Zurek, "Reduction of the wave packet: Preferred observable and decoherence time scale," *Phys. Rev. D* **47**, 488 (1993).

[120] Juan Pablo Paz and Wojciech Hubert Zurek, "Quantum Limit of Decoherence: Environment Induced Superselection of Energy Eigenstates," *Phys. Rev. Lett.* **82**, 5181 (1999).

[121] Wojciech H. Zurek, Salman Habib, and Juan Pablo Paz, "Coherent States via Decoherence," *Phys. Rev. Lett.* **70**, 1187 (1993).

[122] E. Wigner, "On the Quantum Correction For Thermodynamic Equilibrium," *Phys. Rev.* **40**, 749 (1932).

[123] Wolfgang P. Schleich, *Quantum Optics in Phase Space* (Wiley, New York, 2001).

[124] M. Hillery, R. F. O'Connell, M. O. Scully, and E. P. Wigner, "Distribution Functions in Physics: Fundamentals," *Phys. Rep.* **106**, 121 (1984).

[125] J. E. Moyal, "Quantum Mechanics as a Statistical Theory," *Proc. Cambridge Phil. Soc.* **45**, 99 (1949).

[126] K. Shiokawa and B. L. Hu, "Decoherence, delocalization, and irreversibility in quantum chaotic systems," *Phys. Rev. E* **52**, 2497 (1995).

[127] E. Schrödinger, "Der stetige Übergang von der Mikro- zur Makromechanik," *Naturwissenschaften* **14**, 664 (1926).

[128] Salman Habib, Kosuke Shizume, and Wojciech Hubert Zurek, "Decoherence, Chaos, and the Correspondence Principle," *Phys. Rev. Lett.* **80**, 4361 (1998).

[129] Salman Habib, Kurt Jacobs, Hideo Mabuchi, Robert Ryne, Kosuke Shizume, and Bala Sundaram, “The Quantum-Classical Transition in Nonlinear Dynamical Systems,” arXiv.org preprint quant-ph/0010093 (2000).

[130] Todd A. Brun, Ian C. Percival, and Rüdiger Schack, “Quantum chaos in open systems: a quantum state diffusion analysis,” *J. Phys. A* **29**, 2077 (1996).

[131] Jiangbin Gong and Paul Brumer, “Decoherence and correspondence in conservative chaotic dynamics,” *Phys. Rev. E* **60**, 1643 (1999).

[132] Tanmoy Bhattacharya, Salman Habib, and Kurt Jacobs, “Continuous Quantum Measurement and the Emergence of Classical Chaos,” *Phys. Rev. Lett.* **85**, 4852 (2000).

[133] E. Ott, T. M. Antonsen, Jr., and J. D. Hanson, “Effect of Noise on Time-Dependent Quantum Chaos,” *Phys. Rev. Lett.* **53**, 2187 (1984).

[134] Rainer Scharf and Bala Sundaram, “Role of parametric noise in nonintegrable quantum dynamics,” *Phys. Rev. E* **49**, R2509 (1994).

[135] B. S. Helmkamp and D. A. Browne, “Role of the Environment in Chaotic Quantum Dynamics,” *Phys. Rev. Lett.* **76**, 3691 (1996).

[136] Tanmoy Bhattacharya, Salman Habib, Kurt Jacobs, and Kosuke Shizume, “Strange happenings at the quantum-classical boundary: The delta-kicked rotor,” arXiv.org preprint quant-ph/0105086 (2001).

[137] T. P. Spiller and J. F. Ralph, “The emergence of chaos in an open quantum system,” *Phys. Lett. A* **194**, 235 (1994).

[138] A. J. Scott and G. J. Milburn, “Quantum nonlinear dynamics of continuously measured systems,” *Phys. Rev. A* **63**, 042101 (2001).

[139] Giulio Casati and B. V. Chirikov, “Comment on ‘Decoherence, Chaos, and the Second Law,’ ” *Phys. Rev. Lett.* **75**, 350 (1995). A comment on [109].

[140] Michael S. Chapman, Troy D. Hammond, Alan Lenef, Jörg Schmiedmayer, Richard A. Rubenstein, Edward Smith, and David E. Pritchard, “Photon Scattering from Atoms in an Atom Interferometer: Coherence Lost and Regained,” *Phys. Rev. Lett.* **75**, 3783 (1995).

[141] David A. Kokorowski, Alexander D. Cronin, Tony D. Roberts, and David E. Pritchard, "From Single- to Multiple-Photon Decoherence in an Atom Interferometer," *Phys. Rev. Lett.* **86**, 2191 (2001).

[142] M. Brune, E. Hagley, J. Dreyer, X. Maître, A. Maali, C. Wunderlich, J. M. Raimond, and S. Haroche, "Observing the Progressive Decoherence of the 'Meter' in a Quantum Measurement," *Phys. Rev. Lett.* **77**, 4887 (1996).

[143] C. J. Myatt, B. E. King, Q. A. Turchette, C. A. Sackett, D. Kielpinski, W. M. Itano, C. Monroe, and D. J. Wineland, "Decoherence of quantum superpositions through coupling to engineered reservoirs," *Nature* **403**, 269 (2000).

[144] Q. A. Turchette, C. J. Myatt, B. E. King, C. A. Sackett, D. Kielpinski, W. M. Itano, C. Monroe, and D. J. Wineland, "Decoherence and decay of motional quantum states of a trapped atom coupled to engineered reservoirs," *Phys. Rev. A* **62**, 053807 (2000).

[145] James E. Bayfield, "Near-classical noise enhancement of microwave ionization of Rydberg atoms," *Chaos* **1**, 110 (1991).

[146] L. Sirko, M. R. W. Bellermann, A. Haffmans, P. M. Koch, and D. Richards, "Probing Quantal Dynamics of Mixed Phase Space Systems with Noise," *Phys. Rev. Lett.* **71**, 2895 (1993).

[147] L. Sirko, A. Haffmans, M. R. W. Bellermann, and P. M. Koch, "Microwave 'ionization' of excited hydrogen atoms: frequency dependence in a resonance zone," *Europhys. Lett.* **33**, 181 (1996).

[148] R. Blümel, R. Graham, L. Sirko, U. Smilansky, H. Walther, and K. Yamada, "Microwave Excitation of Rydberg Atoms in the Presence of Noise," *Phys. Rev. Lett.* **62**, 341 (1989).

[149] M. Arndt, A. Buchleitner, R. N. Mantegna, and H. Walther, "Experimental Study of Quantum and Classical Limits in Microwave Ionization of Rubidium Rydberg Atoms," *Phys. Rev. Lett.* **67**, 2435 (1991).

[150] R. Blümel, A. Buchleitner, R. Graham, L. Sirko, U. Smilansky, and H. Walther, "Dynamical localization in the microwave interaction of Rydberg atoms: The influence of noise," *Phys. Rev. A* **44**, 4521 (1991).

[151] Oliver Benson, Andreas Buchleitner, Georg Raithel, Markus Arndt, Rosario N. Mantegna, and Herbert Walther, "From coherent to noise-induced microwave ionization of Rydberg atoms," *Phys. Rev. A* **51**, 4862 (1995).

[152] R. M. Clarke, I. H. Chan, C. M. Marcus, C. I. Duruöz, J. S. Harris, Jr., K. Campman, and A. C. Gossard, "Temperature dependence of phase breaking in ballistic quantum dots," *Phys. Rev. B* **52**, 2656 (1995).

[153] A. G. Huibers, M. Switkes, C. M. Marcus, K. Campman, and A. C. Gossard, "Dephasing in Open Quantum Dots," *Phys. Rev. Lett.* **81**, 200 (1998).

[154] Brian E. King, *Quantum State Engineering and Information Processing with Trapped Ions*, Ph.D. thesis, University of Colorado at Boulder (1999).

[155] Alan L. Migdall, John V. Prodan, William D. Phillips, Thomas H. Bergeman, and Harold J. Metcalf, "First Observation of Magnetically Trapped Neutral Atoms," *Phys. Rev. Lett.* **54**, 2596 (1985).

[156] Fujio Shimizu, "Specular Reflection of Very Slow Metastable Neon Atoms from a Solid Surface," *Phys. Rev. Lett.* **86**, 987 (2001).

[157] David W. Keith, Christopher R. Ekstrom, Quentin A. Turchette, and David E. Pritchard, "An interferometer for atoms," *Phys. Rev. Lett.* **66**, 2693 (1991).

[158] R. Frisch, "Experimenteller Nachweis des Einsteinischen Straklungsrückstosses," *Z. Phys.* **86**, 42 (1933).

[159] T. Hänsch and A. Schawlow, "Cooling of gases by laser radiation," *Opt. Comm.* **13**, 68 (1975).

[160] D. Wineland and H. Dehmelt, "Proposed $10^{14}\Delta\nu < \nu$ laser fluorescence spectroscopy on TI^+ mono-ion oscillator III," *Bull. Am. Phys. Soc.* **20**, 637 (1975).

[161] D. J. Wineland, R. E. Drullinger, and F. L. Walls, "Radiation-Pressure Cooling of Bound Resonant Absorbers," *Phys. Rev. Lett.* **40**, 1639 (1978).

[162] W. Neuhauser, M. Hohenstatt, P. Toschek, and H. Dehmelt, "Optical-Sideband Cooling of Visible Atom Cloud Confined in Parabolic Well," *Phys. Rev. Lett.* **41**, 233 (1978).

[163] William D. Phillips and Harold Metcalf, "Laser Deceleration of an Atomic Beam," *Phys. Rev. Lett.* **48**, 596 (1982).

[164] Steven Chu, L. Hollberg, J. E. Bjorkholm, Alex Cable, and A. Ashkin, "Three-Dimensional Viscous Confinement and Cooling of Atoms by Resonance Radiation Pressure," *Phys. Rev. Lett.* **55**, 48 (1985).

[165] Steven Chu, J. E. Bjorkholm, A. Ashkin, and A. Cable, "Experimental Observation of Optically Trapped Atoms," *Phys. Rev. Lett.* **57**, 314 (1986).

[166] Steven Chu, "The manipulation of neutral particles," *Rev. Mod. Phys.* **70**, 685 (1998).

[167] E. L. Raab, M. Prentiss, Alex Cable, Steven Chu, and D. E. Pritchard, "Trapping of Neutral Sodium Atoms with Radiation Pressure," *Phys. Rev. Lett.* **59**, 2631 (1987).

[168] C. Monroe, W. Swann, H. Robinson, and C. Wieman, "Very Cold Trapped Atoms in a Vapor Cell," *Phys. Rev. Lett.* **65**, 1571 (1990).

[169] Carl Wieman, Gwenn Flowers, and Sarah Gilbert, "Inexpensive laser cooling and trapping experiment for undergraduate laboratories," *Am. J. Phys.* **63**, 317 (1995).

[170] C. S. Adams and E. Riis, "Laser Cooling and Trapping of Neutral Atoms," *Prog. Quant. Electr.* **21**, 1 (1997).

[171] M. H. Anderson, J. R. Ensher, M. R. Matthews, C. E. Wieman, and E. A. Cornell, "Observation of Bose-Einstein condensation in a dilute atomic vapor," *Science* **269**, 198 (1995).

[172] C. C. Bradley, C. A. Sackett, J. J. Tollett, and R. G. Hulet, "Evidence of Bose-Einstein Condensation in an Atomic Gas with Attractive Interactions," *Phys. Rev. Lett.* **75**, 1687 (1995).

[173] K. B. Davis, M.-O. Mewes, M. R. Andrews, N. J. van Druten, D. S. Durfee, D. M. Kurn, and W. Ketterle, "Bose-Einstein Condensation in a Gas of Sodium Atoms," *Phys. Rev. Lett.* **75**, 3969 (1995).

[174] Mark Kasevich and Steven Chu, "Atomic Interferometry using Stimulated Raman Transitions," *Phys. Rev. Lett.* **67**, 181 (1991).

[175] J. R. Gardner, R. A. Cline, J. D. Miller, D. J. Heinzen, H. M. J. M. Boesten, and B. J. Verhaar, "Collisions of Doubly Spin-Polarized, Ultracold ^{85}Rb Atoms," *Phys. Rev. Lett.* **74**, 3764 (1995).

[176] M. Bijlsma, B. J. Verhaar, and D. J. Heinzen, "Role of collisions in the search for an electron electric-dipole moment," *Phys. Rev. A* **49**, R4285 (1994).

[177] Kurt Gibble and Steven Chu, “Laser-Cooled Cs Frequency Standard and a Measurement of the Frequency Shift due to Ultracold Collisions,” *Phys. Rev. Lett.* **70**, 1771 (1993).

[178] G. Timp, R. E. Behringer, D. M. Tennant, J. E. Cunningham, M. Prentiss, and K. K. Berggren, “Using light as a lens for submicron, neutral-atom lithography,” *Phys. Rev. Lett.* **69**, 1636 (1992).

[179] J. J. McClelland, R. E. Scholten, E. C. Palm, and R. J. Celotta, “Laser Focused Atomic Deposition,” *Science* **262**, 877 (1993).

[180] Claude N. Cohen-Tannoudji, “Manipulating atoms with photons,” *Rev. Mod. Phys.* **70**, 707 (1998).

[181] P. S. Jessen and I. H. Deutsch, “Optical Lattices,” *Adv. At. Mol. Opt. Phys.* **37**, 95 (1996).

[182] Qian Niu, Xian-Geng Zhao, G. A. Georgakis, and M. G. Raizen, “Atomic Landau-Zener Tunneling and Wannier-Stark Ladders in Optical Potentials,” *Phys. Rev. Lett.* **76**, 4504 (1996).

[183] K. W. Madison, M. C. Fischer, R. B. Diener, Qian Niu, and M. G. Raizen, “Dynamical Bloch band suppression in an optical lattice,” *Phys. Rev. Lett.* **81**, 5093 (1998).

[184] Martin Christian Fischer, *Atomic Motion in Optical Potentials*, Ph.D. dissertation, The University of Texas at Austin (2001).

[185] S. R. Wilkinson, C. F. Bharucha, K. W. Madison, Qian Niu, and M. G. Raizen, “Observation of Atomic Wannier-Stark Ladders in an Accelerating Optical Potential,” *Phys. Rev. Lett.* **76**, 4512 (1996).

[186] Maxime Ben Dahan, Ekkehard Peik, Jakob Reichel, Yvan Castin, and Christophe Salomon, “Bloch Oscillations of Atoms in an Optical Potential,” *Phys. Rev. Lett.* **76**, 4508 (1996).

[187] M. C. Fischer, K. W. Madison, Qian Niu, and M. G. Raizen, “Observation of Rabi oscillations between Bloch bands in an optical potential,” *Phys. Rev. A* **58**, R2648 (1998).

[188] Kirk William Madison, *Quantum Transport in Optical Lattices*, Ph.D. dissertation, The University of Texas at Austin (1998).

[189] K. W. Madison, M. C. Fischer, and M. G. Raizen, "Observation of the Wannier-Stark fan and the fractional ladder in an accelerating optical lattice," *Phys. Rev. A* **60**, R1767 (1999).

[190] Patrick Russel Morrow, *Quantum Tunneling of Atoms in an Optical Potential*, Ph.D. dissertation, The University of Texas at Austin (1996).

[191] C. F. Bharucha, K. W. Madison, P. R. Morrow, S. R. Wilkinson, Bala Sundaram, and M. G. Raizen, "Observation of atomic tunneling from an accelerating optical potential," *Phys. Rev. A* **55**, R857 (1997).

[192] K. W. Madison, C. F. Bharucha, P. R. Morrow, S. R. Wilkinson, Q. Niu, Bala Sundaram, and M. G. Raizen, "Quantum Transport of Ultra-Cold Atoms in an Accelerating Optical Potential," *Appl. Phys. B* **65**, 693 (1997).

[193] S. R. Wilkinson, C. F. Bharucha, M. C. Fischer, K. W. Madison, P. R. Morrow, Qian Niu, Bala Sundaram, and M. G. Raizen, "Experimental evidence for non-exponential decay in quantum tunnelling," *Nature* **387**, 575 (1997).

[194] M. C. Fischer, B. Gutiérrez-Medina, and M. G. Raizen, "Observation of the Quantum Zeno and Anti-Zeno Effects in an Unstable System," *Phys. Rev. Lett.* **87**, 040402 (2001).

[195] R. Graham, M. Schlautmann, and P. Zoller, "Dynamical localization of atomic-beam deflection by a modulated standing light wave," *Phys. Rev. A* **45**, R19 (1992).

[196] John Charles Robinson, *Atom Optics: A New Testing Ground for Quantum Chaos*, Ph.D. dissertation, The University of Texas at Austin (1995).

[197] Cyrus Farrokh Bharucha, *Experiments in Dynamical Localization of Ultra-Cold Sodium Atoms Using Time-Dependent Optical Potentials*, Ph.D. dissertation, The University of Texas at Austin (1997).

[198] F. L. Moore, J. C. Robinson, C. Bharucha, P. E. Williams, and M. G. Raizen, "Observation of Dynamical Localization in Atomic Momentum Transfer: A New Testing Ground for Quantum Chaos," *Phys. Rev. Lett.* **73**, 2974 (1994).

[199] J. C. Robinson, C. Bharucha, F. L. Moore, R. Jahnke, G. A. Georgakis, Q. Niu, M. G. Raizen, and Bala Sundaram, "Study of Quantum Dynamics in the Transition from Classical Stability to Chaos," *Phys. Rev. Lett.* **74**, 3963 (1995).

[200] F. L. Moore, J. C. Robinson, C. F. Bharucha, Bala Sundaram, and M. G. Raizen, "Atom Optics Realization of the Quantum δ-Kicked Rotor," *Phys. Rev. Lett.* **75**, 4598 (1995).

[201] C. F. Bharucha, J. C. Robinson, F. L. Moore, Qian Niu, Bala Sundaram, and M. G. Raizen, "Dynamical localization of ultracold sodium atoms," *Phys. Rev. E* **60**, 3881 (1999).

[202] B. G. Klappauf, W. H. Oskay, D. A. Steck, and M. G. Raizen, "Quantum Chaos with Cesium Atoms: Pushing the Boundaries," *Physica D* **131**, 78 (1999).

[203] Bruce George Klappauf, *Experimental Studies of Quantum Chaos with Trapped Cesium*, Ph.D. dissertation, The University of Texas at Austin (1998).

[204] B. G. Klappauf, W. H. Oskay, D. A. Steck, and M. G. Raizen, "Observation of Noise and Dissipation Effects on Dynamical Localization," *Phys. Rev. Lett.* **81**, 1203 (1998). Also **82**, 241(E) (1998).

[205] H. Ammann, R. Gray, I. Shvarchuck, and N. Christensen, "Quantum Delta-Kicked Rotor: Experimental Observation of Decoherence," *Phys. Rev. Lett.* **80**, 4111 (1998).

[206] Salman Habib, Hideo Mabuchi, Kozuke Shizume, and Bala Sundaram, "Comment on 'Quantum Delta-Kicked Rotor: Experimental Observation of Decoherence,'" unpublished (1998).

[207] Daniel A. Steck, Valery Milner, Windell H. Oskay, and Mark G. Raizen, "Quantitative study of amplitude noise effects on dynamical localization," *Phys. Rev. E* **62**, 3461 (2000).

[208] V. Milner, D. A. Steck, W. H. Oskay, and M. G. Raizen, "Recovery of classically chaotic behavior in a noise-driven quantum system," *Phys. Rev. E* **61**, 7223 (2000).

[209] W. H. Oskay, D. A. Steck, V. Milner, B. G. Klappauf, and M. G. Raizen, "Ballistic Peaks at Quantum Resonance," *Opt. Comm.* **179**, 137 (2000).

[210] M. K. Oberthaler, R. M. Godun, M. B. d'Arcy, G. S. Summy, and K. Burnett, "Observation of Quantum Accelerator Modes," *Phys. Rev. Lett.* **83**, 4447 (1999).

[211] R. M. Godun, M. B. d'Arcy, M. K. Oberthaler, G. S. Summy, and K. Burnett, "Quantum accelerator modes: A tool for atom optics," *Phys. Rev. A* **62**, 013411 (2000).

[212] K. Vant, G. Ball, H. Ammann, and N. Christensen, "Experimental evidence for the role of cantori as barriers in a quantum system," *Phys. Rev. E* **59**, 2846 (1999).

[213] J. Ringot, P. Szriftgiser, J. C. Garreau, and D. Delande, "Experimental Evidence of Dynamical Localization and Delocalization in a Quasiperiodic Driven System," *Phys. Rev. Lett.* **85**, 2741 (2000).

[214] Jianxin Zhong, R. B. Diener, Daniel A. Steck, Windell H. Oskay, Mark G. Raizen, E. Ward Plummer, Zhenyu Zhang, and Qian Niu, "Shape of the Quantum Diffusion Front," *Phys. Rev. Lett.* **86**, 2485 (2001).

[215] Daniel A. Steck, Windell H. Oskay, and Mark G. Raizen, "Observation of Chaos-Assisted Tunneling between Islands of Stability," *Science* **293**, 274 (2001).

[216] W. K. Hensinger, H. Häffner, A. Browaeys, N. R. Heckenberg, K. Helmerson, C. McKenzie, G. J. Milburn, W. D. Phillips, S. L. Rolston, H. Rubinsztein-Dunlop, and B. Upcroft, "Dynamical tunneling of ultracold atoms," *Nature* **412**, 52 (2001).

[217] W. K. Hensinger, A. G. Truscott, B. Upcroft, N. R. Heckenberg, and H. Rubinsztein-Dunlop, "Atoms in an amplitude-modulated standing wave – dynamics and pathways to quantum chaos," *J. Opt. B: Quant. Semiclass. Opt.* **2**, 659 (2000).

[218] Windell Haven Oskay, Ph.D. dissertation (in preparation), The University of Texas at Austin (2001).

[219] Windell H. Oskay, Daniel A. Steck, and Mark G. Raizen, in preparation (2001).

[220] J. Dalibard and C. Cohen-Tannoudji, "Dressed-atom approach to atomic motion in laser light: the dipole force revisited," *J. Opt. Soc. Am. B* **2**, 1707 (1985).

[221] Marlan O. Scully and M. Suhail Zubairy, *Quantum Optics* (Cambridge University Press, Cambridge, 1997).

[222] R. Loudon, *The Quantum Theory of Light*, 2nd ed. (Oxford University Press, 1983).

[223] Pierre Meystre, "Light-Matter Interaction," in *Atomic, Molecular, and Optical Physics Handbook*, Gordon W. F. Drake, Ed. (American Institute of Physics Press, Woodbury, 1996).

[224] Claude Cohen-Tannoudji, "Atoms in strong resonant fields," in *Les Houches, Session XXVII, 1975 — Frontiers in Laser Spectroscopy*, R. Balian, S. Haroche, and S. Liberman, Eds. (North-Holland, Amsterdam, 1977).

[225] R. Dum, P. Zoller, and H. Ritsch, "Monte Carlo simulation of the atomic master equation for spontaneous emission," *Phys. Rev. A* **45**, 4879 (1992).

[226] Stig Stenholm, "The semiclassical theory of laser cooling," *Rev. Mod. Phys.* **58**, 699 (1986).

[227] J. P. Gordon and A. Ashkin, "Motion of atoms in a radiation trap," *Phys. Rev. A* **21**, 1606 (1980).

[228] V. I. Balykin and V. S. Letokhov, *Atom Optics with Laser Light* (Harwood, Switzerland, 1995).

[229] Harold J. Metcalf and Peter van der Straten, *Laser Cooling and Trapping* (Springer, New York, 1999).

[230] B. S. Mathur, H. Tang, and W. Happer, "Light Shifts in the Alkali Atoms," *Phys. Rev.* **171**, 11 (1968).

[231] M. Arndt, M. Ben Dahan, D. Guéry-Odelin, M. W. Reynolds, and J. Dalibard, "Observation of a Zero-Energy Resonance in Cs-Cs Collisions," *Phys. Rev. Lett.* **79**, 625 (1997).

[232] Peter J. Martin, Bruce G. Oldaker, Andrew H. Miklich, and David E. Pritchard, "Bragg scattering of atoms from a standing light wave," *Phys. Rev. Lett.* **60**, 515 (1988).

[233] David M. Giltner, Roger W. McGowan, and Siu Au Lee, "Theoretical and experimental study of the Bragg scattering of atoms from a standing light wave," *Phys. Rev. A* **52**, 3966 (1995).

[234] M. Kozuma, L. Deng, E. W. Hagley, J. Wen, R. Lutwak, K. Helmerson, S. L. Rolston, and W. D. Phillips, "Coherent Splitting of Bose-Einstein Condensed Atoms with Optically Induced Bragg Diffraction," *Phys. Rev. Lett.* **82**, 871 (1999).

[235] Armand Eugéne Albert Koolen, *Dissipative Atom Optics with Cold Metastable Helium Atoms*, Doctoral thesis, Technische Universiteit Eindhoven (2000).

[236] Walter R. Leeb, "Algorithm 537: Characteristic Values of Mathieu's Differential Equation," *ACM Trans. Math. Soft.* **5**, 112 (1979).

[237] Randall B. Shirts, "Algorithm 721: MTIEU1 and MTIEU2: Two Subroutines to Compute Eigenvalues and Solutions of Mathieu's Differential Equation for Noninteger and Integer Order," *ACM Trans. Math. Soft.* **19**, 391 (1993).

[238] Randall B. Shirts, "The Computation of Eigenvalues and Solutions of Mathieu's Differential Equation for Noninteger Order," *ACM Trans. Math. Soft.* **19**, 377 (1993).

[239] K. B. MacAdam, A. Steinbach, and C. Wieman, "A narrow-band tunable diode laser system with grating feedback, and a saturated absorption spectrometer for Cs and Rb," *Am. J. Phys.* **60**, 1098 (1992).

[240] P. G. Pappas, M. M. Burns, D. D. Hinshelwood, M. S. Feld, and D. E. Murnick, "Saturation spectroscopy with laser optical pumping in atomic barium," *Phys. Rev. A* **21**, 1955 (1980).

[241] Joseph T. Verdeyen, *Laser Electronics*, third ed. (Prentice Hall, Englewood Cliffs, 1995).

[242] G. C. Bjorklund, M. D. Levenson, W. Lenth, and C. Ortiz, "Frequency Modulation (FM) Spectroscopy," *Appl. Phys. B* **32**, 145 (1983).

[243] Carl E. Wieman and Leo Hollberg, "Using diode lasers for atomic physics," *Rev. Sci. Inst.* **62**, 1 (1991).

[244] Patrick McNicholl and Harold J. Metcalf, "Synchronous cavity mode and feedback wavelength scanning in dye laser oscillators with gratings," *Appl. Opt.* **24**, 2757 (1985).

[245] Christopher Roy Monroe, *Experiments with Optically and Magnetically Trapped Cesium Atoms*, Ph.D. thesis, University of Colorado (1992).

[246] Martin Christian Fischer, *Design and Performance of a Ring Dye Laser*, Master's thesis, The University of Texas at Austin (1993).

[247] M. H. Dunn and A. I. Ferguson, "Coma Compensation in Off-Axis Laser Resonators," *Opt. Comm.* **20**, 214 (1977).

[248] T. W. Hänsch and B. Couillaud, "Laser frequency stabilization by polarization spectroscopy of a reflecting reference cavity," *Opt. Comm.* **35**, 441 (1980).

[249] John H. Moore, Christopher C. Davis, and Michael A. Coplan, *Building Scientific Apparatus*, second ed. (Perseus Books, Reading, 1991).

[250] W. Petrich, M. H. Anderson, J. R. Ensher, and E. A. Cornell, "Behavior of Atoms in a Compressed Magneto-optical Trap," *J. Opt. Soc. Am. B* **11**, 1332 (1994).

[251] C. G. Townsend, N. H. Edwards, C. J. Cooper, K. P. Zetie, C. J. Foot, A. M. Steane, P. Szriftgiser, H. Perrin, and J. Dalibard, "Phase-space density in the magneto-optical trap," *Phys. Rev. A* **52**, 1423 (1995).

[252] B. G. Klappauf, W. H. Oskay, D. A. Steck, and M. G. Raizen, "Experimental Study of Quantum Dynamics in a Regime of Classical Anomalous Diffusion," *Phys. Rev. Lett.* **81**, 4044 (1998).

[253] John M. Greene, "A method for determining a stochastic transition," *J. Math. Phys.* **20**, 1183 (1979).

[254] A. B. Rechester and R. B. White, "Calculation of Turbulent Diffusion for the Chirikov-Taylor Model," *Phys. Rev. Lett.* **44**, 1586 (1980).

[255] A. B. Rechester, M. N. Rosenbluth, and R. B. White, "Fourier-space paths applied to the calculation of diffusion for the Chirikov-Taylor model," *Phys. Rev. A* **23**, 2664 (1981).

[256] Charles F. F. Karney, "Long-Time Correlations in the Stochastic Regime," *Physica D* **8**, 585 (1983).

[257] B. V. Chirikov and D. L. Shepelyansky, "Correlation Properties of Dynamical Chaos in Hamiltonian Systems," *Physica D* **13**, 395 (1984).

[258] Ryuji Ishizaki, Takehiko Horita, Tatsuharu Kobayashi, and Hazime Mori, "Anomalous Diffusion Due to Accelerator Modes in the Standard Map," *Prog. Theor. Phys.* **85**, 1013 (1991).

[259] Joseph Klafter, Michael F. Schlesinger, and Gert Zumofen, "Beyond Brownian Motion," *Physics Today* p. 33 (February 1996).

[260] T. Geisel, A. Zacherl, and G. Radons, "Generic $1/f$ Noise in Chaotic Hamiltonian Dynamics," *Phys. Rev. Lett.* **59**, 2503 (1987).

[261] S. Benkadda, S. Kassibrakis, R. B. White, and G. M. Zaslavsky, "Self-similarity and transport in the standard map," *Phys. Rev. E* **55**, 4909 (1997).

[262] G. Zumofen and J. Klafter, "Comment on 'Self-similarity and transport in the standard map,' " *Phys. Rev. E* **59**, 3756 (1999).

[263] G. M. Zaslavsky, M. Edelman, and B. A. Niyazov, "Self-similarity, renormalization, and phase space nonuniformity of Hamiltonian chaotic dynamics," *Chaos* **7**, 159 (1997).

[264] Alexander I. Saichev and George M. Zaslavsky, "Fractional kinetic equations: solutions and applications," *Chaos* **7**, 753 (1997).

[265] George M. Zaslavsky, "Chaotic Dynamics and the Origin of Statistical Laws," *Physics Today* p. 39 (August 1999).

[266] Charles F. F. Karney, "Effect of Noise on the Standard Mapping," *Physica D* **4**, 425 (1982).

[267] V. B. Berestetskii, E. M. Lifshitz, and L. P. Pitaevskii, *Relativistic Quantum Theory* (Pergamon Press, Oxford, 1971).

[268] Shmuel Fishman, "Quantum Localisation," in *Quantum Dynamics of Simple Systems: Proceedings of the Forty Fourth Scottish Universities Summer School in Physics, Stirling, August 1994*, G. L. Oppo, S. M. Barnett, E. Riis, and M. Wilkinson, Eds. (Scottish Universities Summer School in Physics and Institute of Physics Publishing, Bristol, 1996).

[269] R. P. Feynman and A. R. Hibbs, *Quantum Mechanics and Path Integrals* (McGraw-Hill, New York, 1965).

[270] F. M. Izrailev and D. L. Shepelyanskii, "Quantum resonance for a rotor in a nonlinear periodic field," *Sov. Phys. Dokl.* **24**, 996 (1979).

[271] F. M. Izrailev and D. L. Shepelyanskii, "Quantum Resonance for a Rotator in a Nonlinear Periodic Field," *Theor. Math. Phys.* **43**, 553 (1980).

[272] M. V. Berry and E. Bodenschatz, "Caustics, multiply reconstructed by Talbot interference," *J. Mod. Opt.* **46**, 349 (1999).

[273] A. C. Doherty, K. M. D. Vant, G. H. Ball, N. Christensen, and R. Leonhardt, "Momentum distributions for the quantum δ-kicked rotor with decoherence," *J. Opt. B: Quant. Semiclass. Opt.* **2**, 605 (2000).

[274] Doron Cohen, "Non Perturbative Destruction of Localization in the Quantum Kicked Particle Problem," arXiv.org preprint chao-dyn/9909016 (1999).

[275] D. L. Shepelyanskii, "Dynamical Stochasticity in Nonlinear Quantum Systems," *Theor. Math. Phys.* **49**, 925 (1982).

[276] D. L. Shepelyansky, "Localization of Diffusive Excitation in Multi-Level Systems," *Physica D* **28**, 103 (1987).

[277] Bala Sundaram and G. M. Zaslavsky, "Anomalous transport and quantum-classical correspondence," *Phys. Rev. E* **59**, 7231 (1999).

[278] Indubala I. Satija, Bala Sundaram, and Jukka A. Ketoja, "Localization and fluctuations in quantum kicked rotors," *Phys. Rev. E* **60**, 453 (1999).

[279] R. M. Wilcox, "Exponential Operators and Parameter Differentiation in Quantum Physics," *J. Math. Phys.* **8**, 962 (1967).

[280] C. Salomon, J. Dalibard, W. D. Phillips, A. Clairon, and S. Guellati, "Laser Cooling of Cesium Atoms below 3μK," *Europhys. Lett.* **12**, 683 (1990).

[281] A. Kastberg, W. D. Phillips, S. L. Rolston, and R. J. C. Spreeuw, "Adiabatic Cooling of Cesium to 700 nK in an Optical Lattice," *Phys. Rev. Lett.* **74**, 1542 (1995).

[282] S. E. Hamann, D. L. Haycock, G. Klose, P. H. Pax, I. H. Deutsch, and P. S. Jessen, "Resolved-Sideband Raman Cooling to the Ground State of an Optical Lattice," *Phys. Rev. Lett.* **80**, 4149 (1998).

[283] Vladan Vuletić, Cheng Chin, Andrew J. Kerman, and Steven Chu, "Degenerate Raman Sideband Cooling of Trapped Cesium Atoms at Very High Atomic Densities," *Phys. Rev. Lett.* **81**, 5768 (1998).

[284] Andrew J. Kerman, Vladan Vuletić, Cheng Chin, and Steven Chu, "Beyond Optical Molasses: 3D Raman Sideband Cooling of Atomic Ceium to High Phase-Space Density," *Phys. Rev. Lett.* **84**, 439 (2000).

[285] S. Lukman Winoto, Marshall T. DePue, Nathan E. Bramall, and David S. Weiss, "Laser cooling at high density in deep far-detuned optical lattices," *Phys. Rev. A* **59**, R19 (1999).

[286] Sugiharto Lukman Winoto, *Laser Cooling of Cesium Atoms in Far-Detuned Optical Lattices*, Ph.D. dissertation, University of California, Berkeley (1999).

[287] Marshall T. DePue, Colin McCormick, S. Lukman Winoto, Steven Oliver, and David S. Weiss, "Unity Occupation of Sites in a 3D Optical Lattice," *Phys. Rev. Lett.* **82**, 2262 (1999).

[288] Steffen Wolf, Steven J. Oliver, and David S. Weiss, "Suppression of Recoil Heating by an Optical Lattice," *Phys. Rev. Lett.* **85**, 4249 (2000).

[289] D. J. Han, Marshall T. DePue, and David S. Weiss, "Loading and compressing Cs atoms in a very far-off-resonant trap," *Phys. Rev. A* **63**, 023405 (2001).

[290] G. Grynberg, B. Lounis, P. Verkerk, J.-Y. Courtois, and C. Salomon, "Quantized motion of cold cesium atoms in two- and three-dimensional optical potentials," *Phys. Rev. Lett.* **70**, 2249 (1993).

[291] J. Dalibard and C. Cohen-Tannoudji, "Laser cooling below the Doppler limit by polarization gradients: simple theoretical models," *J. Opt. Soc. Am. B* **6**, 2023 (1989).

[292] D. W. Sesko, T. G. Walker, and C. E. Wieman, "Behavior of neutral atoms in a spontaneous force trap," *J. Opt. Soc. Am. B* **8**, 946 (1991).

[293] K. Ellinger, J. Cooper, and P. Zoller, "Light-pressure force in N-atom systems," *Phys. Rev. A* **49**, 3909 (1994).

[294] Y. Castin, J. I. Cirac, and M. Lewenstein, "Reabsorption of Light by Trapped Atoms," *Phys. Rev. Lett.* **80**, 5305 (1998).

[295] Wolfgang Ketterle, Kendall B. Davis, Michael A. Joffe, Alex Martin, and David E. Pritchard, "High Densities of Cold Atoms in a *Dark* Spontaneous-Force Optical Trap," *Phys. Rev. Lett.* **70**, 2253 (1993).

[296] J. Reichel, F. Bardou, M. Ben Dahan, E. Peik, S. Rand, C. Salomon, and C. Cohen-Tannoudji, "Raman Cooling of Cesium below 3 nK: New Approach Inspired by Lévy Flight Statistics," *Phys. Rev. Lett.* **75**, 4575 (1995).

[297] Jakob Reichel, *Refroidissement Raman et vols de Lévy: atomes de césium au nanokelvin*, Thése de doctorat, École Normale Supérieure (1996).

[298] Mark Kasevich and Steven Chu, "Laser cooling below a photon recoil with three-level atoms," *Phys. Rev. Lett.* **69**, 1741 (1992).

[299] Nir Davidson, Heun Jin Lee, Mark Kasevich, and Steven Chu, "Raman Cooling of Atoms in Two and Three Dimensions," *Phys. Rev. Lett.* **72**, 3158 (1994).

[300] Mark Adams Kasevich, *Atom interferometry in an atomic fountain*, Ph.D. dissertation, Stanford University (1992).

[301] A. V. Taichenachev, A. M. Tumaikin, V. I. Yudin, and L. Hollberg, "Two-dimensional sideband Raman cooling and Zeeman-state preparation in an optical lattice," *Phys. Rev. A* **63**, 033402 (2001).

[302] J. Reichel, O. Morice, G. M. Tino, and C. Salomon, “Subrecoil Raman Cooling of Cesium Atoms,” *Europhys. Lett.* **28**, 477 (1994).

[303] Hans C. Ohanian, *Principles of Quantum Mechanics* (Prentice Hall, Englewood Cliffs, 1990).

[304] M. Hug and G. J. Milburn, “Quantum slow motion,” *Phys. Rev. A* **63**, 023413 (2001).

[305] L. D. Landau and E. M. Lifshitz, *Quantum Mechanics: Non-Relativistic Theory* (Pergamon, Oxford, 1977).

[306] Steven Tomsovic and Denis Ullmo, “Chaos-assisted tunneling,” *Phys. Rev. E* **50**, 145 (1994).

[307] S. C. Creagh, “Tunnelling in Two Dimensions,” in *Tunneling in Complex Systems*, Steven Tomsovic, Ed. (World Scientific, Singapore, 1998).

[308] M. J. Davis and E. J. Heller, “Quantum Dynamical Tunneling in Bound States,” *J. Chem. Phys.* **75**, 246 (1981).

[309] E. Doron and S. D. Frischat, “Semiclassical Description of Tunneling in Mixed Systems: Case of the Annular Billiard,” *Phys. Rev. Lett.* **75**, 3661 (1995).

[310] B. V. Chirikov and D. L. Shepelyansky, “Shnirelman Peak in Level Spacing Statistics,” *Phys. Rev. Lett.* **74**, 518 (1995).

[311] Rainer Scharf and Bala Sundaram, “Periodic orbits in quantum standard maps,” *Phys. Rev. A* **46**, 3164 (1992).

[312] S. Sridhar and E. J. Heller, “Physical and numerical experiments on the wave mechanics of classically chaotic systems,” *Phys. Rev. A* **46**, R1728 (1992).

[313] Giulio Casati, Robert Graham, Italo Guarneri, and Felix M. Izrailev, “Tunneling between localized states in classically chaotic systems,” *Phys. Lett. A* **190**, 159 (1994).

[314] John H. Frederick and Eric J. Heller, “Ring torsional dynamics and spectroscopy of benzophenone: a new twist,” *J. Chem. Phys.* **88**, 2169 (1988).

[315] Eric J. Heller, “Wavepacket Dynamics and Quantum Chaology,” in *Chaos and Quantum Physics: Proceedings of the Les Houches Summer School, Session LII, 1–31 August 1989*, M.-J. Giannoni, A. Voros, and J. Zinn-Justin, Eds. (North-Holland, Amsterdam, 1991).

[316] Karl W. Holtzclaw and David W. Pratt, "Prominent, and restricted, vibrational state mixing in the fluorescence excitation spectrum of benzophenone," *J. Chem. Phys.* **84**, 4713 (1986).

[317] P. M. Koch, L. Sirko, and R. Blümel, private communication (2001).

[318] S. Dyrting, G. J. Milburn, and C. A. Holmes, "Nonlinear quantum dynamics at a classical second-order resonance," *Phys. Rev. E* **48**, 969 (1993).

[319] W. A. Lin and L. E. Ballentine, "Quantum Tunneling and Chaos in a Driven Anharmonic Oscillator," *Phys. Rev. Lett.* **65**, 2927 (1990).

[320] Asher Peres, "Dynamical Quasidegeneracies and Quantum Tunneling," *Phys. Rev. Lett.* **67**, 158 (1991). This paper is a comment on [319]; see also the response by Lin and Ballentine, *Phys. Rev. Lett.* **67**, 159 (1991).

[321] R. Utermann, T. Dittrich, and P. Hänggi, "Tunneling and the onset of chaos in a driven bistable system," *Phys. Rev. E* **49**, 273 (1994).

[322] O. Bohigas, S. Tomsovic, and D. Ullmo, "Manifestations of Classical Phase Space Structures in Quantum Mechanics," *Phys. Rep.* **223**, 43 (1993).

[323] Roberto Roncaglia, Luca Bonci, Felix M. Izrailev, Bruce J. West, and Paolo Grigolini, "Tunneling versus Chaos in the Kicked Harper Model," *Phys. Rev. Lett.* **73**, 802 (1994).

[324] Enrique M. Zanardi, Javier Gutiérrez, and Jose M. Gomez Llorente, "Mixed dynamics and tunneling," *Phys. Rev. E* **52**, 4736 (1995).

[325] A. Mouchet, C. Miniatura, R. Kaiser, B. Grémaud, and D. Delande, "Chaos assisted tunnelling with cold atoms," *Phys. Rev. E* **64**, 016221 (2001).

[326] F. Grossman, T. Dittrich, P. Jung, and P. Hänggi, "Coherent Destruction of Tunneling," *Phys. Rev. Lett.* **67**, 516 (1991).

[327] S. D. Frischat and E. Doron, "Dynamical Tunneling in Mixed Systems," *Phys. Rev. E* **57**, 1421 (1998).

[328] Steven Tomsovic, "Tunneling and Chaos," *Physica Scripta* **T90**, 162 (2001).

[329] Jakub Zakrzewski, Dominique Delande, and Andreas Buchleitner, "Ionization via chaos assisted tunneling," *Phys. Rev. E* **57**, 1458 (1998).

[330] Jens U. Nöckel and A. Douglas Stone, "Ray and wave chaos in asymmetric resonant optical cavities," *Nature* **385**, 45 (1997).

[331] Sven Åberg, "Chaos Assisted Tunneling from Superdeformed States," *Phys. Rev. Lett.* **82**, 299 (1999).

[332] D. L. Haycock, P. M. Alsing, I. H. Deutsch J. Grondalski, and P. S. Jessen, "Mesoscopic Quantum Coherence in an Optical Lattice," *Phys. Rev. Lett.* **85**, 3365 (2000).

[333] Shohini Ghose, Paul M. Alsing, and Ivan H. Deutsch, "Atomic motion in magneto-optical double-well potentials: A new testing ground for quantum chaos," arXiv.org preprint quant-ph/0102085 (2001).

[334] Sigmund Kohler, Ralf Utermann, Peter Hänggi, and Thomas Dittrich, "Coherent and incoherent chaotic tunneling near singlet-doublet crossings," *Phys. Rev. E* **58**, 7219 (1998).

[335] Luca Bonci, Andrea Farusi, Paolo Grigolini, and Roberto Roncaglia, "Tunneling rate fluctuations induced by nonlinear resonances: A quantitative treatment based on semiclassical arguments," *Phys. Rev. E* **58**, 5689 (1998).

[336] Olivier Brodier, Peter Schlagheck, and Denis Ullmo, "Resonance-Assisted Tunneling in Near-Integrable Systems," *Phys. Rev. Lett.* **87**, 064101 (2001).

[337] Miroslaw Latka, Paolo Grigolini, and Bruce J. West, "Control of dynamical tunneling in a bichromatically driven pendulum," *Phys. Rev. E* **50**, R3299 (1994).

[338] E. J. Heller, "The Many Faces of Tunneling," *J. Phys. Chem.* **103**, 10433 (1999).

[339] L. C. Allen and J. H. Eberly, *Optical Resonance and Two-Level Atoms* (Dover, New York, 1987).

[340] Miroslaw Latka, Paolo Grigolini, and Bruce J. West, "Chaos and avoided level crossings," *Phys. Rev. E* **50**, 596 (1994).

[341] V. Averbukh, N. Moiseyev, B. Mirbach, and H. J. Korsch, "Dynamical tunneling through a chaotic region," *Z. Phys. D* **35**, 247 (1995).

[342] Clarence Zener, "Non-Adiabatic Crossing of Energy Levels," *Proc. R. Soc. London A* **137**, 696 (1932).

[343] R. Grobe and F. Haake, "Dissipative Death of Quantum Coherences in a Spin System," *Z. Phys. B* **68**, 503 (1987).

[344] B. C. Sanders and G. J. Milburn, "The effect of measurement on the quantum features of a chaotic system," *Z. Phys. B* **77**, 497 (1989).

[345] Frank Grossmann, Thomas Dittrich, Peter Jung, and Peter Hänggi, "Coherent Transport in a Periodically Driven Bistable System," *J. Stat. Phys.* **70**, 229 (1993).

[346] Wojciech Hubert Zurek, "Sub-Planck structure in phase space and its relevance for quantum decoherence," *Nature* **412**, 712 (2001).

[347] S. Dyrting and G. J. Milburn, "Quantum chaos in atom optics: using phase noise to model continuous momentum and position measurement," *Quant. Semiclass. Opt.* **8**, 541 (1996).

[348] T. W. Parks and C. S. Burrus, *Digital Filter Design* (Wiley, New York, 1987).

[349] Peter J. Mohr and Barry N. Taylor, "CODATA recommended values of the fundamental physical constants: 1998," *Rev. Mod. Phys.* **72**, 351 (2000).

[350] Michael P. Bradley, James V. Porto, Simon Rainville, James K. Thompson, and David E. Pritchard, "Penning Trap Measurements of the Masses of ^{133}Cs, ^{87,85}Rb, and ^{23}Na with Uncertainties $\leq$0.2 ppb," *Phys. Rev. Lett.* **83**, 4510 (1999).

[351] David R. Lide (Ed.), *CRC Handbook of Chemistry and Physics*, 81st ed. (CRC Press, Boca Raton, 2000).

[352] A. N. Nesmeyanov, *Vapor Pressure of the Chemical Elements* (Elsevier, Amsterdam, 1963). English edition edited by Robert Gary.

[353] K.-H. Weber and Craig J. Sansonetti, "Accurate energies of nS, nP, nD, nF, and nG levels of neutral cesium," *Phys. Rev. A* **35**, 4650 (1987).

[354] Th. Udem, J. Reichert, T. W. Hänsch, and M. Kourogi, "Absolute optical frequency measurement of the cesium D_2 line," *Phys. Rev. A* **62**, 031801 (2000).

[355] Th. Udem, J. Reichert, R. Holzwarth, and T. W. Hänsch, "Absolute Optical Frequency Measurement of the Cesium D_1 Line with a Mode-Locked Laser," *Phys. Rev. Lett.* **82**, 3568 (1999).

[356] Bengt Edlén, "The Refractive Index of Air," *Metrologia* **2**, 12 (1966).

[357] Robert J. Rafac, Carol E. Tanner, A. Eugene Livingston, and H. Gordon Berry, "Fast-beam laser lifetime measurements of the cesium $6p\ ^2P_{1/2,3/2}$ states," *Phys. Rev. A* **60**, 3648 (1999).

[358] L. Young, W. T. Hill III, S. J. Sibener, Stephen D. Price, C. E. Tanner, C. E. Wieman, and Stephen R. Leone, "Precision lifetime measurements of Cs $6p\ ^2P_{1/2}$ and $6p\ ^2P_{3/2}$ levels by single-photon counting," *Phys. Rev. A* **50**, 2174 (1994).

[359] R. J. Rafac, C. E. Tanner, A. E. Livingston, K. W. Kukla, H. G. Berry, and C. A. Kurtz, "Precision lifetime measurements of the $6p^2P_{1/2,3/2}$ states in atomic cesium," *Phys. Rev. A* **50**, R1976 (1994).

[360] C. E. Tanner, A. E. Livingston, R. J. Rafac, F. G. Serpa, K. W. Kukla, H. G. Berry, L. Young, and C. A. Kurtz, "Measurement of the $6p\ ^2P_{3/2}$ State Lifetime in Atomic Cesium," *Phys. Rev. Lett.* **69**, 2765 (1992).

[361] S. Rydberg and S. Svanberg, "Investigation of the $np\ ^2P_{3/2}$ Level Sequence in the Cs I Spectrum by Level Crossing Spectroscopy," *Physica Scripta* **5**, 209 (1972).

[362] Robert J. Rafac and Carol E. Tanner, "Measurement of the ratio of the cesium D-line transition strengths," *Phys. Rev. A* **58**, 1087 (1998).

[363] Carol E. Tanner, "Precision Measurements of Atomic Lifetimes," in *Atomic Physics 14: The Fourteenth International Conference on Atomic Physics*, D. J. Wineland, C. E. Wieman, and S. J. Smith, Eds. (AIP Press, 1995).

[364] Alan Corney, *Atomic and Laser Spectroscopy* (Oxford, 1977).

[365] E. Arimondo, M. Inguscio, and P. Violino, "Experimental determinations of the hyperfine structure in the alkali atoms," *Rev. Mod. Phys.* **49**, 31 (1977).

[366] Carol E. Tanner and Carl Wieman, "Precision measurement of the hyperfine structure of the ^{133}Cs $6P_{3/2}$ state," *Phys. Rev. A* **38**, 1616 (1988).

[367] Robert J. Rafac and Carol E. Tanner, "Measurement of the ^{1}33Cs $6p\ ^2P_{1/2}$ state hyperfine structure," *Phys. Rev. A* **56**, 1027 (1997).

[368] Hans A. Bethe and Edwin E. Salpeter, *Quantum Mechanics of One- and Two-Electron Atoms* (Springer-Verlag, Berlin, 1957).

[369] Leonti Labzowsky, Igor Goidenko, and Pekka Pyykkö, "Estimates of the bound-state QED contributions to the g-factor of valence ns electrons in alkali metal atoms," *Phys. Lett. A* **258**, 31 (1999).

[370] Hans Kleinpoppen, “Atoms,” in Ludwig Bergmann and Clemens Schaefer, *Constituents of Matter: Atoms, Molecules, Nuclei, and Particles*, Wilhelm Raith, Ed. (Walter de Gruyter, Berlin, 1997).

[371] E. B. Alexandrov, M. P. Chaika, and G. I. Khvostenko, *Interference of Atomic States* (Springer-Verlag, Berlin, 1993).

[372] G. Breit and I. I. Rabi, “Measurement of Nuclear Spin,” *Phys. Rev.* **38**, 2082 (1931).

[373] Lloyd Armstrong, Jr., *Theory of the Hyperfine Structure of Free Atoms* (Wiley-Interscience, New York, 1971).

[374] Robert W. Schmieder, Allen Lurio, and W. Happer, “Quadratic Stark Effect in the $^2P_{3/2}$ States of the Alkali Atoms,” *Phys. Rev. A* **3**, 1209 (1971).

[375] Robert W. Schmieder, “Matrix Elements of the Quadratic Stark Effect on Atoms with Hyperfine Structure,” *Am. J. Phys.* **40**, 297 (1972).

[376] Thomas M. Miller, “Atomic and Molecular Polarizabilities,” in *CRC Handbook of Chemistry and Physics*, David R. Lide, Ed., 81st ed. (CRC Press, Boca Raton, 2000).

[377] D. M. Brink and G. R. Satchler, *Angular Momentum* (Oxford, 1962).

[378] J. Sagle, R. K. Namiotka, and J. Huennekens, “Measurement and modelling of intensity dependent absorption and transit relaxation on the cesium D_1 line,” *J. Phys. B* **29**, 2629 (1996).

[379] Daniel A. Steck, “The Angular Distribution of Resonance Fluorescence from a Zeeman-Degenerate Atom: Formalism,” (1998). Unpublished, available on-line at the time of writing at `http://www.ph.utexas.edu/~quantopt`.

[380] T. A. Brian Kennedy, private communication (1994).

[381] Bo Gao, “Effects of Zeeman degeneracy on the steady-state properties of an atom interacting with a near-resonant laser field: Analytic results,” *Phys. Rev. A* **48**, 2443 (1993).

[382] Bo Gao, “Effects of Zeeman degeneracy on the steady-state properties of an atom interacting with a near-resonant laser field: Probe spectra,” *Phys. Rev. A* **49**, 3391 (1994).

[383] Bo Gao, "Effects of Zeeman degeneracy on the steady-state properties of an atom interacting with a near-resonant laser field: Resonance fluorescence," *Phys. Rev. A* **50**, 4139 (1994).

[384] D. Polder and M. F. H. Schuurmans, "Resonance fluorescence from a $j = 1/2$ to $j = 1/2$ transition," *Phys. Rev. A* **14**, 1468 (1976).

[385] J. Javanainen, "Quasi-Elastic Scattering in Fluorescence from Real Atoms," *Europhys. Lett.* **20**, 395 (1992).

[386] L. R. Hunter, D. Krause, Jr., S. Murthy, and T. W. Sung, "Precision measurement of the Stark shift of the cesium D lines," *Phys. Rev. A* **37**, 3283 (1988).

[387] Carol E. Tanner and Carl Wieman, "Precision measurement of the Stark shift in the $6S_{1/2} \rightarrow 6P_{3/2}$ cesium transition using a frequency-stabilized laser diode," *Phys. Rev. A* **38**, 162 (1988).

[388] Asher Peres, *Quantum Theory: Concepts and Methods* (Kluwer Academic Publishers, Dordrecht, 1993).

Vita

Daniel Adam Steck was born on April 20, 1973 in Dayton, Ohio to Raymond and Shitsuko Steck. He graduated from Archbishop Alter High School in Kettering, Ohio in 1991, and received the degree of Bachelor of Science in Physics and Mathematics from the University of Dayton in 1995. The following fall, he joined the research group of Mark G. Raizen in the Department of Physics at The University of Texas at Austin to perform research on quantum chaos in optical lattices, which is the subject of this dissertation.

Permanent address: 1501 Chelman Pl.
Miamisburg, Ohio 45342-3840

This dissertation was typeset with LaTeX‡ by the author.

---

‡ LaTeX is a document preparation system developed by Leslie Lamport as a special version of Donald Knuth's TeX Program.